

DARK
MATTER

ASTROPHYSICAL
ASPECTS
OF THE
PROBLEM

2
VOLUME



NATIONAL ACADEMY OF SCIENCES OF UKRAINE
INSTITUTE of RADIO ASTRONOMY
MAIN ASTRONOMICAL OBSERVATORY
TARAS SHEVCHENKO NATIONAL UNIVERSITY OF KYIV
V.N. KARAZIN KHARKIV NATIONAL UNIVERSITY

НАЦІОНАЛЬНА АКАДЕМІЯ НАУК УКРАЇНИ
РАДІОАСТРОНОМІЧНИЙ ІНСТИТУТ
ГОЛОВНА АСТРОНОМІЧНА ОБСЕРВАТОРІЯ
КИЇВСЬКИЙ НАЦІОНАЛЬНИЙ УНІВЕРСИТЕТ імені ТАРАСА ШЕВЧЕНКА
ХАРКІВСЬКИЙ НАЦІОНАЛЬНИЙ УНІВЕРСИТЕТ імені В.Н. КАРАЗІНА

Editor
V. Shulga

DARK ENERGY
AND DARK MATTER
IN THE UNIVERSE

IN THREE VOLUMES

M D DARK
ATTER:

2

VOLUME

ASTROPHYSICAL
ASPECTS
OF THE
PROBLEM

PROJECT
«UKRAINIAN SCIENTIFIC BOOK
IN A FOREIGN LANGUAGE»

KYIV
AKADEMPERIODYKA
2014

За редакцією
В. Шульги

ТЕМНА ЕНЕРГІЯ
І ТЕМНА МАТЕРІЯ
У ВСЕСВІТІ

У ТРЬОХ ТОМАХ

М **Т** **ЕМНА**
МАТЕРІЯ:

2 **ТОМ** АСТРОФІЗИЧНІ
АСПЕКТИ
ПРОБЛЕМИ

ПРОЕКТ
«УКРАЇНСЬКА НАУКОВА КНИГА
ІНОЗЕМНОЮ МОВОЮ»

КИЇВ
АКАДЕМПЕРІОДИКА
2014

UDK 524.8, 539
BBK 22.6, 22.3
D20

Reviewers:

I.L. ANDRONOV, Dr. Sci., Prof., Head of Department
of the Odesa National Maritime University

O.L. PETRUK, Dr. Sci., Leading researcher of the Pidstryhach Institute
for Applied Problems of Mechanics and Mathematics of NASU

Approved for publication by:

Scientific Council of the Institute of Radio Astronomy of NASU (June, 2013)

Scientific Council of the Main Astronomical Observatory of NASU (June, 2013)

***Publication was made possible by a State contract promoting
the production of scientific printed material***

Dark energy and dark matter in the Universe: in
D20 three volumes / Editor V. Shulga. — Vol. 2. Dark matter:
Astrophysical aspects of the problem / Shulga V.M., Zhdanov V.I.,
Alexandrov A.N., Berczik P.P., Pavlenko E.P., Pavlenko Ya.V.,
Pilyugin L.S., Tsvetkova V.S. — K.: Akadempriodyka, 2014. —
356 p.

ISBN 978-966-360-239-4

ISBN 978-966-360-253-0 (vol. 2)

This monograph is the second issue of a three volume edition under the general title “Dark Energy and Dark Matter in the Universe”. It concentrates mainly on astrophysical aspects of the dark matter and invisible mass problem including those of gravitational lensing, mass distribution, and chemical abundance in the Universe, physics of compact stars and models of the galactic evolution. The monograph is intended for science professionals, educators and graduate students, specializing in extragalactic astronomy, cosmology and general relativity.

**UDC 524.8, 539
BBK 22.6, 22.3**

**ISBN 978-966-360-239-4
ISBN 978-966-360-253-0 (vol. 2)**

© Shulga V.M., Zhdanov V.I.,
Alexandrov A.N., Berczik P.P.,
Pavlenko E.P., Pavlenko Ya.V.,
Pilyugin L.S., Tsvetkova V.S., 2014
© Akadempriodyka, design, 2014



CONTENTS

	FOREWORD OF THE EDITOR.....	7
	ACKNOWLEDGMENTS.....	9
1	Gravitational lensing as a key	
CHAPTER	to solving the dark matter problem	
	<i>Shulga V.M., Minakov A.A., Vakulik V.G.,</i>	
	<i>Smirnov G.V., Tsvetkova V.S.</i>	
	1.1. Gravitational lensing: general conception.....	11
	1.2. Spatial structure of quasars from microlensing studies	22
	1.3. Dark matter content from probability density distributi-	
	ons of microlensing amplifications.....	51
	1.4. Flux ratio anomalies as a key to detect dark matter	
	substructures.....	59
	1.5. Time delay lenses: impact on the Hubble constant and/or	
	the dark matter problem.....	67
2	Qualitative problems in gravitational microlensing	
CHAPTER	<i>Zhdanov V.I., Alexandrov A.N., Fedorova E.V., Sliusar V.M.</i>	
	2.1. Gravitational lensing: a short overview.....	85
	2.2. Approximate solutions of the lens equation in the vicinity	
	of the high amplification events.....	89
	2.3. Amplification of extended sources near the fold.....	99
	2.4. Astrometric gravitational microlensing.....	111
3	Chemical evolution of late	
CHAPTER	type galaxies of different masses	
	<i>Pilyugin L.S.</i>	
	3.1. Introduction.....	135
	3.2. The chemical abundances in nearby galaxies.....	137
	3.3. The maximum attainable value of the oxygen abundan-	
	ce in spiral galaxies.....	148

	3.4.	The redshift evolution of oxygen and nitrogen abundances in late type galaxies. Galaxy downsizing	159
	3.5.	Galaxy downsizing and the origin of the scatter in the N/H—O/H diagram	173
	3.6.	Summary	180
4	Dissipative N-body & gasodynamical model of the triaxial protogalaxy collapse		
CHAPTER	<i>Berczik P.P., Kravchuk S.G., Spurzem R., Hensler G.</i>		
	4.1.	Introduction	191
	4.2.	Dissipative N-body code for galaxy evolution	193
	4.3.	Galaxy as dynamical system with accreting cold gas halo	200
	4.4.	Gasodynamical model of the triaxial protogalaxies collapse. Isothermal and adiabatic solutions	209
	4.5.	Chemo-dynamical SPH code for evolution of star forming disk galaxies	229
	4.6.	Chemo-photometric evolution of star forming disk galaxy	247
	4.7.	Multi-phase chemo-dynamical hardware accelerated SPH code for galaxy evolution	254
	4.8.	Conclusion	282
5	Cataclysmic variables — the faint interacting close binary stars at the late stage of evolution		
CHAPTER	<i>Pavlenko E.P.</i>		
	5.1.	Introduction	294
	5.2.	Observations and results	297
6	Ultracool dwarfs in our Galaxy		
CHAPTER	<i>Pavlenko Ya.V.</i>		
	6.1.	Introduction	318
	6.2.	M-dwarfs of later spectral classes	320
	6.3.	Brown dwarfs	327
	6.4.	Low mass objects of spectral classes L-T-Y	335
	6.5.	Exoplanets	341
	6.6.	Conclusions	346
	ABOUT THE AUTHORS		354

■

FOREWORD OF THE EDITOR

At present it is no surprise that the major part of matter in the Universe is either invisible or dark. More surprising is the fact that first evidence for the existence of dark matter and dark energy (and the overall matter-energy content in the Universe) have been established by the methods of astronomy, i.e. by observing emissions from baryonic objects which are bright objects. Since the discovery of the dark Universe dominated by dark matter and dark energy, astronomical observations continue to be the main tool for studying the composition and distribution of dark matter, and the effect of dark energy on the evolution of the Universe.

The present book is the second in a three volume monograph under the general title “Dark Energy and Dark Matter of the Universe”. It concentrates mainly on astrophysical aspects of the dark matter problem. The aim of this book is to provide a self-contained description of the data which underlie our present understanding of the physical processes in the baryonic Universe containing dark matter.

The book is divided into several parts according to the content of the material. Chapters 1 and 2 summarize a significant fraction of the theoretical and observational results obtained by two research teams from Kharkov and Kyiv in Ukraine. They are dedicated to problems of gravitational lensing effects that provide a direct proof of the existence of dark matter. Chapter 3 presents material on the composition of galactic objects, focusing on the formation and evolution of galaxies. Chapter 4 contains special topics relating to the evolution of galactic and multi-galactic systems, using the techniques of hydrodynamic simulation and N-body numerical modeling, with account of certain

cosmological assumptions. Chapters 5 and 6 concern compact galactic objects that form a most numerous population of small sized stars and are an important part of the poorly observable baryonic matter. In Chapter 5 close binary stars are discussed with emphasis on the late stage of their evolution, including such compact objects as dwarf stars and neutron stars, or black holes. Studies of physical conditions and evolution processes in low-mass stars of another kind are presented in Chapter 6, also discussing the formation of spectra of ultra cold and brown dwarfs.

The list of contributors to Chapter 1 includes the names of Prof. Anatoly Minakov and Victor Vakulik, two researchers who were pioneers of strong gravitational lensing studies in Ukraine. Both of them left this world too early, passing away before this book has been completed. We will remember.

V. SHULGA

A handwritten signature in blue ink, appearing to read 'Shulga', followed by a horizontal line.



ACKNOWLEDGMENTS

We are grateful to the National Academy of Sciences of Ukraine for the financial support of the Target Scientific Research Programs “Structure and composition of the Universe, hidden mass and dark energy” (2007–2009), “Astrophysical and cosmological problems of hidden mass and dark energy of the Universe” (2010–2012) [“CosmoMicroPhysics”], within which this monograph was originated. We are thankful to academician Valerij Shulga, the editor of this monograph, for the suggestion of its writing, participation in the formation of its content, and organization of its publication. We also thank academician Yaroslav Yatskiv for his generous support of these Programs. We also appreciate helpful and highly professional assistance from the staff of the academic publisher “Akademperiodyka”.

AUTHORS

Kyiv, June, 2013

GRAVITATIONAL LENSING AS A KEY TO SOLVING THE DARK MATTER PROBLEM

*V.M. Shulga, A.A. Minakov, V.G. Vakulik,
G.V. Smirnov, V.S. Tsvetkova*

1.1. Gravitational lensing: general conception

The second part of the XX century occurred to be very successful for astronomers, astrophysicists and cosmologists. In the first 60ths, the most remote sources of radiation, — the quasars — were discovered [85]. A few years later, pulsating sources — the pulsars — were detected [38]. And finally, a decade later existence of space mirages — gravitational lenses (GL) — was confirmed [124]. Discovery of the first GL has stimulated dedicated searches for other lenses. To do this, most powerful instruments of the optical and radio wavelength ranges were being used, and even some new instruments dedicated to the search for manifestations of the gravitational lensing phenomenon have been created¹. Several international programs dedicated to the GL problems have been approved, which remain to be operational so far.

The interest to the space “mirages” is due, first of all, to a possibility of solving a set of topical astrophysical and cosmological problems inherent in this phenomenon. They are, for example, determination of the Hubble constant, as well as studies of the fine structure of the quasars’ emitting regions with the highest resolution that is as yet unachievable for ground-based and even space-based observations.

Last time, the GL phenomenon turned out to be very efficient in searching for the hidden mass in the Universe

¹ Sometimes this phenomenon is also referred to as the “gravitational focusing”.

and estimating its abundance. As it became evident about three quarters of a century ago, the observed rotation curves of galaxies can only be explained by an assumption that the visible matter is immersed into a massive extended but invisible formation, which was named a dark matter halo. A considerable attention has been paid to find out the halo constituents, and several monitoring programs that used the gravitational lensing has been carried out to clear up what fraction of the halo mass is formed by MACHOs — Massive Compact Halo Objects. The answer is that the halo predominantly consists of the non-baryonic dark matter. On the other hand, a lot of compact objects has been found by using gravitational lensing, however not in the halo, but in the Galactic disk. These objects may include brown dwarfs, white dwarfs, planets with masses $10^{-5}M_{\odot} < M < 10^{-3}M_{\odot}$, neutron stars and even low-mass black holes. A question about the relative content of these objects is presently vital for solving the problem of the Universe origin and evolution.

The essence of the gravitational lensing phenomenon is deflection of the light rays in the gravitational field of a massive object. I. Newton was the first to ask a question: can it be that bodies act upon the light at some distance to bend the light rays, and would this action be (all factors being the same) the strongest at the least distance? A history of developing the theory and observations of the GL phenomenon can be found in the books by P. Bliokh and A. Minakov [10], P. Schneider, J. Ehlers and E. Falco [107] and A. Zakharov [147].

In 1804, German astronomer J. Zoldner determined the angle of deviation of the light beam from a star in its transition near the edge of the solar disc and obtained $0''.87$ [107]. A hundred and ten years later, A. Einstein considered the effect of the light ray deflection in the gravitational field of the Sun in the framework of his general relativity theory (GRT). His first result, obtained in 1911, did not differ from that of Zoldner. In 1915, however, a new work by A. Einstein appeared, where a revised value was presented, which is twice as much as compared to the previous estimate. The first experimental confirmation of gravitational deflection of the light rays was obtained in observations of the total solar eclipse on the 29th of May, 1919.

By now a number of various manifestations of the effects of GL in the optical and radio wave length ranges at various spatial scales reaches hundreds. Three types of gravitational lensing are presently differentiated, each of which has its intrinsic potentials as concerned to solving the dark matter problem: weak lensing, microlensing and strong lensing.

The term “weak lensing” is used when a lens produces a single slightly distorted image of a particular source. Weak lensing reveals itself in observations of vast sky areas of very distant objects (quasars, galaxies) through the gravitational fields of massive foreground clusters of galaxies. In addition to small deformations of shapes of the distant source images, minor changes of

their brightness and distribution over the sky occur. In principle, peculiarities of these distortions provide a clue to restore the pattern of the gravitational potential of the cluster. To reveal the dark matter, the restored distribution of the gravitational potential can be then compared to that caused by distribution of the visible (luminous) matter.

Addressing to the weak lensing phenomenon with the aim to detect the hidden mass usually implies statistical analysis of very large sky areas obtained in the deep surveys. For example, the well known work by Jee et al. [42] reports detection of a ring-like dark matter substructure in the rich galaxy cluster Cl0024+17 at a radius of $r \approx 75''$ surrounding a soft, dense core at $r \leq 50''$. To restore distribution of the total gravitational potential of the cluster, the authors fulfilled statistical analysis of 1300 images of background objects produced by both weak and strong lensing. They interpret this ring-like substructure as the result of a line-of-sight collision of two massive clusters. Another impressive result of detecting the peculiar dark matter pattern with the use of the weak lensing is the Bullet cluster 1E0657-558 [18], which consists of two colliding clusters of galaxies.

Microlensing is divided into a “near” microlensing (called also “galactic” microlensing) and a “distant” (extragalactic) one. The galactic microlensing is meant when a star located in the Galaxy or in the Magellanic clouds changes its brightness due to gravitational focusing by a compact object of our Galaxy crossing the line of sight between the star and observer. The extragalactic microlensing is spoken about when a compact object of a lensing galaxy passes close to the line of sight resulting in essential brightness change of a particular lensed quasar image.

In 1986, B. Paczyński [83] proposed a peculiar method to investigate a population of the halo of our Galaxy, which implies observations of the gravitational lensing events of stars in the Milky Way by other stars. Since the probability of observing an individual event of such a kind is very small ($P \approx 10^{-6}$ events per year), Paczyński proposed to monitor several million stars simultaneously, for example, in the Magellanic Clouds. Analogous programs dealt with monitoring of stars near the nucleus of the Milky Way. Several dedicated programs have been launched, such as MACHO, EROS and, somewhat later, OGLE, which resulted in detecting several hundred microlensing events. The amplitudes and durations of light curves of these events contain information about masses of compact bodies and their velocities.

As was noted above, microlensing events may be produced by compact bodies not only in our Galaxy, but also in the other galaxies, which lens remote quasars. Observations of gravitationally lensed quasars show that microlensing is a phenomenon of a rather high occurrence, — almost all of them demonstrate microlensing activity that is different in different objects. Of all the known

gravitationally lensed quasars, the highest microlensing activity is observed in the quadruple lens system Q 2237 + 0305, the Einstein Cross.

Strong lensing is spoken about when either multiple, or arc-like, or ring-like images of a remote source (a quasar) are formed in gravitational focusing. It takes place when a sufficiently massive galaxy occurs to be close to the path of light rays from a distant quasar to the observer. The observer will see then, instead of one source, several distorted images of the same quasar formed by the gravitational field of the galaxy.

The phenomena of strong lensing and microlensing provide several approaches to solving the dark matter problem which are based on the long-term observations of transient events in images of gravitationally lensed quasars. We mention here some of them.

1. *The method of histograms.* Each of the images of a gravitationally lensed quasar (macroimage) may change its brightness because of possible microlensing events, which are signaling that a compact object (a star or a planet) is moving near the line of sight corresponding to a particular macroimage. The method of histograms is based on studying the magnification probability distributions for macroimages due to microlensing events. Numerical simulation shows that such distributions are sensitive to the relationship between the mass fraction in compact objects and that one in the uniformly distributed matter, or in the objects with extremely small masses.

2. *Flux ratio anomaly method.* It has been long noticed that flux ratios of the lensed quasar components are poorly reproduced by the lens models with smooth (regular) distribution of gravitational potential (the problem of flux ratio anomalies). Since 2001, the anomalies of mutual fluxes observed in many quasar lenses are thought to be caused by the presence of the dark matter substructures in lensing galaxies. Existence of these substructures is predicted by the scenario of hierarchical formation of structures in the Universe.

3. *The method of time delays* proposed in 1964 by S. Refsdal [94] to determine the Hubble constant, is based on the fact that fluctuations of the intrinsic brightness of a quasar are seen in its lensed images with the delays, which are determined — at a given system geometry — by the surface mass density distribution in a lens galaxy and by the Hubble constant value.

Below the basic results of observations and theoretical studies of the GL phenomenon will be presented, which were being carried out by a joint Kharkiv and Kiev group consisting of researches from the Institute of Radio Astronomy of the National Academy of Sciences of Ukraine, Institute of Astronomy of V.N. Karazin National University of Kharkiv and Astronomical Observatory of Taras Shevchenko National University of Kyiv. The works were supported by the target Program of the National Academy of Sciences of Ukraine “Investigation of the Universe structure and composition, hidden mass and dark energy” (“Cosmomicrophysics”).

1.1.1. Basic equations of the gravitational focusing phenomenon

In the theory of GL, a system of coordinates presented in Fig. 1.1 is usually used, which is convenient for a terrestrial observer. The OZ axis passes through the point of observations P and the mass center of a gravitating object O . In this coordinate system, a source of radiation with small angular dimensions (a “point source”) is situated in the source plane with angular coordinates \mathbf{y} .

When considering the effect of lensing produced by gravitational fields of complicated objects, such as galaxies and stellar clusters, one should take into account that their masses are contained not only in the large-scale diffusely distributed structures (e.g. dust or gas clouds, dark matter), but also in compact objects. A number of such objects inside a cluster is large enough. For example, a number of stars in a spiral galaxy similar to the Galaxy can reach $N \approx 10^{10} \div 10^{11}$. It should be also noted that in addition to stars, star-like and planet-like bodies can act as microlenses, and their number is also large enough inside a cluster or a galaxy.

As a rule, the effects of microlensing are investigated theoretically with the use of a two-dimensional model for distribution of stars in a cluster. In doing so, a uniform in the average distribution of the microlens stars is considered, with the correlation between their positions being neglected. Though such representation does not allow the “fine” effects to be predicted from the observed brightness fluctuations of microlensed images, it is justified by the following. Firstly, we use the minimal number of free parameters in this representation, and secondly, our ignorance of the actual spatial distributions of stars in the clusters makes the model refinements resulting in minor quantitative corrections to be senseless, (see, e.g. [10, 107]).

The gravitational field averaged over large interstellar volumes of matter distribution provides a global lensing effect of the cluster as a whole. Such lens was called a macrolens in literature. Compact bodies randomly distributed inside the cluster produce the lensing effect too, though of a smaller scale. The phenomenon of focusing in gravitational fields of compact “low-mass” objects was named microlensing. Though the spatial scales of microlenses are small, their effect results in significant brightness variations of macro-images of sources — quasars. An extended large-scale mass constituent in the cluster will be further referred to as a “diffuse” one, while compact masses will be named a “stellar” constituent.

The approximations of quasi-statics, geometrical optics and a thin phase screen form the basis of the theory. A validity of applying the method of the phase screen (MPS) is usually justified by the following considerations. Excepting heavily populated regions around galactic nuclei, the spatial density of

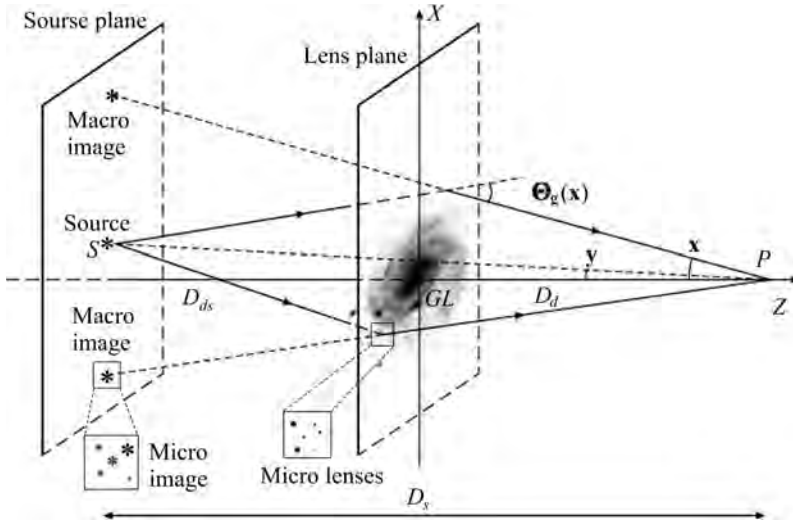


Fig. 1.1. Mutual locations of a source quasar (S), observer (P) and a lens galaxy (GL), where the microlens-stars are present

microlens stars in the galaxy is small enough. In this case, the effects of radiation re-scattering from one microlens to another can be neglected, and this allows the thin screen approximation to be used. All microlenses are assumed in the theory of microlensing as being located in one the same plane coinciding with that passing through the mass center of the macrolens normally to axis OZ , which connects the observer P and the macrolens mass center at the origin $z = 0$ (Fig. 1.1).

The geometrical-optics description of the gravitational focusing phenomenon is as follows. As a rule, a source and observer are both at large distances from a gravitating mass, and deflection of light rays occurs only within a small region around the gravitating mass. These two circumstances make it possible to substitute the actual curved rays by their “linear” asymptotes. So the light rays from the source are assumed to reach the phase screen ($z = -0$) travelling along the “straight” lines and after the phase screen ($z = +0$) the light wave acquires an additional phase shift that produces a sharp bending of the ray at an angle Θ_g that will be treated as a two-dimensional vector on the unit sphere. The rays refracted at the screen propagate again along the “straight” lines into the right semi-space ($z > 0$). According to Fig. 1.1, a vector equation can be written for a point-like element of the source surface. This equation allows to select, of the whole set of rays refracted at the screen, only those ones passing through the point of observation:

$$\mathbf{y} = \mathbf{x} + \frac{D_{ds}}{D_s} \Theta_g(\mathbf{x}), \quad (1.1)$$

where \mathbf{x} and \mathbf{y} are the angular positions of the image and the source, D_d , D_s are angular diameter distances from the observer to the lens and to the source, respectively, and D_{ds} is that from the lens to the source. Because typical angles in GLS are small, vectors $\mathbf{x} = (x_1, x_2)$ and $\mathbf{y} = (y_1, y_2)$ can be viewed as Cartesian coordinates near the origin². Equation (1.1) is the well-known lens equation, or the aberration equation³.

The angle of gravitational deflection of rays $\Theta_{\mathbf{g}}$ is determined in the MPS approximation with the use of projected surface mass density $\sigma(\mathbf{x})$ as

$$\Theta_{\mathbf{g}}(\mathbf{x}) = -\frac{4GD_d}{c^2} \int_{\Sigma_d} d^2\mathbf{x}' \frac{\mathbf{x} - \mathbf{x}'}{|\mathbf{x} - \mathbf{x}'|^2} \sigma(\mathbf{x}'), \quad (1.2)$$

where G is the gravitational constant, c is the velocity of light in the vacuum, and the integration is performed over the whole deflector area projected on the sky. It should be noted that the sign of the two-dimensional deviation angle $\Theta_{\mathbf{g}}$ in equation (1.2) is opposite to that commonly used in the literature (e.g., [107]) (though after substitution into (1.1) we get the equivalent result). To our opinion, the minus sign is more appropriate because it reflects the real physical situation. Indeed, the lensing mass attracts the light from the source (not “repulses”), and the bending angle must be counted off the optical axis, not in the reverse direction.

Equation (1.2) is often written in another form. Using the so called critical surface mass density $\sigma_{cr} = D_s c^2 / 4\pi G D_d D_{ds}$ and normalized surface mass density $\kappa = \sigma / \sigma_{cr}$ (microlensing optical depth), we obtain

$$\mathbf{y} = \mathbf{x} + \eta(\mathbf{x}), \quad (1.3)$$

where a two-dimensional vector of a “normalized” gravitational deflection is introduced

$$\eta(\mathbf{x}) = -\frac{1}{\pi} \int_{\Sigma_d} d^2\mathbf{x}' \frac{\mathbf{x} - \mathbf{x}'}{|\mathbf{x} - \mathbf{x}'|^2} \kappa(\mathbf{x}'). \quad (1.4)$$

Now let us consider focusing of radiation of a source with small angular dimensions (a “point” source), around one isolated image \mathbf{x}_0 of a point source at $\mathbf{y}_0 = \mathbf{x}_0 + \eta(\mathbf{x}_0)$. For a smooth mass distribution the function $\eta(\mathbf{x}_0)$ can be linearized around \mathbf{x}_0 . Then we choose the coordinates origins: at \mathbf{x}_0 in the

² Correspondingly, we speak about the lens plane of coordinates (x_1, x_2) and the source plane of (y_1, y_2) . Thus the left-hand side of (1.1) realizes mapping of the lens plane onto the source plane.

³ Sometimes the lens equation is written in terms of linear distances, i.e. Cartesian coordinates in the real lens and source planes as it is shown in (1). This form of the lens equation is obtained from (1.1) by rescaling $\mathbf{x} \rightarrow D_d \mathbf{x}$, $\mathbf{y} \rightarrow D_s \mathbf{y}$.

lens plane and at \mathbf{y}_0 in the source plane. The linearized lens equation is then

$$\mathbf{y} = \mathbf{Q} \mathbf{x}, \quad (1.5)$$

where \mathbf{Q} is a so-called (two-dimensional) amplification matrix with the elements

$$Q_{ij} = \delta_{ij} + \frac{\partial \eta_i}{\partial x_j}, \quad i, j = 1, 2.$$

It can be shown that (see, e.g., Schneider et al. [106])

$$\frac{\partial \eta_1}{\partial x_2} = \frac{\partial \eta_2}{\partial x_1}, \quad \frac{\partial \eta_1}{\partial x_1} + \frac{\partial \eta_2}{\partial x_2} = -2\kappa(\mathbf{x}).$$

Therefore the spur $\text{tr } \mathbf{Q} = 2(1 - \kappa)$. In a proper reference frame

$$\mathbf{Q} = \text{diag} [\lambda_-, \lambda_+] = \begin{pmatrix} 1 - \kappa - \gamma, & 0 \\ 0, & 1 - \kappa + \gamma \end{pmatrix}, \quad (1.6)$$

$\lambda_{\pm} = 1 - \kappa \pm \gamma$ being the eigenvalues of the amplification matrix, and we introduced the shear $\gamma = (\lambda_+ - \lambda_-)/2$.

It is known from the theory of nonabsorbing lenses (including GLs) that the brightness along an infinitely thin light ray does not change in focusing. Therefore, change of the source magnitude as observed through the lens is due to the change of angular dimensions. The amplification factor μ_j for the j -th image of a point source can be determined from comparison of the image area and the source area. The result can be expressed by means of the determinant of the amplification matrix [10, 107]:

$$\mu_j = \left| (1 - \kappa)^2 - \gamma^2 \right|_{\mathbf{x}=\mathbf{x}_j}^{-1}. \quad (1.7)$$

The total amplification of a gravitational lens is equal to the sum of μ_j for individual images:

$$\mu = \sum_{j=1}^N \mu_j. \quad (1.8)$$

The quantity

$$\mu(\mathbf{x}) = \left| [1 - \kappa(\mathbf{x})]^2 - \gamma^2(\mathbf{x}) \right|^{-1} \quad (1.9)$$

can be regarded as an amplification field for images of some ‘‘point’’ source. Sometimes a magnitude sign is omitted in considering $\mu(\mathbf{x})$, that is, a relationship $\mu(\mathbf{x}) = \{[1 - \kappa(\mathbf{x})]^2 - \gamma^2(\mathbf{x})\}^{-1}$ is merely considered. In doing so, images with $\mu > 0$ are called direct, and those with $\mu < 0$ are referred to as inverted ones.

The field of amplification $\mu(\mathbf{x})$ may reach infinitely large values at some points $\mathbf{x} = \mathbf{x}_{cr}$ of the lens plane which are called critical points. The locus of

points where $\mu(\mathbf{x}) \rightarrow \infty$ is called a critical curve. Substituting \mathbf{x}_{cr} into the lens equation yields the caustics in the source plane:

$$\mathbf{y}_{cs} = \mathbf{x}_{cr} + \eta(\mathbf{x}_{cr}). \quad (1.10)$$

When the point source approaches the caustic curve from the caustic “light” side ($\mathbf{y} \rightarrow \mathbf{y}_{cs}$), some of the observed images (called critical) are coming closer. When the source is projected exactly at the caustic ($\mathbf{y} = \mathbf{y}_{cs}$), the images approach each other and merge to form a single image situated exactly at the lens critical curve. The magnitude of the merging pair is growing infinitely in the process. As the source is moving further (a transit to the caustic “shadow”), the merged images are gradually disappearing.

Besides amplification of an image, there is another important characteristic of GLS: the time delay of signals coming from a source and seen in its lensed images (macroimages). S. Refsdal [94] was the first to notice that the time delays, which are different for different quasar images, can be used to derive the estimates of the Hubble constant, which is one of the most important cosmological parameters determining the age and scale of the Universe. The analysis presented for the first time in [21] has shown that for cosmological distances the formulas for propagation times of signals differ from those for the flat space-time only by a multiplier $(1 + z_d)$, which takes into account the Universe expansion during the time as the signal comes to an observer. Omitting the details of derivation (for this see, e.g., in [75, 107]), we present the final expression for the time delay difference $\Delta t(\mathbf{x}_j, \mathbf{x}_m)$ between the signals from two visible quasar images \mathbf{x}_j and \mathbf{x}_m coming to the observer [30, 107]:

$$c\Delta t(\mathbf{x}_j, \mathbf{x}_m) = (1 + z_d) D_d \int_{\mathbf{x}_m}^{\mathbf{x}_j} \left\{ \Theta_{\mathbf{g}}(\mathbf{x}') - \frac{1}{2} [\Theta_{\mathbf{g}}(\mathbf{x}_j) + \Theta_{\mathbf{g}}(\mathbf{x}_m)] \right\} d\mathbf{x}'. \quad (1.11)$$

The integration is performed in the lens plane along an arbitrary path connecting points \mathbf{x}_j and \mathbf{x}_m .

The expressions presented above form a basis not only for a geometrical-optics analysis of the GL phenomenon, but also play an important role in solving the inverse problem of recovering parameters of gravitating masses from deformations of images of remote sources as observed through the gravitational fields.

1.1.2. Recovery of gravitating objects' parameters from observations of the GL phenomenon

Before coming to specific results of investigations in the framework of the program “Cosmomicrophysics”, some peculiarities of solving the inverse problems should be mentioned, which concern recovering parameters of gravitating objects from observations of the GL phenomenon.

In studying characteristics of the GL phenomenon provided by observations, the latter can be divided into two groups: 1) observations of distorted images of remote objects, and 2) observations of gravitating masses which produce the lensing effect. The observables for images are their redshifts, shapes and angular positions, relative amplifications, as well as differential time delays. It should be noted that, because of the GL effect, observations of undistorted source images are impossible. For deflectors, the principal observables are their redshifts, velocity dispersions and positions of centroids of their brightness distributions. For nearby galaxies, however, more detailed characteristics of mass distributions can be obtained from observations (certainly, without a contribution from a “hidden” constituent).

It was as early as in 1964 that S. Refsdal proposed a simple method to independently determine the Hubble constant and the mass of a gravitating object [94]. The idea of his method can be demonstrated with the use of the aforementioned expression (1.11) for the time delays between the signals seen in different lensed images. The angular coordinates \mathbf{x}_j of compact images, redshifts of the source z_s and lens z_d , as well as the time delays $\Delta t_{jm}(\mathbf{x}_j, \mathbf{x}_m)$ are the measured quantities in (1.11). The mass distribution in the galaxy and angular diameter distances, which enter the lens equation (1.1), (1.2), are unknown quantities. Dependence of the angular diameter distance on the source redshift is determined, first of all, by the cosmological model of the Universe. In the theory of gravitational lensing produced by cosmological objects, the models by Friedman—Lemaître with Robertson—Walker metrics (FLRW) are commonly used. This model is characterized by several principal parameters. This is, first of all, the value of the Hubble constant at the present epoch, H_0 , that is often written, in view of the measure of uncertainty, in the form $H_0 = 100 \cdot h$ [km/s Mpc], where the dimensionless parameter h lies within $0.6 < h < 0.9$. In standard Λ CDM cosmological model, in addition to H_0 , we have a parameter of cold matter density, Ω_M , then Ω_Λ related with the cosmological constant Λ , and finally, the curvature parameter Ω_k associated with the current curvature radius R_k of space. It follows from the Friedmann equations that these three parameters must satisfy a condition $\Omega_M + \Omega_\Lambda + \Omega_k = 1$ for a uniform and isotropic model. According to the ideas based on the data of observations, we have the following values of parameters at the present epoch: $\Omega_M + \Omega_\Lambda \approx 1$ ($\Omega_M \approx 0.23$; $\Omega_\Lambda \approx 0.75$), that is, $\Omega_k \approx 0$, [14, 86, 112]. Equality

of parameter $\Omega_k \approx 0$ to zero means that $R_k^{-1} \approx 0$, and the three-dimensional space is Euclidean with a high degree of accuracy. For a model with $\Omega_k = 0$, the angular diameter distance between two objects with redshifts z_1 and z_2 ($z_2 \geq z_1$) is determined as follows [39]:

$$D_{1-2}(z_1, z_2) = \frac{c}{H_0} \frac{1}{1+z_2} \int_{z_1}^{z_2} \frac{dz'}{\sqrt{\Omega_M (1+z')^3 + \Omega_\Lambda}}. \quad (1.12)$$

Setting $z_1 = 0$ (observer), and $z_2 = z_d$ (deflector), one will have $D_{1-2} = D_d$ (the angular diameter distance between the observer and GL). For $z_1 = 0$ and $z_2 = z_s$ (source), we have $D_{1-2} = D_s$ for the angular diameter distance from the source to observer. And finally, if $z_1 = z_d$, and $z_2 = z_s$ then $D_{1-2} = D_{ds}$ (the angular diameter distance from the lens to source). For angular diameter distances for other cosmological FLRW models see, e.g., Kayser et al. [45].

With all the aforesaid taken into account, the initial expression can be written in the following general form:

$$H_0 = \Upsilon(z_d, z_s; \text{the Universe model}) \times \text{T}(\mathbf{x}_j, \mathbf{x}_m; \text{deflector model}) / \Delta t(\mathbf{x}_j, \mathbf{x}_m), \quad (1.13)$$

where $\Upsilon(z_d, z_s; \text{the Universe model})$ and $\text{T}(\mathbf{x}_j, \mathbf{x}_m; \text{deflector model})$ are dimensionless functions, which depend on particular values of redshifts and on the accepted model of the Universe, as well as on the observed angular coordinates of the lensed images and the assumed deflector model, respectively. If the cosmological parameters (the Universe model) and surface mass distribution in a deflector, including its hidden constituent (deflector model) were known precisely enough we would easily determine the unknown quantity H_0 having measured z_d , z_s , \mathbf{x}_j , \mathbf{x}_m and $\Delta t(\mathbf{x}_j, \mathbf{x}_m)$. For a simple GL model, e.g. central point mass model, [94], the deflector mass can also be determined from Equation (1.2). Unfortunately, an attractive idea of Refsdal had met a number of formidable difficulties in reality. Without going into details, note briefly the following.

- Mathematically, the inverse problem is an ill-posed one. The detailed analysis made by Falco et al. [30] has shown that there exists a class of mathematical transformations, which remain the data of optical observations without changes. This means that an unambiguous determination of the desired parameters from observations of only GL phenomenon is impossible. Involving additional data on interaction of matter and on gravitational fields in a broad wavelength range is necessary.

- Determining the time delay is often difficult because of a high level of various random noises. Microlensing events play a particular role in this case. They occur when star-like compact bodies intersect, in their random motions in the lens galaxy, the light rays corresponding to individual quasar images. The

microlensing events result in random variations of brightness of the observed source images.

- Serious problems occur also in the attempts to account for the hidden mass, for which the distribution in galaxies and clusters of galaxies in the wide range of spatial scales is unknown so far. Though the hidden mass has a gravitational effect on propagation of radiation from a distant source, only indirect estimates of a spatially local distribution of the invisible matter can be made from the GL phenomenon.

- In fact, we cannot even formulate the inverse problem in its strict statement. Cosmologically, we deal with the data of observations referring to a “single” point of the space, “single” direction of arriving the radiation, and “single” time moment. Estimating parameters of the Universe and sources of radiation, and determining the total mass is only possible in the framework of solving direct problems with the use of simulation. The final result is determined by the available initial data of observations and by intuition of a researcher.

Summarizing, we may conclude that the inverse problem of determining the parameters of the Universe and searching for the hidden mass with the use of the GL phenomenon is an intricate problem which needs joint efforts both from observers and theoreticians working in various fields.

1.2. Spatial structure of quasars from microlensing studies

As was noted above, images of a gravitationally lensed quasar (macroimages) may change its brightness because of possible microlensing events. The effect of microlensing is totally analogous to the phenomenon of scintillations on the medium inhomogeneities, which is well known in optics and radio physics. While the effects of scintillation in optics and radio astronomy are produced by moving irregularities of the atmosphere or space plasma, in gravitational focusing we deal with irregularities of gravitational fields produced by compact objects (microlenses). Various applications of this phenomenon are known from the theory of scintillations. In particular, valuable information about spatial scales and velocities of the medium irregularities can be obtained from the statistical analysis of the data of observations, and fine structure of the sources of radiation can be examined with a high angular resolution. Similarly, the analysis of observations of microlensing is capable of providing information about mass function of microlenses and about their velocities in galaxies. Also, a possibility emerges to estimate dimensions of quasar structure with a resolution, which is presently inaccessible for observations. The recent work by Minakov and Vakulik [75] is dedicated to application of the methods of statistical radio physics to the analysis of gravitational microlensing.

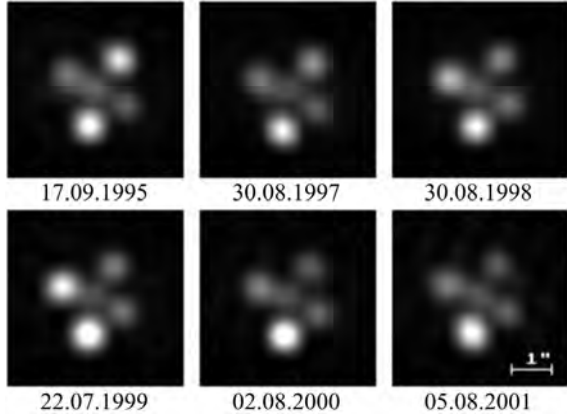


Fig. 1.2. Images of the gravitationally lensed quasar Q 2237 + 0305 (the Einstein Cross) obtained from the Maidanak Observatory at six different epochs. The magnitudes of the components caused by microlensing events are clearly seen to change in time

The following inferences from observations of the “near” and “distant” microlensing can be regarded as most important: 1) only a minor fraction of the Galaxy dark matter (about 20%) is represented by compact masses; 2) the masses responsible for the microlensing effects observed are rather small: $M \sim 10^{-1} M_{\odot}$.

As was already noted, the phenomenon of microlensing provides the unprecedented possibility to study spatial structure of remote quasars at microarcsecond angular scales. This is a vital issue for astrophysics in itself, but in addition, parameters of the quasar structure model provide important constraints to adequately interpret transient events in gravitationally lensed quasars. In particular, as will be demonstrated in section 1.3, the source quasar dimensions have an effect on amplification probability density distributions caused by microlensing, which are assumed to be diagnostic of the dark matter abundance in lensing galaxies.

The quadruply lensed quasar Q 2237 + 0305 (Fig. 1.2) is the most promising object for microlensing studies, as was noted immediately after its discovery [43, 44]. This is explained by the high optical density for microlensing and by proximity of the lensing galaxy to the observer. Large amount of observational data in the optical, IR, radio wavelengths, and in the X-rays is assembled for this object, which have become the basis to determine the effective source sizes in different spectral ranges and to infer the principal macro- and microlensing parameters. The Kharkov group made a noticeable contribution into the total database on this object, having provided it with the monitoring data in three filters. The data cover the time period from 1997 till at least 2008. In the next two sections, we show how these data can be used to investigate the spatial structure of the Q 2237 + 0305 quasar and to estimate abundance of smoothly distributed (dark) matter in the lensing galaxy.

The approaches to infer microlensing parameters from the light curves may be divided into two classes. One of them is based upon the analysis of

individual microlensing events interpreted as the source crossing of a caustic fold or cusp (e.g., [33,110,132,142]). Another approach referred hereafter as the statistical one, utilizes all the available observational data to infer the statistical parameters of interest. This approach is represented, e.g., by the structure function analysis by Lewis and Irwin [65], or the analysis of distribution of the Q 2237 light curve derivatives by Wyithe, Webster & Turner [138–140]. Recently, Kochanek [58] applied a method of statistical trials to analyse the well-sampled light curves of Q 2237 + 0305 obtained in the framework of the OGLE monitoring campaign.

Both approaches have their intrinsic weak points and advantages. In particular, in analysing an individual microlensing event, it is necessary to presume that the source actually crosses a single caustic, and that the source size is significantly smaller than the Einstein ring radius of typical microlenses. Moreover, there must be some complexity caused by the unknown vector difference between the microlens trajectory and the macrolens shear.

In applying the statistical approach, the microlensing parameters are obtained through the analysis of the light curves as a whole, where a variety of microlensing events with different circumstances may contribute simultaneously. This approach may encounter the problem of insufficiency of statistics, however, and Q 2237 + 0305 is not an exclusion, in spite of its uniqueness: according to [126] and [132], light curves of more than 100 years in duration are needed to obtain reliable statistical estimates of microlensing parameters.

It should be noted here that in analysing microlensed light curves, one deals with the well-known degeneracy between the principal parameters derived from the observed microlensing light curves, namely, between the source size, microlens mass and transverse velocity. In fact, at least one of this parameters should be fixed to determine the rest. To do this, some additional considerations are involved, which are not always applicable to an individual microlensing event. This may be an important reason to give preference to statistical methods. A significant complication inherent in both approaches is due to the fact that the actual brightness distribution over the source quasar can not be restored from the microlensed light curves, but instead, one may estimate only a characteristic size parameter describing a certain photometric model of the quasar adopted in simulations, e.g., full width on half-maximum (FWHM), or parameter σ for a Gaussian brightness profile, etc. This is a well-known consequence of difficulties associated with solving the inverse problems, noted in the previous section.

1.2.1. The problem of spatial structure of quasars

The mechanism of accretion onto the massive black hole is presently believed to provide the most efficient power supply in AGNs and quasars, and effectively all researchers use various accretion disk models when interpreting microlensing events in gravitationally lensed quasars. However, with the accretion disc being generally accepted as a central engine in quasars, the difficulties in explaining the amplitudes of the long-term microlensed light curves still remain, as well as in interpreting polarization and spectral properties of quasar radiation and their variety.

It has long been understood that introducing of some additional structural elements could resolve these discrepancies. In 1992, Jaroszyński, Wambsgans and Paczyński [41] admitted existence of an outer feature of the quasar, that reprocesses emission from the disk and may contribute up to 100% light in B or V spectral bands. A bit later, Witt & Mao [137] demonstrated in their simulations of microlensed light curves of Q 2237, that a source model consisting of a small central source surrounded by a much larger halo structure, would better explain the observed amplitudes of the Q 2237 light curves.

Various candidates for the extended structural elements have been proposed, such as, e.g., an envelope of high-velocity clouds or wind re-emitting the hard X-ray radiation from the central engine as a network of broad emission lines; gas outflows, which are believed to be launched from the central engine; an equatorial torus containing the dark clouds that re-absorb the radiation emanating in some directions (e.g., [6, 13, 29] and references therein).

There are many observational evidences for existence of these extended structures in the Q 2237 + 0305 quasar. Mid-infrared observations of Q 2237 + 0305 by Agol et al. [1] favor existence of a shell of hot dust extending between 1 pc and 3 pc from the quasar nucleus and intercepting about half of the quasar luminosity. The flux ratios of the four Q 2237 macroimages measured at 3.6 cm and 20 cm by Falco et al. [31] were also interpreted as originating in a source much larger than that radiating in the optical wavelengths. Observations in the broad emission lines (BEL) also suggest that they originate in a very large structure, much larger than that emitting the optical continuum, [66, 71, 92, 98, 111, 131]. This is consistent with determinations of spatial scales of the broad-line regions in AGNs obtained through reverberation mapping, [87]. Recently, Pooley et al. [89] found out, through a comparison of the flux ratio anomalies in the X-ray and optical bands for ten quadruply lensed quasars, that the optical emission regions of quasars are much (by factors of 10–100) larger than the basic disc models predict.

Microlensing light curves of these complicated source structures may noticeably differ from those for a simple source structure represented by an accretion disc alone. In particular, the accretion disc alone cannot reproduce in si-

mulations the observed amplitudes of the Q 2237 + 0305 light curves. While providing good fits for the peaks, which are most sensitive to the effect of the central source, it fails to provide the actual amplitudes of the rest of light curves, [41]. In this respect, the results by Yonehara [142], Shalyapin et al. [110], and Gil-Merino et al. [33], who analysed the regions of the light curves near the peaks of HME, provide successful estimates of the central source, but ignore the effect of a possible quasar outer feature. In 2003, Schild & Vakulik [104] have shown how the double-ring model of the quasar surface brightness distribution, resulting from the Elvis's [29] quasar spatial structure model, successfully explains the rapid low-amplitude brightness fluctuations in light curves of the First Lens Q0957 + 561. Interestingly, recent analysis [67] of brightness records of 55 radio-quiet quasars monitored by the MACHO project indicates the presence of large-scale outflow structures consistent with the Elvis [29] and 'dusty torus' [6] models of quasars.

A current concept of spatial structures of active galactic nuclei (AGN) and quasars implies that there is a dusty torus lying outside the accretion disc on the scale of several tenths of kiloparsec, with a broad-line emitting region (BLR) in between. According to the recent inferences of Agol et al. [2] made from their IR observations of Q 2237 + 0305, the accretion disc and the torus may contribute in the total luminosity almost equally near one micron.

Polarimetric observations (e.g. [54]) raised a question about existence of an additional electron scattering region (ESR) in quasars, [46], which has been earlier detected around some AGNs and is presently believed to be responsible for reprocessing emission from the accretion disk into polarized radiation [6, 113]. The exact geometry of the ESR, its dimensions and mutual location with respect to the BLR are still poorly constrained at present, and seem to differ in different objects. Future spectropolarimetric observations at different phases of microlensing events are expected to be diagnostic concerning this issue.

In the sections to follow, we present the results of our analysis of two most extensive monitoring data sets of Q 2237 + 0305 — those of the OGLE (Optical Gravitational Lensing Experiment) group, obtained in filter V and covering the time period from 1997 to 2008, and the data of monitoring the Einstein Cross from the Maidanak observatory in filters V , R and I during 2001–2008, but with slightly lower sampling rate. We analyse these data sets to test a two-component model of the Q 2237 quasar structure and to determine parameters of this source model. In contrast to the ring model proposed earlier, [104], we used a simplified model, consisting of a compact central source and an extended outer structure with a much smaller surface brightness. Such a model, being much easier for calculations, possesses the principal property of the ring model to produce sharp peaks of the simulated light curves, while damping the amplitudes of the entire microlensed light curves.

Thus, our basic approach is to accept existence of the inner and outer structural elements as detailed above, and to derive from parameter fitting only the size of the inner luminous feature and the fraction of the total UV-optical energy from the extended outer feature as compared to the luminosity originating in the compact central feature. We will show that the structural elements of this two-component quasar model satisfactorily explain the observed light curves amplitudes of the Q 2237 + 0305 image components and variations of their color indices caused by microlensing.

1.2.2. Testing of the two-component quasar model: application to Q 2237 + 0305

In the vicinity of a selected macroimage, the equation (1.5) describes only a smooth part of the lens equation. In order to take into account an effect of a highly inhomogeneous gravitational field due to stars (as well as other compact objects) on the line of sight one must add an ensemble of microlenses that may be assumed randomly distributed in the lens plane [43, 84]. This yields

$$\mathbf{y} = \begin{pmatrix} 1 - \kappa_c - \gamma, & 0 \\ 0, & 1 - \kappa_c + \gamma \end{pmatrix} \mathbf{x} - \sum_i m_i \frac{\mathbf{x} - \mathbf{x}_i}{|\mathbf{x} - \mathbf{x}_i|^2}, \quad (1.14)$$

$$m_i = \frac{4GM_i D_d D_{ds}}{c^2 D_s},$$

κ_c is the microlensing optical depth of a smooth background, and M_i are microlens masses.

Using equation (1.14) and the ray tracing method [107], it is possible to calculate the distribution of magnification rate $M(\mathbf{y})$ for a small (quasi-point) source for all its possible locations \mathbf{y} — the so-called magnification map. Magnification of an extended source with a surface brightness distribution $B(\mathbf{y})$ can be calculated from the formula:

$$\mu(\mathbf{y}) = \frac{\int B(\mathbf{y}') M(\mathbf{y} - \mathbf{y}') d^2 \mathbf{y}'}{\int B(\mathbf{y}') d^2 \mathbf{y}'}. \quad (1.15)$$

For moving source we have a set of consecutive shifts of $B(\mathbf{y})$ along the source trajectory which generate dependence $\mu(t)$ and the light curve $m(t) = -2.5 \lg [\mu(t)] + C$. Once calculated, the magnification map can be used to produce a large set of simulated light curves for various models of surface light distribution $B(\mathbf{y})$ over the source.

We simulated microlensing of a two-component source, with one of them the compact, central luminous source having a surface brightness distribution $B_1(\mathbf{y})$. The other, outer, structure, is associated with the larger structural elements — a shell, a torus, Elvis's biconics, [29] — and is characterized by

substantially lower surface brightness $B_2(\mathbf{y})$. For such a source the magnification μ_{12} can be written as [120]:

$$\mu_{12}(\mathbf{y}) = \frac{\mu_1(\mathbf{y}) + \varepsilon\mu_2(\mathbf{y})}{1 + \varepsilon}. \quad (1.16)$$

The magnifications μ_1 and μ_2 are calculated according to (1.15) for the surface brightness distributions B_1 and B_2 , while ε is determined as a ratio of the integral luminosities of these structures:

$$\varepsilon = \frac{\int B_2(\mathbf{y}) d^2\mathbf{y}}{\int B_1(\mathbf{y}) d^2\mathbf{y}}. \quad (1.17)$$

The characteristic time-scale of the observed Q2237 microlensing brightness fluctuations is known to be almost a year. We infer from known cosmological transverse velocities that such a scale is due to microlensing of the compact inner quasar structure. Since the predicted spatial scale of the outer structure is more than an order of magnitude larger as compared to the inner part [29, 104], the expected time scale of its microlensing brightness variations must exceed ten years. So, because of the large dimensions of the extended structure, the amplitudes of its magnification in microlensing must be noticeably less, as compared to microlensing of the compact structure. Thus we conclude, that on time-scales near 4 years, the magnification rate $\mu_2(\mathbf{y})$ is almost invariable and does not differ noticeably from the average magnification rate of the j -th image component μ_j resulting from macrolensing: $\mu_2(\mathbf{y}) \approx \langle \mu_2(\mathbf{y}) \rangle \approx \mu_j$ ($j = 1, 2, 3, 4$). Under these assumptions, equation (1.16) can be rewritten:

$$\mu_{12}(\mathbf{y}) = \frac{\mu_1(\mathbf{y}) + \varepsilon\mu_j}{1 + \varepsilon}. \quad (1.18)$$

It is clear that, under such assumptions, microlensing of the extended (outer) structure does not produce noticeable variations of magnification or brightness fluctuations on the observationally sampled time-scales, and therefore is effectively a brightness plateau above which the inner structure brightness fluctuations are seen. So the observed inner region brightness fluctuations are reduced by $1/(1 + \varepsilon)$.

Therefore, when analysing the light curves, we did not attempt to estimate the size of the extended structure, and the accepted value of ε was the only parameter which characterized the outer structure. The inner compact structure of the source was simulated by the Gaussian surface brightness distribution, and with its characteristic size expressed in units of the Einstein ring radius of a typical microlens $r_s = r/r_E$ at the one-sigma level as a fitted parameter. We used this simple central source model because it is more easy for computation. In doing so, we relied on the work by Mortonson et al. [80], who

examined the effect of the source brightness profile on the observed magnitude fluctuations in microlensing. They used a variety of accretion disc models, including Gaussian disk, and concluded that the statistics of microlensing fluctuations depends mainly on the effective radius of the source, while being relatively insensitive to a particular light distribution over the source disc.

In producing magnification maps, we accepted the values for microparameters κ_* and γ (shear) taken from Kochanek [58]: 0.392, 0.375, 0.743, and 0.635 for κ_* , and 0.395, 0.390, 0.733, 0.623 for γ , for the A, B, C and D components, respectively. For each of the four Q 2237 + 0305 components, we calculated five magnification maps with dimensions of 30×30 microlens Einstein radii, (a pixel scale of $0.02 r_E$). We assumed here that the entire mass is concentrated only in stars — that is, κ_c equals zero. To simplify computations, all the stars were accepted as having the same mass. We are well aware that this assumption is rather artificial, but in doing so, we refer to the works by Wambsganss [128] and Lewis & Irwin [64], who demonstrated, having used various mass functions, that the resulting magnification probability distributions are independent of the mass function of the compact lensing objects. For the sake of completeness, the more recent works by Schechter, Wambsganss & Lewis [101] and Lewis & Gil-Merino [63] should be mentioned, where simulations with two populations of microlenses with noticeably differing masses were carried out to show that the magnification probability distributions do depend on the mass function. It is not surprising that such an exotic case has demonstrated the effect the authors wanted to demonstrate. But it is of little relevance for our work, since the more relevant calculation of Lewis & Irwin [64] was made for more realistic mass functions — for microlenses in $0.3M_\odot$, $10.0M_\odot$ stars, and for the Salpeter mass function; these do not show appreciable dependence of the magnification probability distribution on the adopted mass function.

For our analysis, we used the Q 2237 + 0305 light curves obtained in the V filter by the OGLE group in 1997–2000. High sampling rate (2–3 datapoints weekly) and low random errors are inherent in the photometric data from this program. To compare with the simulated light curves, results of the OGLE photometry were averaged within a night, thus providing 108 data points in the light curve of each image component. For every set of the source model parameters, we estimated the probability to produce good approximations to the observed brightness curves. The values of the source model parameters providing the maximum probabilities, were accepted as the parameter estimates. To estimate consistency of the results, the analysis was carried out for each of the four image components separately.

Quasars are known to be variable objects, and their luminosity may change noticeably on time-scales of several years, months, and even days [26, 35, 91]. If a variable source is macrolensed, the intrinsic brightness variations will be observed in each lensed image with some time delays. This is just the fact

that allows the Hubble constant to be determined from measurement of the time delays. In analysing microlensing, however, variability of the source is an interfering factor, which needs to be taken into account. In the Q 2237 + 0305 system, because of an extreme proximity of the lensing galaxy, ($z_d = 0.04$), and because of almost symmetric locations of the macroimages with respect to the lens galaxy center, the expected time delays do not exceed a day, (e.g. [105, 129]). This is why the intrinsic brightness variations of the source would reveal themselves as almost synchronous variations of brightnesses of all lensed images. This was observed in 2003 [119], when the microlensing activity was substantially subdued in all the four image components.

Generally, separation of the intrinsic brightness variations of the source from the light curves containing microlensing events is a poorly defined and intricate task. In our attempts to obtain the intrinsic source light curve for Q 2237 + 0305, we introduced the following assumptions:

1. No effects of microlensing on the brightnesses of the components were observed during the time interval from January to June, 2002 (JD 2090–2250), when the magnitudes of all the components were almost unchanged. The magnitude of each component was accepted as a zero level, and its brightness variations were analysed relative to this level.

2. Relative to this zero level, we regarded that the closer these light curves were to each other, the higher the probability that the components are not microlensed within this time interval, while almost synchronous variations of their brightness are due to changes of the quasar brightness. And vice versa, the more the light curve of a component deviates from others, the larger the probability that the component undergoes microlensing, which veils and distorts the source variations.

Thus, the weighted average variations of the component brightnesses with respect to their zero levels were adopted as the estimate of the source brightness curve, with the statistical weight for variations of every component being selected depending on how close this brightness variation to variations of other components is. The quasar intrinsic brightness curve, obtained on the basis of these assumptions, as well as the OGLE light curves for the individual images, reduced to their zero levels, are shown in Fig. 1.3. We expect the largest source of error in estimating this intrinsic source brightness history to be encountered during the time interval from August 1998 to December 1999, when, possibly, all the components underwent microlensing.

To characterize similarity of the simulated and observed light curves, a χ^2 statistics for each image component was chosen:

$$\chi_j^2 = \sum_j^{N_S} \frac{[m_j(t_i) - M_j(t_i, p)]^2}{\sigma_j^2}, \quad (1.19)$$

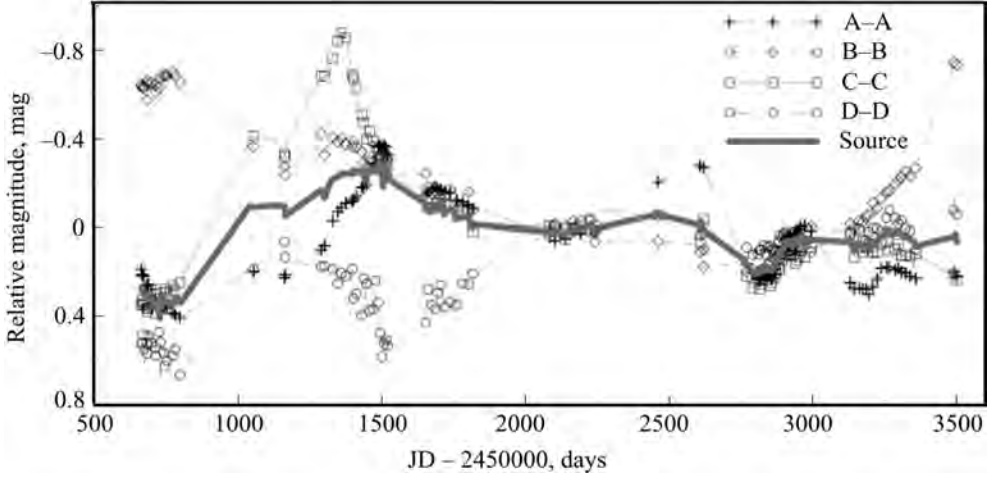


Fig. 1.3. The OGLE light curves obtained in the V filter in 1997–2005. The light curves are reduced to the same (zero) level at the time interval JD 2090–2250. The solid grey line is our estimate of brightness variations of the source quasar

where $m_j(t_i)$ is the observed light curve of the j -th component, and $M_j(t_i, p)$ is one of the simulated light curves, produced from a source trajectory at the magnification map, and N_S is a number of points in the observed light curve. The magnification map was calculated for the source model described by a set of parameters p , which could be varied. The quantity σ_j^2 characterizes the errors of the observed light curve measurements, which are 0.032^m , 0.039^m , and 0.038^m for the A, B and C components, and 0.057^m for the faintest D component.

The probability that, for a given set of parameters p , a simulated light curve will be close enough to the observed light curve, — that is, the value of χ^2 will happen to be less than some boundary value χ_0^2 , — such a probability will be:

$$P(\chi^2 < \chi_0^2) = \lim_{N \rightarrow \text{inf}} \frac{N_{\chi^2 < \chi_0^2}}{N_{\text{tot}}}, \quad (1.20)$$

where $N_{\chi^2 < \chi_0^2}$ is a number of successful trials, and N_{tot} is a total number of trials. The boundary value $\chi_0^2/N_S = 3$ was adopted for calculations.

The direction of an image motion with respect to the shear is an important parameter, which affects the probabilities noticeably. In [58], directions of motion of each component were chosen randomly and independently of directions of other components. This is not quite correct, since the directions of motion of components are not independent, and are determined by the motion of the source. Therefore, specifying the motion of one of the components must automatically specify motions of other components, if the bulk velocities and

velocity dispersion of microlenses can be neglected [130, 139]. As a result of almost perfect symmetry of Q 2237 + 0305, for any direction of the source motion, directions of the opposite components with respect to the shear direction must coincide, while motion for the two other images must be perpendicular to the shear direction. That's why, unlike the work by Kochanek [58], we analysed trajectories for two selected directions at the magnification maps, — when the A and B components are moving along the shear, with the C and D moving transversely to it, and vice versa, when A and B are moving transversely to the shear. Also, we did not undertake the local optimization of trajectories, as in [58], since this may distort the estimates of probabilities.

Thus, for each magnification map, and for each of the two selected directions, a map of distribution of the initial points of the trajectories can be calculated, for which $\chi^2 < \chi_0^2$. The probability (1.20) can then be calculated as the relative area of such regions on the map.

To reduce computing time, the map of χ^2 was calculated initially with a coarse mesh, ($\sim 0.3 r_E$), to localize the regions with low values of χ^2 . Then, more detailed calculations with a finer mesh were carried out for only these regions.

In our simulation, the following parameters could be varied: the radius of the central compact feature r_s , expressed in units of a microlens Einstein ring radius r_E ; the brightness ratio, ε , expressing the ratio of the total outer structure brightness to the total inner structure brightness; and the relative transverse velocity of the source, $V_t(r_E/\text{year})$, expressed in the units of the Einstein ring radius of a microlens per year, which is also a scaling factor for simulated light curves.

The search of probabilities for our three fitting parameters, r/r_E , ε and V_t is a rather complicated task, which needs much computing time. We attempted to simplify it in the following way. Assuming that the effect of the outer structure on the characteristic time scales of microlensing brightness variations is insignificant, we put $\varepsilon = 0$ at the first stage. Hence, a dependence of probabilities on two parameters, — the scaling factor and relative dimension of the compact feature, — was evaluated at the first stage. In Fig. 1.4, the diagrams are presented, which demonstrate distributions of probabilities to find simulated light curves, which would be close to the observed ones, — depending on the scaling factor and the compact feature dimension. The diagrams are built for all the four components for two directions of the source motion: A and B along the shear, C and D transversely — at the left, and C and D along the shear, A and B transversely — at the right. Overall, a nearly linear dependence of the scaling factor from the source dimension is seen. The largest values of probability occur for $r/r_E \approx 0.4$ in the first case, and for $r/r_E \approx 0.3$ in the second case. Since the maximum of probability distribution is, on average, at the source radius of $0.35 r_E$ and the velocity of $1.82 r_E$ per year (see Fig. 1.4),

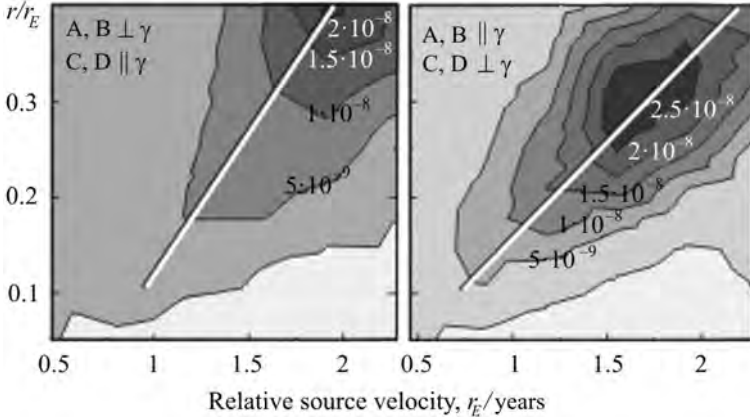


Fig. 1.4. Probability distributions to find “good” simulated light curves as functions of the scaling factor and compact source size. Directions of the source motion are indicated in the left upper corner. The probability scale is shown in levels of grey

and taking into account a nearly linear dependence between these values, we adopted the following expression for the further calculations:

$$V_t = 1.82_{-0.52}^{+1.18} \frac{r/r_E}{0.35}. \quad (1.21)$$

Here, the source velocity V_t is expressed in the units of the microlens Einstein ring radius per year.

At the second stage of our simulation, the distribution of the probabilities to find simulated light curves similar to the observed ones was estimated, depending on the source’s compact feature dimension $r_s = r/r_E$, and on the relative integral brightness of the outer feature ε . The scaling factor V_t was determined according to (1.21) for each determination of the source dimension. The diagrams constructed for two different directions of the source motion, — along the shear γ and transversely to it for each component, — are shown in Fig. 1.5. Joint probability distributions for all the four components, calculated as $P_{all} = P(A)P(B)P(C)P(D)$, are also shown in the third row in this figure.

It is very significant that the probability maxima for all the components are found for values of ε larger than zero. This means that the outer quasar structures must noticeably contribute to the total quasar brightness in the optical wavelengths. The outer structure decreases the amplitudes of microlensing brightness fluctuations and is at the core of the conundrum that in Q 2237, observed microlensing events are lower in amplitude than inferred for simple luminous accretion disc models.

Interestingly, we also see from Fig. 1.5 that the statistics and locations of probability maxima in the domain of parameters ε and r/r_E found

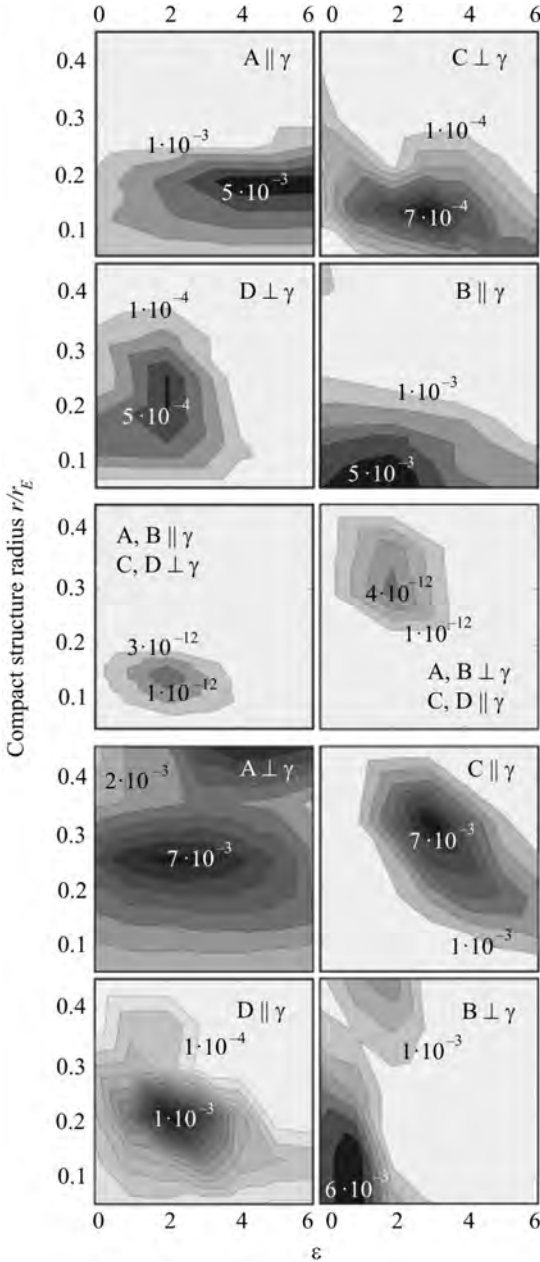


Fig. 1.5. Probability distributions to find “good” simulated light curves as functions of the compact structure dimension, r/r_E , and of the ratio ε of the integral brightnesses of the outer and inner source structures. Directions of the source motion are indicated in the right upper corner. The 3-d row shows the joint probability distributions

for each of the components separately, differ for different directions of motion of the image components with respect to the lens shear, γ . Examining four upper and four bottom panels of our Fig. 1.5, we see that the values of probabilities for the A and B components at their maxima are almost the same for the two selected directions of the source motion, while the C and D components both exhibit higher probabilities for the source to move parallel to the line connecting C and D rather than A and B. However, the joint probabilities calculated for all the four components, (the third row panels of Fig. 1.5), though giving slightly differing values of ε and r/r_E , favor neither of these two cases in terms of the maximal values of probabilities. Much larger statistics is needed to solve this important problem, which is beyond our current computational resources.

In Fig. 1.6, some of the most successful simulated light curves are shown together with the corresponding observed light curves reduced to their zero level. (The quasar light variations have been subtracted as described previously.) It should be noted that the simulated light curves reproduce the observed ones well enough within the time interval of the

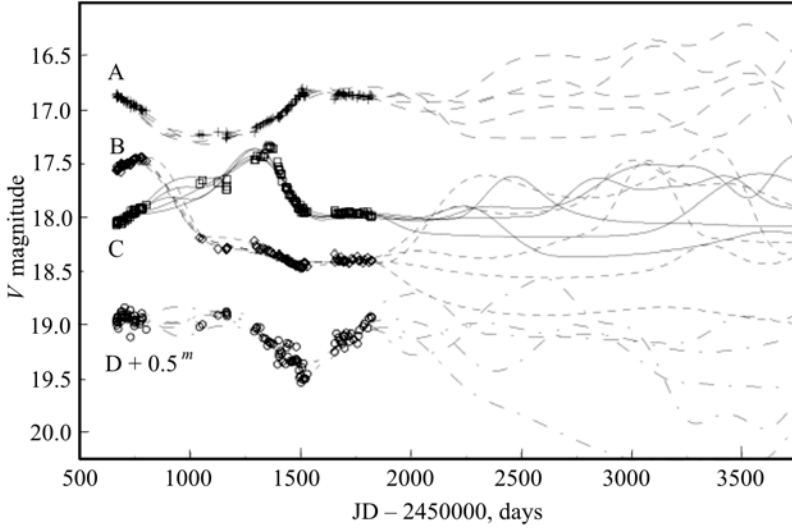


Fig. 1.6. Some of the most successful simulated light curves plotted against the observed light curves. Microlensing brightness fluctuations beyond the time interval of fitting are approximately of the amplitude and duration observed. The time scale is in the Julian dates

fitting, and no unacceptably large brightness fluctuations are observed outside this interval, unlike the results in fig. 10 of Kochanek [58].

Thus, the two-component source model consisting of a compact inner structure and much larger outer structure with lower surface brightness, allows to successfully model the brightness monitoring data and, importantly, to avoid the effect from the standard accretion disc model that large amplitudes of microlensing brightness fluctuations are predicted but not observed [41, 58].

The proposed source model consisting of two structures, — an inner compact structure and an extended outer region, — provides higher values of probability to find “good” simulated light curves as compared to the central compact source alone, and produces better fits to long-term light curves.

The calculated distributions of the joint probabilities has well-marked maxima, and their locations in the domain of parameters ε and r/r_E allow reasonable confidence in their determined values which provide the best fit of the simulated light curves to the observed ones. The range for the most probable values of the relative luminosity ε of the extended feature, determined from probability distributions of the individual macroimages, is between 1 and 3, while the estimate of the relative size of the compact central feature of the quasar varies within a range of $0.1 < r/r_E < 0.45$. When determined from distributions of the joint probabilities, the values of ε equal 2 in both cases, while r/r_E is about 0.4 for A and B motion perpendicular to γ , and 0.15 for A and B moving parallel to the shear γ .

Very significantly, the simulated light curves calculated for the proposed two-component source model with the parameters indicated above, do not tend to unacceptably increase their amplitudes outside the time interval where they were objectively selected according to the $\chi^2 < \chi_0^2$ criterion, as is seen in fig. 10 from the work by Kochanek [58].

For better comparison with other authors, we adopted, following [58], a probable projected cosmological transverse source velocity of $V_t = 3300$ km/s to determine a linear size of the compact central source of $r \approx 2 \cdot 10^{15}$ cm, ($1.2 \cdot 10^{15}$ cm $< r < 2.8 \cdot 10^{15}$ cm). This size was estimated by Kochanek to be between $r \approx 1.4 \cdot 10^{15} h^{-1}$ cm and $4.5 \cdot 10^{15} h^{-1}$ cm for the accretion disc model and for the same transverse velocity, ($h = 100/H_0$, where H_0 is the expected value of the Hubble constant). For the relative size of the source of $0.3r_E$, ($0.1r_E < r < 0.45r_E$), the estimate for the average microlens mass is $\langle m \rangle = 1.88 \cdot 10^{-3} h^2 M_\odot$, ($3.08 \cdot 10^{-4} h^2 M_\odot < \langle m \rangle < 3.3 \cdot 10^{-2} h^2 M_\odot$).

1.2.3. Two-component quasar model in interpreting chromatic microlensing

Though the gravitational lensing phenomenon is known to be achromatic, the importance of observations at several spectral bands has become understood long ago. As far back as in 1986, Kayser, Refsdal & Stabell [43] suggested that chromatic phenomena can be expected for microlensing of a source with a radial temperature gradient. This possibility was later confirmed in simulations by Wambsganss & Paczyński [127]. In 1992, Jaroszyński, Wambsganss and Paczyński [41] demonstrated in simulations that microlensing maxima tend to be “bluer” than the rest of the light curve, with the expected ($B - R$) microlensing colour changes in Q 2237 + 0305 as large as a few tenths of a magnitude.

Rix et al. [95] and Corrigan et al. [22] were the first to conclude independently that the colour indices of the Q 2237 + 0305 components seem to vary in time. Their suggestion was later confirmed independently by Vakulik et al. [122] and Burud et al. [12]. The first detailed analysis of variations of colour indices in Q 2237 + 0305 was made by Vakulik et al. [118], who presented their long-term V , R and I observations of Q 2237 + 0305 from the Maidanak Observatory with the subsequent statistical analysis. Variations of the $V - I$ colour indices turned out to be correlated with the brightness changes. A tendency of the components to become bluer towards the microlensing peaks predicted in [127] and [41], has been confirmed. Moreau et al. [78] built the ($V - R$) vs V diagrams from the data of the GLITP collaboration [3], and noted their similarity with that reported in [118].

Observations of Q 2237 + 0305 in spectral ranges other than optical continuum (IR, radio and in the quasar emission lines, see references in section 1.2.1) — all indicate that the Q 2237 quasar structures emitting in these spectral

regions are almost nonsusceptible to microlensing and thus, must be much larger than those emitting the UV and optical continuum.

Very interesting results concerning microlensing chromatic phenomena in Q 2237 + 0305 have been recently reported in [27, 28, 81, 111] and [4]. Mosquera et al. [81] detected a chromatic microlensing event in image A of Q 2237 + 0305 through a single-epoch narrow-band photometry in eight different filters covering the wavelength interval 3510–8130 Å. Considering a Gaussian brightness profile for the accretion disc (in a simple thin-disc model) they found from simulations that the effective disc size varies in wavelength according to the $R_\lambda \propto \lambda^{4/3}$ law, which follows from the thin accretion disc model by Shakura–Syunyaev [109]. They also confirmed that the emission line regions of quasars are much larger than that emitting the UV and visual light.

Eigenbrod et al. [27, 28] presented the results of spectroscopic monitoring of Q 2237 + 0305 during October 2004–December 2006, with the wavelength coverage 4000–8000 Å. They conclude that the continuum and broad line regions of the quasar are subjected to microlensing. They found that, according to theoretic predictions, microlensing brightness variations are stronger at shorter wavelengths, and restored the energy profile of the accretion disc. The relative sizes of the accretion disc emitting at different wavelengths turned out to follow the $R_\lambda \propto \lambda^\beta$ law, with $\beta = 1.2 \pm 0.3$ for the UV/optical continuum, that is close to the result of Mosquera et al. [81].

Similar results for wavelength dependence of the effective source size are reported by Anguita et al. [4], who used their g'- and r'-band photometry at the Apache Point Observatory 3.5-m telescope together with the OGLE V-band data to obtain 1.2–1.45 for the ratio of the source sizes in the r'-band to that in the g'-band, with the 0.5–0.9 uncertainty, however.

Thus, as compared to the single-band observations, multi-colour observations are capable of providing a more comprehensive idea of a quasar's spatial structure and thus, of physical processes responsible for the observed properties of quasar radiation.

Our data obtained at the Maidanak Observatory allow to see the signatures of chromatic phenomena directly from comparison of the V , R and I light curves of a particular microlensing event. This is illustrated by Fig. 1.7, where the V , R and I light curves of the high-magnification event in image A started in 2005 are shown. A tendency of amplitudes to decrease towards the longer wavelengths is clearly seen in this picture.

However, a single microlensing event, no matter how prominent it may be, is of a lower diagnostic value as compared to the statistics of all available microlensing history of all the four Q 2237 image components. Below, we find and analyse statistical relationships between the observed variations of colour indices and magnitudes, and compare them to the results of microlensing simulation fulfilled for a set of the quasar structure parameters.

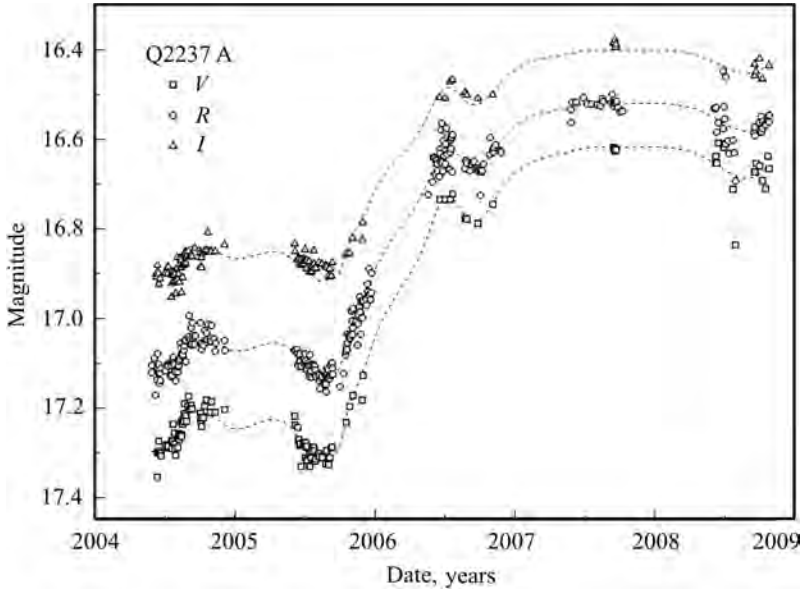


Fig. 1.7. Brightness changes of the A component of Q2237+0305 in the V , R and I filters during the high magnification event started in 2005 (observations from the Maidanak Observatory). The amplitudes of the event are clearly seen to decrease consecutively from filter V to R and I

To properly investigate microlensing phenomena, one has to disentangle them from the intrinsic variability of quasars and from the effects of dust extinction in lensing galaxies, which are known to act simultaneously and in a similar way.

Yonehara, Hirashita & Richter [143] have made an attempt to evaluate relative contributions from these three factors. They conclude that the intrinsic quasar variability is hardly a dominant factor for the observed chromatic phenomena in gravitationally lensed quasars from their sample counting about 25 systems. They claim that both dust extinction and microlensing are capable of producing the observed behavior of colour indices of the lensed quasar images.

We regard that one should be more careful concerning this issue. According to [134] and [34], variability of quasars increases towards the shorter wavelengths, and most of quasars exhibits hardening of their spectra in the bright phases. Giveon et al. [34] undertook an extensive statistical analysis of variability properties of 42 quasars from the Palomar Green (PG) sample having used the results of the 7-years monitoring in the Johnson-Cousins B and R bands with the Wisa Observatory 1-m telescope. The main goal of their study was to search for correlations between the variability properties and other parameters of quasars, such as luminosity, redshift, radio loudness, etc.

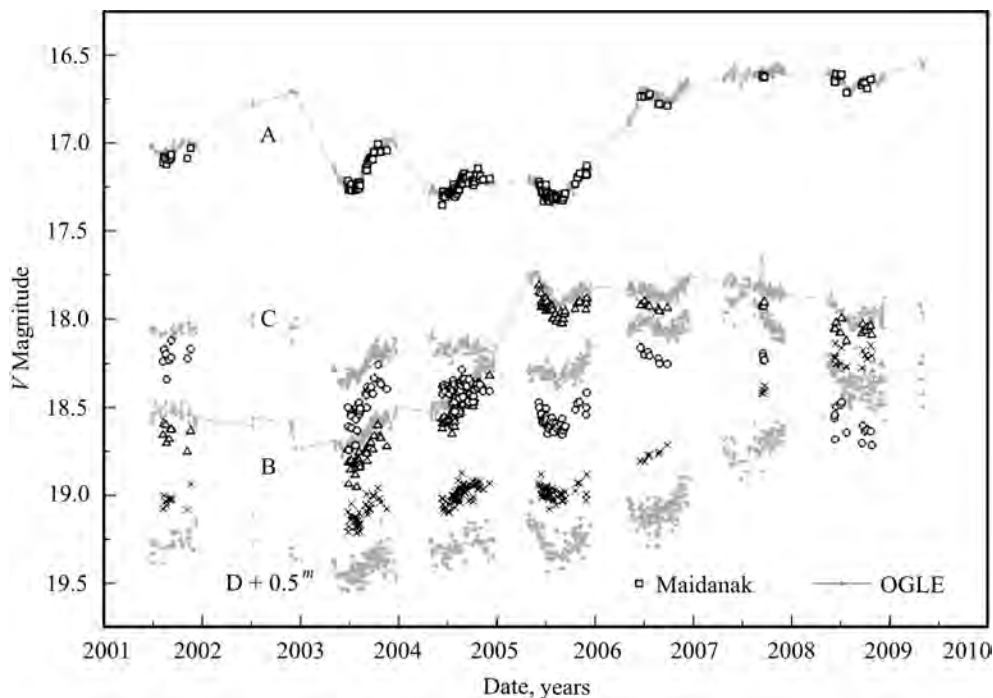


Fig. 1.8. Q 2237 + 0305 light curves in filter V from 2001 to 2008; grey symbols — the OGLE data, the Maidanak data are shown in darker symbols. The D light curve is 0.5 mag shifted for better view

They confirmed previous finding that the spectra of quasars become harder (bluer) at brighter phases, but found out that this trend holds for only a half of their subsample. They presented the diagrams which demonstrate a rather high correlation between variations of the $B - R$ colours and variations of the B and R magnitudes, with a regression line slope of approximately 0.25.

The Q 2237 + 0305 system is usually referred to as that one, where brightness changes of all the four lensed quasar images are dominated by microlensing events. Recent observations have shown, however, that quasar variability may contribute noticeably to the Q 2237 + 0305 light curves. It is seen especially during 2003–2006 (Fig. 1.8), when the microlensing activity was somewhat subdued for images A, C and D (for image B, a noticeable microlensing event has happened during this time period). Recall that this fact had made it possible to estimate the time delays in Q 2237 + 0305 [119]. Observations of this time period have shown that the contribution of the source variations to the observed light curves can not be neglected. To be sure of this, we estimated contributions from the microlensing and quasar intrinsic variabilities quantitatively, having applied a simple statistical approach to the whole R light curve during 1997–2008. Having made use of the fact that the time

delays in Q 2237 + 0395 are negligibly small as compared to the variability time-scales, we analysed the sums and differences of light curves for all the six combinations of pairs of images to obtain the following values of the RMS fluctuations: $\sigma_S = 0.10 \pm 0.03$ mag for the intrinsic quasar brightness variations, and $\sigma_{micr} = 0.16 \pm 0.04$ mag for microlensing variability (averaged over all the four image components). Similar results were obtained from the analysis of the OGLE V light curves.

Thus, the intrinsic brightness fluctuations of the Q 2237 + 0305 quasar do contribute significantly to the observed light curves of the lensed images, and therefore one must find a possibility to exclude the quasar constituent to study the net microlensing colour and magnitude variations.

The most simple way to exclude the quasar variability is to analyse the difference light curves in the units of stellar magnitudes, where these two constituents are additive. Thus, we may form the difference light curves ΔR_{A-B} , ΔR_{A-C} , ΔR_{A-D} , ΔR_{B-C} , ΔR_{B-D} , ΔR_{C-D} , and the corresponding difference colour curves, $\Delta(V - I)$, where Δ means, similar to [118], deviations of the corresponding quantities from their average values over the time interval under consideration.

At first, we built the $\Delta(V - I)$ vs. ΔR diagram for all the four quasar components from our VRI photometry of 2001–2008 and compared it to the similar diagram for the 1995–2000 data shown in fig. 2 from [118]. The diagrams turned out to be very similar both in the regression line slopes and in correlation factors, with the difference well within the error bars. However, both the $V - I$ colour indices and magnitudes in R varied within a larger range for the 1995–2000 data as compared to the observations of 2001–2008. This can be naturally explained by two unprecedented high-magnification events happened to images A and C in 1999. Taking into account obviously different mutual contributions of the microlensing variability and quasar intrinsic variability to the observed light curves during these two periods, the likeliness of the diagrams can be regarded as an indication to the similar statistical characteristics of these two types of variability (compare the $B - R$ vs. R regression line slope of 0.25 for PG quasars in fig. 6 from [34] with 0.28 in [118]).

Thus, to analyse the net microlensing statistics, we will further address the difference colour and magnitude variations curves. Besides, it is reasonable to expect that the difference curves calculated as described above will be less affected by the inevitable photometry errors, both random, such as, e.g., night-to-night error, and systematic ones. The difference $\Delta(V - I)$ vs. ΔR diagram built for all possible combinations of pairs of images is shown in Fig. 1.9. Here we used the photometry results obtained in observations from the Maidanak Observatory during the time period from 2001 to 2008.

The regression line slope for these difference data points is insignificantly larger than that in fig. 2 from the work by Vakulik et al. [118], while the

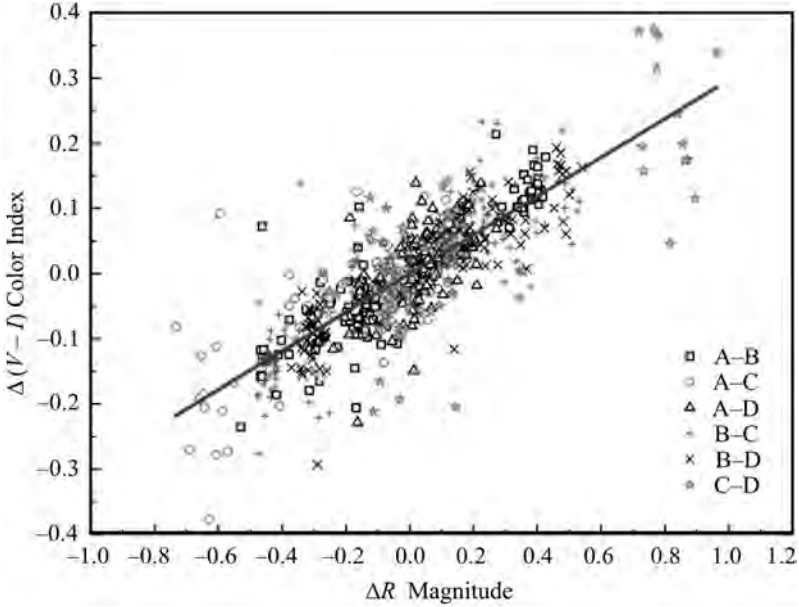


Fig. 1.9. A diagram showing correlation between variations of the $(V - I)$ colour indices (vertical axis) and variations of magnitudes in filter R , calculated from the VRI observations in 2001–2008 with the 1.5-m telescope at Maidanak Observatory

correlation index turned out to be noticeably higher, in accordance with expectations noted above. Hence, we have a diagram representing statistics of microlensing variations of colour indices exempted from the interfering effects of the quasar variability, and therefore suitable for the further interpreting in simulations. We argue that the regression line slope and correlation factor of the $\Delta(V - I)$ vs. ΔR diagram are important parameters of microlensing statistics, which are diagnostic for a spatial structure of the source quasar.

Wambsganss & Paczynski [127] seem to be the first to simulate statistical dependencies between variations of colour indices and variations of brightness for Q 2237 + 0305 caused by microlensing of a source with a radial temperature gradient. They simulated the B and R microlensing light curves for Q 2237 + 0305 for the Gaussian brightness profile of the quasar with the half width radius varying between $2 \cdot 10^{14}$ cm and $3.2 \cdot 10^{15}$ cm, and found out that $|\Delta(B - R)|$ may be approximately proportional to $|\Delta B|$ for some source dimensions and for the ratios of the source sizes at the two spectral bands of at least 1.3 or larger.

Similar to the previous section, we considered a photometric model of the Q 2237 + 0305 quasar consisted of a compact central source at some brightness pedestal as a case that is much more simple computationally, but results in similar effects. We, again, did not attempt to specify the size and brightness

profile of the extended feature in our simulations, but intended to find the relative energy contribution of the extended feature into the total quasar luminosity that would provide the best fit of the simulated $\Delta(V-I)$ vs. ΔR diagram to that obtained from our *VRI* photometry.

The magnification maps were calculated using the inverse ray tracing method, with the local lensing parameters κ_* and γ accepted, similar to the previous section, to be the same as in Kochanek [58]. To utilize all the statistics available from the generated magnification maps, we did not select source trajectories and thus, did not use the corresponding light curves in the further analysis, but instead, operated directly with data points of the maps themselves to find the desired parameters. In this way, we excluded the unknown direction of the source motion over the map, as well as its relative velocity.

To decrease the amount of calculations while having the size of magnification maps sufficient enough to provide reasonable accuracy of the calculated model parameters, we produced two sets of magnification maps differing in their scales. For the source radii from $r_s = 0.05r_E$ to $r_s = 1.0r_E$, three maps of $(46 \times 46)r_E$ in dimension with a $44\text{pix}/r_E$ scale were calculated for each image component, while for r_s ranging from $0.5r_E$ to $3r_E$, one $(205 \times 205)r_E$ map with a scale of $10\text{pix}/r_E$ was used for each image component.

Since the correlation coefficient of the colour-magnitude diagram must be sensitive to errors in the values of $V - I$ and R , we added a random noise to our magnification maps, thus making our simulations more realistic. The RMS values of the imitated errors were accepted to equal those estimated for the actual errors of our *VRI* photometry: 0.019^m , 0.037^m , 0.042^m and 0.039^m for images A, B, C and D, respectively, and were made to be distributed normally.

As was shown in the previous section, the value of magnification μ_{12} in microlensing of the two-component source consisting of a compact central structure and an extended outer structure, can be represented by equation (1.18).

The average magnifications can be adopted to equal those determined by the local lensing parameters. With these taken from [105], and using the known relationship between the normalized surface density in stars, normalised shear parameter and macroamplification, (see equation (1.7) in section 1.1.1), we have the following values of amplifications for the A, B, C and D components: $\mu_A \approx 4$, $\mu_B \approx 4.3$, $\mu_C \approx 2.45$ and $\mu_D \approx 4.9$.

As was noted in section 1.2.1, some authors, e.g. Mortonson et al. [80], claim that the effective size is a universal parameter of a source model for microlensing simulations, and that a particular type of the brightness profile virtually does not affect fluctuations of the simulated light curves. To check if this is valid for simulation of colour fluctuations, we considered both the accretion disc and a source with Gaussian surface brightness distribution as the quasar models. We adopted a generalized power law for wavelength dependence

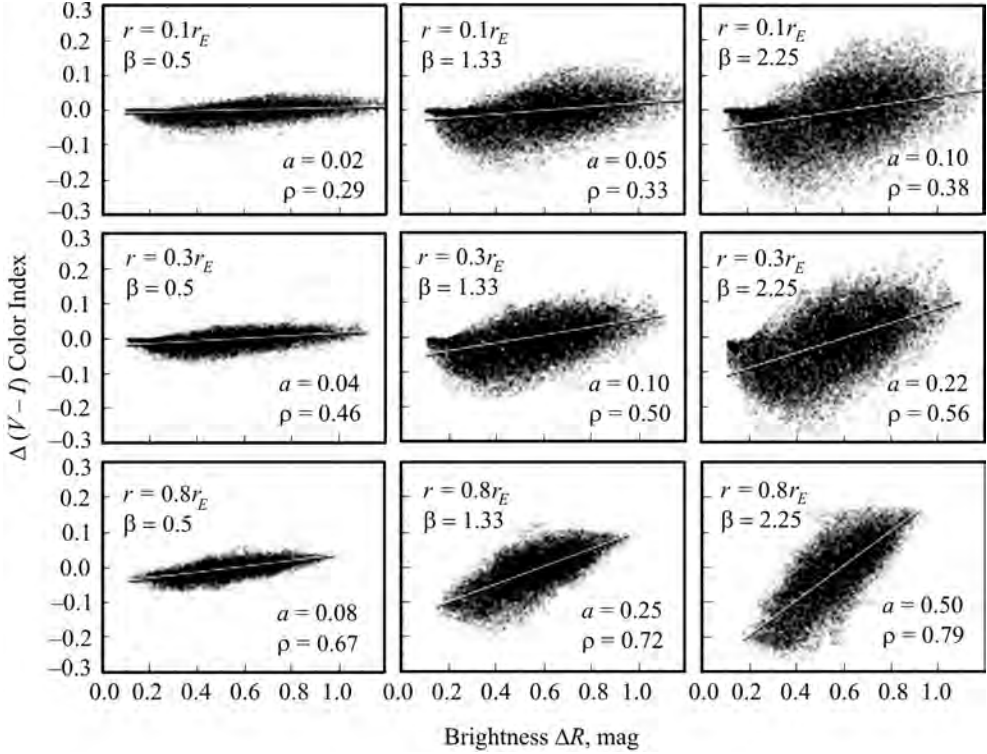


Fig. 1.10. Diagrams $\Delta(V - I)$ vs. ΔR simulated for image A of Q2237 + 0305 as described above for a central source with Gaussian brightness profile. The calculations were made for three different effective sizes of the source and three values of the parameter β in the $r_\lambda \sim \lambda^\beta$ law (shown in the left upper corners). The resulting values of the correlation coefficient ρ and regression line slope a are indicated in the right bottom corner of each panel

of the Gaussian source effective radius, $r_\lambda \propto \lambda^\beta$. The value of β varied from 0.5 to 2.5 for the Gaussian source brightness profile, with $\beta = 4/3$ valid for the Shakura–Syunyaev accretion disc. Then, we simulated the colour-brightness diagrams for our two-component source structure, with the accretion disc as the compact central source surrounded by an extended feature with its relative energy contribution ε_λ varying in wavelength.

Fig. 1.10 is presented to qualitatively illustrate appearances of the $\Delta(V - I)$ vs. ΔR diagrams simulated for a compact source with Gaussian brightness profile for three values of the effective radius and for three different values of β . None of the resulting regression line slopes and correlation factors (shown in the plots) can be regarded as consistent with those of the color-magnitude diagram built from the observations.

Fig. 1.11 demonstrates typical appearances of colour-magnitude diagrams for three different sizes of the classical accretion disc with no contribution

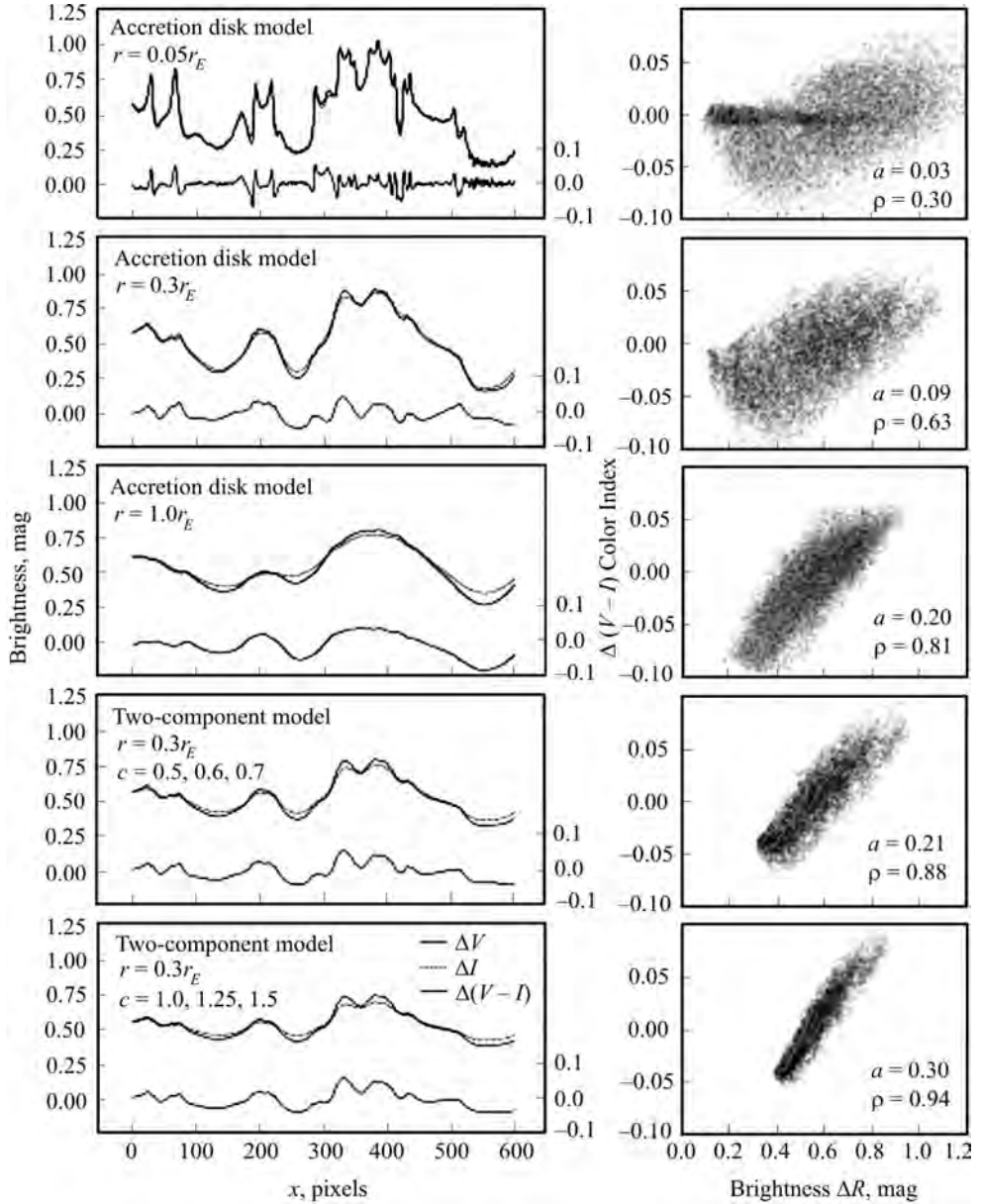


Fig. 1.11. Illustration of the effect of the source model on appearance of the $\Delta(V-I)$ vs. ΔR diagrams simulated for image A of Q 2237 + 0305. The light curves in filters V and I (denoted as ΔV and ΔI) and the curves ($\Delta(V-I)$) corresponding to a particular source trajectory, are in the left column. The time scale is presented by pixels on the magnification map. The source model parameters are also indicated in the left panels. The $\Delta(V-I)$ vs. ΔR diagrams built from the whole amplification maps as described in the text are presented in the right column. The entangled curves at the diagrams correspond to particular source trajectories and are shown to illustrate the ambiguity of the color-magnitude relationship produced by microlensing

from the extended feature (three upper panels in the right-hand column), and for the two-component source model with two sets of ε_λ (right-hand panels in two bottom rows). For the central compact source alone, both Gaussian and accretion disc, the parameters ρ and a of the $\Delta(V - I)$ vs. ΔR diagram are seen to approach those of actually observed ones only for unrealistically large sources (indicated in the plot). For the two-component source model, the simulated diagrams are consistent with the observed ones for quite reasonable values of the central source size.

It is interesting to note a horizontal strip-like condensation of data points seen in the uppermost diagrams both in Fig. 1.10 and Fig. 1.11, that is stretched parallel to the magnitude axis against the zero colour indices. A similar condensation can also be seen in the $\Delta(V - I)$ vs. ΔV diagram simulated by Mosquera et al. [81] for image A of Q 2237 + 0305 and shown in their fig. 5. The origin of the strip becomes evident from the color curves in the upper left panels of our Fig. 1.11, showing variations of the $(V - I)$ colour index for a very small source ($R_s = 0.05r_E$) moving along a certain trajectory over the magnification map, (the appropriate light curves in filters V and I are plotted above the colour curves). The color curves clearly shows a high probability for a small source to have low values of $\Delta(V - I)$, close to zero. Our simulations show that the strip is gradually disappearing as the source size is increasing. Since there is no signs of such a strip in the diagram built from the data of observations (Fig. 1.9), its presence in the simulated diagrams can serve as an indication to the unrealistically small source size.

One more important feature of the simulated $\Delta(V - I)$ vs. ΔV diagrams should be noted. We overlaid the individual $\Delta(V - I)$ vs. ΔR curves resulted from a particular source trajectory over the amplification map against the clouds of points, which form the simulated diagrams (right-hand column in Fig. 1.11). We see the entangled curves at the diagrams, which demonstrate that relationship between variations of colour indices and magnitudes in microlensing is ambiguous. This curves demonstrate why the analysis of a single event may produce wrong inferences about a quasar structure and thus, provide a strong argument in favour of statistical approach to studying chromatic events in microlensing.

To quantitatively interpret our multi-colour data, we abandoned simulation of many individual $V - I$ vs. R diagrams calculated for a set of specific source parameters, but instead, chose to analyse behaviors of the diagram parameters, namely, the correlation factor ρ and regression line slope a as functions of the source parameters. At first, we analyzed if Gaussian source alone can reproduce the observed ρ and a pair of the diagram parameters. This can be seen in Fig. 1.12, where three curves illustrate three sets of the ρ and a pairs calculated for three different values of β in the $r_\lambda \sim \lambda^\beta$ law adopted for the Gaussian source profile (indicated in the plot). Each data

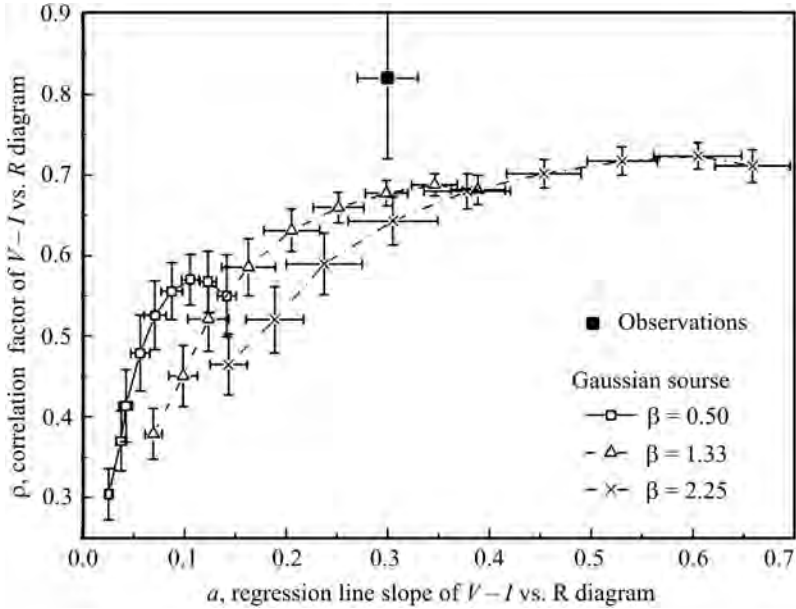


Fig. 1.12. Sequence of values for the pair of parameters ρ and a of the $\Delta(V - I)$ vs. ΔR diagram simulated for the Gaussian central source alone with the effective source radius r_s varying in wavelength according to the $r_s(\lambda) \propto \lambda^\beta$ law. The data points in the curves (crosses, triangles and squares) are the values of the ρ and a pair simulated for source sizes that increase discretely from $0.05r_E$ to $3r_E$ from left to right. The actually observed ρ and a are marked with a black square above the curves

point in this plot (denoted by crosses, triangles and squares) corresponds to the ρ and a pair calculated by averaging over the whole magnification maps for a particular source size, which increases progressively from left to right. The error bars demonstrate the RMS deviations of the estimates from their average values. An isolated point in the upper part of the plot corresponds to the values of ρ and a of the diagram obtained from our VRI photometry (Fig. 1.9). The curves calculated for $\beta = 1.33$ and $\beta = 2.25$ do provide the needed value of a , but fail to provide the correlation factor ρ actually observed: it reaches its maximal values for unrealistically large source radii r_s , though remaining to be lower than that obtained from observations.

A similar set of values for the ρ and a pair was also calculated for the standard accretion disc model with the source size varying from $0.05r_E$ to $3r_E$, (Fig. 1.13). The squares along the curve correspond to the source size growing from left to right again. General trend of this set resembles that one obtained for the Gaussian source with the power index $\beta \approx 1.33$. Though slightly larger values of the correlation index are obtained for this model, they still remain to be less than $\rho = 0.82 \pm 0.1$ of the diagram built from the data of observations.

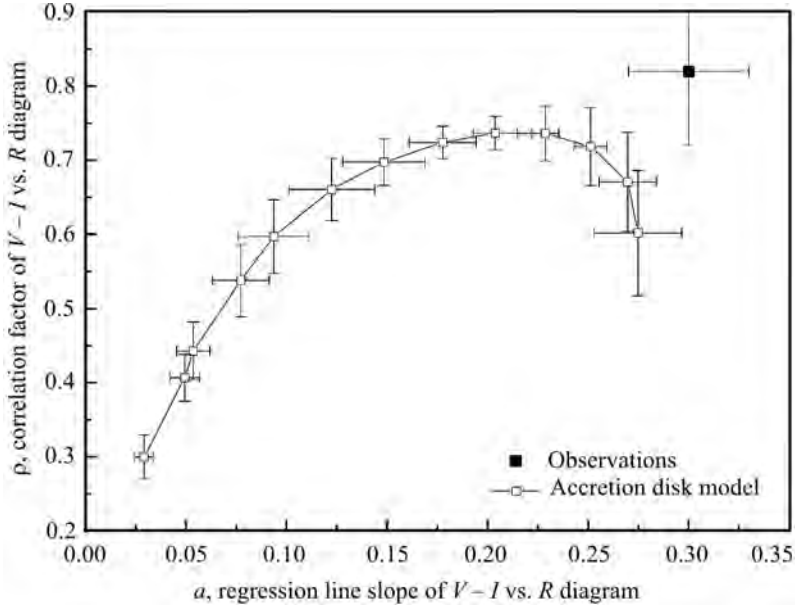


Fig. 1.13. Sequence of values for the pair of parameters ρ and a of the $\Delta(V - I)$ vs. ΔR diagram simulated for the accretion disc as a model for the Q 2237 quasar, with the effective source radius r_s varying in wavelength according to the $r_s(\lambda) \propto \lambda^{4/3}$ law. The effective source size grows from $0.05r_E$ to $3r_E$ from left to right again

Also, a tendency of the regression line slope a to approach the observed value $a = 0.30 \pm 0.03$ for very large source dimensions is observed again.

Thus, both Gaussian and accretion disc do not reproduce in simulations the parameters of the $\Delta(V - R)$ vs. ΔR diagram (Fig. 1.9), built from our VRI photometry, — $a = 0.3 \pm 0.03$, $\rho = 0.82 \pm 0.10$. As has been shown above and presented in [120], a two-component photometric model of the source structure provides much better fit to the observed **amplitudes** of the V light curves of Q 2237 + 0305 as compared to the single central source model. The central source size was estimated in that work to lie within $0.15r_E$ and $0.4r_E$. This is consistent with determinations of the Q 2237 + 0305 source size obtained by other authors, from the early works, such as e.g., [125, 126, 132], and up to the recent studies by, e.g., Kochanek et al. (2004) [58], Eigenbrod et al. (2008) [27], Mosquera et al. (2009) [81]. Summarizing all available estimates of the central source radius, we may adopt $r = (0.3 \pm 0.1)r_E$ as the most probable value.

Therefore, our next step was to simulate microlensing $\Delta(V - I)$ vs. ΔR diagrams for the two-component source model and to find the model parameters, which would provide a and ρ of the simulated diagram consistent with those actually observed. Fig. 1.14 shows behaviors of the a and ρ pair simulated for the two-component source model with three different values of the relative

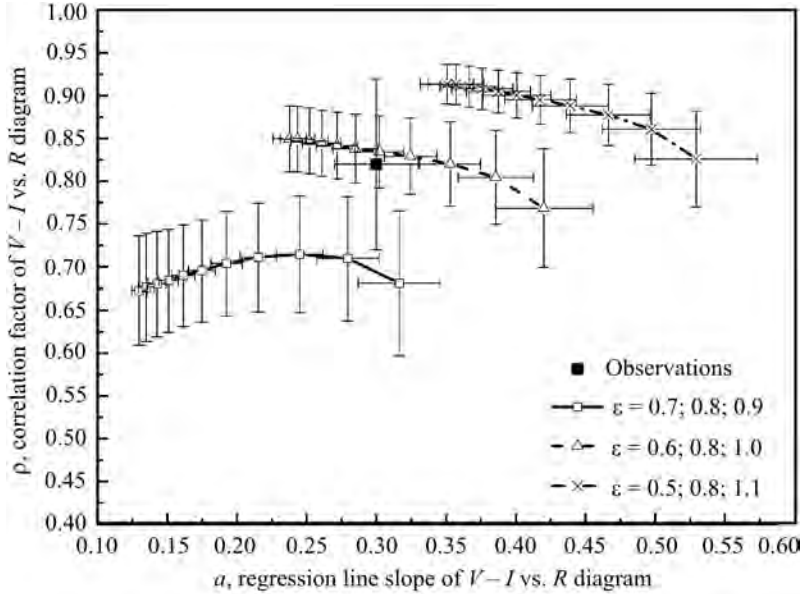


Fig. 1.14. Sequence of values for the pair of parameters ρ and a of the $\Delta(V - I)$ vs. ΔR diagram simulated for the two-component model of the Q 2237 quasar with three different sets of ε_V , ε_R , ε_I . The effective radius of the central source decreases from left to right in this case from $0.05r_E$ to $1.6r_E$

energy contribution from the extended source in filters V , R and I (shown in the sidebar). Similar to Fig. 1.12 and Fig. 1.13, the data points fix the a and ρ pairs calculated for the central source size increasing consecutively from left to right.

We see from Fig. 1.14 that the two-component source model provides much better fit to the a and ρ pair obtained from observations as compared to the single central source model, with both Gaussian and accretion disc profiles. However, we cannot find a unique solution from the analysis of this plot, because in contrast to the single source model, the two-component model is described by three additional parameters, ε_V , ε_R and ε_I , which we need to be constrained in some way.

To search for necessary observational constraints, we addressed Eq. (1.18) that describes a relationship between amplifications of the two-component (μ_{12}) and single-component (μ_1) source models, resulted from microlensing. Taking into account that the extended structure is almost insusceptible to microlensing ($\mu_2(\mathbf{y}) \approx \langle \mu_2(\mathbf{y}) \rangle \approx \mu_j$, see section 1.2.2), — we can write for deviations of the corresponding magnifications μ_{12} and μ_1 from their values $\langle \mu_{12} \rangle$ and $\langle \mu_1 \rangle$ averaged over the ensemble under consideration:

$$\mu_{12} - \langle \mu_{12} \rangle = \frac{\mu_1 - \langle \mu_1 \rangle}{1 + \varepsilon}. \quad (1.22)$$

Having averaged these differences over the whole magnification map, we can calculate the RMS variations σ_{12}^μ and σ_1^μ for μ_{12} and μ_1 . Both magnifications and their RMS variations are understood to be functions of the central source size r : $\sigma_1^\mu = \sigma_1^\mu(r)$ and $\sigma_{12}^\mu = \sigma_{12}^\mu(r)$. This will result in ε being a function of r too and thus, we can write for $\varepsilon(r)$:

$$\varepsilon(r) = \frac{\sigma_1^\mu(r)}{\sigma_{12}^\mu(r)} - 1. \quad (1.23)$$

When checking the hypothesis of the two-component source model, $\sigma_{12}^\mu(r)$ should be treated as the actually observed RMS flux variations σ^{obs} of quasar images, while $\sigma_1^\mu(r) = \sigma^{sim}(r)$ are those obtained from simulations with a single-source model for a set of the central source sizes. Applying Eq. (1.23) to the data taken in different filters, we have:

$$\varepsilon_V(r) = \frac{\sigma_V^{sim}(r)}{\sigma_V^{obs}} - 1; \quad \varepsilon_R(r) = \frac{\sigma_R^{sim}(r)}{\sigma_R^{obs}} - 1; \quad \varepsilon_I(r) = \frac{\sigma_I^{sim}(r)}{\sigma_I^{obs}} - 1, \quad (1.24)$$

where the observed flux variations in filters V , R and I were obtained from our light curves to equal $\sigma_V^{obs} = 0.167$, $\sigma_R^{obs} = 0.142$ $\sigma_I^{obs} = 0.124$. Using these observational constraints and the values of $\sigma^{sim}(r)$ obtained from simulation, we can calculate the corresponding values of the relative integral brightness of the extended structure as functions of the central source size. The result is presented in Fig. 1.15.

For all the three filters the relative contributions of the extended feature needed to explain parameters of the $\Delta(V-I)$ vs. ΔR diagram of Q 2237 + 0305 are seen to decrease as the central source radius increases. Now, to obtain a reasonable solution, we must fix the size of the central source. Adopting $r = (0.3 \pm 0.2)r_E$ mentioned above for the compact source radius, we obtain $\varepsilon_V \approx 1.3$, $\varepsilon_R \approx 1.5$, $\varepsilon_I \approx 1.6$ for the relative energy contributions of the extended structure of our two-component quasar model. The uncertainties are ± 0.5 , ± 0.6 and ± 0.8 , respectively.

As is seen, the values of ε obtained with the approach based on comparison of fluctuations of the observed and simulated light curves expressed by equations (1.24) are larger than those selected in a rather random manner in direct simulation to fit the observed values of a and ρ (Fig. 1.14). This can easily be understood from Eq. (1.24): the values of σ_V^{obs} , σ_R^{obs} and σ_I^{obs} were obtained from the observed light curves, which, in contrast to the simulated ones, cannot be regarded as the representative samples of microlensing brightness variations (see, e.g. [84]). This must result in underestimation of σ^{obs} and thus, in overestimation of ε from expressions (1.24). Therefore, the values ε_V , ε_R , ε_I indicated above should be considered as the upper limits for the relative energy contributions of the extended feature in filters V , R and I .

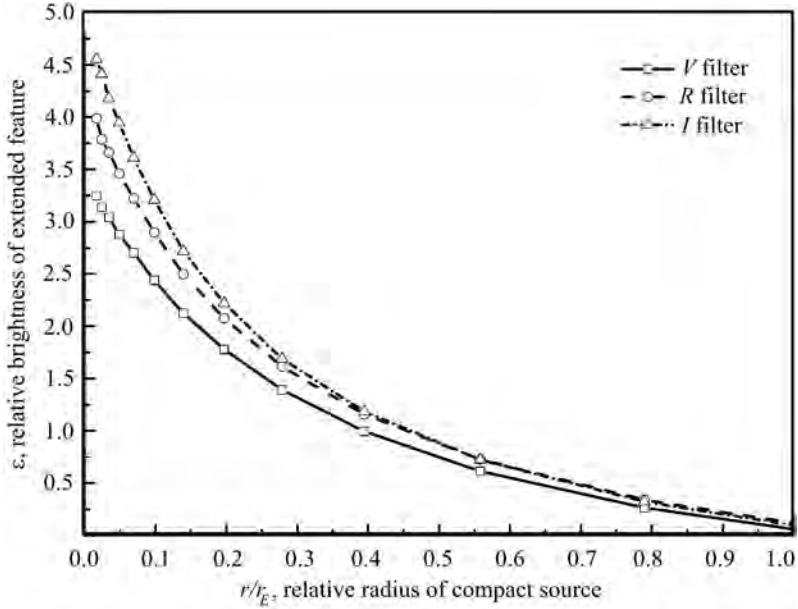


Fig. 1.15. Relative brightness of the extended feature in filters V , R and I as a function of the quasar compact structure relative size expressed in units of a microlens Einstein ring radius, r_s/r_E

Indeed, simulations show that lower values of ϵ_V , ϵ_R and ϵ_I much better reproduce the observed ρ and a pair. Moreover, simulations show that a family of solutions exists diverging not only in the values of ϵ , but also in the ratios of ϵ in different spectral bands. Therefore, additional constraints are needed, which would be based on more reliable data about the spectral properties of the supposed extended feature. At the present level of our knowledge, we can only argue that a contribution of the extended structure into the total quasar emission grows towards the longer wavelengths, with the upper limits in the V , R and I bands of $\epsilon_V \approx 1.3$, $\epsilon_R \approx 1.5$, $\epsilon_I \approx 1.6$

Thus, to explain the parameters of our $\Delta(V-I)$ vs. ΔR diagram, we, again, had to admit existence of an extended structure around a compact central source, with a rather large contribution into the total quasar emission. It is obvious that the effect of such structure, when treated in terms of the $R_\lambda \propto \lambda^\beta$ law, is equivalent to the steeper wavelength dependence of the effective source size as compared to that expected for the accretion disc. Meanwhile, the most recent observations of chromatic microlensing in Q 2237 + 0305 [2, 5, 28, 81] and in other lensed quasars give the value of β in the λ^β law varying around $4/3$ predicted by the thin accretion disc model.

To comment discrepancy between our results and the results of the authors cited above, we would like to refer to the recent work by Mosquera et al. [81],

who reported detection of chromatic microlensing in image A of Q 2237 + 0305 in the single-epoch multiband observations with the NOT. Having noted that their results are consistent with a simple thin disc model, with the effective source radius $r_s(\lambda)$ obeying in general the $\lambda^{4/3}$ law, they noted however, that other accretion disc size-wavelength relationships also lead to good solutions. Moreover, according to their finding, the probability of solutions increases for laws with larger ratios of the source radius in filter I to that in V , than the $\lambda^{4/3}$ law predicts. They conclude also that a single microlensing event seems to be insufficient to study chromatic phenomena.

Our Fig. 1.11, where entangled curves corresponding to particular source trajectories at the magnification map are shown, confirms this statement. The relationship between variations of colour indices and magnitudes in microlensing turned out to be ambiguous, and thus, analysis of a small number of events, no matter how prominent they might be, can provide a wrong result. This is just understanding of this fact that has made us to refuse deterministic analysis of chromatic phenomena in microlensing events in Q 2237 + 0305 as early as in 2004 [118]. Instead, we analysed them statistically, addressing a relationship between variations of colour indices $\Delta(V - I)$ of the Q 2237 + 0305 image components and variations of their magnitudes in filter R . We addressed the same relationship in the present work to compare parameters of the observed $\Delta(V - I)$ vs. ΔR diagram with those obtained from simulations. Having tested several photometric models of the Q 2237 + 0305 quasar in simulations of the $\Delta(V - I)$ vs. ΔR diagram for a variety of the model parameters, we conclude that the microlensing color-magnitude diagram is diagnostic to distinguish between various source structure models.

It should be noted that our two-component quasar model is a photometric one, that is, it concerns only the quasar surface brightness distribution as seen in projection on the sky. Little can be said about the physics, origin and geometry of this outer structure contributing such an appreciable amount of the UV/optical continuum emission into the total quasar luminosity. But perhaps, the existing quasar models mentioned in section 1.2.1, either outflows, or dusty tori and electron scattering regions, — all are capable, in principle, of being possible candidates for the structure that would efficiently reprocess continuum radiation from the accretion disk.

1.3. Dark matter content from probability density distributions of microlensing amplifications

The microlensing events or, more exactly, statistics of the resulting brightness changes, are informative to infer the ratio between the galaxy mass in compact objects and in uniformly distributed (dark) matter. The idea to use microlensing events in determining the dark matter content in

galaxies lensing remote quasars was reported for the first time as early as in 1991 [132] and published somewhat later in the work dedicated to statistical analysis of microlensing light curves [128], though its basics are contained in the so-called scaling relations obtained by Paczyński in 1986 [84].

In 2002–2004, Schechter and Wambsganss [99–101], having noted the above-mentioned predecessors, returned to the idea and proposed the method to estimate the relative contribution of dark matter into the total surface mass density of lensing galaxies that is based on the analysis of probability density distribution for microlensing amplifications (the method of histograms hereafter). They showed in computer simulation [99, 100] that, contrary to intuitive expectations, substitution of a part of gravitating mass in compact objects for uniformly distributed matter in some cases results in the increase of brightness fluctuations in microlensing on the rest of compact objects. As this takes place, fluctuations increase much more for images corresponding to the saddle points of the Fermat surface as compared to those corresponding to the minima of this surface. Moreover, introducing of the uniformly distributed matter noticeably changes the appearance of probability density distribution for amplification, with the effect of the smooth component being different for images of different parity.

Thus, the problem of estimating the fraction of smoothly distributed matter in lensing galaxies by the method of histograms seems, in principle, to be rather simple: it requires either a long-term monitoring of brightness changes in macroimages of some selected gravitationally lensed quasar, or observations of a sample of such objects in arbitrary time moments, with the subsequent statistical analysis [128]. But in reality, the situation is not so simple.

1. Firstly, simulations show that distributions of amplification probabilities strongly depend on the accepted model for surface brightness distribution over the quasar, in particular, on its effective size.

2. Secondly, the mass function of microlenses can principally have an effect on statistics of microlensing brightness fluctuations. This question has been repeatedly discussed in literature, for example, [64, 101, 141]. Wambsganss [128] presented a large number of various probability distributions for microlensing amplification obtained in simulations with the use of various combinations of microlensing parameters. His results confirmed the analytical result of Schneider [106], which demonstrated that the appearance of probability distribution for microlensing amplifications weakly depends on the mass function of compact objects. This conclusion remained to be undoubted for a rather long time and, though it was understood that population of compact objects in actual galaxies must be represented within a broad range of masses, from planets to stars, until the present time all microlenses were usually accepted to have the same mass in simulations and analytical studies. This noticeably simplified numerical simulations and theoretic analysis and thus, was convenient.

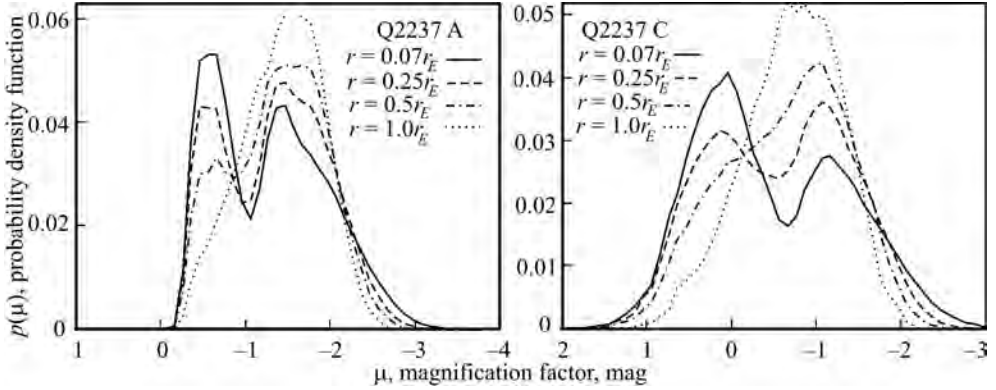


Fig. 1.16. Demonstration of the effect of the source size on probability density distributions for microlensing amplifications. Simulation was carried out for components A and C of Q 2237 + 0305 with the zero contribution of the smoothly distributed matter. The source dimensions ranges from 0.07 to 1.0 Einstein ring radius r_E of a microlens (indicated in the insert)

3. Then, in analyzing the data of observations, there is a necessity to separate brightness fluctuations of components caused by microlensing from those which are due to the quasar intrinsic flux variations. This is an intricate problem even for quadruple systems with small values of time delays, such as, for example, Q 2237 + 0305 (see sections 1.2.2 and 1.2.3). The actual quasar light curve and even statistical characteristics of variability are unknown for each particular quasar, while simulation must be carried out for a quasar flux fixed, i.e., the “net” microlensing must be analyzed.

4. Finally, poor statistics and uneven sampling of light curves are important factors, which strongly complicate statistical analysis of the observed light curves of gravitationally lensed quasars.

1.3.1. The effect of a source structure on distribution of amplification probability in microlensing

The effect of the source size on statistics of microlensing brightness variations analyzed in numerical simulations by several authors, [8, 20, 63, 80, 116], can be seen from Fig. 1.16 taken from [116]. Here, simulation for Q 2237 + 0305 was fulfilled for the sources of various dimensions. The distributions of microlensing amplification probabilities for images A (minimum of the arrival time surface, Fermat surface) and C (saddle point) were calculated for microlensing parameters taken from [58] again. The curves are normalized so that a sum of all possible brightness amplifications remained to be constant. The brightness distribution over the source was accepted to be Gaussian for simplicity.

The bimodal character of probability distributions accompanied by a more frequent occurrence of deamplifications (positive values at the horizontal axis), is clearly seen to reveal more and more distinctly for the “saddle” images as the source size is decreasing. An important difference in microlensing statistics for the “saddle” and “minimum” images demonstrated earlier in [64, 99, 128] is also seen clearly: the histograms for “saddle” images are systematically broader than those corresponding to minima of Fermat surface.

Thus, the source size and structure shown above to be important for interpreting the microlensing light curves and color-magnitude statistics, must be also taken into account in interpreting probability distributions of microlensing amplifications. Distributions presented in Fig. 1.16, as well as similar results of other authors indicated in the first paragraph of this section, all have been obtained for a single-component quasar structure model.

However, as was shown in sections 1.2.2 and 1.2.3, a central compact source alone is not capable of reproducing in simulations parameters of the observed light curves and statistical relationship between variations of color indices and magnitudes resulted from microlensing. The two-component source model, composed of a compact central source surrounded by an extended feature was shown there to provide the simulation results consistent with observations. The extended structure is thought to damp variations of brightness caused by microlensing of a central compact source. As concerns the microamplification probability distributions, the effect of this structure is qualitatively understood to result in narrowing these distributions.

Thus probability distributions of amplifications in microlensing are shown to be sensitive to the quasar spatial structure. Moreover, the quasar size and the mass function of compact objects in a lensing galaxy have been recently shown to interact in a rather intricate manner, determining statistical characteristics of microlensing light curves jointly. In particular, Schechter, Wambsgans and Lewis [101] simulated a rather exotic mass function — two populations of compact objects with masses of 1.0 and 0.003 Solar mass, — and showed that distributions of microlensing amplification probabilities for these two populations look very much like those when a population with more massive compact objects is submerged in a smoothly distributed matter. In 2006 Lewis and Gil-Merino [63] continued analyzing a bi-modal mass function with masses differing significantly, and found out that a critical mode exists, which is determined by the source quasar dimensions, such that small masses still reveal themselves as compact objects. As the source size increases, the small masses begin to act as smoothly distributed matter.

1.3.2. Distributions of microlensing amplification probabilities for Q 2237 + 0305

The quadruply lensed quasar Q 2237 + 0305 (the Einstein Cross) is virtually an ideal object to investigate the dark matter problem with the use of statistics of brightness variations caused by microlensing. Because of closeness of the lensing galaxy to the observer ($z_L \approx 0.04$) and due to the extraordinary compactness of the system — the light rays of all the four images pass through the densely populated galaxy regions at distances of about $1''$ from its centre — microlensing events are happening almost uninterruptedly and have the typical time scales from several months to a few years, with the amplitudes reaching 1^m . The microlensing history of Q 2237 + 0305 during 1986–2008 can be seen from Fig. 1.17, where four light curves were built with the use of all available observational data in filter R since 1986. The observations of the Kharkov group from the Maidanak Observatory are marked with grey background. The light curves in this figure clearly demonstrate the problems arising in their statistical analysis: the data points are burdened with inevitable random errors of photometry, which are larger for fainter components, the samples are essentially irregular, with the seasonal and weather-induced gaps, which are especially harmful for analysis.

Therefore, the method to correctly interpolate the uneven data is needed. Then, to analyze pure microlensing statistics, a method to exclude a consti-

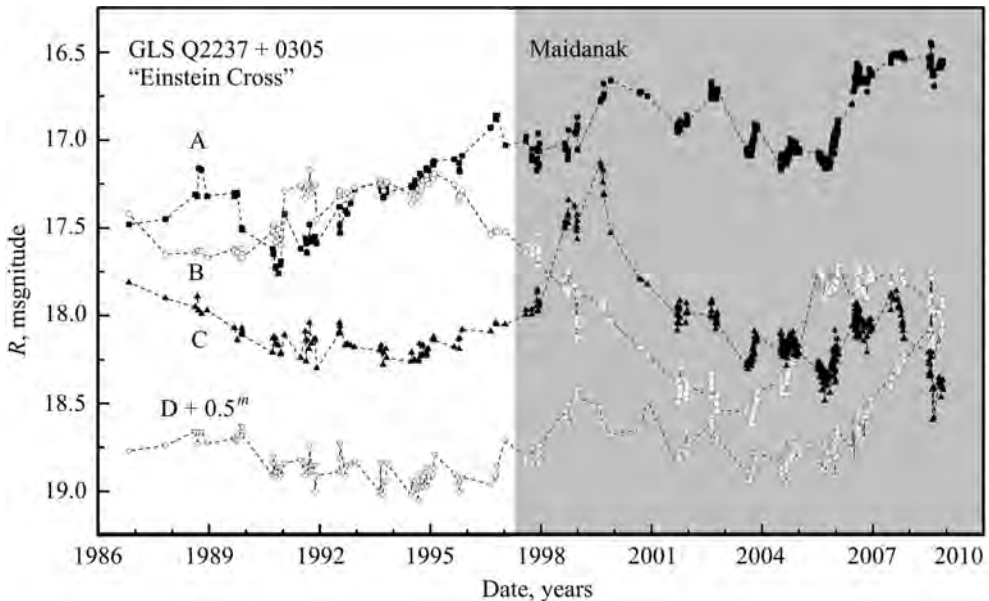


Fig. 1.17. Synthetic light curves of the Q 2237 + 0305 image components composed of all available photometric data in filter R . The data obtained at the Maidanak Observatory are marked with the grey background

tuent caused by the intrinsic variability of the source quasar should be applied. As is shown in sections 1.2.2 and 1.2.3, a contribution from the quasar variability cannot be neglected even for Q 2237 + 0305, where high-amplification microlensing events are observed. To prepare the light curves of macroimages for the further statistical analysis, an approximation algorithm based on the sampling theorem was proposed. The algorithm was successfully applied to the Q 2237 + 0305 light curves and described in greater detail in [74]. The methods to exclude a contribution of the intrinsic variability of the Q 2237 quasar are presented in sections 1.2.2 and 1.2.3.

As described above, statistics of brightness variations caused by microlensing is very sensitive to the presence of continuously distributed (presumably dark) matter or compact objects with extremely small masses, for which the Einstein ring radii are essentially less than the source emitting region dimensions. A relationship between this constituent of the lens galaxy population and that one represented by solar-mass objects, can be obtained from comparison of simulated distributions of magnification probabilities with the histograms built from the results of observations. There is only a single work, however, where such a comparison has been made [116]. This can be explained by the fact that even for Q 2237 + 0305, which has been regularly monitored for about a quarter of a century, the available data sample is not representative. Recall that, according to [84], more than 100 years of regular observations of Q 2237 + 0305 are needed to provide reliable estimates of statistical characteristics for microlensing brightness variations.

To build the histograms of microlensing amplification probabilities for the Q 2237 components, we used virtually all available photometry results obtained in filter R from 1986 to 2009, which are presented in Fig. 1.17. After subtraction of the source light curve from the light curves of each of the components calculated as described in section 1.2.2, with the approximation according to [74], smooth microlensing light curves were obtained. The RMS errors of approximation are $0.^m023$, $0.^m019$, $0.^m024$, $0.^m026$ for components A, B, C, D, respectively, which are comparable with the errors of photometry. The resulting histograms of amplification probability distributions for images A and C of Q 2237 + 0305 are shown in Fig. 1.18 [116]. Since, according to the existing macrolens models for Q 2237 + 0305, the expected microlensing parameters for pairs of adverse image components (A and B, C and D) are rather similar, we combined the histograms for images A and B, and for C and D to obtain the joint histograms for pairs of the same parity.

First of all, a significant difference of histograms for these two pairs should be noted, which is a result of different parities: as was noted above, A and B correspond to the points of minima of Fermat surface, while C and D are the so-called “saddle” images. This difference has been noted for the first time by Schechter and Wambsganss [99] in their computer simulations. The microlensi-

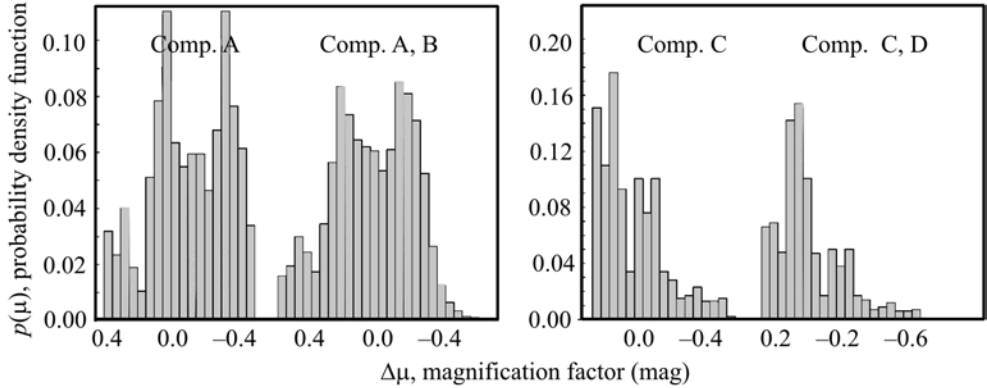


Fig. 1.18. Histograms of the amplification probability distributions for components A and B (left) and C and D (right) of the quadruple system Q 2237 + 0305. The histograms are built with the use of all available photometric data in filter *R* (see Fig. 1.17)

ng parameters γ and κ are different for these pairs, and besides, because of different distances of these pairs from the galaxy nucleus, the relative contributions from the stellar population and smoothly distributed (dark) matter can be expected to differ.

The width of amplification probability distribution for the A-B pair is noticeably larger than for C-D and is clearly bimodal. Also, higher probabilities of deamplification for the C and D pair as compared to A and B should be noted (positive values at the horizontal axis), which is also consistent with simulation results by Schechter and Wambsganss [99]. The further steps imply simulation of microlensing events for the source with the spatial structure and dimensions supposed to be known, and the subsequent comparison of the histograms simulated for various contributions of diffusely distributed matter with those built from the data of observations.

Figure 1.19 shows amplification probability distributions calculated for microlensing of image A of Q 2237 + 0305 for various relative contents of diffusely distributed matter κ_c/κ_{tot} , and for the zero contribution ε of the extended structure to the total quasar radiation (central source alone). Omitting the details, we will note only that the relative content of diffusely distributed matter κ_c/κ_{tot} and relative energy contribution of the extended structure have different effects on the microlensing magnification probability distribution. While variations of κ_c noticeably change the shape of the probability distribution and only slightly affect the range of brightness changes, the quantity ε controls mainly the width of the amplification probability distribution.

The distributions of amplification probability have been built for the first time for microlensing light curves of Q 2237 + 0305. It should be noted that in spite of pessimistic prediction for possibility to analyze variability statistics in

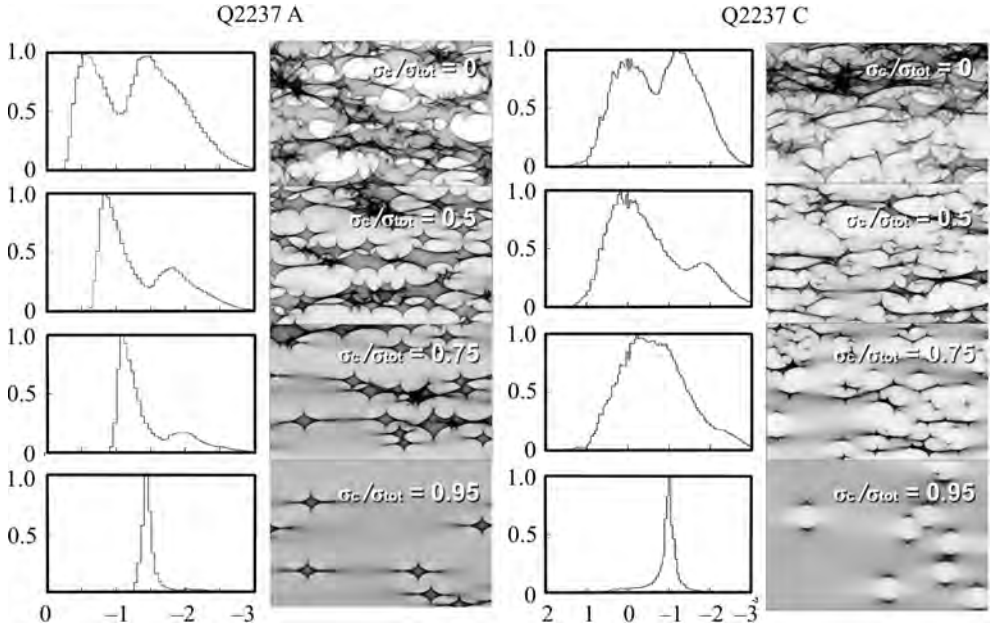


Fig. 1.19. Microlensing amplification probability distributions simulated for components A and C of the quadruple system Q 2237 + 0305 for four different contributions of the smoothly distributed (dark) matter into the total surface mass density (σ_c/σ_{tot}). The corresponding amplification maps are shown as well

this object, some attempts have been made earlier on the basis of observations of the first 8–10 years (for example, [64, 65]). But it was for the first time in [116] that the most full and homogeneous data sample in filter R for the time period of more than 20 years has been used to build the histograms of amplification probability distributions. A majority of the data points in the combined light curves are those obtained in observations with the 1.5-meter telescope of the high-altitude Maidanak Observatory.

Taking into account recent predictions for the expected dark matter fraction in the total mass of the galaxy matter, simulations in [116] were carried out for rather high values of the quantity κ_c/κ_{tot} , which varied from 0.5 to 0.95. The resulting histograms count in favor of smaller values of κ_c/κ_{tot} , however. At the present state of our knowledge, a preliminary conclusion is: the dark matter fraction in the total surface mass density in Q 2237 lens galaxy is $<50\%$ at the distance 0.8 Kpc from the galaxy nucleus, where the lensed images are situated.

1.4. Flux ratio anomalies as a key to detect dark matter substructures

It has long been known that the observed positions of multiple quasar macroimages are well predicted by smooth regular models of mass distribution in lensing galaxies, while their brightness ratios are reproduced by such models poorly, (e.g., [53, 61, 70]). The first systematic analysis of this problem called “flux ratio anomalies” was made by Mao & Schneider [70], who assumed that the anomalies of mutual fluxes of the components in some lenses can be explained by the presence of small-scale structures (substructures) in lensing galaxies or somewhere near the line of sight.

A popular model of forming hierarchical structures in the Universe with a dominant content of dark matter is currently known to poorly explain the observed distribution of matter at small scales. In particular, the expected number of satellite galaxies with masses of the order of $M_G \approx 10^8 M_\odot$ remained after the process of hierarchical formation is completed, is an order of magnitude larger than a number of dwarf galaxies with such masses actually observed within the Local Group [55, 77]. One of the solutions of this contradiction is a suggestion that some substructures, especially those with low masses, are not luminous.

Metcalf and Madau [72] were the first to note that the dark matter paradigm can naturally explain existence of substructures in galaxies lensing the remote quasars, as proposed by Mao and Schneider [70] to interpret the anomalies of mutual fluxes of quasar macroimages, and vice versa, confirmation of substructures with masses from $10^6 M_\odot$ to $10^8 M_\odot$ is capable of removing the contradiction between the predicted number of the low-mass satellite galaxies and that one actually observed. The idea turned out to be intriguing and was immediately taken up [11, 15, 25, 47, 73]. Investigation of flux ratio anomalies in gravitationally lensed quasars is presently believed to be a powerful tool in solving the problem of the dark matter abundance in the Universe. It is intensively discussed in numerous recent publications [19, 47–49, 59, 68, 73, 76, 79, 88–90].

The idea to detect substructures in lensing galaxies using the anomalies of flux ratios is based on fundamental relationships between coordinates and magnifications of the quasar images, which result from the general lens equation. These relationships have been obtained for the first time by Schneider & Weiss [108] and Mao [69] for several “smooth” distributions of lensing potential. In principle, the lens equation is capable of providing six independent relationships between the coordinates and magnifications for a quadruple lens, but only one of them can be checked with the data of observations. This is the well-known magnification sum rule for a source within a macrocaustic cusp, when three close images emerge: magnification of the central image must be equal

to the sum of magnifications of two outer images (Schneider & Weiss [108]). When the source lies near a caustic fold, two images of the same brightness must arise, [49].

Since the absolute values of magnifications in macroimages are unknown (the unlensed quasar cannot be observed), Mao & Schneider [70] proposed to use the dimensionless quantities

$$R_{cusp} = \frac{|\mu_1| - |\mu_2| + |\mu_3|}{|\mu_1| + |\mu_2| + |\mu_3|} = \frac{F_1 - F_2 + F_3}{F_1 + F_2 + F_3} \quad (1.25)$$

for three images emerging when the source is in a caustic cusp, and

$$R_{fold} = \frac{|\mu_m| - |\mu_s|}{|\mu_m| + |\mu_s|} = \frac{F_m - F_s}{F_m + F_s} \approx 0 \quad (1.26)$$

for the case when the source is at the caustic fold. Here, F_i are the fluxes from corresponding macroimages, indices m and s in the second expression denote the images at the minimum and saddle points of Fermat surface.

Ideally, cusp relation $R_{cusp} = 0$ and fold relation $R_{fold} = 0$ hold only when the source lies exactly at the caustic cusp or fold, respectively. In real lenses these relations hold only approximately. The authors of [48, 49] fulfilled a detailed study of asymptotic behaviours of the cusp and fold relations and calculated probability distributions of R_{fold} values for several smooth lens models. The value of deviation of R_{cusp} and R_{fold} from zero can be regarded as a measure of probability for the lensing potential to have substructures on scales smaller than the separation between the closest images [48, 49]. The authors of [49] warn, however, that for fold lenses, the observed violation of the fold relation may just mean that the source is far enough from a caustic fold.

It should be noted that, in principle, the observed anomalies of brightness ratios in images of gravitationally lensed quasars can be explained by other factors, such as microlensing by compact bodies and the effects of propagation phenomena in the interstellar medium (extinction and scattering, scintillations). These factors are studied in details by Kochanek & Dalal [59]. They concluded that substructures of cold dark matter is the best explanation for the flux ratio anomalies in some quadruply lensed quasars. They reminded also that, as was stated for the first time by Mao & Schneider [70], the fluxes of highly magnified saddle images are very sensitive to small gravitational perturbations as compared to low-magnification images and, even more importantly, these perturbations bias the fluxes towards demagnification, as was also noted by Schechter & Wambsganss [99].

Recently, Keeton & Moustakas [50] proposed a new approach to detection of the CDM substructures in strong gravitational lens systems, having shown that, in addition to distortions of flux ratios and astrometric perturbations,

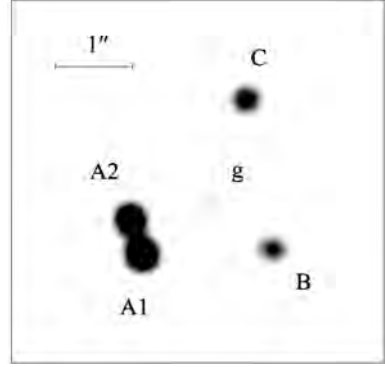


Fig. 1.20. PG 1115 + 080 from observations in filter R with the 1.5-m telescope of the Maidanak Observatory. The image was obtained by averaging of six frames from a series obtained in February 24, 2004, with a subsequent Richardson–Lucy processing

substructures may also perturb the time delays between images. Moreover, the time delay ratios were shown to be immune to the central concentration degeneracy in lens modeling. This finding is very challenging and can be expected to provide a new insight into the problem.

1.4.1. The A2/A1 flux ratio anomaly in PG 1115 + 080; a bit of history

The quadruply imaged quasar PG 1115 + 080 (Fig. 1.20) is one of the most promising candidates both to investigate the dark matter problem and to determine the H_0 value from measurements of the time delays between the image components. The source with a redshift of $z_S = 1.722$ is lensed by a galaxy with $z_G = 0.31$ [17, 37, 114], which forms four quasar images, with an image pair A1 and A2 bracketing the critical curve very close to each other. It is the second gravitationally lensed quasar discovered over a quarter of century ago, at first as a triple quasar, [133]. Later on, the brightest image component was resolved into two images separated by 0.48 arcsec. Further observations [23, 62, 123, 146] have provided positions of quasar images and information about the lensing object, which allowed construction of a macrolens model (e.g., [52]). They have shown, in particular, that the observed quasar image positions and fluxes and the galaxy position can be fit well by an ellipsoidal galaxy with an external shear rather than by only an ellipsoidal galaxy, or by a circular galaxy with an external shear. They noted that a group of nearby galaxies detected by Young et al. [146] could provide the needed external shear.

The A1 + A2 image pair in PG 1115 + 080 consists of a highly magnified minimum point image (A1) and saddle point image (A2). According to theoretical expectations (e.g. Schneider et al. [108]), the ratio of their fluxes must be close to 1.

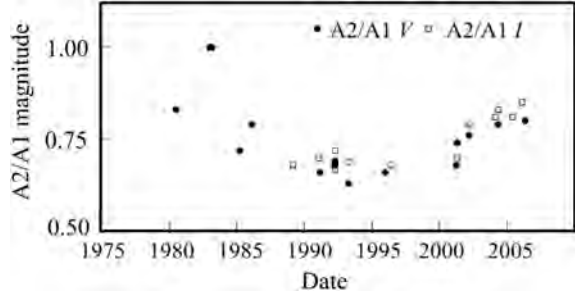
There are numerous measurements of the A2/A1 brightness ratio in PG 1115 + 080 made at different spectral ranges and at different epochs si-

Table 1.1. Estimates of the A2/A1 brightness ratios in PG 1115 + 030 for the time period 1980–2006 from all available data

Date	A2/A1 flux ratio	Spectral range	Instrument	Reference
1980 June	0.83	<i>V</i>	MMT	Hege et al. (1980)
1981 April 30	1.0	<i>B</i>	CFHT	Vanderriest (1986)
1983 March 8	1.0	<i>V</i>	Some	Some
1984 March 26	0.95	<i>B</i>	"	"
1985 March 16	0.75	<i>B</i>	"	"
1985 March 19	0.79	<i>V</i>	"	"
1986 February 19	0.79	<i>V</i>	CFHT	Christian (1987)
Some	0.8	<i>R</i>	Some	Some
"	0.79	<i>B</i>	"	"
1989 April	0.68	<i>I</i>	CFHT	Schechter (1993)
1991 March 3	0.66	<i>V</i>	HST	Kristian (1993)
Some	0.7	<i>I</i>	Some	Some
1992 April	0.67	<i>I</i>	Hiltner	Schechter 1993
Some	0.69	<i>V</i>	Some	Some
"	0.72	<i>I</i>	CTIO	"
"	0.68	<i>V</i>	Some	"
1993 April	0.69	<i>I</i>	Hiltner	"
Some	0.63	<i>V</i>	Some	"
1995 December 20	0.66	<i>V</i>	Magellan	Pooley et al. (2006)
1996 June 7	0.68	<i>I</i>	NOT	Courbin et al. (1997)
1997 November 17	0.64	<i>H</i>	HST	Impey et al. (1998)
?	0.52	<i>V</i>	HST	Morgan et al. (2008)
?	0.67	<i>I</i>	Some	Some
?	0.63	<i>H</i>	"	"
2001 March 26	0.66	<i>V</i>	Magellan	Pooley et al. (2006)
2001 April 20–27	0.74	<i>V</i>	1.5 m Maidanak	Vakulik et al.(2010)
Some	0.67	<i>R</i>	Some	Some
"	0.72	<i>I</i>	"	"
2002 March	0.76	<i>V</i>	"	"
Some	0.71	<i>R</i>	"	"
"	0.72	<i>I</i>	"	"
2004 February 22	0.81	Sloan <i>i'</i>	Magellan	Pooley et al.(2006)
2004 May 5–6	0.93	11.67 μm	Subaru	Chiba et al. (2005)
2004 Jan. 17–June 8	0.79	<i>V</i>	1.5 m Maidanak	Vakulik et al. (2010)
"	0.81	<i>R</i>	Some	Some
2004 Apr. 11–June 8	0.83	<i>I</i>	"	"
2005 June 07	0.81	Sloan <i>i'</i>	Magellan	Pooley et al. (2006)
2006 Jan. 5–Apr. 15	0.8	<i>V</i>	1.5 m Maidanak	Vakulik et al.(2010)
2006 Jan. 5–June 2	0.83	<i>R</i>	Some	Some
2006 Jan. 5–Apr. 15	0.85	<i>I</i>	"	"

nce 1980, which we tried to assemble in Table 1.1. Some of these data have been used by Pooley et al. [90] to analyse a long-term history of the A2/A1 variations in the optical band and to compare it with the X-ray data, (see, e.g.,

Fig. 1.21. A history of the A2/A1 flux ratios in PG 1115 + 080 from the data in filters *V* (filled circles) and *I* (empty squares) as listed in Table 1.1



Pooley et al. [88–90]). Fig. 2 from [90] demonstrates changes in the A2/A1 optical flux ratio during the time period from 1980 to 2008, and much more dramatic changes of this ratio in X-rays. Pooley et al. [90] noted that, according to all the observations since the system discovery, the A2/A1 flux ratio varied within 0.65–0.85.

In Table 1.1 the telescopes and filter bands are indicated for all estimates of the A2/A1 flux ratios. The table does not contain the results of the Chandra X-rays observations, which exhibited strong flux ratio anomaly and can be found, e.g., in [88–90]. Flux ratios in filters *V* and *I* from Table 1.1 are displayed in Fig. 1.21. These flux ratios behave similarly in time for both filters, and in general features resemble those in fig. 2 from [90]. Based upon their fig. 2, Pooley et al. [90] argue that the optical flux ratio anomaly in PG 1115 + 080 is slight and “nearly constant in time”. Our analysis described below has shown, however, that it is not quite so. Our Fig. 1.21, where the available previous data in *V* and *I* are supplemented by our measurements, shows that variations of the A2/A1 flux ratio in time are indeed rather small and slow. However, even if we exclude a marginal value for the date 1983, March 8 (Vanderriest et al. 1986 [123]), which equals 1 with the uncertainty of 0.1, we will have the A2/A1 flux ratio varying in some regular manner with the amplitude of about 0.15 during the last 25 years. Somewhere between 1991 and 1996, the ratio reached its minimal value of about 0.65 in filter *V*, and increased up to 0.8 by 2006. It should be noted that the fact that A2/A1 flux ratio varies in time is in itself an argument in favour of microlensing as the main reason for the anomalous flux ratio in PG 1115 + 080. Also, it should be mentioned that the A2/A1 flux ratio is slightly but steadily higher in filter *I* (empty squares) than in *V* (dark circles).

1.4.2. Light curves of PG 1115 + 080 in 2001–2006: flux ratio anomaly or microlensing?

Observations of PG 1115 + 080 were started at the 1.5-meter telescope of the high-altitude Maidanak Observatory (Central Asia, Uzbekistan) in 2001. Our algorithm for photometric image processing is similar to that applied to Q 2237 + 0305 and described in detail in [118]. The light curves of PG 1115 + 080 A1, A2, B,C in filter R for the time period from April 2001 to June 2006 are shown in Fig. 1.22.

In Fig. 1.20 one of the best Maidanak images of PG 1115 + 080 obtained through the R filter is shown. For better view, the image was restored with an algorithm similar to that known as the Richardson-Lucy iterative method. Thanks to the spatially resolved photometry of the A1 and A2 image pair in filters V , R and I , our data have made it possible to measure flux ratios for these components for five seasons of observations, and to study their behavior in time and in wavelength. As is noted above, deviations of flux ratios in quasar macroimages from the theoretical predictions (flux ratio anomalies) are presently believed to be diagnostic for detection of substructures in lensing galaxies, which may represent the dark matter.

Unfortunately, observations were not carried out in 2003, and the data are very scanty for the 2001 and 2002 seasons in all the three filters. The most numerous data were obtained in filter R . The data demonstrate noticeable variations of the quasar brightness, with the total amplitude reaching approximately 0.4 mag in 2004–2006, and smaller amplitudes of about

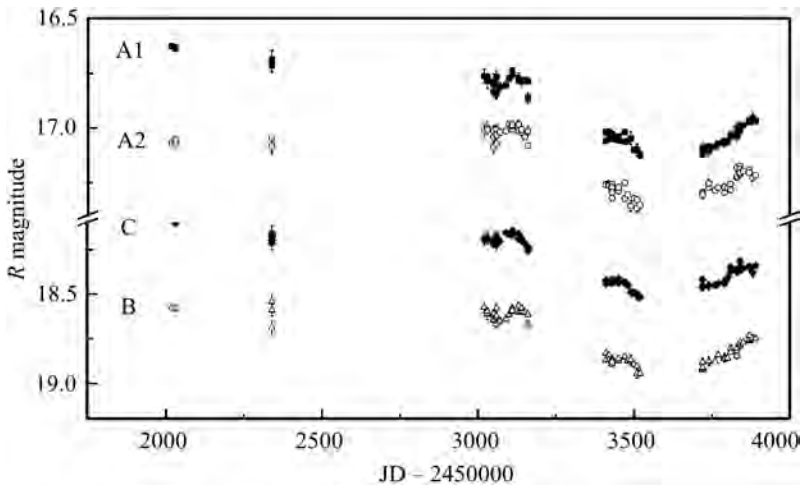


Fig. 1.22. The light curves of PG 1115 + 080 A1, A2, B, C from observations in filter R with the 1.5-m telescope of the Maidanak Observatory in 2001, 2002, 2004, 2005 and 2006 (Julian dates are at the horizontal axis)

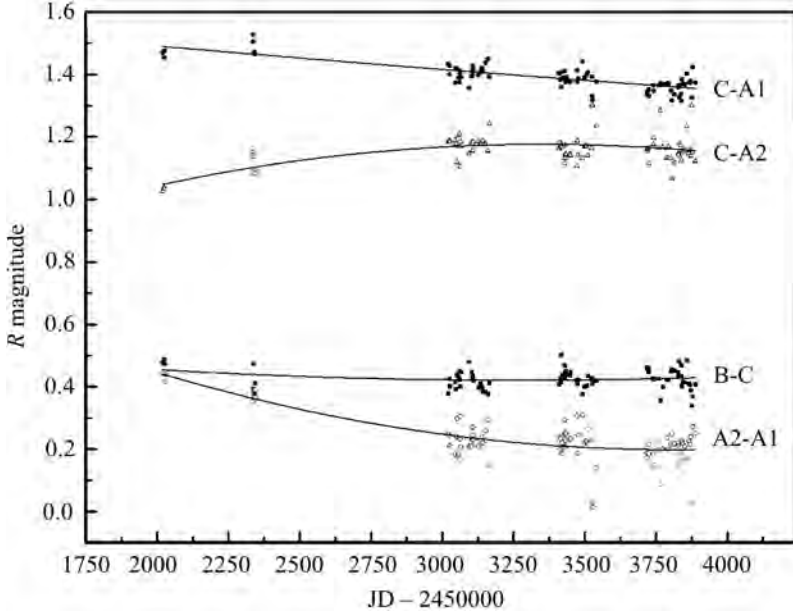


Fig. 1.23. Behaviors of the C-A1, C-A2, B-C and A2-A1 magnitude differences in time from the results of our photometry in filter R ; approximation by the second-order polynomials is shown

0.05 mag on a time-scale of two months, which are clearly seen in all the four light curves in 2004.

To determine which component (or components) exactly underwent microlensing, we addressed only our data as more homogeneous ones, and analysed behaviors in time of the long-term constituents of the A2-A1, C-A1, B-C and C-A2 magnitude differences for filters R and I . These difference light curves in filter R are shown in Fig. 1.23 taken from [117]. We did not correct the individual light curves for the time delays, which are small as compared to the characteristic time-scale of quasar flux variations. This might result only in some increase of the data points scatter with respect to the approximating curves, which are the second-order polynomials in Fig. 1.23.

The largest decrease of the magnitude difference is for the A2-A1 image pair — about 0.23 mag during 2001–2005. Pair C-A1 shows an almost linear decrease of the magnitude difference in time, with only 0.12 mag during 2001–2005. Since the mutual brightness of images B and C was almost invariable in 2001–2006, one might conclude that it is an image A1 that became fainter during this time period. But the C-A2 magnitude difference curve shows however, that, in addition to the obvious dimming of image A1, brightening of image A2 makes a certain contribution to the decrease of the A2-A1 magnitude difference in 2001–2005.

Therefore, we can conclude that a decay of A1 and brightening of A2 took place simultaneously in PG 1115 + 080 during 2001–2006. We may also conclude that it is the A1 image that underwent microlensing in the previous years, with the maximum near 1992–1995, as seen from Fig. 1.21, and the final phase in 2006 or, perhaps, later. With the previous data taken into account (see Fig. 1.21 and Table 1.1), the total time-scale of the 0.3-magnitude event is about 25 years. Image A2 underwent microlensing as well, with its rising branch occurring in 2001–2005. The brightening of image A2 reached about 0.14 mag during this time period, while the total brightening in the whole event may be larger. In calculation of the time delays, more subtle variations of the magnitude differences during 2004–2006 were found, (see Sec. 1.5).

It should be noted that our results are well consistent with measurements of the A1-A2 magnitude difference presented by Morgan et al. [79], who reported approximately 0.2-mag growth of this quantity during 2001–2006. However, they do not present the magnitude differences between other images and A1 or A2 separately, which has led us to a conclusion about the final phase of microlensing in image A1 and, seemingly, the initial phase of a microlensing event in image A2. This conclusion is also indirectly confirmed by the results of Pooley et al. [90], who reported a dramatic rise in the X-ray flux from image A2 between 2001 and 2008. Larger microlensing amplitudes at shorter wavelengths are often detected for many lensed quasars and are known to be naturally explained by smaller effective sizes of quasars at shorter wavelengths.

The observed time-scales and amplitudes of the microlensing brightness fluctuations are known to depend on the relative velocity of a quasar and lensing galaxy, and on the relationship between the source size and the Einstein ring radius of a microlens. For PG 1115 + 080, the expected duration of a microlensing event is estimated to be of the order of 10 to 20 years for the subsolar mass microlens, [16], well consistent with that in image A1 observed in 1980–2006.

Thus, if our interpretation of the observed brightness variations in the A1, A2, B and C images is valid, then the A2/A1 flux ratio would be expected to

Table 1.2. Flux ratios in PG 1115 + 080 as predicted by the most recent lens models and determined from the results of our photometry in 2006 (filter *I*); the uncertainty of our flux ratio estimates is 0.02 for all ratios

Lens model	A2/A1	B/A1	C/A1	B/C
Chiba (2002)	0.92	0.22	0.28	0.8
Chiba (2005)	0.92	0.22	0.28	0.79
Pooley (2006)	0.96		0.26	0.67
Pooley (2007)	0.92	0.21	0.27	0.78
This work	0.85	0.19	0.29	0.68

approach its undisturbed value in a few years, unless a new event takes place in at least one image. Our estimates of the A2/A1, B/A1, C/A1 and B/C flux ratios calculated from the photometry data of 2006, are presented in Table 1.2 along with the model predictions by Chiba [15], Chiba et al. [16], Pooley et al. [88, 89]. The ratios for filter *I* are presented, where the effect of microlensing is expected to be minimal as compared to *V* and *R*. As is seen from Table 1.2, the A1/A2 flux ratio is still less than predicted by the most recent lens models. However, when expressed in terms of R_{fold} , it would equal 0.08, which means that, according to simulations described in [49], this flux ratio is within a region admissible by a smooth lensing potential model for the finite source distances from the caustic fold, that is, it is not anomalous in the sense implied by Mao & Schneider [70].

1.5. Time delay lenses: impact on the Hubble constant and/or the dark matter problem

As is noted in Introduction, gravitationally lensed quasars are known to potentially provide estimates of the Hubble constant H_0 from measurements of the time delays between the quasar intrinsic brightness variations seen in different quasar images (Refsdal [94]). Since a phenomenon of gravitational lensing is controlled by the surface density of the total matter (dark plus luminous), it provides a unique possibility both to determine the value of H_0 and to probe the dark matter content in lensing galaxies and along the light paths in the medium between the quasar and observer.

By now the time delays have been measured in more than 20 gravitationally lensed quasars resulting in the values of H_0 that are generally noticeably less than the most recent estimate of H_0 obtained in the HST Hubble Constant Key Project with the use of Cepheids — $H_0 = 72 \pm 8 \text{ km s}^{-1} \text{ Mpc}^{-1}$ (Freedman et al. [32]). This discrepancy is large enough and, if the Hubble constant is really a universal constant, needs to be explained. A detailed analysis of the problem of divergent H_0 estimates inherent in the time delay method and the ways to solve it can be found, e.g., in [51, 57, 60, 93, 97, 102, 147], and in many other works.

The main sources of uncertainties in determining H_0 are:

- low accuracy of the time delay estimates caused by poorly sampled and insufficiently accurate light curves of quasar components, as well as by microlensing events and, as a rule, by low amplitudes of the quasar intrinsic variability;
- difference in the values of cosmological constants adopted in deriving H_0 ;
- invalid models of mass distribution in lensing galaxies.

The way to reduce the effect of the first source of errors is clear enough: more accurate and better sampled light curves of a sufficient duration are

needed. A choice of the cosmological model is usually just indicated — this is mostly a question of agreement. As to the third item, here the problem of estimating the Hubble constant encounters the problem of the dark matter abundance in lensing galaxies.

The problem of determining the Hubble constant from the time delay lenses is known to suffer from the so-called central concentration degeneracy, which means that, given the measured time delay values, the estimates of the Hubble constant turn out to be strongly model-dependent. In particular, models with more centrally concentrated mass distribution (lower dark matter content) provide higher values of H_0 , more consistent with the results of the local H_0 measurements than those with lower mass concentration towards the center (more dark matter). Moreover, it has long been noticed that the time delays are sensitive not only to the total radial mass profiles of lensing galaxies, but also to the small perturbations in the lensing potential, e.g., [9, 82, 136].

The Hubble constant — central concentration degeneracy is a part of the well known total problem of lensing degeneracies mentioned in Section 4: all lensing observables, even if they were determined with zero errors, are consistent with a variety of the mass distribution laws in lensing galaxies. A strategy for solving this non-uniqueness problem could be a search through a family of lens models that are capable of reproducing the lensing observables, [82, 135]. Then many models can be run in order to infer a probability density for a parameter under investigation, e.g. for H_0 , [135]. The most recent studies [93, 96] have shown that, in such an approach, discrepancy between the H_0 value determined from lensing and with other methods can be substantially reduced if non parametric models for mass reconstruction are used, which can provide much broader range of models as compared to the parametric ones.

In defining priors on the allowed space of lens models, it is naturally to assume that lensing galaxies in the time delay lenses are similar in their mass profiles to other early-type ellipticals, that are presently believed to be close to isothermal and admit the presence of the cold dark matter haloes. The isothermal models are also consistent with stellar dynamics, as well as with the effects of strong and weak lensing.

The quadruply lensed quasars are known to be more promising for solving these problems as compared to the two-image lenses since they provide more observational constraints to fit the lens model. Ten astrometric constraints can be presently regarded as measured accurately enough for most systems. This especially concerns the relative coordinates of quasar images. As to the lensing galaxies, their less accurate coordinates are often the only reliable information about the lensing object known from observations, with other important characteristics being derived indirectly. This situation is inherent, e.g. in PG 1115 + 080 with its faint, 0.31 — redshift galaxy. Of other observational constraints, the time delays and their ratios are very important. In quadruple

lenses, the time delay between one of the image pairs is usually used to determine H_0 , while the other ones form the H_0 -independent time delay ratios to constrain the lens model, [51].

The time delays in PG 1115 + 080 were determined for the first time by Schechter et al. [103] to be 23.7 ± 3.4 days between B and C, and 9.4 ± 3.4 days between A1 + A2 and C (image C is leading). Barkana [7] re-analyzed their data using another algorithm and reported $25_{-3.8}^{+3.3}$ days for the time delay between B and C, and this is quite consistent with 23.7 ± 3.4 days from [103]. But the other time delays, and hence the time delay ratio $r_{ABC} = \tau_{AC}/\tau_{BA}$ differ significantly: $r_{ABC} = 1.13_{-0.17}^{+0.18}$ as calculated by Barkana [7] and 0.7 ± 0.3 according to Schechter et al. [103]. Since 1997, just these values, either the first or the second ones, were being used to constrain the PG 1115 + 080 model and determine the Hubble constant.

Determination of the time delays has generated a flow of models for the system [15, 23, 40, 51, 52, 56, 76, 88, 97, 103, 115, 144, 145, 148], all illustrating how strongly the estimated value of H_0 depends on the adopted mass profile of the lens galaxy for the given values of time delays.

The detailed analysis of the uncertainties in determining Hubble constant from the time delay lenses can be found in, e.g., [57, 60, 102], where the paths to eliminate or at least to lessen the uncertainties have been also outlined. Kochanek & Schechter [60] indicated, in particular, the importance of improving the accuracy of time delays for PG 1115 + 080.

1.5.1. Time delays in PG 1115 + 080 from observations on the Maidanak Mountain: algorithm and results

The R light curves from our Maidanak data in 2004–2006 (Fig. 1.22) clearly demonstrate their applicability to determine the time delays. As compared to the data used by Schechter et al. [103] and Barkana [7], we were lucky to detect the quasar brightness variation with an amplitude of almost a factor of three larger, and with rather well-sampled data points within every season of observations. In addition, the accuracy of our photometry has made it possible to confidently detect flux variations with an amplitude as small as 0.05 mag that can be seen in the data of 2004.

The methodology to determine the time delays in pairs is simple enough and obvious. A common feature of all known methods of time delay measurements is the use, in one way or another, of the cross-correlation maximum or mutual dispersion minimum criteria, while they may differ in the algorithms of the initial data interpolation.

Analysis of the light curves of quasar images in pairs can also be applied when a lens consists of more than two images. To determine the time delays from the light curves shown in Fig. 1.22, we used another approach

however, as described in more detail in [119, 121]. Here we shall only remind the fundamentals of our approach.

We determined the source light curve from a joint analysis of light curves of all image components. The individual time delays for pairs of images can be then determined with respect to this model source light curve jointly from the corresponding system of equations.

Since, according to predictions of all lens models and to measurements in X-rays by Dai et al. [24] and Grant et al. [36], the time delay between images A1 and A2 does not exceed a small fraction of the day, their fluxes were summed to form a single curve, which we call the A light curve. Thus, we may write the following functional for the three light curves:

$$\Phi(\Delta t, \tau_0, \tau_1, \tau_2) = \frac{1}{3N} \sum_{j=0}^2 \sum_{i=0}^N \frac{[m_j(t_i) + dm_j - f(t_i, \Delta t, \tau_j)]^2}{\sigma_j^2(t_i)}, \quad (1.27)$$

where $m_j(t_i)$ are the data points in the light curve of the j th image at the time moments t_i ; dm_j and τ_j are the shifts of a corresponding light curve in stellar magnitude and in time, respectively, N is a number of points in the light curves, Δt is the parameter of the approximating function $f(t_i, \Delta t, \tau_j)$, and $\sigma_j^2(t_i)$ are the photometry errors.

We adopted $dm_0 = 0$ and $\tau_0 = 0$ in our calculations, that is, we fitted the light curves of B and C to the A light curve, and thus, dm_1 and dm_2 are the magnitude differences A-B and A-C, respectively. At given values of τ_1 and τ_2 , we minimize $\Phi(\Delta t, \tau_1, \tau_2)$ in dm_j and in coefficients of the approximating function. The values of minimum of $\Phi(\Delta t, \tau_1, \tau_2)$ were being looked for at a rectangular mesh τ_1, τ_2 with a step of 0.5 days in preliminary calculations, and of 0.2 days at a final stage. The values of τ_1, τ_2 corresponding to the minimal value of $\Phi(\Delta t, \tau_1, \tau_2)$ were adopted as the estimates of the time delays τ_{BA} and τ_{AC} . Fig. 1.24 shows a distribution of $\Phi(\Delta t, \tau_1, \tau_2) - \Phi_{min}$ in the space of parameters τ_{BA} and τ_{AC} calculated for parameter $\Delta t = 0.12$ years. Thus, our estimates of the time delays that can be read out at the τ_{AC} and τ_{BC} axes against the centre of contours in Fig. 1.24, are $\tau_{BA} = 4.4$, $\tau_{AC} = 12.0$ days. The time delay τ_{BC} is not an independent quantity in our method, and can be determined as a linear combination $\tau_{BC} = \tau_{BA} + \tau_{AC}$, that is, $\tau_{BC} = 16.4$ days.

To test our method for robustness and absence of systematics, and to estimate the accuracy inherent in our time delay measurements, we fulfilled a numerical simulation as described in detail in [121]. The simulated light curves of the components were obtained by shifting the approximating curve $f(t_i, \Delta t, \tau_j)$ by the proper time delays τ_1, τ_2 and magnitude differences, and by adding random quantities to imitate the photometry errors. We simulated 2000 light curves synthesized as described above, and calculated the resulting time delays using the procedure, which was exactly the same as in the

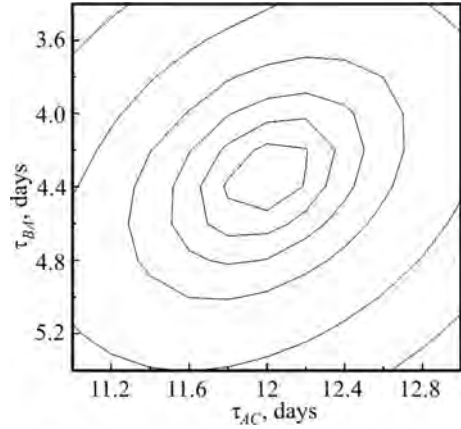


Fig. 1.24. Distribution of $\Phi(\Delta t, \tau_1, \tau_2) - \Phi_{min}$ in the space of parameters τ_{AC} and τ_{AB} . The innermost contour corresponds to $\Phi(\Delta t, \tau_1, \tau_2) - \Phi_{min}$ equalling 0.0001, with every next level twice as much than preceding

analysis of the actual light curves. The results of simulations were used to build the distribution functions for errors and to estimate the 95-percent confidence intervals. The final values of the time delays and the corresponding uncertainties are presented in Table 1.3, where they can be compared with the estimates reported in [103] and [7].

It is interesting to note that using only the data of 2004, where a small-amplitude turn-over in the light curves is detected, we obtained $\tau_{BA} = 5.0$ days, $\tau_{AC} = 9.4$ days, and $\tau_{BC} = 14.4$ days, consistent with the estimates obtained from the whole data set. However, simulation of errors for only the data of 2004 demonstrates noticeably larger uncertainties, as compared to those calculated from the entire light curve.

The light curves of images A, B and C shifted by the corresponding time delays and reduced to image A in magnitude are shown in Fig. 1.25 for the approximating function parameter $\Delta t = 0.12$ years. As is seen from this picture, the data points for all the three images are very well consistent with each other and with the approximating curve.

Thus we obtained the time delay values, which differ noticeably from those reported by Schechter et al. [103] and Barkana [7] and used in a variety of models of many authors to derive the Hubble constant value. The largest differences are for τ_{BC} and τ_{BA} : our estimate of τ_{BC} is a factor of 1.5 smaller,

Table 1.3. The time delays (days) for PG 1115 + 080 as reported earlier and in our previous work [121]

Author	τ_{BA}	τ_{AC}	τ_{BC}
Schechter (1997)	14.3 ± 3.4	9.4 ± 3.4	23.7 ± 3.4
Barkana (1997)	$11.7_{-3.2}^{+2.9}$	$13.3_{-2.2}^{+2.0}$	$25.0_{-3.8}^{+3.3}$
Vakulik(2009)	$4.4_{-2.5}^{+3.2}$	$12.0_{-2.0}^{+2.5}$	$16.4_{-2.5}^{+3.5}$

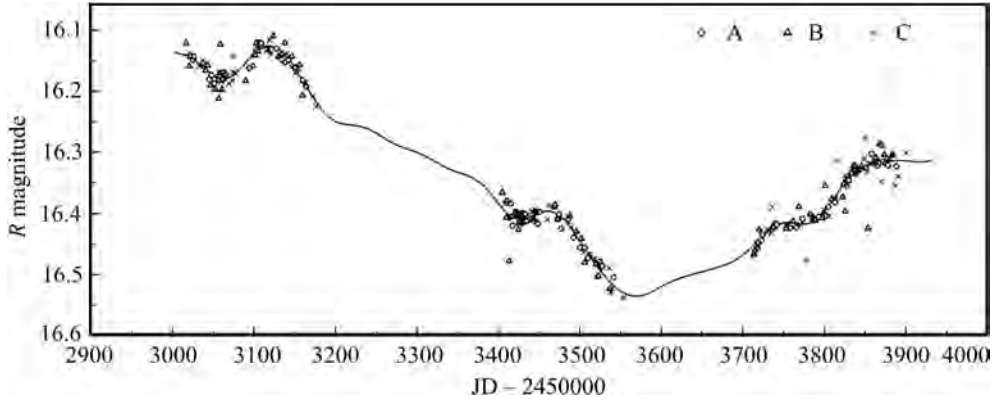


Fig. 1.25. The data points of the A, B and C light curves superposed with each other after shifting by the corresponding magnitude differences and time delays $\tau_{BA} = 4.4^{+3.2}_{-2.5}$, $\tau_{AC} = 12.0^{+2.5}_{-2.0}$ and $\tau_{BC} = 16.4^{+3.5}_{-2.5}$ obtained in this work. The parameter Δt of the approximating function $f(t_i, \Delta t, \tau_j)$ in Eq. (27) is 0.12 years

while for τ_{BA} , it is almost three times smaller as compared to the results of [103] and [7]. Meanwhile, our values of τ_{AC} are rather similar to those of Schechter and, especially, of Barkana.

As is noted above, the time delay between one of the image pairs, say, τ_{BC} , can be used to determine H_0 , while the time delay ratio $r_{ABC} = \tau_{AC}/\tau_{BA}$ is independent of the H_0 value and can be used to constrain the lens model. Most of the PG 1115 + 080 macromodels are consistent in predicting r_{ABC} to within 0.15. As far as can be expected from Table 1.3, the three measurements of time delays do not provide the time delay ratios consistent with each other and with model predictions. This can be seen from Table 1.4, where we collected several model predictions for r_{ABC} together with the measurements presented in [103] and [7] and those obtained in this work. Also, we presented here the time delay

Table 1.4. Time delay ratios τ_{AC}/τ_{BA} and τ_{AC}/τ_{BC} for PG 1115 + 080 as predicted by several lens models (the upper part of the table) and determined from the existing measurements of the time delays for the system (the last three lines)

Author	τ_{AC}/τ_{BA}	τ_{AC}/τ_{BC}
Schechter et al. (1997)	1.33–1.80	0.57–0.64
Keeton&Kochanek (1997)	1.35–1.47	—
Impey et al. (1998)	1.3	—
Chartas et al. (2004)	1.3	0.56
Keeton et al. (2009)	1.54	0.61
Schechter et al. (1997)	0.66	0.40
Barkana (1997)	1.14	0.53
Vakulik et al. (2009)	2.73	0.73

ratios $r_{CBA} = \tau_{AC}/\tau_{BC}$, which demonstrate better agreement between model predictions and measurements.

The time delay ratios calculated from measurements of Schechter and Barkana are seen to be lower as compared to the model predictions, while our measurements provide the estimates of this quantities exceeding the model predictions, especially for $r_{ABC} = \tau_{AC}/\tau_{BA}$, which is as large as 2.73 from our data. One should admit that such discrepancy is too large, since the largest r_{ABC} we have found in the literature is that calculated by Schechter et al. [103] for their isothermal ellipsoid model — $r_{ABC} = 1.8$.

The reason for this becomes qualitatively clear when addressing the data in Table 1.3: the shortest time delay τ_{BA} is measured with almost the same absolute error as the longest one, τ_{BC} , that is, of all the three time delays, τ_{BA} has the largest relative error. Therefore, we are far from arguing our value of τ_{BA} to be more trustworthy than those obtained by Schechter and Barkana. We regard, however, that the values of τ_{BC} and τ_{AC} are more reliable and trustworthy. Also, it should be noted that none of the macrolens models we could find in the literature predicts the values of τ_{BC} larger than 18^d , — the value 19.9^d from the unrealistic point-mass model in Schechter et al. [103] may hardly be taken into account.

To derive the estimates of the Hubble constant resulted from our measurements of the time delays, we have made use of the results of Schechter et al. [103], who calculated five models for the gravitational potential of PG 1115 + 080. The time delays τ_{AC} and τ_{BC} as predicted by their five models for $\Omega = 1$ and $H_0 = 100 \text{ km s}^{-1} \text{ Mpc}^{-1}$, and the corresponding estimates of H_0 obtained with their time delays are shown in Table 1.5 (columns 2–4). We remind that, according to Schechter et al. [103], model PMXS means a point mass with external shear, the ISXS model is an isothermal sphere with external

Table 1.5. Time delays as predicted by the lens models calculated by Schechter et al. [103] (columns 2, 3) and the values of the Hubble constant H_0 obtained from comparison of these time delays with those obtained by Schechter et al. [103] (column 4); the H_0 values ($\text{km s}^{-1} \text{ Mpc}^{-1}$) calculated for the same lens models, but with the time delays determined in this work (columns 5–7)

τ and H_0 from Schechter et al.				H_0 with τ from our work		
Model	τ_{AC}	τ_{BC}	H_0	$\tau_{AC} = 12.0^d$	$\tau_{BC} = 16.4^d$	H_0 (mean)
PMXS	12.5^d	19.9^d	84	104	121	113
ISXS	6.6^d	10.4^d	44	55	63	59
ISEP	9.7^d	15.1^d	64	81	92	86
ISIS	5.6^d	9.7^d	41	47	59	53
ISIS+	5.7^d	10.0^d	42	48	61	54

shear, and ISEP is an isothermal elliptical potential. The ISIS model uses a second isothermal sphere for a group of galaxies at approximately the same redshift as the main lensing galaxy (Young et al. [146]; Henry & Heasley [37]) to represent shear. In the ISIS + model, the uncertainty in the galaxy position is not regarded to be negligible, as in the ISXS and ISIS, but its coordinates were taken as two additional free parameters.

Columns 5 to 7 of Table 1.5 contain the H_0 values estimated for the Schechter et al. models with our values of the time delays for image pairs AC and BC separately (column 5 and 6), and the average between the pairs (column 7). We may conclude that, as could be expected, our new estimates of τ_{BC} and τ_{AC} provide higher values of the Hubble constant, which are closer to the most recent value obtained in the HST Key Project from observations of Cepheids (Freedman et al. [32]).

Thus, the time delays for PG 1115 + 080 obtained from our monitoring data in 2004–2006 differ from those determined by Schechter et al. [103] and Barkana [7] earlier. The differences for τ_{BA} and τ_{BC} are well beyond the uncertainties reported in both publications and determined in the present work. While our time delay estimates for images A and C are rather close to the two previous ones, the delays for two other image pairs can not be regarded as consistent even marginally.

The new estimates of time delays in PG 1115 + 080 provide additional support for the family of models close to isothermal, which admit existence of dark matter. As analyzed in details by Kochanek and Schechter [60], the estimates of H_0 with the use of time delay lenses are bounded by two limiting models: models with less dark matter (more centrally concentrated mass profiles) produce higher values of H_0 than those with more dark matter. In particular, the constant mass-to-light ratio models set an upper limit on estimates of H_0 , while the isothermal mass distribution models are responsible for the lower limit of H_0 . Our result is very important in this respect, since an isothermal model is preferred for the lensing galaxy in PG 1115 + 080 for the reasons listed in [102]: 1) the velocity dispersions observed for an ensemble of lensing galaxies are consistent with the fundamental plane relations for ellipticals; 2) a majority of the nearby galaxies, as well as those lensing galaxies for which the radial mass distributions can be measured, are very nearly isothermal. Since the PG 1115 + 080 lensing galaxy is by no means unusual, the isothermal hypothesis is most probable.

In conclusion, recently published observations of PG 1115 + 080 in filter R during almost the same time periods in 2004–2006 should be mentioned [79]. We have used their table 3 photometry to compare to our light curves. The quasar brightness fluctuations which allowed us to determine the time delays are seen in their A1 + A2 light curve quite well, but become undetectable in the B and C light curves because of a much larger scatter of the data points.

■

BIBLIOGRAPHY

1. E. Agol, B. Jones, O. Blaes, Keck Mid-Infrared imaging of QSO 2237 + 0305, *Astrophys. J.* **545** (2000), 657–663.
2. E. Agol, S.M. Gogarten, V. Gorjian, A. Kimball, Spitzer observations of a gravitationally lensed quasar, QSO 2237 + 0305, *Astrophys. J.* **697** (2009), 1010–1019.
3. D. Alcalde, E. Mediavilla, O. Moreau, J.A. Munoz, C. Libbrecht, L.J. Goicoechea, J. Surdej, E. Puga, Y. De Rop, R. Barrena, R. Gil-Merino, B.A. McLeod, V. Motta, A. Oscoz, M. Serra-Ricart, QSO 2237 + 0305 VR light curves from gravitational LensES international time project optical monitoring, *Astrophys. J.* **572** (2002), 729–734.
4. T. Anguita, R.W. Schmidt, E.L. Turner, J. Wambsganss, R.L. Webster, K.A. Loomis, D. Long, R. McMillan, The multiple quasar Q 2237 + 0305 under a microlensing caustic, *Astron. Astrophys.* **480** (2008), 327–334.
5. T. Anguita, C. Faure, A. Yonehara, J. Wambsganss, J. Kneib, G. Covone, D. Alloin, Integral field spectroscopy of four lensed quasars: analysis of their neighborhood and evidence for microlensing, *Astron. Astrophys.* **481** (2008), 615–627.
6. R. Antonucci, Unified models for active galactic nuclei and quasars, *Ann. Rev. Astron. Astrophys.* **31** (1993), 473–521.
7. R. Barkana, Analysis of time delays in the gravitational lens PG 1115+ 080, *Astrophys. J.* **489** (1997), 21–28.
8. N. Bate, R. Webster, J. Wyithe, Smooth matter and source size in microlensing simulations of gravitationally lensed quasars, *Mon. Not. R. Astron. Soc.* **381** (4) (2007), 1591–1596.
9. R. Blandford, R. Narayan, Fermat’s principle, caustics, and the classification of gravitational lens images, *Astrophys. J.* **310** (1986), 568–582.
10. P. Bliokh, A. Minakov, *Gravitational lenses* (Kiev, Naukova Dumka, 1989), (in Russian).
11. M. Bradač, P. Schneider, M. Steinmetz, M. Lombardi, L.J. King, R. Porcas, B 1422 + 231: The influence of mass substructure on strong lensing, *Astron. Astrophys.* **388** (2002), 373–382.
12. I. Burud, R. Stabell, P. Magain, F. Courbin, R. Ostensen, S. Refsdal, M. Remy, J. Teuber, Three photometric methods tested on ground-based data of Q 2237 + 0305, *Astron. Astrophys.* **339** (1998), 701–708.

13. D. Chelouche, Gravitational microlensing and the structure of quasar outflows, *Astrophys. J.* **629** (2005), 667–672.
14. A. Chernin, Dark energy and universal antigravitation, *Phys. Usp.* **51** (3) (2008), 253–282.
15. M. Chiba, Probing dark matter substructure in lens galaxies, *Astrophys. J.* **565** (2002), 17–23.
16. M. Chiba, Deciphering cold dark matter substructure with Subaru, *Astronomical Herald* **98** (2005), 783–789.
17. C.A. Christian, D. Crabtree, P. Waddell, Detection of the lensing galaxy in PG 1115 + 080, *Astrophys. J.* **312** (1987), 45–49.
18. D. Clowe, M. Bradač, A.H. Gonzalez, M. Markevitch, S.W. Randall, C. Jones, D. Zaritsky, A direct empirical proof of the existence of dark matter, *Astrophys. J. Let.* **648** (2006), L109–L113.
19. A.B. Congdon, C.R. Keeton, Multipole models of four-image gravitational lenses with anomalous flux ratios, *Mon. Not. R. Astron. Soc.* **364** (2005), 1459–1466.
20. A.B. Congdon, C.R. Keeton, S.J. Osmer, Microlensing of an extended source by a power-law mass distribution, *Mon. Not. R. Astron. Soc.* **376** (2007), 263–272.
21. J.H. Cooke, R. Kantowski, Time delay for multiply imaged quasars, *Astrophys. J. Let.* **195** (1975), L11–L14.
22. R.T. Corrigan, M.J. Irwin, J. Arnaud, G.G. Fahlman, J.M. Fletcher, P.C. Hewett, J.N. Hewitt, O. Le Fevre, R. McClure, C.J. Pritchett, D.P. Schneider, E.L. Turner, R.L. Webster, H.K.C. Yee, Initial light curve of Q 2237 + 0305, *Astron. J.* **102** (1991), 34–40.
23. F. Courbin, P. Magain, C. R. Keeton, C.S. Kochanek, C. Vandierriest, A.O. Jaunsen, J. Hjorth, The geometry of the quadruply imaged quasar PG 1115 + 080: implications for H_0 , *Astron. Astrophys.* **324** (1997), L1–L4.
24. X. Dai, G. Chartas, G.P. Garmire, M.W. Bautz, Chandra observations of the gravitational lenses PG 1115 + 080 and APM 08279 + 5255; determination of a time-delay and constraints on H_0 , in: American Astronomical Society, 199th AAS Meeting; *Bulletin of the American Astronomical Society*, **33** (2001), 1334.
25. N. Dalal, C.S. Kochanek, Direct detection of cold dark matter substructure, *Astrophys. J.* **572** (2002), 25–33.
26. W.H. de Vries, R.H. Becker, R.L. White, C. Loomis, Structure function analysis of long-term quasar variability, *Astron. J.* **129** (2005) 615–629.
27. A. Eigenbrod, F. Courbin, G. Meylan, E. Agol, T. Anguita, R.W. Schmidt, J. Wambsganss, Microlensing variability in the gravitationally lensed quasar QSO 2237 + 0305: the Einstein cross II. energy profile of the accretion disk, *Astron. Astrophys.* **490** (2008), 933–943.
28. A. Eigenbrod, F. Courbin, D. Sluse, G. Meylan, E. Agol, Microlensing variability in the gravitationally lensed quasar QSO 2237 + 0305: the Einstein cross I. spectrophotometric monitoring with the VLT, *Astron. Astrophys.* **480** (2008), 647–661.
29. M. Elvis, A structure for quasars, *Astrophys. J.* **545** (2000), 63–76.
30. M.V. Gorenstein, I.I. Shapiro, E.E. Falco, Degeneracies in parameter estimates for models of gravitational lens systems, *Astrophys. J.* **327** (1988), 693–711.
31. E.E. Falco, J. Lehar, R.A. Perley, J. Wambsganss, M.V. Gorenstein, VLA observations of the gravitational lens system Q 2237 + 0305, *Astron. J.* **112** (1996), 897–901.

32. W.L. Freedman, B.F. Madore, B.K. Gibson, L. Ferrarese, D.D. Kelson, S. Sakai, J.R. Mould, R.C. Kennicutt, H.C. Ford, J.A. Graham, J.P. Huchra, S.M.G. Hughes, G.D. Illingworth, L.M. Macri, P.B. Stetson, Final results from the hubble space telescope key project to measure the hubble constant, *Astrophys. J.* **553** (2001), 47–72.
33. R. Gil-Merino, J. González-Cadelo, L.J. Goicoechea, V.N. Shalyapin, G.F. Lewis, Is there a caustic crossing in the lensed quasar Q 2237 + 0305 observational data record?, *Mon. Not. R. Astron. Soc.* **371** (2006) 1478–1482.
34. U. Giveon, D. Maoz, S. Kaspi, H. Netzer, P.S. Smith, Long-term optical variability properties of the Palomar-Green quasars, *Mon. Not. R. Astron. Soc.* **306** (1999), 637–654.
35. Gopal-Krishna, C.S. Stalin, R. Sagar, P.J. Wiita, Clear evidence for intranight optical variability in radio-quiet quasars, *Astrophys. J. Let.* **586** (2003), L25–L28.
36. C.E. Grant, M.W. Bautz, G. Chartas, G.P. Garmire, Detection of X-Rays from galaxy groups associated with the gravitationally lensed systems PG 1115 + 080 and B 1422 + 231, *Astrophys. J.* **610** (2004), 686–690.
37. J.P. Henry, J.N. Heasley, High-resolution imaging from mauna kea — the triple quasar in 0.3-arc s seeing, *Nature* **321** (1986), 139–142.
38. A. Hewish, S.J. Bell, J.D.H. Pilkington, P.F. Scott, R.A. Collins, Observation of a rapidly pulsating radio source, *Nature* **217** (1968) 709–713.
39. D.W. Hogg, Distance measures in cosmology, e-print arXiv: 9905116v4 (1999).
40. C.D. Impey, E.E. Falco, C.S. Kochanek, J. Lehar, B.A. McLeod, H. Rix, C.Y. Peng, C.R. Keeton, An infrared einstein ring in the gravitational lens PG 1115 + 080, *Astrophys. J.* **509** (1998), 551–560.
41. M. Jaroszynski, J. Wambsganss, B. Paczynski, Microlensed light curves for thin accretion disks around schwarzschild and kerr black holes, *Astrophys. J. Let.* **396** (1992), L65–L68.
42. M.J. Jee, H.C. Ford, G.D. Illingworth, R.L. White, T.J. Broadhurst, D.A. Coe, G.R. Meurer, A. van der Wel, N. Bentez, J.P. Blakeslee, R.J. Bouwens, L.D. Bradley, R. Demarco, N.L. Homeier, A.R. Martel, S. Mei, Discovery of a ringlike dark matter structure in the core of the galaxy cluster Cl0024 + 17, *Astrophys. J.* **661** (2007), 728–749.
43. R. Kayser, S. Refsdal, R. Stabell, Astrophysical applications of gravitational micro-lensing, *Astron. Astrophys.* **166** (1986), 36–52.
44. R. Kayser, S. Refsdal, Detectability of gravitational microlensing in the quasar QSO 2237 + 0305, *Nature* **338** (1989), 745–746.
45. R. Kayser, P. Helbig, T. Schramm, A general and practical method for calculating cosmological distances, *Astron. Astrophys.* **318** (1997) 680–686.
46. D.J. Kedziora, H. Garsden, G.F. Lewis, Gravitational microlensing as a probe of the electron-scattering region in Q 2237 + 0305, *Mon. Not. R. Astron. Soc.* **415** (2011), 1409–1418.
47. C.R. Keeton, Cold dark matter and strong gravitational lensing: Concord or conflict?, *Astrophys. J.* **561** (2001), 46–60.
48. C.R. Keeton, B.S. Gaudi, A.O. Petters, Identifying lenses with Small-Scale structure. I. cusp lenses, *Astrophys. J.* **598** (2003), 138–161.

49. C.R. Keeton, B.S. Gaudi, A.O. Petters, Identifying lenses with Small-Scale structure. II. fold lenses, *Astrophys. J.* **635** (2005), 35–59.
50. C.R. Keeton, L.A. Moustakas, A new channel for detecting dark matter substructure in galaxies: Gravitational lens time delays, *Astrophys. J.* **699** (2009), 1720–1731.
51. C.R. Keeton, C.S. Kochanek, Determining the hubble constant from the gravitational lens PG 1115 + 080, *Astrophys. J.* **487** (1997), 42–54.
52. C.R. Keeton, C.S. Kochanek, U. Seljak, Shear and ellipticity in gravitational lenses, *Astrophys. J.* **482** (1997), 604–620.
53. S.M. Kent, E.E. Falco, A model for the gravitational lens system 2237 + 0305, *Astron. J.* **96** (1988), 1570–1574.
54. M. Kishimoto, R. Antonucci, O. Blaes, A. Lawrence, C. Boisson, M. Albrecht, C. Leipski, AGN accretion disks as spatially resolved by polarimetry, *J. Phys. Conf. Ser.* **131** (2008), 012039.
55. A. Klypin, S. Gottloeber, A.V. Kravtsov, A.M. Khokhlov, Galaxies in N-Body simulations: Overcoming the overmerging problem, *Astrophys. J.* **516** (1999), 530–551.
56. C.S. Kochanek, C.R. Keeton, B.A. McLeod, The importance of einstein rings, *Astrophys. J.* **547** (2001), 50–59.
57. C.S. Kochanek, What do gravitational lens time delays measure?, *Astrophys. J.* **578** (2002), 25–32.
58. C.S. Kochanek, Quantitative interpretation of quasar microlensing light curves, *Astrophys. J.* **605** (2004), 58–77.
59. C.S. Kochanek, N. Dalal, Tests for substructure in gravitational lenses, *Astrophys. J.* **610** (2004), 69–79.
60. C.S. Kochanek, P.L. Schechter, The hubble constant from gravitational lens time delays, in: *Measuring and Modeling the Universe, from the Carnegie Observatories Centennial Symposia*. Published by Cambridge University Press, as part of the *Carnegie Observatories Astrophysics Series*, 2004, p. 117.
61. C.S. Kochanek, The implications of lenses for galaxy structure, *Astrophys. J.* **373** (1991), 354–368.
62. J. Kristian, E.J. Groth, E.J. Shaya, D.P. Schneider, J.A. Holtzman, W.A. Baum, B. Campbell, A. Code, D.G. Currie, G.E. Danielson, S.P. Ewald, J.J. Hester, R.M. Light, C.R. Lynds, E.J. O’Neil, P.K. Seidelmann, J.A. Westphal, Imaging of the gravitational lens system PG 1115 + 080 with the hubble space telescope, *Astron. J.* **106** (1993), 1330–1336.
63. G.F. Lewis, R. Gil-Merino, Quasar microlensing: When compact masses mimic smooth matter, *Astrophys. J.* **645** (2006), 835–840.
64. G.F. Lewis, M.J. Irwin, The statistics of microlensing light curves – I. amplification probability distributions, *Mon. Not. R. Astron. Soc.* **276** (1995), 103–114.
65. G.F. Lewis, M.J. Irwin, The statistics of microlensing light curves. II. temporal analysis., *Mon. Not. R. Astron. Soc.* **283** (1996), 225–240.
66. G.F. Lewis, M.J. Irwin, P.C. Hewett, C.B. Foltz, Microlensing-induced spectral variability in Q 2237 + 0305, *Mon. Not. R. Astron. Soc.* **295** (1998), 573–586.
67. J. Lovegrove, R.E. Schild, D. Leiter, Discovery of universal outflow structures above and below the accretion disc plane in radio-quiet quasars, *Mon. Not. R. Astron. Soc.* **412** (2011), 2631–2640.

68. S. Mao, Y. Jing, J.P. Ostriker, J. Weller, Anomalous flux ratios in gravitational lenses: For or against cold dark matter?, *Astrophys. J. Let.* **604** (2004), L5–L8.
69. S. Mao, Gravitational microlensing by a single star plus external shear, *Astrophys. J.* **389** (1992), 63–67.
70. S. Mao, P. Schneider, Evidence for substructure in lens galaxies?, *Mon. Not. R. Astron. Soc.* **295** (1998), 587–594.
71. E. Mediavilla, S. Arribas, C. del Burgo, A. Oscoz, M. Serra-Ricart, D. Alcalde, E.E. Falco, L.J. Goicoechea, B. Garcia-Lorenzo, J. Buitrago, Two-dimensional spectroscopy reveals an arc of extended emission in the gravitational lens system Q 2237 + 0305, *Astrophys. J. Let.* **503** (1998), L27–L30.
72. R.B. Metcalf, P. Madau, Compound gravitational lensing as a probe of dark matter substructure within galaxy halos, *Astrophys. J.* **563** (2001) 9–20.
73. R.B. Metcalf, H. Zhao, Flux ratios as a probe of dark substructures in Quadruple-Image gravitational lenses, *Astrophys. J. Let.* **567** (2002), L5–L8.
74. A.A. Minakov, R.E. Schild, V.G. Vakulik, G.V. Smirnov, V.S. Tsvetkova, Microlensing events in gravitationally lensed quasar Q 2237 + 0305: stars or dark matter, in: *Problems of Practical Cosmology, Proceedings of the International Conference held at Russian Geographical Society, 23-27 June, 2008 in St. Petersburg, 2008*, pp. 180–186.
75. A. Minakov, V. Vakulik, *Statistical analysis of gravitational microlensing* (Kiev, Naukova Dumka, 2010) (in Russian).
76. M. Miranda, P. Jetzer, Substructures in lens galaxies: PG 1115 + 080 and B 1555 + 375, two fold configurations, *Astrophys. Space Sci.* **312** (2007), 203–214.
77. B. Moore, C. Calcáneo-Roldán, J. Stadel, T. Quinn, G. Lake, S. Ghigna, F. Governato, Dark matter in draco and the local group: Implications for direct detection experiments, *Phys. Rev. D* **64** (2001), 63508.
78. O. Moreau, C. Libbrecht, D. Lee, J. Surdej, Accurate photometric light curves of the lensed components of Q 2237 + 0305 derived with an optimal image subtraction technique: Evidence for microlensing in image a, *Astron. Astrophys.* **436** (2005), 479–492.
79. C.W. Morgan, C.S. Kochanek, X. Dai, N.D. Morgan, E.E. Falco, X-Ray and optical microlensing in the lensed quasar PG 1115 + 080, *Astrophys. J.* **689** (2008), 755–761.
80. M.J. Mortonson, P.L. Schechter, J. Wambsganss, Size is everything: Universal features of quasar microlensing with extended sources, *Astrophys. J.* **628** (2005), 594–603.
81. A.M. Mosquera, J.A. Munoz, E. Mediavilla, Detection of chromatic microlensing in Q 2237 + 0305 A, *Astrophys. J.* **691** (2009) 1292–1299.
82. M. Oguri, Gravitational lens time delays: A statistical assessment of lens model dependences and implications for the global hubble constant, *Astrophys. J.* **660** (2007), 1–15.
83. B. Paczynski, Gravitational microlensing by the galactic halo, *Astrophys. J.* **304** (1986), 1–5.
84. B. Paczynski, Gravitational microlensing at large optical depth, *Astrophys. J.* **301** (1986), 503–516.

85. T. Page, Qso's, the brightest things in the universe (quasi-stellar objects), *Astron. Soc. Pacif. Leaflets* **9** (1964), 161–166.
86. P.J.E. Peebles, *Principles of Physical Cosmology* (Princeton University Press, 1993).
87. B.M. Peterson, Reverberation mapping of active galactic nuclei, *Publ. Astron. Soc. Pac.* **105** (1993), 247–268.
88. D. Pooley, J.A. Blackburne, S. Rappaport, P.L. Schechter, W.-f. Fong, A strong X-Ray flux ratio anomaly in the quadruply lensed quasar PG 1115 + 080, *Astrophys. J.* **648** (2006), 67–72.
89. D.A. Pooley, X-Ray and optical flux ratio anomalies in quadruply lensed quasars, in: *American Astronomical Society Meeting 210; Bulletin of the American Astronomical Society*, Vol. 38, 2007, p. 238.
90. D. Pooley, S. Rappaport, J. Blackburne, P.L. Schechter, J. Schwab, J. Wambsganss, The dark-matter fraction in the elliptical galaxy lensing the quasar PG 1115 + 080, *Astrophys. J.* **697** (2009), 1892–1900.
91. M. Rabbette, B. McBreen, N. Smith, S. Steel, A search for rapid optical variability in radio-quiet quasars, *Astron. Astrophys. Suppl. Ser.* **129** (1998), 445–454.
92. R. Racine, Continuum and semiforbidden C III microlensing in Q 2237 + 0305 and the quasar geometry, *Astrophys. J. Let.* **395** (1992), L65–L67.
93. J.I. Read, P. Saha, A.V. Macciò, Radial density profiles of Time-Delay lensing galaxies, *Astrophys. J.* **667** (2007), 645–654.
94. S. Refsdal, On the possibility of determining hubble's parameter and the masses of galaxies from the gravitational lens effect, *Mon. Not. R. Astron. Soc.* **128** (1964), 307–310.
95. H. Rix, D.P. Schneider, J.N. Bahcall, Hubble space telescope wide field camera imaging of the gravitational lens 2237 + 0305, *Astron. J.* **104** (1992), 959–967.
96. P. Saha, L.L.R. Williams, Gravitational lensing model degeneracies: Is steepness All-Important?, *Astrophys. J.* **653** (2006), 936–941.
97. P. Saha, L.L.R. Williams, Non-parametric reconstruction of the galaxy lens in PG 1115 + 080, *Mon. Not. R. Astron. Soc.* **292** (1997), 148–156.
98. A.B. Saust, Determining the size of the emission line region in Q 2237 + 031 from microlensing, *Astron. Astrophys. Suppl. Ser.* **103** (1994) 33–37.
99. P.L. Schechter, J. Wambsganss, Quasar microlensing at high magnification and the role of dark matter: Enhanced fluctuations and suppressed saddle points, *Astrophys. J.* **580** (2002), 685–695.
100. P.L. Schechter, J. Wambsganss, G.F. Lewis, Qualitative aspects of quasar microlensing with two mass components: Magnification patterns and probability distributions, *Astrophys. J.* **613** (2004), 77–85.
101. P.L. Schechter, J. Wambsganss, The dark matter content of lensing galaxies at $1.5 R_e$, in: *International Astronomical Union Symposium no. 220*, held 21–25 July, 2003 in Sydney, Australia, 2004, p. 103.
102. C.S. Kochanek, P.L. Schechter, The hubble constant from gravitational lens time delays, in: *Measuring and Modeling the Universe, from the Carnegie Observatories Centennial Symposia*. Published by Cambridge University Press, as part of the *Carnegie Observatories Astrophysics Series*, 2004, p. 117.

103. P.L. Schechter, C.D. Bailyn, R. Barr, R. Barvainis, C.M. Becker, G.M. Bernstein, J.P. Blakeslee, S.J. Bus, A. Dressler, E.E. Falco, R.A. Fesen, P. Fischer, K. Gebhardt, D. Harmer, J.N. Hewitt, J. Hjorth, T. Hurt, A.O. Jaunsen, M. Mateo, D. Mehlert, D.O. Richstone, L.S. Sparke, J.R. Thorstensen, J.L. Tonry, G. Wegner, D.W. Willmarth, G. Worthey, The quadruple gravitational lens PG 1115 + 080: Time delays and models, *Astrophys. J. Let.* **475** (1997), L85–L88.
104. R. Schild, V. Vakulik, Microlensing of a ring model for quasar structure, *Astron. J.* **126** (2003), 689–695.
105. R. Schmidt, R.L. Webster, G.F. Lewis, Weighing a galaxy bar in the lens Q 2237 + 0305, *Mon. Not. R. Astron. Soc.* **295** (1998), 488–496.
106. P. Schneider, An analytically soluble problem in fully nonlinear statistical gravitational lensing, *Astrophys. J.* **319** (1987), 9–13.
107. P. Schneider, J. Ehlers, E.E. Falco, *Gravitational Lenses* (Springer-Verlag: Berlin, Heidelberg, New York, 1992).
108. P. Schneider, A. Weiss, The gravitational lens equation near cusps, *Astron. Astrophys.* **260** (1992), 1–13.
109. N.I. Shakura, R.A. Sunyaev, Black holes in binary systems. observational appearance, *Astron. Astrophys.* **24** (1973), 337–355.
110. V.N. Shalyapin, L.J. Goicoechea, D. Alcalde, E. Mediavilla, J.A. Munoz, R. Gil-Merino, The nature and size of the optical continuum source in QSO 2237 + 0305, *Astrophys. J.* **579** (2002), 127–135.
111. D. Sluse, R. Schmidt, F. Courbin, D. Hutsemékers, G. Meylan, A. Eigenbrod, T. Anguita, E. Agol, J. Wambsganss, Zooming into the broad line region of the gravitationally lensed quasar QSO 2237 + 0305 the einstein cross. III. determination of the size and structure of the c iv and c iii] emitting regions using microlensing, *Astron. Astrophys.* **528** (2011) 100–117.
112. D.N. Spergel, R. Bean, O. Doré, M.R. Nolta, C.L. Bennett, J. Dunkley, G. Hinshaw, N. Jarosik, E. Komatsu, L. Page, H.V. Peiris, L. Verde, M. Halpern, R. S. Hill, A. Kogut, M. Limon, S.S. Meyer, N. Odegard, G.S. Tucker, J.L. Weiland, E. Wollack, E.L. Wright, Three-Year wilkinson microwave anisotropy probe (WMAP) observations: Implications for cosmology, *Astrophys. J. Suppl. Ser.* **170** (2007), 377–408.
113. Y. Taniguchi, N. Anabuki, The electron-scattering region in seyfert nuclei, *Astrophys. J. Let.* **521** (1999), L103–L106.
114. J.L. Tonry, Redshifts of the gravitational lenses B 1422 + 231 and PG 1115 + 080, *Astron. J.* **115** (1998), 1–5.
115. T. Treu, L.V.E. Koopmans, The internal structure of the lens PG 1115 + 080: breaking degeneracies in the value of the hubble constant, *Mon. Not. R. Astron. Soc.* **337** (2002), L6–L10.
116. V.S. Tsvetkova, V.M. Shulga, V.G. Vakulik, G.V. Smirnov, V.N. Dudinov, A.A. Minakov, Search for dark matter using the phenomenon of strong gravitational lensing, *Kinemat. Phys. Celest. Bod.* **25** (2009) 28–37.
117. V.S. Tsvetkova, V.G. Vakulik, V.M. Shulga, R.E. Schild, V.N. Dudinov, A.A. Minakov, S.N. Nuritdinov, B.P. Artamonov, A.Y. Kochetov, G.V. Smirnov, A.A. Sergeev, V.V. Konichek, I.Y. Sinelnikov, A.P. Zheleznyak, V.V. Bruevich, R. Gaisin, T. Akhunov, O. Burkhanov, PG 1115 + 080: variations of the A2/A1

- flux ratio and new values of the time delays, *Mon. Not. R. Astron. Soc.* **406** (2010), 2764–2776.
118. V.G. Vakulik, R.E. Schild, V.N. Dudinov, A.A. Minakov, S.N. Nuritdinov, V.S. Tsvetkova, A.P. Zheleznyak, V.V. Konichek, I.Y. Sinelnikov, O.A. Burkxonov, B.P. Artamonov, V.V. Bruevich, Color effects associated with the 1999 microlensing brightness peaks in gravitationally lensed quasar Q 2237 + 0305, *Astron. Astrophys.* **420** (2004), 447–457.
119. V. Vakulik, R. Schild, V. Dudinov, S. Nuritdinov, V. Tsvetkova, O. Burkxonov, T. Akhunov, Observational determination of the time delays in gravitational lens system Q 2237 + 0305, *Astron. Astrophys.* **447** (2006), 905–913.
120. V.G. Vakulik, R.E. Schild, G.V. Smirnov, V.N. Dudinov, V.S. Tsvetkova, Q 2237 + 0305 source structure and dimensions from light-curve simulation, *Mon. Not. R. Astron. Soc.* **382** (2007), 819–825.
121. V.G. Vakulik, V.M. Shulga, R.E. Schild, V.S. Tsvetkova, V.N. Dudinov, A.A. Minakov, S.N. Nuritdinov, B.P. Artamonov, A.Y. Kochetov, G.V. Smirnov, A.A. Sergeyev, V.V. Konichek, I.Y. Sinelnikov, V.V. Bruevich, T. Akhunov, O. Burkxonov, Time delays in PG 1115 + 080: new estimates, *Mon. Not. R. Astron. Soc.* **400** (2009), L90–L93.
122. V.G. Vakulik, V.N. Dudinov, A.P. Zheleznyak, V.S. Tsvetkova, P. Notni, V.N. Shalyapin, B.P. Artamonov, VRI photometry of the einstein cross Q 2237 + 0305 at maidanak observatory, *Astron. Nachr.* **318** (1997) 73–80.
123. C. Vanderriest, G. Wlerick, G. Lelievre, J. Schneider, H. Sol, D. Horville, L. Renard, B. Servan, Variability of the gravitational mirage PG 1115 + 080, *Astron. Astrophys.* **158** (1986), L5–L8.
124. D. Walsh, R.F. Carswell, R.J. Weymann, 0957 + 561 A, B — twin quasistellar objects or gravitational lens, *Nature* **279** (1979), 381–384.
125. J. Wambsganss, B. Paczynski, N. Katz, A microlensing model for QSO 2237 + 0305, *Astrophys. J.* **352** (1990), 407–412.
126. J. Wambsganss, B. Paczynski, P. Schneider, Interpretation of the microlensing event in QSO 2237 + 0305, *Astrophys. J. Let.* **358** (1990) L33–L36.
127. J. Wambsganss, B. Paczynski, Expected color variations of the gravitationally microlensed QSO 2237 + 0305, *Astron. J.* **102** (1991), 864–868.
128. J. Wambsganss, Probability distributions for the magnification of quasars due to microlensing, *Astrophys. J.* **386** (1992), 19–29.
129. J. Wambsganss, B. Paczynski, Parameter degeneracy in models of the quadruple lens system Q 2237 + 0305, *Astron. J.* **108** (1994), 1156–1162.
130. J. Wambsganss, T. Kundic, Gravitational microlensing by random motion of stars: Analysis of light curves, *Astrophys. J.* **450** (1995), 19–26.
131. R.B. Wayth, M. O’Dowd, R.L. Webster, A microlensing measurement of the size of the broad emission-line region in the lensed quasar QSO 2237 + 0305, *Mon. Not. R. Astron. Soc.* **359** (2005), 561–566.
132. R.L. Webster, A.M.N. Ferguson, R.T. Corrigan, M.J. Irwin, Interpreting the light curve of Q 2237 + 0305, *Astron. J.* **102** (1991), 1939–1945.
133. R.J. Weymann, D. Latham, J. Roger, P. Angel, R.F. Green, J.W. Liebert, D.A. Turnshek, D.E. Turnshek, J.A. Tyson, The triple QSO PG 1115 + 08 — another probable gravitational lens, *Nature* **285** (1980), 641–643.

-
134. B.C. Wilhite, D.E. Vanden Berk, R.G. Kron, D.P. Schneider, N. Pereyra, R.J. Brunner, G.T. Richards, J.V. Brinkmann, Spectral variability of quasars in the sloan digital sky survey I. wavelength dependence, *Astrophys. J.* **633** (2005), 638–648.
 135. L.L.R. Williams, P. Saha, Pixelated lenses and H_0 from Time-Delay quasars, *Astron. J.* **119** (2000), 439–450.
 136. H.J. Witt, S. Mao, C.R. Keeton, Analytic time delays and H_0 estimates for gravitational lenses, *Astrophys. J.* **544** (2000), 98–103.
 137. H.J. Witt, S. Mao, Interpretation of microlensing events in Q 2237 + 0305, *Astrophys. J.* **429** (1994), 66–76.
 138. J.S.B. Wyithe, R.L. Webster, E.L. Turner, Interpretation of the OGLE Q 2237 + 0305 microlensing light curve (1997–1999), *Mon. Not. R. Astron. Soc.* **318** (2000), 1120–1130.
 139. J.S.B. Wyithe, R.L. Webster, E.L. Turner, A small source in Q 2237 + 0305?, *Mon. Not. R. Astron. Soc.* **318** (2000), 762–768.
 140. J.S.B. Wyithe, R.L. Webster, E.L. Turner, The distribution of microlensed light-curve derivatives: the relationship between stellar proper motions and transverse velocity, *Mon. Not. R. Astron. Soc.* **312** (2000) 843–852.
 141. J.S.B. Wyithe, E.L. Turner, Determining the microlens mass function from quasar microlensing statistics, *Mon. Not. R. Astron. Soc.* **320** (2001), 21–30.
 142. A. Yonehara, Evidence for a source size of less than 2000 AU in quasar 2237 + 0305, *Astrophys. J. Let.* **548** (2001), L127–L130.
 143. A. Yonehara, H. Hirashita, P. Richter, Origin of chromatic features in multiple quasars. variability, dust, or microlensing, *Astron. Astrophys.* **478** (2008), 95–109.
 144. J. Yoo, C.S. Kochanek, E.E. Falco, B.A. McLeod, The lens galaxy in PG 1115 + 080 is an ellipse, *Astrophys. J.* **626** (2005), 51–57.
 145. J. Yoo, C.S. Kochanek, E.E. Falco, B.A. McLeod, Halo structures of gravitational lens galaxies, *Astrophys. J.* **642** (2006), 22–29.
 146. P. Young, R.S. Deverill, J.E. Gunn, J.A. Westphal, J. Kristian, The triple quasar Q1115 + 080A, B, C – a quintuple gravitational lens image, *Astrophys. J.* **244** (1981), 723–735.
 147. A. Zakharov, Gravitational lenses and microlenses (Moscow, Yanus-K, 1997) (in Russian).
 148. H. Zhao, D. Pronk, Systematic uncertainties in gravitational lensing models: a semi-analytical study of PG 1115 + 080, *Mon. Not. R. Astron. Soc.* **320** (2001), 401–416.

2

CHAPTER

QUALITATIVE PROBLEMS IN GRAVITATIONAL MICROLENSING

V.I. Zhdanov, A.N. Alexandrov, E.V. Fedorova, V.M. Sliusar

Gravitational lensing theory contains a number of nice qualitative results and beautiful theorems [116, 147]. However, their use in case of a particular gravitational lens system (GLS) can be rather complicated, and this requires an additional numerical and analytical studies. The present article deals mainly with some topics on the latter subject basing on results of the authors. The main attention is paid to qualitative results, and to photometric and astrometric effects of gravitational microlensing that can be investigated either without using extensive numerical computations or where such computations can be reduced to a minimum.

The paper begins with a short overview of the most famous achievements obtained with the help of the gravitational lensing (Section 2.1) — weak lensing, strong lensing, MACHOs.

Then we discuss the High Amplification Events (HAE) in the microlensing processes [101, 116, 147] that are associated with the source crossings of the GLS caustics. In Sections 2.2, 2.3 we discuss approximation methods that allow us to get solutions of the lens equation near caustics with any prescribed accuracy. We consider both the cases of a fold caustic and a cusp point using a general procedure of a power reduction [151]. The case of the fold is considered in more detail. We find an analytic form of the solution using two approximation methods of [5, 6]. The results are applied to derive a formula for amplification of a point source near the fold and then to obtain the amplifications in case of some extended source models (Gaussian, power-law and

limb-darkening). In section 2.3.5 we discuss the possibility to distinguish different source models from observations of microlensed light curves.

Section 2.4 deals with astrometric microlensing on account of some of our results [8, 36, 149, 151, 153–155, 157]. We show that the trajectory of the image centroid depends strongly on the source size and on an external gravitational field (external shear); a microlensing by extended lenses is also discussed including a simple “toy” model of microlensing by extended dark matter clumps. Then we discuss a statistics of weak astrometric microlensing of a distant source by a large number of foreground point masses in case of a small optical depth; this case corresponds to a weak microlensing by the Milky Way objects. Variable gravitational field of moving foreground masses induces small motions of remote sources’ images. We present compact analytical relations describing a statistics of these motions; it is different in case of a continuous (e.g., dark) matter and discrete masses (stars). This effect leads to a small apparent rotation of an extragalactic reference frame.

2.1. Gravitational lensing: a short overview

2.1.1. General remarks

There is a number of books and reviews on basics and various applications of gravitational lensing (GL, see, e.g., [16, 77, 91, 101, 116, 147], see also the previous article of this book). In this view, we give in this Section only a short sketch of achievements of GL which are important for determination of mass distributions and for the dark matter (DM) investigations. This text does not purport to be a complete overview of all directions of GL.

The GL theory may be considered as a part of the wave propagation theory in a curved space-time describing the effect of gravitational field on the electromagnetic radiation in the geometrical optics approximation. The main lensing effects include the well-known light bending (leading also to the important effect of image deformation of lensed objects) and the gravitational time delay. The cosmological contributions are taken into account through the angular diameter distances in the equations of GL. Typical derivation of gravitational lens equations presupposes that GLS is almost static, i.e. velocities in the system are much less than the speed of light $c = 1$. Generalization to the relativistic case has been given in [79]; this result can be applied to the lensing by hypothetical oscillating cosmic strings. The only signal that presumably can be regarded as being associated with an object of this type has been found in observations of GLS Q 0957 + 561 images [114]. However, it seems that this signal may be a consequence of random factors in the quasar light curve, because since then no other observations have not revealed such relativistic objects.

All applications of GL dealing with real observations at present use the geometrical optics approximation. However, manifestations of the diffraction

and interference phenomena in GLS have also been studied by a number of authors (see bibliography in monographs [16, 91, 116], also [27, 83–85, 89, 146, 150]). Typically these effects are washed out due to a poor coherence of emitting astronomical sources. Nevertheless, it has been repeatedly pointed out that in some situations such effects deserve an astrophysical interest (see, e.g., [55, 56]). On the other hand, observations of the wave optics effects in GLS could present new independent confirmation of the General Relativity. A considerable attention (see, e.g., [89, 123] and references therein) has been paid to the wave effects in GLS in connection with the future gravitational wave experiments. Indeed, gravitational wave sources generate much larger wavelengths than in the case of the electromagnetic radiation, leading to much larger lensing masses where the wave effects must be significant.

2.1.2. GLS on different scales

Weak lensing. Weak GL is a unique probe of the mass distribution in the Universe. The method of weak GL uses the measurements of lensing induced distortions of the shapes of many distant galaxies and distribution of their orientations. This can be used to reconstruct the maps of a “cosmic shear” in certain sky regions and then to constrain the mass distributions in these regions. The very first attempts in this direction are probably due to Tyson et al. [127, 128]. A lensing signal can be estimated using some averaging over an ensemble of galaxies in a small region of the sky. The lensing image distortions induced by intergalactic gravitational fields are rather small, so one must have a deep survey to observe a sufficiently large number of the galaxies in order to detect the cosmic shear signal on the background of proper ellipticities of these galaxies.

A detailed bibliography on the weak GL can be found in reviews [53, 57, 63, 95]. Statistics of the ellipticities of galaxy images with different redshifts can be related to the power spectrum of cosmological mass fluctuations in the Universe and more delicate statistical characteristics [61, 68, 69], see also reviews [57, 63, 77].

One of the most well known applications of the weak GL is related to the investigations of the Bullet Cluster [22, 23] yielding a direct confirmation of the DM existence. Determination of mass distributions in this cluster by means of the weak GL provides a convincing argument against theories that do not recognize DM and try to explain the missing mass effects by an alteration of the gravitational force law [53].

Extragalactic GLS. The gravitational lensing manifest itself most vividly in extragalactic GLSs. Typical extragalactic GLS contains a remote quasar and a foreground galaxy or cluster on its line of sight. Several tenth of such systems can be found in the Castle Lenses database

(<http://www.cfa.harvard.edu/castles/> [76]). We shall mention only a few very interesting GLSs.

- The First Lens Q 0957 + 561 (1979) [134]. Two images are separated by 6 arcsec. The redshift of the lensing galaxy is $z_l = 0.36$ and that of the source $z_s = 1.41$.

- The Nearest Lensing Galaxy is in the system Q 2237 + 0305 [62] (Einstein Cross, 1985). This GLS has rather symmetric positions of four images separated by 1–2 arcsec; $z_l = 0.04$, $z_s = 1.69$. Due to the small distance to the lensing galaxy this is a unique GLS to study microlensing.

- The Nearest Gravitationally Lensed Quasar is in the system 1RXS J 113155.4–123155 [122]. In this GLS four quasar images are observed along with the arc representing the image of the host galaxy of the quasar; $z_l = 0.29$, $z_s = 0.66$. This is not of course the nearest of all lensed objects including, e.g., stars of our Galaxy or stars in the Magellanic Clouds.

- The Largest Gravitational Lens is recently discovered MACS J0717.5 + 3745 ($z_l = 0.546$, $z_s \sim 2.5$) [158]. This is a cluster of galaxies having the Einstein ring radius $\theta_E = 55 \pm 3''$ corresponding to $r_E = 350 \pm 20$ kpc at the cluster redshift, the mass inside is $\sim 7 \cdot 10^{14}$ solar masses.

There are several images of one quasar in extragalactic GLS; these images may be stretched to form luminous arcs. The typical angular separation between the images are of the arcsecond order, however, as in the case of the latter example, there may be GLS with separations of several tenth of arcseconds (cf. [54, 96, 98]). It is sometimes rather difficult to distinguish such lenses from the real quasar pairs [156]. Arcminute-separation GLS are very helpful to measure the mass function of massive galaxy clusters; by comparison with the results of large scale structure simulation they can provide an important test of the standard cosmological model.

Besides the geometry of the images and the redshifts, the important characteristics of GLS are the relative delay times between images with different angular positions. The delay times can be determined experimentally by considering correlations between the light curves of the different quasar images. Refsdal [107, 108] was the first to point out that information on delay times and angles between the source images can be used for an independent determination of the Hubble constant H_0 . Indeed, the angular distances in the lens equation and in the equation for the time delay involve the cosmological parameters. In the very first paper Refsdal [107] considered the spherically symmetric compact deflecting galaxy; in this case the galaxy mass can be determined from observations along with H_0 . However, for a general GLS the result of this determination depends on the model of mass distribution in the lensing galaxy.

In a more general case, provided that mass distributions in lensing galaxies were known, one can derive an estimate of cosmological parameters Ω_Λ, Ω_M .

The main drawback of this method is that it is also model dependent [73, 74] in view of the unknown distribution of DM mass. A statistical averaging over a larger number of GLSs might improve this situation; nevertheless it would be difficult to prove that the result does not involve systematic errors.

Extragalactic microlensing. The gravitational field of a lensing galaxy in GLS is very inhomogeneous due to gravitational fields of stars on the line of sight. This strongly affects the apparent brightness of a quasar image leading sometimes to HAE [19, 20]. The brightness variations are independent in different images of multiply imaged quasars; therefore comparison of light curves of different images allows one to distinguish them from proper brightness variations of the lensed quasar. Such effects due to the local inhomogeneities of the gravitational field are known as “*microlensing*” ones (as distinct from *macrolensing* due to smoothed field of the lensing galaxy). Mosquera & Kochanek [94] present estimates of characteristic microlensing parameters for a sample of 87 GLSs. In particular, the median source crossing time scale is $t_s \sim 7$ months; and during 10 years roughly half the lenses will show features of the microlensing activity [94].

Lensing on the Milky Way objects. The events with a considerable brightness amplification of remote objects are possible in the Milky Way microlensing. When a foreground star passes near the line of sight to a remote star, e.g., either in Magellanic Clouds or in the bulge of the Milky Way, the brightness of the latter can increase several times. The probability of microlensing of a single remote star is less than 10^{-6} , so Paczynski [99] proposed an idea of simultaneous observations of a few million stars in the Magellanic Clouds. Soon this idea became technically possible [2, 10, 13, 129] and three teams started a hunt for microlensing events towards Magellanic Clouds and then towards the Galactic bulge: OGLE (The Optical Gravitational Lensing Experiment; <http://ogle.astrouw.edu.pl/>), EROS (Expérience pour la Recherche d’Objets Sombres; <http://eros.in2p3.fr/>), MACHO (MASSive Compact Halo Object; <http://en.wikipedia.org/wiki/MACHO>). Later a number of new teams joined to these investigations. These studies yielded estimates of the microlensing optical depth in different directions and the mass fraction of compact objects in different parts of the Galaxy, e.g., in the Galactic Halo. The latter is especially important for DM investigations, because it is the Halo that seems to contain the bulk of the Milky Way dark matter. Though thousands of microlensing events have been detected in the course of monitoring in several directions, but very small portion of these events can be associated with true MACHOs (i.e., Halo Objects). Moreover, the stars within the Magellanic Clouds themselves seem to be microlenses, and the contribution of MACHOs to the Halo dark matter is rather small [109]. This analysis has been confirmed by further observations [124]. EROS found that the mass fraction of microlenses residing in the Halo is less than 8% and MACHOs of the stellar mass are ruled out as

the primary occupants of the Milky Way Halo. In a quite recent study OGLE team claims more definitely [142–144] that the Galactic invisible matter is not made of compact objects in the mass range $10^{-7}M_{Sun} < M < 5M_{Sun}$. This indicates that the Milky Way’s dark matter is unlikely to form compact objects in the subsolar-mass range.

It is an important advantage of star-by-star microlensing that this process typically deals with a stable source brightness, nearly isolated lenses (very small optical depth) and simple behavior of the corresponding light curves. Nevertheless, microlensing of quasars on a Galactic objects is also discussed [136] having in mind that the proper brightness variations may be discriminated by taking into account the larger amplitude of HAE and the forms of microlensing light curves in the multi-band photometry.

Though the Galactic events are not limited to the microlensing by single stars. There is a lot of events of microlensing by binary star and by star with a planetary system [135]. In case of binary systems we have a more complicated structure of the amplification pattern; in particular, the caustic crossing events are possible.

2.2. Approximate solutions of the lens equation in the vicinity of the high amplification events

2.2.1. Basic equations and notations

Typically HAE occurs when the source passes near the singular point (caustic) of the lens mapping in the source plane or crosses this point. Investigation of the lens mapping near singular points is an important part of the HAE studies. It is well known that the only stable caustics of the two-dimensional mapping are folds and cusps [101, 116]. The crossing of the fold caustic is most probable (see, e.g., [43] in case of Q 2237 + 0305), though the role of the cusps is also significant [116].

General notions of the gravitational lensing can be found e.g. in book [116]. We use the normalized lens equation in the form:

$$\mathbf{y} = \mathbf{x} - \nabla\Phi(\mathbf{x}), \quad (2.1)$$

$\Phi(\mathbf{x})$ is the lens mapping potential; this equation relates every point $\mathbf{x} = (x_1, x_2)$ of the image plane to the point $\mathbf{y} = (y_1, y_2)$ of the source plane. In the general case, there are several solutions $\mathbf{X}_{(i)}(\mathbf{y})$ of the lens equation (2.1) that represent images of one point source at \mathbf{y} ; we denote solution number with the index in parentheses.

In case of no continuous matter on the line of sight the potential must be a harmonic function $\Delta\Phi = 0$. Below we will assume that this condition is fulfilled in the considered neighborhood of the critical point. We note however, if we suppose that during HAE the continuous matter density is constant, the lens

equation may be represented in the same form by a suitable renormalization of the variables.

The amplification of a separate image of a point source is $|J|^{-1}$, where $J(\mathbf{x}) \equiv |D(\mathbf{y})/D(\mathbf{x})|$ is the Jacobian of the lens mapping. The critical curves of the lens mapping (2.1) are defined by equation $J(\mathbf{x}) = 0$; they are mapped onto the caustics on the source plane. The stable critical points of two-dimensional mapping may be folds and cusps only, the folds being more probable in HAE. When a point source approaches the fold caustic from its convex side, two of its images approach the critical curve and their amplification tends to infinity; they disappear after the source crossing of the caustic. These two images are called critical. In case of the cusp point there can be either three or one bright images near the critical curve depending on location of the source inside or outside of the caustic.

Below we outline general procedures that allow to find approximate solutions of the lens equation near folds and cusps, the main attention being paid to the case of the folds. The standard consideration of the caustic crossing events deals with the Taylor expansion of the potential near some point p_{cr} of the critical curve in the image plane. Let this point be the coordinate origin and we suppose that (2.1) maps p_{cr} onto the coordinate origin on the source plane. We assume that the lens equation gives the coordinates of a point source as analytic functions of its image coordinates measured from the critical point p_{cr} . The problem is to construct the inverse dependence of the image position as functions of the source coordinates.

2.2.2. Approximate solutions of the lens equation near the fold

The lens equation near a fold can be expanded in powers of local coordinates; in the lowest order of this expansion the caustic is represented by a straight line; so this approximation is often referred to as “the linear caustic approximation”. In this approximation the point source flux amplification depends on the distance to the caustic and contains two parameters [116]. In most cases the linear caustic approximation is sufficient to treat the observed light curves over the range of HAEs at modern accuracy of the flux measurement. The need for a modification of this formula, e.g. by taking into account the caustic curvature, is nevertheless being discussed for a long time [38, 100, 120]. One may hope that future improvement of the photometric accuracy will make it possible to obtain additional parameters of the lens mapping, which are connected to the mass distribution in the lensing galaxy. At the same time, consideration of the “post-linear” terms is sometimes sensible in order to explain even the presently available observational data [5, 6]. Note also that the corrections to the amplification on a macro-lensing level were the

subject of investigations in connection with the problem of “anomalous flux ratios” [71].

We consider two different methods. The first one deals with analytical expansions in powers of a small parameter, however it results in non-analytical functions of coordinates leading to non-integrable terms in the amplification. The second method does not lead to such problems though it uses a somewhat more complicated representation of the solutions of the lens equation (containing roots of analytical functions). Both methods agree with each other in a common domain of validity; moreover, we use the second method to justify some expressions in the amplification formulas in terms of distributions to validate applications to the extended source models.

Lens mapping near the fold. We consider the folds in case of a harmonic potential, that is in case of no continuous matter on the line of sight. Nevertheless, we note that in a more general case we obtain analogous results [3].

For the harmonic potential near the fold one can write (see, e.g., [116])

$$\begin{aligned} y_1 &= 2x_1 + a(x_1^2 - x_2^2) + 2bx_1x_2 + c(x_1^3 - 3x_1x_2^2) - \\ &\quad - d(x_2^3 - 3x_2x_1^2) + gx_2^4 + \dots, \\ y_2 &= b(x_1^2 - x_2^2) - 2ax_1x_2 + d(x_1^3 - 3x_1x_2^2) + \\ &\quad + c(x_2^3 - 3x_2x_1^2) + fx_2^4 + \dots, \end{aligned} \quad (2.2)$$

a, b, c, d, g, f are the expansion coefficients. If the y_2 axis is directed toward the convexity of the caustic, then $b < 0$ (at the fold points $b \neq 0$).

First we shall use a regular procedure [6] in order to construct solutions of Eqs. (2.2) with a desired accuracy. This procedure is useful to study the light curve of the point source, which has a trajectory crossing the fold caustic under some non-zero angle. For $y_2 > 0$ we substitute

$$y_i \rightarrow t^2 \tilde{y}_i; \quad x_1 \rightarrow t^2 \tilde{x}_1, \quad x_2 \rightarrow t \tilde{x}_2, \quad (2.3)$$

where $i = 1, 2$ and t may be considered as a (small) parameter describing a vicinity to the caustic. In fact for small y_i and for an appropriate choice of t we can work with $\tilde{y}_i = O(1)$, $\tilde{x}_i = O(1)$. This is a formal substitution that makes easier operations with different orders of the expansion. On the other hand for small y_i the value $t = 1$ also may be considered as “small”; in this case $y_i = \tilde{y}_i$. Therefore, in the other treatment, after performing calculations we can put $t = 1$ and thus return to the initial variables.

Substitution of (2.3) into Eqs.(2.2) yields

$$\tilde{y}_1 = 2\tilde{x}_1 - a\tilde{x}_2^2 + tF(t, \tilde{x}_1, \tilde{x}_2), \quad \tilde{y}_2 = -b\tilde{x}_2^2 + tG(t, \tilde{x}_1, \tilde{x}_2), \quad (2.4)$$

where F, G are analytical functions of all their variables. However, it should be emphasized that in fact we need finite orders of t for some approximation order; therefore we always deal with polynomials of a finite order in powers of $t, \tilde{y}_1, \tilde{y}_2, \tilde{x}_1, \tilde{x}_2$.

Direct expansion of a solution in powers of t . System (2.4) can be considered for fixed \tilde{y}_i and variable t , then the solution of (2.4) forms a curve which is useful to study a local behavior of critical image trajectories [7]. In this case $t = 0$ corresponds to a crossing of a caustic by a point source and t^2 may be considered as a time counted from the moment when two critical images appear. The results of [7] show that the solutions of Eqs. (2.2) in terms of \tilde{x}_i can be represented as the expansions in powers of t . This can be seen directly for $y_2 > 0, b < 0$ if we rewrite (2.4) in the form ready for iterations

$$\begin{aligned} \tilde{x}_1 &= \frac{1}{2} [\tilde{y}_1 - a\tilde{y}_2/b - tF_1(t, \tilde{x}_1, \tilde{x}_2)], \\ \tilde{x}_2 &= \varepsilon \{-\tilde{y}_2/b\}^{1/2} \left[1 - \frac{1}{2}(t/\tilde{y}_2)G(t, \tilde{x}_1, \tilde{x}_2) + \dots \right], \end{aligned} \quad (2.5)$$

$F_1 \equiv F - aG/b$, where either $\varepsilon = 1$ or $\varepsilon = -1$ corresponding to different critical images.

Therefore, from the very beginning we can look for the solutions in the form

$$\tilde{x}_1 = \tilde{x}_{10} + \tilde{x}_{11}t + \dots, \quad \tilde{x}_2 = \tilde{x}_{20} + \tilde{x}_{21}t + \dots \quad (2.6)$$

From zeroth iteration we have

$$\tilde{x}_{10} = \frac{1}{2} \left[\tilde{y}_1 - \frac{a}{b}\tilde{y}_2 \right], \quad \tilde{x}_{20} = \varepsilon \left\{ \frac{\tilde{y}_2}{|b|} \right\}^{1/2}. \quad (2.7)$$

The first iteration yields

$$\tilde{x}_1 = \tilde{x}_{10} - \frac{t}{2}F_1(0, \tilde{x}_{10}, \tilde{x}_{20}), \quad \tilde{x}_2 = \tilde{x}_{20} \left[1 - \frac{t}{\tilde{y}_2}G(0, \tilde{x}_{10}, \tilde{x}_{20}) + \dots \right],$$

whence we obtain $\tilde{x}_{11}, \tilde{x}_{21}$ and so on.

Evidently, for every step of the iterative procedure we obtain some polynomials of t , but the dependence on $\tilde{y}_2 > 0$ is not analytical one. Moreover, the higher orders of approximation involve higher orders of $(\tilde{y}_2)^{-1}$ leading to formally non-integrable terms in the amplification factor (see below). This is a well-known phenomenon when we represent a non-analytical expression (e.g., square root) as formal asymptotic expansion in powers of some parameter¹.

Alternative representation of solutions. Now we aim to obtain the other representation of the solution $\mathbf{x} = (x_1, x_2)$ as an explicit algebraic function of analytical expansions in powers of coordinates $\mathbf{y} = (y_1, y_2)$ of the source

¹ For example, expansion in powers of t : $\sqrt{x+t} = x^{1/2} + t/(2x^{1/2}) - t^2/(8x^{3/2}) + \dots$

plane. For this purpose we use a power reduction which allows to obtain a simple approximate form of the lens equation on every step of the procedure.

The first equation of system (2.5) for sufficiently small t can be solved iteratively with respect to \tilde{x}_1 yielding a solution in the form

$$\tilde{x}_1 = \frac{1}{2} \left(\tilde{y}_1 - \frac{a}{b} \tilde{y}_2 \right) + tF_2(t, \tilde{y}_1, \tilde{y}_2, \tilde{x}_2). \quad (2.8)$$

In fact we need finite orders of approximations, so only finite number of the iterations are involved. Then, after appropriate truncation, $F_2(t, \tilde{y}_1, \tilde{y}_2, \tilde{x}_2)$ becomes a finite order polynomial of all the arguments. Substitution of (2.8) into the second equation of system (2.4) leads to one equation with respect to one variable \tilde{x}_2 :

$$\tilde{y}_2 = -b\tilde{x}_2^2 + tG_1(t, \tilde{y}_1, \tilde{y}_2, \tilde{x}_2) \quad (2.9)$$

with (again after some truncation) a polynomial $G_1(t, \tilde{x}_2)$ of t, \tilde{x}_2 .

Now we use the power reduction procedure so as to eliminate the terms containing \tilde{x}_2^m with $m > 2$ and to obtain a quadratic equation with respect to \tilde{x}_2 . We put $z = \tilde{x}_2^2$ and write the terms containing \tilde{x}_2 as

$$(\tilde{x}_2)^{2k} = z^k, \quad (\tilde{x}_2)^{2k+1} = \tilde{x}_2 z^k, \quad k = 0, 1, 2, \dots \quad (2.10)$$

Then in the r.h.s. of equation (2.9) we can write ($b < 0!$)

$$G_1 = b \cdot \left(G_1^{(1)}(z) + \tilde{x}_2 H_1^{(1)}(z) \right), \quad G_1^{(1)}(z) = \sum_{k=0}^n g_k z^k, \quad H_1^{(1)}(z) = \sum_{k=0}^n h_k z^k,$$

where to be specific we have truncated the order of the expansion by some degree n , coefficients g_k, h_k are polynomial functions of $t, \tilde{y}_1, \tilde{y}_2$. Thus equation (2.9) can be written as

$$z = z_0 + tG_1^{(1)}(z) + t\tilde{x}_2 H_1^{(1)}(z), \quad (2.11)$$

$z_0 = -\tilde{y}_2/b$. Note that the right-hand side is a linear function of \tilde{x}_2 .

Now we solve equation (2.11) iteratively with respect to z , and every step of the iteration procedure being combined with reduction (2.10) so as to exclude powers of \tilde{x}_2 larger than 1. In the order $\sim O(t)$ we have

$$z = z_0 + tG_1^{(1)}(z_0) + t\tilde{x}_2 H_1^{(1)}(z_0). \quad (2.12)$$

In the next order we must substitute (2.12) into the right-hand side of (2.11). This will yield the higher orders of \tilde{x}_2 ; these orders must be reduced making use of substitution (10) and the result of previous iterations. Thus we again have an equation analogous to (2.12) with a linear function of \tilde{x}_2 in r.h.s. At the end we obtain

$$z = z_0 + tA(t, \tilde{y}_1, \tilde{y}_2) + t\tilde{x}_2 B(t, \tilde{y}_1, \tilde{y}_2)$$

with analytical functions A, B of their arguments.

At last we return from z to \tilde{x}_2 to obtain a quadratic equation

$$\tilde{x}_2^2 - t\tilde{x}_2 B(t, \tilde{y}_1, \tilde{y}_2) - z_0 - tA(t, \tilde{y}_1, \tilde{y}_2) = 0,$$

yielding a solution

$$\tilde{x}_2 = \frac{t}{2} B(t, \mathbf{y}) + \varepsilon \left[z_0 + tA(t, \mathbf{y}) + \frac{1}{4} t^2 B^2(t, \mathbf{y}) \right]^{1/2}. \quad (2.13)$$

The above approximation procedure can be fulfilled to yield approximate solutions with any degree of accuracy required. Note that in reality the calculations up to the order $\sim O(t^2)$ involve a very limited number of coefficients g_k, h_k after truncation of higher order terms in t on every step of approximation. After derivation of \tilde{x}_2 we find \tilde{x}_1 owing to (2.8).

From these considerations it is easy to see that analytical structure of the solutions of the lens Eqs. (2.2) near the fold is

$$\tilde{x}_1 = p + t\varepsilon r\sqrt{w}, \quad \tilde{x}_2 = ts + \varepsilon\sqrt{w}, \quad \varepsilon = \pm 1, \quad (2.14)$$

where p, r, w, s are analytical functions of $t, \tilde{y}_1, \tilde{y}_2$. This allows us to seek for the solution in this form from the very beginning by substitution of (2.14) into the initial equations. This will be considered in more detail in Section 2.2.4.

2.2.3. Lens mapping near the cusp

The coefficients of Taylor expansion in (2.2) depend on the caustic point near which the expansion is performed. If this point is a cusp, then $b = 0$ and the above approximation methods of Section 2.2.2 are no longer valid. In this case the lens equation is

$$\begin{aligned} y_1 &= 2x_1 + a(x_1^2 - x_2^2) + c(x_1^3 - 3x_1x_2^2) - d(x_2^3 - 3x_2x_1^2) + \dots, \\ y_2 &= -2ax_1x_2 + d(x_1^3 - 3x_1x_2^2) + c(x_2^3 - 3x_2x_1^2) + fx_2^4 + \dots \end{aligned} \quad (2.15)$$

The lower order terms correspond to a familiar form of the lens equation near the cusp as described in [116, 118].

In order to perform a formal expansion we write, instead of (2.3),

$$y_1 \rightarrow t^2\tilde{y}_1, \quad y_2 \rightarrow t^3\tilde{y}_2; \quad x_1 \rightarrow t^2\tilde{x}_1, \quad x_2 \rightarrow t\tilde{x}_2.$$

Then the substitution into (2.15) yields, up to the first order terms in t ,

$$\begin{aligned} \tilde{y}_1 &= 2\tilde{x}_1 - a\tilde{x}_2^2 + t(-d\tilde{x}_2^3 + \dots), \\ \tilde{y}_2 &= -2a\tilde{x}_1\tilde{x}_2 + c\tilde{x}_2^3 + t(f\tilde{x}_2^4 - 3d\tilde{x}_1\tilde{x}_2^2 + \dots). \end{aligned} \quad (2.16)$$

A detailed analysis of properties of this lens mapping in zeroth approximation (with respect to t) was carried out in [41, 118]. First-order corrections

in a general case when the matter density in a vicinity of the line of sight is not zero were found in [25], see also [4].

The solution can be sought by using the expansion in powers of t . Here we outline an alternative method using the power reduction like one described in Section 2.2.2, which allows determining an analytical structure of the solutions. First one must express \tilde{x}_1 by means of the other variables; this can be done iteratively using the first equation of system (2.16). Practically we need a finite number of iterations. Then we apply a power reduction to eliminate terms \tilde{x}_2^m with $m > 3$ so as to obtain a cubic equation for \tilde{x}_2 . We put

$$\tilde{x}_2^{3k} = z^k, \quad \tilde{x}_2^{3k+1} = z^k \tilde{x}_2, \quad \tilde{x}_2^{3k+2} = z^k \tilde{x}_2^2. \quad (2.17)$$

On account of the second equation of system (2.16) after substitutions we get an equation for \tilde{x}_2 of the form

$$z = K_0(\mathbf{y}) + K_1(\mathbf{y}) \tilde{x}_2 + t \left\{ L_0(t, \mathbf{y}, z) + L_1(t, \mathbf{y}, z) \tilde{x}_2 + L_2(t, \mathbf{y}, z) \tilde{x}_2^2 \right\}. \quad (2.18)$$

Using an iterative procedure combined with (2.17) this enables us to obtain z as follows

$$z = K_0(\mathbf{y}) + K_1(\mathbf{y}) \tilde{x}_2 + t \left\{ \tilde{L}_0(t, \mathbf{y}) + \tilde{L}_1(t, \mathbf{y}) \tilde{x}_2 + \tilde{L}_2(t, \mathbf{y}) \tilde{x}_2^2 \right\}, \quad (2.19)$$

where $K_0, K_1, \tilde{L}_0, \tilde{L}_1, \tilde{L}_2$ are polynomial functions of t and \mathbf{y} , the order of the polynomials depending upon the order of the approximation required. Thus we come to the cubic equation with respect to \tilde{x}_2

$$\tilde{x}_2^3 - t \tilde{L}_2 \tilde{x}_2^2 - (K_1 + t \tilde{L}_1) \tilde{x}_2 - (K_0 + t \tilde{L}_0) = 0. \quad (2.20)$$

The roots can be obtained via the Cardano–Tartaglia formulas or the Viète trigonometric solution. Depending on sign of the discriminant of this equation there are either three real roots (inside the cusp), or one real root (outside the cusp). The analytic properties of the solution are completely defined by the coefficients of (2.20), in particular for $t \rightarrow 0$ they are defined by K_0 and K_1 . It is important that for a general cusp these coefficients are finite order polynomials of $t, \tilde{y}_1, \tilde{y}_2$. This structure will be preserved for any order of approximation leading to (2.20).

2.2.4. Amplification near the fold

Solutions of the lens equation. Further we deal with the results concerning the folds that follow from Section 2.2.2. The result of the expansions near the fold

$$\tilde{x}_1 = \tilde{x}_{10} + \tilde{x}_{11}t + \tilde{x}_{12}t^2, \quad \tilde{x}_2 = \tilde{x}_{20} + \tilde{x}_{21}t + \tilde{x}_{22}t^2 \quad (2.21)$$

as applied to the lens equation (2.2) in zeroth order is given by (2.7):

$$\tilde{x}_{10} = \frac{1}{2} \left[\tilde{y}_1 - \frac{a}{b} \tilde{y}_2 \right], \quad \tilde{x}_{20} = \varepsilon \left[\frac{\tilde{y}_2}{|b|} \right]^{1/2}. \quad (2.22)$$

The next orders are as follows

$$\begin{aligned} \tilde{x}_{11} &= -\varepsilon \sqrt{\frac{\tilde{y}_2}{|b|}} \frac{(ac - aR^2 + bd) \tilde{y}_2 + bR^2 \tilde{y}_1}{2b^2}, \\ \tilde{x}_{21} &= \frac{1}{2} \left(\frac{a^2 - c}{b^2} \tilde{y}_2 - \frac{a}{b} \tilde{y}_1 \right), \end{aligned} \quad (2.23)$$

where $R^2 = a^2 + b^2$. The solutions up to this accuracy level have been obtained earlier in [7] and [71]. The contributions of this order are cancelled in calculations of the total amplification of two critical images. Therefore to get a nontrivial correction to zero order amplification we need the higher order approximations.

The second order terms contain an expression, which is singular in \tilde{y}_2 :

$$\begin{aligned} \tilde{x}_{12} &= \frac{1}{4b^4} \left(3a^5 + 5a^3b^2 + 2ab^4 - 2b^3d - 2b^2g + 3ac^2 - 6a^3c + 3bcd - 8a^2bd + \right. \\ &\quad \left. + 2abf \right) \tilde{y}_2^2 + \frac{1}{2b^3} \left(2a^2c - b^2c + 3abd - 2a^2R^2 - b^2R^2 \right) \tilde{y}_1 \tilde{y}_2 + \frac{aR^2}{4b^2} \tilde{y}_1^2, \end{aligned} \quad (2.24)$$

$$\begin{aligned} \tilde{x}_{22} &= \varepsilon \sqrt{\frac{\tilde{y}_2}{|b|}} \left[\frac{1}{8b^3} (10a^2c - 5c^2 - 5a^2R^2 + 10abd - 4bf) \tilde{y}_2 - \right. \\ &\quad \left. - \frac{3}{4b^2} (ac + bd - aR^2) \tilde{y}_1 - \frac{R^2}{8b} \frac{\tilde{y}_1^2}{\tilde{y}_2} \right]. \end{aligned} \quad (2.25)$$

Now we proceed to second approach to construct approximate solutions of the lens equation in a vicinity of folds, which is free from such singularities. We look for two critical solutions (2.14) $\tilde{x}_1 = p + \varepsilon r \sqrt{w}$, $\tilde{x}_2 = ts + \varepsilon \sqrt{w}$ corresponding to different signs of $\varepsilon = \pm 1$. After substitution into the lens equation we separate the terms containing integer and half-integer powers of w , e.g.:

$$\sum_{n,m} a_{n,m} (p + \varepsilon r \sqrt{w})^n (ts + \varepsilon \sqrt{w})^m = A_0 + \varepsilon w^{1/2} A_1,$$

where A_0, A_1 are analytical in t, p, r, s, w . This yields a system of four independent equations for the variables p, r, w, s ; this system can be reduced to a form convenient for iteration procedure [5]. It is important to note that at every iteration step we obtain an approximate solution in the form of finite order polynomials of $t, \tilde{y}_1, \tilde{y}_2$, as it was stated above. The solution of this

system up to the terms $\sim t^2$ is [5]

$$\begin{aligned}
 p &= \tilde{x}_{10} + t^2 \tilde{x}_{12}, \\
 r &= -\frac{R^2 \tilde{y}_1}{2b} + \frac{\tilde{y}_2}{2b^2} [aR^2 - (ac + bd)], \\
 s &= -\frac{a}{2b} \tilde{y}_1 + \frac{a^2 - c}{2b^2} \tilde{y}_2, \quad w = -\frac{\tilde{y}_2 + t^2 Z}{b}, \\
 Z &= -\frac{R^2}{4b} \tilde{y}_1^2 + \frac{3}{2b^2} [a(a^2 - c) + b(ab - d)] \tilde{y}_1 \tilde{y}_2 - \\
 &\quad - \frac{\tilde{y}_2^2}{4b^3} [5a^2(R^2 - 2c) + 5c^2 - 10abd + 4bf].
 \end{aligned} \tag{2.26}$$

Total amplification of critical images of a point source near the fold. The solutions of the lens equation are then used to derive the Jacobians of the lens mapping (for both images near the critical curve). The value of J^{-1} yields the amplification of individual images. As we pointed out above, we need the total amplification of two critical images (the sum of two amplifications of the separate critical images). In the second order approximation (using the expansion up to the terms t^2) this is

$$K_{cr} = \frac{1}{2} \frac{\Theta(y_2)}{\sqrt{|b|y_2}} \left[1 + Py_2 + Qy_1 - \frac{\kappa y_1^2}{4y_2} \right], \tag{2.27}$$

where the constants P , Q , are expressed via the Taylor expansion coefficients from equation (2.1), and

$$\kappa = \frac{a^2 + b^2}{2|b|};$$

$\Theta(y_2)$ is the Heaviside step function. Note that κ is the caustic curvature at the origin which enters explicitly into the amplification formula. Parameters P and Q are independent; explicit formulae for them may be found in [5, 6]. However, this is not needed when we use equation (2.27) for fitting the observational data, because these constants are whatever considered as free fitting parameters.

Formula (2.27) yields an effective approximation for the point source amplification near the coordinate origin provided that $y_2 > 0$, and y_2/y_1^2 is not too small (see the term containing κ). For a fixed source position, this can be satisfied always by an appropriate choice of the coordinate origin, so that the source will be situated almost on a normal to the tangent to the caustic.

If the source is on the caustic tangent or in the region between the caustic and the tangent, then formula (2.27) does not represent a good approximation to the point source amplification. Nevertheless, in case of an extended source, we will show that result (2.27) can be used to obtain approximations to the amplification of this source even as it intersects the caustic. However, to do

this, we need to redefine correctly the convolution of (2.27) with a brightness distribution.

Dark matter on the line of sight. It is well known that the non-baryonic dark matter (DM) dominates in galactic masses, though exact small-scale distribution of DM is a subject of studies. Simulations show that a complicated subhalo structure is possible [28]. In this connection it is interesting to study how a *variable* DM density can affect the HAE characteristics.

Formulae (2.22)–(2.27) have been obtained under an assumption that there is no continuous matter on the line of sight $k = 0$. It is easy to take into account an effect of a non-zero constant density $k = \text{const} \neq 0$ by means of a rescaling of variables and change of coefficients in equations (2.2) [5].

For $k \neq 0$ the lens potential in (2.1) satisfies equation $\Delta\Phi = 2k(\mathbf{x})$. The Taylor expansion analogous to (2.2) after substitution (2.3) takes on the form in the second approximation:

$$\begin{aligned} \tilde{y}_1 &= 2(1 - k_0)\tilde{x}_1 - a_2\tilde{x}_2^2 + t(2b_1\tilde{x}_1\tilde{x}_2 - d\tilde{x}_2^3) + \\ &\quad + t^2(a_1\tilde{x}_1^2 - 3c_1\tilde{x}_1\tilde{x}_2^2 + g\tilde{x}_2^4), \\ \tilde{y}_2 &= -b_2\tilde{x}_2^2 + t(-2a_2\tilde{x}_1\tilde{x}_2 + c_2\tilde{x}_2^3) + t^2(b_1\tilde{x}_1^2 - 3d\tilde{x}_1\tilde{x}_2^2 + f\tilde{x}_2^4). \end{aligned} \quad (2.28)$$

Here $k_0 = k(0)$ is the matter density at the origin, and the coefficients of expansion in (2.28) are expressed by means of derivatives of the lens potential Φ . If k is constant, then $a_1 = a_2 = a$, $b_1 = b_2 = b$, $c_1 = c_2 = c$. Thus, system (2.28) contains four additional parameters as compared to the previously studied case $k(\mathbf{x}) \equiv 0$. The solutions of system (2.28) have been studied in [3]; they are analogous to (2.22)–(2.25) and they have the same analytic structure. The formula for the amplification also preserves its form (2.27); the difference is only due to a change of explicit expressions for P , Q and κ in terms of new Taylor coefficients, which anyway cannot be determined from observations for realistic models of mass distributions. We however must make a reservation that here we suppose that the Taylor expansion in the lens equation is possible and it is effective (which presupposes that the continuous matter is sufficiently smooth); therefore very inhomogeneous case of small objects with size $\ll R_E$ is not involved in our consideration.

2.2.5. Resume of Section 2.2

The main results of this Section deal with solutions of the lens equation in the caustic region, namely, near the folds and cusps. We propose a general procedure of the power reduction that provides an approximate solution with a prescribed accuracy. Most attention is paid to the case of the fold caustic. We outlined two methods that enable us to obtain the critical solutions of the gravitational lens equation near a fold with any desired accuracy.

In order to obtain nontrivial corrections to K_{cr} near the fold obtained in the linear caustic approximation, the higher orders of the expansion of the lens equation must be taken into account as compared to works [7, 71]. The modified formula for K_{cr} contains 3 extra parameters in addition to those of the linear caustic approximation. We point out that any presence of a continuous (cf. dark) matter on the line of sight (with the same typical scales of Taylor expansion) does not change analytical structure and the number of fitting parameters in the formula for K_{cr} .

2.3. Amplification of extended sources near the fold

2.3.1. Preliminary comments

In this section we proceed to applications of the previous results to some extended source models typically used in fittings of the observed light curves. Interest to HAE in extragalactic GLSs is due to possibilities to study brightness distributions in sources. This is especially interesting in connection with investigation of central regions of distant quasars. The idea, first proposed by Grieger, Kayser and Refsdal [48], uses an approximate formula of flux amplification during HAE, which contains a few fitting parameters. This makes possible some estimations of certain GLS characteristics, in particular, the source size [48]. For example, in case of the well known GLS Q 2237 + 0305 (Einstein Cross) several HAEs was observed [1, 130, 137] and the estimates of the source size have been obtained within different source models [17, 120, 121, 139–141, 145].

A possibility do distinguish different source models is widely discussed elsewhere. Typical problems arising in determination of the source brightness distribution are as follows.

First, it is impossible to get complete information about the brightness distribution from the light curve observations. Information from separate HAE only, without making recourse to the whole light curve etc, is still more limited. Observations provide only a one-dimensional luminosity profile of the source (integrated along the caustic); then, without using additional information, we cannot determine even the source size because we do not know the value and direction of the source velocity, ellipticity and orientation with respect to the caustic.

Second, even for a circularly symmetric source and known normal velocity with respect to the fold caustic, determination of the luminosity profile is a kind of ill-posed mathematical problems: small variations of input data may lead to considerable changes of the solution. A standard way to mitigate this difficulty involves additional restrictions and/or using some simple “fiducial” models for brightness distribution. Some of these models are considered below

in this paper. However, it should be clearly understood that the real picture of the central quasar region is more complicated than the simple brightness distributions of the following section; these models can be considered rather as reference ones. On the other hand, in view of the present-day accuracy of observations, it is difficult to distinguish even these simple source models on the basis of observational data. For example, the authors of [93] argue that the accretion disk can be modeled with any brightness profile (Gaussian, uniform, etc.), and this model will agree with the available data provided that an appropriate source size is chosen. On the other hand, a number of authors [9, 17, 43, 44, 75, 93, 120, 121, 132] discussed delicate questions concerning determination of a fine quasar structure from HAE. For example, the authors of [44] wrote that the GLTP data [1] on Q 2237 + 0305 admit only accretion disc models (see also [9, 43]). Obviously, the presence of an accretion disk in a central region of quasar is beyond any doubts, as well as the fact that the real appearance of the quasar core can be quite different from our simplified models. However, is it possible to prove the existence of the accretion disk in a concrete GLS *a posteriori*? This is an open question.

We note that since the work by Kochanek [75], followed by a number of authors [9, 43, 93, 102–104, 132], statistical methods dealing with the complete light curves of the GLS images have been developed. This approach is very attractive because it allows taking into account the whole aggregate of observational data on image brightness variations yielding estimates of the microlens masses and source model parameters. However this treatment involves a large number of realizations of the microlensing field and requires a considerable computer time for such simulation. On the other hand, we must remember that (i) the source structure manifests itself only in the HAEs; far from the caustics the source looks like the point one and all the information about its structure is being lost; (ii) in reality we have only one light curve, not a statistical ensemble, so probabilistic estimates of GLS parameters obtained in statistical simulations can differ from the real values in a concrete GLS. If we restrict ourselves to the HAE neighborhood, then part of the information is lost, but instead we use the most general model of the microlensing field described by a small set of coefficients in the lens mapping.

2.3.2. From a point source to extended one

After these reservations, we turn to the amplification of some extended source models.

Let $I(\mathbf{y})$ be a surface brightness distribution of an extended source. If the source center is located at the point $\mathbf{Y} = (Y_1, Y_2)$ in the source plane, then the total microlensed flux from the source is

$$F(\mathbf{Y}) = \iint I(\mathbf{y}(\mathbf{x}) - \mathbf{Y}) dx_1 dx_2, \quad (2.29)$$

$\mathbf{x} = (x_1, x_2)$; $\mathbf{x} \rightarrow \mathbf{y}(\mathbf{x})$ is the lens mapping. The result of using Eq. (2.29) obviously is equivalent to the result of the well-known ray-tracing method [116] (when the pixel sizes tend to zero).

An equivalent representation of this formula is

$$F(\mathbf{Y}) = \iint K(\mathbf{y})I(\mathbf{y} - \mathbf{Y}) dy_1 dy_2, \quad (2.30)$$

where the point source amplification $K(\mathbf{y}) = \sum_i K_i(\mathbf{y})$ is the sum of amplifications of all the images. We remind that in microlensing events separate micro-images are not resolved in observations.

Near a caustic, one can approximate $K(\mathbf{y}) = K_0 + K_{cr}(\mathbf{y})$, where K_0 is an amplification of all noncritical images that is supposed to be constant during HAE, and K_{cr} is the amplification of the critical images. Due to a relative motion of the lensing galaxy and the source (quasar), the flux of some quasar image in GLS is a function of time; this function is represented by the lightcurve of this image.

Formula (2.27) for K_{cr} contains the nonintegrable term $\sim \Theta(y_2)(y_2)^{-3/2}$. Therefore, the question arises of how formula (2.27) can be used in situation when the extended source intersects a caustic and some part of the source is in the zone between the tangent and the caustic. In view of Subsections 2.2.2 and 2.2.4, it is evident that the mentioned term is a result of the asymptotic expansion of the root $\sqrt{y_2 + \kappa y_1^2 t^2 / 2 + \dots}$ in the approximate solution (2.14). Direct usage of the solution in the form (2.14) for calculation of the Jacobians of the lens mapping and then for the derivation of amplifications does not lead to any divergences and any nonintegrable terms in K_{cr} do not arise without using this expansion. Nevertheless, it is convenient to have a representation of K_{cr} in the form of expansion in powers of small parameter. Such an expansion can be fulfilled correctly after substitution of K_{cr} into integral (2.30). On this way starting from the form (2.14) it is easy to show that to define K_{cr} correctly, one must replace the term $\Theta(y_2)(y_2)^{-3/2}$ in (2.27) by the distribution (generalized function) $(y_2)_+^{-3/2}$ [42]. We recall that the distribution $y_+^{-3/2}$ of the variable y is defined by the expression

$$\int y_+^{-3/2} f(y) dy = 2 \int_0^\infty y^{-1/2} \frac{\partial f(y)}{\partial y} dy$$

for any test function $f(y)$.

After this redefinition, we have

$$K_{cr} = \frac{\Theta(y_2)}{2\sqrt{|b|}y_2} \left[1 + Py_2 + Qy_1 \right] - \frac{\kappa}{8\sqrt{|b|}} y_1^2 (y_2)_+^{-3/2}. \quad (2.31)$$

This formula can be used to correctly derive an approximate amplification of a sufficiently smooth extended source including the case where the source crosses the caustic.

2.3.3. The extended source models

Gaussian and power-law models. Below we list most simple and commonly used brightness distributions of a source in GLS; without loss of generality they are chosen to be normalized to 1:

$$\iint I(\mathbf{y}) dy_1 dy_2 = 1.$$

To compare different models of the brightness distribution we have to use the same parameter that characterizes the size of an object. The r.m.s. size R_{rms} is often used:

$$R_{rms}^2 = \iint \mathbf{y}^2 I(\mathbf{y}) dy_1 dy_2. \quad (2.32)$$

However, for slowly decreasing brightness profile (e.g., $I(\mathbf{y}) \sim |\mathbf{y}|^{-\alpha}$, $\alpha \leq 4$) the r.m.s. size diverges. In case of the circularly symmetric sources the half-brightness radius $R_{1/2}$ is also widely used; it is defined by the relation:

$$2\pi \int_0^{R_{1/2}} I(r)r dr = \pi \int_0^{\infty} I(r)r dr. \quad (2.33)$$

In case of Gaussian source model

$$I_G(r) = \frac{1}{\pi R^2} \exp \left[- \left(\frac{r}{R} \right)^2 \right], \quad (2.34)$$

where R stands for a size parameter; $R_{rms} = R$, $R_{1/2} = R\sqrt{\ln(2)}$.

Limb-darkening model (see, e.g., [30]):

$$I_{LD}(r) = \frac{q+1}{\pi R^2} \Xi(r/R; q), \quad (2.35)$$

where

$$\Xi(\xi; q) = \Theta(1 - \xi^2)(1 - \xi^2)^q,$$

and $R_{rms} = R/\sqrt{q+2}$. Here we assume $q > 0$. The half-brightness radius is $R_{1/2} = R\sqrt{1 - (1/2)^{1/(q+1)}}$. For fixed R_{rms} and $q \rightarrow \infty$, the brightness distribution (2.35) tends to the Gaussian one.

The models (2.35) and (2.34) describe a class of compact sources with fast brightness decrease. On the contrary, the power-law models [120, 121] describe a slow decrease at large r :

$$I_{PL}(r) = \frac{p-1}{\pi R^2} [1 + r^2/R^2]^{-p}, \quad (2.36)$$

where $p > 1$ is the power index, and R is related to the r.m.s. radius R_{rms} as $R^2 = (p-2)R_{rms}^2$. The model (2.36) may be considered as an alternative to (2.35). The half-brightness radius of the source for this model is

$R_{1/2} = R\sqrt{2^{1/(p-1)} - 1}$. Like (2.35), for fixed R_{rms} and $p \rightarrow \infty$, the brightness distribution (2.36) tends to the Gaussian one. For small p we have a “long-range” distribution; R_{rms} diverges for $p \leq 2$.

Linear combinations of different distributions (2.34, 2.35, 2.36) with different parameters yield rather a wide class of symmetric source models to fit any kind of data. On the other hand (2.34) may be considered as a fiducial model to determine some parameters such as the source size and (2.35), (2.36) are useful in case when in addition we are interested in investigation of a brightness behavior at large r . More physical models are considered in the next subsection.

Accretion disk models. The accretion disk (AD) of Shakura—Sunyaev [119] has a more complicated profile. This model gives the energy density of the radiation from accretion disk around a non-rotating black hole as a function of radius whence the (normalized) brightness distribution is

$$I_{AD}(r) = \frac{3R\theta(r-R)}{2\pi r^3} \left[1 - \sqrt{\frac{R}{r}} \right], \quad (2.37)$$

here R being the radius of the inner edge of the accretion disk. For this AD model the half-brightness radius is $R_{1/2} = 4R$, $R_{rms} = \infty$. This formula describes a total brightness integrated over all radiation frequencies. The maximum brightness is at $r = r_m = 49R/36$.

For a blackbody radiation the temperature scales as $T \sim I_{AD}^{1/4}$, whence the specific intensity as a function of radius $\sim \lambda^{-5}(e^{hc/\lambda T} - 1)^{-1}$ for wavelength λ (AD1)

$$I_{AD1}(r) = \frac{C_{AD1}}{R^2} \left[\exp\left(\frac{\kappa_1 \rho^{3/4}}{(1 - \rho^{-1/2})^{1/4}}\right) - 1 \right]^{-1} \theta(r-R), \quad \rho = r/R, \quad (2.38)$$

here C_{AD1} is a normalization factor. For the maximum disk temperature (at $r = r_m$), the peak value of intensity as a function of λ corresponds to $\kappa_1 = 2.422$ and $C_{AD1} = 9.61$. Further we adopt this value of κ_1 for which $R_{1/2}/R = 2.021$. Intensity (2.38) can be easily rewritten for any wavelength taking into account that $\kappa_1 \sim \lambda^{-1}$.

Though intensities (2.37), (2.38) are quite different, their light curves in HAE can look very similar for an appropriate choice of parameters. The main feature that distinguishes the accretion disk models from the Gaussian one is the concavity of the light curve owing to the dark “hole” in the accretion disk center. We shall return to this question in Section 2.3.5.

2.3.4. Amplifications including the post-linear corrections

Gaussian source. Formula (2.31) has been used [5] to derive the amplification of a Gaussian source with the brightness distribution (2.34), the limb-darkening source, and the power-law source (see the next subsections).

Further, we use the dimensionless coordinates $s = Y_1/R$, $h = Y_2/R$ of the source center and the functions

$$\begin{aligned} I_k(h) &= \int_0^{\infty} u^{k-1/2} \exp(-u^2 + 2uh) du = \\ &= \frac{1}{2} \sum_{n=0}^{\infty} \frac{\Gamma\left(\frac{1}{4} + \frac{k+n}{2}\right)}{n!} (2h)^n. \end{aligned} \quad (2.39)$$

These functions can be expressed in terms of the confluent hypergeometric function ${}_1F_1$ or the parabolic cylinder function D :

$$I_k(h) = 2^{-\left(\frac{k}{2} + \frac{1}{4}\right)} \Gamma\left(k + \frac{1}{2}\right) e^{\frac{h^2}{2}} D_{-(k+\frac{1}{2})}(-\sqrt{2} \cdot h). \quad (2.40)$$

The substitution of (2.31) and (2.34) in (2.30) yields

$$\begin{aligned} K_G(s, h) &= \frac{1}{2\sqrt{\pi|b|R}} \left\{ \Phi_0(h) + \right. \\ &\left. + R \left[P\Phi_1(h) - \frac{\kappa}{2}\Phi_2(h) + Qs\Phi_0(h) - \kappa s^2\Phi_2(h) \right] \right\}. \end{aligned} \quad (2.41)$$

Here,

$$\Phi_0(h) = I_0(h) \exp(-h^2),$$

$$\Phi_1(h) = I_1(h) \exp(-h^2),$$

$$\Phi_2(h) = [hI_0(h) - I_1(h)] \exp(-h^2).$$

Note that the main term of (2.41) which corresponds to the linear caustic approximation was first obtained in the paper [117].

Limb-darkening source. Analogous considerations allow us to obtain formulas for the amplification of extended sources for the limb-darkening (2.35) and power-law (2.36) brightness profiles; the results are represented analytically in terms of hypergeometric function ${}_2F_1$ [11].

Denote

$$X_{k,q}(h) = \frac{\Gamma(q+2)}{\Gamma\left(q+\frac{3}{2}\right)} \int_0^{\infty} y^{k-\frac{1}{2}} \Xi(y-h; q+1/2) dy,$$

$k = 1, 2$. We have

$$X_{k,q}(h) = 2^{q+\frac{1}{2}}(1+h)^{q+k+1} \frac{\Gamma(q+2)\Gamma(k+\frac{1}{2})}{\Gamma(q+k+2)} \times \\ \times {}_2F_1\left(-q-\frac{1}{2}, q+\frac{3}{2}; q+k+2; \frac{1+h}{2}\right)$$

for $-1 < h < 1$ and

$$X_{k,q}(h) \sqrt{\pi} (h+1)^{k-\frac{1}{2}} {}_2F_1\left(q+\frac{3}{2}, \frac{1}{2}-k; 2q+3; \frac{2}{h+1}\right)$$

for $h > 1$.

Also for $k = -1$ we define

$$X_{-1,q}(h) = 4(q+1)(hX_{0,q-1} - X_{1,q-1}).$$

Then in case of the model with limb darkening (2.35), the critical images disappear when the source lies on the outer side of the caustic (i.e., for $h < -1$). The amplification due to critical images takes on the form

$$K_{LD}(s, h) = \frac{1}{2\sqrt{\pi|b|R}} \left\{ X_{0,q}(h) + R \left[PX_{1,q}(h) - \right. \right. \\ \left. \left. - \frac{\kappa}{8(q+2)} X_{-1,q+1}(h) + Qs X_{0,q}(h) - \frac{\kappa}{4} s^2 X_{-1,q}(h) \right] \right\}.$$

Power-law source. The result for the amplification involves integrals:

$$\Psi_{k,p}(h) = \frac{\Gamma(p-\frac{1}{2})}{\Gamma(p-1)} \int_0^\infty \frac{y^{k-\frac{1}{2}} dy}{(1+(y-h)^2)^{p-1/2}} = \\ = \frac{\Gamma(p-\frac{1}{2})}{\Gamma(p-1)} B\left(k+\frac{1}{2}, 2p-k-\frac{3}{2}\right) (1+h^2)^{k/2+3/4-p} \times \\ \times {}_2F_1\left(k+\frac{1}{2}, 2p-k-\frac{3}{2}; p; \frac{1}{2}\left(1+\frac{h}{\sqrt{1+h^2}}\right)\right)$$

for $k = 0, 1$, $B(x, y)$ being the Beta-function.

We extend this to $k = -1$ having in mind the definition of $(y)_+^{-3/2}$, so that

$$\Psi_{-1,p}(h) = 4(p-1)[h\Psi_{0,p+1}(h) - \Psi_{1,p+1}(h)].$$

Now, the amplification due to critical images takes on the form

$$K_{PL}(s, h) = \frac{1}{2\sqrt{\pi|b|R}} \left\{ \Psi_{0,p}(h) + R \left[P\Psi_{1,p}(h) - \right. \right. \\ \left. \left. - \frac{\kappa}{8(p-2)} \Psi_{-1,p-1}(h) + Qs \Psi_{0,p}(h) - \frac{\kappa}{4} s^2 \Psi_{-1,p}(h) \right] \right\}.$$

The zeroth approximation to this formula has been derived in [120].

2.3.5. Simulations of microlensing light curves with different source models

Parameters of simulations. Though we expect that a source structure reveals itself just during HAEs, it is instructive to compare whole light curves corresponding to different source models; this is fulfilled below. Nevertheless we point out that below we mainly deal with an estimate for η_m (see Eq. (2.44) below), which is just a characteristic of HAE. We assume the lens equation

$$\mathbf{y} = \mathbf{x} - \sum_{n=1}^N R_{E,n}^2 \frac{\mathbf{x} - \mathbf{x}_n}{|\mathbf{x} - \mathbf{x}_n|^2 + a_n^2}, \quad (2.42)$$

which describes microlensing by N extended masses (clumps) in absence of any external field; the surface mass density corresponding to (2.42) is

$$\sigma(\mathbf{x}) = \sum_{n=1}^N f(a_n, M_n, \mathbf{x} - \mathbf{x}_n), \quad (2.43)$$

where the surface mass density of one clump is $f(a, M, \mathbf{x}) \sim a^2 M (\mathbf{x}^2 + a^2)^{-2}$; here \mathbf{x}_n, a_n, M_n stand for the position, size and mass of n -th clump. In case of point masses $a_n = 0$; however in simulations of the point mass microlensing we have chosen some small positive values of $a_n \ll R_{E,n}$ so as not to have problems with singularities. In Section 2.4 we also consider the case of finite-size extended masses.

Here we present results of straightforward calculations of a microlensed flux according to equation (2.29) to obtain the light curves for different realizations of the point microlenses positions. The parameters of numerical integration are presented in Table 2.1 along with the parameters of the microlensing field. The microlens positions were chosen in a random way with uniform distribution over the field. The length of trajectory has been taken sufficiently long so as to provide the caustic crossings. However the trajectory in the simulations was situated far from the field boundaries, and the size of the field was chosen large enough to avoid boundary effects.

Table 2.1. Parameters of simulation

Parameter	Value
Number of pixels	1.23×10^6
Pixel size	$0.01 R_E$
Source trajectory length	$2 R_E; 5 R_E$
Radius of field	$70 R_E$
Microlensing optical depth, σ	0.3
Source speed, V	1
Time discretization, δt	$0.01 R_E/V$

Here we compare the light curves for Gaussian, PL, LD, AD and AD1 source models with brightness distributions from Section 2.3.3. The simulations were performed for a set of 100 random realizations of microlensing field with optical depth $\sigma = 0.3$ in order to have possibility to compare

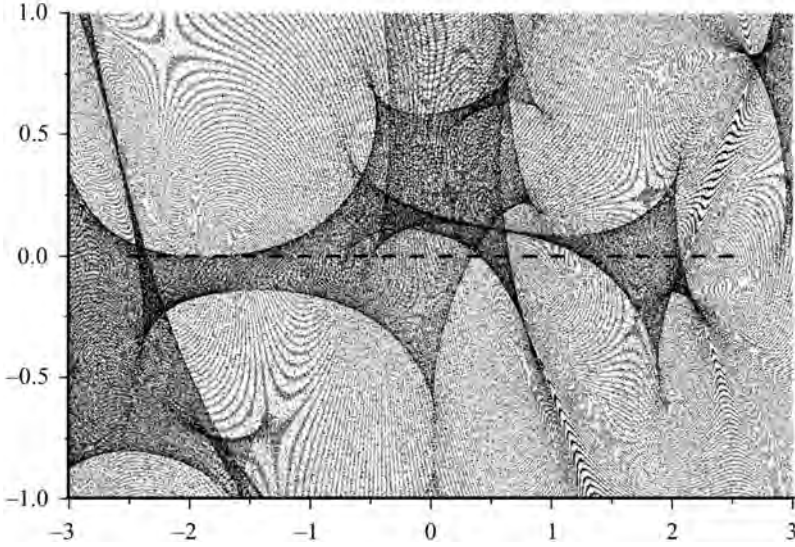


Fig. 2.1. Magnification pattern with the trajectory of the source in the source plane. The source moves from left to right along the straight line with uniform speed

with some of the results of papers [26, 37, 115, 131]. All source models had the same half-brightness radius, the light curves for all source models have been calculated for the same microlensing fields. All the microlenses were static, the total number of microlenses was 1470. The typical magnification pattern is shown on Fig. 2.1; here the speed of source is $V = 1$ so we can identify the source position as a function of time.

The simulations were carried out with half-brightness radius $R_{1/2} = 0.21$ for all models; the power-law index was $p = 3/2$ for the “long range” PL model; note that AD model also corresponds to this class of the power-law asymptotic dependence (with $p = 3/2$). For LD model we have chosen $q = 1$.

To compare the light curves for different source models 1 and 2 we used the relative value

$$\eta_m = 2 \langle \max_t \{ \eta(t) \} \rangle, \quad \eta(t) = \frac{|K_1(t) - K_2(t)|}{K_1(t) + K_2(t)}, \quad (2.44)$$

where $K_i(t)$ is the amplification for i -th model along the trajectory of source linear motion; $\langle \dots \rangle$ is an average over a number of realizations. Because we expect that maximum difference of brightness on lightcurves for different source models takes place during HAE, so η_m typically is a characteristic of HAE.

From the “light curves” on Fig. 2.2 we observe a significant difference between the “compact” (LD and Gaussian) and the “long-range” models. The long-range character of the latter reveals itself even on considerable distances

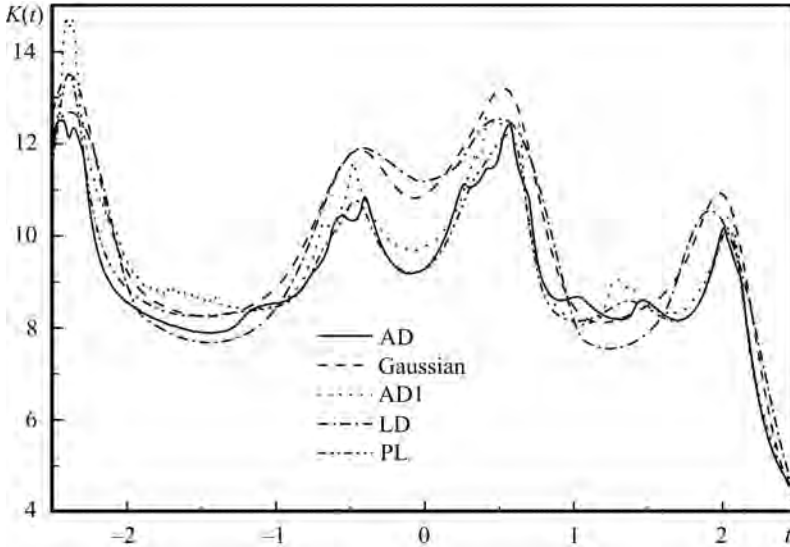


Fig. 2.2. “Light curves”: amplification as a function of time for different source models that correspond to magnification pattern of Fig. 2.1

from the caustics, where we expect that brightness of all the sources must have the same behavior as that of a point source. The differences between these two groups of models are essentially larger than the differences within each group (e.g. between Gaussian and LD models). This conclusion is confirmed by results of the statistical considerations over 100 realizations shown in Table 2.2 for half-brightness radius $R_{1/2} = 0.21$ as the example.

We note that the results of comparison may depend on a complexity of the caustics involved into our consideration. One can expect e.g. that in case of complicated caustic crossing (such as crossing of the fold caustics in a vicinity of cusp, intersection of dense aggregations of caustics etc) the light curve

Table 2.2. Relative difference between the light curves in HAE

i -th model	j -th model	η_m
AD	Gaussian	0.074 ± 0.0012
AD	AD1	0.085 ± 0.002
AD	LD	0.091 ± 0.002
AD	PL	0.038 ± 0.001
Gaussian	AD1	0.073 ± 0.0017
Gaussian	LD	0.042 ± 0.001
Gaussian	PL	0.073 ± 0.0013
AD1	LD	0.094 ± 0.002
AD1	PL	0.052 ± 0.0012
LD	PL	0.090 ± 0.002

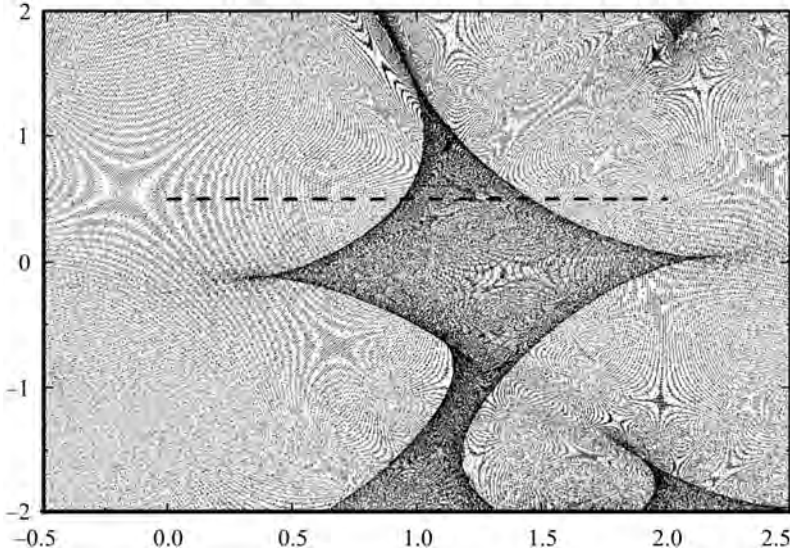


Fig. 2.3. Magnification pattern with simple caustic crossing events

difference for different source models may be more significant. Previous our simulations involved *all* possible realizations of the microlensing field that may invoke the complicated caustic crossings. However, in case of a concrete GLS we deal with a *single* light curve. One may ask: is it relevant to apply the results of statistical simulations to this single light curve, where we may have a kind of an observational selection. Therefore it is necessary to check how this “complexity” affects the average value of η . In this connection we considered some modification of our statistical procedure: we have chosen (“by eye”) such realizations rather simple fold caustic crossings involved. However, the numerical results for simple caustic crossing events, such as shown as the example on Fig. 2.3, appeared to be nearly the same as that of the Table 2.2. Though, we must note that we had smaller number of the “simple” caustic realizations. Additional simulations are needed to have better statistics.

Gaussian fittings of accretion disk and limb-darkening source models. Table 2.2 concerns a comparison of different models *with the same* $R_{1/2}$. However, in reality we do not know what source we must fit and one must check whether we can replace one model with a different one with some other source parameters to get better fitting.

We have fitted the limb-darkening and accretion disk model light curves with that of the Gaussian source of different radii. The half-brightness radius of LD and AD models was fixed: $R_{1/2} = 0.2R_E$ (this choice was determined by the AD1 model, see comments after formula (2.38)) and that of the Gaussian source was varied to get better fitting; here $p = 3/2$ for PL model and $q = 1$ for LD model. One example of the relative light curve differences $\eta(T)$ according

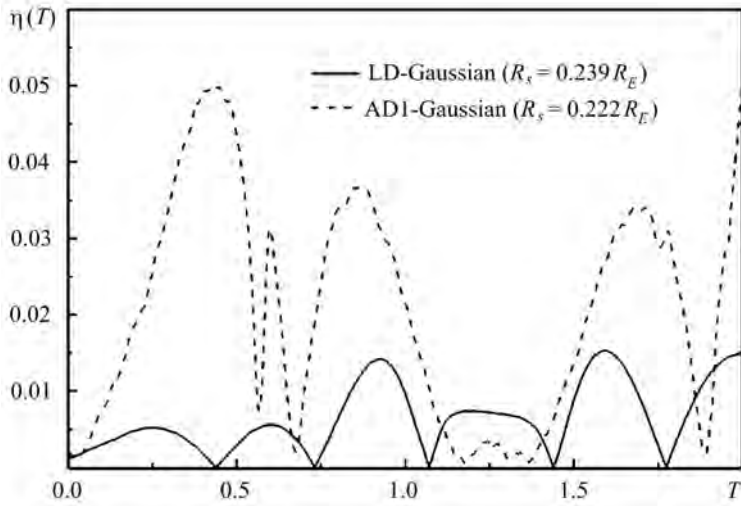


Fig. 2.4. Relative differences $\eta(t)$ between Gaussian and LD ($q = 1$), AD1 models for the best fitted curves corresponding to magnification pattern of Fig. 2.3

to (2.44) between LD, AD1 and the best fitted Gaussian models is shown in Fig. 2.4. As we see from this figure, usage of an optimal size of the Gaussian model can diminish η_m as compared to the estimate dealing with the same $R_{1/2}$ for all the models.

To test this statement statistically, we carried out simulations with 20 magnification patterns having the “simple” caustic crossing. We found, that fitting of AD light curves by the Gaussian model (with different $R_{1/2}$) yields $\eta_m = 0.07 \pm 0.006$; this is roughly the same as in Table 2.2. Fittings of LD model light curves by the Gaussian model (with different $R_{1/2}$) yielding $\eta_m = 0.026 \pm 0.002$ (less than half of Table 2.2); in this case an improvement is noticeable. Therefore, the Gaussian source cannot reproduce all the models, though for some compact models the fitting results are rather good. Then in the caustic crossing events different models may be distinguished on the accuracy level of modern photometric observations.

2.3.6. Resume of Section 2.3

Here the formulas of Section 2.2 are applied to the Gaussian, power-law and limb darkening models of an extended source. The analytical formulas for these source models are obtained. We note that a fitting of the light curve of GLS Q 2237 + 0305C [5, 6] showed that some of these higher order corrections can be statistically significant even at the present accuracy level. This means that when we are looking for some fine effects in HAE due to the source size, a consistent treatment must also take into account possible effects of the above corrections.

In case of the accretion disk models we have not succeeded to find compact “workable” expressions for K_{cr} , so this case has been treated numerically to compare possible observational differences of various source models.

Now we remind the main assumptions and the class of models used in order to discuss the results of the subsection 2.3.5. The simulations use the GLS parameters similar to that of Q 2237 + 030 [115, 138]. We consider the equal mass microlenses; we do not consider any mass distributions and/or populations of small (planetary) masses. Next, we consider most simple circular symmetric source models without effects of ellipticity etc. The results of subsection 2.3.5 can be summed up as follows. There are special classes of models: (i) accretion disk models having the dark region in the center and (ii) source models with a slow decrease of the (“long-range”) brightness distribution at large distances from the center. From our results we see that (i) and (ii) show in HAEs a behavior which is different from that of the Gaussian and the limb-darkening models on a relative accuracy level of $\sim 4\div 7\%$. There is then a possibility to distinguish such models on account of observations during HAEs. Outside HAE the surface brightness profile typically has little effect on microlensing (see [24, 93]).

We note that our conclusions involve concrete source models with a special choice of parameters (source sizes, microlensing optical depth etc) and a considerable work is to be fulfilled to obtain more general results. Also, our results are of a statistical nature, so our average estimate of η_m may be different from analogous one in a separate light curve observation.

Note that adding a sufficient number of microlenses having a small (e.g., planetary) masses (cf. [66, 87, 126, 138]) must produce an additional caustics that in its turn can give rise to fine features of light curves during HAE. One may expect that this can mimic features due to brightness distribution over the source. This question deserves further investigation.

2.4. Astrometric gravitational microlensing

2.4.1. General remarks

Besides photometric observations of microlensed sources, additional information about the source and lens structure may come from astrometric effects. We say about the astrometric gravitational microlensing when we deal with shifts and motions of the distant source images due to the gravitational fields of foreground stellar-mass objects (stars, black holes, dark matter substructures etc, either in the Milky Way or in the other galaxies).

Possibilities to detect an image motion of the remote source caused by the gravitational field of the Milky Way stars have been discussed for a long time [21, 59, 60, 78, 97]. The problem gained a new interest in connection with investigations of massive compact halo objects [58, 92, 133], see also [14, 18, 31,

45, 50–52, 125] and references therein; for the extended source and extended lens effects see [81, 88, 152, 154]. The extragalactic topics are less studied [82, 110, 125, 155]. Nevertheless the microarcsecond accuracy level appears to be sufficient to resolve the shape of a source image trajectory in extragalactic GLS in microlensing events. The corresponding image shifts can achieve the level of $\sim 10 \mu\text{as}$.

Astrometric measurements can provide valuable information about mass distributions of microlenses, which can complement the photometric observations of GLS images [135]. Observations of trajectories of the remote source images during the microlensing events, in addition to the photometric data, would give us a possibility to estimate the foreground field parameters and the optical depth of the continuous and discrete matter. This may be helpful in connection with the dark matter (DM) problem; in particular, this can be used to test the existence of the putative DM subhalos [34]. Though such positional effects are still beyond the accuracy of observations, the astrometric microlensing attracts a considerable attention during the last decade in connection with perspectives of spaceborn micro-arcsecond astrometry (the forthcoming Gaia mission, space based VLBI missions, optical Space Interferometry Mission). It should be pointed out that, typically, the accuracy of astrometric positioning is essentially higher than the image resolution. The other positive feature of astrometric microlensing events is the slow dependence on the impact parameter ($\sim p^{-1}$) and, hence, there is a larger probability of observing such events, once a required accuracy will be achieved.

There is a number of candidates for astrometric microlensing in our Galaxy that can be detected in the near future [12, 105, 112]. On the other hand, the unpredictable microlensing noise can spoil positions and proper motions of the objects resulting from future astrometric missions on a sub-micro-arcsecond level (e.g., [72]). The gravitational image motion due to microlensing effects may be comparable to proper motion of quasars [70, 111, 113, 149, 157].

2.4.2. Extended source and extended lens

Further, dealing with trajectories of the microlensed source images we mean the trajectory of the source image centroid (SIC), i.e. a weighted average over all elements of all the source images. The position of SIC can be defined as

$$\mathbf{R}(\mathbf{Y}) = \frac{1}{F(\mathbf{Y})} \iint \mathbf{x} I(\mathbf{y}(\mathbf{x}) - \mathbf{Y}) dx_1 dx_2, \quad (2.45)$$

$\mathbf{x} = (x_1, x_2)$, $\mathbf{y}(\mathbf{x})$ is the lens mapping, $\mathbf{Y} = (Y_1, Y_2)$ is the center of the source in the source plane; $F(\mathbf{Y})$ is given by formula (2.29).

Having in mind that most of the astrometric microlensing effects are still outside observational possibilities, for astrometric purposes it is quite reasonable to confine ourselves to the most simple source brightness profiles described in

Section 2.3.3. We only note that for the microlensing of a star the limb darkening model is most appropriate, and structures of real extragalactic sources (e.g. quasars) are more complicated.

In this subsection we consider microlensing by one mass in presence of an external shear. This can be the case of microlensing of a remote source by a small mass (planet) in presence of a background gravitational field of a star or microlensing by a star in the field of a putative DM clump.

First we consider a weak microlensing system, i.e. the linear distance from a microlensing mass to the line of sight is much larger than its Einstein radius. In this case if a remote point source is microlensed by a foreground moving point mass, the trajectory of the source image is approximately the circle in the rest frame of the source [31, 149]. In case of strong lensing HAE (linear distance from the microlens to the line of sight is of the order of the Einstein radius) this circle will be distorted. In any case the point source image is “repulsed” from the lensing point mass.

The trajectory qualitatively changes when the projection of the point mass onto the source plane crosses the extended source. In this case the SIC motion trajectory typically has a three-leaf form [88, 154]. This has been first shown in case of a source with uniform surface brightness [88] and in case of the Gaussian source [154]. The reason for such behavior is that when the lens is projected onto the internal part of the source, the “repulsion” of SIC is changed by its “attraction” to the lens due to larger amplification near it. For a sufficiently small values of impact parameter p of the lens with respect to the extended source center, the SIC trajectory bends and passes through the source center forming a self-intersection.

The external field effects, which are essential in extragalactic GLS, distort considerably the trajectory of SIC [35, 36, 155]. Below we present some simple examples of microlensing of an extended Gaussian source in presence of an external shear (Chang-Refsdal lens [20]). The configuration of the figures is as follows: the left hand panels show the SIC trajectories; the right-hand ones show corresponding dependencies of the amplification $K(t)$ as functions of time. The SIC trajectories are shown in the rest frame of the source; in the right upper corner the source center trajectory is shown (schematically) with respect to the caustic. We show in figures the impact parameter (p) and the shear (γ).

Fig. 2.5 shows the differences between the point-like source and the extended Gaussian one (2.34) in presence of an external shear. To compare astrometrical and photometrical effects for different source models we represent in (Figs. 2.6–2.7) the SIC trajectories and light curves of the Gaussian source and accretion disk (2.38) in band V, both with the same half-brightness radius of $0.08R_E$. The last one, Fig. 2.8 shows the SIC trajectories in case of finite-size microlensing masses. We note that the SIC trajectory depends on the source trajectory and upon the source model more distinctly than the light curve.

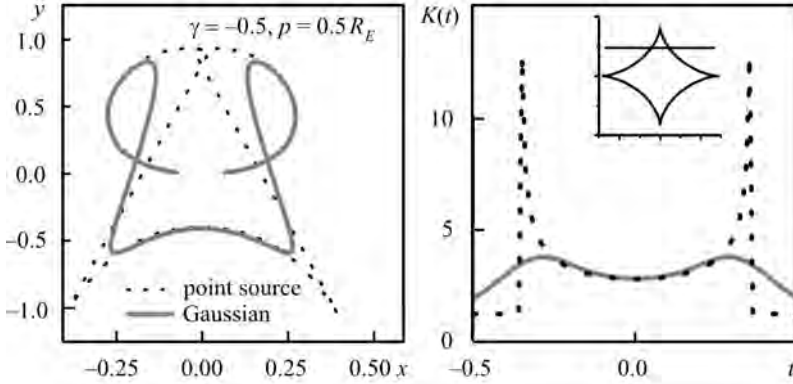


Fig. 2.5. Microlensing in the Chang–Refsdal lens for two different sources: point-like one and Gaussian one (2.34) with r.m.s. radius $R = 0.1R_E$ (see (2.32); this corresponds to the half-brightness radius (2.33) $R_{1/2} \approx 0.08R_E$). The source center crosses two caustic folds, left panel shows source image centroid trajectory, right one — the light curve

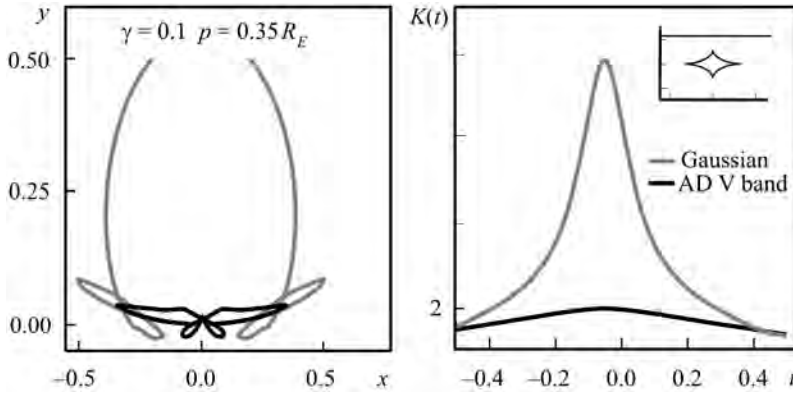


Fig. 2.6. Microlensing in the Chang–Refsdal lens: the source center passes over the cusp of the caustic. Source models: Gauss (2.34) and AD1 (2.38)

The simplest situation is when the source track passes far from the caustic. In this case the SIC trajectory is oval-like and light curve is continuous. However, when the source center track is close to the caustic, even if it does not cross it, the trajectory becomes much more complicated. In general, it can be self-intersected several times. When point source crosses the caustic, its SIC suffers a jump (Fig. 2.5). This is explained by the emergence or by disappearance of pairs of images of infinite brightness, leading to sudden jumps of the weighted average of positions of the source elements. Analytical expressions for such jumps can be found in [36]. For an extended source, corresponding discontinuities of the trajectory are smoothed out but may be quite noticeable. When the small source passes near the cusp or crosses it, the total images brightness increases dramatically, but no jump of image motion occurs because

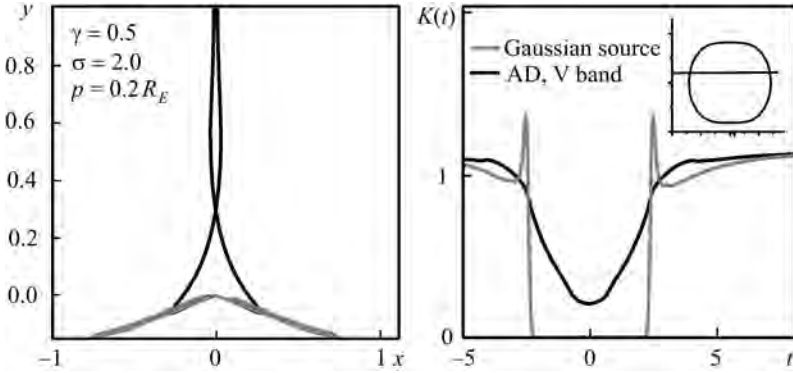


Fig. 2.7. Microlensing in the Chang–Refsdal lens with large convergence. Source models: Gauss (2.34) and AD1 (2.38)

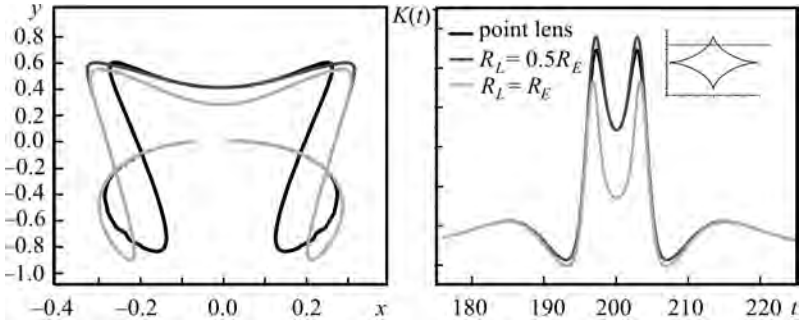


Fig. 2.8. Microlensing of the Gaussian source by the Zakharov & Sazhin lens [148] of different lens sizes R_L . The source size is $0.1R_E$

of the existence of one more image of infinite (in case of a point source) brightness which does not disappear. This distinguishes the high amplification events corresponding to the fold and cusp caustic crossings.

The effect of high optical depth of continuous matter is demonstrated in Fig. 2.7 to show possible observational signals of continuous DM near the line of the sight.

In papers [81, 148] astrometric and photometric effects of GLS with an extended microlens were considered. The microlensing effect caused by a compact body (for example, a star) must be distinguished from the eclipse-like effect in case of a presence of quite dense but essentially continuous background (cf. “subhalos”) of DM. Such “subhalos” are supposed to be extended clumps of DM. The size of these clumps predicted by Λ CDM model is larger than typical Einstein radius (see, e.g., Diemand et al. [29]). Such an object can manifest itself in microlensing process acting together with another compact object. In this case, smooth-shaped or even quasi-elliptical caustics can exist instead of, or together with, cusped ones (Fig. 2.7). When the source crosses the fold of

the smooth caustic, two images of it disappear. As a result after some peak of the image brightness there may be swift diminution. Thus DM can cause the effect like “eclipse”, demonstrated on Fig. 2.7. In an opposite case, when a subhalo has a finite size smaller than the Einstein radius, finite-size lens models can be applied to describe the situation. As it was shown in [148], the finite-size opaque lens can cause “ears” on the trajectory when one of the images is obscured by the lens, and the convergence causes the trajectory disruption when the source crosses caustic. In the light curve a finite lens size manifest itself in the magnification jumps when the image enters in the lens shadow. In case of an overcritical convergence the brightness decreases when the source is inside the caustic.

In case of the other “toy-example” of microlensing by one subhalo of the size a modelled by lens equation (2.42) with $N = 1$, the finite size of the subhalo causes an apparition of the additional quasielliptical caustic. Meanwhile the SIC trajectories do not differ principally from the point-lens situation. However, there is also a dip on the lightcurve similar to that obtained in Zakharov & Sazhin lens model [148].

The effect of the finite-size lens manifests itself in smoother way if the source is extended. In this case it changes the SIC trajectory and the light curve have no jumps or gaps. The most prominent effect on the light curve is in the recession of the dip between two caustic crossings, i.e. when the source is inside the caustic.

2.4.3. Statistics of weak astrometric microlensing

Correlation tensor of image shifts. In a general case of a complicated microlensing system we need some statistical measure of image motion; possible characteristic is proposed below.

Let $\delta\mathbf{x}$ describe a deviation of the point source image from unperturbed position. In case of one microlens this value typically varies as r^{-1} , where r is a distance of the microlens from the line of sight. Because of this we expect that in case of uniform distribution of many microlenses the usual correlation function and $\langle\delta\mathbf{x}^2\rangle$ diverge, and so we prefer to deal with a correlation tensor like that used in the turbulence theory [80]

$$D_{ij}(\tau) \equiv \langle(\delta x_i(t) - \delta x_i(t - \tau))(\delta x_j(t) - \delta x_j(t - \tau))\rangle. \quad (2.46)$$

This tensor is symmetric and it has a diagonal form in a system where the source moves along one of coordinate axes, e.g. along y_1 -axis. So a determination of $D_{ij}(\tau)$ from observations may help to constrain a direction of the source motion.

We shall illustrate calculation of D_{ij} in case of weak astrometric microlensing by N clumps having a uniform distribution over the lens plane. The system is described by the lens equation (2.42). We suppose that all the clumps are

independent, and \mathbf{x}_n has a uniform distribution over the lens plane. To be precise, we assume that the spatial distribution function for every \mathbf{x}_n is

$$\begin{cases} S^{-1}, & \mathbf{x}_n \in \Omega, \\ 0, & \mathbf{x}_n \notin \Omega, \end{cases} \quad (2.47)$$

where S is the area of domain Ω . Further considerations deal with the limit of Ω that will be blown up to cover the whole plane assuming

$$\frac{S(\Omega)}{N} = s(a, M) = \text{const}, \quad N \rightarrow \infty, \quad (2.48)$$

where we take into account that the surface per one clump $s(a, M)$ may be different for clumps of different mass and size. Density $f(a, M, \mathbf{x}) \sim |\mathbf{x}|^{-4}$ goes to zero sufficiently fast as $\mathbf{x} \rightarrow \infty$, so the clumps have a finite size and integral $M = \int d^2\mathbf{x} f(a, M, \mathbf{x}) < \infty$ is convergent. To save the space we do not consider a distribution of parameters a, M assuming that these parameters are the same for all the clumps. This means that in the general case the results below must be averaged over possible a, M .

According to (2.42) in case of weak microlensing the shift of the point source image is

$$\delta\mathbf{x} = \sum_{n=1}^N R_{E,n}^2 \frac{\mathbf{y} - \mathbf{x}_n}{|\mathbf{y} - \mathbf{x}_n|^2 + a_n^2}. \quad (2.49)$$

For a straight line motion of a source we put $y_1 = vt$, $y_2 = \text{const}$. Then we have a diagonal form of D_{ij} with

$$\begin{aligned} D_{11}(\tau) &= \frac{R_E^4}{s} \int d^2\mathbf{x} \left[\frac{x_{1,-}}{x_{1,-}^2 + x_2^2 + a^2} - \frac{x_{1,+}}{x_{1,+}^2 + x_2^2 + a^2} \right]^2, \\ D_{22}(\tau) &= \frac{R_E^4}{s} \int d^2\mathbf{x} \left[\frac{x_2}{x_{1,-}^2 + x_2^2 + a^2} - \frac{x_2}{x_{1,+}^2 + x_2^2 + a^2} \right]^2, \\ x_{1,\pm} &= x_1 \pm y_\tau, \quad y_\tau \equiv |\mathbf{v}| \tau/2. \end{aligned}$$

Calculation of the integrals yields

$$D_{11}(\tau) = \frac{\pi R_E^4}{s} F_{11}(y_\tau/a), \quad D_{22}(\tau) = \frac{\pi R_E^4}{s} F_{22}(y_\tau/a), \quad (2.50)$$

where

$$F_{11}(\xi) = \eta \ln \frac{1+\eta}{1-\eta}, \quad F_{22}(\xi) = \frac{1}{\eta} \ln \frac{1+\eta}{1-\eta} - 2, \quad \eta \equiv \frac{\xi}{\sqrt{\xi^2 + 1}}.$$

Statistical effect of gravitational dragging of a distant source image. In this section we consider statistical effects in the motion of the GLS images due to the variable gravitational field of a large number of moving

stars. Here we consider a rarefied collection of lensing masses, when a typical distances between the source and the microlens are much larger than the corresponding Einstein radius. For brevity we call this “weak” microlensing; this must be distinguished from the well-known extragalactic weak lensing, i.e. image distortions caused by the cosmic shear. Unlike the previous sections here we rule out strong microlensing events that are accompanied by considerable brightness amplification.

In some situations it will be difficult to separate the gravitational image motion (GIM) from the real proper motions, and this is important for accuracy of the fundamental reference frame based on extragalactic sources [72, 111, 113]. The gravitational field of moving point masses (which is essentially inhomogeneous) induces a stochastic motion of the source image in the reference frame of the source. On the other hand, smoothly distributed masses also induce a stochastic motion, but typical amplitude of the effect will be weaker. Indeed, we cannot take into account positions of all stars [72]; we only can work with their probability distribution leading to distribution of image motions of a source [149, 157]. The situation could be further complicated in presence of invisible DM clumps, if they exist on small scales.

In case of the point masses it is possible to estimate the probability distribution $P(\mathbf{u})$ of image motions \mathbf{u} (i.e. angular velocities) of the distant source image microlensed by collection of a randomly moving point masses [157]

$$P(\mathbf{u}) = \frac{u_0}{2\pi(u_0^2 + \mathbf{u}^2)^{3/2}}, \quad (2.51)$$

where u_0 is a characteristic value depending upon the transverse velocity of point masses, their value and their spatial density. It should be noted that the distribution (2.51) is obtained under the approximation of the weak microlensing [157], so that HAEs must be excluded.

The distribution (2.51) has a slowly decreasing tail yielding an infinite estimate of velocity squared $\langle \mathbf{u}^2 \rangle$. This tail is a formal consequence of pointness of the microlenses that makes possible very high GIMs. In fact this case is not covered by formula (2.51), which is valid for weak microlensing only. In case of smooth DM concentrations such very high GIMs will be absent.

If a bulk motion of microlensing masses is present, the average $\langle \mathbf{u} \rangle$ requires a special consideration. It has been pointed out in [149, 157] that stochastic GIM of an extragalactic source induced by stellar motions is accompanied with a systematic component (not a statistical average) which depends upon bulk velocity of microlensing stars, including stars that are far away from the line of sight. The typical velocity of this component remains non-zero even for a homogeneous distribution of microlensing masses which move in certain direction (all masses have the same collective velocity component). This needs some explanation because the average position of the unmoving source image

(averaged over a very long time) must be unchanged and, evidently, the statistical average of image velocity must be zero. However, when dealing with the extragalactic reference frame, in reality we do not deal with a very large observational time and/or with a sufficiently large number of sources to obtain a statistical average. In this case, because the strong microlensing events yielding the fast image motions are very rare, they in practice are not observable unless the number of simultaneously observed sources is of the order of millions or more. This is well known from theory and observations of MACHOs. Then the statistical average over set of all events is not a good characteristic of GIM; the most probable value of GIM (which is different from zero) would be a better measure.

Otherwise, we can estimate probability for all necessary velocity intervals. Detailed approach on this way, however, involves consideration of strong lensing events with different extended source models. However, to have an order-of-magnitude estimate, we can avoid calculations of probability distributions, if we confine ourselves to the domain of weak microlensing events (“ W ”, for brevity) [149, 153]. Typical velocity which is a characteristic of such events is a statistical average over the domain W , with HAE being excluded. Note that these rare strong lensing events (“ S ”) essentially contribute to the usual statistical average velocity $\langle \mathbf{u} \rangle_{W+S}$ (i.e. average over all the space of events $S + W$). If we exclude S -events (this is easy to do in real observations because of strong brightness amplification of a source), then we deal with “truncated” average velocity $\langle \mathbf{u} \rangle_W$ over W -events. This value is non-zero even in case of a homogeneous distribution of microlenses having a collective velocity. It is important to note that this value practically does not depend upon the exact definition of S -domain (that is upon a value of minimal impact parameter of microlensing masses with respect to the line of sight, which determines events “ S ”).

Note that this “truncated” average would better correspond to realistic observations when the typical velocity is estimated as an arithmetic mean over all reference sources used in extragalactic International Celestial Reference Frame (ICRF). In a near future the number of these sources will not exceed thousand. Therefore in fact we deal with most probable dispositions of lensing masses which typically do not produce the S -events: it is well known that the probability of such events is of the order of 10^{-6} per year in the Milky Way galaxy. Then in ICRF considerations it is reasonable to exclude such rare events that would hardly occur during the century.

In case of microlensing of distant sources by Milky Way stars we may neglect cosmological curvature. Evidently this does not contradict to assumption that the radiation source is at the infinity. Let unperturbed light ray moves from the infinitely distant radiation source in negative direction of z -axis of Cartesian coordinates $\{x, y, z\}$, the observer being at the origin. Let position

of microlensing point mass M be (\mathbf{r}, z) , where $\mathbf{r} = (x, y)$ is a two-dimensional vector in the transverse plane; i.e. $r = |\mathbf{r}|$ is the impact distance of the unperturbed ray with respect to the mass. In the case of weak microlensing $r \gg (mz)^{1/2}$, $m = GM/c^2$. Equations for the source image angular shift can be found in [106, 111, 149]. Because of smallness of the effect it can be calculated by taking a sum over contributions of all Milky Way stars.

We assume that a star at point (\mathbf{r}, z) has velocity $\mathbf{V}_p = \{\mathbf{v}_p(\mathbf{r}, z), w_p(\mathbf{r}, z)\}$, w_p is the velocity component parallel to the line of sight and \mathbf{v}_p represents the transversal component. Then we consider sum over all stars, which must further be averaged with the mass density $\rho(\mathbf{r}, z)$. This enables us [151, 153] to obtain an average GIM in domain W

$$\langle \mathbf{U}_{tot} \rangle_W = \frac{G}{c^2} \int dz \int d^2\mathbf{r} \rho(\mathbf{r}, z) \mathbf{U}(\mathbf{r}, z, \mathbf{V}_p(\mathbf{r}, z)), \quad (2.52)$$

where we denote

$$\begin{aligned} \mathbf{U}(\mathbf{r}, z, \mathbf{V}_p) = & -2 \left\{ \frac{1}{r^4} [\mathbf{v}_p r^2 - 2\mathbf{r}(\mathbf{r} \cdot \mathbf{v}_p)] \times \right. \\ & \left. \times \left[1 + \frac{z}{\sqrt{z^2 + r^2}} + \frac{zr^2}{2(z^2 + r^2)^{3/2}} \right] + \frac{w_p \mathbf{r} - z\mathbf{v}_p/2}{(z^2 + r^2)^{3/2}} \right\}, \end{aligned} \quad (2.53)$$

and we suppose that $\rho(\mathbf{r})$ vanishes outside a bounded domain, and this function is sufficiently smooth so as we can use approximation of weak microlensing inside the domain where $\rho(\mathbf{r}) \neq 0$.

Taking into account the explicit form (2.53) it is easy to see that a considerable contribution may be due to stars at large impact distances from the line of sight. Also one can show that the singularities in (2.52) for small r are integrable and the integral is convergent. This allows us to avoid the question about exact value of a lower limit of r in the definition of the domain W . However, the domain S appears to be also important! To see this directly we must compare GIM (2.52) with an average over all $S + W$ events in case of the same continuous mass distribution $\rho = \rho(\mathbf{r}, z, t)$. The shift of remote source image in case of continuous mass distribution has been treated in [90]. These shifts are of the order of $10^{-5} \div 10^{-6}$ radians; they are large but they cannot be observed from the Solar system because they are almost unchanged. The observable (at least in principle) value is the change of angular position with time [151, 153]:

$$\mathbf{U}_{tot}^* \equiv \frac{d\mathbf{\Psi}_{tot}}{dt} = \frac{G}{c^2} \int dz \int d^2\mathbf{r} \frac{\partial \rho}{\partial t} \tilde{\mathbf{\Psi}}(\mathbf{r}, z), \quad (2.54)$$

$$\tilde{\mathbf{\Psi}} = -2 \frac{\mathbf{r}}{r^2} \left[1 + z(z^2 + r^2)^{-1/2} \right], \quad (2.55)$$

where $\tilde{\mathbf{\Psi}}$ is a two dimensional vector describing the source image angular displacement per unit point mass m . Formula (2.54) represents an average image velocity over all $S + W$ events:

$$\mathbf{U}_{tot}^* = \langle \mathbf{U}_{tot} \rangle_{S+W}.$$

This average differs from (2.52). To compare (2.52) with (2.54) one must use the continuity equation, avoid singular points at $r = 0$ in \mathbf{U}_{tot}^* and apply the Ostrogradsky–Gauss theorem [153].

The result is as follows $\mathbf{U}_{tot}^* = \langle \mathbf{U}_{tot} \rangle_W + \mathbf{U}^{(1)}$, where the second term can be written as

$$\mathbf{U}^{(1)} \equiv \langle \mathbf{U}_{tot} \rangle_{S+W} - \langle \mathbf{U}_{tot} \rangle_W = -\frac{4\pi G}{c^2} \int_0^\infty dz \rho(z) \mathbf{V}_\perp(z), \quad (2.56)$$

where $\rho(z)$ stands for the density of microlensing masses along the line of sight, $\mathbf{V}_\perp = \mathbf{v}_p(\mathbf{0}, z)$ is the transverse velocity of microlenses (in radians per second) on the line of sight. Evidently (2.56) differs from zero. For example, if an observer at rest is situated in the center of Milky Way (stationary mass distribution), we have $\mathbf{U}_{tot}^* = 0$ (see Eq. (2.54)), but GIM does not equal to zero.

For an observer in the Solar system this effect yields a non-zero GIM value leading to apparent rotation of extragalactic reference frame in the direction of the Milky Way rotation [153]. For sources near the Galactic plane the effect amounts about $\approx 10^{-8}$ arcseconds per year [153]. The effect will be even smaller for sources with higher Galactic latitudes. Therefore, in principle (if the corresponding accuracy be achieved!), the effect can be observed from the Solar system.

2.4.4. Resume of Section 2.4

In this Section we review main points of astrometric microlensing. We demonstrate effects due to a finite size of the source and extended lens as well; a special attention is paid to effects that may serve as signals of dark matter. Several examples of microlensing by one mass in presence of an external shear are given. This can be the case of microlensing of a remote source by a small mass (planet) in presence of a background gravitational field of a star or microlensing by a star in the field of a putative DM clump.

Then we proceed to some statistical subjects of astrometric microlensing. We introduced the correlation tensor as a statistical characteristic of a stochastic image motion and applied this to a “toy” model of weak microlensing by dark matter clumps.

We have shown that gravitational field of foreground stars induces an image motion, which differs for a continuous and discrete mass density distribution. In the latter case image performs random walks, as distinct from a regular motion in case of continuous matter, plus some additional motion due to the collective motion of the microlensing masses. This effect leads to apparent rotation of extragalactic reference frame in the direction of the Milky Way rotation. In principle, the effect can be observed, however it is far beyond modern possibilities.

■

BIBLIOGRAPHY

1. D. Alcalde, E. Mediavilla, O. Moreau, J.A. Munoz, C. Libbrecht et al., QSO 2237 + 0305 VR Light Curves from Gravitational Lenses International Time Project Optical Monitoring, *Astrophys. J.* **572** (2002), 729–734.
2. C. Alcock, C.W. Akerlof, R.A. Allsman, Possible gravitational microlensing of a star in the Large Magellanic Cloud *Nature* **365**, Iss. 6447 (1993), 621–623.
3. A.N. Alexandrov, S.M. Koval, V.I. Zhdanov, Asymptotic relations for high magnification events in presence of the dark matter, *Visnyk Kyivskogo Universytetu, Astronomiya*, Iss. 49 (2012), 17–20.
4. A.N. Alexandrov, S.M. Koval, V.I. Zhdanov, Gravitational lens equation: critical solutions and magnification near folds and cusps, *Advances in Astron. and Space Phys.* **2**(2) (2012), 184–187.
5. A.N. Alexandrov, V.I. Zhdanov, Asymptotic expansions and amplification of a gravitational lens near a fold caustic, *Mon. Not. R. Astron. Soc.* **417** (2011), 541–554.
6. A.N. Alexandrov, V.I. Zhdanov, E.V. Fedorova, Asymptotic formulas for the magnification of a gravitational lens system near a fold caustic, *Astronomy Letters* **36** (2010) 329.
7. A.N. Alexandrov, V.I. Zhdanov, E.V. Fedorova, Analytical relations for gravitational lens mapping in the vicinity of a critical curve. *Visnyk Kyivskogo Universytetu, Astronomiya*, **39–40** (2003), 52–59 (in Ukrainian).
8. A.N. Alexandrov, V.I. Zhdanov, V.M. Sliusar, Caustic Crossing Events and Source Models in Gravitational Lens Systems, *Ukrainian J. Phys.* **56** (2011), 389–400.
9. T. Anguita, R.W. Schmidt, E.L. Turner, J. Wambsganss, R.L. Webster et al., The multiple quasar Q 2237 + 0305 under a microlensing caustic, *Astron. Astrophys.* **480** (2008) 327–334.
10. E. Aubourg, P. Barette, S. Brehin et al. The EROS Search for Dark Halo Objects, *The Messenger* **72** (1993) 20–27.
11. H. Bateman, A. Erdélyi, *Higher Transcendental Functions*, Vol. **1**. New York, McGraw-Hill, 1953.
12. V.A. Belokurov, N.W. Evans, Astrometric microlensing with the GAIA satellite, *Mon. Not. Roy. Astron. Soc.* **331** (2002), 649–665.

13. D.P. Bennett, C. Akerlof, C. Alcock, The First Data from the MACHO Experiment, Texas/PASCOS '92: Relativistic Astrophysics and Particle Cosmology. Eds.: Carl W. Akerlof and Mark A. Srednicki, Annals of the New York Academy of Sciences **688** (1993), 612.
14. D. Bennett, S. Rhie, A. Becker, N. Butler, J. Dann et al., Gravitational Microlensing Evidence for a Planet Orbiting a Binary Star System, Nature **402** (1999), 57–67.
15. J.A. Blackburne, C.S. Kochanek, The Effect of a Time-varying Accretion Disk Size on Quasar Microlensing Light Curves, Astrophys. J. **718** (2010), 1079–1084.
16. P.V. Bliokh, A.A. Minakov, Gravitational lenses (in Russian) Kiev, Naukova Dumka, 1989.
17. M.B. Bogdanov, A.M. Cherepashchuk, Reconstruction of the Strip Brightness Distribution in a Quasar Accretion Disk from Gravitational Microlensing Data, Astronomy Repts. **46** (2002), 626–633.
18. V. Bozza, Trajectories of the images in binary microlensing, Astron. Astrophys. **274** (2001), 13–27.
19. K. Chang, S. Refsdal, Flux variations of QSO 0957 + 561 A, B and image splitting by stars near the light path. Nature **282** (1979), 561–564.
20. K. Chang, S. Refsdal, Star disturbances in gravitational lens galaxies, Astron. Astrophys. **132** (1984) 168–178 [Erratum: Astron. Astrophys. **132** (1984), 168–178.
21. F. Chollet, A new method of measuring stellar masses, Academie des Sciences (Paris), Comptes Rendus. Sciences Physiques B **288** (1979), 163–165 (in French).
22. D. Clowe, A. Gonzalez, M. Markevitch, Weak-lensing mass reconstruction of the interacting cluster 1E 0657–558: direct evidence for the existence of dark matter, Astrophys. J. **604** (2004), 596–603.
23. D. Clowe, M. Bradac, A. Gonzalez, M. Markevitch, S.W. Randall, C. Jones, D. Zaritsky A direct empirical proof of the existence of dark matter, Astrophys. J. **648** (2006) L109–L113.
24. A.B. Congdon, C.R. Keeton, S.J. Osmer, Microlensing of an extended source by a power-law mass distribution, Mon. Not. R. Astron. Soc. **376** (2007), 263–272.
25. A.B. Congdon, C.R. Keeton, C.E. Nordgren, Analytic relations for magnifications and time delays in gravitational lenses with fold and cusp configurations, Mon. Not. R. Astron. Soc. **389** (2008), 398–406.
26. X. Dai, E. Agol, M.W. Bautz, G.P. Garmire, Chandra Observations of QSO 2237 + 0305, Astrophys. J. **589** (2003) 100–110.
27. S. Deguchi, W.D. Watson, Diffraction in gravitational lensing for compact objects of low mass, Astrophys. J. **307** (1986), 30–37.
28. J. Diemand, M. Kuhlen, P. Madau et al., Clumps and streams in the local dark matter distribution, Nature **454** (2008), 735–738.
29. J. Diemand, B. Moore, J. Stadel, Earth-mass dark-matter haloes as the first structures in the early Universe, Nature **433**, Iss. 7024 (2005), 389–391.
30. M. Dominik, Revealing stellar brightness profiles by means of microlensing fold caustics, Mon. Not. R. Astron. Soc. **353** (2004), 118–132.
31. M. Dominik, K. Sahu, Astrometric Microlensing of Stars, Astron. J. **534** (2000), 213–226.

32. S. Dong, I.A. Bond, A. Gould, S. Kozlowski, N. Miyake et al., Microlensing Event MOA-2007-BLG-400: Exhuming the Buried Signature of a Cool, Jovian-Mass Planet, *Astrophys. J.* **698** (2009), 1826–1837.
33. S. Dong, D.L. DePoy, B.S. Gaudi, A. Gould, C. Han et al., Planetary Detection Efficiency of the Magnification 3000 Microlensing Event OGLE-2004-BLG-343, *Astrophys. J.* **642** (2006), 842–860.
34. A.L. Erickcek, N.M. Law Astrometric microlensing by local dark matter subhalos, *Astrophys. J.* **729** (2011), 49.
35. E. Fedorova, Binary gravitational microlensing of extragalactic sources, *Visnyk Kyivskogo Universytetu. Astronomiya* **45** (2009), 33–39.
36. E.V. Fedorova, V.I. Zhdanov, A.N. Alexandrov, Motion of source image in Chang–Refsdal lens, *Journal of Phys. Studies* **4** (2002), 465–468.
37. E.V. Fedorova, V.I. Zhdanov, C. Vignali, G.G.C. Palumbo, Q 2237 + 0305 in X-rays: spectra and variability with XMM-Newton, *Astron. Astrophys.* **490** (2008), 989–994.
38. C.J. Fluke, R.L. Webster, Investigating the geometry of quasars with microlensing, *Mon. Not. R. Astron. Soc.* **302** (1999), 68–74.
39. B.S. Gaudi, D. Bennett, A. Udalski, A. Gould, G. Christie et al., Discovery of a Jupiter/Saturn Analog with Gravitational Microlensing, *Science* **319** (2008), 927–937.
40. B.S. Gaudi, A.O. Petters, Gravitational Microlensing near Caustics. I. Folds, *Astrophys. J.* **574** (2002), 970–984.
41. B.S. Gaudi, A.O. Petters, Gravitational Microlensing near Caustics. II. Cusps, *Astrophys. J.* **580** (2002), 468–489.
42. I.M. Gel’fand, G.E. Shilov, *Generalized Functions*, Vol. 1, New York, Academic Press, 1964.
43. R. Gil-Merino, J. Gonzalez-Cadello, L.J. Goicoechea, V.N. Shalyapin, G.F. Lewis, Is there a caustic crossing in the lensed quasar Q 2237 + 0305 observational data record?, *Mon. Not. R. Astron. Soc.* **371** (2006), 1478–1482.
44. L.J. Goicoechea, D. Alcalde, E. Mediavilla, J.A. Muñoz, Determination of the properties of the central engine in microlensed QSOs, *Astron. Astrophys.* **397** (2003), 517–525.
45. A. Gould, C. Han, Astrometric Resolution of Severely Degenerate Binary Microlensing Events, *Astrophys. J.* **538** (2000), 653–656.
46. A. Gould, A. Loeb, Discovering planetary systems through gravitational microlenses, *Astrophys. J.* **396** (1992) 104–114.
47. A. Gould, A. Udalski, D. An, D.P. Bennett, A.-Y. Zhou et al., Microlens OGLE-2005-BLG-169 Implies That Cool Neptune-like Planets Are Common, *Astrophys. J.* **644** (2006) L37–L40.
48. B. Grieger, R. Kayser, S. Refsdal, Gravitational micro-lensing as a clue to quasar structure, *Astron. Astrophys.* **194** (1988), 54–64.
49. K. Griest, N. Safizadeh, The Use of High-Magnification Microlensing Events in Discovering Extrasolar Planets, *Astrophys. J.* **500** (1998), 37.
50. C. Han, On the Astrometric Behavior of Binary Microlensing Events, *Mon. Not. Roy. Astron. Soc.* **325** (2001), L1281–L1287.
51. C. Han, M. Chun, K. Chang, Astrometric properties of gravitational binary-microlens events and their applications, *Astrophys. J.* **526** (1999), 405–410.

52. C. Han, S. Park, Y. Lee, Distribution of caustic-crossing intervals for galactic binary-lens microlensing events, *Mon. Not. R. Astron. Soc.* **314** (2000), 59–64.
53. A. Heavens, Weak lensing: Dark Matter, Dark Energy and Dark Gravity, *Nucl. Phys. Proceedings Suppl.* **194 B** (2009), 76–81.
54. J.F. Hennawi, N. Dalal, P. Bode, Statistics of Quasars Multiply Imaged by Galaxy Clusters, *Astrophys. J.* **654**, Is. 1 (2007), 93–98.
55. J.S. Heyl, Diffractive microlensing – I. Flickering planetesimals at the edge of the Solar system, *Mon. Not. Roy. Astron. Soc. (Letters)* **402** (2010), L39–L43.
56. J.S. Heyl, Diffractive microlensing – II. Substellar disc and halo objects, *Mon. Not. Roy. Astron. Soc.* **411** (2011), 1780–1786.
57. H. Hoekstra, D. Jain, Weak Gravitational Lensing and its Cosmological Applications, *Ann. Rev. Nucl. Part. Sci.* **58** (2008), 99–123.
58. E. Hog, I.D. Novikov, A.G. Polnarev, MACHO photometry and astrometry, *Astron. Astrophys.* **294** (1995), 287–294.
59. M. Hosokawa, K. Ohnishi, T. Fukushima, Astrometric Microlensing and Degradation of Reference Frames, In: *Highlights of Astronomy, Vol. 13, Proc. XXVth General Assembly of the IAU-2003*. Ed. by O. Engvold. (San Francisco, CA: Astronomical Society of the Pacific, 2005), p. 602.
60. M. Hosokawa, K. Ohnishi, T. Fukushima, M. Takeuti, Parallaxic variation of gravitational lensing and measurement of stellar mass, *Astron. Astrophys.* **278** (1993), L27–L30.
61. W. Hu, Power Spectrum Tomography with Weak Lensing, *Astrophys. J.* **522** (1999), L21–L24.
62. J. Huchra, V. Gorenstein, S. Kent, I. Shapiro, G. Smith et al., 2237 + 0305: A new and unusual gravitational lens, *Astron. J.* **90** (1985), 691–696.
63. D. Huterer, Weak lensing, dark matter and dark energy, *General Relativity and Gravitation*, **42**, Iss. 9 (2010), 2177–2195.
64. M.J. Irwin, R.L. Webster, P.C. Hewett, R.T. Corrigan, R.I. Jedrzejewski, Photometric variations in the Q 2237 + 0305 system – First detection of a microlensing event, *Astron. J.* **98** (1989), 1989–1994.
65. J. Janczak, A. Fukui, S. Dong, B. Monard, S. Kozłowski et al., Sub-Saturn Planet MOA-2008-BLG-310Lb: Likely to be in the Galactic Bulge, *Astrophys. J.* **711** (2010), 731–743.
66. M. Jaroszynski, B. Paczynski, A Possible Planetary Event OGLE-2002-BLG-055, *Acta Astron.* **52** (2002) 361–367.
67. M. Jaroszynski, J. Skowron, Microlensing of Q 2237 + 0305: Simulations and Statistics, *Acta Astron.* **56** (2006), 171–182.
68. N. Kaiser, Weak gravitational lensing of distant galaxies, *Astrophys. J.* **388** (1992), 272–286.
69. N. Kaiser, G. Squires, Mapping the dark matter with weak gravitational lensing, *Astrophys. J.* **404** (1993) 441–450.
70. N.S. Kardashev, Cosmological proper motion, *Astronomicheskii Zhurnal.* **63** (1986), 845–849.
71. C.R. Keeton, B.S. Gaudi, A.O. Petters, Identifying Lenses with Small-Scale Structure. II. Fold Lenses, *Astrophys. J.* **635** (2005), 35–59.
72. S.A. Klioner, A practical relativistic model for microarcsecond astrometry in space, *Astron. J.* **125** (2003), 1580–1597.

73. C.S. Kochanek, What Do Gravitational Lens Time Delays Measure?, *Astrophys. J.* **578**, Iss. 1 (2002) 25–32.
74. C.S. Kochanek, Gravitational Lens Time Delays in Cold Dark Matter, *Astrophys. J.* **583**, Iss. 1 (2003) 49–57.
75. C.S. Kochanek, Quantitative Interpretation of Quasar Microlensing Light Curves, *Astrophys. J.* **605** (2004) 58–77.
76. C.S. Kochanek, E.E. Falco, C. Impey, J. Lehar, B. McLeod, H.-W. Rix, CASTLES Survey, <http://www.cfa.harvard.edu/castles/>
77. C.S. Kochanek, P. Schneider, J. Wambsganss, Gravitational Lensing: Strong, Weak & Micro, Proceedings of the 33rd Saas-Fee Advanced Course. Edited by G. Meylan, P. Jetzer, P. North. (Springer-Verlag: Berlin, 2006).
78. J. Kovalevsky, F. Mignard, M. Froeschle, Space astrometry prospects and limitations, Proc. IAU Symp. 114, eds. J. Kovalevsky and V.A. Brumberg (1979), 369–382.
79. A.A. De Laix, T. Vachaspati, Gravitational lensing by cosmic string loops, *Phys. Rev. D.* **54** (1996), 4780–4791.
80. L.D. Landau, E.M. Lifshitz, Fluid mechanics (Pergamon, New York, 1959).
81. C.-H. Lee, S. Seitz, A. Riffeser, R. Bender, Finite-source and finite-lens effects in astrometric microlensing, *Mon. Not. R. Astron. Soc.* **407** (2010), 1597–1608.
82. G.F. Lewis, R.A. Ibata, Quasar Image Shifts Resulting from Gravitational Microlensing, *Astrophys. J.* **501** (1998), 478–485.
83. A.V. Mandzhos, The Mutual Coherence of Gravitational Lens Images, *Pis'ma Astron. Zh.* **7** (1981), 387–389 (in Russian).
84. A.V. Mandzhos, Mutual coherence properties of images of a quasar observed through a gravitational lens, Microlensing by a double star. *Astronomicheskii Zh.* **68** (1991), 236–243 (in Russian)
85. A.V. Mandzhos, Mutually-Interferometric and structural properties of the images of an object in the vicinity of the gravitational lens cusp: The degree of mutual coherence of the images, *Astronomicheskii Zh.* **72** (1995), 153–160 (in Russian).
86. S. Mao, Y. Jing, J.P. Ostriker, J. Weller, Anomalous Flux Ratios in Gravitational Lenses: For or against Cold Dark Matter?, *Astrophys. J.* **604**, Issue 1 (2004), L5–L8.
87. S. Mao, B. Paczynski, Gravitational microlensing by double stars and planetary systems, *Astrophys. J.* **374** (1991), L37–L40.
88. S. Mao, H.J. Witt, Extended source effects in astrometric gravitational microlensing, *Mon. Not. Roy. Astron. Soc.* **300** (1998), 1041–1046.
89. N. Matsunaga, K. Yamamoto, The finite source size effect and the wave optics in gravitational lensing. *Journal of Cosmology and Astroparticle Physics*, **01** (2006), 023.
90. A.A. Minakov, V.N. Shalyapin, Effect of the gravitational field of the Galaxy on the apparent position, brightness and spatial density of remote radiation sources. I. A lens model of the Galaxy and deflection angles of rays, *Kinematics and Physics of Celestial Bodies* **6** (1990), 49–59.
91. A.A. Minakov, V.G. Vakulik, Statistical analysis of gravitational microlensing (in Russian), Kiev, Naukova Dumka, 2010.

92. M. Miyamoto, Y. Yoshii, Astrometry for Determining the MACHO Mass and Trajectory, *Astron. J.* **110** (1995), 1427–1432.
93. M.J. Mortonson, P.L. Schechter, J. Wambsganss, Size Is Everything: Universal Features of Quasar Microlensing with Extended Sources, *Astrophys. J.* **628** (2005), 594–603.
94. A.M. Mosquera, C.S. Kochanek, The Microlensing Properties of a Sample of 87 Lensed Quasars, *Astrophys. J.* **738** (2011), article id. 96.
95. D. Munshi, P. Valageas, L. Van Waerbeke, A. Heavens, Cosmology with Weak Lensing Surveys, *Phys. Rept.* **462** (2008), 67–121.
96. M. Oguri, How many arcminute-separation lenses are expected in the 2dF QSO Survey, *Mon. Not. Roy. Astron. Soc.* **339**, Iss. 2 (2003), L23–L27.
97. K. Ohnishi, M. Hosokawa, T. Fukushima, Secular Component of Apparent Proper Motion of QSOs Induced by Gravitational Lens of the Galaxy, *ASP Conf. Proc.* **289** (2003), 461–464.
98. L. Miller, A. Lopes, R. Smith, S. Croom, B. Boyle, T. Shanks, P. Outram, Possible arcminute-separation gravitational lensed QSOs in the 2dF QSO Survey, *Mon. Not. Roy. Astron. Soc.* **348**, Is. 2. (2004) L395–L405.
99. B. Paczynski, Gravitational microlensing by the galactic halo, *Astrophysical Journ.* **304**, Iss. 1 (1986) 1–5.
100. O. Pejcha, D. Heyrovský, Extended-Source Effect and Chromaticity in Two-Point-Mass Microlensing, *Astrophys. J.* **690** (2009), 1772–1796.
101. A.O. Petters, H. Levine, J. Wambsganss, *Singularity Theory and Gravitational Lensing* (Birkhauser, Boston, 2001).
102. S. Poindexter, C.S. Kochanek, The Transverse Peculiar Velocity of the Q2237+0305 Lens Galaxy and the Mean Mass of Its Stars, *Astrophys. J.* **712** (2010), 658–667.
103. S. Poindexter, C.S. Kochanek, Microlensing Evidence that a Type 1 Quasar is Viewed Face-On, *Astrophys. J.* **712** (2010), 668–673.
104. S. Poindexter, N. Morgan, C.S. Kochanek, The Spatial Structure of an Accretion Disk, *Astrophys. J.* **673** (2008), 34–38.
105. S. Proft, M. Demleitner, J. Wambsganss, Prediction of astrometric microlensing events during the Gaia mission, *Astron. Astrophys.* **536** (2011), A50, 11P.
106. K.A. Pyragas, V.I. Zhdanov, V.V. Zhdanova, I.T. Zhuk, Light propagation in a weak gravitational field of a stochastic system of pointlike sources, *Soviet Physics Journal* **29**, Iss. 12 (1986), 1019–1023 (*Izvestiya Vuzov. Fizika*. No. 12, 1986, p. 79)
107. S. Refsdal, On the possibility of determining Hubble’s parameter and the masses of galaxies from the gravitational lens effect, *Mon. Not. Roy. Astron. Soc.* **128** (1964) 307–310.
108. S. Refsdal, On the possibility of determining the distances and masses of stars from the gravitational lens effect, *Mon. Not. Roy. Astron. Soc.*, **134** (1966), 315–319.
109. K.C. Sahu, Microlensing towards the Magellanic Clouds: nature of the lenses and implications on dark matter. In: *The Dark Universe: Matter Energy and Gravity*, M. Livio (ed.), (Cambridge Univ. Press: Cambridge), (2003), p. 14, also astro-ph/0302325.

110. S.A. Salata, V.I. Zhdanov, Statistical Astrometric Microlensing of Extended Sources, *Astron. J.* **125** (2003) 1033–1037.
111. M.V. Sazhin, A fundamental limit to the accuracy of astrometric measurements, *Pis'ma Astron. Zh.* **22** (1996) 573–577.
112. M.V. Sazhin, O.S. Sazhina, M.S. Pshirkov, Apparent motions of quasars due to microlensing, *Astronomy Reports*, **55** (2011), 954–961.
113. M.V. Sazhin, V.E. Zharov, A.V. Volynkin, T.A. Kalinina, Microarcsecond instability of the celestial reference frame, *Mon. Not. R. Astron. Soc.* **300** (1998), 287–291.
114. R. Schild, I.S. Masnyak, B.I. Hnatyk, V.I. Zhdanov, Anomalous fluctuations in observations of Q 0957 + 561 A,B: Smoking gun of a cosmic string? *Astron. Astrophys.* **422** (2004) 477–482.
115. R. Schmidt, R.L. Webster, F.G. Lewis, Weighing a galaxy bar in the lens Q 2237 + 0305, *Mon. Not. Roy. Astron. Soc.* **295** (1998), 488.
116. P. Schneider, J. Ehlers, E.E. Falco, *Gravitational Lenses* (Springer, New York, 1992).
117. P. Schneider, A. Weiss, A gravitational lens origin for AGN-variability? Consequences of microlensing, *Astron. Astrophys.* **171** (1987), 49–65.
118. P. Schneider, A. Weiss, The gravitational lens equation near cusps, *Astron. Astrophys.* **260** (1992) 1–13
119. N.I. Shakura, R.A. Sunyaev, Black holes in binary systems. Observational appearance, *Astron. Astrophys.* **24** (1973), 337–355.
120. V.N. Shalyapin, Caustic Crossing in the Gravitational Lens Q 2237 + 0305, *Astron. Lett.* **27** (2001) 150–155.
121. V.N. Shalyapin, L.J. Goicoechea, D. Alcalde, E. Mediavilla, J.A. Muñoz, R. Gil-Merino, The Nature and Size of the Optical Continuum Source in QSO 2237 + 0305, *Astrophys. J.* **579** (2002), 127–135.
122. D. Sluse, J. Surdej, J.-F. Claeskens, D. Hutsemekers, C. Jean, F. Courbin, T. Nakos, M. Billeres, S.V. Khmil, A quadruply imaged quasar with an optical Einstein ring candidate: 1RXS J113155.4-123155, *Astron. Astrophys.* **406** (2003), L43–L46.
123. R. Takahashi, T. Suyama, S. Michikoshi, Scattering of gravitational waves by the weak gravitational fields of lens objects, *Astron. Astrophys.* **438**, Iss. 1 (2005), L5–L8.
124. P. Tisserand, L. Le Guillou, C. Afonso et al. Limits on the Macho content of the Galactic Halo from the EROS-2 Survey of the Magellanic Clouds, *Astron. Astrophys.* **469** (2007), 387–404.
125. M. Treyer, J. Wambsganss, Astrometric microlensing of quasars. Dependence on surface mass density and external shear, *Astron. Astrophys.* **416** (2004), 19–34.
126. Y. Tsapras, K. Horne, S. Kane, K. Carson, Microlensing limits on numbers and orbits of extrasolar planets from the 1998–2000 OGLE events, *Mon. Not. Roy. Astron. Soc.* **343** (2003), 1131–1144.
127. J.A. Tyson, R.A. Wenk, F. Valdes, Detection of systematic gravitational lens galaxy image alignments. Mapping dark matter in galaxy clusters, *Astrophys. J. (Part 2 – Letters)* **349** (1990), L1–L4.
128. J.A. Tyson, F. Valdes, J.E. Jarvis, A.P. Mills (Jr.), Galaxy mass distribution from gravitational light deflection, *Astrophys J.* **281**(1984), L59–L62.

129. A. Udalski, M. Szymanski, J. Kaluzny et al. The Optical Gravitational Lensing Experiment, *Acta Astronomica* **42**, No. 4 (1992), 253–284.
130. A. Udalski, M.K. Szymanski, M. Kubiak, G. Pietrzynski, I. Soszynski et al., The Optical Gravitational Lensing Experiment. OGLE-III Long Term Monitoring of the Gravitational Lens QSO 2237 + 0305, *Acta Astron.* **56** (2006) 293–305.
131. V. Vakulik, R. Schild, V. Dudinov, S. Nuritdinov, V. Tsvetkova et al., Observational determination of the time delays in gravitational lens system Q 2237 + 0305, *Astron. Astrophys.* **447** (2006), 905–913.
132. V. Vakulik, R. Schild, G. Smirnov, V. Dudinov, V. Tsvetkova, Q 2237 + 0305 source structure and dimensions from light-curve simulation, *Mon. Not. Roy. Astron. Soc.* **382** (2007), 819–825.
133. M.A. Walker, Microlensed Image Motions, *Astrophys. J.* **453** (1995), 37–39.
134. D. Walsh, R.F. Carswell, R.J. Weymann, 0957 + 561 A, B – Twin quasistellar objects or gravitational lens?, *Nature* **279** (1979), 381–384.
135. J. Wambsganss, Gravitational microlensing. Part 4 of “Gravitational Lensing: Strong, Weak, and Micro”, Saas-Fee Advanced Course 33. Edited by G. Meylan, P. North, P. Jetzer (Berlin, Springer, 2006), p. 453–540.
136. J. Wang, M.C. Smith, Using microlensed quasars to probe the structure of the Milky Way, *Mon. Not. Roy. Astron. Soc.* **410**, Iss. 2 (2011) 1135–1144.
137. P.R. Wozniak, C. Alard, A. Udalski, M. Szymański, M. Kubiak et al., The Optical Gravitational Lensing Experiment Monitoring of QSO 2237 + 0305, *Astrophys. J* **529** (2000), 88–92.
138. J.S. Wyithe, E.L. Turner, Determining the microlens mass function from quasar microlensing statistics, *Mon. Not. Roy. Astron. Soc.* **320** (2001), 21–30.
139. J.S. Wyithe, R.L. Webster, E.L. Turner, A measurement of the transverse velocity of Q 2237 + 0305, *Mon. Not. Roy. Astron. Soc.* **309** (1999), 261–272.
140. J.S. Wyithe, R.L. Webster, E.L. Turner, Interpretation of the OGLE Q 2237 + 0305 microlensing light curve (1997–1999), *Mon. Not. R. Astron. Soc.* **318** (2000) 1120–1130.
141. J.S. Wyithe, R.L. Webster, E.L. Turner, D.J. Mortlock, A gravitational microlensing determination of continuum source size in Q 2237 + 0305, *Mon. Not. Roy. Astron. Soc.* **315** (2000), 62–68.
142. L. Wyrzykowski, S. Kozłowski, J. Skowron et al., The OGLE view of microlensing towards the Magellanic Clouds. I. A trickle of events in the OGLE-II LMC data, *Mon. Not. Roy. Astron. Soc.* **397** (2009), 1228–1242.
143. L. Wyrzykowski, S. Kozłowski, J. Skowron, et al., The OGLE view of microlensing towards the Magellanic Clouds. II. OGLE-II Small Magellanic Cloud data, *Mon. Not. Roy. Astron. Soc.* **407** (2010), 189–200.
144. L. Wyrzykowski, S. Kozłowski, J. Skowron et al., The OGLE View of Microlensing microlensing toward the Magellanic Clouds. III. Ruling out OGLE-III LMC data, *Mon. Not. Roy. Astron. Soc.* **413** (2011), 493–508.
145. A. Yonehara, Evidence for a Source Size of Less than 2000 AU in Quasar 2237 + 0305, *Astrophys. J.* **548** (2001) L127–L130.
146. S.A. Zabel, J.B. Peterson, Extended Source Diffraction Effects near Gravitational Lens Fold Caustics, *Astrophys. J.* **594** (2003), 456–463.
147. A.F. Zakharov, Gravitational lenses and microlenses (Yanus-K, Moscow, 1997) (in Russian).

148. A.F. Zakharov, M.V. Sazhin, Non-compact astronomical objects as microlenses, *Astron. Astrophys.* **18** (1999), 27–38.
149. V.I. Zhdanov, The General Relativistic Potential of Astrometric Studies at Microarcsecond Level, in: *Astronomical and Astrophysical Objectives of Sub-Milliarcsecond Optical Astrometry*, Eds. E. Hog, P.K. Seidelmann (Dordrecht: Kluwer, 1995), P. 295–300.
150. V.I. Zhdanov, Autocorrelation function of microlensed radio emission, *Astronomy Lett.* **25**, Iss. 12 (1999), 793–796.
151. V.I. Zhdanov, A.N. Alexandrov, E.V. Fedorova, V.M. Sliusar, Analytical methods in gravitational microlensing, *ISRN Astron. Astrophys.* **2012** (2012), ID 906951, 21 p.
152. V.I. Zhdanov, A.N. Alexandrov, S.A. Salata, Motion of images of microlensed extended sources: analytical relations and numerical estimates for moderate optical depths, *Kinematika i Fizika Nebesnykh Tel.* **16** (2000), 336–345 (in Russian).
153. V.I. Zhdanov, E.V. Fedorova, A.N. Alexandrov, Gravitational dragging of distant source images caused by Galaxy stars, *Kinematika i Fizika Nebesnykh Tel.* **20** (2004), 422–429 (in Russian).
154. V.I. Zhdanov, S.A. Salata, Motion of the image of a distant object microlensed by stars in a foreground galaxy, *Kinematics Phys. Celest. Bodies.* **14** (1998), 156–161.
155. V.I. Zhdanov, S.A. Salata, E.V. Fedorova, Background field effects in astrometric microlensing, *Astron. Lett.* **27** (2001), 562–567.
156. V.I. Zhdanov, J. Surdej, Quasar pairs with arcminute angular separations, *Astron. Astrophys.* **372** (2001), 1–7.
157. V.I. Zhdanov, V.V. Zhdanova, Analytical relations for time-dependent statistical microlensing, *Astron. Astrophys.* **299** (1995), 321–325.
158. A. Zitrin, T. Broadhurst, Y. Rephaeli, S. Sadeh, The Largest Gravitational Lens: MACS J0717.5 + 3745 ($z = 0.546$), *Astrophys. J. Lett.* **707** (2009), L102–L106.

3

CHAPTER

CHEMICAL EVOLUTION OF LATE TYPE GALAXIES OF DIFFERENT MASSES

L.S. Pilyugin

Foreword. Big Bang Nucleosynthesis: the initial chemical composition of galaxies

The chemical elements we see in nature have two origins: primordial and stellar. For a brief time in its early evolution the Universe was a cosmic nuclear reactor. The expansion and cooling of the Universe limited this epoch to the first few minutes [127, 128]. During Big Bang Nucleosynthesis, in the first ~ 20 minutes of the evolution of the Universe, the light nuclides, D, ^3He , ^4He , and ^7Li were manufactured. Since the baryon density at Big Bang Nucleosynthesis is relatively low and the time-scale short, only reactions involving two-particle collisions occur. The absence of a stable nuclide at mass-5 ensures that the primordial abundance of ^7Li is much smaller than that of the other light nuclides and the similar gap at mass-8 guarantees negligible primordial abundances for any heavier nuclei. Stars jump the mass-5 and -8 instability by having gravity compress the matter to sufficient densities and have much longer times available so that three-body collisions, $3^4\text{He} \rightarrow ^{12}\text{C}$, can occur. The Big Bang Nucleosynthesis provides not only the initial chemical composition of galaxies but also a key test of the standard models of cosmology and the particle physics. For Big Bang Nucleosynthesis in the standard cosmology (SBBN), there is only one adjustable parameter, the baryon density parameter η_{10} . For the more general Big Bang Nucleosynthesis (BBN) case the relic abundances depend on two adjustable parameters, the baryon density parameter and the expansion rate parameter S (or, equivalently, the “equivalent number of neutrinos” N_ν) [127, 128, 130].

The universal density of baryons can be quantified by the value $\eta_{10} \equiv 10^{10}(n_B/n_\gamma)$, where n_B is the number density of baryons (the only baryons present at Big Bang Nucleosynthesis are nucleons, i.e. protons and neutrons), n_γ is the number density of cosmic background photons. It is convenient to quantify the number density of baryons using a combination of Ω_B , the ratio of the baryon mass density to the critical mass density, and h , the present value of the Hubble constant H_0 measured in units of $100 \text{ km s}^{-1} \text{ Mpc}^{-1}$ [128],

$$\eta_{10} = 273.9 \Omega_B h^2.$$

In the standard model of cosmology, the expansion rate is described by the Hubble parameter H [127, 128]. In contrast to the standard model of cosmology, there is a class of non-standard cosmological models in which the expansion rate may differ from its standard model value. Deviations from the standard model may be parameterised by an expansion rate parameter, $S \equiv H'/H$. Deviations from the standard model may be quantified equally well by the “equivalent number of neutrinos”, $\Delta N_\nu \equiv N_\nu - 3$. At the BBN

$$S^2 = 1 + 0.163 \Delta N_\nu.$$

It should be noted that $\Delta N_\nu \neq 0$ need not be the result of extra neutrino flavors but could be due to other extensions of the standard models. In particular, ΔN_ν need not be an integer and need not be positive [128].

Thus, relic abundances of deuterium, D_P , and helium, Y_p , depend on two adjustable parameters, η_{10} and S . Steigman with co-authors [51, 121, 128, 129] have identified extremely simple but quite accurate analytic fits over a limited range in these variables ($4 < \eta_{10} < 8$, $0.8 < S < 1.1$, corresponding to $0.8 < \Delta N_\nu < 4.3$). These are [121, 129]

$$D_P \equiv 10^5 (\text{D/H})_P = 2.64 \left[\frac{6}{\eta_{10} - 6(S - 1)} \right]^{1.6},$$

$$Y_P = 0.2485 + 0.0016[(\eta_{10} - 6) + 100(S - 1)].$$

As can be seen, primordial abundance of deuterium depends largely on the baryon density parameter, η_{10} (deuterium is a cosmological baryometer), while that of ${}^4\text{He}$ is sensitive to the early Universe expansion rate, S (${}^4\text{He}$ is an early Universe chronometer) [128].

The products of primordial nucleosynthesis, along with the cosmic microwave background photons, are relics from the early evolution of the Universe whose observations probe the standard model of cosmology [127, 128, 130]. The Wilkinson Microwave Anisotropy Probe (WMAP) aimed at understanding cosmology through full-sky observations of the cosmic microwave background

(CMB). The WMAP full-sky maps of the temperature and polarization anisotropy in five frequency bands provide most accurate view to date of conditions in the early Universe. The WMAP allows to derive parameters of the cosmological models including the baryon density, the cold dark matter density, the dark energy density, and the Hubble parameter [24, 52, 53, 57, 126]. Larson et al. (2011) derived the cosmological parameters inferred from the WMAP 7-year data alone [57]. They found the baryon density $\Omega_B = 0.0449 \pm 0.0028$, the cold dark matter density $\Omega_{DM} = 0.222 \pm 0.026$, the dark energy density $\Omega_{DE} = 0.734 \pm 0.029$, and the Hubble parameter $H_0 = 71.0 \pm 2.5 \text{ km s}^{-1} \text{ Mpc}^{-1}$. These values of Ω_B and $h \equiv H_0/100$ results in $\eta_{10} = 6.199$ (see relations above). Then the SBBN (with $S = 1$) predicts the primordial abundance of deuterium $D_P \equiv 10^5(D/H)_P = 2.505$ and the primordial abundance of helium $Y_P \equiv 0.2488$.

The comparison between the predicted and observed primordial abundances of the light nuclides provides a key probe of the standard models of cosmology and the particle physics (for recent review of these tests, see [128, 131, 132]). Reliable measures of $(D/H)_P$ and Y_P are difficult to obtain, however. As gas is cycled through stars, deuterium is destroyed and no significant amounts of D are synthesized in stellar nucleosynthesis [28]. Then the post-BBN abundance of deuterium decreases along with the abundance of the heavy elements. Pettini et al. (2008) have noted that the astrophysical environments which seem most appropriate are the hydrogen-rich clouds absorbing the light of background QSOs at high redshift, but rare combination of: (a) large neutral hydrogen column density; (b) low metallicity corresponding to negligible astration of D; and (c) most importantly, low internal velocity dispersion of the absorbing atoms allowing the isotope shift of only 81.6 km s^{-1} to be adequately resolved, are required for this observational test to succeed [82]. Thus, while the potential of this method was appreciated more than thirty years ago, the number of trustworthy measurements of $(D/H)_P$ is still only five or six. Pettini et al. (2008) have studied the most metal-poor damped $Ly\alpha$ system known to date, at $z = 2.61843$, with an oxygen abundance only $\sim 1/250$ of the solar value. They have concluded that the D/H measurements in damped $Ly\alpha$ systems appear to converge to a mean value $\log(D/H)_P = -4.55 \pm 0.03$ ($D_P = 2.82$).

As gas is cycled through successive generations of stars, hydrogen is burned to helium and beyond, with net effect being that the post-BBN abundance of helium increases with the abundance of heavy elements. This contamination of the relic helium abundance by stellar-produced helium is non-negligible. To derive the primordial helium abundance from the observed helium abundances, they should be corrected for such pollution. The most favored approach is the one pioneered by Peimbert and Torres—Peimbert [77, 78] using observations of extragalactic H II regions, especially in dwarf irregular and blue compact or

H II galaxies with low metallicity. One plots a regression of helium against oxygen (and sometimes also nitrogen) abundance and extrapolates to zero oxygen (nitrogen) to get the primordial mass fraction Y_P . This method of primordial helium abundance determination has been used by many authors [33, 41, 42, 44, 47, 75, 79]. Recently, Peimbert et al. (2007) [79] have obtained $Y_P = 0.2477 \pm 0.0029$ and Izotov and Thuan (2010) [47] have found $Y_P = 0.2565 \pm 0.0010(\text{stat.}) \pm 0.0050(\text{syst.})$. It should be noted that the accuracy in observationally-inferred primordial helium abundance Y_P needed to confirm (or reject) the SBBN extends to the third decimal place.

Steigman (2010) has discussed the recent data and concluded that the SBBN-predicted and observationally-inferred primordial abundances of D and ^4He are in good agreement (within the errors) [132]. He noted however that some challenges remain. For example, what are the sources (and the magnitudes) of the systematic errors in observationally-inferred primordial abundance of helium and, are there observing strategies to reduce them?

The use of a linear regression of helium against oxygen can be the oversimplification and can be the source of the systematic error in observationally-inferred primordial abundance of helium. Indeed, a prominent feature of the $Y\text{--O/H}$ diagram is that the helium abundance Y shows a large scatter at a fixed value of the oxygen abundance (see Fig. 1 in Izotov and Thuan (2010) [47]). A part of this scatter is due to uncertainties in the helium and oxygen abundances. But another part is likely to be real and reflects a real dispersion in the helium abundance at a given oxygen abundance. This fact must be kept in mind when using the observations to infer the primordial abundance. This scatter can suggest that the evolutionary tracks in the $Y\text{--O/H}$ diagram differ from galaxy to galaxy. If this is the case then the observational data points must be fitted by a set of curves rather than by a single line. In order to exclude the ambiguity in the interpretation of the $Y\text{--O/H}$ diagram and provide with the adequate determination of Y_P , the origin of the scatter in the helium abundances in galaxies with a given oxygen abundance should be established.

A similar feature can be seen in the N/H--O/H diagram, i.e. the N/H--O/H diagram (especially in its high-metallicity part) also shows a large scatter in the nitrogen abundances in galaxies with a given oxygen abundance. Here the oxygen and nitrogen abundances in late type galaxies at current epoch and the evolution of the N/H and the O/H abundances with redshift and galaxy stellar mass of galaxy are discussed. The origin of the scatter in the nitrogen abundances in galaxies with a given oxygen abundance is considered. The approach developed in the investigating of the N/H--O/H diagram can be also applied to the study of the $Y\text{--O/H}$ diagram.

3.1. Introduction

The oxygen abundance is one of the fundamental characteristics of a galaxy. Oxygen abundances are mandatory in investigations of different aspects of the formation and evolution of galaxies. Investigating the macroscopic properties of galaxies that could drive their chemical evolution is very important in understanding their global evolution, which has been the goal of many studies over the past decades. It has been found, for example, that the properties of H II regions in late type galaxies are linked to macroscopic characteristics of galaxies such as luminosity or Hubble type. Smith (1975) concluded that excitation differences among the H II regions of Sbc–Scd–Irr galaxies can be best understood in terms of an abundance sequence which progresses from higher to lower heavy-element enrichment as one progresses from earlier to later type galaxies [124]. He also noted that his results show no apparent correlation between the average heavy-element abundance and galaxy mass. The correlation between oxygen abundance and the morphological type of galaxy was later confirmed in [140, 142].

Lequeux et al. (1979) revealed that the oxygen abundance correlates with total galaxy mass for irregular galaxies, in the sense that the higher the total mass, the higher the heavy element content [60]. Since the galaxy mass is a poorly known parameter, the metallicity–luminosity relation instead of the mass–metallicity relation is usually considered [39, 62, 72, 95, 111, 123, 139]. Garnett & Shields (1987) found that spiral disk abundance also correlates very well with galaxy luminosity [34]. They concluded that the metallicity of galaxies correlates better with galaxy luminosity than with morphological type. Zaritsky et al. (1994) found that the characteristic gas-phase abundances and luminosities of spiral galaxies are strongly correlated, and this relationship maps almost directly onto the luminosity–metallicity relationship of irregular galaxies [142].

The origin of this correlation is open to debate. It is widely suggested that there are two mechanisms which can be responsible for a luminosity–metallicity relation for spirals and irregulars: higher astration level and decreasing efficiency of heavy-element loss with increasing luminosity. The mass exchange between a galaxy and its environment can alter the relation between oxygen abundance and gas mass fraction; it mimics the variation in the oxygen yield. To investigate the possibility of a varying yield, Edmunds and Vila-Costas have suggested to use the “effective” oxygen yield, y_{eff} , as the yield that would be deduced if a system was assumed to behave as in the simple model of chemical evolution [26, 140]. The variation of the value of the effective oxygen yield from galaxy to galaxy can be considered as indicative of the efficiency of mass exchange between galaxies and their environments. A similar approach, the concept of the oxygen abundance deficiency in the galaxy which is introduced

as a deficiency of the oxygen abundance observed in the galaxy in comparison with the oxygen abundance predicted by the closed-box model for the same gas mass fraction, has been used in [89, 92, 93].

In recent years, the number of good-quality spectra of emission-line galaxies has increased dramatically due to the completion of several large spectral surveys, and in particular of the Sloan Digital Sky Survey (SDSS) [141]. Measurements of emission lines in those spectra have been carried out for abundance determinations and investigation of the luminosity–metallicity relation. Thus, Melbourne & Salzer (2002) have considered the luminosity–metallicity relation for 519 galaxies in the KPNO International Spectroscopic Survey (KISS) [69], Lamareille et al. (2004) for 6387 galaxies in the 2dF Galaxy Survey [54], Tremonti et al (2004) for about 53000 galaxies in the Sloan Digital Sky Survey (SDSS) [136], Asari et al. (2007) for 82302 SDSS galaxies [3], and Thuan et al. (2010) for around 84000 SDSS galaxies [133]. This opens also the possibility of using the SDSS spectral base to study the evolution of O and N abundances in galaxies in the redshift range $z \leq 0.4$ (e.g. [133, 136]).

Accurate abundance determinations are mandatory for such investigations. In H II regions, they can be derived from measurements of temperature-sensitive line ratios, such as $[\text{OIII}]\lambda\lambda 4959, 5007 / [\text{OIII}]\lambda 4363$. Unfortunately, in oxygen-rich H II regions, the temperature-sensitive lines such as $[\text{OIII}]\lambda 4363$ are often too weak to be detected. For such H II regions, abundance indicators based on more readily observable strong lines were suggested by Alloin et al. (1979) [2] and Pagel et al. (1979) [74]. This approach has found widespread acceptance and use. Many relations have been suggested to convert various metallicity-sensitive emission-line combinations into metallicity or temperature estimations (e.g. see the review in [27, 62]). The calibration relations express the abundances (and electron temperatures) in terms of the fluxes in the strong emission lines of O^{++} , O^+ , N^+ , and S^+ . It should be stressed that “strong lines–oxygen abundance” calibrations do not form an uniform family. The oxygen abundances derived with these different calibrations are not in good agreement, with differences amounting up to 0.7 dex [27, 62, 98]. In fact, there actually exist many different scales of oxygen abundances in H II regions. What metallicity scale is the correct one? There is strong evidence in favor of the metallicity scale defined by the classic T_e method, considered the most reliable one (see the discussion in [10, 98]). Indeed, the oxygen abundances derived with the T_e method have been confirmed by high-precision model-independent determinations of the interstellar oxygen abundance in the solar vicinity, using high-resolution observations of the weak interstellar $\text{OI}\lambda 1356$ absorption line towards stars, and by recent determinations of stellar abundances. A number of empirical calibration relations (derived using spectra of H II regions with well-measured electron temperatures as calibration data-points) produce abundances which are in agreement with the abundance scale

defined by the classic T_e method [9, 81, 102, 103, 106, 108, 133]. Hence, only the abundances determined via the T_e method or through those calibrations are considered here.

Here we have discussed the oxygen and nitrogen abundances at the present epoch and the observed evolution (with redshift) over last ~ 4.5 Gyr in late type galaxies of different masses. In Section 2 the parameters of the radial distributions (the extrapolated central intersect value and the gradient) of the oxygen and nitrogen abundances in 54 nearby late type galaxies are considered. The correlations between characteristic oxygen abundance and macroscopic properties of galaxies are examined. In Section 3 the maximum attainable value of oxygen abundance in spiral galaxies is considered. In Section 4 the evolution of the oxygen and nitrogen abundances with redshift and galaxy stellar mass of galaxy are investigated. In Section 5 the origin of the scatter in the nitrogen abundances in galaxies with a given oxygen abundance is considered. Section 6 is a brief summary.

3.2. The chemical abundances in nearby galaxies

3.2.1. Central abundances and radial gradients

Relatively detailed studies of the chemical composition of the interstellar medium of galaxies can be carried out by using the emission lines in spectra of individual H II regions in nearby galaxies. The oxygen abundance in the interstellar gas is usually used as a tracer of metallicity in late type (spiral and irregular) galaxies at the present epoch. We have carried out a compilation of published spectra of H II regions in late type galaxies [101]. Our list contains more than 1000 individual spectra of H II regions in 54 spiral and irregular galaxies. Only the galaxies with available spectra for at least four H II regions were taken into consideration. Using these spectrophotometric data, the oxygen and nitrogen abundances were derived for this sample of H II regions through the P method [91, 94].

In investigations of the relationships between the oxygen abundances and the macroscopic properties of spiral galaxies, the concept of the characteristic oxygen abundance has been introduced: it is defined as the oxygen abundance in the disk at a predetermined galactocentric distance. Due to the presence of radial abundance gradients in the disks of spiral galaxies, the choice of the characteristic (or representative) value of the oxygen abundance in a galaxy is not trivial. The value of the oxygen abundance at the B -band effective (half-light) radius of the disk [34, 36], the value of the central oxygen abundance extrapolated to zero radius from the radial abundance gradient [140], the value of the oxygen abundance at $r = 0.4 R_{25}$, where R_{25} is the isophotal (or photometric) radius [142], and the value of the oxygen abundance at one disk scale length from the nucleus [35], have been used as the characteristic oxygen

abundance in a galaxy. To estimate the characteristic oxygen abundance in spiral galaxies, the radial distribution of oxygen abundances within the galaxies should be established.

The radial oxygen abundance distribution in every galaxy is well fitted by the following equation:

$$12 + \log(\text{O}/\text{H}) = 12 + \log(\text{O}/\text{H})_0 + C_{\text{O}/\text{H}} \times (R/R_{25}), \quad (3.1)$$

where $12 + \log(\text{O}/\text{H})_0$ is the extrapolated central oxygen abundance, $C_{\text{O}/\text{H}}$ is the slope of the oxygen abundance gradient expressed in terms of dex/ R_{25} , and R/R_{25} is the fractional radius (the galactocentric distance normalized to the disk isophotal radius).

The derived radial distributions of the oxygen abundance in 12 galaxies are presented in Fig. 3.1 (see [101] for more galaxies). The oxygen abundances for individual H II regions are shown by the filled circles. The linear best fits (derived via the least squares method) to these points are presented by solid lines. The galactocentric distances are normalized to the isophotal radius.

As in the case of the oxygen abundance, the radial nitrogen abundance distribution in every galaxy is well fitted by the following equation:

$$12 + \log(\text{N}/\text{H}) = 12 + \log(\text{N}/\text{H})_0 + C_{\text{N}/\text{H}} \times (R/R_{25}), \quad (3.2)$$

and the radial distribution of the nitrogen to oxygen abundance ratios is well fitted by the single equation of the type:

$$\log(\text{N}/\text{O}) = \log(\text{N}/\text{O})_0 + C_{\text{N}/\text{O}} \times (R/R_{25}). \quad (3.3)$$

The derived radial distributions of the nitrogen abundances and nitrogen-to-oxygen abundance ratios in 12 galaxies are also shown in Fig. 3.1. The nitrogen abundances for individual H II regions are shown by the open squares. The linear best fits to these points are presented by dashed lines. The nitrogen-to-oxygen abundance ratios for individual H II regions are shown by the open circles. The linear best fits to these points are presented by solid lines.

For the majority of galaxies, all the H II regions with available oxygen and nitrogen emission line measurements were used in the analysis of the abundance gradients. For a few galaxies, however, some H II regions were rejected for the following reason. The adopted relationship between oxygen abundance and strong line intensities (P method) is double-valued with two distinct parts usually known as the “lower” and “upper” branches of the R_{23} -O/H relationship. Thus, one has to know a priori on which of the two branches the H II region lies. The adopted expression for the oxygen abundance determination in H II regions is valid only for H II regions which belong to the upper branch, with $12 + \log(\text{O}/\text{H})$ higher than ~ 8.2 . It has been known for a long time [118, 124]

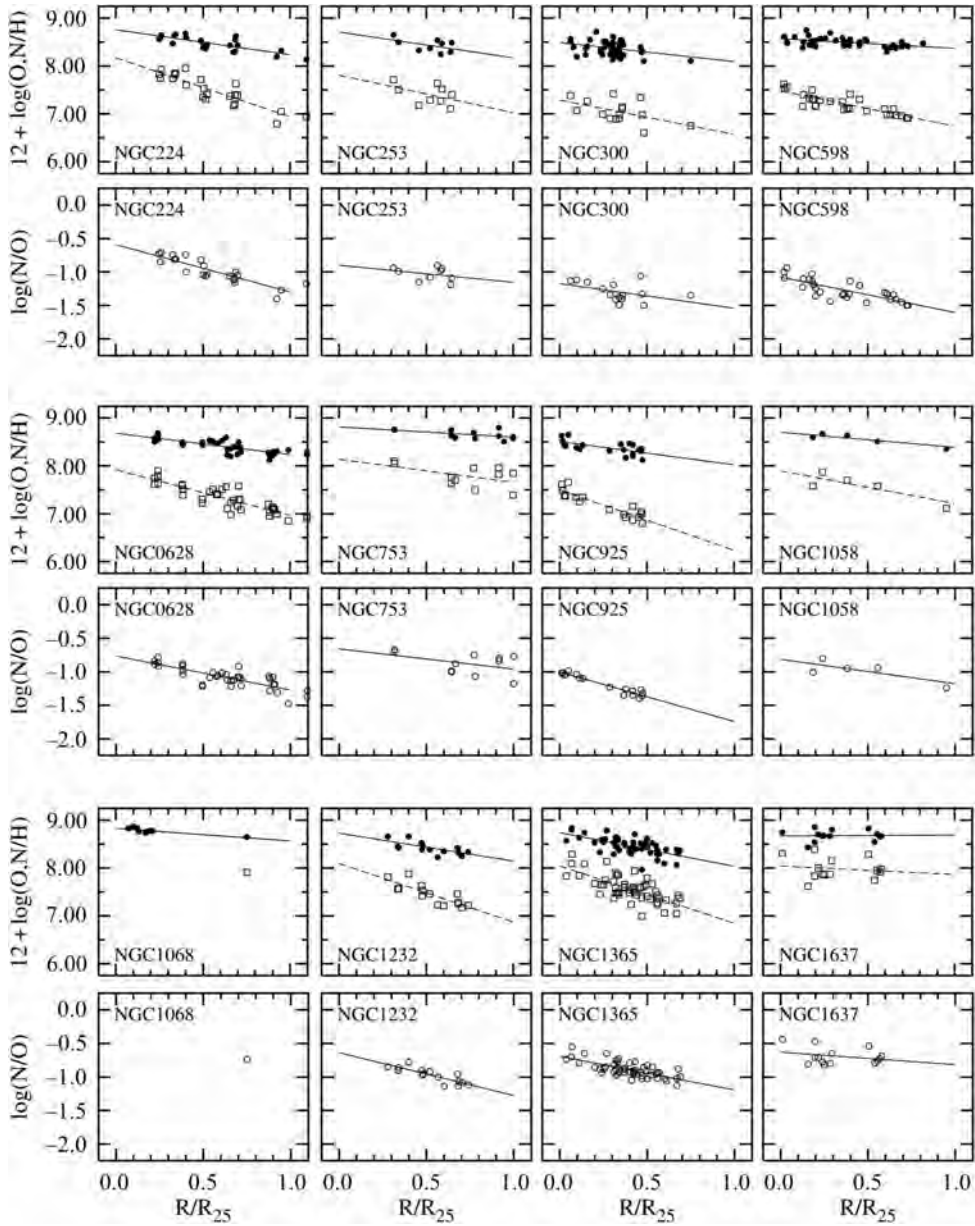


Fig. 3.1. Oxygen and nitrogen abundances, and nitrogen-to-oxygen abundance ratios versus galactocentric distance for late type galaxies. The oxygen abundances are shown by filled circles, the linear least-squares fits to these data are presented by solid lines. The nitrogen abundances are shown by open squares, the linear least-squares fits to these data are presented by dashed lines. The nitrogen-to-oxygen abundance ratios are shown by open circles, the linear least-squares fits to these data are presented by solid lines. The galactocentric distances are normalized to the isophotal radius

that disks of spiral galaxies show radial oxygen abundance gradients, in the sense that the oxygen abundance is higher in the central part of the disk and decreases with galactocentric distance. We thus start from the H II regions in the central part of disks and move outward until the radius R^* where the oxygen abundance decreases to $12 + \log(\text{O}/\text{H}) \sim 8.2$. It should be noted that it is difficult to establish the exact value of R^* due to the scatter in oxygen abundance values at any fixed radius. An unjustified use of the adopted relation in the determination of the oxygen abundance in low-metallicity H II regions beyond R^* would result in overestimated oxygen abundances, and would produce a false bend in the slope of abundance gradients [97]. Therefore, H II regions with galactocentric distances larger than R^* , those with $12 + \log(\text{O}/\text{H})$ less than 8.2 were rejected.

The credibility of the radial oxygen abundance gradients (as well as gradients of the nitrogen abundance and gradients of the nitrogen-to-oxygen abundance ratios) is defined not only by the large number of H II regions and their small dispersion but also by the distribution of these H II regions along the galactic radius. For example, the six H II regions in the galaxy NGC 4651 give a much more reliable value of abundance gradients than the 8 H II regions in the galaxy NGC 4725. The estimated values of the radial oxygen abundance gradient in galaxies NGC 1068, NGC 1637, NGC 2841, NGC 3521, NGC 4571, NGC 4713, NGC 4725, NGC 5033, and NGC 5055 are not beyond question [101].

3.2.2. Characteristic oxygen abundance in spirals as a function of M_B , V_{rot} , and Hubble type

As was noted above, in investigations of the relationships between the oxygen abundances and the macroscopic properties of spiral galaxies, the concept of the characteristic oxygen abundance has been introduced: it is defined as the oxygen abundance in the disk at a predetermined galactocentric distance. Following [142], the value of the oxygen abundance at $r = 0.4R_{25}$ will be used here as the *characteristic* oxygen abundance in a galaxy.

The characteristic oxygen abundance in spiral galaxies as a function of absolute blue magnitude M_B is shown in Fig. 3.2. The solid line is the characteristic oxygen abundance—luminosity relationship (linear best fit derived through the least squares method):

$$12 + \log(\text{O}/\text{H}) = 6.93 (\pm 0.37) - 0.079 (\pm 0.018) M_B. \quad (3.4)$$

The dashed lines correspond to this relation shifted by -0.2 dex and $+0.2$ dex. Fig. 3.2 clearly demonstrates that there is a correlation between the characteristic oxygen abundance of a galaxy and its blue luminosity. The bulk of the galaxies lies within the band defined by the dashed lines (± 0.2 dex

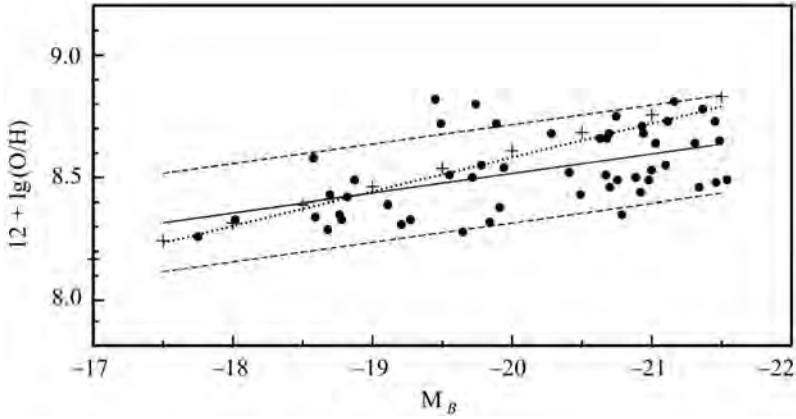


Fig. 3.2. The characteristic oxygen abundance as a function of absolute blue magnitude M_B for sample of spiral galaxies from [101]. The solid line is the derived $O/H-M_B$ relationship. The dashed lines correspond to the lines shifted by ± 0.2 dex along the vertical axes relatively to the $O/H-M_B$ relationship. The dotted line is the $O/H-M_B$ relationship for our sample of irregular galaxies extrapolated to the luminosity range of spiral galaxies. The line presented by the plus signs is the extrapolated $O/H-M_B$ relationship for irregular galaxies from [111]

around the best fit). The dotted line in Fig. 3.2 is the luminosity—metallicity relationship for irregular galaxies (see below) extrapolated to the luminosity range of spiral galaxies. The line presented in Fig. 3.2 by the plus signs is the extrapolated $O/H-M_B$ relationship for irregular galaxies derived by Richer & McCall (1995). Inspection of Fig. 3.2 shows that the slope of the derived luminosity—metallicity relationship for spiral galaxies is lower than the one for irregular galaxies.

We have carried out a search in the literature for measurements of rotation velocities for our sample of spiral galaxies [101]. Unfortunately, a measurement of the rotation velocity is not available for 7 galaxies of our sample. On the contrary, there are two or more measurements of rotation velocities for a number of galaxies. The more recent value (or a mean value if the measurements are close to each other) is taken for these galaxies. The adopted values of the rotation velocity for the galaxies and corresponding references are listed in [101].

The characteristic oxygen abundance in spiral galaxies as a function of rotation velocity V_{rot} is shown in Fig. 3.3. The solid line is the oxygen abundance — rotation velocity relationship (linear best fit)

$$12 + \log(O/H) = 8.18 (\pm 0.06) + 0.00179 (\pm 0.00031) V_{\text{rot}}. \quad (3.5)$$

The dotted lines correspond to this relation shifted by -0.2 dex and $+0.2$ dex. Fig. 3.3 shows that the characteristic oxygen abundance of a galaxy correlates

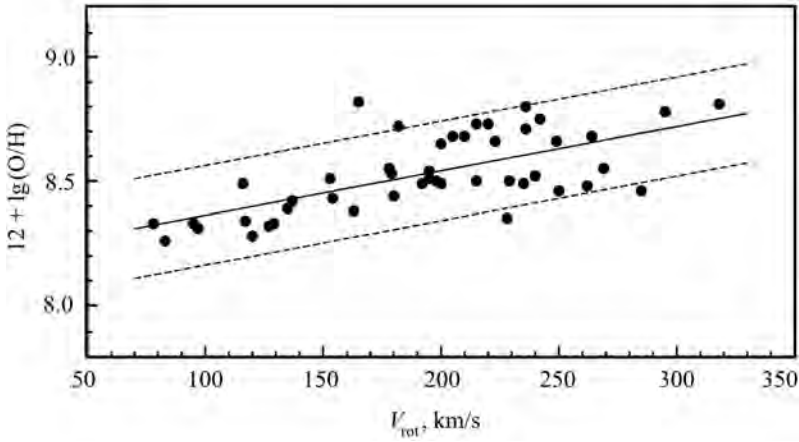


Fig. 3.3. The characteristic oxygen abundance as a function of rotation velocity for sample of spiral galaxies from [101]. The solid line is the O/H– V_{rot} relationship, the dashed lines correspond to the lines shifted by ± 0.2 dex relatively to the O/H– V_{rot} relationship

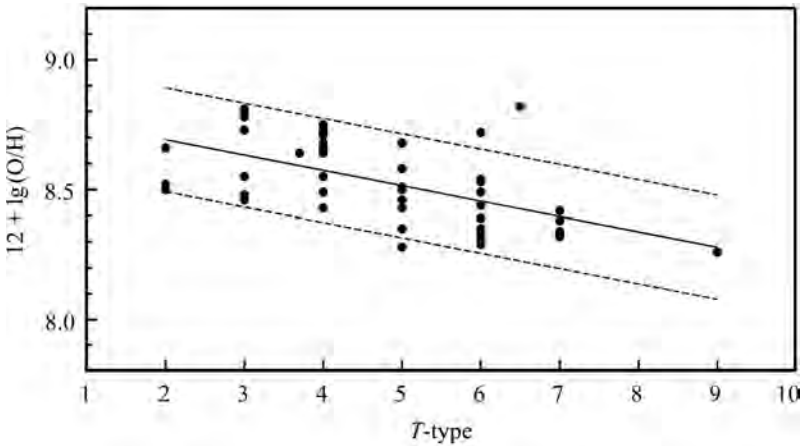


Fig. 3.4. The characteristic oxygen abundance as a function of Hubble type, expressed in the terms of T type, for sample of spiral galaxies from [101]. The solid line is the O/H– T relationship derived through the least squares method. The dashed lines correspond to the lines shifted by -0.2 dex and $+0.2$ dex relatively to the derived O/H– T relationship

with its rotation velocity. The deviation of an individual galaxy from the general trend is usually less than 0.2 dex. The mean value of the scatter in the characteristic oxygen abundances at a given rotation velocity is 0.12 dex for 46 points.

The characteristic oxygen abundance in spiral galaxies as a function of morphological type, expressed in terms of T type, is shown in Fig. 3.4. The

solid line is the characteristic oxygen abundance– T relationship (best fit)

$$12 + \log(\text{O}/\text{H}) = 8.81 (\pm 0.06) - 0.059 (\pm 0.011) T. \quad (3.6)$$

The dotted lines correspond to this relation shifted by -0.2 dex and $+0.2$ dex. Fig. 3.4 shows that the characteristic oxygen abundance of a galaxy correlates with its morphological type. The deviation of an individual galaxy from the general trend usually does not exceed the value ± 0.2 dex, as in the cases of the O/H – M_{B} and the O/H – V_{rot} diagrams. The mean value of the scatter in the characteristic oxygen abundances at a given morphological type is 0.13 dex for 53 points.

One can see that the characteristic oxygen abundance correlates well with both the absolute blue luminosity, the rotational velocity, and the morphological type; the correlation with the rotation velocity perhaps being slightly tighter.

3.2.3. Comparison between O/H – M_{B} relationships for spiral and irregular galaxies

Zaritsky et al. (1994) found that the characteristic gas-phase oxygen abundance–luminosity relation of spiral galaxies extends almost directly to the luminosity–metallicity relationship of irregular galaxies [142]. Melbourne and Salzer (2002) [69] and Lamareille et al. (2004) [54] found that the slope of the oxygen abundance–luminosity relationship for high-luminosity galaxies is steeper than when dwarf galaxies are considered alone and may be evidence that the relationship is not linear over the full luminosity range. Garnett (2002) concluded that the metallicity–luminosity correlation shows a roughly uniform growth in the average present-day O/H abundance over 11 mag in absolute blue magnitude M_{B} [36]. Let us compare the derived metallicity–luminosity relationship for spiral galaxies with that for irregular galaxies.

The irregular galaxies were selected from the samples in [95, 111]. The luminosities, oxygen abundances and the values of the rotation velocity for irregular galaxies are taken from these studies.

The characteristic oxygen abundances in spiral and irregular galaxies are plotted versus absolute blue magnitude M_{B} in Fig. 3.5. The filled circles in Fig. 3.5 are spiral galaxies, and the solid line is the O/H – M_{B} relationship for spiral galaxies, Eq. (3.4). The open squares in Fig. 3.5 are irregular galaxies. The dashed line is the O/H – M_{B} relationship (best fit) for our sample of irregular galaxies

$$12 + \log(\text{O}/\text{H}) = 5.80 (\pm 0.17) - 0.139 (\pm 0.011) M_{\text{B}}. \quad (3.7)$$

The dotted line is the O/H – M_{B} relationship for irregular galaxies

$$12 + \log(\text{O}/\text{H}) = 5.59 (\pm 0.54) - 0.153 (\pm 0.025) M_{\text{B}}, \quad (3.8)$$

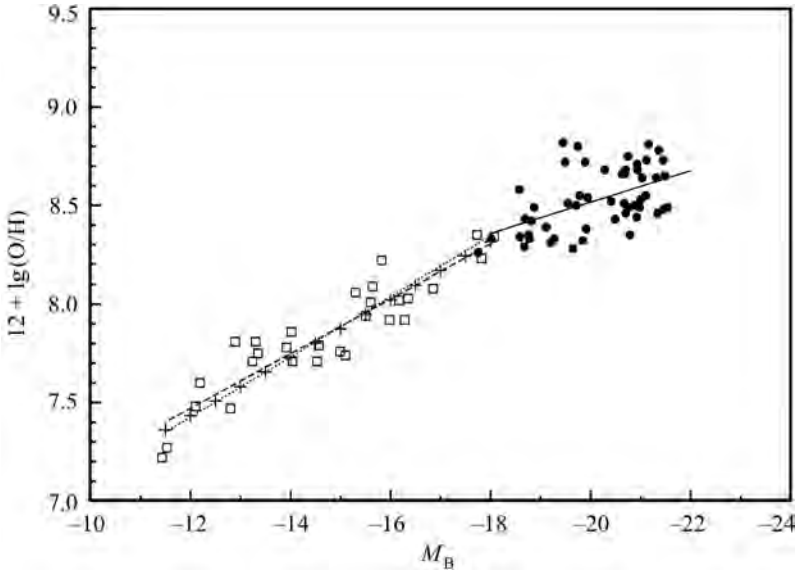


Fig. 3.5. The characteristic oxygen abundance as a function of absolute blue magnitude M_B for sample of spiral galaxies from [101] (the filled circles). The solid line is the best (linear least-squares) fit to these data. The open squares are oxygen abundances in irregular galaxies, the dashed line is the metallicity—luminosity relationship for irregular galaxies. The dotted line is the O/H— M_B relationship for irregular galaxies from [59]. The relationship for irregular galaxies from [111] is presented by the plus signs

derived by Lee et al. (2003) [59]. The O/H— M_B relationship for irregular galaxies

$$12 + \log(\text{O}/\text{H}) = 5.67 (\pm 0.48) - 0.147 (\pm 0.029) M_B, \quad (3.9)$$

derived by Richer and McCall (1995) [111] is presented by the plus signs. Inspection of Fig. 3.5 (as well as the comparison between Eq. (3.7), Eq. (3.8), and Eq. (3.9)) shows that the O/H— M_B relationship for our sample of irregular galaxies agrees, within the uncertainties, with that from [59] and from [111]. Fig. 3.5 shows a familiar oxygen abundance — luminosity correlation for late type galaxies, an increase in metallicity with luminosity over the full range of absolute blue magnitude, M_B from ~ -22 to ~ -11 . Comparison between Eq. (3.4) and Eq. (3.7) shows that the O/H — M_B relationships for spiral and irregular galaxies have slightly different slopes.

Fig. 3.6 shows the oxygen abundance in spiral (filled circles) and irregular (open squares) galaxies as a function of rotation velocity V_{rot} . The most prominent feature is the bend in the O/H— V_{rot} relation. Garnett (2002) also found that the correlation between O/H and V_{rot} does not increase steadily but rather turns over for rotation speeds greater than 125 km s^{-1} [36]. It is worth noting that the presence of the bend in the O/H— V_{rot} relation does not necessary

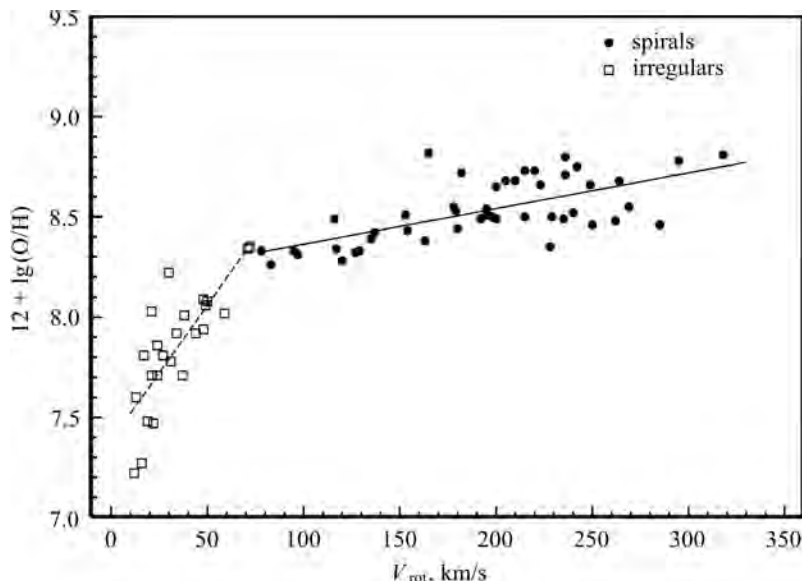


Fig. 3.6. The characteristic oxygen abundance as a function of rotation velocity V_{rot} for sample of spiral galaxies from [101] (the filled circles). The solid line is the best (linear least-squares) fit to these data. The open squares are oxygen abundances in irregular galaxies, the dashed line is the linear least-squares fit to these data

imply the existence of a bend in the O/H – M_B trend. The correlation between M_B and V_{rot} is not linear but rather shows a bend. This bend in the O/H – V_{rot} trend would thus occur even if the increase in oxygen abundance with luminosity can be described by a single linear function over the full magnitude range.

3.2.4. The gas mass fractions

The gas fraction μ in a galaxy is estimated using the following standard relation:

$$\mu = \frac{M_{\text{H I}} + M_{\text{H}_2}}{M_{\text{H I}} + M_{\text{H}_2} + k L_B}, \quad (3.10)$$

where $M_{\text{H I}}$ is the mass of atomic hydrogen in the galaxy, M_{H_2} is the mass of molecular hydrogen in the galaxy (both $M_{\text{H I}}$ and M_{H_2} are corrected for the helium and heavy element contribution), L_B is the blue luminosity of the galaxy, and k is the mass-to-luminosity ratio. The mass of atomic hydrogen is derived in a standard way using the measured H I flux taken from literature and the adopted distance. If the mass of atomic hydrogen instead of the H I flux measurement is reported in literature, this value is rescaled

to the adopted distance. The atomic hydrogen masses expressed in terms of $M_{\text{HI}}/L_{\text{B}}$ and corresponding references to the HI flux measurements are listed in [101].

The mass of molecular hydrogen can only be estimated with indirect methods. The commonly accepted method is the use of the CO line flux and X conversion factor between the flux in the CO line and the amount of molecular hydrogen. The conversion factor $X = N_{\text{H}_2}/I(\text{CO})$ strongly depends on the physical properties of the interstellar medium which are known to vary from galaxy to galaxy. The best-estimated values of the conversion factor for a sample of well-studied nearby galaxies span the range $0.6 \leq X \leq 10 \times 10^{20} \text{ mol cm}^{-2}(\text{K km s}^{-1})^{-1}$ [6]. The high values of the conversion factor correspond to low-luminosity irregular galaxies, and the low values of the conversion factor are found in spiral galaxies. Then the value of $X = 1 \times 10^{20} \text{ mol cm}^{-2}(\text{K km s}^{-1})^{-1}$ (including helium and heavy elements contribution) is adopted here for spiral galaxies. The molecular gas content is derived with this conversion factor using the measured CO flux from literature and distance. If the mass of molecular hydrogen instead of the CO flux measurement is reported in the literature, this value is rescaled to the adopted distance and adopted conversion factor. The molecular hydrogen masses expressed in terms of $M_{\text{H}_2}/L_{\text{B}}$ and corresponding references to the CO flux measurements are given in [101].

The mass of the stellar component of the galaxy is estimated by converting the measured luminosity to mass via the mass-to-luminosity ratio. It is difficult to get a reliable estimation of the mass-to-luminosity ratio for individual galaxies. The μ and $\mu -$ dependent values will be used here only for examination of the general trends of these values with luminosity but not for examination of individual galaxies. A similar investigation was carried out by Garnett (2002) [36]. He considered the impact of the choice of the mass-to-luminosity ratio on the trends by comparing the trends derived with the color-based mass-to-luminosity ratio and constant mass-to-luminosity ratio. Garnett has found that the trends are fairly robust against the choice of mass-to-luminosity ratio. Based on this conclusion, a constant value of the mass-to-luminosity ratio $k = 1.5$ is adopted here for all spiral galaxies, and $k = 1$ is adopted for all irregular galaxies.

Unfortunately, for several spiral galaxies on the list no measurement of the CO flux is available. For these galaxies, the gas mass fraction is based on the atomic hydrogen mass only and is a lower limit. Taking into account that the average value is $M_{\text{H}_2}/M_{\text{HI}} = 0.14$ [6], one can hope that the use of a lower limit instead of the estimated value of gas fraction for several galaxies is quite acceptable.

The values of the gas mass fraction in the irregular galaxies were estimated taking into account the atomic hydrogen mass only since the molecular

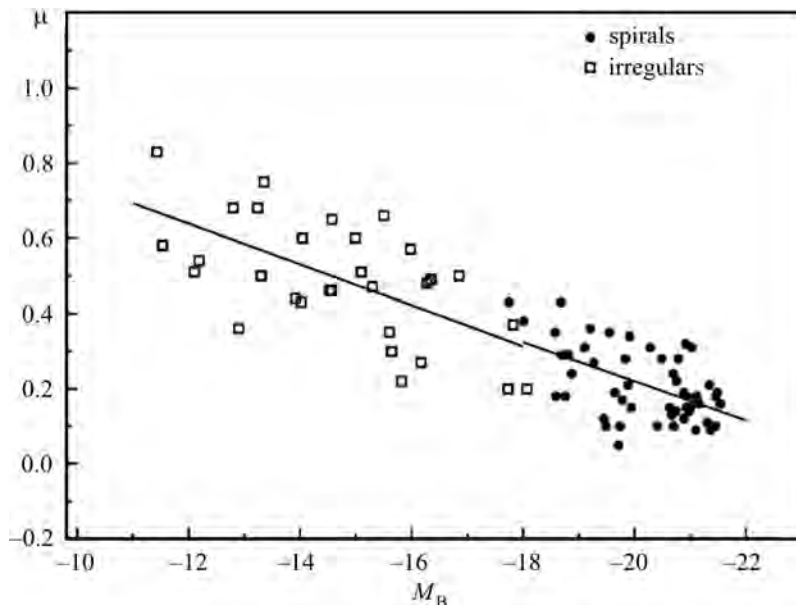


Fig. 3.7. Gas mass fraction as a function of the absolute blue magnitude M_B . The filled circles are spiral galaxies, the open squares are irregular galaxies. The solid line is the μ – M_B relationship for spiral galaxies, the dashed line is the μ – M_B relationship for irregular galaxies

hydrogen in dwarf irregular galaxies is only a small fraction of the total gas mass. The HI fluxes were taken mainly from [48].

The gas mass fraction in spiral galaxies as a function of absolute blue magnitude M_B is shown by the filled circles in Fig. 3.7. The solid line is the gas mass fraction – luminosity relationship (best fit determined via the least squares method) for spiral galaxies

$$\mu = 1.264 (\pm 0.220) + 0.0522 (\pm 0.0109) M_B. \quad (3.11)$$

The open squares in Fig. 7 are irregular galaxies. The dashed line is the gas fraction – luminosity relationship (best fit) for irregular galaxies

$$\mu = 1.289 (\pm 0.198) + 0.0542 (\pm 0.0134) M_B. \quad (3.12)$$

Comparison between Eq. (3.11) and Eq. (3.12) shows that the μ – M_B relationship for spiral galaxies coincides remarkably well with the μ – M_B relationship for irregular galaxies. It can also be seen in Fig. 3.7 that the gas mass fraction–luminosity relation for spiral galaxies is a direct continuation of the gas mass fraction – luminosity relationship for irregular galaxies.

Thus, the characteristic (or representative) oxygen abundance in late type galaxies correlates with its luminosity, rotation velocity, and morphological

type. The gas mass fraction (or astration level) in late type galaxies is also a function of absolute blue magnitude M_B . One can consider these facts as evidence in favor of that the decreasing gas mass fraction with increasing luminosity can be responsible for a luminosity—metallicity relation for spirals and irregulars or at least these facts play an important role in the origin of this relationship. It should be noted however that the scatter in each diagram is rather large.

3.3. The maximum attainable value of the oxygen abundance in spiral galaxies

Which spiral galaxy is the oxygen-richest one? How high is the maximum attainable value of the oxygen abundance? Do the most oxygen rich spiral galaxies reach the maximum attainable value of the oxygen abundance? These questions will be discussed here.

3.3.1. Oxygen abundances in spiral galaxies reported to be the very oxygen-rich

The chemical composition of various samples of spiral galaxies has been discussed in a number of papers [35, 36, 138, 140, 142]. According to those articles, the oxygen-richest galaxies are: NGC 5194 (M 51) with $12 + \log(\text{O}/\text{H})_0 = 9.54$ [140], NGC 3351 with $12 + \log(\text{O}/\text{H})_0 = 9.41$ [142], NGC 3184 with $12 + \log(\text{O}/\text{H})_0 = 9.50$ [138], NGC 6744 with $12 + \log(\text{O}/\text{H})_0 = 9.64$ [35]. Different versions of the one-dimensional method, proposed first by [74] a three decades ago, have been used for oxygen abundance determinations in those papers. It has been shown that the oxygen abundances in galaxies determined with the one-dimensional calibrations are significantly overestimated at the high-metallicity end ($12 + \log \text{O}/\text{H} > 8.25$) [9, 62, 97]. This is for two reasons. First, the then-existing calibrating points at the high-metallicity end were very few and not reliable. Second, the physical conditions in H II regions cannot be taken into account accurately in one-dimensional calibrations. Pilyugin et al. (2004) [101] have used instead a two-dimensional parametric empirical calibration (*P* method) to derive oxygen abundances for a sample of spiral galaxies which includes NGC 3184, NGC 3351, NGC 5194, and NGC 6744. They found generally lower oxygen abundances with $12 + \log(\text{O}/\text{H})_0 \sim 9.0$ (see above).

We have considered the problem of the maximum observed oxygen abundance in spiral galaxies by attempting to derive more accurate oxygen abundances [104]. These can be derived via the classic T_e method, T_e being the electron temperature of the H II region. Measurements of the auroral lines, such as $[\text{OIII}]\lambda 4363$, are necessary to determine T_e . Unfortunately, they are very faint and often drop below the detectability level in the spectra of high-metallicity H II regions. It has been advocated that the faint auroral line flux

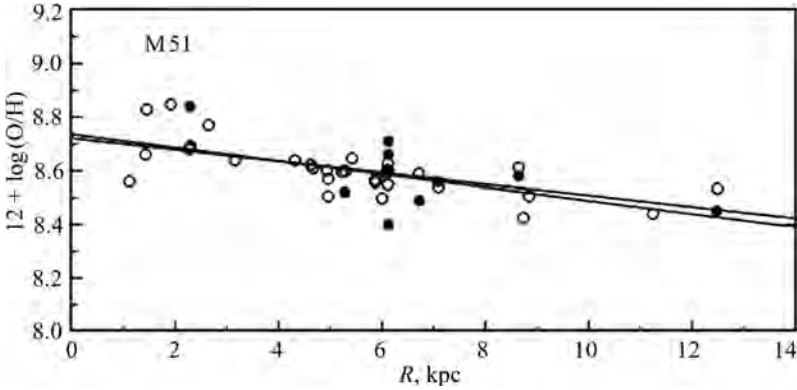


Fig. 3.8. Radial distribution of oxygen abundances in the disk of the spiral galaxy M51 (NGC 5194). The open circles denote $(O/H)_{ff}$ abundances. The solid line is the linear least-square best fit to those data. The filled circles show $(O/H)_{T_e}$ abundances from [7]. The dashed line is their linear regression fit

can be computed from the fluxes in the strong nebular lines via the ff relation [102]. Then, using the obtained flux in the auroral line, accurate oxygen abundances $(O/H)_{ff}$ can be derived using the equations of the T_e method.

The ff relation will be applied to derive the oxygen abundances in the spiral galaxies reported to be the oxygen-richest ones, NGC 3184, NGC 3351, NGC 5194, and NGC 6744. For comparison, we will also consider the Milky Way Galaxy. First, M 51 (NGC 5194), the oxygen-richest spiral galaxy ($12 + \log(O/H)_0 = 9.54$) in the sample from [140] will be considered. The value of $(O/H)_0$ in M 51 was derived recently from determinations of $(O/H)_{T_e}$ abundances in a number of H II regions [7]. Comparison between the radial distributions of $(O/H)_{T_e}$ and $(O/H)_{ff}$ abundances in the disk of M 51 provides possibility to test the reliability of the latter. Second, $(O/H)_{ff}$ abundances in NGC 3184, NGC 3351, and NGC 6744 which have been reported to be the most oxygen-rich spirals, will be determined. Third, the ff – relation will be applied to Galactic H II regions to select high-precision measurements.

The compilation of published spectra of H II regions in M 51 is taken from [101]. The spectra of H II regions from [7] (their Tables 1 and 6) have been added. The $(O/H)_{ff}$ abundances for every H II region have been determined using the ff relation. The $(O/H)_{ff}$ abundances in the H II regions of M 51 are shown as a function of galactocentric distance in Fig. 3.8 by open circles. The solid line is the linear least-square best fit to those data:

$$12 + \log(O/H) = 8.74 (\pm 0.03) - 0.025 (\pm 0.004) \times R. \quad (3.13)$$

The distance of M 51 ($d = 7.64$ Mpc) and the isophotal radius ($R_{25} = 5.61$ arcmin) were taken from [101]. The filled circles are $(O/H)_{T_e}$ abundances

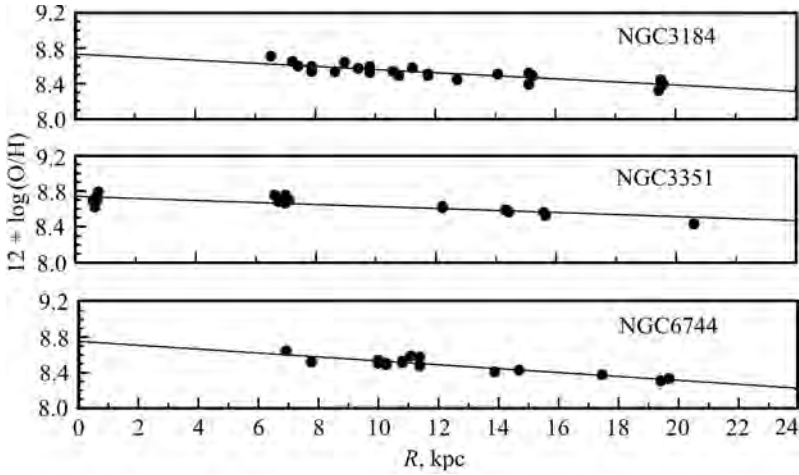


Fig. 3.9. Radial distributions of $(\text{O}/\text{H})_{\text{ff}}$ abundances in the spiral galaxies NGC 3184, NGC 3351, and NGC 6744. The points show individual H II regions. The lines are the best fits to those data

determined by Bresolin et al. (2004) via the direct T_e method [7]. The dashed line is their linear regression:

$$12 + \log(\text{O}/\text{H}) = 8.72 (\pm 0.09) - 0.02 (\pm 0.01) \times R. \quad (3.14)$$

Fig. 3.8 shows that the radial distribution of $(\text{O}/\text{H})_{\text{ff}}$ abundances agrees well with that of the $(\text{O}/\text{H})_{T_e}$ abundances (compare also Eq. (3.13) and Eq. (3.14)). This is a strong argument in favor of the reliability of the $(\text{O}/\text{H})_{\text{ff}}$ abundances.

Some H II regions show large deviations from the general radial trend in oxygen abundances. Some of those deviations can be real, but some are probably caused by uncertainties in the oxygen abundance determinations. It should be emphasized that the uncertainties in the $(\text{O}/\text{H})_{\text{ff}}$ abundances are not necessarily caused by uncertainties in the line flux measurements. It has been noted [102] that the ff relation gives reliable results only if two conditions are satisfied; i) the measured fluxes reflect their relative contributions to the radiation of the whole nebula, and ii) the H II region is ionization-bounded. If these two conditions are not met, then the derived $(\text{O}/\text{H})_{\text{ff}}$ abundances may be significantly in error.

The compilation of published spectra of H II regions in the spiral galaxies NGC 3184, NGC 3351, and NGC 6744 was taken from [101]. The $(\text{O}/\text{H})_{\text{ff}}$ abundances in the H II regions of NGC 3184 is shown as a function of galactocentric distance in the top panel of Fig. 3.9. The solid line is the linear least-square best fit to those data:

$$12 + \log(\text{O}/\text{H}) = 8.73 (\pm 0.03) - 0.035 (\pm 0.004) \times R. \quad (3.15)$$

The same data are shown for the H II regions of NGC 3351 in the middle panel of Fig. 3.9. The solid line is the linear least-square best fit to those data:

$$12 + \log(\text{O}/\text{H}) = 8.74 (\pm 0.02) - 0.023 (\pm 0.004) \times R. \quad (3.16)$$

Similarly, the data for the H II regions of NGC 6744 are shown in the bottom panel of Fig. 3.9. The linear least-square best fit to those data is given by:

$$12 + \log(\text{O}/\text{H}) = 8.75 (\pm 0.04) - 0.022 (\pm 0.003) \times R. \quad (3.17)$$

The distances of the galaxies and the galactocentric distances of the H II regions were taken from [101].

Figs. 3.8 and 3.9 (see also Eqs. (3.13), (3.15)–(3.17)) show that the values of $(\text{O}/\text{H})_0$ in these spiral galaxies are ~ 8.75 .

3.3.2. Oxygen abundances in the Milky Way Galaxy

A compilation of published spectra of Galactic H II regions with an auroral $[\text{O III}]\lambda 4363$ line has been carried out in [99]. The list contains 69 individual measurements of 13 H II regions in the range of galactocentric distances from 6.6 to 14.8 kpc. Recent measurements of six Galactic H II regions from [32] were added to that list, resulting in a total of 75 measurements. The derived $(\text{O}/\text{H})_{\text{T}_e}$ abundances are shown as a function of galactocentric distance by the open circles in the left panel of Fig. 3.10. The linear least-square best fit to those data (with two points with a deviation more than 0.2 dex rejected)

$$12 + \log(\text{O}/\text{H}) = 8.79 (\pm 0.05) - 0.034 (\pm 0.005) \times R \quad (3.18)$$

is shown by the solid line in the left panel of Fig. 3.10.

There is a relative large number of measurements of abundances in the Milky Way Galaxy. They show a large scatter since the quality of the data obtained over a period of more than thirty years is necessarily heterogeneous. Some measurements have a low accuracy. The ff relation provides a way to select out the H II regions with high quality measurements [103]. We can make use of the ff relation to define a “discrepancy index”, equal to the difference between the logarithm of the observed flux R in the $[\text{O III}]\lambda 4363$ line and that of the flux R_{ff} of that line derived from the strong $[\text{O II}]\lambda 3727$, $[\text{O III}]\lambda\lambda 4959, 5007$ lines using the ff relation:

$$D_{\text{ff}} = \log R_{\text{ff}} - \log R. \quad (3.19)$$

That discrepancy index will allow us to eliminate low-quality measurements with large D_{ff} , while retaining high-quality ones with small D_{ff} .

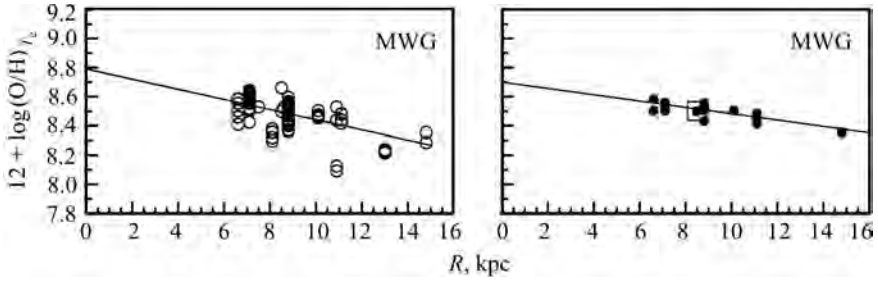


Fig. 3.10. Radial distribution of $(\text{O}/\text{H})_{T_e}$ abundances in the disk of the Milky Way Galaxy. *Left panel.* The open circles show $(\text{O}/\text{H})_{T_e}$ for all H II regions. The solid line is the best fit to those data. *Right panel.* The filled circles show $(\text{O}/\text{H})_{T_e}$ abundances for H II regions with an absolute value of the discrepancy index D_{ff} less than 0.05 dex. The solid line is the best fit to those data. The open square shows the oxygen abundance in the interstellar gas at the solar galactocentric distance

The right panel of Fig. 3.10 shows the $(\text{O}/\text{H})_{T_e}$ abundances as a function of galactocentric distance for objects with an absolute value of the discrepancy index D_{ff} less than 0.05 dex. The linear least-square best fit to those data

$$12 + \log(\text{O}/\text{H}) = 8.70 (\pm 0.04) - 0.022 (\pm 0.004) \times R \quad (3.20)$$

is shown by the solid line in the right panel of Fig. 3.10. The open square is the oxygen abundance of the interstellar gas at the solar galactocentric distance.

High-resolution observations of the weak interstellar $\text{O}\text{I}\lambda 1356$ absorption lines towards stars allow one to determine the interstellar oxygen abundance in the solar vicinity with a very high precision. It should be noted that this method is model-independent. These observations yield a mean interstellar oxygen abundance of 284–390 O atoms per 10^6 H atoms (or $12 + \log(\text{O}/\text{H}) = 8.45\text{--}8.59$) [13, 71, 125]. Oliveira et al. (2005) have determined a mean O/H ratio of 345 ± 19 O atoms per 10^6 H atoms (or $12 + \log(\text{O}/\text{H}) = 8.54$) for the Local Bubble [73]. Thus, an oxygen abundance $12 + \log(\text{O}/\text{H}) = 8.50$ in the interstellar gas at the solar galactocentric distance seems to be a reasonable value. The value of the oxygen abundance at the solar galactocentric distance traced by $(\text{O}/\text{H})_{T_e}$ abundances in H II regions is then in good agreement with the oxygen abundance derived with high precision from the interstellar absorption lines towards stars (open square in the right panel of Fig. 3.10). This is strong evidence that the classic T_e method provides accurate oxygen abundances in high-metallicity H II regions.

The central oxygen abundance in the Milky Way obtained here, $12 + \log(\text{O}/\text{H})_0 \sim 8.70$, is significantly lower than that $12 + \log(\text{O}/\text{H})_0 = 9.38$ from [120]. It should be noted that the central oxygen abundance obtained here for the Milky Way is close to that in other large spirals.

3.3.3. A plateau in the L–Z diagram at high luminosities

We have examined the problem of the maximum attainable value of the oxygen abundance in spiral galaxies in [105]. Since the maximum value of the observed oxygen abundance is expected to occur at the centers of the most luminous galaxies, we have derived the radial distribution of the oxygen abundance in the disks of the four most luminous spiral galaxies in the sample from [101]: NGC 1068 with an absolute blue magnitude $M_B = -22.18$, NGC 6384 with $M_B = -22.22$, NGC 7331 with $M_B = -22.20$, and IC 342 with $M_B = -22.27$. We use the compilation from [101] of a large sample of published spectra of H II regions in nearby spiral galaxies. Recent measurements from [7, 8, 22] have been added to that list. The distances and luminosities of the galaxies are taken from [101].

Fig. 3.11 shows the oxygen abundance as a function of galactocentric distance in the disks of the four most luminous spiral galaxies in our sample. The points are $(O/H)_{\text{ff}}$ abundances in individual H II regions. The lines are linear least-square best fits to those points. Inspection of Fig. 3.11 shows that the central oxygen abundance in the most luminous spiral galaxies can be as large as $12 + \log(O/H) \sim 8.87$. Are those galaxies indeed the most oxygen-rich ones as expected from the L–Z correlation? To clarify this point, we next derive the central oxygen abundances of all the spiral galaxies in our sample and examine their dependence on galaxian luminosity.

The left panel of Fig. 3.12 shows the familiar L–Z diagram. It should be stressed that while the characteristic oxygen abundance (the oxygen abundance in the disk at a predetermined galactocentric distance) is used in the “standard” L–Z diagram (e.g. Fig. 3.3 and Fig. 3.5), Z in Fig. 3.12 denotes the central oxygen abundance. The squares show the central $(O/H)_{\text{ff}}$ abundances of the

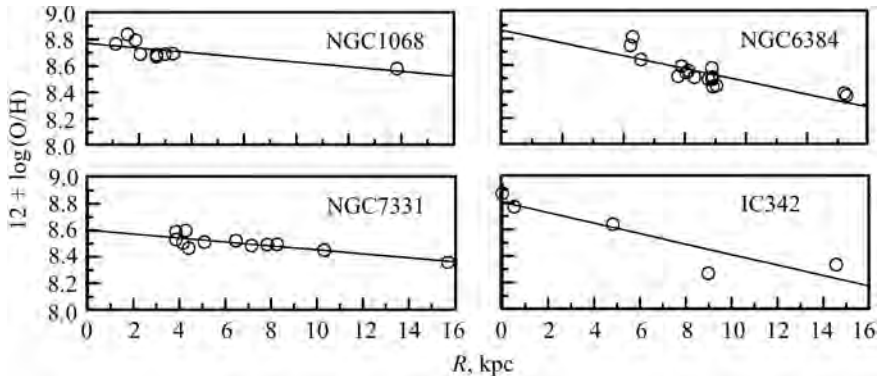


Fig. 3.11. The oxygen abundance as a function of galactocentric distance in the disks of the four most luminous spiral galaxies in our sample: NGC 1068, NGC 6384, NGC 7331 and IC 342. The circles are $(O/H)_{\text{ff}}$ abundances in individual H II regions. The lines are linear least-square best fits to those data points

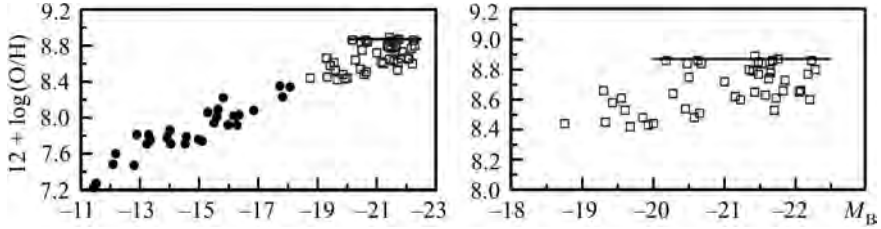


Fig. 3.12. The luminosity – central metallicity diagram. *Left panel.* The open squares show the central $(\text{O}/\text{H})_{\text{ff}}$ abundances in the disks of spiral galaxies plotted against their luminosities. The filled circles denote irregular galaxies from [101]. *Right panel.* A blow-up of the high-luminosity part of the L–Z diagram in the left panel

spiral galaxies in our sample. The filled circles in Fig. 3.12 show irregular galaxies from [95, 101]. Examination of Fig. 3.12 shows that the central oxygen abundances in galaxies with $M_{\text{B}} \sim -20.25$ are in the same range as those of galaxies with $M_{\text{B}} \sim -22.25$, i.e. the central oxygen abundances in luminous galaxies with $M_{\text{B}} < -20.25$ do not show an appreciable correlation with galaxy luminosity. This flattening of the L–Z relation can be seen more clearly in the right panel of Fig. 3.12 which shows a blow-up of the high-luminosity end of the relation. The presence of an upper envelope in the L–Z relation at $12 + \log(\text{O}/\text{H}) \sim 8.87$, is clearly seen. It should be noted that the presence of an upper envelope can also be seen in the “standard” L–Z diagram [29, 72, 101] (see also Fig. 3.3 and Fig. 3.5).

What is the meaning of such a plateau? There are two known reasons for the existence of the L–Z relation. First, it can be caused by a dependence of the efficiency of galactic winds to get rid of metals on the galaxy’s luminosity: more luminous and massive galaxies are less efficient in losing heavy elements by galactic winds. In this case, the L–Z relation represents the ability of a given galaxy to retain the products of its own chemical evolution rather than its ability to produce metals [58]. It is believed that the galactic winds do not play a significant role in the chemical evolution of the largest spiral galaxies (e.g. [23, 36, 101, 136]). The second reason that has been invoked to explain the L–Z relation is that the astration level increases (the gas mass fraction decreases) as the luminosity of a galaxy increases [14, 15, 68, 114] (see Fig. 3.7). The existence of a plateau at high luminosities in the L–Z relation thus implies that, on average, the central parts of large luminous spiral galaxies have similar astration levels.

Another prominent feature of the L–Z relation is the rather large scatter in oxygen abundances at a given luminosity, $\Delta \log(\text{O}/\text{H}) \sim 0.25$. Part of this scatter may be due to uncertainties in the oxygen abundances. But another part is likely to be real. This scatter may be explained by fluctuations of

the gas mass fraction μ among galaxies of a given luminosity. The simple model of chemical evolution of galaxies predicts that a decrease of μ by 0.1 results in an increase of the oxygen abundance by ~ 0.13 dex, in the range of μ from ~ 0.50 to ~ 0.05 . Then, a scatter $\Delta \log(\text{O}/\text{H}) \sim 0.25$ may be explained by fluctuations of the gas mass fraction as large as $\Delta \mu \sim 0.2$ among galaxies of a given luminosity. The global gas mass fractions in the sample spiral galaxies have been estimated to be low, $\mu < 0.25$ ([36, 101] and Fig. 3.7 above). This suggests that the gas in the centers of the most metal-rich galaxies has been almost completely converted into stars. Consequently, the observed oxygen abundance in the centers of those galaxies represents the maximum attainable value of the oxygen abundance. This provides a natural explanation for the constant maximum value of the observed central oxygen abundance in the most oxygen-rich galaxies (Fig. 3.12).

The maximum value of the gas-phase oxygen abundance in H II regions of spiral galaxies is thus $12 + \log(\text{O}/\text{H}) \sim 8.87$. Some fraction of the oxygen is locked into dust grains [30, 71]. According to Esteban et al. (1998) [30], the fraction of the dust-phase oxygen abundance in the Orion nebula is about 0.08 dex (but see [122]). Then, the maximum value of the gas+dust oxygen abundance in H II regions of spiral galaxies is $12 + \log(\text{O}/\text{H}) \sim 8.95$.

What is the minimum value of the observed gas-phase oxygen abundance in galaxies in the local universe? The oxygen abundances in H II regions of the most metal-poor galaxies known (blue compact galaxies and dwarf irregulars) are $12 + \log(\text{O}/\text{H}) = 7.0\text{--}7.1$ [45, 46, 109]. Thus, the minimum value of the observed gas-phase oxygen abundance in galaxies in the local universe is around two orders of magnitude lower than the maximum attainable value of the oxygen abundance.

The Sun is one of the widely used reference objects in astrophysics. Standard practice is to express the element content in a cosmic object via the corresponding value for the Sun, i.e. the composition of the Sun is used as standard unit. For many years, the recommended solar oxygen abundance was $12 + \log(\text{O}/\text{H})_{\odot} \approx 8.9$. This high abundance was obtained from a one-dimensional hydrostatic model of the solar atmosphere. Recently the solar oxygen abundance has been significantly reduced as a result of a time-dependent, three-dimensional hydrodynamical model of the solar atmosphere. Taking the average of recent determinations ($12 + \log(\text{O}/\text{H})_{\odot} = 8.70$ in [1], 8.66 in [4], 8.59 in [70]), 8.62–8.68 [80]), 8.71 [117]), the solar abundance is now $12 + \log(\text{O}/\text{H})_{\odot} \sim 8.65$. Thus, the maximum value of the gas+dust oxygen abundance of H II regions in spiral galaxies is higher by a factor of ~ 2 than the solar value.

3.3.4. The oxygen yield

The simple model of chemical evolution of galaxies predicts that the oxygen abundance of the interstellar matter of a galaxy is related to the gas mass fraction μ and the oxygen yield Y_{O} by the following formula

$$Y_{\text{O}} = \frac{Z_{\text{O}}}{\ln(\frac{1}{\mu})}, \quad (3.21)$$

where the oxygen yield Y_{O} is defined as the mass of new manufactured oxygen ejected into the interstellar medium by the star generation per unit mass locked up in long-lived stars and stellar remnants. In a real situation, the oxygen abundance is also affected by the mass exchange between a galaxy and its environment [76, 119]. This mass exchange can alter the above relation and mimic a variation in the oxygen yield. In that case, the simple chemical evolution model is used to estimate the “effective” oxygen yield Y_{eff} [26, 140].

As noted above, it is believed that galactic winds do not play a significant role in the chemical evolution of the largest spiral galaxies. For these, is the oxygen yield derived by using Eq. (3.21) close to the true oxygen yield? This may not be the case for two reasons. First, the simple model is based on the instantaneous recycling approximation. Oxygen is produced and ejected into the interstellar medium by massive stars with lifetimes much shorter than the evolution time of spiral galaxies. From this point of view, the instantaneous recycling approximation is justified. However, the value of Y_{O} depends not only on the amount of oxygen but also on the total mass of matter ejected in the interstellar medium. In other words, the instantaneous recycling approximation assumes that the next generation of star is formed when all stars from previous generations have finished their evolution. This never occurs in a real galaxy. As a consequence, the simple model predicts slightly higher oxygen abundances than numerical models for the chemical evolution of galaxies with realistic star formation histories [85]. Fortunately, this difference is small and can be neglected in the case of oxygen.

Furthermore, it is well known that the simple model predicts many more low-metallicity stars than are observed in the solar neighbourhood, the so called “G—dwarf” paradox. Various versions of the infall model, in which an infall of gas onto the disk takes place for a long time, have been proposed to account for the observed metallicity distribution in the solar neighborhood ([16, 87, 88, 134, 135] among many others). An infall model has also been applied to other spiral galaxies ([76] and references therein). It is thus generally accepted that gas infall plays an important role in the chemical evolution of disks of spiral galaxies. Therefore, the application of the simple model to large spiral galaxies to estimate the true oxygen yields may appear unjustified. It is expected that the rate of gas infall onto the disk decreases exponentially with time [12, 67, 87,

88]. It has been shown [89] that the present-day location of a system in the μ —O/H diagram is governed by its evolution in the recent past, but is independent of its evolution on long timescales. Therefore, the fact that the present-day location of spiral galaxies is near the one predicted by the simple model is not in conflict with a picture in which an infall of gas onto the disk takes place during a long time (the latter is necessary to satisfy the observed abundance distribution function and the age—metallicity relation in the solar neighbourhood) since these observational data reflect the evolution of the system in the distant past. Therefore, one can expect that the application of the simple model to large spiral galaxies, Eq. (3.21), provides a more or less reasonable estimate of the true oxygen yield Y_{O} . Certainly, to find an accurate value of the true oxygen yield Y_{O} , an appropriate models of chemical evolution of galaxies should be computed.

From Eq. (3.21), it is clear that a precise determination of the oxygen yield depends on accurate oxygen abundance and gas mass fraction measurements. The $(\text{O}/\text{H})_{\text{ff}}$ abundances are rather accurate. However, a precise estimate of the gas mass fraction is not a trivial task (see above). Thus, the value of the oxygen yield derived from Eq. (3.21) can be strongly affected by the uncertainty in the gas mass fraction determination.

The use of the maximum attainable value of the oxygen abundance allows to overcome the above problem in the following way. One can compare the derived maximum attainable value of the oxygen abundance in galaxies with oxygen abundances predicted by the simple models with different oxygen yields for $\mu = 0$. Fig. 3.13 shows the oxygen abundance as a function of the gas mass fraction predicted by the simple model with $Y_{\text{O}} = 0.0030$ (solid line) and with $Y_{\text{O}} = 0.0035$ (dashed line). Since the oxygen abundances are expressed in units of number of oxygen atoms relative to hydrogen, while Z_{O} in Eq. (3.21) have units of mass fraction, we adopt the following conversion equation for oxygen [36]

$$Z_{\text{O}} = 12 \frac{\text{O}}{\text{H}}. \quad (3.22)$$

The simple model breaks down as the gas mass fraction approaches zero because the term $\ln(1/\mu)$ blows up. Therefore the oxygen abundance predicted by the simple model at $\mu = 0$ should be estimated by extrapolation of the model predictions to $\mu = 0$. The extrapolations of the simple models for two values of the oxygen yield are shown in Fig. 3.13 by the dotted lines. The fact that the central oxygen abundances in galaxies are derived here, not as oxygen abundances of H II regions in the very central parts of galaxies, but also as extrapolations of linear fits, justifies the above method.

The maximum value of the observed gas-phase oxygen abundance in H II regions of spiral galaxies is shown by the open square in Fig. 3.13. The maximum attainable value of the gas + dust oxygen abundance is shown by the open

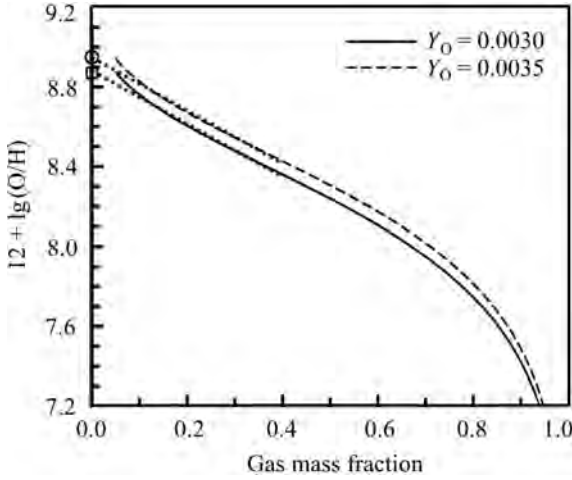


Fig. 3.13. The oxygen abundance as a function of the gas mass fraction predicted by the simple models of chemical evolution of galaxies, with an oxygen yield $Y_{\text{O}} = 0.0030$ (solid line) and with $Y_{\text{O}} = 0.0035$ (dashed line). The extrapolations to $\mu = 0$ for these models are shown by the dotted lines. The open square is the maximum value of the observed gas-phase oxygen abundance in H II regions of spiral galaxies. The open circle is the maximum attainable value of the gas + dust oxygen abundance

circle. Examination of Fig. 3.13 shows that the maximum value of the observed gas-phase oxygen abundance in H II regions of spiral galaxies corresponds to the simple model with $Y_{\text{O}} \sim 0.0030$, and the maximum attainable value of the gas+dust oxygen abundance in spiral galaxies corresponds to the simple model with $Y_{\text{O}} \sim 0.0035$. The value of the oxygen yield derived from the gas-phase oxygen abundance ($Y_{\text{O}} \approx 0.0030$) is close to that obtained recently for spiral galaxies in [101] ($Y_{\text{O}} \approx 0.0027$) and in [7] ($Y_{\text{O}} \approx 0.0032$), but is significantly lower than the oxygen yield obtained in [36] ($Y_{\text{O}} \approx 0.010$).

Thus, there exists a plateau in the luminosity—central metallicity diagram at high luminosities ($-22.3 \leq M_{\text{B}} \leq -20.3$). This provides strong evidence that the oxygen abundance in the centers of the most metal-rich luminous spiral galaxies reaches the maximum attainable value of oxygen abundance. The maximum value of the gas-phase oxygen abundance in H II regions of spiral galaxies is $12 + \log(\text{O}/\text{H}) \sim 8.87$. Because some fraction of the oxygen (about 0.08 dex) is expected to be locked into dust grains, the maximum value of the true gas+dust oxygen abundance in H II regions of spiral galaxies is $12 + \log(\text{O}/\text{H}) \sim 8.95$. This value is a factor of ~ 2 higher than the recently estimated solar value. Based on our derived maximum value of the oxygen abundance in spiral galaxies, one can estimate the oxygen yield. It has been obtained that the oxygen yield is around 0.0035, depending on the fraction of oxygen incorporated into dust grains.

3.4. The redshift evolution of oxygen and nitrogen abundances in late type galaxies. Galaxy downsizing

3.4.1. Preliminary remarks

As it was noted above, in recent years, the number of good-quality spectra of emission-line galaxies has increased dramatically due to the completion of several large spectral surveys. Measurements of emission lines in those spectra have been used for abundance determinations. This opens the possibility to study the evolution of O and N abundances with redshift in galaxies of different stellar masses. In the last decade, the evolution of the mass–metallicity relation with redshift has been examined by many investigators [21, 29, 55, 56, 61, 64, 116, 133]. It has been found that, when mass can be determined, the mass–metallicity correlation is considerably tighter than the luminosity–metallicity correlation, suggesting that mass may be a more meaningful physical parameter than luminosity. In those investigations, oxygen abundances have been derived using various methods. The general conclusion from those studies is that the oxygen abundance change of star-forming galaxies over the last half of the age of the Universe appears to be somewhat moderate, with $\Delta(\log(\text{O}/\text{H})) \sim 0.3$ or lower.

A little attention has been paid to the redshift evolution of nitrogen abundances in galaxies, despite the fact that they present several advantages for the study of the chemical evolution of galaxies. First, since at $12 + \log(\text{O}/\text{H}) \geq 8.3$, secondary nitrogen becomes dominant and the nitrogen abundance increases at a faster rate than the oxygen abundance [40], then the change in nitrogen abundances with redshift should show a larger amplitude in comparison to oxygen abundances and, as a consequence, should be easier to detect. Furthermore, there is a time delay in the nitrogen production as compared to oxygen production [63, 76, 137]. This provides an additional constraint on the chemical evolution of galaxies.

We have considered not only the redshift evolution of oxygen abundances but also that of nitrogen abundances [133]. Our study is based on the SDSS data base of a million spectra. To study the redshift evolution of oxygen and nitrogen abundances, accurate oxygen and nitrogen abundance determinations are mandatory. The determination of accurate abundances in H II regions from SDSS spectra poses two problems. First, line fluxes in SDSS spectra are measured by an automatic procedure. This inevitably introduces large flux errors for some objects. One needs to devise a way to recognize those objects and exclude them from consideration. Second, the SDSS galaxy spectra span a large range of redshifts. There is thus an aperture-redshift effect in SDSS spectra. Indeed, they are obtained with 3-arcsec-diameter fibers. At a redshift of $z = 0.05$ the projected aperture diameter is ~ 3 kpc, while it is ~ 15 kpc at a

redshift of $z = 0.25$. This means that, at large redshifts, SDSS spectra are closer to global spectra of whole galaxies, i.e. to that of composite nebulae including multiple star clusters, rather than to spectra of individual H II regions. One should then expect that some SDSS objects will not follow the fundamental H II region sequence. These need also to be identified and excluded from our sample.

We have proposed a method to recognize objects that suffer from one or both of these problems [133]. It is based on the idea that if *i*) an object belongs to the fundamental H II region sequence, and *ii*) its line fluxes are measured accurately, then the different relations between the line fluxes and the physical characteristic of H II regions, based on different emission lines, should yield similar physical characteristics (such as electron temperatures and abundances) of that object.

3.4.2. Sample selection

Line flux measurements in SDSS spectra have been carried out by several groups. We have used the data in several catalogs made available publicly by the MPA/JHU group¹. These catalogs give line flux measurements, redshifts and various other derived physical properties such as stellar masses for a large sample of SDSS galaxies. The techniques used to construct the catalogues are described in [11, 136] and other publications of those authors. It is preferable to use these catalogues instead of the original SDSS spectral database because they contain generally more accurate line flux measurements (see a discussion of the errors in the line flux measurements in [11]).

We have extracted from the MPA/JHU catalogs all emission-line objects with measured fluxes in the H β , H α , [OII] $\lambda\lambda$ 3727,3729, [OIII] λ 4959, [OIII] λ 5007, [NII] λ 6548, [NII] λ 6584, [SII] λ 6717, and [SII] λ 6731 emission lines. The hydrogen, oxygen and nitrogen lines serve to estimate oxygen and nitrogen abundances relative to hydrogen, and the ratio of the sulfur line intensities is an indicator of electron density. Since the calibrations for abundance determination are only valid in the low-density limit, we have included only those objects with a reasonable value of the [SII] ratio, i.e. those with $1.25 < F_{[\text{SII}]\lambda 6717}/F_{[\text{SII}]\lambda 6731} < 1.5$. This results in a sample containing 118544 objects which will be referred to hereafter as the total sample. The wavelength range of the SDSS spectra is 3800–9300 Å so that for nearby galaxies with redshift $z \leq 0.023$, the [O II] λ 3727 + λ 3729 emission line is out of that range. The absence of this line prevents the determination of the oxygen abundance, so all SDSS galaxies with $z \leq 0.023$ were also excluded. Thus, all galaxies in their total sample have redshifts greater than ~ 0.023 , i.e. they are more distant than ~ 100 Mpc. The redshift z and stellar mass M_S of each galaxy were also

¹ The catalogs are available at <http://www.mpa-garching.mpg.de/SDSS/>

taken from the MPA/JHU catalogs. The emission-line fluxes are corrected for interstellar reddening using the theoretical $H\alpha$ to $H\beta$ ratio and the analytical approximation to the Whitford interstellar reddening law from [41].

For each galaxy, we have estimated three values of the nitrogen abundance and three values of the electron temperature, using the suggested calibrations [133]. Since measurements of the $[\text{NII}]\lambda 6584$ line are more reliable than those of the $[\text{NII}]\lambda 6548$ line, we have used $N_2 = 1.33[\text{NII}]\lambda 6584$ instead of the standard $N_2 = [\text{NII}]\lambda 6548 + [\text{NII}]\lambda 6584$. Then the mean value N/H of the nitrogen abundance for each galaxy is determined as

$$\log(N/H)_{\text{mean}} = \frac{\log(N/H)_{N_2} + \log(N/H)_{N_2/R_2} + \log(N/H)_{N_2/R_3}}{3}. \quad (3.23)$$

The mean value of the electron temperature t_2 is determined in a similar way. Using N/H and the mean t_2 , the N/O ratio and the oxygen abundance O/H are then derived using T_e method equations.

It has been suggested that if *i*) the object belongs to the fundamental sequence of H II regions, and *ii*) its line fluxes are measured accurately, then the calibrations based on different lines should result in similar abundances. We have calculated for each galaxy the deviations of individual values of the nitrogen abundance from the mean value $\Delta\log(N/H)_{N_2, N_2/R_2, N_2/R_3} = \log(N/H)_{N_2, N_2/R_2, N_2/R_3} - \log(N/H)_{\text{mean}}$. The mean deviation $\Delta\log(N/H)_{\text{mean}}$ and the maximum deviation $\Delta\log(N/H)_{\text{max}}$ were also computed for each object. We have then used the value of $\Delta\log(N/H)_{\text{max}}$ as a selection criterion to extract from the total sample three subsamples of star-forming galaxies with accurate line flux measurements, going from the most stringent requirement to the least stringent one:

- Subsample A contains only objects with $\Delta\log(N/H)_{\text{max}} \leq 0.05$, a total of 15548 galaxies.
- Subsample B contains only objects with $\Delta\log(N/H)_{\text{max}} \leq 0.10$, a total of 55189 galaxies.
- Subsample C contains only objects with $\Delta\log(N/H)_{\text{max}} \leq 0.15$, a total of 84364 galaxies.

Does selecting objects in such a way give only 1) star-forming galaxies and 2) with accurate line flux measurements? We can test the reliability of our selection criterion concerning the first point by appealing to the $[\text{OIII}]\lambda 5007/H\beta$ vs $[\text{NII}]\lambda 6584/H\alpha$ diagram which is often used to distinguish between star-forming galaxies and AGNs. Fig. 3.14 shows such diagrams for subsamples A, B, C and for the total sample. The solid line, taken from [49], shows the dividing line between H II regions ionized by star clusters and AGNs. Fig. 3.14 clearly shows that, while the total sample contains both star-forming galaxies and AGNs (lower right panel), the suggested criterion does select out subsamples containing only star-forming galaxies.

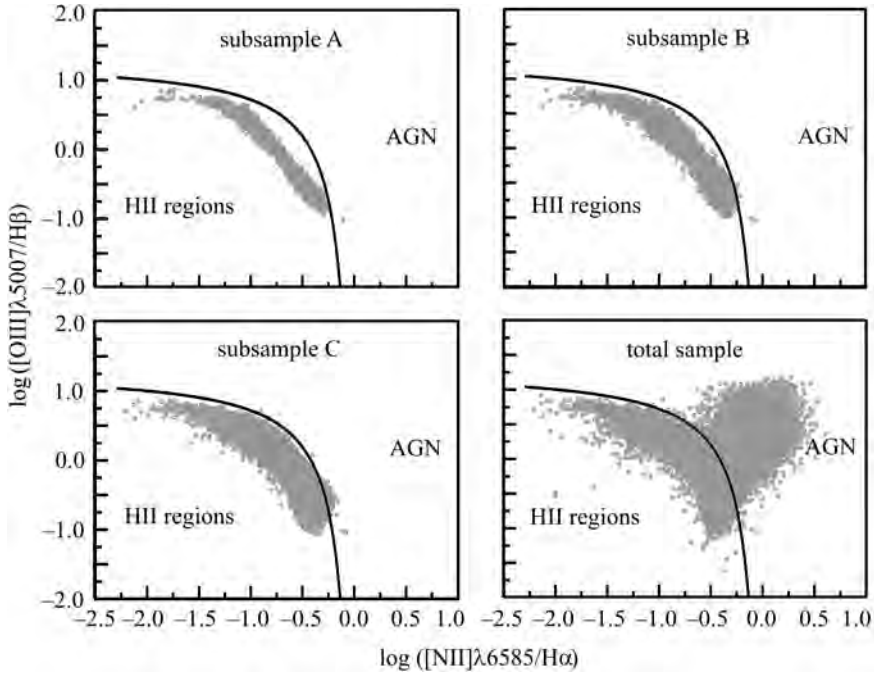


Fig. 3.14. The $[\text{OIII}]\lambda 5007/\text{H}\beta$ vs $[\text{NII}]\lambda 6585/\text{H}\alpha$ diagram for subsamples A, B, and C and the total sample. The solid line shows the dividing line between H II regions ionized by star clusters and AGNs [49]

Concerning the second point, Fig. 3.15 shows the classical R_3 – R_2 diagram for subsamples A, B, and C and the total sample (where $R_3 = ([\text{OIII}]\lambda 4959 + [\text{OIII}]\lambda 5007)/\text{H}\beta$ and $R_2 = ([\text{OII}]\lambda 3727 + [\text{OII}]\lambda 3729)/\text{H}\beta$). Each galaxy is plotted as a gray open circle. For comparison, H II regions in nearby galaxies with accurate line flux measurements, from the compilation in [101], are shown as black filled circles. Inspection of Fig. 3.15 shows that the selected subsamples of galaxies occupy the same area in the R_3 – R_2 diagram as the H II regions in nearby galaxies with accurate measurements, while the total sample covers a considerably larger area. Evidently, selection criterion picks out objects which have line intensities that are in agreement with the well-measured line intensities of H II regions in nearby galaxies.

We now compare the properties of the galaxies in subsamples A, B, and C. The histograms of galaxy stellar masses, redshifts, oxygen and nitrogen abundances for the three subsamples are shown in Fig. 3.16. Examination of the distributions of the parameters in the three subsamples reveals that, while they are somewhat similar for subsamples B and C, the distribution for subsample A differs significantly. In particular, there is a shift toward higher masses (by about 0.2 dex) of the galaxy mass distribution in subsample A

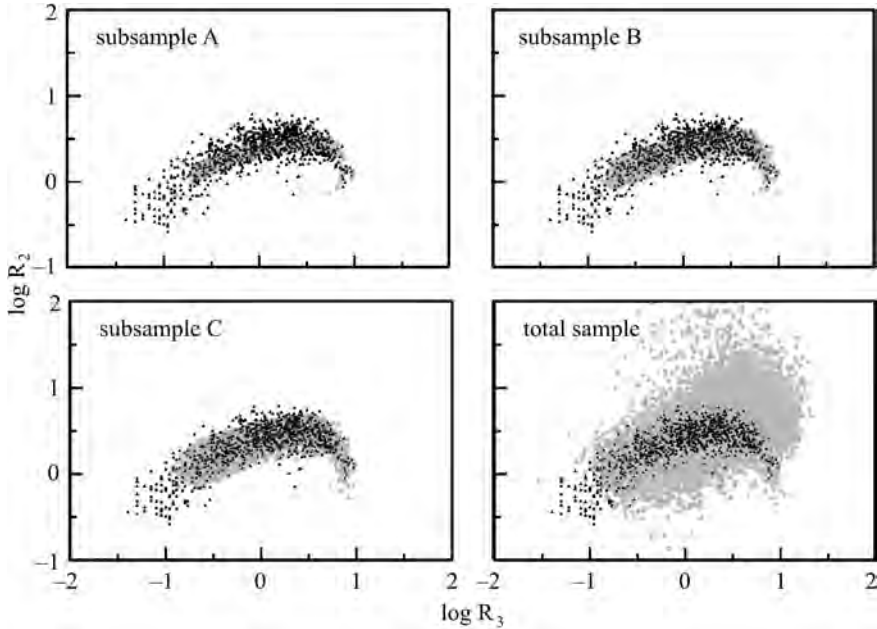


Fig. 3.15. The R_3 – R_2 diagram for subsamples A, B, and C and the total sample (where $R_3 = ([\text{OIII}]\lambda 4959 + [\text{OIII}]\lambda 5007)/\text{H}\beta$ and $R_2 = ([\text{OII}]\lambda 3727 + [\text{OII}]\lambda 3729)/\text{H}\beta$). The SDSS objects are shown by gray circles. The H II regions in nearby galaxies (the compilation from [101]) are shown by black triangles

relative to the other two subsamples. There is also a shift toward higher nitrogen abundances (by about 0.1 dex) of galaxies in subsample A relative to subsamples B and C (see Fig. 3.16). These shifts seem to be caused by a too restrictive selection criterion. The selection condition for subsample A, $\Delta \log(N/H)_{\max} \leq 0.05$, appears to be too constraining, eliminating too many galaxies and, as a consequence, causing a selection effect. In order not to bias the results, we have considered subsample B as the basic subsample, while subsample C will be used as a control subsample.

3.4.3. The redshift evolution of oxygen and nitrogen abundances

We have investigated the changes in oxygen and nitrogen abundances with galaxy stellar mass and redshift [133]. Examination of Fig. 3.16 shows that such a study is justified only in the range of stellar galaxy masses from $\sim 10^{9.5} M_{\odot}$ to $\sim 10^{11.5} M_{\odot}$, where the number of galaxies is large enough to give good statistics.

The z – M_S – O/H relation. The left panel of Fig. 3.17 shows the oxygen abundances of galaxies in subsample B, with redshifts in the range $0.04 < z <$

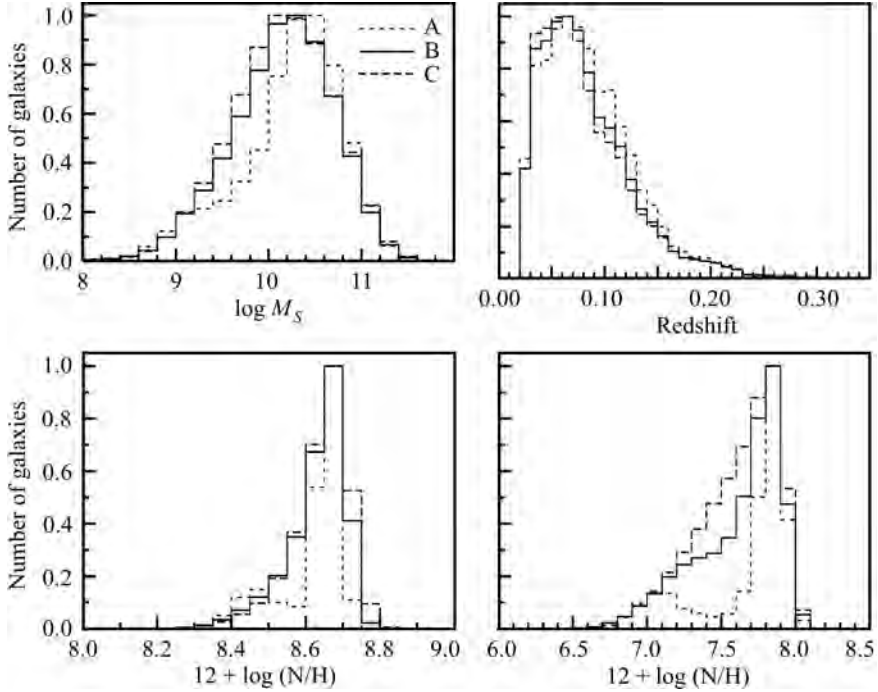


Fig. 3.16. Normalized histograms of observed and derived properties for SDSS galaxies in subsamples A (short-dashed line), B (solid line), and C (long-dashed line)

< 0.06 , as a function of galaxy stellar mass. The right panel of Fig. 3.17 shows the same diagram, but for galaxies in a higher redshift range, $0.23 < z < 0.27$. We note that our M_S –O/H diagram is very similar to that from [29] (see their Fig. 3). This may not be surprising since those authors also used a N_2 calibration to estimate the oxygen abundances of their SDSS galaxies. Fig. 3.17 shows that the oxygen abundance increases with increasing galaxy stellar mass up to a value M_S^* . For galaxies with $M_S > M_S^*$, the oxygen abundance becomes constant. Comparison of the left and right panels of Fig. 3.17 reveals that the value of M_S^* depends on redshift, shifting to higher values at higher redshifts.

To be more quantitative, the change in oxygen abundance with redshift and galaxy stellar mass has been approximated by the following “redshift–galaxy stellar mass–oxygen abundance” z – M_S –O/H relation:

$$\begin{aligned}
 12 + \log(\text{O}/\text{H}) &= a_1 + a_2 z + (a_3 + a_4 z) \log\left(\frac{M_S}{M_S^*}\right), \quad M_S \leq M_S^*, \\
 12 + \log(\text{O}/\text{H}) &= a_1 + a_2 z, \quad M_S \geq M_S^*,
 \end{aligned}
 \tag{3.24}$$

$$\log(M_S^*/M_\odot) = a_5 + a_6 z.$$

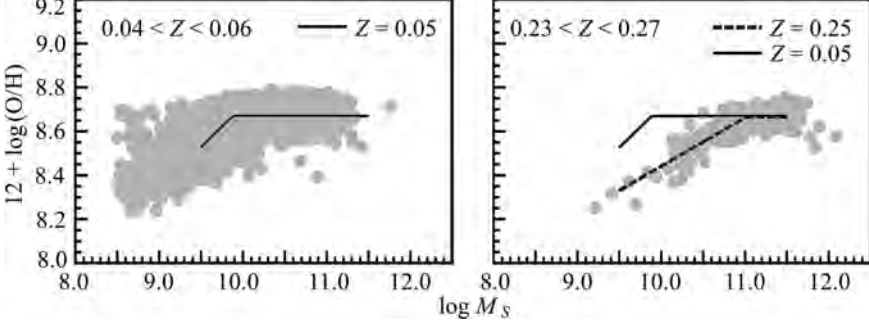


Fig. 3.17. The oxygen abundance—galaxy stellar mass diagrams for subsample B at $z = 0.05$ (left panel) and $z = 0.25$ (right panel). The Z — M_S — O/H relation (Eq. 3.25) is shown by the solid line for $z = 0.05$ and by the dashed line for $z = 0.25$

Fitting the data for galaxies in subsample B gives the following:

$$12 + \log(O/H) = 8.67 - 0.027 z + (0.41 - 0.76 z) \log\left(\frac{M_S}{M_S^*}\right), \quad M_S \leq M_S^*,$$

$$12 + \log(O/H) = 8.67 - 0.027 z, \quad M_S \geq M_S^*, \quad (3.25)$$

$$\log(M_S^*/M_\odot) = 9.60 + 5.65 z.$$

The derived z — M_S — O/H relation for subsample B is shown in Fig. 3.17 by the solid line for $z = 0.05$, and by the dashed line for $z = 0.25$.

To test the robustness of the derived z — M_S — O/H relation, subsample C has also been analyzed in a similar way. Fitting the subsample C data gives the following:

$$12 + \log(O/H) = 8.67 - 0.020 z + (0.39 - 0.63 z) \log\left(\frac{M_S}{M_S^*}\right), \quad M_S \leq M_S^*,$$

$$12 + \log(O/H) = 8.67 - 0.020 z, \quad M_S \geq M_S^*, \quad (3.26)$$

$$\log(M_S^*/M_\odot) = 9.54 + 5.90 z.$$

The obtained z — M_S — O/H relations for subsamples B and C are very similar, so that the results appear to be robust. The derived relations should approximate well the redshift evolution of oxygen abundances for $z \leq 0.25$, corresponding to lookback times of up to ~ 3 Gyr. Beyond $z = 0.25$, the number of galaxies in each subsample becomes very small and the redshift evolution of abundances cannot be studied with enough statistics. At the low-redshift end, to reduce errors from aperture effects and following the recommendations of [50], the objects with redshifts $z > 0.04$ only examined. Objects with $0.04 < z < 0.06$ will be considered as representative of the present-day epoch.

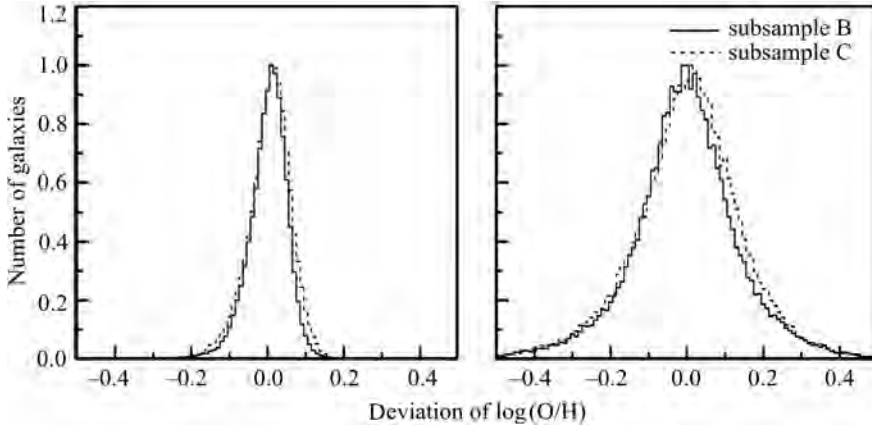


Fig. 3.18. Normalized histograms of oxygen abundance deviations from the $Z-M_S-O/H$ relation (left panel) and nitrogen abundances deviations from the $Z-M_S-N/H$ relation (right panel). In both panels, subsample B is shown by the solid line and subsample C by the dashed line

Fig. 3.18 shows the distribution of the deviations of the oxygen abundances from the derived $z-M_S-O/H$ relation for both subsamples B and C. It is seen that the scatter of oxygen abundances about the $z-M_S-O/H$ relation is slightly larger for galaxies in subsample C than in subsample B. Nevertheless, it can be said that, for both subsamples of galaxies, the oxygen abundances follow reasonably well the derived $z-M_S-O/H$ relation. The mean deviation is small, being ~ 0.06 dex. One can thus conclude that the derived relations can be used, in principle, to obtain a rough estimate of the metallicities of SDSS galaxies.

The metallicity plateau and the oxygen enrichment as a function of galaxy stellar mass. For the sake of definiteness, we will discuss the results for subsample B. The oxygen abundance increases with galaxy stellar mass until $M_S = 10^{9.9} M_\odot$, but then remains approximately constant, equal to $12 + \log(O/H) = 8.67$, in galaxies with $M_S \geq 10^{9.9} M_\odot$ (see the left panel of Fig. 17). The luminosity–central metallicity relation for nearby spiral galaxies also shows a plateau at high luminosities [105]. This plateau was interpreted above as evidence that the gas in the centers of the most metal-rich galaxies has been almost completely converted into stars and that the oxygen abundance in the centers of the most luminous metal-rich galaxies has reached its maximum attainable value of $12 + \log(O/H) \sim 8.87$. The plateau for oxygen abundances in the SDSS galaxies is at the level of $12 + \log(O/H) = 8.67$, i.e. 0.2 dex smaller. The simple model of chemical evolution of galaxies predicts that a decrease of μ by 0.1 results in an increase of oxygen abundance by ~ 0.13 dex, in the range of μ from ~ 0.50 to ~ 0.05 [105]. Then, the difference between the maximum attainable value of the oxygen abundance and the mean oxygen abundance

in high-mass SDSS galaxies, $\Delta(\log(\text{O}/\text{H})) \sim 0.2$, corresponds to a difference in gas mass fraction $\Delta\mu \sim 0.15$. Since the maximum attainable oxygen value corresponds to complete astration, i.e. $\mu = 0$, the mean μ in high-mass SDSS galaxies at the present epoch should be $\sim 15\%$, with a probable range of μ from $\sim 5\%$ to $\sim 25\%$.

Why do our SDSS subsamples not contain galaxies with abundances as high as the maximum attainable value? The reason has to do with the gas content of the SDSS galaxies in our subsamples. The maximum attainable value of the oxygen abundance corresponds to the limiting case where the gas has been completely converted into stars. The galaxies in our SDSS subsamples are all characterized by strong emission lines in their spectra, meaning that they are undergoing strong starbursts. This requires in turn that they contain an appreciable amount of gas. In other words, because our galaxies are gas-rich, they have not reached the maximum attainable value of the oxygen abundance which requires complete gas exhaustion. If galaxies were not gas-rich, they would have weak emission lines, unlikely to be measured accurately. There exists thus a lower limit on the gas mass fraction for a galaxy to have accurately measured lines and to be included in our subsamples. In that sense, the observed plateau is likely affected by the selection criteria. We note however that, even in the most evolved nearby spiral galaxies, the H II region oxygen abundances are generally lower than the maximum attainable value. There is furthermore an aperture effect that slightly lowers the metallicities observed for SDSS galaxies. The maximum attainable value oxygen abundance observed in the central part of some nearby galaxies is usually derived by linearly fitting the variations of H II region abundances with galactocentric distance, and extrapolating to $R = 0$. In the distant SDSS galaxies, because one fiber includes many H II regions that show decreasing metallicities towards larger galactocentric distances, the oxygen abundances are slightly diluted when averaged over a large region.

In the right panel of Fig. 3.17, we compare the M_S –O/H relation for local ($z \approx 0.05$) galaxies (solid line) with that for distant ($z \approx 0.25$) ones (dashed line). Three features are to be noted. First, it can be seen that, for the galaxies of highest stellar masses, those with masses $\geq 10^{11} M_\odot$, the plateau value of the oxygen abundance does not change in the redshift interval from 0.05 to 0.25. This implies that the galaxies of highest mass in our SDSS subsamples have reached their highest astration level some 3 Gyr ago, and have been somewhat “lazy” in their evolution afterwards. Second, for lower mass galaxies with stellar masses $\leq 10^{11} M_\odot$, it is seen that the value of the oxygen enrichment during the last 3 Gyr increases with decreasing galaxy mass, in the mass interval from $10^{11} M_\odot$ to $10^{9.9} M_\odot$, as shown by the widening gap between the solid and dashed curves toward lower masses. At $M_S = 10^{9.9} M_\odot$, there is a difference $\Delta\log(\text{O}/\text{H}) \sim 0.25$ between a local galaxy and one at redshift 0.25. For galaxies

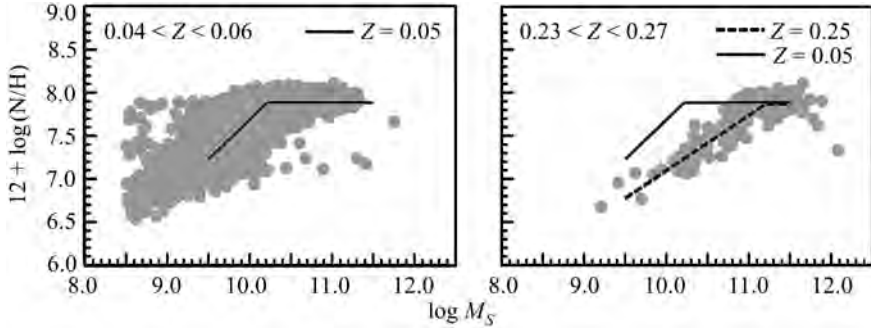


Fig. 3.19. The nitrogen abundance–galaxy stellar mass diagrams for subsample B at $z = 0.05$ (left panel) and $z = 0.25$ (right panel). The Z – M_S – N/H relation (Eq. 3.27) is shown by the solid line for $z = 0.05$ and by the dashed line for $z = 0.25$

with $M_S \leq 10^{9.9} M_\odot$, the oxygen enrichment during the last 3 Gyr slightly decreases with decreasing galaxy mass, the slope of the solid line being slightly steeper than that of the dashed line. Third, the value of M_S^* , the mass where the oxygen abundance becomes constant with galaxy stellar mass, is redshift-dependent, becoming higher at larger redshifts.

In summary, analysis of the z – M_S – O/H relation has led to the following main conclusions.

- The galaxies of highest masses, those with $M_S \geq 10^{11} M_\odot$, have reached their highest astration level in the past and have not had an appreciable oxygen abundance enrichment during the last ~ 3 Gyr.
- The mean value of the oxygen enrichment during the last 3 Gyr in galaxies with stellar masses in the range from $10^{10} M_\odot$ to $10^{11} M_\odot$ is $\Delta(\log(O/H)) \sim \sim 0.11$, with $\Delta(\log(O/H)) \sim 0.23$ at $10^{10} M_\odot$ and $\Delta(\log(O/H)) = 0$ at $10^{11} M_\odot$.

The above picture will now be put to the test through the study of the redshift evolution of nitrogen abundances, which we consider next.

The z – M_S – N/H relation. We proceed in the same way as in our analysis of the oxygen abundances. The left panel of Fig. 3.19 shows the nitrogen abundances of the local galaxies in subsample B, with redshifts $0.04 < z < < 0.06$, as a function of galaxy stellar mass. The right panel of Fig. 3.19 shows the same diagram, but for more distant galaxies, with redshifts $0.23 < z < 0.27$. Fig. 3.19 shows that the general behavior of nitrogen abundances with redshift and galaxy stellar mass is similar to that of oxygen abundances. The nitrogen abundance increases with increasing galaxy stellar mass up to a value M_S^* of the stellar mass. Then, for galaxies with $M_S > M_S^*$, the nitrogen abundance remains approximatively constant, reaching a plateau. The value of M_S^* is redshift-dependent, becoming higher at larger redshifts.

The change of nitrogen abundance with redshift and galaxy stellar mass can be approximated by a z – M_S – N/H relation, similar to the one for oxygen

abundances. Fitting the data for galaxies in subsample B results in the following relation:

$$\begin{aligned}
 12 + \log(\text{N}/\text{H}) &= 7.89 - 0.110 z + (0.99 - 1.40 z) \log\left(\frac{M_S}{M_S^*}\right), \quad M_S \leq M_S^*, \\
 12 + \log(\text{N}/\text{H}) &= 7.89 - 0.110 z, \quad M_S \geq M_S^*, \\
 \log(M_S^*/M_\odot) &= 9.97 + 4.92 z.
 \end{aligned}
 \tag{3.27}$$

The derived relation is shown in Fig. 3.19 by a solid line for $z = 0.05$, and by a dashed line for $z = 0.25$.

Again, to test the robustness of the obtained z – M_S – N/H relation, we have examined subsample C in a similar way. Fitting those data gives:

$$\begin{aligned}
 12 + \log(\text{N}/\text{H}) &= 7.88 - 0.027 z + (0.85 - 1.14 z) \log\left(\frac{M_S}{M_S^*}\right), \quad M_S < M_S^*, \\
 12 + \log(\text{N}/\text{H}) &= 7.88 - 0.027 z, \quad M_S > M_S^*, \\
 \log(M_S^*/M_\odot) &= 10.04 + 5.03 z.
 \end{aligned}
 \tag{3.28}$$

The derived z – M_S – N/H relations for subsample B and C are very similar and that the derived z – M_S – N/H relation is robust.

While the general behavior of nitrogen abundances with redshift and galaxy stellar mass is quite similar to that of oxygen abundances (compare Figs. 3.17 and 3.19), there are significant differences, due to the different production mechanisms of these two elements. The dependence of the nitrogen abundance on galaxy stellar mass for $M_S < M_S^*$ is considerably steeper than that for oxygen abundances. This is caused by the fact that at oxygen abundances higher than about $12 + \log(\text{O}/\text{H}) = 8.3$, the metallicity-dependent nitrogen production by intermediate-mass stars starts to dominate. Another remarkable difference concerns M_S^* , the mass which marks the transition from the linear regime to the plateau regime: at all redshifts, M_S^* is shifted towards higher values in the M_S – N/H diagram as compared to in the M_S – O/H diagram. Thus, $\log M_S^*$ is equal to 10.2 and 11.2 at $z = 0.05$ and $z = 0.25$ respectively in the M_S – N/H diagram, as compared to 9.9 and 11.0 in the M_S – O/H diagram.

We now attempt to understand this M_S^* shift. The time delay in nitrogen production relative to oxygen production plays an important role. Examination of Figs. 3.17 and 3.19 shows that galaxies with masses $\geq 10^{11.2} M_\odot$ are in the plateau regime in both the M_S – O/H and in M_S – N/H diagrams, at both $z = 0.05$ and $z = 0.25$. This means that those galaxies have not undergone appreciable enrichment in both oxygen and nitrogen during the last ~ 3 Gyr.

Evidently, there has not been appreciable star formation in those galaxies over the redshift range from $z = 0.25$ to $z = 0.05$. Significant star formation in those galaxies has occurred so long ago that stars have returned their nucleosynthesis products to the interstellar medium before the epoch corresponding to $z = 0.25$.

Galaxies with masses between $\sim 10^{11.0} M_{\odot}$ and $\sim 10^{11.2} M_{\odot}$ do not show an appreciable enrichment in oxygen abundance from $z = 0.25$ to $z = 0.05$ but do show some enrichment in nitrogen over this period. This suggests that there has not been appreciable star formation in those galaxies over the period from $z = 0.25$ to $z = 0.05$. However, they do contain stars that were formed before $z = 0.25$, but later in comparison to the galaxies of highest masses. The massive oxygen-producing stars die after a few million years, releasing oxygen in the interstellar medium. By contrast, the nitrogen-producing intermediate-mass stars have longer lifetimes, and so they have not returned nitrogen to the interstellar medium before $z = 0.25$ because they have not had enough time to evolve. This also suggests that stars that make a contribution to the nitrogen production have lifetimes of a few Gyr.

The galaxies with masses $\leq 10^{11.0} M_{\odot}$ show enrichment in both oxygen and nitrogen abundances after the period corresponding to $z = 0.25$. This means that appreciable star formation has taken place in those galaxies during the last ~ 3 Gyr. The nitrogen production increases with decreasing galaxy mass from $10^{11.2} M_{\odot}$ to $\sim 10^{10.2} M_{\odot}$ where it reaches a value $\Delta \log(\text{N}/\text{H}) \sim 0.65$, then it decreases with further decrease of galaxy mass.

The right panel of Fig. 3.18 shows the deviations of nitrogen abundances from the derived z - M_S -N/H relation for galaxies from both subsamples B (solid line) and C (dashed line). Examination of the left and right panels of Fig. 3.18 shows that the right histogram is broader than the left one, i.e. that the nitrogen abundances show a larger scatter around the z - M_S -N/H relation as compared to oxygen abundances around the z - M_S -O/H relation. The mean deviation for nitrogen abundances is $\Delta(\log(\text{N}/\text{H})) \sim 0.15$ against $\Delta(\log(\text{O}/\text{H})) \sim 0.06$ for oxygen abundances. However, nitrogen also spans a significantly larger abundance range, from $12 + \log(\text{N}/\text{H}) \sim 6.5$ to $12 + \log(\text{N}/\text{H}) \sim 8.0$, as compared to oxygen which goes only from $12 + \log(\text{O}/\text{H}) \sim 8.25$ to $12 + \log(\text{O}/\text{H}) \sim 8.75$. Taking into account the differences in range, then the relative scatters around the z - M_S -N/H and z - M_S -O/H relations are comparable. It should be emphasized that the larger scatter of nitrogen abundances around the z - M_S -N/H relation in comparison to the scatter of oxygen abundances around the z - M_S -O/H relation cannot be attributed to larger errors in nitrogen abundance determinations. Indeed, the O/H values are derived from the N/H and N/O values, and any error in the nitrogen abundance determination is propagated into the error in the oxygen abundance determination. Then, if the large scatter of nitrogen abundances around the z - M_S -N/H is caused by large errors in the nitrogen abundance

determinations, then the oxygen abundances would show a similar or larger scatter around the z – M_S –O/H relation. Just the opposite is observed.

Thus, the consideration of the nitrogen abundance evolution with redshift and galaxy stellar mass has confirmed the general picture obtained from the oxygen abundance evolution analysis. Examination of both the z – M_S –N/H and the z – M_S –O/H relations has led to the following conclusions:

- The galaxies of highest masses, those with masses $\geq 10^{11.2} M_\odot$, have reached their high astration level more than 3 Gyr ago, so that stars in those galaxies have returned their nucleosynthesis products to the interstellar medium before $z = 0.25$.

- The galaxies with masses in the range from $\sim 10^{11.0} M_\odot$ to $\sim 10^{11.2} M_\odot$ also form their stars before $z = 0.25$, but later in comparison to the galaxies of highest masses. The intermediate-mass stars in those galaxies have not returned nitrogen to the interstellar medium before $z = 0.25$ because they have not had enough time to evolve.

- Significant star formation has occurred in galaxies with masses lower than $\sim 10^{11} M_\odot$ during the last 3 Gyr. Those galaxies have converted up to 20% of their total mass into stars over this period.

- Stars with lifetimes of a few Gyr contribute to the nitrogen production.

The evolution of the mass–metallicity relation of galaxies with redshift has been considered by several groups, as described in the introduction. But, as discussed before, each group uses a different calibration to derive abundances which show as a result sometimes large discrepancies. So it is difficult to directly compare, or put on the same scale, the abundances derived by other groups and our own. Thus, we will not attempt such a comparison. Rather, we will limit ourselves to comparing the evolution in oxygen abundances with redshift which seems to be less sensitive to the adopted calibration.

Lilly et al. (2003) have estimated the oxygen abundance in a sample of 66 Canada–France Redshift Survey galaxies in the redshift range $0.47 < z < 0.92$, using the flux ratios of bright oxygen emission lines [61]. They concluded that, at half the present age of the Universe, the overall oxygen abundance of the galaxies in their sample, with luminosities ranging from $M_B = -20$ to $M_B = -22$ (or $\log(L_B/L_{B\odot}) \sim 10.2$ – 11.0), is only slightly lower than the oxygen abundance in similar luminous galaxies today. They found a variation $\Delta(\log(\text{O}/\text{H})) = 0.08 \pm 0.06$.

Savaglio et al. (2005) have investigated the mass–metallicity relation using galaxies from the Gemini Deep Deep Survey and the Canada–France Redshift Survey in the redshift range $0.4 < z < 1.0$ [116]. Their galaxies with $M_S > 10^{10} M_\odot$ have oxygen abundances close to those in local galaxies of comparable mass, while the oxygen abundances in galaxies with $M_S < 10^{10} M_\odot$ are lower on average (with a large scatter) than those in galaxies of similar masses at the present epoch (see their Fig. 13).

Cowie et al. (2008) have studied the oxygen abundance evolution from $z = 0.9$ to $z = 0.05$ using a large sample of galaxies in the Great Observatories Origins Deep Survey—North (GOODS—N) [21]. They have found an evolution of the metallicity—mass relation corresponding to a decrease of 0.21 ± 0.03 dex between the value at $z = 0.77$ and the local value in the 10^{10} – $10^{11} M_{\odot}$ range. They also found that star formation in the most massive galaxies ($>10^{11} M_{\odot}$) ceases at $z < 1.5$ because of gas starvation.

Lamareille et al. (2009) have derived the mass—metallicity relation of star-forming galaxies up to $z \sim 0.9$ using data from the VIMOS VLT Deep Survey [55]. They found that the galaxies of $10^{10.2}$ solar masses show a larger oxygen enrichment ($\Delta(\log(\text{O}/\text{H})) \sim 0.28$) from $z \sim 0.77$ to $z = 0$) than the galaxies of $10^{9.4}$ solar masses ($\Delta(\log(\text{O}/\text{H})) \sim 0.18$).

Lara-López et al. (2009) have studied the oxygen abundance of relatively massive ($\log(M_S/M_{\odot}) \geq 10.5$) star-forming galaxies from SDSS/DR5 at different redshift intervals from 0.4 to 0.04 [56]. They found an oxygen enrichment $\Delta(\log(\text{O}/\text{H})) \sim 0.1$ from redshift 0.4 to 0.

Cid Fernandes et al. (2009) have derived the mass—metallicity relation at different lookback times for SDSS galaxies using the stellar metallicities estimated with their spectral synthesis code [18]. They have found that the more massive galaxies show very little evolution since a lookback time of 9 Gyr.

Examination of all these studies shows good qualitative agreement between them, but with a rather large scatter in the estimated values of the oxygen enrichment. The results of these investigations can be summarized as followed: 1) the most massive galaxies (those with masses $>10^{11} M_{\odot}$) do not show an appreciable enrichment in oxygen from $z \sim 0.7$ to $z = 0$; 2) in the 10^{10} – $10^{11} M_{\odot}$ mass range, an increase of the oxygen abundance $\Delta(\log(\text{O}/\text{H})) \sim 0.08$ – 0.28 is observed in the redshift range from $z \sim 0.7$ to $z \sim 0$. Our results are also in good qualitative agreement with those previous results. We also see no change in oxygen abundance with redshift for galaxies with masses greater than $10^{11} M_{\odot}$, in the redshift range from ~ 0.25 to 0. We estimate the mean increase of the oxygen abundance with redshift in the 10^{10} – $10^{11} M_{\odot}$ galaxy stellar mass range to be $\Delta(\log(\text{O}/\text{H})) \sim 0.11$, with $\Delta(\log(\text{O}/\text{H})) \sim 0.23$ at $10^{10} M_{\odot}$ and $\Delta(\log(\text{O}/\text{H})) = 0$ at $10^{11} M_{\odot}$. This is in agreement with the upper range of values found in previous works, especially when we take into account the fact that we have considered a smaller redshift interval than previous investigators.

Thus, the O and N abundance evolutions with redshift of the galaxies clearly show the galaxy downsizing effect [20, 115], where enrichment (and hence star formation) is shifted from high-mass galaxies at earlier cosmic times to lower-mass galaxies at later epochs.

3.5. Galaxy downsizing and the origin of the scatter in the N/H—O/H diagram

3.5.1. The N/O—O/H diagram

Oxygen and nitrogen are key elements in the study of the chemical evolution of galaxies. The N/O—O/H (or N/H—O/H) diagram has been considered by many authors [25, 40, 43, 66, 83, 84]. A prominent feature of this diagram is that, in its high-metallicity part ($12 + \log(\text{O}/\text{H}) \geq 8.3$), the N/H abundance ratio shows a large scatter at a fixed value of the O/H abundance ratio [40, 62, 100]. The N/H value for a given O/H contains important information about the heavy element enrichment history of a galaxy, and consequently, about its star formation history. Therefore, an explanation of the origin of the scatter in the N/H—O/H diagram is key to understanding the evolution of galaxies.

Two main explanations are presently considered to account for the scatter in normal spiral galaxies: 1) the time delay between nitrogen and oxygen enrichment; and 2) the local enrichment in nitrogen by Wolf–Rayet (WR) stars. Concerning the first explanation, Edmunds and Pagel (1978) [25] have noted that, due the fact that O and N are produced in stars of different masses, there can be a significant time delay between the release of O, produced in high-mass stars, and that of N, produced in intermediate-mass stars, into the interstellar medium (ISM). The N/O ratio of a galaxy then becomes an indicator of the time that has elapsed since the last episode of star formation. Current stellar evolution models predict that N is mainly manufactured and ejected into the ISM by intermediate-mass stars with masses greater than $3\text{--}4M_{\odot}$ [37, 65, 110, 137], although massive stars can contribute, at least at low metallicities [17]. This suggests that the time delay between N and O enrichment in galaxies is 250–400 Myr, depending on the adopted stellar mass–lifetime relation [113]. Properties of the observed N/O—O/H diagram can generally be reproduced by chemical evolution models of galaxies by taking into account a time delay [19, 38, 40, 66, 83, 84, 90]. The exact value of the time delay is however still a subject of debate [100, 112, 133].

Concerning the second explanation, it is known ([62] and references therein) that some galaxies with WR features have a high N/O ratio. This suggests that the ejecta of WR stars may locally enrich the ISM in N. Henry et al. (2000) noted that most points in the N/O—O/H diagram cluster at relatively low N/O values [40]. This led them to conclude that the lower envelope is the “equilibrium” unperturbed locus and that the observed scatter is the result of intermittent increases in N, caused by the local contamination by WR stars or luminous blue variables. Izotov et al. (2006) also arrived at the same conclusion [43].

Selective heavy element loss through enriched galactic winds may also introduce scatter in the N/O ratios [86]. It is believed, however, that galactic

winds play an important role in the chemical evolution of only dwarf galaxies, not of giant spirals (e.g. [101]).

In a previous section we have considered the evolution of O and N abundances in galaxies with different stellar masses. We have found clear evidence for galaxy downsizing, where the sites of active star formation and hence of metal enrichment shift from high-mass galaxies at early cosmic times to lower-mass systems at later epochs [20,115]. All enrichment ceases in the most massive galaxies at late cosmic times. This downsizing effect provides a remarkable opportunity for clarifying the origin of the scatter in the N/H—O/H diagram. Indeed, if the scatter is caused by a time delay between O and N enrichment in galaxies, then it should be minimized for the most massive galaxies where enrichment has stopped. On the other hand, one should expect that the N/H ratios of the less massive galaxies (those with significant star formation at the current epoch) to be shifted towards lower values relative to the massive galaxies in the N/H—O/H diagram, because there is a time delay between N and O enrichment and N has not yet been released in the ISM.

The study discussed in previous Section was based on the MPA/JHU catalogs of automatic line flux measurements of the SDSS spectra (see [11,136] and other publications of those authors). The accuracy of such automatic line flux measurements seems is not good enough for investigating the origin of scatter in the N/H — O/H diagram. Therefore we have carried out the manually measure the line fluxes of the SDSS spectra [107]. This provides with more accurate line flux measurements, especially for spectra of objects with the largest redshifts, those with redshifts between 0.3 and 0.4. Here we will discuss whether the time delay is in fact responsible for the large scatter in the nitrogen abundances in galaxies with a given oxygen abundance.

3.5.2. The data

We have extracted from the MPA/JHU catalogs four subsamples of emission-line galaxies, each covering a different interval of galaxy stellar mass, centered respectively on the mass values $M_S = 10^{11.3}M_\odot$, $10^{11.0}M_\odot$, $10^{10.6}M_\odot$, and $10^{10.2}M_\odot$. To have a reasonable number of galaxies in each subsample and in order for the galaxies to cover the whole redshift range in a roughly uniform fashion, the mass interval dM was chosen to be small and to vary from 0.0015 to 0.10 dex, depending on the redshift and M_S . For each mass interval, we have extracted from the MPA/JHU catalogs emission-line galaxies with automatic measurements of fluxes in the H β , H α , [O II] $\lambda\lambda 3727, 3729$, [O III] $\lambda 5007$, [N II] $\lambda 6584$ emission lines. We impose the additional restrictions that the galaxies have equivalent widths $EW(\text{H}\beta) > 10 \text{ \AA}$ (this criterion applies only to galaxies with redshifts < 0.3 , as we did not wish to reduce further the very small number of galaxies with $z > 0.3$), $EW([\text{O II}]\lambda\lambda 3727, 3729) > 3 \text{ \AA}$,

$EW([\text{O III}]\lambda 5007) > 3 \text{ \AA}$, and $EW([\text{N II}]\lambda 6584) > 2 \text{ \AA}$. These additional restrictions insure that the chosen galaxies have a reasonably high star formation rate, giving rise to reasonably strong emission lines that can be measured with good accuracy.

Each so chosen spectrum was then examined visually and the noisy spectra were rejected. The line fluxes of the remaining galaxies were then measured with IRAF². The $[\text{O III}]\lambda 5007/\text{H}\beta$ vs $[\text{N II}]\lambda 6584/\text{H}\alpha$ diagram was then used to reject AGNs [5], with the dividing line between H II regions ionized by star clusters and AGNs taken from [49].

The wavelength range of the SDSS spectra is 3800 \AA –9300 \AA , so that for nearby galaxies with redshift $z \leq 0.023$, the $[\text{O II}]\lambda 3727 + \lambda 3729$ emission line is out of the observed range. Thus, all galaxies in our total sample have redshifts greater than ~ 0.023 . For distant galaxies with redshift $z \geq 0.33$, the $[\text{S II}]\lambda\lambda 6717, 6731$ emission lines are out of the observed range. The sulfur line intensities are usually used as indicators of the electron density. They serve also to distinguish between hot and warm H II regions, in the framework of the ON calibrations [106]. Since the sulfur lines are not present, we will assume the electron density to be equal to 100 cm^{-3} and that our sample does not contain hot H II regions (i.e. those with $12 + \log(\text{O}/\text{H}) \leq 8.0$). The redshift z and stellar mass M_S of each galaxy were taken from the MPA/JHU catalogs. When the stellar mass of a galaxy with redshift $z > 0.3$ is not available in the MPA/JHU catalogs, the mass of a galaxy was estimated from its absolute magnitude M_z , its colour $m_z - m_r$ and its $\text{H}\beta$ equivalent width, using the relation

$$\begin{aligned} \log M_S &= -0.459 M_z - 0.775 (m_z - m_r) + 0.363 + 0.083 \log EW(\text{H}\beta) \\ &\quad \text{for } (m_z - m_r) < -0.3, \\ \log M_S &= -0.61 M_z + 0.43 (m_z - m_r) - 2.58 - 0.24 \log EW(\text{H}\beta) \\ &\quad \text{for } (m_z - m_r) > -0.3, \end{aligned} \tag{3.29}$$

where the galaxy stellar mass M_S is in units of solar masses. This relation was derived by fitting the data for galaxies in the redshift interval $0.3 < z < 0.4$ with available stellar masses in the MPA/JHU catalogs. We caution that this relation is not a general relation for the determination of galaxy stellar masses. It applies only within the small particular redshift interval defined above. It should also be stressed that the derived masses serve only to select galaxies with various masses to populate our different subsamples and are not used in any calculation.

²IRAF is distributed by National Optical Astronomical Observatories, which are operated by the Association of Universities for Research in Astronomy, Inc., under cooperative agreement with the National Science Foundation.

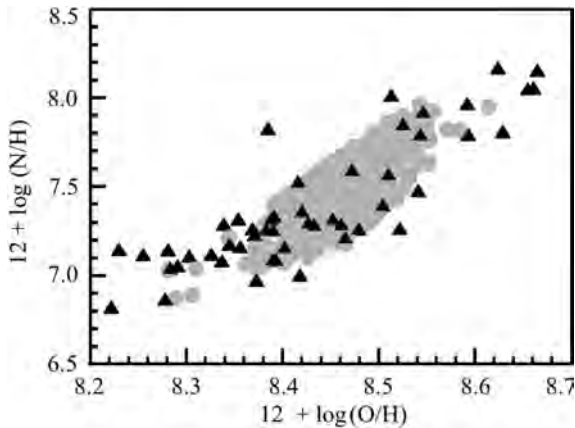


Fig. 3.20. The N/H–O/H diagram. The gray points represent individual galaxies from our four SDSS subsamples with oxygen and nitrogen abundances derived from the ON calibrations from [106]. The dark triangles show H II regions in nearby galaxies (a compilation in [106]) with oxygen and nitrogen abundances derived with the T_e method

The final database consists of 221 spectra of galaxies with $M_S = 10^{11.3} M_\odot$ (with 74 objects with M_S derived from Eq. 3.29), 259 spectra of galaxies with $M_S = 10^{11.0} M_\odot$ (60 objects with M_S from Eq. 3.29), 244 spectra of galaxies with $M_S = 10^{10.6} M_\odot$ (32 objects with M_S from Eq. 3.29), and 152 spectra of galaxies with $M_S = 10^{10.2} M_\odot$ (7 objects with M_S from Eq. 3.29). The measured emission-line fluxes are then corrected for interstellar reddening using the theoretical $H\alpha$ to $H\beta$ ratio, in the same way as in [133]. O and N abundances are then estimated for each galaxy, using the recent ON calibrations [106]. These calibrations give both O and N abundances over the whole metallicity range with a satisfactory precision: the mean differences between O abundances determined from these calibrations and from the direct T_e method based on the $[\text{O III}]\lambda 4363$ line is only ~ 0.075 dex for O abundances, and only ~ 0.05 dex for N abundances.

3.5.3. Galaxy downsizing and the origin of the scatter in the N/H – O/H diagram

We first check the accuracy of our abundance determinations. Fig. 3.20 shows the N/H–O/H diagram. The gray points represent galaxies in our four SDSS subsamples with O and N abundances derived from the ON calibrations. The dark triangles show H II regions in nearby galaxies [106], with O and N abundances derived with the T_e method, commonly thought to be the most accurate one. It is seen that the galaxies in our SDSS subsamples occupy the same region in the N/H – O/H diagram as the H II regions in nearby galaxies with O and N abundances derived through the T_e method. This confirms that our ON-calibration-based O and N abundances are quite reliable. The remarkable feature to note in the N/H–O/H diagram is the large scatter in N/H values at a given O/H value. This holds as much for SDSS objects as for H II regions in nearby galaxies.

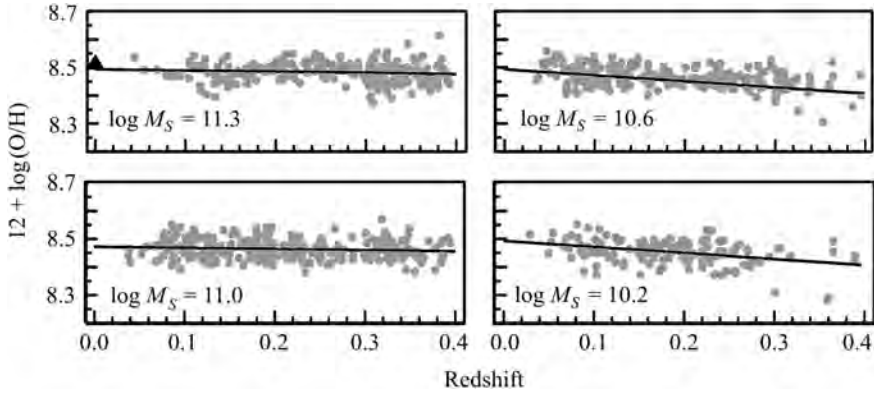


Fig. 3.21. Oxygen abundances as a function of redshift for the four subsamples of galaxies with different stellar masses. In each panel, labeled by the galaxy stellar mass, the gray points represent individual galaxies. The solid line is the least-squares best fit to those data. The dark filled triangle in the top panel shows the Orion Nebula

We next investigate the redshift evolution of O abundances in each of the four galaxy mass ranges (Fig. 3.21). In each panel labeled by the galaxies’ masses, the filled gray circles show individual galaxies. The solid line is the best least-squares fit to those data. Inspection of the upper left panel shows that there is no systematic variation with redshift of the O abundance in galaxies with masses $\sim 10^{11.3} M_{\odot}$ up to $z = 0.4$. This implies that these galaxies have reached a high astration level some 4 Gyr ago, and have been somewhat “lazy” in their evolution afterwards. The average value of the O abundances for galaxies with stellar mass $M_S = 10^{11.3} M_{\odot}$ is remarkably close to the O abundance in the Orion nebula ($12 + \log(\text{O}/\text{H}) = 8.51$) obtained by Esteban et al. (2004) [31]. It is also in good agreement with the O abundances in nearby luminous galaxies obtained by Moustakas et al. (2010) [72], using the calibration from [103].

Comparison between the different panels of Fig. 3.21 shows clearly the effect of galaxy downsizing. Massive galaxies do not show O enrichment: they already reach a relatively high O abundance at $z = 0.4$, and that abundance remains nearly constant until $z = 0$. The less massive galaxies do show O enrichment: they have lower O abundances at $z = 0.4$, but these increase from $z = 0.4$ to $z = 0$, and at the present epoch, they are nearly the same as in massive galaxies.

We next investigate the origin of the scatter in the N/H–O/H diagram. The upper left panel of Fig. 3.22 shows that diagram for the subsample that contains our most massive galaxies, those with masses $\sim 10^{11.3} M_{\odot}$. It is seen that the scatter in the N/H–O/H diagram for this subsample of galaxies is small, especially for galaxies with $z \leq 0.3$ (see Fig. 3.23, to be discussed later).

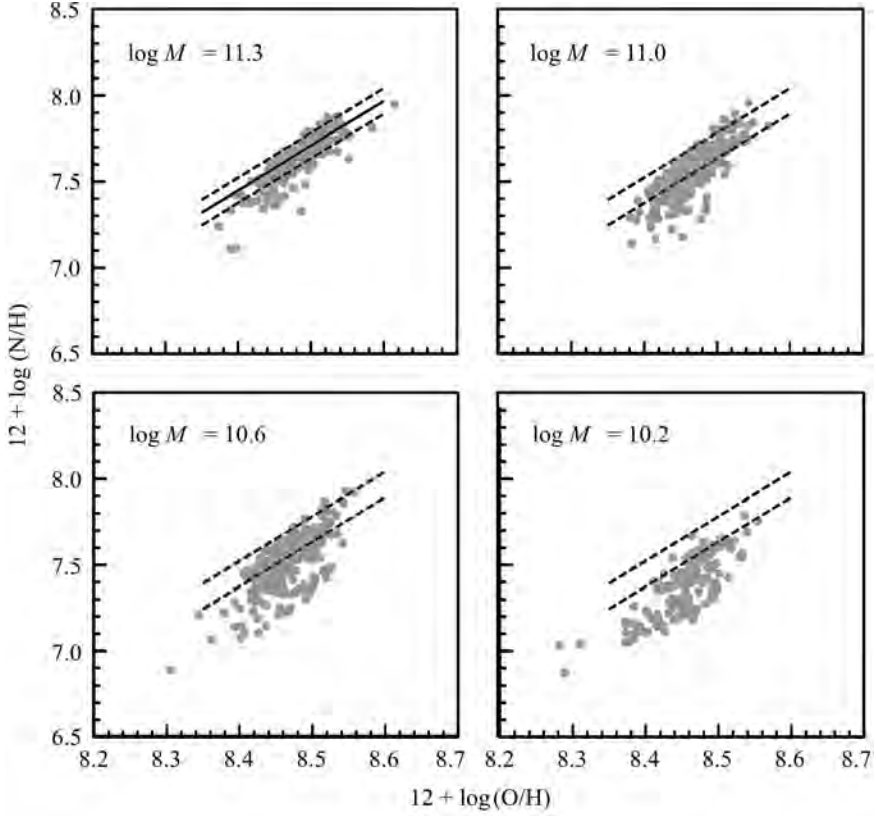


Fig. 3.22. N/H–O/H diagrams for the four subsamples of galaxies with different stellar masses. In each panel, labeled by the galaxy stellar mass, the gray points represent individual galaxies. The solid line in the left upper panel is the derived N/H–O/H relation for the most massive galaxy subsample, with masses $\sim 10^{11.3} M_{\odot}$. The dashed lines show the $\pm 2\sigma$ shifts from this relation. These dashed lines are reproduced in all other panels

Using this subsample, we have derived the following relation between N/H and O/H abundances

$$\log(\text{N}/\text{H}) = 2.596 (\pm 0.118) \log(\text{O}/\text{H}) - 14.359 (\pm 1.001). \quad (3.30)$$

This relation has been derived in an iterative manner. First, a least-squares fit was obtained for all data points with $z < 0.3$. Then, objects with deviations larger than 2σ were rejected and a new least-squares fit derived. The final fit is obtained when, after several iterations, the fits for two consecutive ones coincide. The scatter in the N/H values relative to the final fit is $\sigma = 0.037$ dex. The derived N/H–O/H relation is shown in the upper left panel of Fig. 3.22 by a solid line, while the dashed lines show $\pm 2\sigma$ shifts from that relation. It

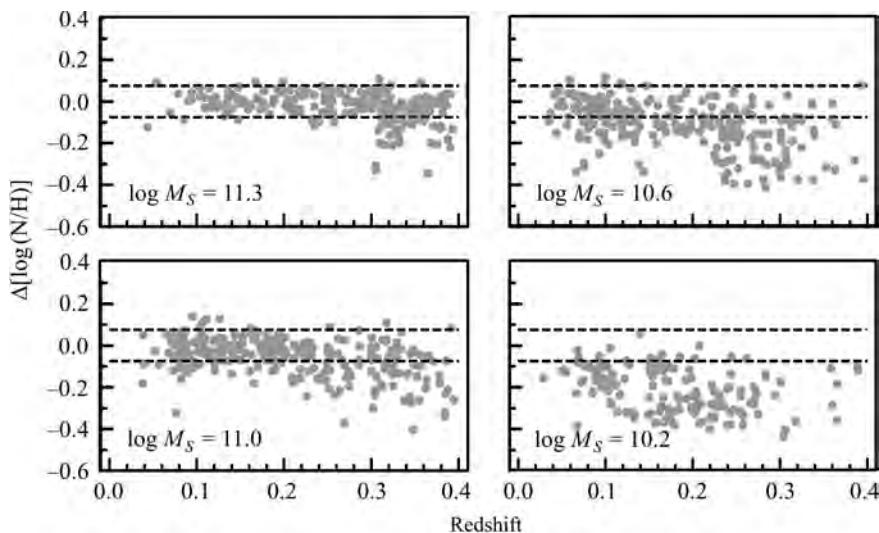


Fig. 3.23. Deviations of the nitrogen abundance from the N/H–O/H relation, derived for the most massive galaxy subsample (Eq. 3.30), as a function of redshift for all four subsamples of galaxies with different stellar masses. In each panel, labeled by the galaxy stellar mass, the gray points represent individual galaxies. The dashed lines show the $\pm 2\sigma$ deviations from the N/H–O/H relation

should be noted that this N/H–O/H relation is derived for a relatively small range of O/H and, consequently, its slope cannot be determined with a high precision. Therefore, it should not be used for O/H values beyond the above specified range. To establish a more general N/H–O/H relation, a sample of objects covering a more extended range in O/H would be needed.

The above relation links N/H and O/H in galaxies where O and N enrichment has already ceased. One would expect that galaxies with significant star formation in the near past would be displaced towards lower N/H values in the N/H–O/H diagram relative to this relation, because of the time delay between N and O enrichment. Comparison between the four panels of Fig. 3.22 clearly shows this effect. The most massive galaxies define an upper envelope in the N/H–O/H diagram and they do not show significant star formation in the last 4 Gyr (Fig. 3.21). The lower-mass galaxies are shifted towards lower N/H values and they show significant star formation during the same period (Fig. 3.21). This is solid evidence that the differences in N/H for galaxies with a given O/H are caused by the time delay between N and O enrichment.

Fig. 3.23 shows how the deviations of the N abundance from the N/H–O/H relation (Eq. 3.30) vary with mass and redshift. The gray points represent individual galaxies. The dashed lines show $\pm 2\sigma$ deviations from that relation. The N evolution with redshift in galaxies of different masses is a clearly due to a galaxy downsizing effect. As the Universe ages, the sites of star formation

shift from high-mass galaxies ($\log M = 11.3$), where star formation and O and N enrichment have ceased more than 4 Gyr ago, to lower-mass galaxies ($\log M < 11.3$) where active star formation and O and N enrichment are still ongoing. Comparison of Figs. 3.23 and 3.21 shows that the downsizing effect is more prominent for N than for O. This is because N is a secondary element while O is a primary one.

To have comparable numbers of galaxies with low redshifts ($0.02 < z < 0.15$) in the highest-mass subsample of galaxies ($M_S = 10^{11.3}M_\odot$) and in the lowest-mass subsample ($M_S = 10^{10.2}M_\odot$), we had to use a mass interval $dM = 0.10$ in the first case, and a value about 66 times lower, $dM = 0.0015$, in the second case. This implies that, at the current epoch, star formation events occur nearly two orders of magnitude more often in low-mass galaxies than in high-mass ones. Because of the time delay between O and N enrichment, there is a downward shift towards lower N/H values for low-mass galaxies in the N/H–O/H diagram (Fig. 3.23). This naturally explains the finding of [40] that most of the local dwarf star-forming galaxies cluster at relatively low N/O values in the N/O–O/H diagram.

Thus, the O and N abundance evolutions with redshift of the galaxies clearly show the galaxy downsizing effect [20, 115], where enrichment (and hence star formation) is shifted from high-mass galaxies at earlier cosmic times to lower-mass galaxies at later epochs. The most massive galaxies where O and N enrichment and star formation has already stopped, occupy a narrow band in the N/H–O/H diagram, defining an upper envelope. On the other hand, the less massive galaxies with significant star formation at the current epoch are shifted downwards, towards lower N/H values. The scatter of N/H for a given O/H is caused by the time delay between N and O enrichment and the different star formation histories in different galaxies (the galaxy downsizing effect).

3.6. Summary

We have performed a detailed study of the chemical composition of the interstellar medium of nearby late type galaxies. A compilation of more than 1000 published spectra of H II regions in 54 nearby spiral and irregular galaxies was carried out. The oxygen and nitrogen abundances in each H II region were recomputed in a homogeneous way. The parameters of the radial distributions (the extrapolated central intersect value and the gradient) of the oxygen and nitrogen abundances were derived. The correlations between oxygen abundance and macroscopic properties of galaxies are examined. The oxygen abundance in the disk of a galaxy at $r = 0.4R_{25}$, where R_{25} is the isophotal radius, is used as a characteristic (or representative) oxygen abundance for spiral galaxies. The oxygen abundance in spiral galaxies correlates with its luminosity, rotation velocity, and morphological type: the

correlation with the rotation velocity may be slightly tighter. The slope of the characteristic oxygen abundance—luminosity relationship for spiral galaxies is slightly more shallow than the one for irregular galaxies.

We search for the maximum attainable value of oxygen abundance in spiral galaxies. The luminosity—central metallicity diagram for spiral galaxies is examined. There exists a plateau in the luminosity—central metallicity diagram at high luminosities ($-22.3 \leq M_B \leq -20.3$). This provides strong evidence that the oxygen abundance in the centers of the most metal-rich luminous spiral galaxies reaches the maximum attainable value of oxygen abundance. The maximum value of the gas-phase oxygen abundance in H II regions of spiral galaxies is $12 + \log(\text{O}/\text{H}) \sim 8.87$. Because some fraction of the oxygen (about 0.08 dex) is expected to be locked into dust grains, the maximum value of the true gas+dust oxygen abundance in H II regions of spiral galaxies is $12 + \log(\text{O}/\text{H}) \sim 8.95$. This value is a factor of ~ 2 higher than the recently estimated solar value.

The redshift evolution of oxygen and nitrogen abundances in star-forming galaxies has been studied. Our study has been based on the SDSS data base of a million spectra. The MPA/JHU catalogs of automatic line flux measurements of the SDSS spectra have been used. We have paid particular attention to the construction of a galaxy sample. We have devised a way to recognize and exclude from consideration not only AGNs, but also star-forming galaxies with large errors in their line flux measurements. We have found that the requirement that nitrogen abundances, derived with different calibration relations based on different emission lines, agree, can be used as a reliable criterion to select star-forming galaxies with accurate line fluxes measurements. Subsamples of star-forming SDSS galaxies have been extracted from the MPA/JHU catalogs, using this criterion. The nitrogen and oxygen abundances are estimated for these galaxies. The general picture of the oxygen abundance evolution with redshift and galaxy stellar mass obtained here and in previous work is confirmed and strengthened by consideration of the nitrogen abundance evolution. The following main results have been obtained.

1. The galaxies of highest masses (those more massive than $\sim 10^{11.2} M_\odot$) do not show an appreciable enrichment in both oxygen and nitrogen from $z = 0.25$ to $z = 0.05$. Those galaxies have reached their high astration level in such a distant past that their stars have returned their nucleosynthesis products to the interstellar medium before $z = 0.25$.

2. The galaxies in the mass range from $\sim 10^{11.0} M_\odot$ to $\sim 10^{11.2} M_\odot$ do not show an oxygen enrichment, but do show some enrichment in nitrogen. Those galaxies also formed stars before $z = 0.25$, but at a later epoch in comparison to the galaxies of highest masses. Their stars have not returned nitrogen to the interstellar medium before $z = 0.25$ because they have not had enough time to evolve.

3. The late-type galaxies with masses lower than $\sim 10^{11} M_{\odot}$ show enrichment in both oxygen and nitrogen abundances over the redshift period from $z = 0.25$ to $z = 0.05$, i.e. during the last 3 Gyr. The oxygen enrichment increases with decreasing galaxy mass, from $M_S = 10^{11} M_{\odot}$ to $M_S = 10^{9.9} M_{\odot}$. It reaches a value $\Delta \log(\text{O}/\text{H}) \sim 0.25$ at $M_S = 10^{9.9} M_{\odot}$ and slightly decreases with further decrease of galaxy mass. The nitrogen enrichment increases with decreasing galaxy mass, from $\sim 10^{11} M_{\odot}$ to $\sim 10^{10.2} M_{\odot}$. It reaches a value $\Delta \log(\text{N}/\text{H}) \sim 0.65$ at $\sim 10^{10.2} M_{\odot}$ and slightly decreases with further decrease of galaxy mass. Significant star formation has occurred in those galaxies during the last 3 Gyr. They have converted up to 20% of their total mass to stars over this period.

We have examined the origin of the scatter of N/H among the galaxies for a given O/H. The accuracy of automatic line flux measurements seems is not good enough for investigating the origin of scatter in the N/H–O/H diagram. Therefore we have carried out the manually measure the line fluxes of selected galaxies in four intervals of galaxy stellar masses, ranging from $10^{11.3} M_{\odot}$ to $10^{10.2} M_{\odot}$. The oxygen and nitrogen abundances have been derived using the recent accurate calibrations from [106]. The oxygen and nitrogen abundance evolutions with redshift of the galaxies clearly show the galaxy downsizing effect [20, 115], where enrichment (and hence star formation) is shifted from high-mass galaxies at earlier cosmic times to lower-mass galaxies at later epochs. The most massive galaxies where oxygen and nitrogen enrichment and star formation has already stopped, occupy a narrow band in the N/H–O/H diagram, defining an upper envelope. On the other hand, the less massive galaxies with significant star formation at the current epoch are shifted downwards, towards lower N/H values. Thus, the scatter of N/H for a given O/H is caused by the time delay between N and O enrichment and the different star formation histories in different galaxies (the galaxy downsizing effect).

■

BIBLIOGRAPHY

1. C. Allende Prieto, M. Asplund, P. Fabiani Bendicho, Center-to-limb variation of solar line profiles as a test of NLTE line formation calculations, *Astron. and Astrophys.* **423** (2004), 1109–1117.
2. D. Alloin, S. Collin-Souffrin, M. Joly, L. Vigroux, Nitrogen and oxygen abundances in galaxies, *Astron. and Astrophys.* **78** (1979), 200–216.
3. N.V. Asari, R. Cid Fernandes, G. Stasińska et al., The history of star-forming galaxies in the Sloan Digital Sky Survey, *Mon. Not. Roy. Astron. Soc.* **381** (2007), 263–279.
4. M. Asplund, N. Grevesse, A.J. Sauval, C. Allende Prieto, D. Kiselman, Line formation in solar granulation. IV. [O I], O I and OH lines and the photospheric O abundance, *Astron. and Astrophys.* **417** (2004), 751–768.
5. J.A. Baldwin, M.M. Phillips, R. Terlevich, Classification parameters for the emission-line spectra of extragalactic objects, *Publ. Astron. Soc. Pacific.* **93** (1981), 5–19.
6. A. Boselli, J. Lequeux, G. Gavazzi, Molecular gas in normal late type galaxies, *Astron. and Astrophys.* **384** (2002), 33–47.
7. F. Bresolin, D.R. Garnett, R.C. Kennicutt, Jr., Abundances of metal-rich H II regions in M 51, *Astrophys. J.* **615** (2004), 228–241.
8. F. Bresolin, D. Schaerer, R.M. González Delgado, G. Stasińska, A VLT study of metal-rich extragalactic H II regions. I. Observations and empirical abundances, *Astron. and Astrophys.* **441** (2005), 981–997.
9. F. Bresolin, The oxygen abundance in the inner H II regions of M 101. Implications for the calibration of strong-line metallicity indicators, *Astrophys. J.* **656** (2007), 186–197.
10. F. Bresolin, W. Gieren, R.-P. Kudritzki, G. Pietrzyński, M.A. Urbaneja, G. Carraro, Extragalactic chemical abundances: do H II regions and young stars tell the same story? The case of the spiral galaxy NGC 300, *Astrophys. J.* **700** (2009), 309–330.
11. J. Brinchmann, S. Charlot, S.D.M. White, C. Tremonti, G. Kauffmann, T. Heckman, J. Brinkmann, The physical properties of star-forming galaxies in the low-redshift Universe, *Mon. Not. Roy. Astron. Soc.* **351** (2004), 1151–1179.
12. F. Calura, A. Pipino, C. Chiappini, F. Matteucci, R. Maiolino, The evolution of the mass-metallicity relation in galaxies of different morphological types, *Astron. and Astrophys.* **504** (2009), 373–388.

13. S.I.B. Cartledge, J.T. Lauroesch, D.M. Meyer, U.J. Sofia, The homogeneity of interstellar oxygen in the galactic disk, *Astrophys. J.* **613** (2004), 1037–1048.
14. B. Catinella, M.P. Haynes, R. Giovanelli, J.P. Gardner, A.J. Connolly, A pilot survey of H I in field galaxies at redshift $z \sim 0.2$, *Astrophys. J.* **685** (2008), L13–L17.
15. B. Catinella, D. Schiminovich, G. Kauffmann et al., The *GALEX* Arcibo SDSS Survey — I. Gas fraction scaling relations of massive galaxies and first data release, *Mon. Not. Roy. Astron. Soc.* **403** (2010), 683–708.
16. C. Chiappini, F. Matteucci, D. Romano, Abundance gradients and the formation of the Milky Way, *Astrophys. J.* **554** (2001), 1044–1058.
17. C. Chiappini, F. Matteucci, S.K. Ballero, The origin of nitrogen. Implications of recent measurements of N/O in Galactic metal-poor halo stars, *Astron. and Astrophys.* **437** (2005), 429–436.
18. R. Cid Fernandes, N.V. Asari, L. Sodré, G. Stasińska, A. Mateus, J.P. Torres-Papaqui, W. Schoenell, Uncovering the chemical enrichment and mass-assembly histories of star-forming galaxies, *Mon. Not. Roy. Astron. Soc.* **375** (2007), L16–L20.
19. T. Contini, M.A. Treyer, M. Sullivan, R.S. Ellis, Chemical abundances in a UV-selected sample of galaxies, *Mon. Not. Roy. Astron. Soc.* **330** (2002), 75–91.
20. L.L. Cowie, A. Songaila, E.M. Hu, J.G. Cohen, New insight on galaxy formation and evolution from Keck spectroscopy of the Hawaii Deep Fields, *Astron. J.* **112** (1996), 839–864.
21. L.L. Cowie, A.J. Barger, An integrated picture of star formation, metallicity evolution, and galactic stellar mass assembly, *Astrophys. J.* **686** (2008), 72–116.
22. N.R. Crockett, D.R. Garnett, P. Masey, G. Jacoby, Neon and oxygen abundances in M 33, *Astrophys. J.* **637** (2006), 741–751.
23. J.J. Dalcanton, The metallicity of galaxy disks: infall versus outflow, *Astrophys. J.* **658** (2007), 941–959.
24. J. Dunkley, E. Komatsu, M.R. Nolte et al., Five-year Wilkinson Microwave Anisotropy Probe observations: likelihoods and parameters from the WMAP data, *Astrophys. J. Suppl. Ser.* **180** (2009), 306–329.
25. M.G. Edmunds, B.E.J. Pagel, Nitrogen synthesis and the “age” of galaxies, *Mon. Not. Roy. Astron. Soc.* **185** (1978), 77P–80P.
26. M.G. Edmunds, General constraints on the effect of gas flows in the chemical evolution of galaxies, *Mon. Not. Roy. Astron. Soc.* **246** (1990), 678–685.
27. S.L. Ellison, D.R. Patton, L. Simard, A.W. McConnachie, Galaxy pairs in the Sloan Digital Sky Survey. I. Star formation, active galactic nucleus fraction, and the luminosity/mass–metallicity relation, *Astron. J.* **135** (2008), 1877–1899.
28. R.I. Epstein, J.M. Lattimer, D.N. Schramm, The origin of deuterium, *Nature* **263** (1976), 198–202.
29. D.K. Erb, A.E. Shapley, M. Pettini, C.C. Steidel, N.A. Reddy, K.L. Adelberger, The mass–metallicity relation at $z > 2$, *Astrophys. J.* **644** (2006), 813–828.
30. C. Esteban, M. Peimbert, S. Torres-Peimbert, V. Escalante, Chemical composition of the Orion nebula derived from echelle spectrophotometry, *Mon. Not. Roy. Astron. Soc.* **295** (1998), 401–422.

31. C. Esteban, M. Peimbert, J. García-Rojas, M.T. Ruiz, A. Peimbert, M. Rodríguez, A reappraisal of the chemical composition of the Orion nebula based on Very Large Telescope echelle spectrophotometry, *Mon. Notic. Roy. Astron. Soc.* **355** (2004), 229–247.
32. C. Esteban, J. García-Rojas, M. Peimbert, A. Peimbert, M.T. Ruiz, M. Rodríguez, L. Carigi, Carbon and oxygen galactic gradients: observational values from H II region recombination lines, *Astrophys. J.* **618** (2005), L95–L98.
33. M. Fukugita, M. Kawasaki, Primordial helium abundance: a reanalysis of the Izotov–Thuan spectroscopic sample, *Astrophys. J.* **646** (2006), 691–695.
34. D.R. Garnett, G.A. Shields, The composition gradient across M 81, *Astrophys. J.* **317** (1987), 82–101.
35. D.R. Garnett, G.A. Shields, E.D. Skillman, S.P. Sagan, R.J. Dufour, Interstellar abundance gradients in NGC 2403: comparison to M 33, *Astrophys. J.* **489** (1997), 63–86.
36. D.R. Garnett, The luminosity-metallicity relation, effective yields, and metal loss in spiral and irregular galaxies, *Astrophys. J.* **581** (2002), 1019–1031.
37. M. Gavilán, F. Buell, M. Mollá, Low and intermediate mass star yields: the evolution of carbon abundances, *Astron. and Astrophys.* **432** (2005), 861–877.
38. M. Gavilán, M. Mollá, F. Buell, Low and intermediate mass star yields. II. The evolution of nitrogen abundances, *Astron. and Astrophys.* **450** (2006), 509–521.
39. N.G. Guseva, P. Papaderos, H.T. Meyer, Y.I. Izotov, K.J. Fricke, An investigation of the luminosity–metallicity relation for a large sample of low-metallicity emission-line galaxies, *Astron. and Astrophys.* **505** (2009), 63–72.
40. R.B.C. Henry, M.G. Edmunds, J. Köppen, On the cosmic origin of carbon and nitrogen, *Astrophys. J.* **541** (2000), 660–674.
41. Y.I. Izotov, T.X. Thuan, V.A. Lipovetsky, The primordial helium abundance from a new sample of metal-deficient blue compact galaxies, *Astrophys. J.* **435** (1994), 647–667.
42. Y.I. Izotov, T.X. Thuan, V.A. Lipovetsky, The primordial helium abundance: systematic effects and a new determination, *Astrophys. J. Suppl. Ser.* **108** (1997), 1–39.
43. Y.I. Izotov, G. Stasińska, G. Meynet, N.G. Guseva, T.X. Thuan, The chemical composition of metal-poor emission-line galaxies in the Data Release 3 of the Sloan Digital Sky Survey, *Astron. and Astrophys.* **448** (2006), 955–970.
44. Y.I. Izotov, T.X. Thuan, G. Stasińska, The primordial abundance of ^4He : a self-consistent empirical analysis of systematic effects in a large sample of low-metallicity H II regions, *Astrophys. J.* **662** (2007), 15–38.
45. Y.I. Izotov, T.X. Thuan, MMT Observations of new extremely metal-poor emission-line galaxies in the Sloan Digital Sky Survey, *Astrophys. J.* **665** (2007), 1115–1128.
46. Y.I. Izotov, N.G. Guseva, K.J. Fricke, P. Papaderos, SBS 0335-052E + W: deep VLT/FORS+UVES spectroscopy of the pair of the lowest-metallicity blue compact dwarf galaxies, *Astron. and Astrophys.* **503** (2009), 61–72.
47. Y.I. Izotov, T.X. Thuan, The primordial abundance of ^4He : evidence for non-standard Big Bang nucleosynthesis, *Astrophys. J.* **710** (2010), L67–L71.
48. I.D. Karachentsev, D.I. Makarov, W.K. Huchtmeier, HI properties of nearby galaxies from a volume-limited sample, *Astron. and Astrophys. Suppl. Ser.* **139** (1999), 97–103.

49. G. Kauffmann, T.M. Heckman, C. Tremonti et al., The host galaxies of active galactic nuclei, *Mon. Not. Roy. Astron. Soc.* **346** (2003), 1055–1077.
50. L.J. Kewley, R.A. Jansen, M.J. Geller, Aperture Effects on Star Formation Rate, Metallicity, and Reddening, *Publ. Astron. Soc. Pac.* **117** (2005), 227–244.
51. J.P. Kneller, G. Steigman, BBN for pedestrians, *New Journal of Physics* **6** (2004), 117–244.
52. E. Komatsu, J. Dunkley, M.R.olta et al., Five-year Wilkinson Microwave Anisotropy Probe observations: cosmological interpretation, *Astrophys. J. Suppl. Ser.* **180** (2009), 330–376.
53. E. Komatsu, K.M. Smith, J. Dunkley et al., Seven-year Wilkinson Microwave Anisotropy Probe (WMAP) observations: cosmological interpretation, *Astrophys. J. Suppl. Ser.* **192** (2011), 18.
54. F. Lamareille, M. Mouhcine, T. Contini, I. Lewis, S. Maddox, The luminosity–metallicity relation in the local Universe from the 2dF Galaxy Redshift Survey, *Mon. Not. Roy. Astron. Soc.* **350** (2004), 396–406.
55. F. Lamareille, J. Brinchmann, T. Contini et al., Physical properties of galaxies and their evolution in the VIMOS VLT Deep Survey. I. The evolution of the mass–metallicity relation up to $z \sim 0.9$, *Astron. and Astrophys.* **495** (2009), 53–72.
56. M.A. Lara-López, J. Cepa, A. Bongiovanni et al., Study of star-forming galaxies in SDSS up to redshift 0.4. I. Metallicity evolution, *Astron. and Astrophys.* **505** (2009), 529–539.
57. D. Larson, J. Dunkley, G. Hinshaw et al., Seven-year Wilkinson Microwave Anisotropy Probe (WMAP) observations: Power spectra and WMAP-derived parameters, *Astrophys. J. Suppl. Ser.* **192** (2011), 16.
58. R.B. Larson, Effects of supernovae on the early evolution of galaxies, *Mon. Not. Roy. Astron. Soc.* **169** (1974), 229–246.
59. H. Lee, M.L. McCall, R.L. Kingsburgh, R. Ross, C.C. Stevenson, Uncovering additional clues to galaxy evolution. I. Dwarf irregular galaxies in the field, *Astron. J.* **125** (2003), 146–165.
60. J. Lequeux, M. Peimbert, J.F. Rayo, A. Serrano, S. Torres-Peimbert, Chemical composition and evolution of irregular and blue compact galaxies, *Astron. and Astrophys.* **80** (1979), 155–166.
61. S.J. Lilly, C.M. Carollo, A.N. Stockton, The metallicities of star-forming galaxies at intermediate redshifts $0.47 < z < 0.92$, *Astrophys. J.* **597** (2003), 730–750.
62. Á.R. López-Sánchez, C. Esteban, Massive star formation in Wolf-Rayet galaxies. IV. Colours, chemical composition analysis and metallicity–luminosity relations, *Astron. and Astrophys.* **517** (2010), A85.
63. A. Maeder, Stellar yields as a function of initial metallicity and mass limit for black hole formation, *Astron. and Astrophys.* **264** (1992), 105–120.
64. R. Maiolino, T. Nagao, A. Grazian et al., AMAZE. I. The evolution of the mass–metallicity relation at $z > 3$, *Astron. and Astrophys.* **488** (2008), 463–479.
65. P. Marigo, Chemical yields from low- and intermediate-mass stars: Models predictions and basic observational constraints, *Astron. and Astrophys.* **370** (2001), 194–217.
66. F. Matteucci, M. Tosi, Nitrogen and oxygen evolution in dwarf irregular galaxies, *Mon. Not. Roy. Astron. Soc.* **217** (1985), 391–405.

67. F. Matteucci, P. François, Galactic chemical evolution — Abundance gradients of individual elements, *Mon. Not. Roy. Astron. Soc.* **239** (1989), 885–904.
68. S.S. McGaugh, W.J.G. de Blok, Gas mass fractions and the evolution of spiral galaxies, *Astrophys. J.* **481** (1997), 689–702.
69. J. Melbourne, J.J. Salzer, Metal abundances of KISS galaxies. I. Coarse metal abundances and the metallicity–luminosity relation, *Astron. J.* **123** (2002), 2302–2311.
70. J. Meléndez, A low solar oxygen abundance from the first-overtone OH lines, *Astrophys. J.* **615** (2004), 1042–1047.
71. D.M. Meyer, M. Jura, J.A. Cardelli, The definitive abundance of interstellar oxygen, *Astrophys. J.* **493** (1998), 222–229.
72. J. Moustakas, R.C. Kennicutt, Jr., C.A. Tremonti, D.A. Dale, J.-D.T. Smith, D. Calzetti, Optical spectroscopy and nebular oxygen abundances of the *SPI-TZER/SING* galaxies, *Astrophys. J. Suppl. Ser.* **190** (2010), 233–266.
73. C.M. Oliveira, J. Dupius, P. Chayer, H.W. Moos, O/H in the local bubble, *Astrophys. J.* **625** (2005), 232–241.
74. B.E.J. Pagel, M.G. Edmunds, D.E. Blackwell, M.S. Chun, G. Smith, On the composition of H II regions in southern galaxies — I. NGC 300 and 1365, *Mon. Not. Roy. Astron. Soc.* **189** (1979), 95–113.
75. B.E.J. Pagel, E.A. Simonson, R.J. Terlevich, M.G. Edmunds, The primordial helium abundance from observations of extragalactic H II regions, *Mon. Notic. Roy. Astron. Soc.* **255** (1992), 325–345.
76. B.E.J. Pagel, *Nucleosynthesis and chemical evolution of galaxies* (Cambridge University Press, Cambridge, 1997), 392 p.
77. M. Peimbert, S. Torres-Peimbert, Chemical composition of H II regions in the Large Magellanic Cloud and its cosmological implications, *Astrophys. J.* **193** (1974), 327–333.
78. M. Peimbert, S. Torres-Peimbert, Chemical composition of H II regions in the Small Magellanic Cloud and the pregalactic helium abundance, *Astrophys. J.* **203** (1976), 581 – 586.
79. M. Peimbert, V. Luridiana, A. Peimbert, Revised primordial helium abundance based on new atomic data, *Astrophys. J.* **666** (2007), 636–646.
80. T.M.D. Pereira, M. Asplund, D. Kiselman, Oxygen lines in solar granulation. II. Centre-to-limb variation, NLTE line formation, blends, and the solar oxygen abundance, *Astron. and Astrophys.* **508** (2009), 1403–1416.
81. M. Pettini, B.E.J. Pagel, [O III]/[N II] as an abundance indicator at high redshift, *Mon. Notic. Roy. Astron. Soc.* **348** (2004), L59–L63.
82. M. Pettini, B.J. Zych, M.T. Murphy, A. Lewis, C.C. Steidel, Deuterium abundance in the most metal-poor damped Ly α system: converging on $\Omega_{b,0}h^2$, *Mon. Notic. Roy. Astron. Soc.* **391** (2008), 1499–1510.
83. L.S. Pilyugin, The evolution of nitrogen and oxygen abundances in dwarf irregular galaxies, *Astron. and Astrophys.* **260** (1992), 58–66.
84. L.S. Pilyugin, On the evolution of helium, nitrogen and oxygen abundances in dwarf irregular galaxies, *Astron. and Astrophys.* **277** (1993), 42–52.
85. L.S. Pilyugin, On the evolution of helium, nitrogen and oxygen abundances in dwarf irregular galaxies, *Astronomy Reports* **38** (1994), 735–741.

86. L.S. Pilyugin, The chemical evolution of irregular galaxies with mass loss, *Astron. and Astrophys.* **287** (1994), 387–389.
87. L.S. Pilyugin, M.G. Edmunds, Chemical evolution of the Milky Way Galaxy. I. On the infall model of galactic chemical evolution, *Astron. and Astrophys.* **313** (1996), 783–791.
88. L.S. Pilyugin, M.G. Edmunds, Chemical evolution of the Milky Way Galaxy. II. On the origin of scatter in the age-metallicity relation, *Astron. and Astrophys.* **313** (1996), 792–802.
89. L.S. Pilyugin, F. Ferrini, On the oxygen abundance deficiency in spiral galaxies, *Astron. and Astrophys.* **336** (1998), 103–115.
90. L.S. Pilyugin, On the origin of nitrogen in low-metallicity galaxies. Blue compact galaxies versus damped Ly α absorbers, *Astron. and Astrophys.* **346** (1999), 428–431.
91. L.S. Pilyugin, On the oxygen abundance determination in H II regions. The problem of the line intensities – oxygen abundance calibration, *Astron. and Astrophys.* **362** (2000), 325–332.
92. L.S. Pilyugin, F. Ferrini, The oxygen abundance deficiency in irregular galaxies, *Astron. and Astrophys.* **354** (2000), 874–880.
93. L.S. Pilyugin, F. Ferrini, On the origin of the luminosity–metallicity relation for late type galaxies. Spirals to irregulars transition, *Astron. and Astrophys.* **358** (2000), 72–76.
94. L.S. Pilyugin, On the oxygen abundance determination in H II regions. High-metallicity regions, *Astron. and Astrophys.* **369** (2001), 594–604.
95. L.S. Pilyugin, Oxygen abundances in dwarf irregular galaxies and the metallicity–luminosity relationship, *Astron. and Astrophys.* **374** (2001), 412–420.
96. L.S. Pilyugin, The oxygen abundance distribution in M 101, *Astron. and Astrophys.* **373** (2001), 56–62.
97. L.S. Pilyugin, The bends in the slopes of radial abundance gradients in the disks of spiral galaxies – Do they exist?, *Astron. and Astrophys.* **397** (2003), 109–114.
98. L.S. Pilyugin, Abundance determinations in H II regions. Model fitting versus T_e method, *Astron. and Astrophys.* **399** (2003), 1003–1007.
99. L.S. Pilyugin, F. Ferrini, R.V. Shkvarun, On the oxygen abundance in our Galaxy, *Astron. and Astrophys.* **401** (2003), 557–563.
100. L.S. Pilyugin, T.X. Thuan, J.M. Vílchez, On the origin of nitrogen, *Astron. and Astrophys.* **397** (2003), 487–501.
101. L.S. Pilyugin, J.M. Vílchez, T. Contini, Oxygen and nitrogen abundances in nearby galaxies. Correlations between oxygen abundance and macroscopic properties, *Astron. and Astrophys.* **425** (2004), 849–869.
102. L.S. Pilyugin, On the relationship between auroral and nebular oxygen line intensities in spectra of H II regions, *Astron. and Astrophys.* **436** (2005), L1–L4.
103. L.S. Pilyugin, T.X. Thuan, Oxygen abundance determination in H II regions: the strong line intensities – abundance calibration revisited, *Astrophys. J.* **631** (2005), 231–243.
104. L.S. Pilyugin, T.X. Thuan, J.M. Vílchez, Oxygen abundances in the most oxygen-rich spiral galaxies, *Mon. Not. Roy. Astron. Soc.* **367** (2006), 1139–1146.

105. L.S. Pilyugin, T.X. Thuan, J.M. Vílchez, On the maximum value of the cosmic abundance of oxygen and the oxygen yield, *Mon. Not. Roy. Astron. Soc.* **376** (2007), 353–360.
106. L.S. Pilyugin, J.M. Vílchez, T.X. Thuan, New improved calibration relations for the determination of electron temperatures and oxygen and nitrogen abundances in H II regions, *Astrophys. J.* **720** (2010), 1738–1751.
107. L.S. Pilyugin, T.X. Thuan, Galaxy Downsizing and the Redshift Evolution of Oxygen and Nitrogen Abundances: Origin of the Scatter in the N/H-O/H Diagram, *Astrophys. J.* **762** (2011), L23–L28.
108. L.S. Pilyugin, L. Mattsson, Abundance determination in HII regions from spectra without the [O II] $\lambda 3727 + \lambda 3729$ line, *Mon. Not. Roy. Astron. Soc.* **412** (2011), 1145–1150.
109. S.A. Pustilnik, A.L. Tepliakova, A.Y. Kniazev, J.-M. Martin, A.N. Burenkov, SDSS J092609.45 + 334304.1: a nearby unevolved galaxy, *Mon. Not. Roy. Astron. Soc.* **401** (2010), 333–341.
110. A. Renzini, M. Voli, Advanced evolutionary stages of intermediate-mass stars. I. Evolution of surface compositions, *Astron. and Astrophys.* **94** (1981), 175–193.
111. M.G. Richer, M.L. McCall, Oxygen abundances in diffuse ellipticals and the metallicity–luminosity relations for dwarf galaxies, *Astrophys. J.* **445** (1995), 642–659.
112. M.G. Richer, M.L. McCall, Bright Planetary Nebulae and their Progenitors in Galaxies Without Star Formation, *Astrophys. J.* **684** (2008), 1190–1209.
113. D. Romano, C. Chiappini, F. Matteucci, M. Tosi, Quantifying the uncertainties of chemical evolution studies. I. Stellar lifetimes and initial mass function, *Astron. and Astrophys.* **430** (2005), 491–505.
114. E.E. Salpeter, G.L. Hoffman, Correlation statistics of irregular and spiral galaxies mapped in H I, *Astrophys. J.* **465** (1996), 595–607.
115. A. Sandage, Star formation rates, galaxy morphology, and the Hubble sequence, *Astron. and Astrophys.* **161** (1986), 89–101.
116. S. Savaglio, K. Glazebrook, D. Le Borgne et al., The Gemini deep deep survey. VII. The redshift evolution of the mass-metallicity relation, *Astrophys. J.* **635** (2005), 260–279.
117. P. Scott, M. Asplund, N. Grevesse, A.J. Sauval, On the Solar Nickel and Oxygen Abundances, *Astrophys. J.* **691** (2009), L119–L122.
118. L. Searle, Evidence for composition gradients across the disks of spiral galaxies, *Astrophys. J.* **168** (1971), 327–341.
119. L. Searle, W.L.W. Sargent, Inferences from the composition of two dwarf blue galaxies, *Astrophys. J.* **173** (1972), 25–33.
120. P.A. Shaver, R.X. McGee, L.M. Newton, A.C. Danks, S.R. Pottasch, The galactic abundance gradient, *Mon. Not. Roy. Astron. Soc.* **204** (1983), 53–112.
121. V. Simha, G. Steigman, Constraining the early-Universe baryon density and expansion rate, *Journal of Cosmology and Astroparticle Physics* **6** (2008), 16.
122. S. Simón-Díaz, A. Herrero, C. Esteban, F. Najarro, Detailed spectroscopic analysis of the Trapezium cluster stars inside the Orion nebula. Rotational velocities, stellar parameters, and oxygen abundances, *Astron. and Astrophys.* **448** (2006), 351–366.

123. E.D. Skillman, R.C. Kennicutt, Jr., P.W. Hodge, Oxygen abundances in nearby dwarf irregular galaxies, *Astrophys. J.* **347** (1989), 875–882.
124. H.E. Smith, Spectrophotometric observations of ionized hydrogen regions in nearby spiral and irregular galaxies, *Astrophys. J.* **199** (1975), 591–610.
125. U.J. Sofia, D.M. Meyer, Interstellar abundance standards revisited, *Astrophys. J.* **554** (2001), L221–L224.
126. D.N. Spergel, R. Bean, O. Doré et al., Three-year Wilkinson Microwave Anisotropy Probe (WMAP) observations: implications for cosmology, *Astrophys. J. Suppl. Ser.* **170** (2007), 377–408.
127. G. Steigman, Primordial nucleosynthesis: successes and challenges, *International Journal of Modern Physics E* **15** (2006), 1–35.
128. G. Steigman, Primordial nucleosynthesis in the precision cosmology era, *Annual Review of Nuclear and Particle Systems* **57** (2007), 463–491.
129. G. Steigman, Neutrinos and BBN (and the CMB), 2008, astro-ph. 0807.3004.
130. G. Steigman, Primordial helium and the cosmic background radiation, *Journal of Cosmology and Astroparticle Physics.* **4** (2010), 29.
131. G. Steigman, Primordial nucleosynthesis: A cosmological probe, in: *Light Elements in the Universe*, Proceedings of the IAU Symposium, edited by C. Charbonnel, M. Tosi, F. Primas, C. Chiappini, **268** (2010), p. 19–26.
132. G. Steigman, Primordial Nucleosynthesis: The Predicted and Observed Abundances and Their Consequences, 2010, astro-ph 1008.4765.
133. T.X. Thuan, L.S. Pilyugin, I.A. Zinchenko, The redshift evolution of oxygen and nitrogen abundances in emission-line SDSS galaxies, *Astrophys. J.* **712** (2010), 1029–1048.
134. M. Tosi, Models of galactic chemical evolution: the problem of uniqueness, *Astron. and Astrophys.* **197** (1988), 33–46.
135. M. Tosi, The effect of metal-rich infall on galactic chemical evolution, *Astron. and Astrophys.* **197** (1988), 47–51.
136. C.A. Tremonti, T.M. Heckman, G. Kauffmann et al., The origin of the mass–metallicity relation: insight from 53000 star-forming galaxies in the Sloan Digital Sky Survey, *Astrophys. J.* **613** (2004), 898–913.
137. L.B. van den Hoek, M.A.T. Groenewegen, New theoretical yields of intermediate mass stars, *Astron. and Astrophys. Suppl. Ser.* **123** (1997), 305–328.
138. L. van Zee, J.J. Salzer, M.P. Haynes, A.A. O’Donoghue, T.J. Balonek, Spectroscopy of outlying H II regions in spiral galaxies: abundances and radial gradients, *Astron. J.* **116** (1998), 2805–2833.
139. L. van Zee, M.P. Haynes, Oxygen and Nitrogen in Isolated Dwarf Irregular Galaxies, *Astrophys. J.* **636** (2006), 214–239.
140. M.B. Vila-Costas, M.G. Edmunds, The relation between abundance gradients and physical properties of spiral galaxies, *Mon. Not. Roy. Astron. Soc.* **259** (1992), 121–145.
141. D.G. York, J. Adelman, J.E. Anderson et al., The Sloan Digital Sky Survey: technical summary, *Astron. J.* **120** (2000), 1579–1587.
142. D. Zaritsky, R.C. Kennicutt, Jr., J.P. Huchra, H II regions and the abundance properties of spiral galaxies, *Astrophys. J.* **420** (1994), 87–109.

4

CHAPTER

DISSIPATIVE N-BODY & GASODYNAMICAL MODEL OF THE TRIAXIAL PROTOGALAXY COLLAPSE

P.P. Berczik, S.G. Kravchuk, R. Spurzem, G. Hensler

4.1. Introduction

This work is devoted to the study of complex modelling of the formation and evolution of galaxies and galactic structures using multivariate methods of numerical simulation based on particle methods (the N-body problem). Multi-dimensional gas-dynamic calculations were carried out in the work with a particle-based method, namely SPH — Smoothed Particle Hydrodynamics. In this this work a newly-developed Chemo-Dynamical Smoothed Particle Hydrodynamic (CD-SPH) code is presented. The disk galaxy is described as a multi-fragmented gas and star system, embedded in a cold dark matter halo with a rigid potential field. The star formation process, SNII, SNIa and PN events, and the chemical enrichment of gas, have all been considered within the framework of the standard SPH model, which we use to describe the dynamical and chemical evolution of triaxial disk-like galaxies. It is found that such an approach provides a realistic description of the process of formation, chemical and dynamical evolution of disk galaxies over a cosmological timescale. As a first application, the model is used to describe the chemical and photometric evolution of a disk galaxy like the Milky Way. We also present our recently developed 3D multi-phase chemo-dynamical code for galaxy evolution. It follows the evolution of all components of a galaxy such as dark matter, stars, and molecular clouds and diffuses interstellar matter (ISM). Dark matter and stars are treated as collisionless N-body systems. The ISM is numerically described by a SPH

approach for the diffuse (hot/warm) gas and a sticky particle scheme for the (cool) molecular clouds. Additionally, the galactic components are coupled by several phase transitions such as star formation, stellar death or condensation and evaporation processes within the ISM. As an example here we present the dynamical, chemical and photometric evolution of a star forming dwarf galaxy.

The formation and evolution of galaxies and galactic subsystems is one of the most intensively developing areas of modern astrophysics. This is primarily defined by the huge quantity and very good quality of modern astrophysical observations and the extremely rapid development of current computer technology. Modern computer systems can not only effectively handle large amounts of observational data, but also can simulate complex astrophysical systems with unprecedented numerical resolution. Hence it is increasingly important to provide effective and appropriate software that allows maximum use of the available computing resources on modern parallel computer clusters.

The actuality of numerical simulations of a baryonic halo is determined by a number of modern observations [65] and theoretical models [114, 115], which show that our Galactic halo may contain a large amount of baryonic matter, along with nonbaryonic “dark matter”. Our numerical simulation further develops this idea and models the evolution of this baryonic halo and its relationship with the Galactic disc itself.

Protogalactic triaxial collapse is a natural prerequisite for the formation of large galactic systems with complex kinematics. The actuality of these simulations directly follows from the general conditions of the forming protogalactic perturbations in the early stages of fragmentation in the universe [6, 54, 158]. Our numerical calculations follow the gas-dynamical evolution of such a triaxial collapsing system. We demonstrate the effectiveness of such models to explain the complex kinematic structures of the galactic disc and bulge.

Modern observations of the galactic disk, which give us the kinematic [28, 90, 91, 150] and chemical [53, 92, 146] data, especially in the solar neighborhood, put forward absolutely clear boundary conditions for the possible scenarios of dynamic and chemical modelling of our Galaxy. Our self-consistent chemo-dynamical modelling using a combined and integrated approach (N -body + SPH gas-dynamic methods together) allows us to describe all of the above observations in one unified scenario for the formation of the Galaxy and Galactic disk.

Spectroscopic observations carried out by the space telescope FUSE (Far Ultraviolet Spectroscopic Explorer) [100] for a number of dwarf galaxies have shown [38] a significant difference (a factor of several, and sometimes up to one order of magnitude) in the content of heavy elements in the different gas phases of these objects. Only our multi-phase gas-dynamic calculations can naturally explain such a difference between these chemical abundances, as seen for oxygen and other heavy elements in the different gas phases.

4.2. Dissipative N-body code for galaxy evolution

4.2.1. Introduction

Recent advances in galactic and extragalactic astrophysics show the close link of a disk galaxy dynamical evolution and its chemical and photometric behavior over the Hubble timescale. In spite of remarkable success of the modern theory of galaxy chemical evolution in explaining the properties of evolving galaxies [109] its serious shortcomings concern the multi parameter character and practical neglecting of dynamical effects. The inclusion of simplified dynamic into the chemical network [126] and vice versa the inclusion of simplified chemical scheme into the sophisticated 3D hydrodynamical code [138] gives very promising results and allows to avoid a formal approach typical to standard theory.

In this paper the interplay between a disk galaxy dynamical evolution and its chemical behavior is studied in a frame of a simplified model which provides a realistic description of the process of galaxy formation and evolution over the cosmological timescale.

4.2.2. Initial conditions

The evolving galaxy is treated as a system of baryonic fragments embedded into the extended halo composed of dark nonbaryonic and baryonic matter. The halo is modeled as a static structure with dark (DH) and diluted baryonic (BH) halo components having Plummer — type density profiles [47]:

$$\rho_{BH}(r) = \frac{M_{BH}}{\frac{4}{3}\pi b_{BH}^3} \frac{b_{BH}^5}{(r^2 + b_{BH}^2)^{\frac{5}{2}}}$$

and

$$\rho_{DMH}(r) = \frac{M_{DMH}}{\frac{4}{3}\pi b_{DMH}^3} \frac{b_{DMH}^5}{(r^2 + b_{DMH}^2)^{\frac{5}{2}}},$$

where

$$M_{DMH} = 10^{12} M_{\odot}, \quad b_{DMH} = 25 \text{ kpc},$$

$$M_{BH} = 10^{11} M_{\odot}, \quad b_{BH} = 15 \text{ kpc}.$$

The dense baryonic matter (future galaxy disk and bulge) of total mass of $M_{gas} = 10^{11} M_{\odot}$ is assumed to be distributed among $N = 2109$ particles — fragments. The single particle density profile is also assumed to be a Plummer one. Its mass is taken to be $m_i = M_{gas}/N$ and radius $h_i = 1$ kpc. Initially all particles are smoothly placed inside the sphere of radius $R_{gas} = 50$ kpc and are involved into the Hubble flow ($H_0 = 75$ km/s/Mpc) and solid — body rotation around z axis. The initial motion of this system is described as:

$$\mathbf{V}(x, y, z) = [\Omega(x, y, z) \times \mathbf{r}] + H_0 \mathbf{r} + \mathbf{D}\mathbf{V}(x, y, z),$$

where $\Omega(x, y, z) = (0, 0, 1) \cdot \Omega_{cir}$ is an angular velocity of the rotating sphere, $\Omega_{cir} = V_{cir}/R_{gas}$ and

$$V_{cir} = \sqrt{G \frac{M_{gas} + M_{DMH} + M_{BH}}{R_{gas}}}.$$

The components DV_x , DV_y , DV_z of the random velocity \mathbf{DV} vector are assumed to be initially randomly distributed within an interval $0 \div 10$ km/s.

4.2.3. N-body code

The dynamical evolution of baryonic matter fragments which are subjected to gravitational influences of DM–baryonic halo and interfragment interactions is followed by means of effective N-body integrator with individual time step. The dynamics of such N-body system is described by following equations:

$$\begin{cases} d\mathbf{R}_i/dt = \mathbf{V}_i, \\ d\mathbf{V}_i/dt = \mathbf{A}_i(\mathbf{R}, \mathbf{V}). \end{cases} \quad (4.1)$$

The acceleration of i -th particle \mathbf{A}_i is defined as a sum of three components.

$$\mathbf{A}_i = \mathbf{A}_i^{INT} + \mathbf{A}_i^{EXT} + \mathbf{A}_i^{VISC}, \quad (4.2)$$

where the first term \mathbf{A}_i^{INT} accounts for gravitational interactions between fragments. The second one \mathbf{A}_i^{EXT} is defined as an external gravitational acceleration caused by the DM and baryonic halo. The last term \mathbf{A}_i^{VISC} corresponds to the viscous deceleration of fragment when passing through the baryonic halo.

The gravitational interaction between fragments is defined as the interaction of N Plummer profile elements:

$$\mathbf{A}_i^{INT} = -G \cdot \sum_{j=1, j \neq i}^N \frac{m_j}{(\mathbf{R}_{ij}^2 + h_{ij}^2)^{\frac{3}{2}}} \cdot \mathbf{R}_{ij}, \quad (4.3)$$

here $h_{ij} = (h_i + h_j)/2$ and $\mathbf{R}_{ij} = \mathbf{R}_i - \mathbf{R}_j$.

Accounting for that the halo DM and baryonic components are also Plummer spheres the second term becomes:

$$\mathbf{A}_i^{EXT} = -G \cdot \left(\frac{M_{DMH}}{(\mathbf{R}_i^2 + b_{DMH}^2)^{\frac{3}{2}}} + \frac{M_{BH}}{(\mathbf{R}_i^2 + b_{BH}^2)^{\frac{3}{2}}} \right) \cdot \mathbf{R}_i. \quad (4.4)$$

The form of the last term \mathbf{A}_i^{VISC} will be discussed in the next subsection.

The characteristic time step δt_i in the integration procedure for each particle is defined as:

$$\delta t_i = \text{Const} \cdot \min_j \left[\sqrt{\frac{|\mathbf{R}_{ij}|}{|\mathbf{A}_{ij}|}}, \frac{|\mathbf{R}_{ij}|}{|\mathbf{V}_{ij}|} \right], \quad (4.5)$$

where the $\mathbf{V}_{ij} = \mathbf{V}_i - \mathbf{V}_j$ and the $\mathbf{A}_{ij} = \mathbf{A}_i - \mathbf{A}_j$.

Here the Const is a numerical parameter equal to $\text{Const} = 10^{-2}$ that provides a nice momentum and energy conservation over the integration interval of about 15 Gyr. For example, in the conservative case (when viscosity of the system is set equal to 0), the final total error in the energy equation is less than 1%.

4.2.4. Viscosity model

The viscosity term \mathbf{A}_i^{VISC} is artificially introduced into the model so as to match the results of more sophisticated SPH approach on dynamical evolution of disk galaxies. The best fitness of results of this simplified approach with SPH modeling data (see e.g. [11]) is achieved when the momentum exchange between the baryonic halo and moving particles is modeled by the following expression:

$$\mathbf{A}_i^{VISC} = -k \cdot \mathbf{V}_i \cdot \frac{|\mathbf{V}_i|}{R_{VISC}} \cdot \frac{\rho_{BH}(r)}{\rho_{VISC}} \cdot \frac{m_i^{gas}}{m_i^{gas} + m_i^{star}}, \quad (4.6)$$

here ρ_{VISC} and R_{VISC} are numerical parameters set equal to $\rho_{VISC} = 0.2 \text{ cm}^{-3}$ and $R_{VISC} = 10 \text{ kpc}$. The vector \mathbf{V}_i is a particle velocity vector. It is to be noted that single particle is assumed to have a total mass which doesn't change with time and is defined as sum $m_i \equiv m_i^{gas} + m_i^{star}$. But masses of its gas and star components m_i^{gas} and m_i^{star} are variable values and are defined by the temporal evolutionary status of the given fragment. Initially $m_i^{star} = 0$. The results of fitness show that for z component of viscosity term $k = 1$. In the galaxy plane where it is necessary to account for baryonic halo and baryonic fragments partial corotation the dynamical friction is decreased and for x, y component of viscosity term k reduced to the value 0.15.

4.2.5. Density definition

In the frame of the multi fragmented model the definition of local gas density is introduced in the SPH manner, e.g. local gas density depends on the total mass of matter contained in the sphere of radius H_i around the i -th particle. For each i -th particle the value of its smoothing radius H_i is chose (using the quicksort algorithm) requiring that the volume of such radius compraises $N_B = 21$ nearest particles (i.e. $\approx 1\%$ of total number of particles N). Therefore, the total mass M_i and density of gas ρ_i inside this sphere are defined as

$$M_i = \sum_{j=1}^N \Delta m_{ij}^{gas}, \quad \rho_i = \frac{M_i}{\frac{4}{3}\pi H_i^3}, \quad (4.7)$$

where Δm_{ij}^{gas} is defined as

$$\text{if } |\mathbf{R}_{ij}| > (H_i + h_j) \Rightarrow \Delta m_{ij}^{gas} = 0,$$

$$\begin{aligned} \text{if } |\mathbf{R}_{ij}| < (H_i - h_j) &\Rightarrow \Delta m_{ij}^{gas} = m_j^{gas}, \\ \text{else } \Delta m_{ij}^{gas} &= m_j^{gas} \cdot \frac{H_i + h_j - |\mathbf{R}_{ij}|}{2 \cdot h_j}. \end{aligned}$$

4.2.6. Star formation and SN explosions

A forming disk galaxy is modelled as a system of interacting fragments (named as particles) embedded into the extended halo. Each particle is composed of gas and stellar components and its total mass is defined as $m_i \equiv m_i^{gas} + m_i^{star}$. Initially all particles are purely gaseous and, therefore, initially $m_i^{star} = 0$. To follow a particle star formation (SF) activity a special timemark t_i^{begSF} is introduced which initially is set equal to $t_i^{begSF} = 0$. The particles eligible to star formation events are chosen as particles which still have a sufficient amount of the gas component and their densities exceed some critical value ρ_{minSF} during some fixed time interval Δt_{SF} (of order of free-fall time):

$$\begin{cases} \rho_i > \rho_{minSF}, \\ t_i - t_i^{begSF} > \Delta t_{SF}, \\ m_i^{gas} / (m_i^{gas} + m_i^{star}) > 10^{-4}, \end{cases} \quad (4.8)$$

here $\Delta t_{SF} = 50$ Myr, and $\rho_{minSF} = 0.01 \text{ cm}^{-3}$ (this last value is not crucial and is only limiting one).

If the particle was subjected to SF activity the parameter t_i^{begSF} is set equal to $t_i^{begSF} = t_i$, and m_i^{star} and m_i^{gas} are redefined as

$$\begin{cases} m_i^{star} := \epsilon \cdot (1 - R) \cdot m_i^{gas} + m_i^{star}, \\ m_i^{gas} := (1 - \epsilon \cdot (1 - R)) \cdot m_i^{gas}, \end{cases} \quad (4.9)$$

here ϵ is a SF efficiency which is defined as:

$$\epsilon = \alpha \cdot \frac{\rho_i}{\rho_{SF}} \left(1 - \exp \left(-\frac{\rho_{SF}}{\rho_i} \right) \right), \quad (4.10)$$

therefore:

$$\begin{aligned} \text{if } \frac{\rho_i}{\rho_{SF}} \rightarrow 0 &\Rightarrow \epsilon \rightarrow \alpha \cdot \frac{\rho_i}{\rho_{SF}}, \\ \text{if } \frac{\rho_{SF}}{\rho_i} \rightarrow 0 &\Rightarrow \epsilon \rightarrow \alpha. \end{aligned}$$

To match available observational data on star formation efficiency (see e.g. [159]) parameters α and ρ_{SF} are set equal to $\alpha = 0.5$ and $\rho_{SF} = 10 \text{ cm}^{-3}$. The chemical evolution of each separate fragment is treated in the frame of one — zone close box model with instantaneous recycling. In the frame of this approach for the returned fraction of gas from evolved stars is taken a standard value $R = 0.25$.

Following the instanteneuous recycling approximation it is assumed that after each SF and SN explosions the heavy element enriched gas is returned to the system and mixed with old (heavy element deficient) gas. After each act of SF and SN explosions the value of heavy element abundances of gas in particle is upgraded according to:

$$Z_i := Z_i + \frac{\epsilon \cdot R \cdot \Delta Z}{1 - \epsilon \cdot (1 - R)}, \quad (4.11)$$

the value $\Delta Z = 0.01$ is used as an average value for all values of $Z = 0.001 \div 0.04$ (see [11]). Initially $Z_i = 0.0$ in all particles.

4.2.7. Conclusion

The proposed simple model provides the self-consistent picture of the process of galaxy formation, its dynamical and chemical evolution is in agreement with the results of more sophisticated approaches (see e.g. [11, 120, 126, 138]).

- The rapidly rotating protogalaxy finally formed a three – component system resembling a typical spiral galaxies: a thin disk and spheroidal component made of gas and/or stars and a dark matter halo.

Fig. 4.1 and Fig. 4.2 show respectively the star formation rate and the galaxy total stellar mass as a function of time. Fig. 4.3 shows the cylindrical

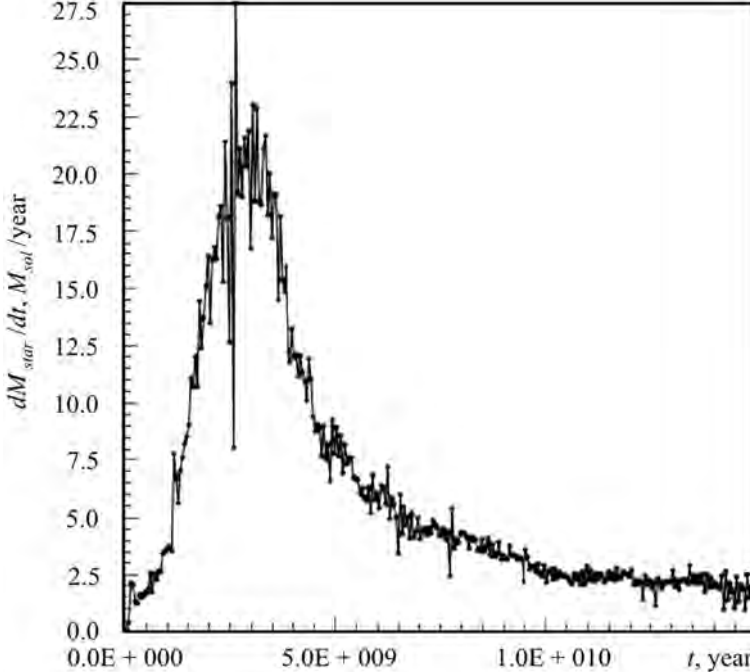


Fig. 4.1. The variation of total star formation rate of forming disk galaxy with time

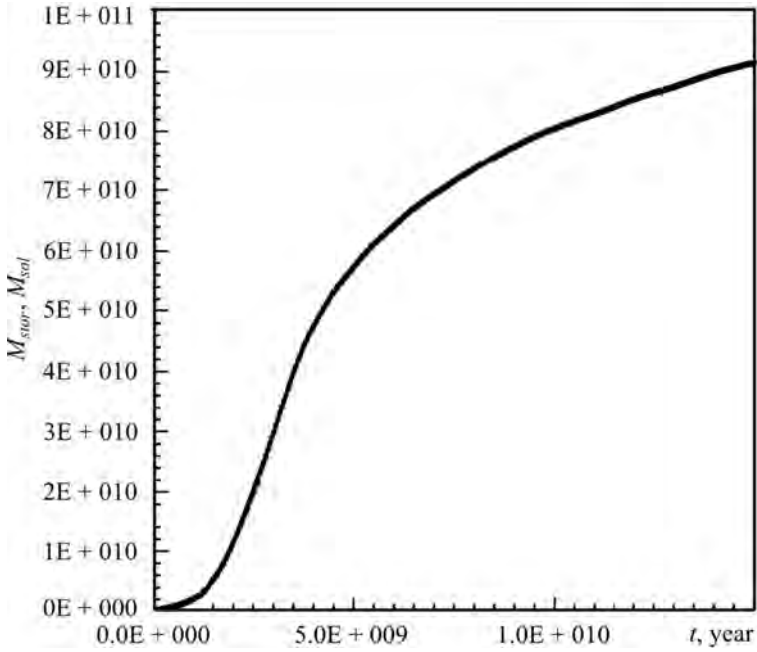


Fig. 4.2. The growth of galaxy stellar mass with time

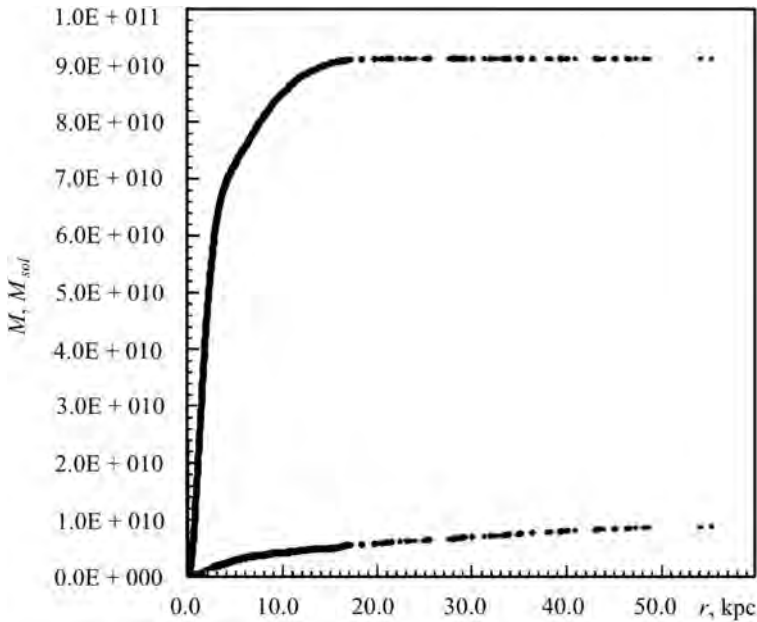


Fig. 4.3. The cylindrical distribution of masses of stellar (upper curve) and gaseous (lower one) components as a function of distance from galaxy center in a galactic plane

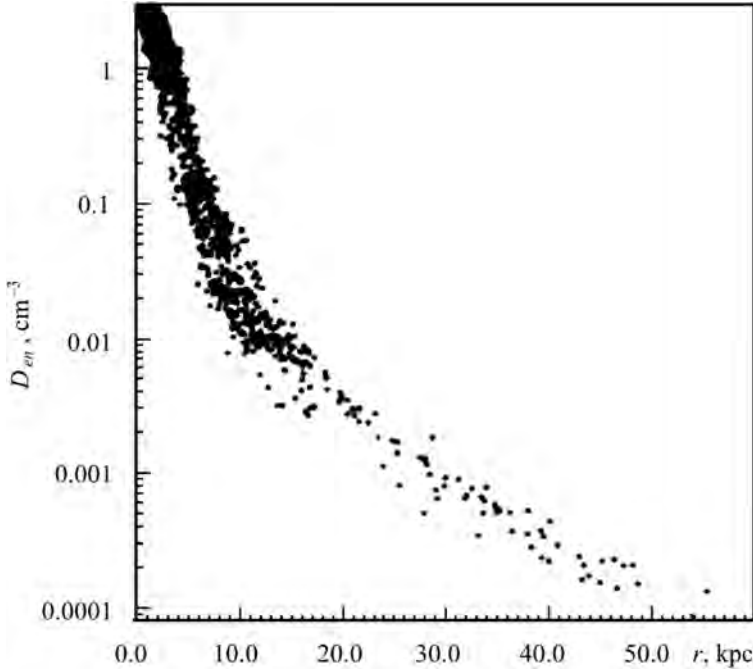


Fig. 4.4. The model galaxy gaseous component volume density radial distribution

distribution of stellar (upper curve) and gaseous (lower one) components of the final model disk galaxy as a function of a distance from the galaxy center in the galactic plane. The total star formation rate (SFR) is a succession of short bursts which doesn't exceed $28 M_{\odot}/\text{yr}$. During first 2 Gyr of evolution only about 20 % of total galaxy mass is transforms into the stars. The SFR gradually decreases, during the further evolution, to the value of about $2 M_{\odot}/\text{yr}$ typical for our own Galaxy. The final total stellar and gas mass of the model galaxy disk are about 92 % and 8 %. All these data as well as volume (see Fig. 4.4) and surface (see Fig. 4.5) densities distributions of stellar and gaseous components are in nice agreement with present date observational data [78, 109].

- The disk component possesses a typical spiral galaxy rotation curve and the distribution of radial and V_z -th velocities of baryonic particles clearly show the presence of the central bulge (see Fig. 4.7 and Fig. 4.8).

- The metallicities and the global metallicity gradient resemble distributions observed in our own Galaxy (Fig. 4.6). The averaged observed value of global metallicity $Z/Z_{\odot}(r)$ (see [109]) is shown in this Fig. 4.6 as a solid line.

4.3. Galaxy as dynamical system with accreting cold gas halo

4.3.1. Introduction

The structural properties of present-day galaxies strongly depend on physical parameters of initial proto-galactic clouds. In the standard scenario it is believed that a universe was seeded at some early epoch with small density fluctuations of dark non-baryonic matter. These small fluctuations, implied by self-gravity, provided the formation of quasy-equilibrium structures — future dark halos. Next processes of galaxy formation involved collapse of baryons within potential wells of such dark halos [157].

The dark matter problem is rather controversial one. Primordial nucleosynthesis constraints allow the significant fraction of dark matter in galactic halos to be ordinary baryonic matter [50]. Moreover, considerable amount of dark matter of baryonic nature could be tied up in hidden, low surface brightness galaxies [48]. Recent observational data (e.g. [4, 83, 84]) provide serious

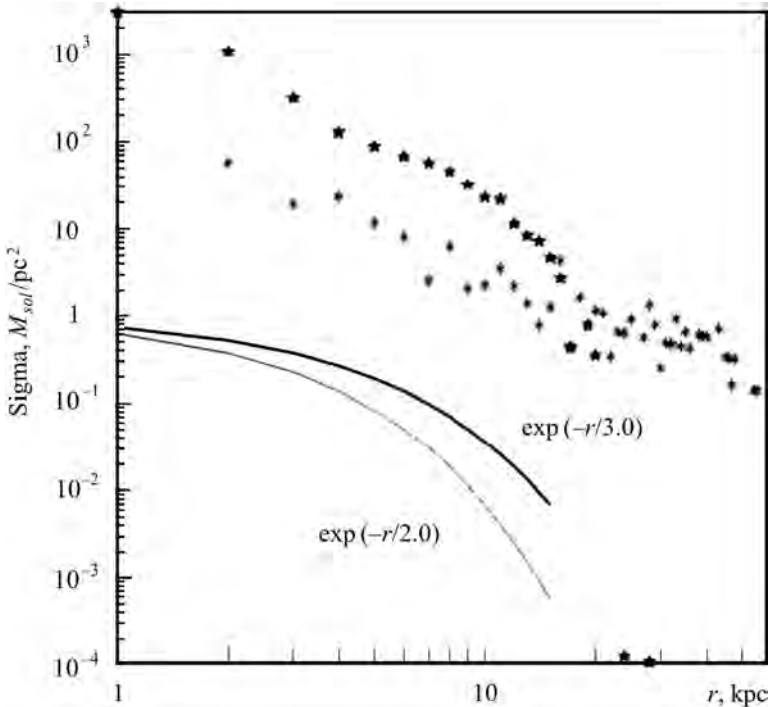


Fig. 4.5. The surface density radial distributions of stellar and gaseous components (stellar component is shown by filled stars, gaseous one by asterisks). Theoretical distributions (not scaled) of surface density for radial exponential scale lengths 2.0 and 3.0 kpc are shown below by lines

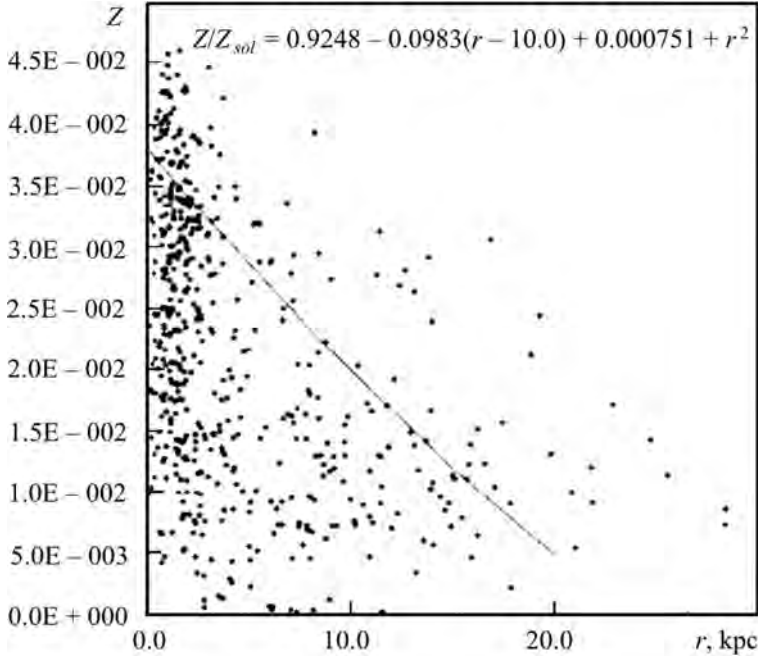


Fig. 4.6. The radial distribution of heavy element abundances (averaged observed distribution of z for our Galaxy is shown by solid line)

arguments on the existence of large amount of cold molecular and neutral hydrogen in outer regions of galaxies.

Recent observations of microlensing events in the Large Magellanic Cloud and in the Galactic bulge also suggest that the essential part of the galactic halo could be in the form of Massive Halo Objects (MHO) of average mass of about $0.1 M_{\odot}$ [2, 149]. De Paolis *et al.* [49] argue that the halo of our Galaxy is mainly baryonic and propose a scenario in which dark cluster of MHO and/or H_2 molecular clouds are formed in the halo at galactocentric distances larger than $10 \div 20$ kpc. Henriksen & Widrow [65] also support the idea that MACHO/EROS events correspond to the gravitational amplification by small clouds formed from a primordial mixture of hydrogen and helium with M of about $0.1 M_{\odot}$ and R of about 10^{14} cm. On the other hand galaxy chemical evolution simulations inevitably require the existence of the permanent inflow of baryonic material into the galactic disc [116, 147]. The observed rate of the baryonic matter delivering from the Galactic disk into the halo by means of wind and/or explosion phenomena and back via accretion into the disk is insufficient to compensate the rate of gas consumption in the Galactic disk (e.g. [109, 147]).

In the paper [115] the authors suppose that at the level of individual disc galaxies the essential part of dark matter could be in the form of cold molecular

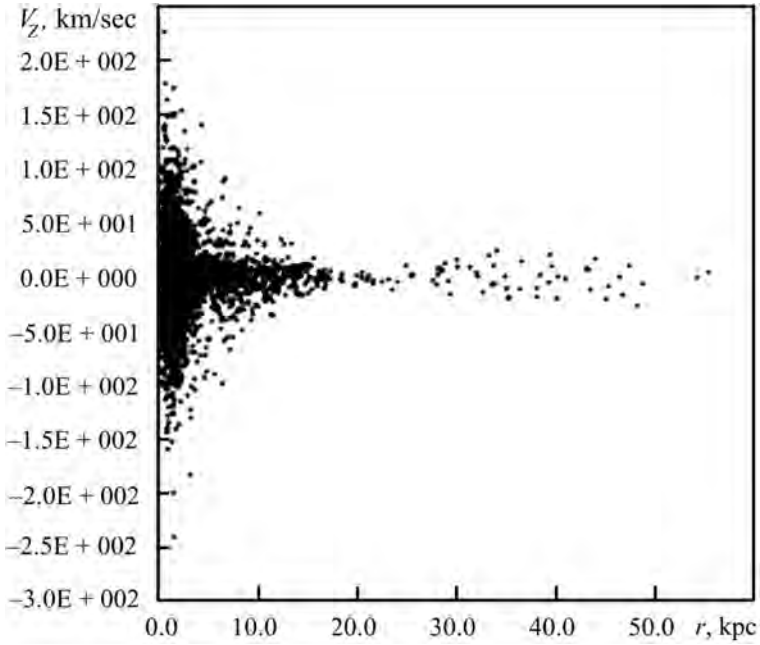


Fig. 4.7. The final distribution of V_z -th velocities of baryonic gas — stellar particles

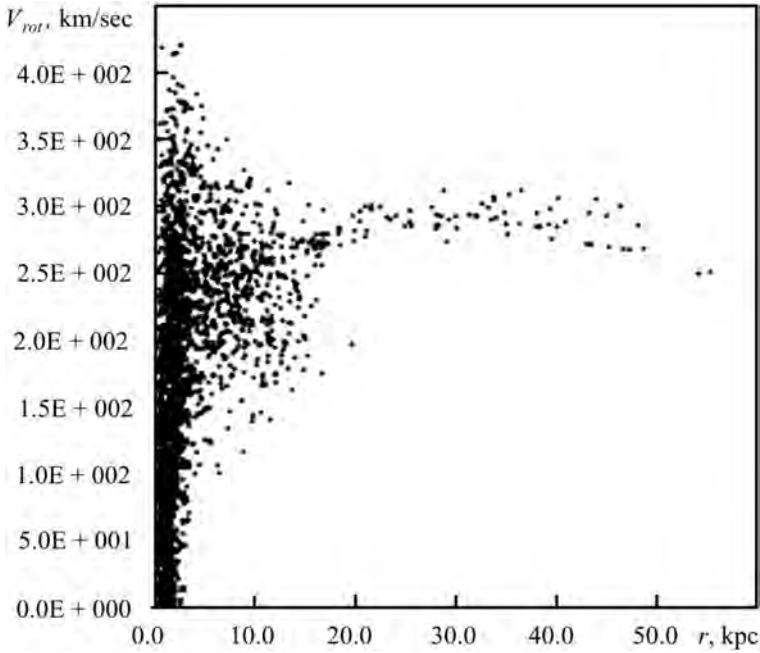


Fig. 4.8. The final galaxy rotation curve

gas cloudlets, which have radii of about 30 AU and masses of the order of Jupiter. And, what is essential, such objects cannot be detected and therefore are really “invisible” [160]. This hypothesis provides reasonable explanation of flat rotation curves, constant ratio of dark matter to HI mass in the outer spiral discs, the larger amount of visible gas in interacting galaxies with respect to the isolated ones, solution of gas consumption problem of spiral galaxies (e.g. [115]), morphology of nearby star formation regions [82] etc.

In this paper, taking into account the existence of the strong link between the behavior of the galactic disk surface density and baryonic halo parameters, we try to determine global system parameters which fit observed properties of the galactic disk in the Solar cylinder.

4.3.2. The model

Consider the galactic system having the halo which contain beside non-baryonic component baryonic matter in the form of small cold molecular cloudlets.

4.3.3. “Particles” representing the baryonic halo

According to [114] baryonic dark matter was supposed to exist in the form of molecular cloudlets having radii of about 30 AU, masses of the order of Jupiter. Their average density and column density are respectively 10^9 cm^{-3} and 10^{24} cm^{-2} . They are gravitationally bound, and almost isothermal with a temperature of about 3 K. The total mass of this baryonic dark matter M_{halo} is a model parameter and to be determined via model fitting with existing observational and model data.

It is to be noted that due to numerical problems the number of considered particles can’t be chosen arbitrary large. But as was checked by our numerical simulation, instead of detailed treatment of dynamics of each elementary cloudlet we can study the evolution of the dark baryonic halo which contain some large but limited number of effective “particles” of significantly larger masses. Therefore, the total number of “particles” was chosen to be $N = 2109$ providing the relevant description of system’s dynamics. The mass of separate elementary “particle” was taken to be $m_i = M_{halo}/N$.

At the initial moment $t = 0$ the initially spherical halo of radius $A_{halo} = 100 \text{ kpc}$ was divided onto homogeneous cubic cells and the center of each “particle” was placed into each cubic cell. It was assumed that initially all “particles” had isotropic chaotic velocities and were involved into the general halo rotational motion.

The initial rotational velocity field was defined by the initial angular velocity $\Omega_0(x, y, z)$ as:

$$\mathbf{V}_0(x, y, z) = [\Omega_0(x, y, z) \times \mathbf{r}],$$

where $\Omega_0(x, y, z)$ is the additional model parameter which is to be determined by fitting procedure.

In numerical simulations initial velocity components were generated as:

$$\begin{cases} V_{x_i} = (\Omega_{0y} \cdot z - \Omega_{0z} \cdot y) + (\Delta V_x - rand() \cdot 2 \cdot \Delta V_x), \\ V_{y_i} = (\Omega_{0z} \cdot x - \Omega_{0x} \cdot z) + (\Delta V_y - rand() \cdot 2 \cdot \Delta V_y), \\ V_{z_i} = (\Omega_{0x} \cdot y - \Omega_{0y} \cdot x) + (\Delta V_z - rand() \cdot 2 \cdot \Delta V_z), \end{cases} \quad (4.12)$$

here the function $rand()$ generates the random numbers between $0 \div 1$ and $\Delta V_x = \Delta V_y = \Delta V_z = 7.7$ km/s. These additional motions can be interpreted as the initial kinetic temperature T_{kin} of “cloudlets gas”, which is about $T_{kin} = 10^4$ K.

The integration of equation of motion for every “particle” was carried out by N-body integrator realized as the modified Smoothed Particle Hydrodynamics (SPH) algorithm of individual time step [20].

System gravitational potential. The process of galaxy formation involves the collapse of baryons within the potential well of the quasy-equilibrium dark halo. In spite of the fact that the total gravitational potential of such system is determined by the bulge, disk and dark non-baryonic and baryonic halo components its global properties depend mainly on the parameters of the dark halo and initial protogalaxy angular momentum. Therefore, for estimations as the starting value we can use the present-day form of galaxy gravitational potential. According to [85] it can be described by three-component model:

$$\begin{aligned} \Phi_1(x, y, z) &= -\frac{G \cdot M_1}{\sqrt{x^2 + y^2 + (a_1 + \sqrt{b_1^2 + z^2})^2}}, \\ \Phi_2(x, y, z) &= -\frac{G \cdot M_2}{\sqrt{x^2 + y^2 + (a_2 + \sqrt{b_2^2 + z^2})^2}}, \end{aligned}$$

where $M_1 = 2.05 \cdot 10^{10} M_\odot$, $a_1 = 0.0$ kpc, $b_1 = 0.495$ kpc, $M_2 = 2.547 \cdot 10^{11} M_\odot$, $a_2 = 7.258$ kpc, $b_2 = 0.52$ kpc.

If $a = 0$ this is simply the Plummer spherical potential and for $b = 0$ this is the Kuzmin thin – disk one.

For third component:

$$\Phi_3(x, y, z) = -\frac{G \cdot M_3}{r_{nbh}} \cdot \left(\ln(1 + q) + \frac{1}{1 + q} \right) - \Phi_0, \quad (4.13)$$

where the parameter q is defined as $q = \frac{\sqrt{x^2 + y^2 + z^2}}{r_{nbh}}$ and $M_3 = 1.35 \times 10^{11} M_\odot$, $r_{nbh} = 13.0$ kpc, $\Phi_0 = 1.4 \cdot 10^{11} (\text{m/s})^2$.

In order to follow the process of Galaxy formation in numerical simulations additional term was included, which account for the evolving baryonic halo and growing disk. This last variable term was calculated in the process of numerical modeling of the whole system evolution.

The gravitational potential of captured matter in the disk was determined as potential of homogeneous ellipsoidal figure [40]:

$$\Phi_{ac}(x, y, z) = \pi \cdot G \cdot \rho_{ac} \frac{a_{ac} b_{ac} c_{ac}}{a'_{ac} b'_{ac} c'_{ac}} \times [A_1(a'^2_{ac} - x^2) \cdot A_2(b'^2_{ac} - y^2) \cdot A_3(c'^2_{ac} - z^2)],$$

where:

$$\begin{cases} A_1 = 2 \cdot b'_{ac} \cdot c'_{ac} \frac{F - E}{a'^2_{ac} \cdot \sin^3(\phi) \cdot \sin^2(\theta)}, \\ A_2 = 2 \cdot b'_{ac} \cdot c'_{ac} \frac{E - F \cdot \cos^2(\theta) - c'_{ac}/b'_{ac} \cdot \sin^2(\theta) \cdot \sin(\phi)}{a'^2_{ac} \cdot \sin^3(\phi) \cdot \sin^2(\theta) \cdot \cos^2(\theta)}, \\ A_3 = 2 \cdot b'_{ac} \cdot c'_{ac} \frac{b'_{ac}/c'_{ac} \cdot \sin(\phi) - E}{a'^2_{ac} \cdot \sin^3(\phi) \cdot \cos^2(\theta)}, \end{cases}$$

and:

$$\begin{cases} a'_{ac} = a_{ac} + \lambda, \\ b'_{ac} = b_{ac} + \lambda, \\ c'_{ac} = c_{ac} + \lambda, \end{cases}$$

the λ is the largest root value of the equation:

$$\frac{x^2}{a_{ac} + \lambda} + \frac{y^2}{b_{ac} + \lambda} + \frac{z^2}{c_{ac} + \lambda} = 1,$$

and:

$$\begin{cases} \sin(\theta) = k = \sqrt{\frac{a'^2_{ac} - b'^2_{ac}}{a'^2_{ac} - c'^2_{ac}}}, \\ \cos(\phi) = \frac{c'_{ac}}{a'_{ac}}. \end{cases}$$

Here E and F are elliptical integrals:

$$\begin{cases} E = \int_0^\phi \sqrt{1 - k^2 \cdot \sin^2(\phi)} d\phi, \\ F = \int_0^\phi \frac{1}{\sqrt{1 - k^2 \cdot \sin^2(\phi)}} d\phi. \end{cases}$$

For more detailed information the reader is referred to [19].

The capturing disk. Simple estimations show that owing to the halo low density, the process of ram pressure retardation of gas cloudlets in this region is

negligible. The effective process of gravitational and ram pressure retardation is confined only to the region of the galactic disk. In order to estimate the role of the process of capturing of halo “particles” by the galactic disk (via ram pressure retardation) into the numerical model we artificially introduce the region of capturing disk as an ellipsoid with semiaxes $a_{ac} > b_{ac} > c_{ac}$, which mimic the parameters of our Galaxy disk:

$$a_{ac} = 20.0 \text{ kpc}, \quad b_{ac} = 19.9 \text{ kpc}, \quad c_{ac} = 1.0 \text{ kpc}.$$

For the initial moment capturing disk mass defined as M_{ac} was set equal zero. For any other moment t its total mass included as captured and temporarily occupying disk transient “particles”.

When the halo “particle” dropped into the region occupied by the capturing disk, with probability P , which was the model parameter, it was added to the disk. This process caused the changing of following parameters:

$$\begin{cases} M_{ac} = M_{ac} + m_i, \\ M_{halo} = M_{halo} - m_i. \end{cases}$$

To follow surface density variations, the capturing disk was divided onto $M = 11$ circular rings of width $\Delta r = a_{ac}/M$ or about $\Delta r \approx 1.8$ kpc. The ring radius was defined as: $r_j = j \cdot a_{ac}/M$. For any given moment t the mass in the circular ring (between radii $r_j \div r_j + \Delta r$) was $\Delta M_{ac}(r_j; t)$ and, therefore, the captured gas surface density was defined as:

$$\sigma(r_j; t) = \frac{\Delta M_{ac}(r_j; t)}{\pi \cdot (2 \cdot r_j \cdot \Delta r + \Delta r^2)}.$$

4.3.4. Results and discussion

Our numerical simulations of the evolution of the galactic system, having baryonic halo in the form of “invisible” small hydrogen clouds, have shown that the behavior of the galactic disk surface density as a function of time and galactocentric distance is very sensitive to the adopted halo parameters. This allowed to determine baryonic halo parameters by fitting results of model calculations for different initial conditions with available data on age, mass inflow rate and the galactic disk surface density.

Modern observational data show that the present baryonic matter surface density in the Solar cylinder is $\sigma \approx 50 M_{\odot}/\text{pc}^2$. The age estimation provide the value of about $t \approx 13$ Gyr. (e.g. [57, 109]). Additionally, in [148] the authors, estimating the maximum accretion rate consistent with both vertical scalelength in the disk and local velocity dispersion, argue that not more than 10% of the total disk mass were accreted in past 5 Gyr.

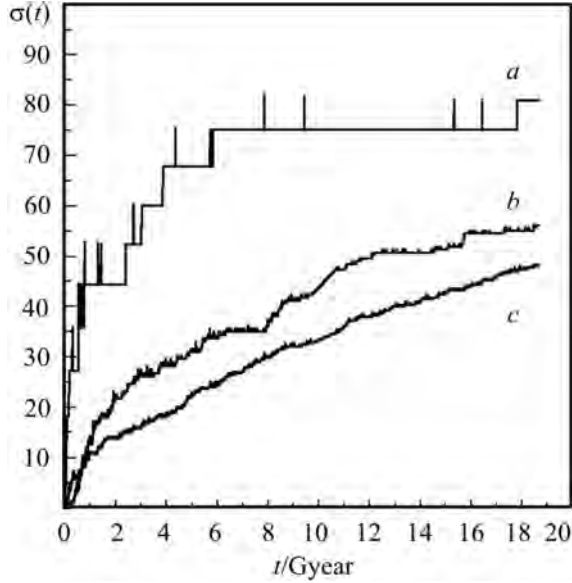


Fig. 4.9. The evolution of disk surface density at different Galactic radii ($\sigma(t)$ in M_{\odot}/pc^2)

Our numerical simulations show that only model with additional baryonic halo of initial mass of $M_{halo} = 2 \cdot 10^{11} M_{\odot}$, which have the flat rotation curve of type:

$$\Omega_{0z} = \omega \cdot \frac{\sqrt{G \cdot M_{HALO} / A_{HALO}}}{\sqrt{A_{HALO}^2 / 100 + x^2 + y^2}},$$

which mimics the disk rotation curve, fits well these observational data. Here ω is the dimensionless parameter of angular velocity equal to 1.0. The present shape of such baryonic halo could be described as an oblate ellipsoidal figure (thick disk) with large semiaxis of about 70 kpc and small one of about 30 kpc.

The other model parameter, concerning the capturing disk, is the value of capturing probability. It was taken to be $P = 0.01$. The comparison of column density of molecular cloudlet with that of typical Giant Molecular Cloud show that such value is a typical one for the probability of cloudlet capturing in the galactic disk. But our simulations show that the influence of of this parameter on the system behavior is rather weak as the main role plays here the process of gravitational capture.

The most controversial moment in our treatment concerns the adopted form of initial galactic potential. But it should be noted that the main role in the process of galaxy formation plays dark nonbaryonic matter. The global properties of forming galaxy are determined mainly by nonbaryonic matter

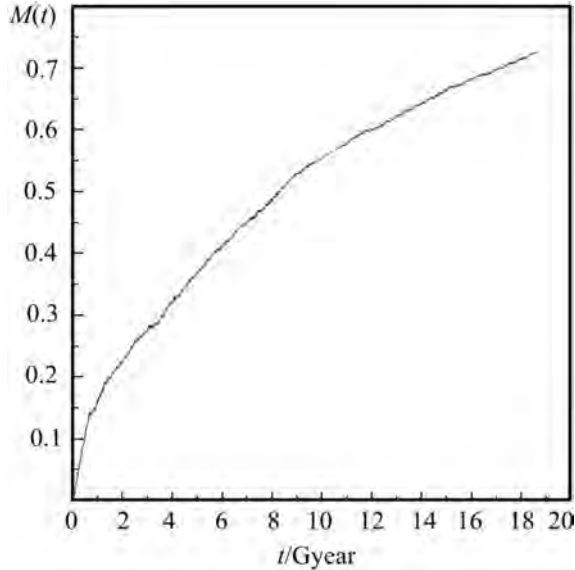


Fig. 4.10. The variation of disk mass (mass in $10^{11} M_{\odot}$)

parameters as the process of galaxy formation involves the collapse of baryons within the potential well of quasy-equilibrium dark halo.

The resulting surface density $\sigma(t)$ variations with time for different radii are shown in Fig. 4.9, where the surface density variation in the central region of the disk is presented by the curve a), the surface density in the Solar vicinity (between radii $\approx 9 \div 11$ kpc) is shown by the curve b) and the surface density at the edge of the disk is referred to the curve c). In Fig. 4.10 the evolution of the disk mass as the function of time is presented.

Finally, it is to be noted that the accretion of halo cloudlets onto the galactic disc can significantly modify the Galaxy chemical evolution and can serve as an efficient supporting mechanism of supersonic turbulent motions observed in Giant Molecular Clouds (GMC). Such selfgravitating cloudlets, captured by GMC, could be seeds triggering a formation of stars with cores which initially are almost depleted of heavy elements and such process can seriously affect their observational properties such as evolutionary time — scale, neutrino fluxes etc.

4.4. Gasodynamical model of the triaxial protogalaxies collapse. Isothermal and adiabatic solutions

4.4.1. Introduction

We not discuss here in detail the process lead to the formation of triaxial protogalaxy. This is the independent cosmological problem that needs the separate investigation. But, as we know, the protogalactic perturbation in early universe may be triaxial [6, 54, 158]. Therefore, when the galaxy is formed through the evolution of triaxial protogalaxy fragment the resulting galaxy also may be triaxial.

The problem of origin of the initial angular momentum of protogalaxy have many different solutions [41, 154]. But, in common cases, the models shows that there exists probability that the protogalaxy have the initial total angular momentum vector which doesn't coincide with any of main axis of triaxial initial protogalactic figure. Then, in a result of dynamical collapse we can expect a triaxial galaxy having complicated internal kinematics [44].

The number of data, that galaxies are triaxial in their majority, increases steadily. First of all, elliptical galaxies are triaxial [29, 30, 70]. This conclusion, in many cases, follows from the analysis of shape and brightness distribution of images of elliptical galaxies. Still more convincing data on the triaxial shape of ellipticals give their kinematical properties. New investigations confirm this idea and now we may make the conclusion that all ellipticals are triaxial [51, 58, 59, 75].

The warping processes in the disk system also possible to examine as evidence of general triaxiality of this system [31]. Asymmetries in the distribution of light and neutral hydrogen also often observed in disk galaxies [122]. On the base of data about the bar-galaxies we conclude that in a considerable part of such systems have essentially triaxial gravitational potential [113]. Now the number of data about triaxiality of bulges in spiral galaxies steadily increases [27, 156]. The Milkyway galaxy and M31 also may be have the extended triaxial bulges [33, 34].

In real, exists some various processes that can lead to the formation of triaxial galaxies as for example "cold" dissipatinless collapse of spherical systems [1, 153]. But, for great number of triaxial shaping among galaxies generates the idea that triaxial configuration can initially exists on a protogalactic stage of evolution. We expect that this triaxial form already exists on the early state of evolution of protogalaxies, when the star formation still not start and protogalaxies have only pure gas components. From our point of view, the triaxiality of protogalaxies may be the main generating factor of present triaxial shape of galaxies.

In this paper we consider a case, when in initial state a protogalaxy is a homogeneous triaxial ellipsoide having an angular momentum directed arbitrary in space. Simulations were carried out by SPH method. The properties of early gas galaxies, that can be formed in a result of isothermal or adiabatic collapse, are considered.

In the next paper, we will describe the result of the next series of models, in which we will include the star formation process in evolution of triaxial protogalaxy.

4.4.2. The SPH code for simulations of galaxy formation

Basic principles. Continuous hydrodynamic fields in SPH are described by the interpolation functions constructed from the known values of these functions at randomly positioned particles. In this case the mean value of a physical field $f(\mathbf{r})$ at the point \mathbf{r} can be written as [96, 98]:

$$\langle f(\mathbf{r}) \rangle = \int f(\mathbf{r}') \cdot W(\mathbf{r} - \mathbf{r}'; h) d\mathbf{r}', \quad (4.14)$$

where $W(\mathbf{r} - \mathbf{r}'; h)$ is the kernel function and h is the softening constant.

The function $W(\mathbf{u}; h)$ is strongly peaked at $|\mathbf{u}| = 0$, and we can consider it without any loss of generality as belonging to the class of even functions. In this case it is not difficult to demonstrate [67] that the average value $\langle f(\mathbf{r}) \rangle$ represents the real function $f(\mathbf{r})$, with an error not higher then $O(h^2)$:

Consider a fluid with the density $\rho(\mathbf{r})$. We rewrite (4.14) in the form:

$$\langle f(\mathbf{r}) \rangle = \int \frac{f(\mathbf{r}')}{\rho(\mathbf{r}')} \cdot W(\mathbf{r} - \mathbf{r}'; h) \cdot \rho(\mathbf{r}') d\mathbf{r}'. \quad (4.15)$$

Let us imagine that $f(\mathbf{r})$ and $\rho(\mathbf{r})$ are known only at N discrete points \mathbf{r}_i . Then, equation (4.15) gives:

$$f_i = \sum_{j=1}^N m_j \cdot \frac{f_j}{\rho_j} \cdot W_{ij}, \quad (4.16)$$

here $f_i \equiv f(\mathbf{r}_i)$, $\rho_i \equiv \rho(\mathbf{r}_i)$, $W_{ij} \equiv W(\mathbf{r}_i - \mathbf{r}_j; h)$ and m_i is a mass of particle i .

Using (4.16), we approximate the hydrodynamic field by an analytical function which is differentiable as many times as the kernel W_{ij} .

Following to [98] for the kernel function W_{ij} we will use the spline expression in the form:

$$W_{ij} = \frac{1}{\pi h^3} \begin{cases} 1 - \frac{3}{2} \left(\frac{u_{ij}}{h}\right)^2 + \frac{3}{4} \left(\frac{u_{ij}}{h}\right)^3, & \text{if } 0 \leq \frac{u_{ij}}{h} \leq 1; \\ \frac{1}{4} \left(2 - \frac{u_{ij}}{h}\right)^3, & \text{if } 1 \leq \frac{u_{ij}}{h} \leq 2; \\ 0, & \text{otherwise.} \end{cases} \quad (4.17)$$

The local resolution in SPH is defined by the chosen smoothing length h . If it is the same for all points, the hydrodynamic field will be evidently approximated more smoothly in the regions where the points lie more closely, i.e. where the density is higher.

To achieve the same level of accuracy for all points in the fluid it is necessary to use a spatially variable smoothing length. In this case each particle has its individual value of h . Following to [67], instead of (4.14) we will write:

$$\langle f(\mathbf{r}) \rangle = \int f(\mathbf{r}') \cdot \frac{1}{2} \cdot [W(\delta\mathbf{r}; h) + W(\delta\mathbf{r}; h')] d\mathbf{r}', \quad (4.18)$$

here $\delta\mathbf{r} \equiv \mathbf{r} - \mathbf{r}'$, $h \equiv h(\mathbf{r})$ and $h' \equiv h(\mathbf{r}')$. For the density $\rho(\mathbf{r})$ it gives:

$$\langle \rho(\mathbf{r}_i) \rangle = \sum_{j=1}^N m_j \cdot \frac{1}{2} \cdot [W(r_{ij}; h_i) + W(r_{ij}; h_j)]. \quad (4.19)$$

Other hydrodynamic functions are written in the same manner.

Many different procedures were proposed for choosing of individual smoothing lengths h_i . In our calculations the values of h_i were determined from the condition that the number of particles N_B in the neighborhood of each particle remains constant. The value of N_B is chosen such that a certain fraction from the total number of particles N affect the local flow characteristics [68].

Hydrodynamics equations. If the density is computed according to the equation (4.19), then the continuity equation is satisfied automatically. The equations of motion for particle i are

$$\frac{d\mathbf{r}_i}{dt} = \mathbf{v}_i, \quad (4.20)$$

$$\frac{d\mathbf{v}_i}{dt} = -\frac{\nabla_i P_i}{\rho_i} + \mathbf{a}_i^{vis} - \nabla_i \Phi_i, \quad (4.21)$$

where P_i is the pressure, Φ_i is the gravitational potential, \mathbf{a}_i^{vis} is an artificial viscosity term. Using the equations (4.18) and (4.19) we can write:

$$\begin{aligned} \frac{\nabla_i P_i}{\rho_i} &= \sum_{j=1}^N m_j \cdot \frac{1}{2} \cdot \left(\frac{P_i}{\rho_i^2} + \frac{P_j}{\rho_j^2} \right) \times \\ &\times [\nabla_i W(r_{ij}; h_i) + \nabla_i W(r_{ij}; h_j)]. \end{aligned} \quad (4.22)$$

The artificial viscosity term \mathbf{a}_i^{vis} is introduced to describe the flows with shock waves. In present calculations the viscous acceleration was introduced by replacing $(P_i/\rho_i^2 + P_j/\rho_j^2)$ in equation (4.22) by $(P_i/\rho_i^2 + P_j/\rho_j^2)(1 + \pi_{ij})$. The expression for π_{ij} has the form [69]:

$$\pi_{ij} = -\alpha \cdot \mu_{ij} + \beta \cdot \mu_{ij}^2, \quad (4.23)$$

where α and β are constants, and μ_{ij} is defined by the relation:

$$\mu_{ij} = \begin{cases} \frac{h_{ij}(\mathbf{v}_{ij} \cdot \mathbf{r}_{ij})}{c_{ij}(r_{ij}^2 + n^2 \cdot h_{ij}^2)}, & \text{if } (\mathbf{v}_{ij} \cdot \mathbf{r}_{ij}) < 0; \\ 0, & \text{otherwise,} \end{cases} \quad (4.24)$$

here $c_{ij} = (c_i + c_j)/2$ is the sound speed averaged for points i and j ; $h_{ij} = (h_i + h_j)/2$; $\mathbf{r}_{ij} = (\mathbf{r}_i - \mathbf{r}_j)$ and $\mathbf{v}_{ij} = (\mathbf{v}_i - \mathbf{v}_j)$ is the relative velocity vector for the points i and j . The term $n^2 \cdot h_{ij}^2$ is inserted to prevent divergences when $r_{ij} = 0$ and it should be small enough. The constant n was set equal 0.1. For the constant α and β in (4.23) the values $\alpha = 1$ and $\beta = 2$ give good results in a wide range of the Mach numbers [96].

By using equation (4.17), for the gravitational acceleration $-\nabla_i \Phi_i$ one gets [68]:

$$-\nabla_i \Phi_i = -\frac{1}{2} \cdot \sum_{j=1}^N G \cdot m_j \cdot \frac{\mathbf{r}_{ij}}{r_{ij}^3} \cdot [g(u_i) + g(u_j)], \quad (4.25)$$

where:

$$g(u_k) = \begin{cases} \frac{4}{3} \cdot u_k^3 - \frac{6}{5} \cdot u_k^5 + \frac{1}{2} \cdot u_k^6, & \text{if } 0 \leq u_k \leq 1; \\ -\frac{1}{15} + \frac{8}{3} u_k^3 - 3u_k^4 + \frac{6}{5} u_k^5 - \frac{1}{6} u_k^6, & \text{if } 1 \leq u_k \leq 2; \\ 1, & \text{otherwise,} \end{cases}$$

and $u_k = \frac{r_{ij}}{h_k}$.

When isothermal flows are considered, the system of equations is closed by adding the equation of state:

$$P_i = \rho_i \cdot c_i^2, \quad (4.26)$$

where c_i is the isothermal speed of sound.

For adiabatic flows the energy equation in the particle representation has the form:

$$\begin{aligned} \frac{du_i}{dt} &= \sum_{j=1}^N m_j \cdot \frac{1}{4} \cdot \left(\frac{P_i}{\rho_i^2} + \frac{P_j}{\rho_j^2} \right) \cdot (1 + \pi_{ij}) \times \\ &\times [\nabla_i W(r_{ij}; h_i) + \nabla_i W(r_{ij}; h_j)] \cdot \mathbf{v}_{ij}. \end{aligned} \quad (4.27)$$

where u_i is the specific internal energy of particle i . And to close the system the equation of state must be added, that can be written in the form:

$$P_i = \rho_i \cdot (\gamma - 1) \cdot u_i, \quad (4.28)$$

where γ is the adiabatic index.

The SPH code. To solve the system of equations (4.20), (4.21) and (4.27) we use the algorithm of individual time steps. This system of equations has the form:

$$\begin{cases} d\mathbf{r}_i/dt = \mathbf{v}_i; \\ d\mathbf{v}_i/dt = \mathbf{F}_i(P, \rho, \mathbf{r}, \mathbf{v}); \\ du_i/dt = G_i(P, \rho, \mathbf{r}, \mathbf{v}). \end{cases} \quad (4.29)$$

The time step δt_i for each particle depends on the particle's acceleration \mathbf{a}_i and velocity \mathbf{v}_i , as well on viscous forces.

To define δt_i we will use the relation [68]:

$$\delta t_i = C_n \min \left[\left(\frac{h_i}{|\mathbf{a}_i|} \right)^{1/2}, \frac{h_i}{|\mathbf{v}_i|}, \frac{h_i}{s_i} \right], \quad (4.30)$$

where $s_i = c_i \cdot (1 + \alpha + 0.68 \cdot \beta \cdot \max_j |\mu_{ij}|)$ and C_n is the Courant's number. Usually $C_n = 0.01 \div 0.1$.

The system of equations (4.29) is integrated in five steps.

Step one. Let t_i and δt_i be the current time and time step for i -th particle. We pick out such a particle i_* that have the minimum value of $t_i + \delta t_i$. For this particle $t_* = t_{i_*}$, $\delta t_* = \delta t_{i_*}$. Thereafter we find for other particles:

$$\delta t_i^{(1/2)} = \frac{1}{2} \cdot \delta t_* + (t_* - t_i),$$

and:

$$\delta t_i^{(1)} = \delta t_* + (t_* - t_i).$$

Step two. Using the Euler method ($y_{n+1} - y_n = \Delta x \cdot f(x, y_n)$), we predict the values of $\mathbf{r}_i^{(n+1/2)}$, $\mathbf{v}_i^{(n+1/2)}$, $u_i^{(n+1/2)}$ and $\rho_i^{(n+1/2)}$ for all particles at the moment $t = t_i + \delta t_i^{(1/2)}$. To obtaine $\rho_i^{(n+1/2)}$ for all particles except i_* , we use equation (4.19) in which only \mathbf{r}_{ij} varies with time. The calculation relations are:

$$\begin{cases} \mathbf{r}_i^{(n+1/2)} = \mathbf{r}_i^{(n)} + \delta t_i^{(1/2)} \cdot \mathbf{v}_i^{(n)}; \\ \mathbf{v}_i^{(n+1/2)} = \mathbf{v}_i^{(n)} + \delta t_i^{(1/2)} \cdot \mathbf{F}_i^{(n)}(P, \rho, \mathbf{r}, \mathbf{v}); \\ u_i^{(n+1/2)} = u_i^{(n)} + \delta t_i^{(1/2)} \cdot G_i^{(n)}(P, \rho, \mathbf{r}, \mathbf{v}); \\ \rho_i^{(n+1/2)} = \rho_i^{(n)} + \delta t_i^{(1/2)} \times \sum_{j=1}^N m_j \frac{1}{2} [\dot{W}(r_{ij}; h_i) + \dot{W}(r_{ij}; h_j)], \end{cases} \quad (4.31)$$

where:

$$\dot{W}(r_{ij}; h) = \frac{1}{\pi h^3} \begin{cases} \frac{3}{4} \frac{\mathbf{v}_{ij} \mathbf{r}_{ij}}{h^2} \left(3 \frac{r_{ij}}{h} - 4 \right), & \text{if } 0 \leq \frac{r_{ij}}{h} \leq 1; \\ -\frac{3}{4} \frac{\mathbf{v}_{ij} \mathbf{r}_{ij}}{h r_{ij}} \left(2 - \frac{r_{ij}}{h} \right)^2, & \text{if } 1 \leq \frac{r_{ij}}{h} \leq 2; \\ 0, & \text{otherwise.} \end{cases}$$

The values thus obtained need not be stored in separate arrays, they are used only for exact integration of the equation for the particle i_* .

Step three. The density ρ_* is most sensitive to time variations on the interval δt_* . Therefore, we firstly by the quicksort algorithm find a new value of $h_*^{(n+1/2)}$ based on the predicted values of $\mathbf{r}_i^{(n+1/2)}$ and then determine $\rho_*^{(n+1/2)}$ from the exact equation (4.19). This value of density is used to calculate the particle i_* parameters for the moment $t_* + \frac{1}{2} \cdot \delta t_*$ from equations (4.31).

Step four. We find the particle i_* parameters at the moment $t_* + \delta t_*$:

$$\begin{cases} \mathbf{v}_*^{(n+1)} = \mathbf{v}_*^{(n)} + \delta t_* \cdot \mathbf{F}_*^{(n+1/2)}(P, \rho, \mathbf{r}, \mathbf{v}); \\ \mathbf{r}_*^{(n+1)} = \mathbf{r}_*^{(n)} + \delta t_* \cdot \frac{1}{2} \cdot (\mathbf{v}_*^{(n)} + \mathbf{v}_*^{(n+1)}); \\ u_*^{(n+1)} = u_*^{(n)} + \delta t_* \cdot G_*^{(n+1/2)}(P, \rho, \mathbf{r}, \mathbf{v}). \end{cases} \quad (4.32)$$

Step five. Substituting $\delta t_i^{(1)}$ instead of $\delta t_i^{(1/2)}$ in (4.31), we synchronize the parameters for all particles except i_* at the moment $t_* + \delta t_*$. Thereafter we define the new value of $h_*^{(n+1)}$ based on the values $\mathbf{r}_i^{(n+1)}$ and find $\rho_*^{(n+1)}$ using equation (4.19). After that the current time is set equal to $t_* + \delta t_*$. The new time step for δt_i is determined and all cycle is repeated.

We have carried out [20] a large series of test calculations to check that the code elaborated is correct, the conservation laws are obeyed and the hydrodynamic fields are represented adequately. These tests have shown good results.

4.4.3. Overview of models

Initial conditions. We suppose, the common initial conditions for protogalaxy. The initial body of protogalaxy, we model by homogeneous triaxial $H I$ ellipsoids with semiaxis A , B and C . The mass of protogalaxy, in all models, we take as $M_{HI} = 10^{12} \cdot M_\odot$. The initial temperature of gas we take T_0 . Initial orientation of ellipsoid semiaxis A , B and C is coincide with the axis of coordinate system (x, y, z) . The initial velocity fields are defined through the angular velocity $\Omega_0(x, y, z)$:

$$\mathbf{V}_0(x, y, z) = [\Omega_0(x, y, z) \times \mathbf{r}].$$

The initial angular velocity Ω_0 we take constant in space. Therefore $\Omega_0(x, y, z) \equiv \Omega_0 = \text{Const}$. The orientation of initial angular velocity is defined by its components: $(\Omega_{0x}, \Omega_{0y}, \Omega_{0z})$. We investigate different orientation of initial angular velocity. The standard spin parameter defined as [110]:

$$\lambda = \frac{|\mathbf{L}_0| \cdot \sqrt{|E_0^{gr}|}}{G \cdot M_{HI}^{5/2}}, \quad (4.33)$$

where the \mathbf{L}_0 is the total initial angular momentum and the E_0^{gr} is the total initial gravitational energy of protogalaxy.

In all models we carry out two series of the calculation with $N = 515$ and $N = 4169$ gas particles. The parameter N_B we take equal 5 for the first series of models and 10 to the second series of models. The initial center of particles we take in space with equal step for three coordinate axes. Therefore the initial configuration of particles form the system of homogenous cubic cells. The Table 4.1 lists parameters of models. The $\Omega_{cir} = V_{cir}/A$ and $V_{cir} = (G \cdot M_{HI}/A)^{1/2}$. The A , B and C , in table, are shown in kpc.

In the case when the angular momentum was acquired by the tidal torque of the matter around the protogalaxy, spin parameter does not exceed $\lambda \approx 0.1$ [54, 154, 162]. In our calculations we investigate the case when the protogalaxy may have also the additional own angular momentum in order of or more than the angular momentum defined by the tidal torque. In result, the value of initial spin parameter of the protogalaxy we take $\lambda \approx 0.1 \div 0.3$.

Discussion of results. The global evolution of isothermal models in second series B1, T1, TT1 and adiabatic model TT1A are shown in Fig. 4.11, 4.12, 4.13 and 4.14.

The model B1. The initial body of protogalaxy in model B1 is almost disk structure. The $A = 100$, $B = 90$ and $C = 50$ kpc. The initial angular momentum vector has only two components, the $\Omega_{0x} = 0.8 \cdot \Omega_{cir}$ and $\Omega_{0z} = 0.8 \cdot \Omega_{cir}$. The initial temperature of gas is $T_0 = 5 \cdot 10^5$ K. The initial density of homogenous ellipsoid is $\rho_0 \approx 0.015 \text{ cm}^{-3}$. In all models we use for representation of dynamical data the coordinate system in which the initial angular momentum have only one component Ω_{0z} . The initial distribution of rotation velocity, in this coordinate system, is linear and has a maximum value $V_{rot} \approx 250 \text{ km/s}$.

The first step in Fig. 4.11 is corresponded to the time $t \approx 0.61 \cdot 10^9$ year. During this time, the gas collapse along the rotation axes. This is the shortest dynamical process. This process form the thin disk, with complex velocity fields. The rotational velocity in disk have the linear part (up to 50 kpc) and

Table 4.1. The list of parameters

A	B	C	Ω_0/Ω_{cir}	λ	$T_0 = 10^4$	10^5	$5 \cdot 10^5$	$10^4(\text{adiab})$
100	90	50	(0.8, 0.0, 0.8)	0.28	—	—	B1	—
100	60	50	(0.5, 0.0, 0.5)	0.13	—	—	T1	—
100	75	50	(0.8, 0.0, 0.8)	0.21	—	TT1	—	—
100	75	50	(0.5, 0.0, 0.5)	0.13	—	—	—	TT1A
100	75	50	(0.8, 0.0, 0.4)	0.11	TT2	—	—	—
100	75	50	(0.4, 0.0, 0.8)	0.22	TT4	—	—	—

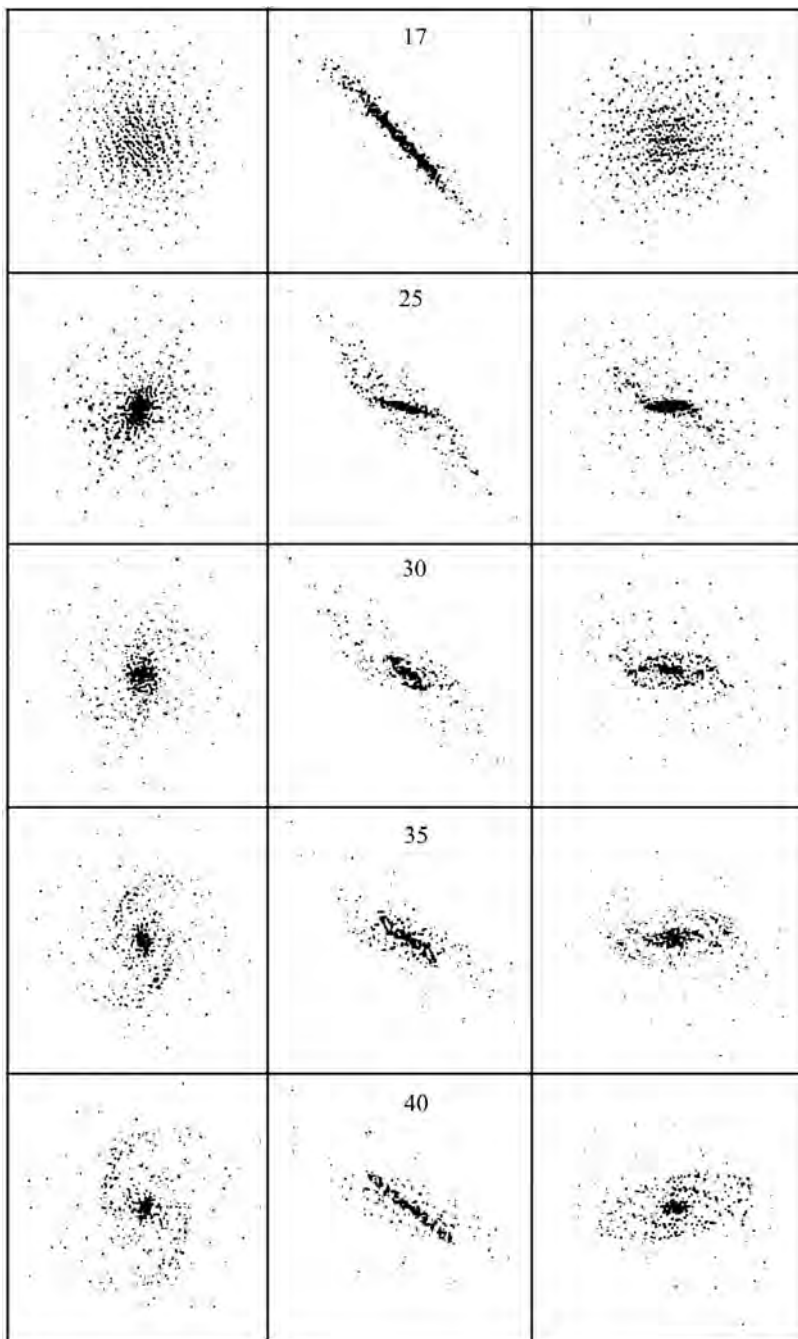


Fig. 4.11. The model B1. The first column is corresponded to **XY** plane, the second – **XZ** plane and the third – **YZ** plane. The step **17** is corresponded to $t \approx 0.61 \cdot 10^9$ year. The step **40** is corresponded to $t \approx 0.98 \cdot 10^9$ year. The diameter of represented cell in figure is 200 kpc

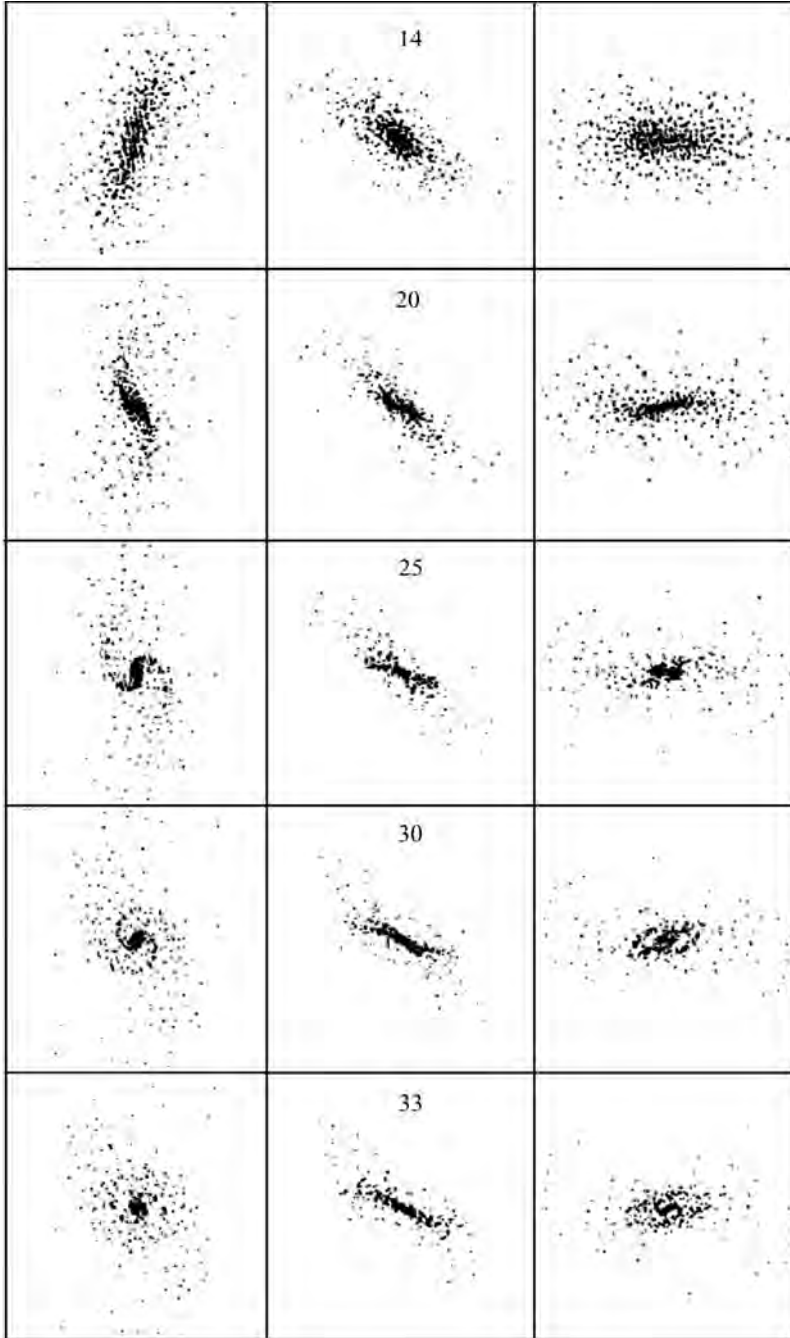


Fig. 4.12. The model T1. The first column is corresponded to **XY** plane, the second – **XZ** plane and the third – **YZ** plane. The step **14** is corresponded to $t \approx 0.46 \cdot 10^9$ year. The step **33** is corresponded to $t \approx 0.78 \cdot 10^9$ year. The diameter of represented cell in figure is 200 kpc

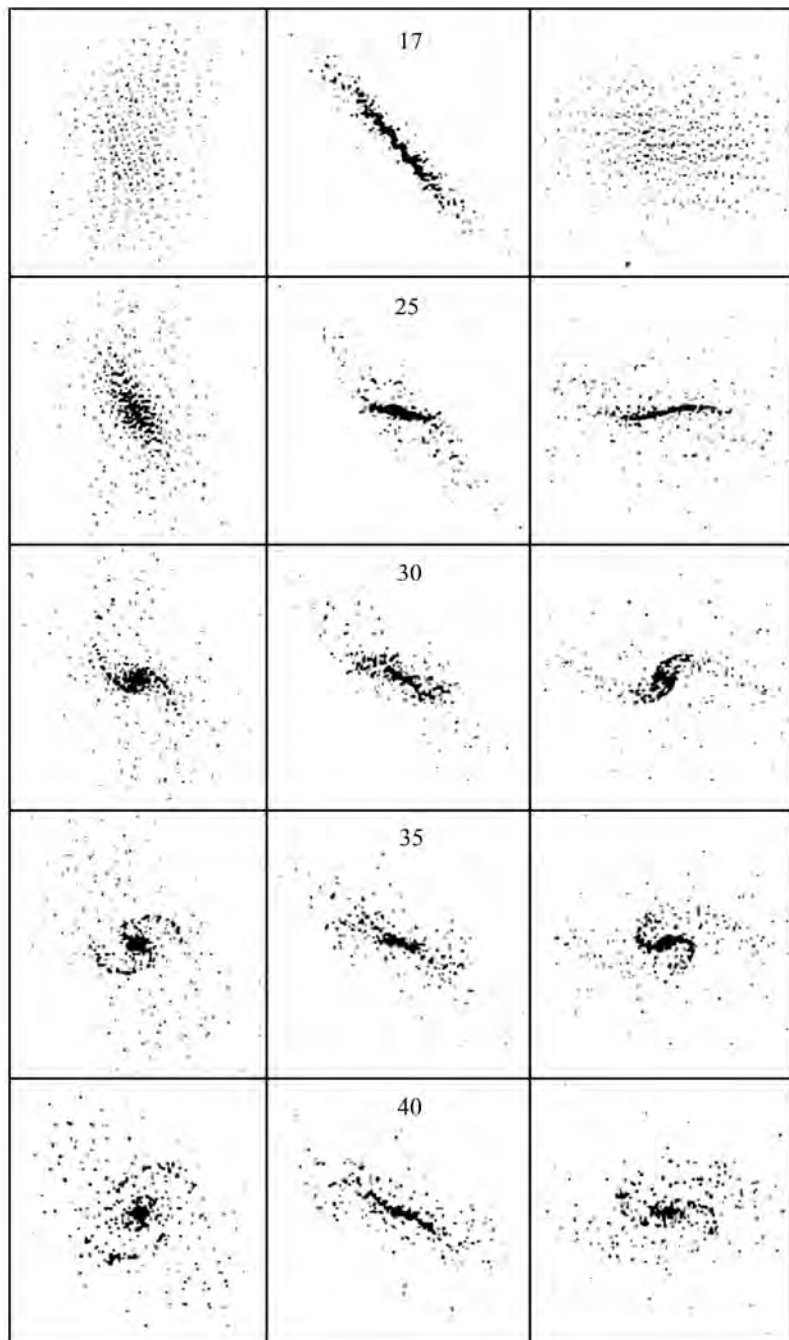


Fig. 4.13. The model TT1. The first column is corresponded to **XY** plane, the second — **XZ** plane and the third — **YZ** plane. The step **17** is corresponded to $t \approx 0.61 \cdot 10^9$ year. The step **40** is corresponded to $t \approx 1.07 \cdot 10^9$ year. The diameter of represented cell in figure is 200 kpc

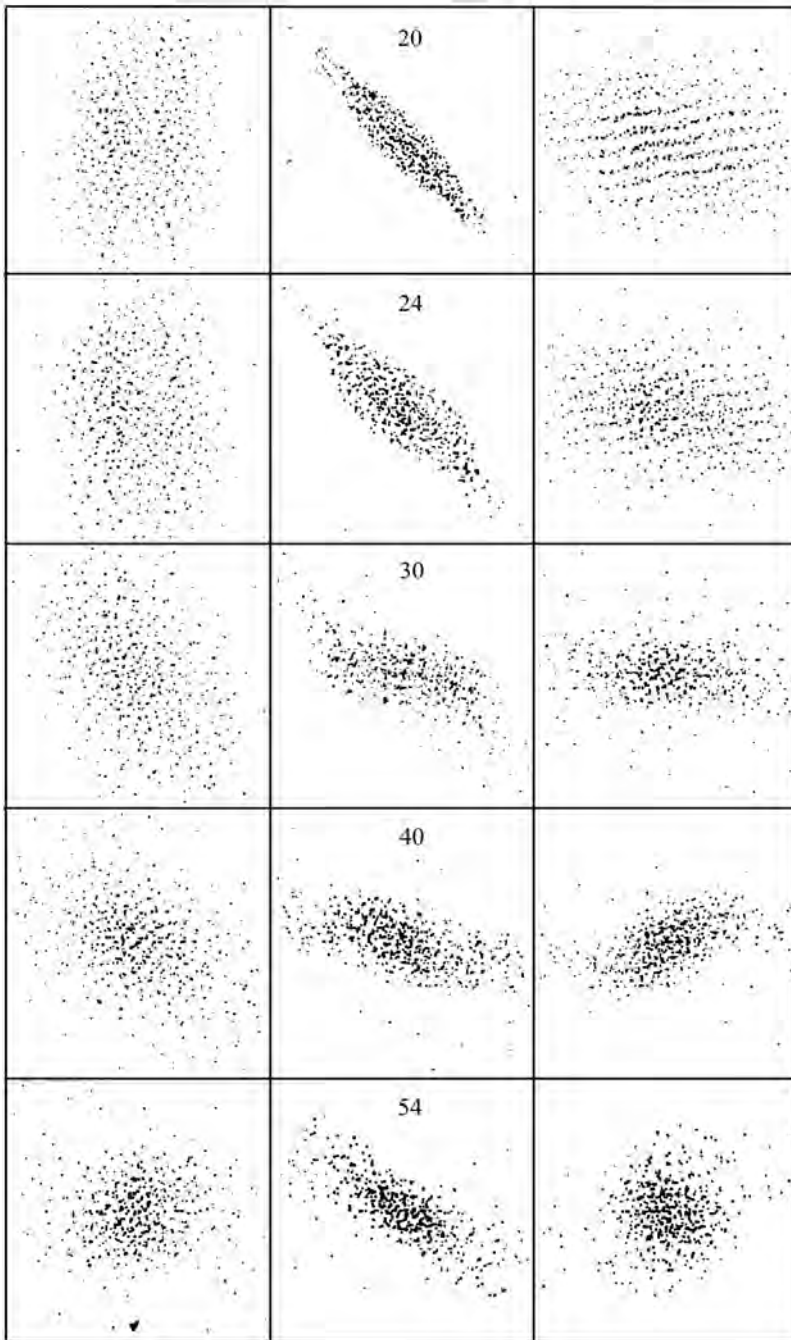


Fig. 4.14. The model TT1A. The first column is coresponded to **XY** plane, the second — **XZ** plane and the third — **YZ** plane. The step **20** is coresponded to $t \approx 0.66 \cdot 10^9$ year. The step **54** is coresponded to $t \approx 1.67 \cdot 10^9$ year. The diameter of represented cell in figure is 200 kpc

flat part (the value of $V_{rot} \approx 200$ km/s). The velocity dispersion along the collapse axis has a maximum value $V_z \approx 150$ km/s. The density in disk have almost power distribution with maximum central value $\rho_c \approx 0.8$ cm $^{-3}$.

The second step in Fig. 4.11 is coresponded to the time $t \approx 0.75 \cdot 10^9$ year. At this time, we see the interesting collapse in the central part of protogalaxy (up to ≈ 20 kpc) which form the thin, compact central disk. The rotational velocity in this disk is almost linear, with maximum value near 20 kpc of $V_{rot} \approx 400$ km/s. The velocity dispersion along the collapse axis has a maximum value $V_z \approx 125$ km/s. The density in the central disk has power distribution with maximum central value $\rho_c \approx 20$ cm $^{-3}$.

The third step in Fig. 4.11 is coresponded to the time $t \approx 0.82 \cdot 10^9$ year. In this picture, we see the strong triaxial bar formation in the central regions with parameters typical for spiral galaxies.

In the Fig. 4.15 we show the more detail view of step **35** in model B1. This step is coresponded to $t \approx 0.89 \cdot 10^9$ year. The diameter of represented cell in figure is 100 kpc.

The final stage in our calculations for this model corespond to the time $t \approx 0.98 \cdot 10^9$ year. At this step the central density already has the maximum value $\rho_c \approx 300$ cm $^{-3}$. The rotation curve is typical for disk galaxies. It has the linear growing part up to 10 kpc and the extended flat tail up to 75 kpc. The maximum value of rotation velocity is $V_{rot} \approx 250$ km/s. After flat tail we have slowly dropping part of rotation curve almost up to 140 kpc.

The density distribution of last step we show in Fig. 4.19, the rotational velocity V_{rot} we show in Fig. 4.21 and the velocity distribution V_z (perpendicular to the plane of forming galaxy) we show in Fig. 4.23.

Because, the body of protogalaxy is not symmetrical and rotates differentially, the collapse process generate the “warp” force, which distors the disk and produce the spiral like structure. During the evolution this “warp” process generates the interesting spiral shape of gas in the protogalaxy, especialy in the central region (up to 20 kpc, see the Fig. 4.15).

The model leads to the development of the triaxial central bar phenomenon. The bar have typical dimensions around 5 kpc. The model also shows the extended gas tail, which have the essential inclination to the central disk. Therefore, we can observe in this case the complicated internal and external motion. The central part have the separate direction of rotation to compare with the external part of forming galaxy.

The model T1. The next model is T1. This model have almost bar like shape. The $A = 100$, $B = 60$ and $C = 50$ kpc. The initial angular momentum vector has two components, the $\Omega_{0x} = 0.5 \cdot \Omega_{cir}$ and $\Omega_{0z} = 0.5 \cdot \Omega_{cir}$. The initial temperature of gas, as in the model B1, is $T_0 = 5 \cdot 10^5$ K. The initial density is $\rho_0 \approx 0.023$ cm $^{-3}$. The initial distribution of rotation velocity has a maximum value $V_{rot} \approx 200$ km/s.

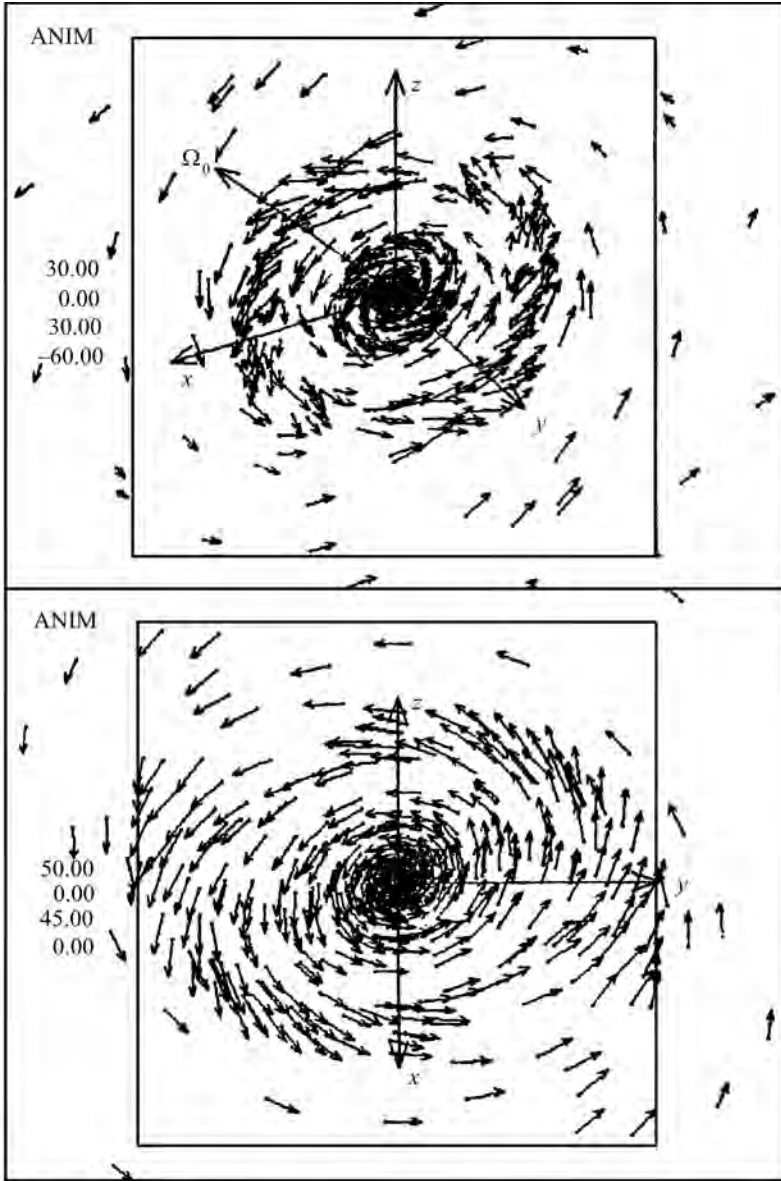


Fig. 4.15. The more detail view of step **35** in model B1. This step is corresponded to $t \approx 0.89 \cdot 10^9$ year. The diameter of represented cell in figure is 100 kpc

The first step in Fig. 4.12 is corresponded to the $t \approx 0.46 \cdot 10^9$ year. This step, corresponds to the moment, when the collapse along rotational axis is maximal. We see in figure the strong elongated bar in collapsed disk. The rotational velocity in disk have the linear part (up to 30 kpc) and wide flat

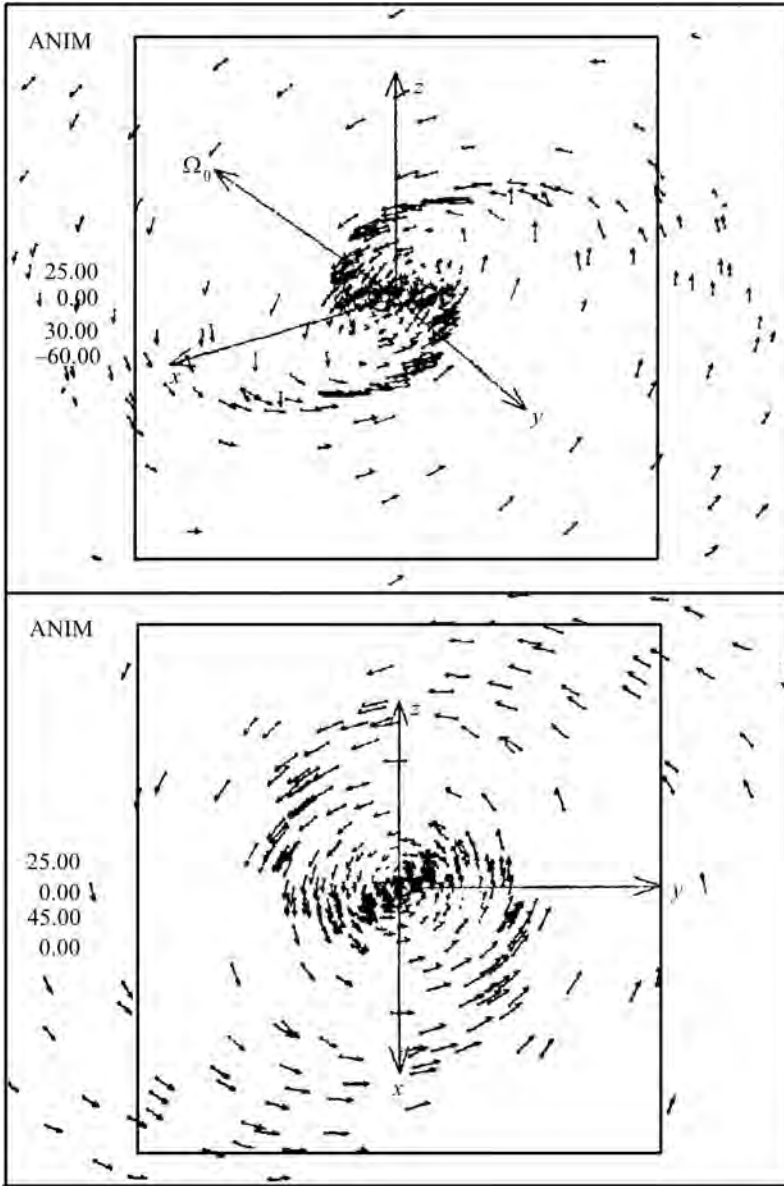


Fig. 4.16. The more detail view of step 25 in model T1. This step is corresponded to $t \approx 0.66 \cdot 10^9$ year. The diameter of represented cell in figure is 50 kpc

part (the value of $V_{rot} \approx 200$ km/s). The velocity dispersion along the collapse axis has a maximum value $V_z \approx 150$ km/s. The density in disk has a maximum central value $\rho_c \approx 0.8 \text{ cm}^{-3}$.

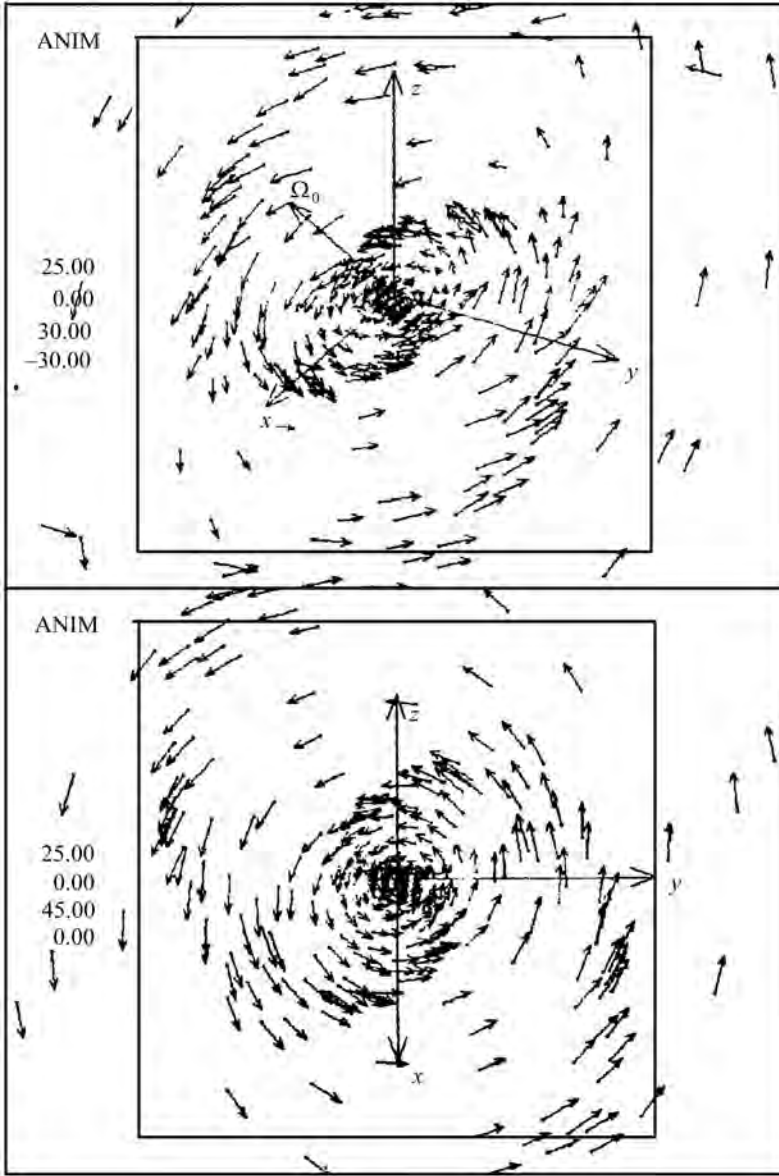


Fig. 4.17. The more detail view of step 35 in model TT1. This step is corresponded to $t \approx 0.95 \cdot 10^9$ year. The diameter of represented cell in figure is 50 kpc

The second step in Fig. 4.12 is corresponded to the $t \approx 0.58 \cdot 10^9$ year. At this time, we see the beginning of the process of generating of spiral perturbation in central part of protogalaxy (up to ≈ 20 kpc). The rotational velocity in central disk is almost linear, with maximum value of $V_{rot} \approx 300$ km/s near

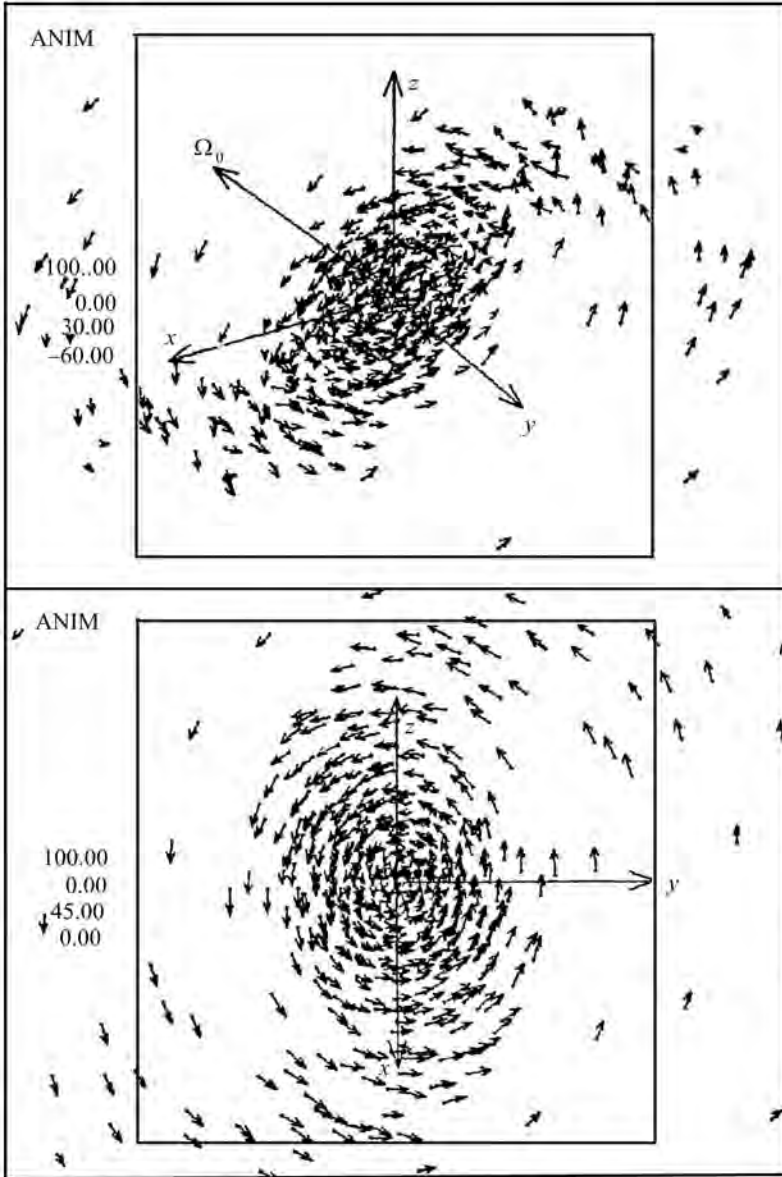


Fig. 4.18. The more detail view of step 54 in model TT1A. This step is corresponded to $t \approx 1.61 \cdot 10^9$ year. The diameter of represented cubic cell in figure is 100 kpc

20 kpc. The velocity dispersion along the collapse axis has a maximum value $V_z \approx 125$ km/s. The density in the central disk has power distribution with maximum central value $\rho_c \approx 100 \text{ cm}^{-3}$.

The third step in Fig. 4.12 is coresponded to the $t \approx 0.66 \cdot 10^9$ year. In this picture, we see the very impressive triaxial spiral shape formation in the central region of protogalaxy. This spiral shape has parameters typical for spiral galaxies.

The more detail view of step **25** we show in the Fig. 4.16. The diameter of represented cell in figure is 50 kpc.

The final state of this model coresponds to the $t \approx 0.78 \cdot 10^9$ year. In this step the central density has the value $\rho_c \approx 500 \text{ cm}^{-3}$. In the central core the rotation curve is linear and has the maximum value $V_{rot} \approx 300 \text{ km/s}$. In the external part rotation curve is almost Keplerian.

Because, the initial rotation fields in this model are less then in the model B1, the final configuration is more compact and dense.

This model shows the very impressive bar instability and spiral pattern generation. The bar has dimensions, as in model B1, about 5 kpc. The spiral structure is very impressive but evolve very quickly.

The model TT1. The model TT1 have the most common triaxial shape. The $A = 100$, $B = 75$ and $C = 50$ kpc. The initial angular momentum vector has two components, $\Omega_{0x} = 0.8 \cdot \Omega_{cir}$ and $\Omega_{0z} = 0.8 \cdot \Omega_{cir}$. The initial temperature of gas is $T_0 = 1 \cdot 10^5 \text{ K}$. The initial density is $\rho_0 \approx 0.018 \text{ cm}^{-3}$. The initial distribution of rotation velocity has a maximum value $V_{rot} \approx 250 \text{ km/s}$.

The first step in Fig. 4.13 is coresponded to the $t \approx 0.61 \cdot 10^9$ year, the second step is coresponded to the $t \approx 0.80 \cdot 10^9$ year and the third step is coresponded to the $t \approx 0.88 \cdot 10^9$ year.

In the Fig. 4.17 we show the more detail view of step **35** in model TT1. This step is coresponded to $t \approx 0.95 \cdot 10^9$ year. The diameter of represented cell in figure is 50 kpc.

The final state of the evolution, shown in last step, is coresponded to the $t \approx 1.07 \cdot 10^9$ year. In this step the central density has the value $\rho_c \approx 300 \text{ cm}^{-3}$. In the central core the rotation curve is linear and has the maximum value $V_{rot} \approx 300 \text{ km/s}$. In external part the velocity distribution shows slowly falling trend.

The model produces very nice spiral system. Two spiral arm extend beyond 20 kpc (see Fig. 4.17).

The model TT1A. The model TT1A has same initial conditions as TT1 but in this case we investigte the adiabatic evolution of gas protogalaxy. The initial temperature of gas is $T_0 = 1 \cdot 10^4 \text{ K}$.

The first step in Fig. 4.14 is coresponded to the $t \approx 0.66 \cdot 10^9$ year, the second step is coresponded to the $t \approx 0.79 \cdot 10^9$ year and the third step is coresponded to the $t \approx 0.99 \cdot 10^9$ year.

The final state of evolution is coresponded to the $t \approx 1.61 \cdot 10^9$ year. In this step the distribution of density is very flat and coresponds to the power law, with central density $\rho_c \approx 0.2 \text{ cm}^{-3}$. In the central core (up to 50 kpc)

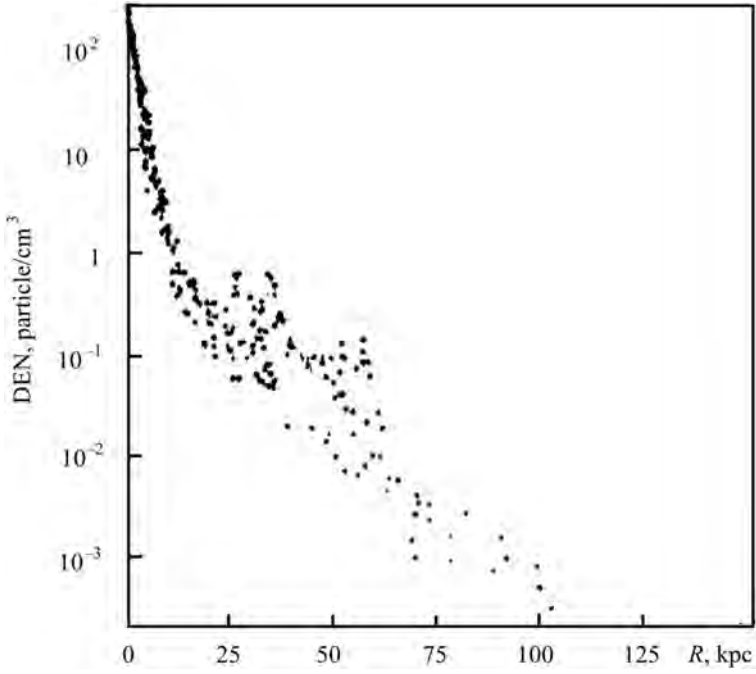


Fig. 4.19. Density distribution of step 40 in model B1

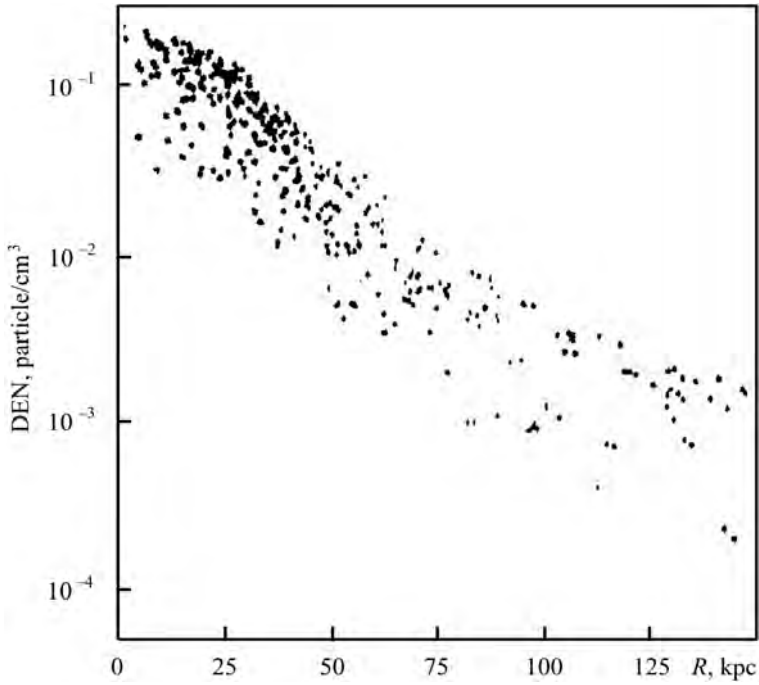


Fig. 4.20. Density distribution of step 54 in model TT1A

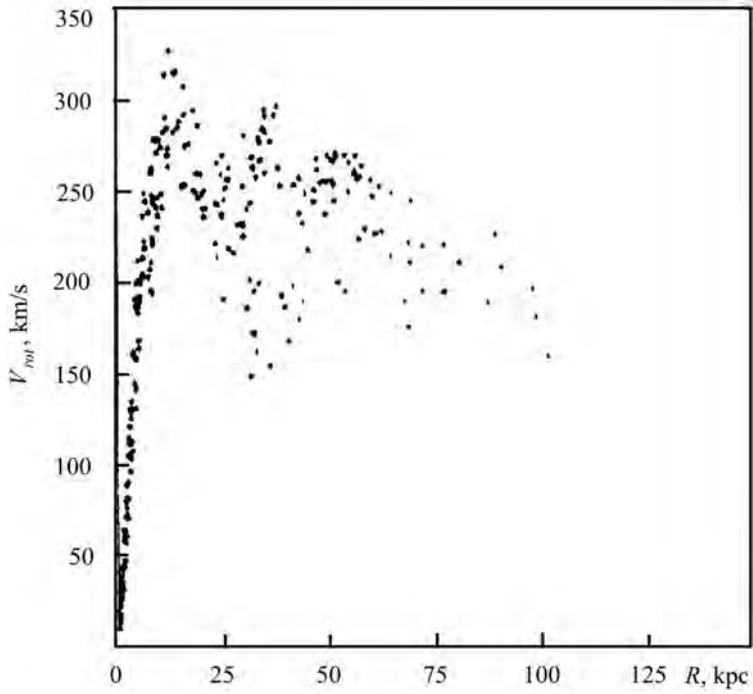


Fig. 4.21. Rotational velocity V_{rot} of step 40 in model B1

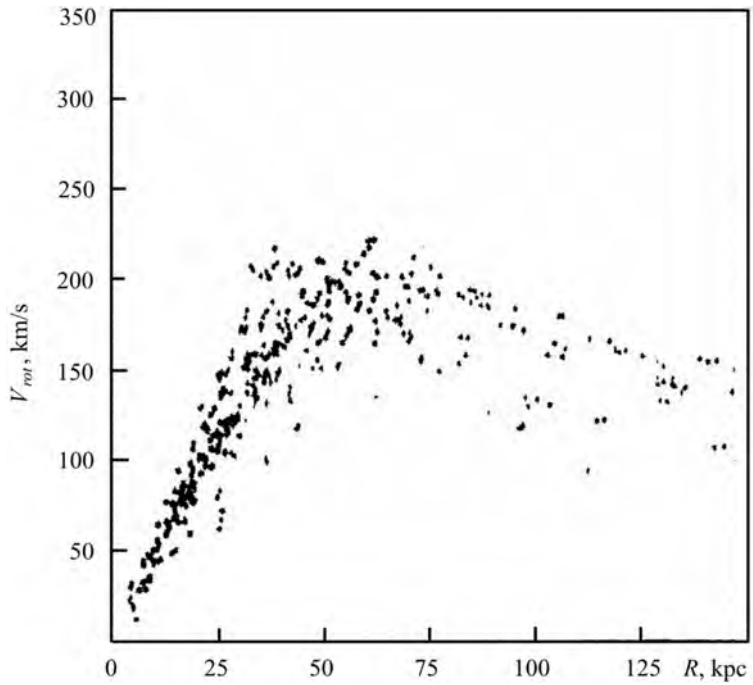


Fig. 4.22. Rotational velocity V_{rot} of step 54 in model TT1A

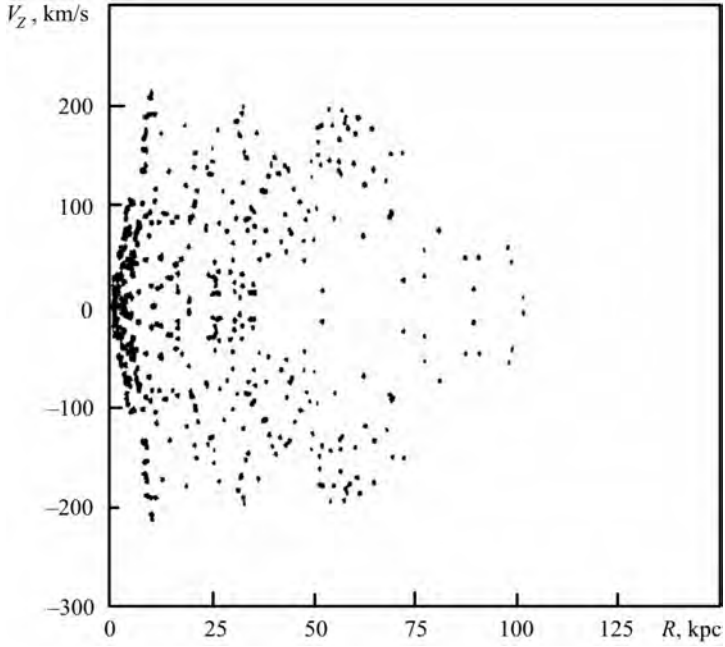


Fig. 4.23. Velocity distribution V_z (perpendicular to the plane of forming galaxy) of step 40 in model B1

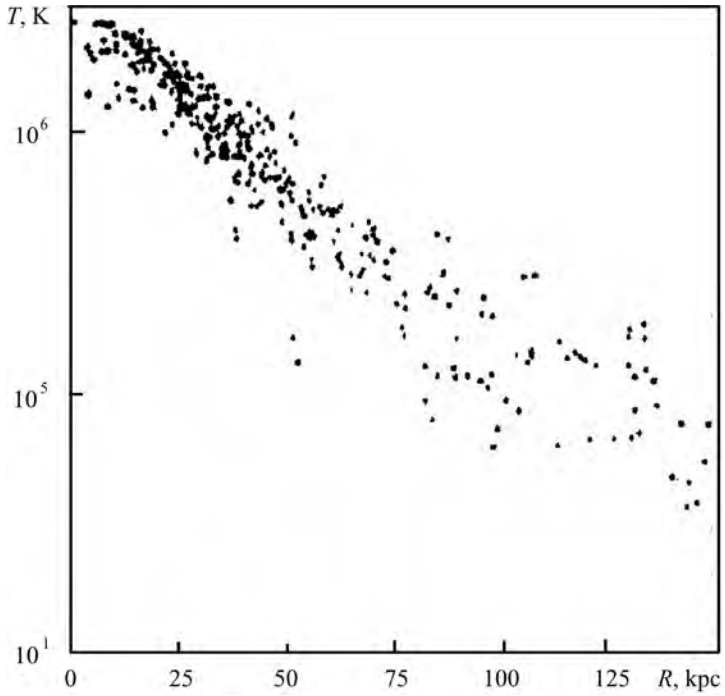


Fig. 4.24. Temperature distribution T of step 54 in model TT1A

the rotation curve is linear and has the maximum value $V_{rot} \approx 200$ km/s. In external part the velocity distribution has the linear, slowly falling trend.

In the Fig. 4.18 we show the more detail view of last step in model TT1A. The diameter of represented cubic cell in figure is 100 kpc.

The density distribution of last step we show in Fig. 4.20, the rotational velocity V_{rot} we show in Fig. 4.22 and the temperature distribution T we show in Fig. 4.24.

This model demonstrates the interesting mechanism of bulge formation. The bulge has triaxial form. Also to be noted, that kinematical properties of central and peripheral part of protogalaxy is definitely different (see Fig. 4.18).

Conclusions. In this paper, we describe the qualitative result of the properties of early, pure gas triaxial protogalaxies, that can be formed in a result of isothermal or adiabatic collapse. We modelling the initial state a protogalaxy as a homogeneous triaxial ellipsoide having an angular momentum directed arbitrary in space.

On the base of model calculation it follows that many interesting and complex properties of galaxies (such as triaxial central bar phenomenon and inclined warp disk structures) we may explain using our suggestion about the initial triaxial shape and angular momentum direction in early protogalaxy.

We may make several general decisions about the early properties of forming protogalaxies:

- In all case the collapse in triaxial model leads to the forming of warp disk structure and the internal bar.
- The dynamical evolution of triaxial model generates the global spiral-like structure. In isothermal model the spiral pattern is more sophisticated and long-living.
- Adiabatic phase of collapse is important for bulge formation and its parameters.
- In case of adiabatic models kinematical properties of core and peripheral parts of protogalactic clouds are extremely different.

4.5. Chemo-dynamical SPH code for evolution of star forming disk galaxies

4.5.1. Introduction

The dynamical and chemical evolution of galaxies is one of the most interesting and complex of problems. Naturally, galaxy formation is closely connected with the process of large-scale structure formation in the Universe.

The main role in the scenario of large-scale structure formation seems to be played by the dark matter. It is believed that the Universe was seeded at some early epoch with low density fluctuations of dark non-baryonic matter, and the

evolving distribution of these dark halos provides the arena for galaxy formation. Galaxy formation itself involves collapse of baryons within potential wells of dark halos [157]. The properties of forming galaxies depend on the amount of baryonic matter that can be accumulated in such halos and the efficiency of star formation. The observational support for this galaxy formation scenario comes from the recent COBE detection of fluctuations in the microwave background (e.g. [8]).

The investigation of galaxy formation is a highly complex subject requiring many different approaches. The formation of self-gravitating inhomogeneities of protogalactic size, the ratio of baryonic and non-baryonic matter [6, 46, 111, 158], the origin of the protogalaxy's initial angular momentum [54, 136, 154, 162], and the protogalaxy's collapse and its subsequent evolution are all usually considered as separate problems. Recent advances in computer technology and numerical methods have allowed detailed modeling of baryon matter dynamics in the universe dominated by collisionless dark matter and, therefore, the detailed gravitational and hydrodynamical description of galaxy formation and evolution. The most sophisticated models include radiative processes, star formation and supernova feedback (e.g. [61, 72, 138]).

The results of numerical simulations are essentially affected by the star formation algorithm incorporated into modeling techniques. The star formation and related processes are still not well understood on either small or large spatial scales, such that the star formation algorithm by which the gas material is converted into stars can only be based on simple theoretical assumptions or on empirical observations of nearby galaxies. The other most important effect of star formation on the global evolution of a galaxy is caused by a large amount of energy released in supernova explosions and stellar winds.

Among numerous methods developed for the modeling of complex three dimensional hydrodynamic phenomena, Smoothed Particle Hydrodynamics (SPH) is one of the most popular [96]. Its Lagrangian nature allows easy combination with fast N-body algorithms, making it suitable for simultaneous description of the complex dynamics of a gas-stellar system [61]. As an example of such a combination, the TREE-SPH code [67, 106] was successfully applied to the detailed modeling of disk galaxy mergers [93] and of galaxy formation and evolution [72]. The second good example is a GRAPE-SPH code [138, 139] which was successfully used to model the evolution of disk galaxy structure and kinematics.

In recent years, there have been excellent papers concerning the complex SPH modeling of galaxy formation and evolution [39, 120]. Our code, proposes new "energetic" criteria for SF, and suggest a more realistic account of returned chemically enriched gas fraction via SNII, SNIa and PN events.

The simplicity and numerical efficiency of the SPH method were the main reasons why we chose this technique for the modeling of the evolution of

complex, multi-fragmented triaxial protogalactic systems. We used our own modification of the hybrid N-body/SPH method [9, 21], which we call the chemo-dynamical SPH (CD-SPH) code.

The “dark matter” and “stars” are included in the standard SPH algorithm as the N-body collisionless system of particles, which can interact with the gas component only through gravitation [72]. The star formation process and supernova explosions are also included in the scheme as proposed by Raiteri et al. [120], but with our own modifications.

4.5.2. The CD-SPH code

The SPH code. Continuous hydrodynamic fields in SPH are described by the interpolation functions constructed from the known values of these functions at randomly positioned particles [96]. Following Monaghan & Lattanzio [98] we use for the kernel function W_{ij} the spline expression in the form of:

$$W_{ij} = \frac{1}{\pi h^3} \begin{cases} 1 - \frac{3}{2}u_{ij}^2 + \frac{3}{4}u_{ij}^3, & \text{if } 0 \leq u_{ij} < 1, \\ \frac{1}{4}(2 - u_{ij})^3, & \text{if } 1 \leq u_{ij} < 2, \\ 0, & \text{otherwise,} \end{cases} \quad (4.34)$$

here $u_{ij} = r_{ij}/h$.

To achieve the same level of accuracy for all points in the fluid, it is necessary to use a spatially variable smoothing length. In this case each particle has its individual value of h . Following Hernquist & Katz [67], we write:

$$\langle \rho(\mathbf{r}_i) \rangle = \sum_{j=1}^N m_j \cdot \frac{1}{2} \cdot [W(r_{ij}; h_i) + W(r_{ij}; h_j)]. \quad (4.35)$$

In our calculations the values of h_i were determined from the condition that the number of particles N_B in the neighborhood of each particle within the $2 \cdot h_i$ remains constant [93]. The value of N_B is chosen such that a certain fraction of the total number of “gas” particles N affects the local flow characteristics [68]. If the defined h_i becomes smaller than the minimal smoothing length h_{min} , we set the value $h_i = h_{min}$. For “dark matter” and “star” particles (with Plummer density profiles) we use, accordingly, the fixed gravitational smoothing lengths h_{dm} and h_{star} .

If the density is computed according to Equation (4.35), then the continuity equation is satisfied automatically. Equations of motion for particle i are

$$\frac{d\mathbf{r}_i}{dt} = \mathbf{v}_i, \quad (4.36)$$

$$\frac{d\mathbf{v}_i}{dt} = -\frac{\nabla_i P_i}{\rho_i} + \mathbf{a}_i^{vis} - \nabla_i \Phi_i - \nabla_i \Phi_i^{ext}, \quad (4.37)$$

where P_i is the pressure, Φ_i is the self gravitational potential, Φ_i^{ext} is a gravitational potential of possible external halo and \mathbf{a}_i^{vis} is an artificial viscosity term [69]. The energy equation has the form:

$$\frac{du_i}{dt} = -\frac{P_i}{\rho_i} \nabla_i \mathbf{v}_i + \frac{\Gamma_i - \Lambda_i}{\rho_i}, \quad (4.38)$$

Here u_i is the specific internal energy of particle i . The term $(\Gamma_i - \Lambda_i)/\rho_i$ accounts for non adiabatic processes not associated with the artificial viscosity (in our calculations $\Gamma_i \equiv 0$). We present the radiative cooling in the form:

$$\Lambda_i = \Lambda_i(u_i, \rho_i) = \Lambda_i^*(T_i) \cdot n_i^2, \quad (4.39)$$

where n_i is the hydrogen number density and T_i the temperature. To follow its subsequent thermal behaviour in numerical simulations, we use an analytical approximation of the standard cooling function $\Lambda^*(T)$ for an optically thin primordial plasma in ionization equilibrium [45, 73]. Its absolute cutoff temperature is set equal to 10^4 K.

The equation of state must be added to close the system.

$$P_i = \rho_i \cdot (\gamma - 1) \cdot u_i, \quad (4.40)$$

where $\gamma = 5/3$ is the adiabatic index.

Time integration. To solve the system of Equations (4.36), (4.37) and (4.38) we use the leapfrog integrator [67]. The time step δt_i for each particle depends on the particle's acceleration \mathbf{a}_i and velocity \mathbf{v}_i , as well as on viscous forces. To define δt_i we use the relation from Hiotelis & Voglis [68], and adopt Courant's number $C_n = 0.1$.

We carried out [20] a large series of test calculations to check that the code is correct, the conservation laws are obeyed and the hydrodynamic fields are represented adequately, all with good results.

The star formation algorithm. It is well known that star formation (SF) regions are associated with giant molecular complexes, especially with regions that are approaching dynamical instability. The early phase of star formation does not seem to crucially affect the dynamics of a galaxy. From the beginning of the collapse, such a system decouples from its surroundings and evolves on a completely different timescale. When the chemically enriched gas content of the galaxy decreases, the heating by winds and supernova explosions [81] begins to play an important role in the dynamics of the galaxy. The overall picture of star formation seems to be understood, but the detailed physics of star formation and accompanying processes, on either small or large scales, remains sketchy [79, 131].

All the above stated as well as computer constraints cause the using of simplified numerical algorithms of description of conversion of the gaseous

material into stars, which are based on simple theoretical assumptions and/or on results of observations of nearby galaxies.

To describe of the process of converting of gaseous material into stars we modify the standard SPH star formation algorithm [72, 106], taking into account the presence of random motions in the gaseous environment and the time lag between the initial development of suitable conditions for star formation and star formation itself [9, 21]. The first reasonable requirement incorporated into this algorithm allows selecting “gas” particles that are potentially eligible to form stars. It states that in the separate “gas” particle the SF can start if the absolute value of the “gas” particle’s gravitational energy exceeds the sum of its thermal energy and the energy of random motions:

$$|E_i^{gr}| > E_i^{th} + E_i^{ch}. \quad (4.41)$$

Gravitational and thermal energies and the energy of random motions for the “gas” particle i in model simulation are defined as:

$$\begin{cases} E_i^{gr} = -\frac{3}{5} \cdot G \cdot m_i^2 / h_i, \\ E_i^{th} = \frac{3}{2} \cdot m_i \cdot c_i^2, \\ E_i^{ch} = \frac{1}{2} \cdot m_i \cdot \Delta v_i^2, \end{cases} \quad (4.42)$$

where $c_i = \sqrt{\mathfrak{R} \cdot T_i / \mu}$ is the isothermal sound speed of particle i . We set $\mu = 1.3$ and define the random or “turbulent” square velocities near particle i as:

$$\Delta v_i^2 = \sum_{j=1}^{N_B} m_j \cdot (\mathbf{v}_j - \mathbf{v}_c)^2 / \sum_{j=1}^{N_B} m_j, \quad (4.43)$$

where:

$$\mathbf{v}_c = \sum_{j=1}^{N_B} m_j \cdot \mathbf{v}_j / \sum_{j=1}^{N_B} m_j. \quad (4.44)$$

For practical reasons, it is useful to define a critical temperature for SF onset in particle i as:

$$T_i^{crit} = \frac{\mu}{3\mathfrak{R}} \cdot \left(\frac{8}{5} \cdot \pi \cdot G \cdot \rho_i \cdot h_i^2 - \Delta v_i^2 \right). \quad (4.45)$$

Then, if the temperature of the “gas” particle i , drops below the critical one, SF can proceed.

$$T_i < T_i^{crit}. \quad (4.46)$$

We think that requirement (4.41), or in another form (4.46), is the only one needed. It seems reasonable that the chosen “gas” particle will produce stars

only if the above condition hold over the interval that exceeds its free – fall time $t_{ff} = \sqrt{3 \cdot \pi / (32 \cdot G \cdot \rho)}$. This condition is based on the well known fact that, due to gravitational instability, all substructures of a collapsing system are formed on such a timescale. Using it, we exclude transient structures, that are destroyed by the tidal action of surrounding matter from consideration.

We also define which “gas” particles remain cool, i.e. $t_{cool} < t_{ff}$. We rewrite this condition as presented in Navarro & White [106]: $\rho_i > \rho_{crit}$. Here we use the value of $\rho_{crit} = 0.03 \text{ cm}^{-3}$.

When the collapsing particle i is defined, we create the new “star” particle with mass m^{star} and update the “gas” particle m_i using these simple equations:

$$\begin{cases} m^{star} = \epsilon \cdot m_i, \\ m_i = (1 - \epsilon) \cdot m_i. \end{cases} \quad (4.47)$$

here ϵ , defined as the global efficiency of star formation, is the fraction of gas converted into stars according to the appropriate initial mass function (IMF). The typical values for SF efficiency in our Galaxy on the scale of giant molecular clouds are in the range $\epsilon \approx 0.01 \div 0.4$ [52, 159]. But it is still a little known quantity. In numerical simulation the model parameter has to be checked by comparison of numerical simulation results with available observational data. Here we define ϵ as:

$$\epsilon = 1 - (E_i^{th} + E_i^{ch}) / |E_i^{gr}|, \quad (4.48)$$

with the requirement that all excess mass of the gas component in a star-forming particle, which provides the inequality $|E_i^{gr}| > E_i^{th} + E_i^{ch}$, is transformed into the star component. In the code we set the absolute maximum value of the mass of such a “star” particle $m_{max}^{star} = 2.5 \cdot 10^6 M_\odot$ i.e. $\approx 5\%$ of the initial particle mass m_i .

At the moment of stellar birth, the position and velocities of new “star” particles are equal to those of parent “gas” particles. Thereafter these “star” particles interact with other “gas”, “star” or “dark matter” particles only by gravitation. The gravitational smoothing length for these (Plummer like) particles is set equal to h_{star} .

The thermal SNII feed-back. We try to include the events of SNII, SNIa and PN in the complex gasdynamic picture of galaxy evolution. But, for the thermal budget of the ISM, only SNII plays the main role. Following [72], we assume that the explosion energy is converted totally into thermal energy. The stellar wind action seems not to be essential in the energy budget [56]. The total energy released by SNII explosions (10^{44} J per SNII) within a “star” particle is calculated at each time step and distributed uniformly between the surrounding (i.e. $r_{ij} < h_{star}$) “gas” particles [120].

The chemical enrichment of gas. Every “star” particle in our SF scheme represents a separate, gravitationally closed star formation macro regi-

on (like a globular cluster). The “star” particle is characterized by its own time of birth t_{begSF} which is set equal to the moment of particle formation. After the formation, these particles return the chemically enriched gas into surrounding “gas” particles due to SNII, SNIa and PN events. For the description of this process we use the approximation proposed by Raiteri et al. [120]. We consider only the production of ^{16}O and ^{56}Fe , and try to describe the full galactic time evolution of these elements, from the beginning to present time (i.e. $t_{evol} \approx 13.0$ Gyr).

With the multi-power IMF law suggested by Kroupa et al. [77], the distribution of stellar masses within a “star” particle of mass m^{star} is then:

$$\Psi(m) = m^{star} \cdot A \cdot \begin{cases} 2^{0.9} \cdot m^{-1.3}, & \text{if } 0.1 \leq m < 0.5, \\ m^{-2.2}, & \text{if } 0.5 \leq m < 1.0, \\ m^{-2.7}, & \text{if } 1.0 \leq m, \end{cases} \quad (4.49)$$

where m is the star mass in solar units. With adopted lower ($m_{low} = 0.1 M_{\odot}$) and upper ($m_{upp} = 100 M_{\odot}$) limits of the IMF, the normalization constant $A \approx 0.31$.

For the definition of stellar lifetimes we use the equation [120]:

$$\log t_{dead} = a_0(Z) - a_1(Z) \cdot \log m + a_2(Z) \cdot (\log m)^2, \quad (4.50)$$

where t_{dead} is expressed in years, m is in solar units, and coefficients are defined as:

$$\begin{cases} a_0(Z) = 10.130 + 0.0755 \cdot \log Z - 0.0081 \cdot (\log Z)^2, \\ a_1(Z) = 4.4240 + 0.7939 \cdot \log Z + 0.1187 \cdot (\log Z)^2, \\ a_2(Z) = 1.2620 + 0.3385 \cdot \log Z + 0.0542 \cdot (\log Z)^2. \end{cases} \quad (4.51)$$

These relations are based on the calculations of the Padova group [3, 26, 36] and give a reasonable approximation to stellar lifetimes in the mass range from $0.6 M_{\odot}$ to $120 M_{\odot}$ and metallicities $Z = 7 \cdot 10^{-5} \div 0.03$ (defined as a mass of all elements heavier than He). In our calculation following Raiteri et al. [120], we assume that Z scales with the oxygen abundance as $Z/Z_{\odot} = ^{16}\text{O}/^{16}\text{O}_{\odot}$. For those metallicities exceeding available data we take the value corresponding to the extremes.

We can define the number of SNII explosions inside a given “star” particle during the time from t to $t + \Delta t$ using a simple equation:

$$\Delta N_{\text{SNII}} = \int_{m_{dead}(t+\Delta t)}^{m_{dead}(t)} \Psi(m) dm, \quad (4.52)$$

where $m_{dead}(t)$ and $m_{dead}(t + \Delta t)$ are masses of stars that end their lifetimes at the beginning and at the end of the respective time step. We assume that

all stars with masses between $8 M_\odot$ and $100 M_\odot$ produce SNII, for which we use the yields from Woosley & Weaver [161]. The approximation formulae from Raiteri et al. [120], defines the total ejected mass by one SNII — m_{ej}^{tot} , as well as the ejected mass of iron — m_{ej}^{Fe} and oxygen — m_{ej}^O as a function of stellar mass (in solar units).

$$\begin{cases} m_{ej}^{tot} = 7.682 \cdot 10^{-1} \cdot m^{1.056}, \\ m_{ej}^{Fe} = 2.802 \cdot 10^{-4} \cdot m^{1.864}, \\ m_{ej}^O = 4.586 \cdot 10^{-4} \cdot m^{2.721}. \end{cases} \quad (4.53)$$

To take into account PN events inside the “star” particle we use the equation, as for (4.52):

$$\Delta N_{PN} = \int_{m_{dead}(t+\Delta t)}^{m_{dead}(t)} \Psi(m) dm. \quad (4.54)$$

Following [125, 127, 152], we assume that all stars with masses between $1 M_\odot$ and $8 M_\odot$ produce PN. We define the average ejected masses (in solar units) of one PN event as [121, 152]:

$$\begin{cases} m_{ej}^{tot} = 1.63, \\ m_{ej}^{Fe} = 0.00, \\ m_{ej}^O = 0.00. \end{cases} \quad (4.55)$$

The method described in [120], and proposed in [63, 88] is used to account for SNIa. In simulations, the number of SNIa exploding inside a selected “star” particle during each time step is given by:

$$\Delta N_{SNIa} = \int_{m_{dead}(t+\Delta t)}^{m_{dead}(t)} \Psi_2(m_2) dm_2. \quad (4.56)$$

The quantity $\Psi_2(m_2)$ represents the initial mass function of the secondary component and includes the distribution function of the secondary’s mass relative to the total mass of the binary system m_B ,

$$\Psi_2(m_2) = m^{star} \cdot A_2 \cdot \int_{m_{inf}}^{m_{sup}} \left(\frac{m_2}{m_B} \right)^2 \cdot m_B^{-2.7} dm_B, \quad (4.57)$$

where $m_{inf} = \max(2 \cdot m_2, 3 M_\odot)$ and $m_{sup} = m_2 + 8 M_\odot$. Following [151] the value of normalization constant we set, equal to $A_2 = 0.16 \cdot A$.

The total ejected mass (in solar units) is [108, 145]:

$$\begin{cases} m_{ej}^{tot} = 1.41, \\ m_{ej}^{Fe} = 0.63, \\ m_{ej}^O = 0.13. \end{cases} \quad (4.58)$$

In summary, a new “star” particle (with metallicity $Z = 10^{-4}$) with mass $10^4 M_\odot$ during the total time of evolution t_{evol} produces:

$$\Delta N_{\text{SNII}} \approx 52.5, \quad \Delta N_{\text{PN}} \approx 1770.0, \quad \Delta N_{\text{SNIa}} \approx 8.48.$$

Fig. 4.27. presents the number of SNII, SNIa and PN events for this “star” particle.

In Fig. 4.29 and Fig. 4.30. we present the returned masses of ^{56}Fe and ^{16}O . We can estimate the total masses (H, He, ^{56}Fe , ^{16}O) (in solar masses) returned to the surrounding “gas” particles due to these processes as:

$$\begin{cases} \Delta m_{\text{SNII}}^{\text{H}} = 477, & \Delta m_{\text{PN}}^{\text{H}} = 2164, & \Delta m_{\text{SNIa}}^{\text{H}} = 4.14, \\ \Delta m_{\text{SNII}}^{\text{He}} = 159, & \Delta m_{\text{PN}}^{\text{He}} = 721.3, & \Delta m_{\text{SNIa}}^{\text{He}} = 1.38, \\ \Delta m_{\text{SNII}}^{\text{Fe}} = 3.5, & \Delta m_{\text{PN}}^{\text{Fe}} = 0.000, & \Delta m_{\text{SNIa}}^{\text{Fe}} = 5.35, \\ \Delta m_{\text{SNII}}^{\text{O}} = 119, & \Delta m_{\text{PN}}^{\text{O}} = 0.000, & \Delta m_{\text{SNIa}}^{\text{O}} = 1.10. \end{cases} \quad (4.59)$$

The cold dark matter halo. In the literature we have found some profiles, sometimes controversial, for the galactic Cold Dark Matter Haloes (CDMH) [5, 103]. For resolved structures of CDMH: $\rho_{halo}(r) \sim r^{-1.4}$ [99]. The structure of CDMH high-resolution N-body simulations can be described by: $\rho_{halo}(r) \sim r^{-1}$ [104, 105]. Finally, in Kravtsov et al. [76], we find that the cores of DM dominated galaxies may have a central profile: $\rho_{halo}(r) \sim r^{-0.2}$.

In our calculations and as a first approximation, it is assumed that the model galaxy halo contains the CDMH component with Plummer-type density profiles [47]:

$$\rho_{halo}(r) = \frac{M_{halo}}{\frac{4}{3}\pi b_{halo}^3} \cdot \frac{b_{halo}^5}{(r^2 + b_{halo}^2)^{\frac{5}{2}}}, \quad (4.60)$$

Therefore for the external force acting on the “gas” and “star” particles we can write:

$$-\nabla_i \Phi_i^{ext} = -G \cdot \frac{M_{halo}}{(r_i^2 + b_{halo}^2)^{\frac{3}{2}}} \cdot \mathbf{r}_i. \quad (4.61)$$

4.5.3. Results and discussion

Initial conditions. After testing our code demonstrated that simple assumptions can lead to a reasonable model of a galaxy. The SPH calculations were carried out for $N_{gas} = 2109$ “gas” particles. According to [106, 120], such a number seems adequate for a qualitatively correct description of the systems behaviour. Even this small a number of “gas” particles produces $N_{star} = 31631$ “star” particles at the end of the calculation.

The value of the smoothing length h_i was chosen to require that each “gas” particle had $N_B = 21$ neighbors within $2 \cdot h_i$. Minimal h_{min} was set equal to

1 kpc, and the fixed gravitational smoothing length $h_{star} = 1$ kpc was used for the “star” particles. Our results show that a value of $N_B \approx 1\% N_{gas}$ provides qualitatively correct treatment of the system’s large scale evolution.

As the initial model (relevant for CDM-scenario) we took a constant-density homogeneous gaseous triaxial configuration ($M_{gas} = 10^{11} M_\odot$) within the dark matter halo ($M_{halo} = 10^{12} M_\odot$). We set $A = 100$ kpc, $B = 75$ kpc and $C = 50$ kpc for semiaxes of system. Such triaxial configurations are reported in cosmological simulations of the dark matter halo formation [54, 60, 155]. Initially, the centers of all particles were placed on a homogeneous grid inside this triaxial configuration. We set the smoothing parameter of CDMH: $b_{halo} = 25$ kpc. These values of M_{halo} and b_{halo} are typical for CDMH in disk galaxies [5, 104, 105].

The gas component was assumed to be cold initially, $T_0 = 10^4$ K. As we see in our calculations, the influence of random motions essentially reduces the dependence of model parameters on the adopted temperature cutoff and, therefore, on the adopted form of the cooling function itself.

The gas was assumed to be involved in the Hubble flow ($H_0 = 65$ km/s/Mpc) and the solid-body rotation around z -axis. We added small random velocity components ($\Delta|\mathbf{v}| = 10$ km/s) to account for the random motions of fragments. The initial velocity field was defined as:

$$\mathbf{v}(x, y, z) = [\Omega(x, y, z) \times \mathbf{r}] + H_0 \cdot \mathbf{r} + \Delta\mathbf{v}(x, y, z), \quad (4.62)$$

where $\Omega(x, y, z)$ is the angular velocity of an initially rigidly rotating system.

The spin parameter in our numerical simulations is $\lambda \approx 0.08$, defined in Peebles [110] as:

$$\lambda = \frac{|\mathbf{L}_0| \cdot \sqrt{|E_0^{gr}|}}{G \cdot (M_{gas} + M_{halo})^{5/2}}, \quad (4.63)$$

\mathbf{L}_0 is the total initial angular momentum and E_0^{gr} is the total initial gravitational energy of a protogalaxy. It is to be noted that for a system in which angular momentum is acquired through the tidal torque of the surrounding matter, the standard spin parameter does not exceed $\lambda \approx 0.11$ [136]. Moreover, its typical values range between $\lambda \approx 0.07_{-0.05}^{+0.04}$, e.g. $0.02 \leq \lambda \leq 0.11$.

Dynamical model. In Fig. 4.25 we present the “XY”, “XZ” and “YZ” distributions of “gas” particles at the final time step ($t_{evol} \approx 13.0$ Gyr). The box size is 50 kpc. In Fig. 4.26 we present the distributions of “star” particles. The “star” distributions have dimensions typical of a disk galaxy. The radial extension is approximately 25–30 kpc. The disk height is around 1–2 kpc. In the center the “bar-like” structure is developed as a result of strong initial triaxial structure whole in the plane of the disk we can see the “spiral-like” distribution of particles, with extended arm filaments. The “gas” particles are located within central 5–10 kpc.



Fig. 4.25. The distribution of “gas” particles in the final step. $t = 13$ Gyr, box size 50 kpc



Fig. 4.26. The distribution of “star” particles in the final step. $t = 13$ Gyr, box size 50 kpc

Except for the central region (< 2 kpc), the gas distribution has an exponential form with radial scale length ≈ 2.8 kpc. The column density distributions of gas $\sigma_{gas}(r)$ and stars $\sigma_*(r)$ are presented in Fig. 4.31. The total column density is defined as: $\sigma_{tot}(r) = \sigma_{gas}(r) + \sigma_*(r)$. The total column density distribution $\sigma_{tot}(r)$ is well approximated (in the interval from 5 kpc to 15 kpc) with an exponential profile characterized by a ≈ 3.5 kpc radial scale length. This value is very close to one reported recently (3.5 kpc) for the radial scale length of the total disk mass surface density distribution obtained for our Galaxy [91]. The value of $\sigma_{tot} \approx 55 M_\odot \text{ pc}^{-2}$ near the location of the Sun ($r \approx 9$ kpc) is close to a recent determination of the total density $52 \pm 13 M_\odot \text{ pc}^{-2}$ [90].

Fig. 4.32 shows both the rotational velocity distribution of gas $V_{rot}(r)$ resulting from the modeled disk galaxy calculation and the rotational curve for our Galaxy [150], both of which are very close.

The gaseous radial $V_{rad}(r)$ and normal $V_z(r)$ velocity distributions are in Fig. 4.33 and Fig. 4.34. The radial velocity dispersion has a maximum value ≈ 60 km/s in the center, a high value mainly caused by the central strong bar structure. Near the Sun this dispersion drops down to ≈ 2 km/s. Such radial

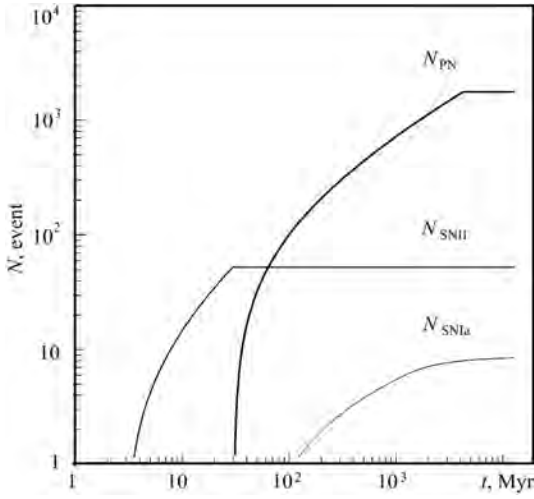


Fig. 4.27. The number of SNIa, SNIa and PN events

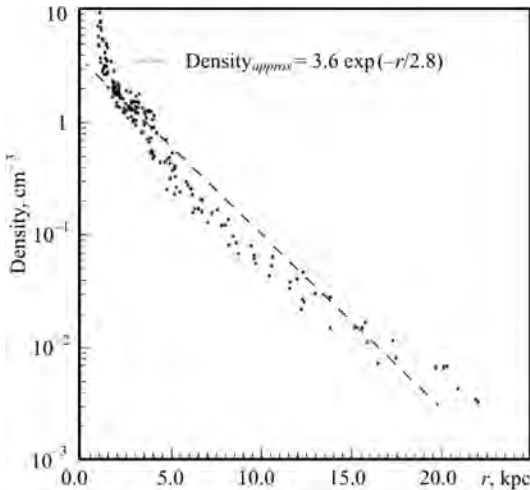


Fig. 4.28. $\rho(r)$. The density distribution of gas in the final step

into stars at the end of calculation. The most intensive SF burst happened in the first ≈ 1 Gyr, with a maximal SFR $\approx 35 M_{\odot}/\text{yr}$. After ≈ 1.5 – 2 Gyr the SFR is decreases like an “exponential function” until it has a value $\approx 1 M_{\odot}/\text{yr}$ at the end of the simulation. To check the SF and chemical enrichment algorithm in our SPH code, we use the chemical characteristics of the disk in the “solar” cylinder ($8 \text{ kpc} < r < 10 \text{ kpc}$).

The age-metallicity relation of the “star” particles in the “solar” cylinder, $[\text{Fe}/\text{H}](t)$, is shown in Fig. 4.37, with observational data taken from [92] and

dispersion is reported in the kinematic study of the stellar motions in the solar neighborhood [9], while the normal dispersion is near $\approx 20 \text{ km/s}$ in the whole disk. This value also coincides with the vertical dispersion velocity near the Sun [9].

We present the temperature distribution of gas $T(r)$ in Fig. 4.35. As seen the distribution of $T(r)$ has a very large scatter from 10^4 K to 10^6 K . In our calculation we set the cutoff temperature for the cooling function at 10^4 K , the gas can’t cool to lower temperatures.

The modeled process of SNIa explosions injects to a great amount of thermal energy into the gas and generates a very large temperature scatter, also typical of our Galaxy’s ISM. At each point even with crude numerical approximations a good fit can be reached for all dynamical and thermal distributions of gas and stars in a typical disk galaxy like our Galaxy.

Chemical characteristics.

Fig. 4.36 shows the time evolution of the SFR in galaxy $SFR(t) = dM_*(t)/dt$. Approximately 90% of gas is converted

[53], while in Fig. 4.38 we presented the metallicity distribution of the “star” particles in the “solar” cylinder $N_*([\text{Fe}/\text{H}])$. The model data are scaled to the observed number of stars [53]. In Fig. 4.37 each model point represents the separate “star” particle. The mass of each “star” particle is different (from $\sim 10^4 M_\odot$ up to $\sim 2.5 \cdot 10^6 M_\odot$), because the star formation efficiency — ϵ is different in each star forming region. The model point is systematically higher than the observations (especially near the $t \approx 5$ Gyr), but if we also analyze the mass of each “star” particle we see that the more massive particles systematically show lower metallicity than the observations. If one divides the metallicity to equal zone and calculate the sum of the mass in each metallicity zone in Fig. 4.37 we get the results in Fig. 4.38 and in this figure we see what the model mass distribution has shifted to the lower metallicities.

The $[\text{O}/\text{Fe}]$ vs. $[\text{Fe}/\text{H}]$ distribution of the “star” particles in the “solar” cylinder one found in Fig. 4.39. In this figure we also present the observational data from [53] and [146]. All these model distributions are in good agreement, not only with presented observational data, but also with other data collected from [117].

The $[\text{O}/\text{H}]$ radial distribution $[\text{O}/\text{H}](r)$ is shown in Fig. 4.40. The approximation presented in the figure is obtained by a least-squares linear fit. At distances $5 \text{ kpc} < r < 11 \text{ kpc}$ the models radial abundance gradient is -0.06 dex/kpc . In the literature we found different values of this gradient defined in objects of different types. From observations of HII regions [112, 129]

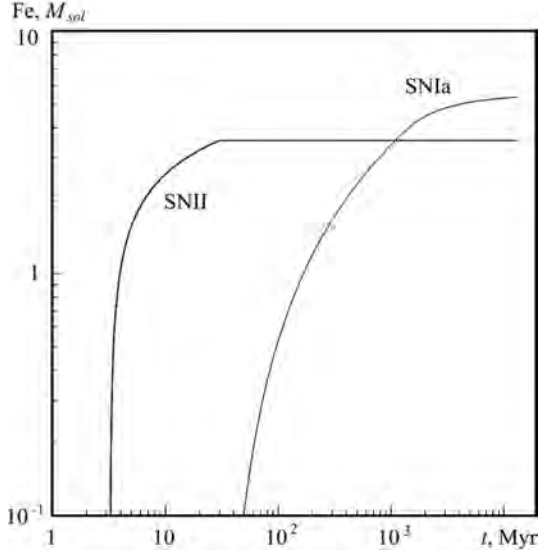


Fig. 4.29. The returned mass of ^{56}Fe

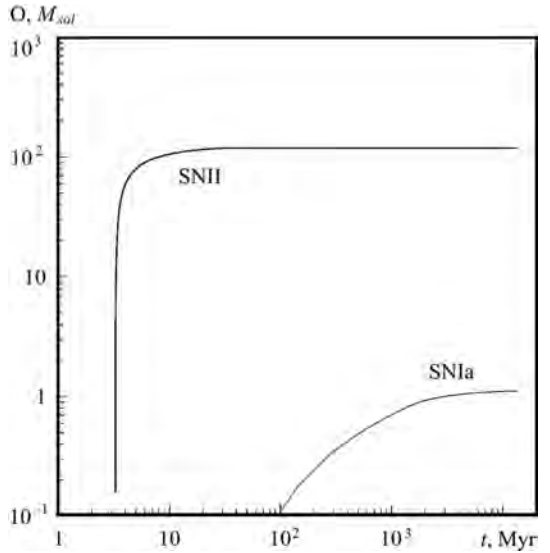


Fig. 4.30. The returned mass of ^{16}O

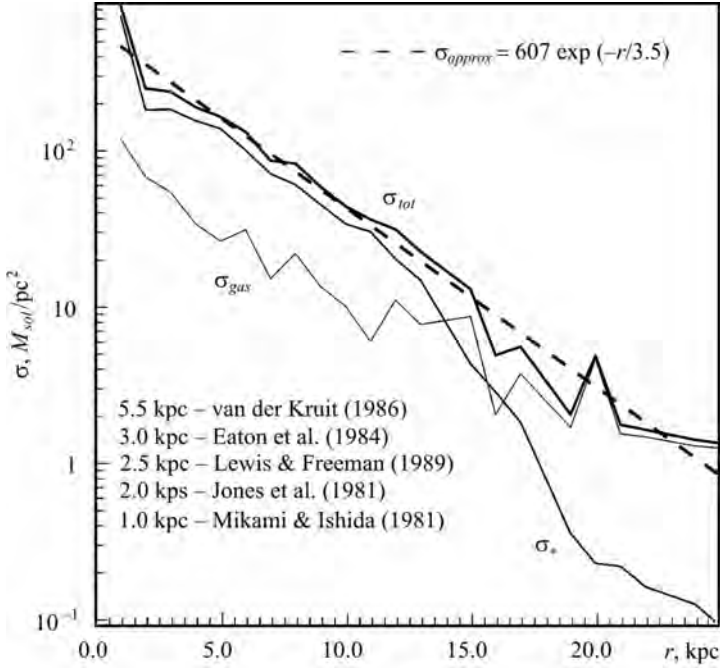


Fig. 4.31. $\sigma_{gas}(r)$, $\sigma_*(r)$ and $\sigma_{tot}(r) = \sigma_{gas}(r) + \sigma_*(r)$. The column density distribution in the disk of gas and stars in the final step

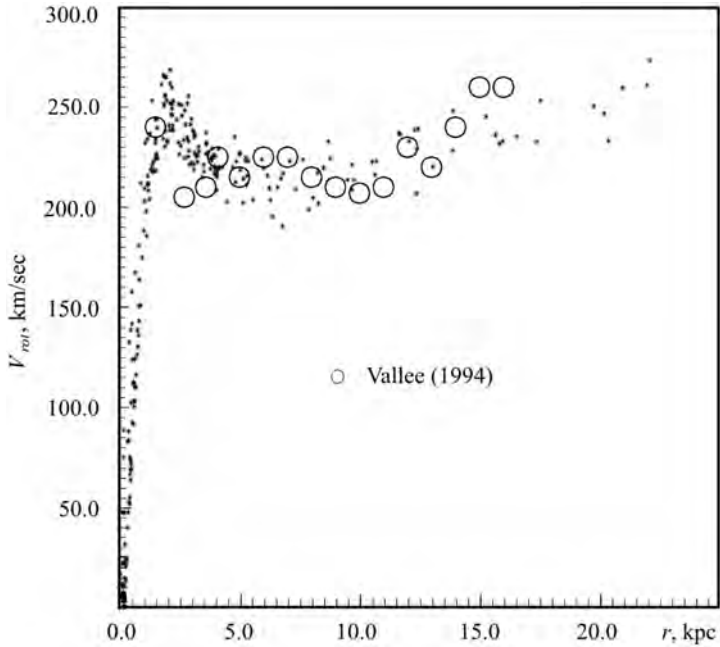


Fig. 4.32. $V_{rot}(r)$. The rotational velocity distribution of gas in the final step

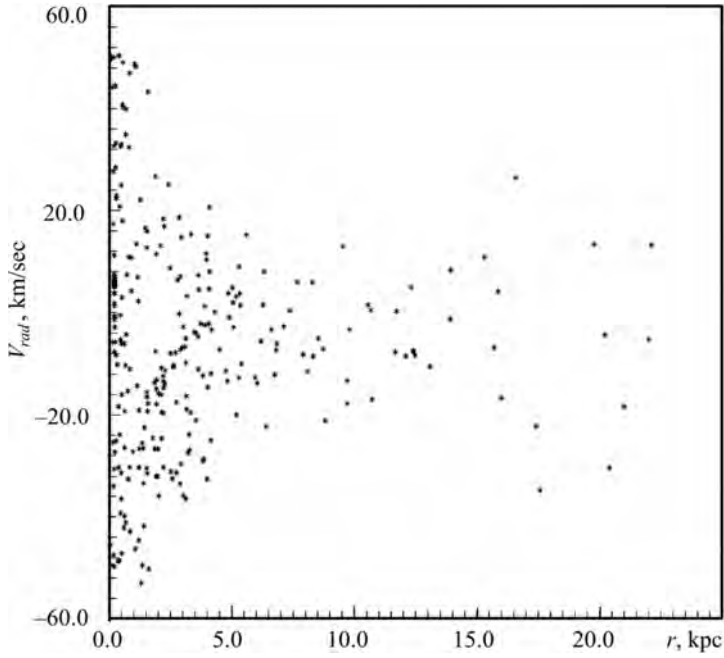


Fig. 4.33. $V_{rad}(r)$. The radial velocity distribution of gas in the final step

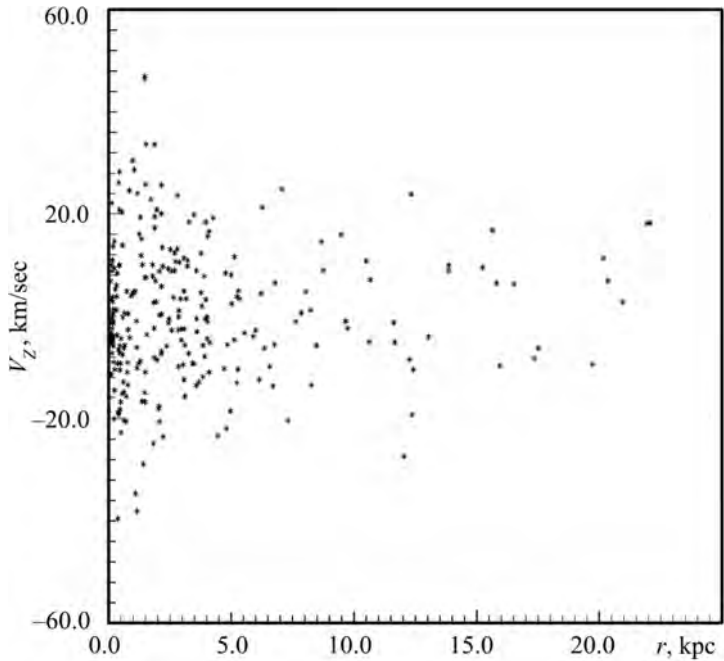


Fig. 4.34. $V_z(r)$. The perpendicular to disk normal velocity distribution of gas in the final step

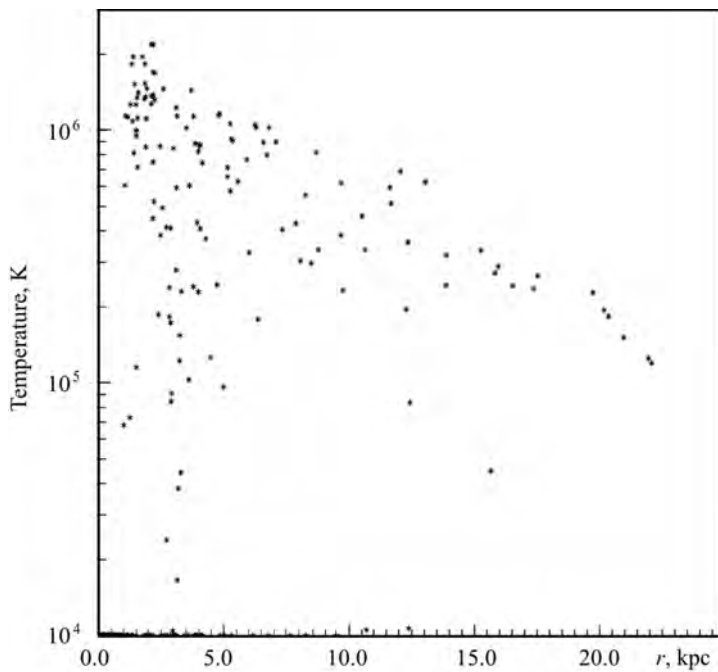


Fig. 4.35. $T(r)$. The temperature distribution of gas in the final step

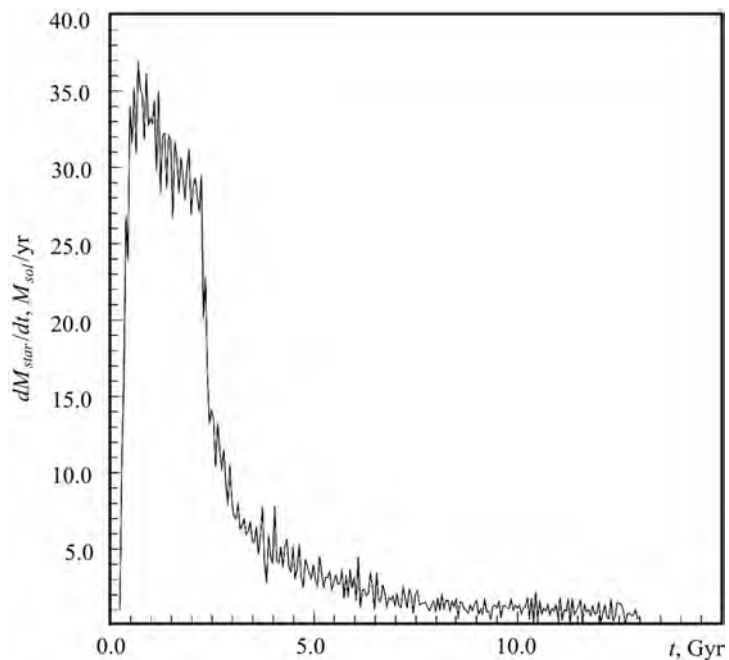


Fig. 4.36. $SFR(t) = dM_*(t)/dt$. The time evolution of the SFR in galaxy

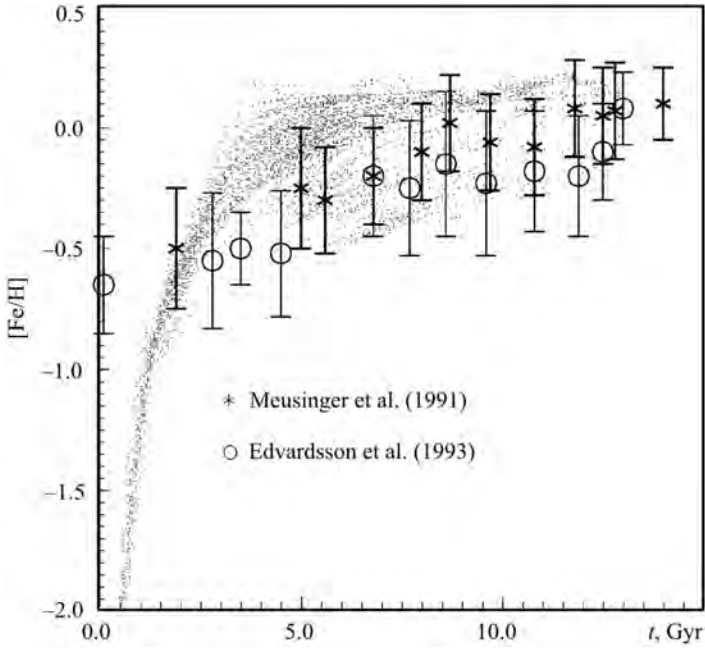


Fig. 4.37. $[\text{Fe}/\text{H}](t)$. The age metallicity relation of the “star” particles in the “solar” cylinder ($8 \text{ kpc} < r < 10 \text{ kpc}$)

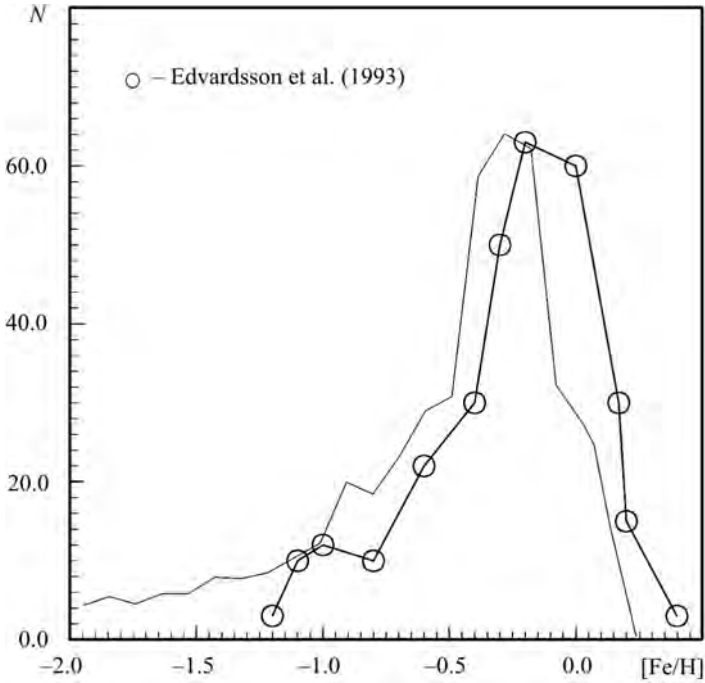


Fig. 4.38. $N_*([\text{Fe}/\text{H}])$. The metallicity distribution of the “star” particles in the “solar” cylinder ($8 \text{ kpc} < r < 10 \text{ kpc}$)

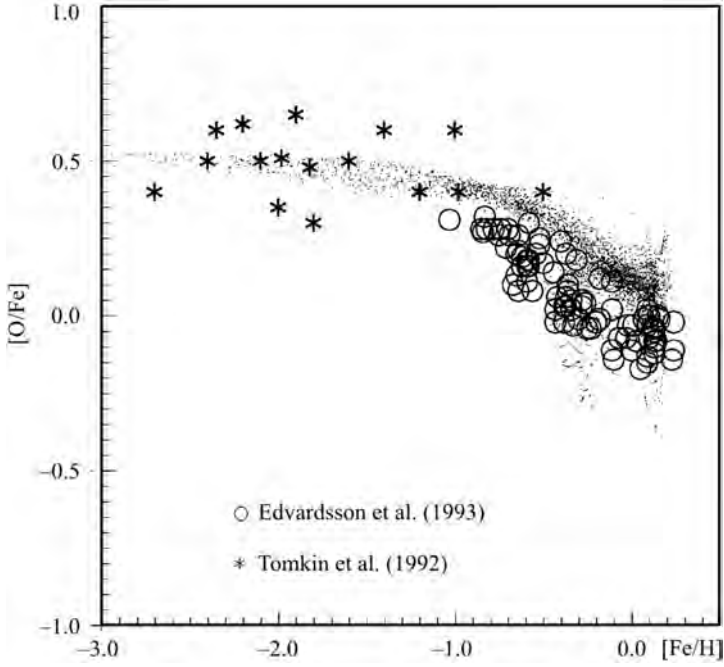


Fig. 4.39. The $[O/Fe]$ vs. $[Fe/H]$ distribution of the “star” particles in the “solar” cylinder ($8 \text{ kpc} < r < 10 \text{ kpc}$)

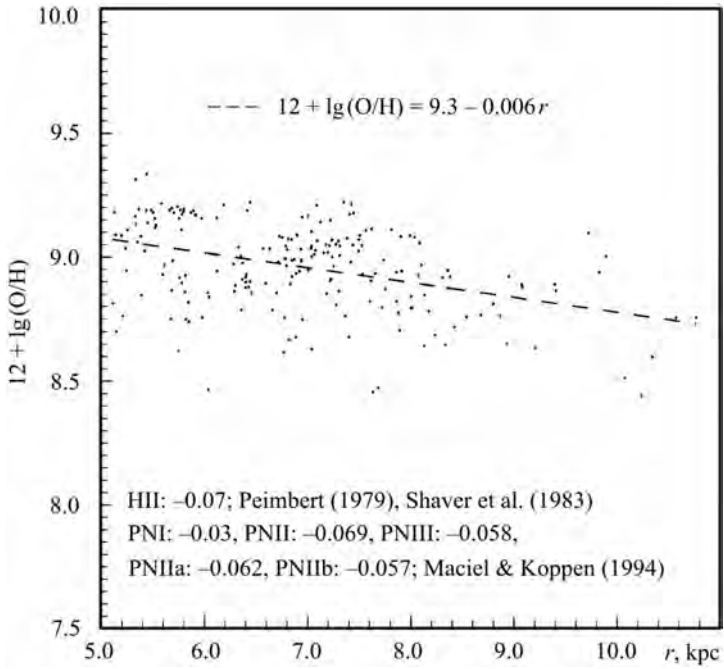


Fig. 4.40. $[O/H](r)$. The $[O/H]$ radial distribution

we obtained oxygen radial gradient -0.07 dex/kpc. From observations of PN of different types [86] we obtained the values: -0.03 dex/kpc for PNI, -0.069 dex/kpc for PNII, -0.058 dex/kpc for PNIII, -0.062 dex/kpc for PNIIa, and -0.057 dex/kpc for PNIIb. All this agrees well with the oxygen radial gradient in our Galaxy.

Conclusion. This simple model provides a reasonable, self-consistent picture of the processes of galaxy formation and star formation in the galaxy. The dynamical and chemical evolution of the modeled disk-like galaxy is coincident with observations for our own Galaxy. The results of our modeling give a good base for a wide use of the proposed SF and chemical enrichment algorithm in other SPH simulations.

4.6. Chemo-photometric evolution of star forming disk galaxy

4.6.1. Introduction

Galaxy formation is a highly complex subject requiring many different approaches of investigation. Recent advances in computer technology and numerical methods have allowed detailed modeling of baryonic matter dynamics in a universe dominated by collisionless dark matter and, therefore, the detailed gravitational and hydrodynamical description of galaxy formation and evolution. The most sophisticated models include radiative processes, star formation and supernova feedback (e.g. [61, 72, 138]).

The results of numerical simulations are fundamentally affected by the star formation algorithm incorporated into modeling techniques. Yet star formation and related processes are still not well understood on either small or large spatial scales. Therefore the star formation algorithm by which gas is converted into stars can only be based on simple theoretical assumptions or on empirical observations of nearby galaxies.

Among the numerous methods developed for modeling complex three dimensional hydrodynamical phenomena, Smoothed Particle Hydrodynamics (SPH) is one of the most popular [96]. Its Lagrangian nature allows easy combination with fast N-body algorithms, making possible the simultaneous description of complex gas-stellar dynamical systems [61]. As an example of such a combination, an TREE-SPH code [67, 106] was successfully applied to the detailed modeling of disk galaxy mergers [93] and of galaxy formation and evolution [72]. A second good example is an GRAPE-SPH code [138, 139] which was successfully used to model the evolution of disk galaxy structure and kinematics.

4.6.2. Model

The hydrodynamical simulations are based on our own coding of the Chemo-Dynamical Smoothed Particle Hydrodynamics (CD-SPH) approach, including feedback through star formation (SF). The dynamics of the “star” component is treated in the frame of a standard N-body approach. Thus, the galaxy consists of “gas” and “star” particles. For a detailed description of the CD-SPH code (the star formation algorithm, the SNII, SNIa and PN production, the chemical enrichment and the initial conditions) the reader is referred to [11, 21]. Here we briefly describe the basic features of our algorithm.

We modify the standard SPH SF algorithm [72, 138, 139], taking into account the presence of chaotic motion in the gaseous environment and the time lag between the initial development of suitable conditions for SF, and SF itself.

Inside a “gas” particle, the SF can start if the absolute value of the “gas” particle gravitational energy exceeds the sum of its thermal energy and energy of chaotic motions:

$$|E_i^{gr}| > E_i^{th} + E_i^{ch}. \quad (4.64)$$

The chosen “gas” particle produces stars only if the above condition holds over the time interval exceeding its free-fall time:

$$t_{ff} = \sqrt{\frac{3 \cdot \pi}{32 \cdot G \cdot \rho}}. \quad (4.65)$$

We also check that the “gas” particles remain cool, i.e. $t_{cool} < t_{ff}$. We rewrite these conditions following [106]:

$$\rho_i > \rho_{crit}. \quad (4.66)$$

We set the value of $\rho_{crit} = 0.03 \text{ cm}^{-3}$.

When the collapsing particle i is defined, we create the new “star” particle with mass m^{star} and update the “gas” particle m_i using these simple equations:

$$\begin{cases} m^{star} = \epsilon \cdot m_i, \\ m_i = (1 - \epsilon) \cdot m_i. \end{cases} \quad (4.67)$$

In the Galaxy, on the scale of giant molecular clouds, the typical values for SF efficiency are in the range $\epsilon \approx 0.01 \div 0.4$ [52, 159].

We did not fix this value but rather also derived ϵ from the “energetics” condition:

$$\epsilon = 1 - \frac{E_i^{th} + E_i^{ch}}{|E_i^{gr}|}. \quad (4.68)$$

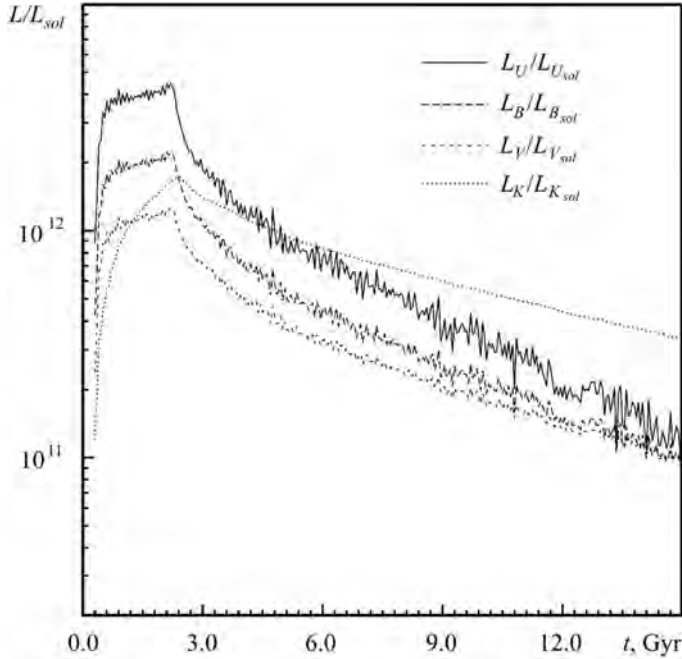


Fig. 4.41. Luminosity evolution of the model galaxy

At the moment of birth, the positions and velocities of new “star” particles are set equal to those of parent “gas” particles. Thereafter these “star” particles interact with other “gas” and “star” or “dark matter” particles only by gravity.

For the thermal budget of the ISM, SNIIs play the main role. Following to [61, 72], we assume that the energy from the explosion is converted totally to thermal energy. The total energy released by SNIi explosions (10^{44} J per SNIi) within “star” particles is calculated at each time step and distributed uniformly between the surrounding “gas” particles [120].

In our SF scheme, every new “star” particle represents a separate, gravitationally bound, star formation macro region (like a globular clusters). The “star” particle has its own time of birth t_{begSF} which is set equal to the moment the particle is formed. After the formation, these particles return the chemically enriched gas into surrounding “gas” particles due to SNIi, SNIa and PN events.

We concentrate our treatment only on the production of ^{16}O and ^{56}Fe , yet attempt to describe the full galactic time evolution of these elements, from the beginning up to present time (i.e. $t_{evol} \approx 15.0$ Gyr).

The code also includes the photometric evolution of each “star” particle, based on the idea of the Single Stellar Population (SSP) [35, 141].

At each time-step, absolute magnitudes: M_U , M_B , M_V , M_R , M_I , M_K , M_M and M_{bol} are defined separately for each “star” particle. The SSP integrated

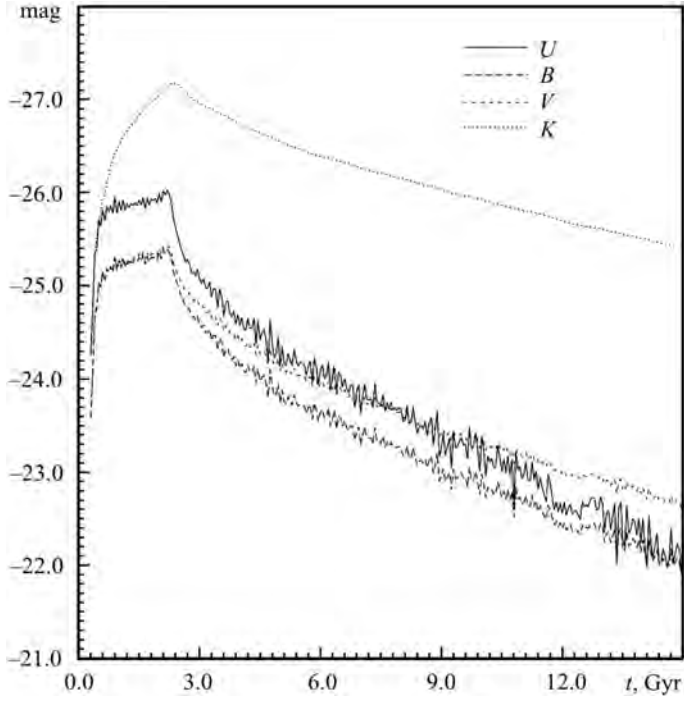


Fig. 4.42. Photometric evolution of the model galaxy

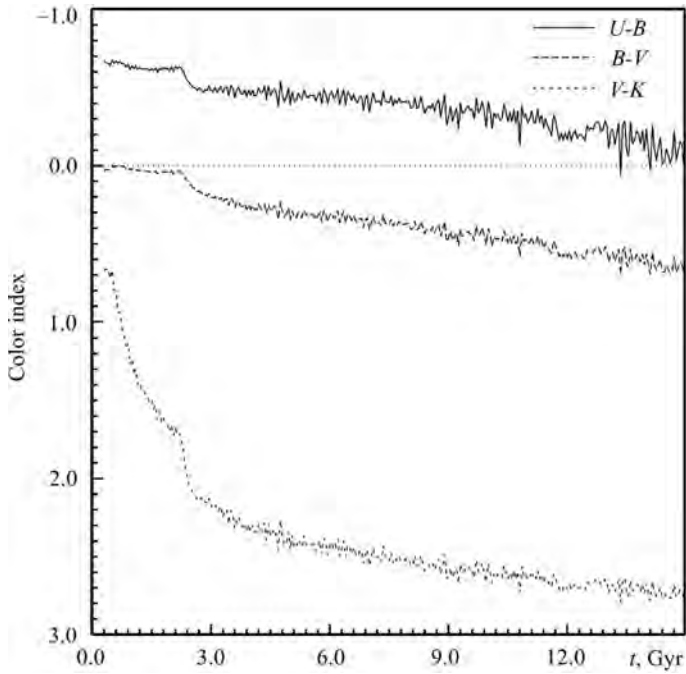


Fig. 4.43. Color index evolution of the model galaxy

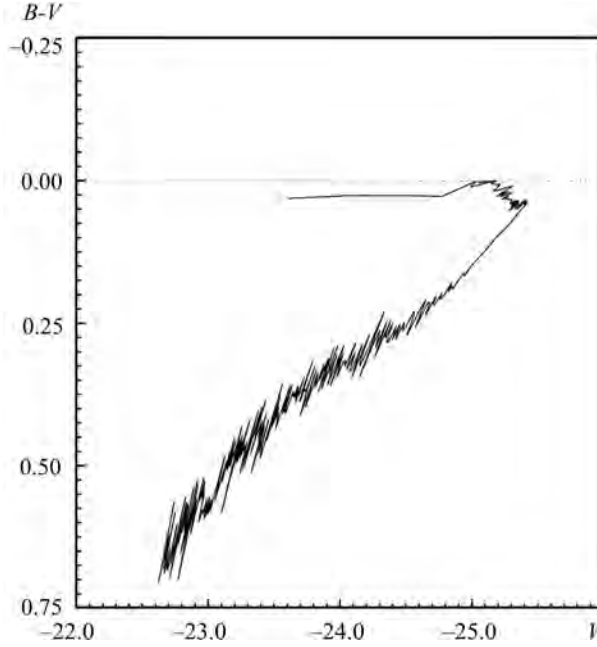


Fig. 4.44. Evolution of the model galaxy in the $(B-V)$ vs. V plane

colours (UBVRIKM) are taken from [141]. The spectro-photometric evolution of the overall ensemble of “star” particles forms the Spectral Energy Distribution (SED) of the galaxy.

We do not model the energy distribution in spectral lines nor the scattered light by dust. However according to [141] our approximation is reasonable, especially in the UBV spectral band.

4.6.3. Results

The model presented describes well the time evolution of the basic chemical and photometric parameters of a disk galaxy similar to the Milky Way. The metallicity, luminosity and colors obtained are typical of such disk galaxies.

- Figure 4.41. Luminosity evolution of the model galaxy.
- Figure 4.42. Photometric evolution of the model galaxy.
- Figure 4.43. Color index evolution of the model galaxy.
- Figure 4.44. Evolution of the model galaxy in the $(B-V)$ vs. V plane.
- Figure 4.45. Evolution of the model galaxy in the $(U-B)$ vs. $(B-V)$ plane.
- Figure 4.46. Evolution of the model galaxy in the $(U-B)$ vs. $(V-K)$ plane.
- Figure 4.47. Evolution of the model galaxy in the $[\text{Fe}/\text{H}]$ vs. V plane.
- Figure 4.48. The “real” M_{star}/L_V evolution of the model galaxy.

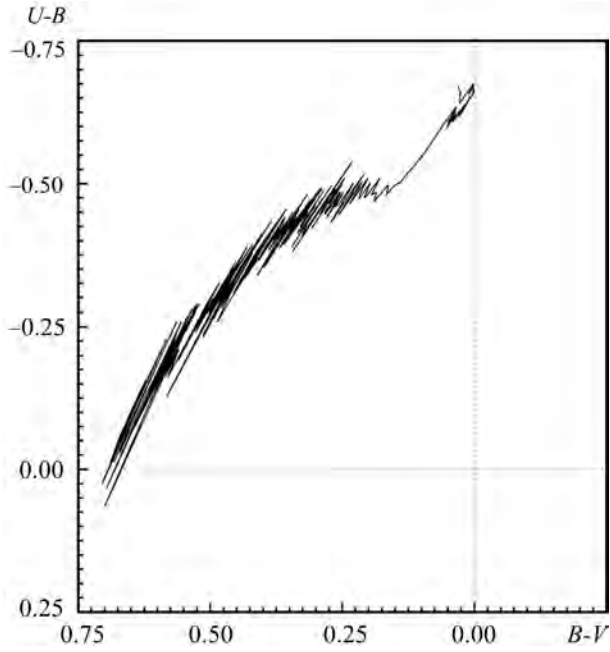


Fig. 4.45. Evolution of the model galaxy in the $(U-B)$ vs. $(B-V)$ plane

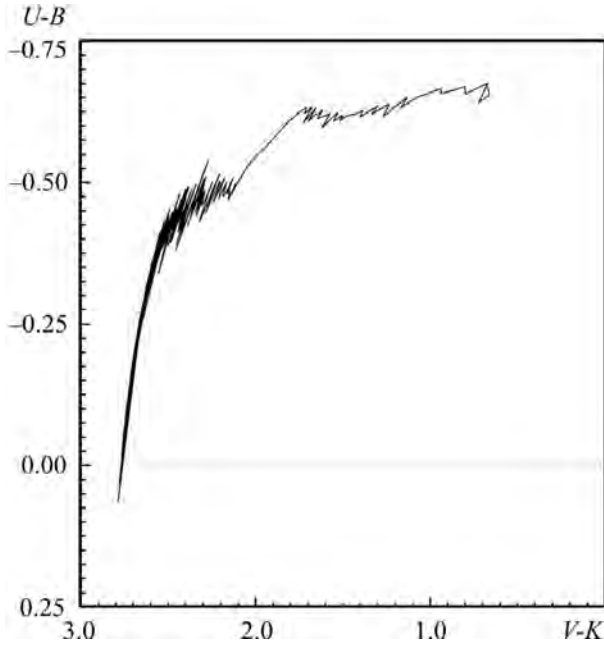


Fig. 4.46. Evolution of the model galaxy in the $(U-B)$ vs. $(V-K)$ plane

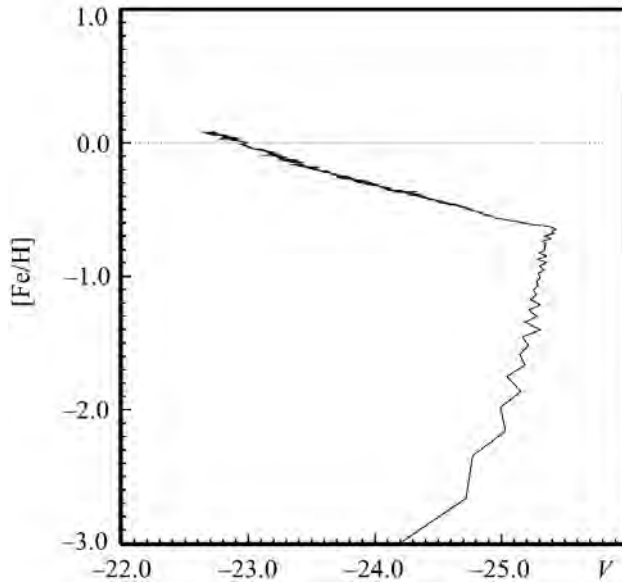


Fig. 4.47. Evolution of the model galaxy in the $[Fe/H]$ vs. V plane

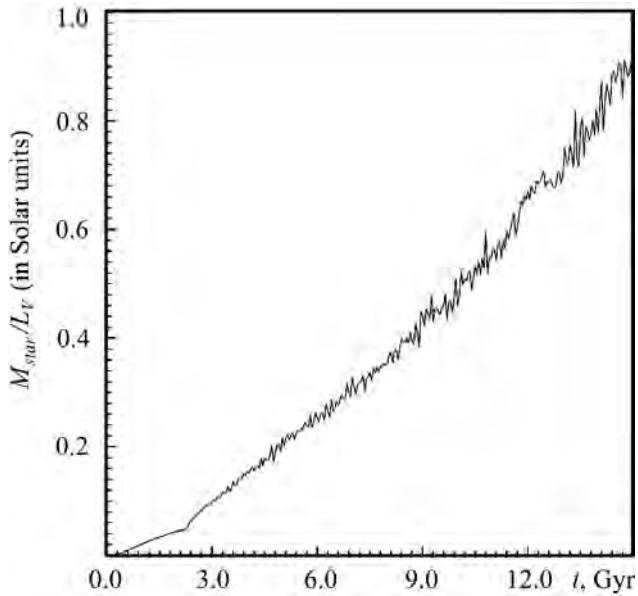


Fig. 4.48. The “real” M_{star}/L_V evolution of the model galaxy

4.7. Multi-phase chemo-dynamical hardware accelerated SPH code for galaxy evolution

4.7.1. Introduction

Since several years the method of smoothed particle hydrodynamics (SPH, [96]) calculations have been applied successfully to study the formation and evolution of galaxies. Its Lagrangian nature as well as its easy implementation together with standard N -body codes allows for a simultaneous description of complex systems consisting of dark matter, gas, and stars [39, 93, 106, 134, 142]. The main features of this SPH variants are: single gas phase, star formation from SPH particles dependent on the mean mass density within each individual particle through their free-fall time, and stellar energy release and mass return to the gas particles. This single-gas phase SPH treatment was successfully applied to the overall evolution of a Milky Way Galaxy model [11, 138, 139] in the sense that they could reproduce main structural and chemical signatures of the global galaxy and of the disk as one substructures like e.g. its density profile and metallicity gradient. The recent largest high resolution single-phase SPH simulations [124] of isolated Milky Way type galaxy (with 10^6 – 10^7 SPH particle numbers) are able to reproduce even the very complex phase substructures in the highly turbulent ISM.

The main critical issue in such a single-phase SPH treatment, that the stellar energy and mass release due to the different processes of stellar feedback (for example SNII and SNIa events) are deposited in the same gas phase particle.

We have therefore developed a 3d chemodynamical code which is based on our single phase galactic evolutionary program. This code includes many complex effects such as a multi-phase ISM, cloud-cloud collisions, a drag force between different ISM components, condensation and evaporation of clouds (CE), star formation (SF) and a stellar feedback (FB). In this sense the multi-phase SPH part of our new code is quite similar to the description proposed on the paper [64].

In our new (multi-phase gas) code we also use a two component gas description of the ISM [127, 143]. The basic idea is to add a cold (10^2 – 10^4 K) cloudy component to the smooth and hot/warm gas (10^4 – 10^7 K) described by SPH. The cold clumps are modeled as sticky N -body particles with some “viscosity” [128, 144]. This “viscosity” modeled the processes of the cloud-cloud collisions and a drag force between clouds and hot/warm gas component. The cloudy component interacts with the surrounding hot/warm gas also via condensation and evaporation processes [43, 74].

In the code we introduce also the star formation from the cold gas component. The “stellar” particles are treated as a dynamically separate (collisionless) N -body component. Each “stellar” particles describes as a separate Single Stellar Population (SSP). Only the cold (cloudy) component forms

the stars. During their evolution, these “stars” return chemically enriched gas material and energy to both gaseous phases. The code also includes the photometric evolution of each “star” particle, based on the idea of the SSP [35, 141]. The summed photometric evolution of the overall ensemble of “star” particles forms the Spectral Energy Distribution (SED) of the whole galaxy. By ideology our “gas” and “star” multi-phase description is significantly different from the recently very popular “hybrid multiphase” model proposed in the paper [133].

In the paper we also present the test results of our newly developed code for galaxy evolution. As a first test, we calculate the self-gravitating collapse of an initially isothermal, cool gas sphere [55, 67, 137]. In this part of the test procedure we concentrate our attention to the test of our “pure” hydro (i.e. SPH) part of the code.

As a second test, we check also our multi-phase description of gas component of the ISM. In this test procedure we compare our condensation and evaporation description with the results of previous 2d mesh multi-phase hydro code [66, 123].

As an example of the complex evolution of the galactic system, here we present the dynamical, chemical and photometric evolution of a star forming dwarf galaxy.

4.7.2. Basic ingredients of the code

“Pure” SPH. Continuous hydrodynamic fields in SPH are described by the interpolation functions constructed from the known values of these functions at randomly positioned N “smooth” particles with individual masses m_i [96]. To achieve the same level of accuracy for all points in the fluid, it is necessary to use a spatially variable smoothing length. In this case each particle has its individual value of smoothing length — h_i .

The more detail and complete description of the basic numerical equations of SPH the reader can find in many previous publications [11, 20, 106, 137] in this reason we here just briefly repeat the skeleton equations of the code. The density at the position of the particle i can be defined as [67]:

$$\rho_i = \sum_{j=1}^N m_j \cdot W_{ij},$$

where:

$$W_{ij} = \frac{1}{2} [W(|\mathbf{r}_i - \mathbf{r}_j|; h_i) + W(|\mathbf{r}_i - \mathbf{r}_j|; h_j)].$$

Following [98] we use for the kernel function W_{ij} the classical spline expression

in the form:

$$W(r; h) = \frac{1}{\pi h^3} \begin{cases} 1 - \frac{3}{2}(r/h)^2 + \frac{3}{4}(r/h)^3, & 0 \leq r/h < 1, \\ \frac{1}{4}(2 - r/h)^3, & 1 \leq r/h < 2, \\ 0, & 2 \leq r/h. \end{cases} \quad (4.69)$$

Equations of motion for particle i are:

$$\begin{aligned} \frac{d\mathbf{r}_i}{dt} &= \mathbf{v}_i, \\ \frac{d\mathbf{v}_i}{dt} &= - \sum_{j=1}^N m_j \left(\frac{P_i}{\rho_i^2} + \frac{P_j}{\rho_j^2} + \tilde{\Pi}_{ij} \right) \nabla_i W_{ij} - \nabla_i \Phi_i - \nabla_i \Phi_i^{ext}, \end{aligned}$$

where P_i is the pressure, Φ_i is the self gravitational potential, Φ_i^{ext} is a gravitational potential of possible external halo and $\tilde{\Pi}_{ij}$ is an artificial viscosity term. This term we write in a form [5, 97, 135]:

$$\tilde{\Pi}_{ij} = \frac{1}{2}(f_i + f_j)\Pi_{ij}f_i = \frac{|(\nabla \cdot \mathbf{v})_i|}{|(\nabla \cdot \mathbf{v})_i| + |(\nabla \times \mathbf{v})_i| + \epsilon c_i/h_i},$$

where:

$$\begin{aligned} \Pi_{ij} &= \begin{cases} \left[-\alpha c_{ij} \mu_{ij} + \beta \mu_{ij}^2 \right] / \rho_{ij}, & \text{if } (\mathbf{r}_{ij} \cdot \mathbf{v}_{ij}) < 0, \\ 0, & \text{else,} \end{cases} \\ \mu_{ij} &= \frac{h_{ij}(\mathbf{v}_i - \mathbf{v}_j) \cdot (\mathbf{r}_i - \mathbf{r}_j)}{|\mathbf{r}_i - \mathbf{r}_j|^2 + \epsilon h_{ij}^2}, \\ h_{ij} &= \frac{1}{2}(h_i + h_j), \rho_{ij} = \frac{1}{2}(\rho_i + \rho_j). \end{aligned}$$

The internal energy equation has the form:

$$\frac{du_i}{dt} = \frac{1}{2} \sum_{j=1}^N m_j \left(\frac{P_i}{\rho_i^2} + \frac{P_j}{\rho_j^2} + \tilde{\Pi}_{ij} \right) (\mathbf{v}_i - \mathbf{v}_j) \nabla_i W_{ij} + \frac{\Gamma_i - \Lambda_i}{\rho_i}.$$

Here u_i is the specific internal energy of particle i . The term $(\Gamma_i - \Lambda_i)/\rho_i$ accounts for non adiabatic processes not associated with the artificial viscosity. We present the radiative cooling in the form proposed by [102] (see case ‘‘B’’) using the MAPPINGS III software [140]:

$$\begin{aligned} \Lambda &= \Lambda(\rho, u, Z, \dots) \simeq \Lambda^*(T, [\text{Fe}/\text{H}]) \cdot n_i^2, \\ n_i &= \rho_i / (\mu \cdot m_p), \end{aligned}$$

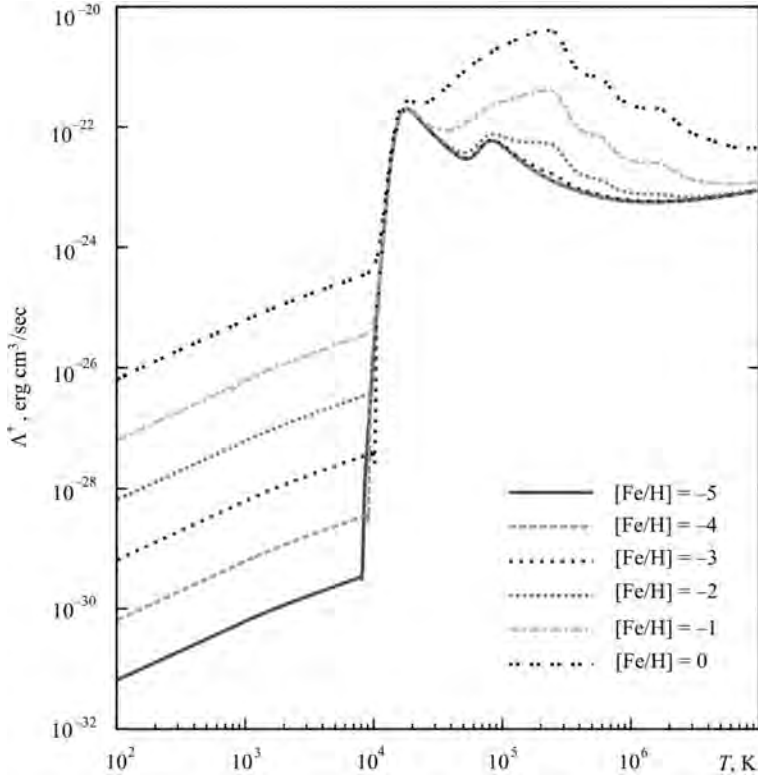


Fig. 4.49. The normalized cooling function used in the code for different metallicities

where n_i is the hydrogen number density, T_i the temperature and μ the molecular weight. The resulting cooling function for the wide range of metallicities are presented in the Fig. 4.49.

The equation of state must be added to close the system:

$$P_i = (\gamma - 1)\rho_i \cdot u_i,$$

where γ is the adiabatic index.

In SPH, one of the basic tasks is to find the nearest neighbors of each SPH particle i.e. to construct its interaction lists for all particles. Basically we need to find all particles with $|\mathbf{r}_{ij}| \leq 2 \max(h_i, h_j)$ in order to estimate the density and also calculate the hydrodynamical forces.

In our code we decide to keep the number of neighbors exactly constant by defining $2h_i$ to be the distance to the N_B – nearest particle [93]. The value of N_B is chosen such that a certain fraction of the total number of “gas” particles N affects the local flow characteristics. From these we need to

SELECT the closest N_B particles. Fast algorithms for doing this exist, see [119]. In computational reason, if the defined h_i becomes smaller than the selected minimal smoothing length h_{min} , we set the value $h_i = h_{min}$.

For calculate the self gravitational potential Φ_i and self gravitational force $-\nabla_i\Phi_i$ we use the GRAPE-6A hardware accelerators. The more detail description of the board and the links to the publication about the GRAPE the reader can find in the <http://www.astrogrape.org/> homepage.

In a present code (which is publicly available from the FTP link¹) we use with the GRAPE the simplest particle-particle (PP) summation scheme for the gravity calculation between the particles. Such a simple routine is directly supported by the GRAPE-6A standard library functions. But such a direct PP scheme is efficient only for the relatively low particle numbers (few 10^4 particles). For the larger particle numbers (from $\sim 10^4$ to few 10^6 particles) we already develop the more efficient (but, of course, less accurate) TREE-GRAPE gravity calculation scheme on the base of the [62] paper.

The simulations have been carried out on the dedicated high-performance GRAPE-6A clusters at the Astronomisches Rechen-Institut in Heidelberg², and at the Main Astronomical Observatory in Kiev³.

To the time integration of the system of hydrodynamical equations we use the quite conservative second order Runge–Kutta–Fehlberg scheme. The time step Δt_i for each particle depends on the particle's acceleration \mathbf{a}_i and velocity \mathbf{v}_i , as well as on the sound speed c_i and the heating *vs.* cooling balance:

$$\Delta t = C_n \cdot \min_i \left[\sqrt{\frac{2h_i}{|\mathbf{a}_i|}}; \frac{h_i}{|\mathbf{v}_i|}; \frac{h_i}{c_i}; \frac{u_i}{\dot{u}_i} \right],$$

where $C_n = 0.1$ is the Courant's number. In computational reason, we also can fix the minimal integration time step Δt_{min} .

The integration doing in a two steps:

Predictor step:

$$\begin{cases} \mathbf{r}_i^{n+\frac{1}{2}} = \mathbf{r}_i^n + \mathbf{v}_i^n \cdot \frac{\Delta t}{2} + \mathbf{a}_i^n \cdot \left(\frac{\Delta t}{2}\right)^2 / 2, \\ \mathbf{v}_i^{n+\frac{1}{2}} = \mathbf{v}_i^n + \mathbf{a}_i^n \cdot \frac{\Delta t}{2}, \\ u_i^{n+\frac{1}{2}} = u_i^n + \dot{u}_i^n \cdot \frac{\Delta t}{2}. \end{cases}$$

¹ <ftp://ftp.ari.uni-heidelberg.de/staff/berczik/mp-cd-sph>

² GRACE: see <http://www.ari.uni-heidelberg.de/grace>

³ golowood: <http://www.mao.kiev.ua/golowood/eng>

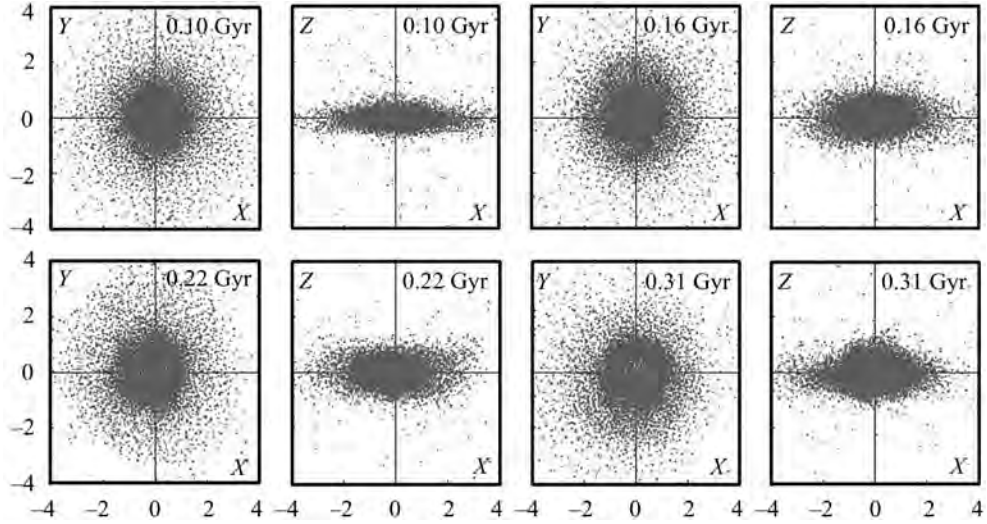


Fig. 4.50. The “hot/warm” (SPH gas) phase particles distribution for the selected different timesteps of the model galaxy. The scale unit is kpc

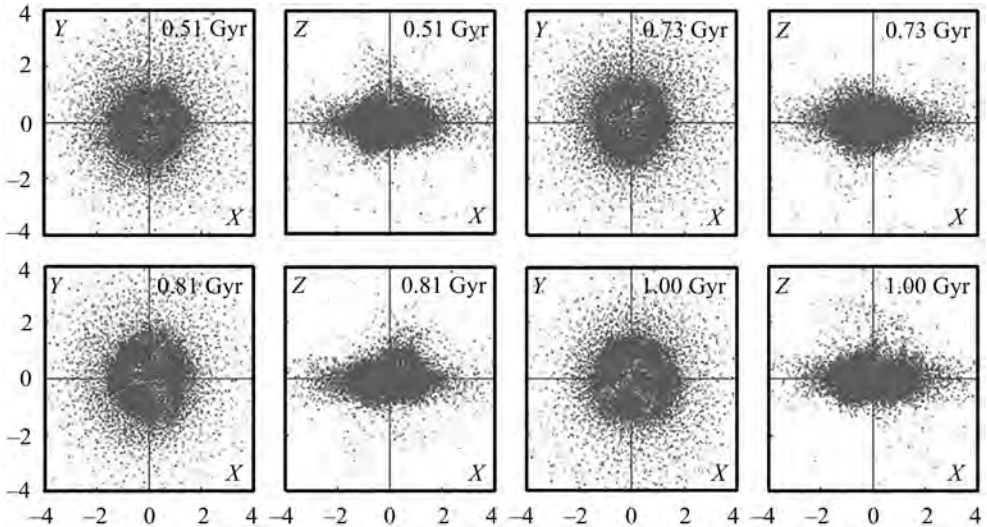


Fig. 4.51. The “hot/warm” (SPH gas) phase particles distribution for the selected different timesteps of the model galaxy. The scale unit is kpc

Corrector step:

$$\begin{cases} \mathbf{r}_i^{n+1} = \mathbf{r}_i^n + \mathbf{v}_i^n \cdot \Delta t + \left[\frac{1}{3} \cdot \mathbf{a}_i^n + \frac{2}{3} \cdot \mathbf{a}_i^{n+\frac{1}{2}} \right] \cdot \frac{\Delta t^2}{2}, \\ \mathbf{v}_i^{n+1} = \mathbf{v}_i^n + \mathbf{a}_i^{n+\frac{1}{2}} \cdot \Delta t, \\ u_i^{n+1} = u_i^n + \dot{u}_i^{n+\frac{1}{2}} \cdot \Delta t. \end{cases}$$

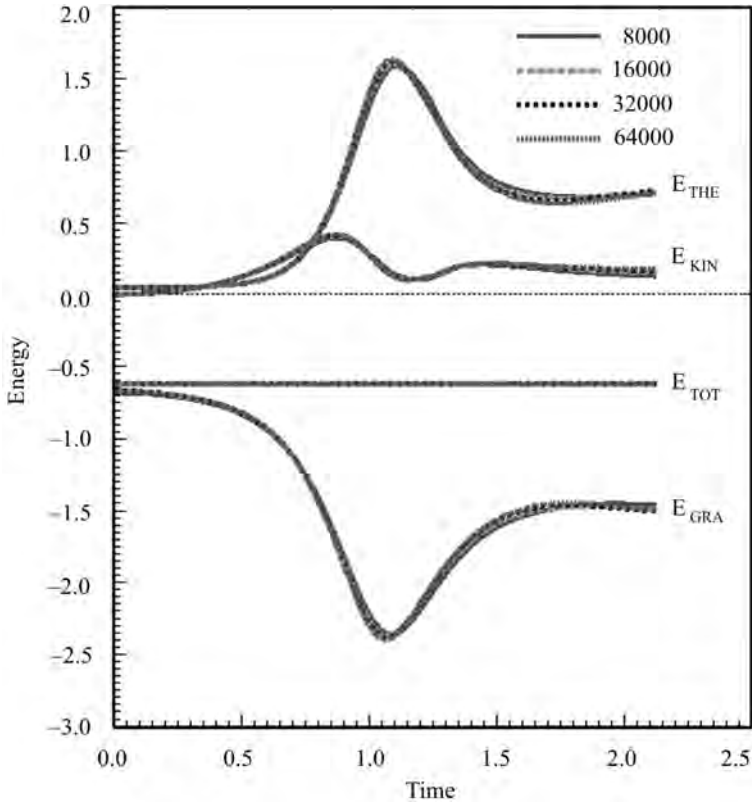


Fig. 4.52. Time evolution of the thermal, kinetic, potential and total energy for the collapse of an initially isothermal gas sphere. The different lines corresponds to the different gas particle numbers

SPH hydro code test. The self-gravitating collapse of an initially isothermal, cool gas sphere has been a common test problem of different SPH codes [39, 55, 67, 134, 137, 142]. Following these authors, we consider a spherically symmetric gas cloud of total mass M , radius R , and initial density profile

$$\rho(r) = \frac{M}{2\pi R^2} \frac{1}{r}.$$

We take the gas to be of constant temperature initially, with an internal energy per unit mass of

$$u = 0.05 \frac{GM}{R}.$$

At the start of the simulation, the gas particles are at rest. We initially distribute randomly the particles inside the set of spherical shells in a manner that reproduces the density profile. We use a system of units with $G = M = R = 1$.

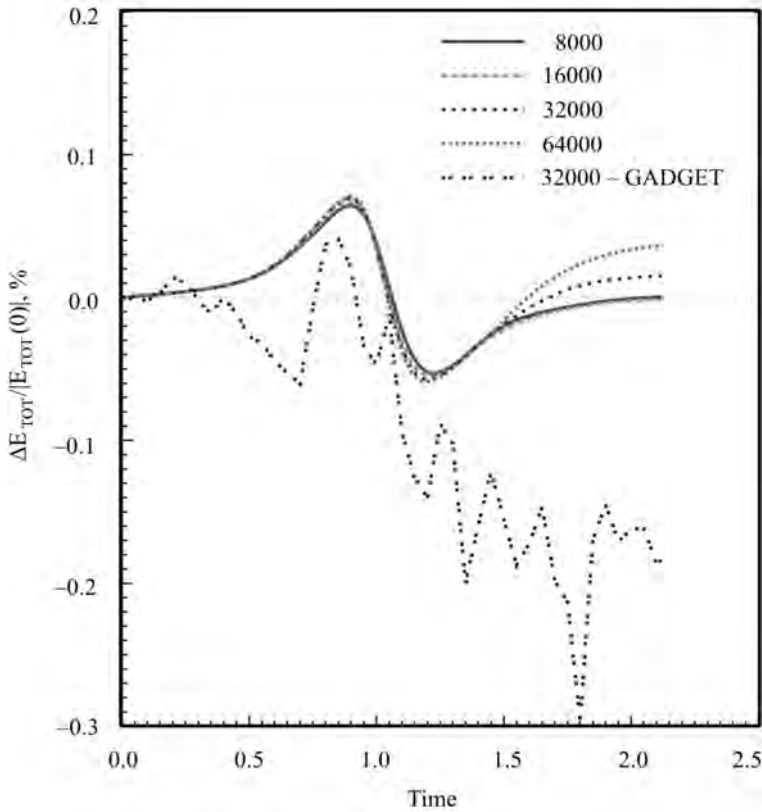


Fig. 4.53. The relative total energy error for different models. The different lines corresponds to the different gas particle numbers. In the figure we also present the energy error results of the GADGET code with “standard” parameters for the 32,000 particles

In Fig. 4.52 and Fig. 4.53 we present the time evolution of the different type of energy and the relative total energy error. In the Fig. 4.53 we also present the energy error results of the public access GADGET SPH code [134] with “standard” parameters for the 32,000 particles. During the central bounce around $t \approx 1.1$ most of the kinetic energy is converted into heat and a strong shock wave travels outward.

For all these runs the number of neighbors was set $N_B = 50$ and the gravitational softening was set $\varepsilon = 0.01$. For the integration of the system of equation we use the second order Runge–Kutta–Fehlberg scheme with fixed time step $\Delta t = 10^{-4}$.

The results presented in the figures agree very well with those of [137] and with [134]. The maximum relative total energy error is around 0.05% even for moderate (8,000) particle numbers.

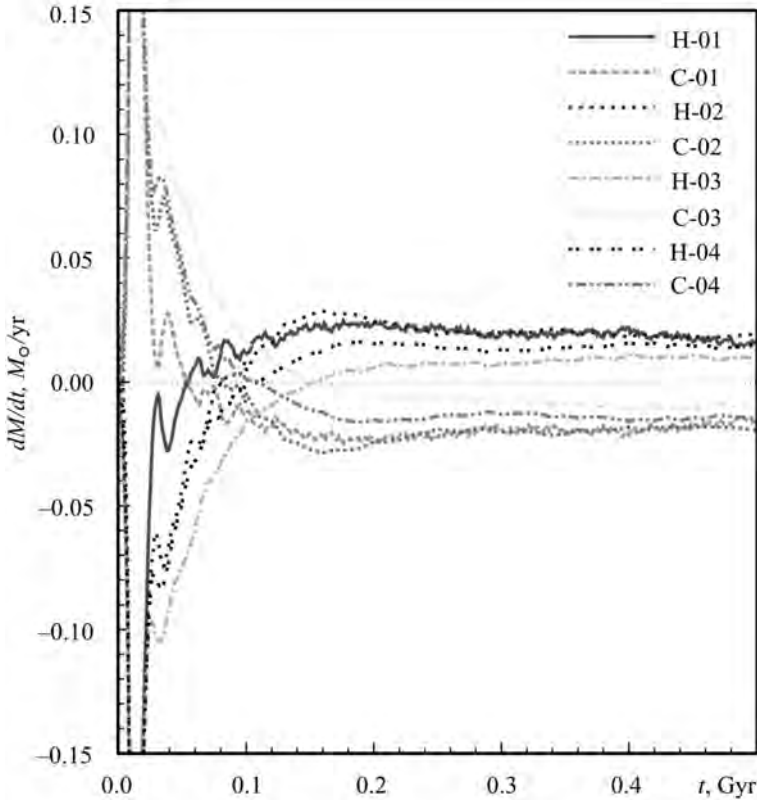


Fig. 4.54. The time evolution of the mass exchange rate due to condensation vs. evaporation (CE) effects (left). The letters indicate the phase (i.e. H – Hot; C – Cold) and the numbers indicate the different models

Multi-phase gas processes. In our (multi-phase gas) code we use a two component gas description of the ISM [127,143]. The basic idea is to add a cold (10^2 – 10^4 K) cloudy component to the smooth and hot/warm gas (10^4 – 10^7 K) described by SPH. The cold clumps are modeled as N-body particles with some “viscosity” [144] (cloud-cloud collisions and drag force between clouds and hot/warm gas component).

For the parametric description of the cold clumps in the code we use the mass *vs.* radius relation for clouds based mainly on observations and also some theoretical work in this direction [80,87,132]:

$$h_{\text{cl}} \simeq 50 \sqrt{\frac{m_{\text{cl}}}{10^6 M_{\odot}}} \text{ (pc)}.$$

This parameterizations has already successfully been applied for the description of the cloudy ISM by [144] and in the cd grid code by [127]. The jump

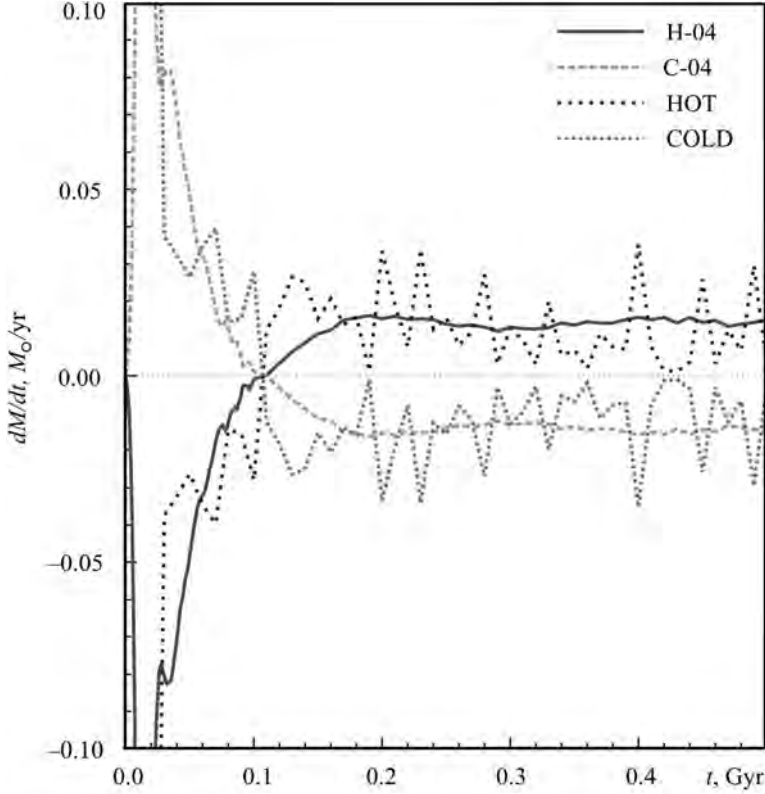


Fig. 4.55. The time evolution of the mass exchange rate due to condensation vs. evaporation (CE) effects. In the figure we compare our “best” model VER-04 with 2d multi phase hydro mesh code results, for the similar initial conditions

in physical conditions of the 2 gas phases causes exchange processes that try to smear out discontinuities. The basic mechanism between “cold” and “hot/warm” gaseous phases is heat conduction that leads to mass and energy exchange as condensation of hot/warm gas or evaporation (CE) of the cold cloud clumps.

In our code we follow the prescription of these processes using the analytical results by [43]. In this model the basic parameter controlling the process of CE is σ_0 , which represents the ratio of the electron mean free path λ_κ and the cloud size h_{cl} :

$$\sigma_0 = \left(\frac{T_{hot}(K)}{1.54 \cdot 10^7} \right)^2 \frac{1}{\Phi n_{hot}(cm^{-3}) h_{cl}(pc)}.$$

If the h_{cl} is smaller than λ_κ ($\sigma_0 > 1$) saturated evaporation occurs. Vice versa, if the temperature of the hot gas becomes low or the cloud size very large,

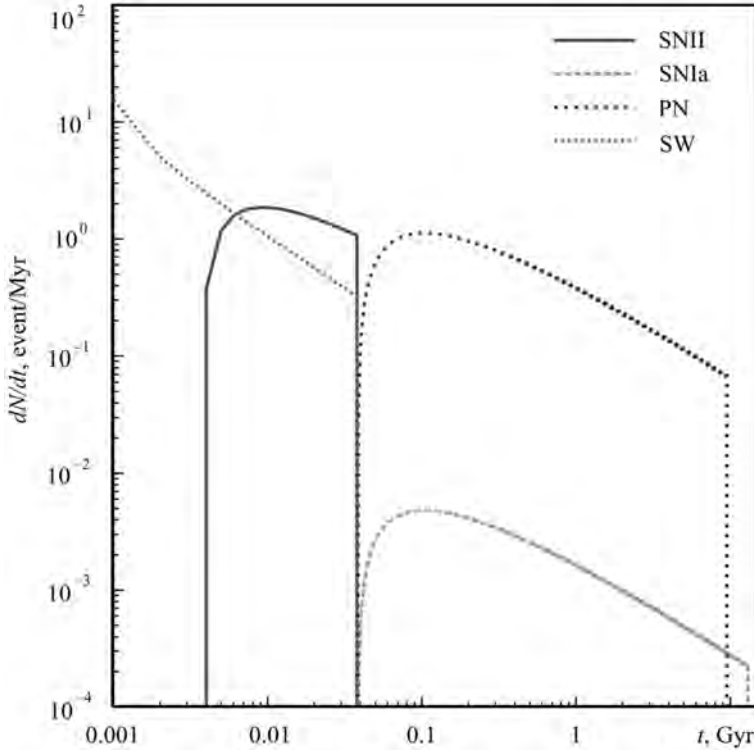


Fig. 4.56. The number rate of SNII, SNIa, PN and SW events for the SSP with the $10^4 M_{\odot}$ and with solar metallicity $Z_{\odot} = 0.02$

the cooling length scale becomes shorter than the cloud size and the conditions change to condensation. For simplicity and as in [43] we just use here $\sigma_0 = 0.03$ as transition value from evaporation to condensation, although a more detailed physical description should invoke the cooling or field length [7, 89].

The rate at which “cold” clouds evaporate to the surrounding “hot/warm” gas or acquire mass from it by condensation is given by:

$$\frac{dm_{\text{cl}}}{dt} (\text{kg/s}) = \begin{cases} 0.825 \cdot T_{\text{hot}}^{5/2} h_{\text{cl}} \sigma_0^{-1}, & \sigma_0 < 0.03, \\ -27.5 \cdot T_{\text{hot}}^{5/2} h_{\text{cl}} \Phi, & 0.03 \leq \sigma_0 \leq 1, \\ -27.5 \cdot T_{\text{hot}}^{5/2} h_{\text{cl}} \Phi \sigma_0^{-5/8}, & \sigma_0 > 1, \end{cases}$$

where we have used $\Phi = 1$ (no inhibition of evaporation by magnetic fields). In the formula we use the (K) and (pc) units for the temperature and cloud radius.

In addition to the mass exchange between the gas phases we include also the momentum transfer by the CE processes.

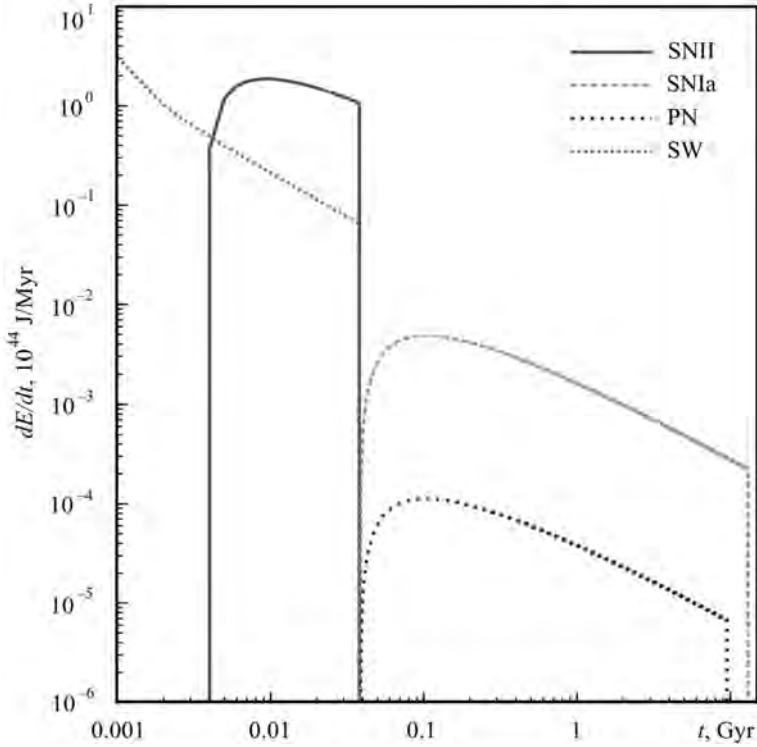


Fig. 4.57. The energy returned rate from the SSP with the $10^4 M_{\odot}$ and with solar metallicity $Z_{\odot} = 0.02$ due to SNIi, SNIa, PN and SW events

Another important effect of dynamical interaction between the two gaseous phases is cloud dragging (DRAG). For this reason we use the prescription proposed in the papers [32, 130]:

$$\frac{d\mathbf{p}_{\text{cl}}}{dt} = -C_{\text{DRAG}} \cdot \pi h_{\text{cl}}^2 \rho_{\text{hot}} \cdot |\mathbf{v}_{\text{cl}} - \mathbf{v}_{\text{hot}}| \cdot (\mathbf{v}_{\text{cl}} - \mathbf{v}_{\text{hot}}),$$

where the drag coefficient C_{DRAG} represents the ratio of the effective cross section of the cloud to its geometrical one πh_{cl}^2 and is set to 0.5. A value of order unity for C_{DRAG} has the physically correct order of magnitude for the forces exerted by a pressure difference before and after a supersonic shock wave [42].

The second important dynamical effect in the evolution of the cloudy medium is a cloud *vs.* cloud collisions (COLL). These processes also can significantly reduce the kinetic energy of the cloudy system. As a first approach for these processes we assume that in each collision the colliding clouds loss only 10% of its kinetic energy.

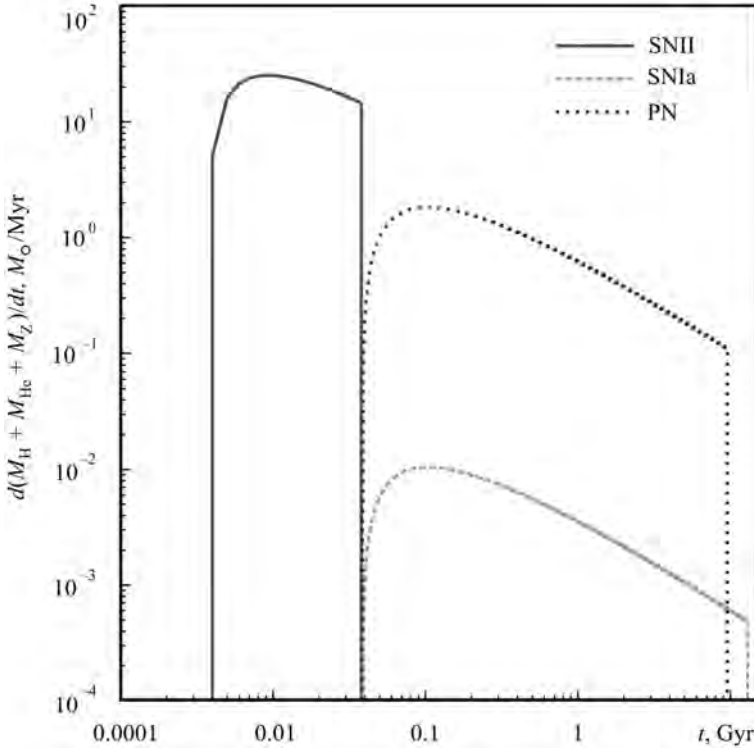


Fig. 4.58. The returned mass rate from the SSP with the $10^4 M_{\odot}$ and with solar metallicity $Z_{\odot} = 0.02$ due to SNII, SNIa and PN events

Condensation/evaporation test. As a CE test for our code, we calculate the isothermal evolution of an isolated “hypothetical” gas system inside a dark matter halo. We directly compare our results with the 2d multi-phase hydro mesh-code [66, 123] for the same system.

The initial total gas content of our test system is $2 \times 10^9 M_{\odot}$ (99% “cold” + 1% “hot/warm”) which is placed inside a fixed dark matter halo with parameters $r_0 = 2$ kpc and $\rho_0 = 2 M_{\odot}/\text{pc}^3$ [37]:

$$\rho_{\text{dm}}(r) = \rho_0 \cdot \frac{r_0^3}{(r + r_0)(r^2 + r_0^2)}.$$

With these parameters the dark matter mass inside the initial gas distribution (20 kpc) is $\simeq 3.2 \times 10^{11} M_{\odot}$. The initial temperatures for the cold gas is set to 2×10^3 K, for the hot gas to 10^6 K. For the initial gas distribution we use a Plummer–Kuzmin disk with parameters $a = 0.1$ kpc and $b = 2$ kpc [94]:

$$\Phi_{\text{gas}}(r, z) = -\frac{G \cdot M_{\text{gas}}}{\sqrt{r^2 + (a + \sqrt{b^2 + z^2})^2}}.$$

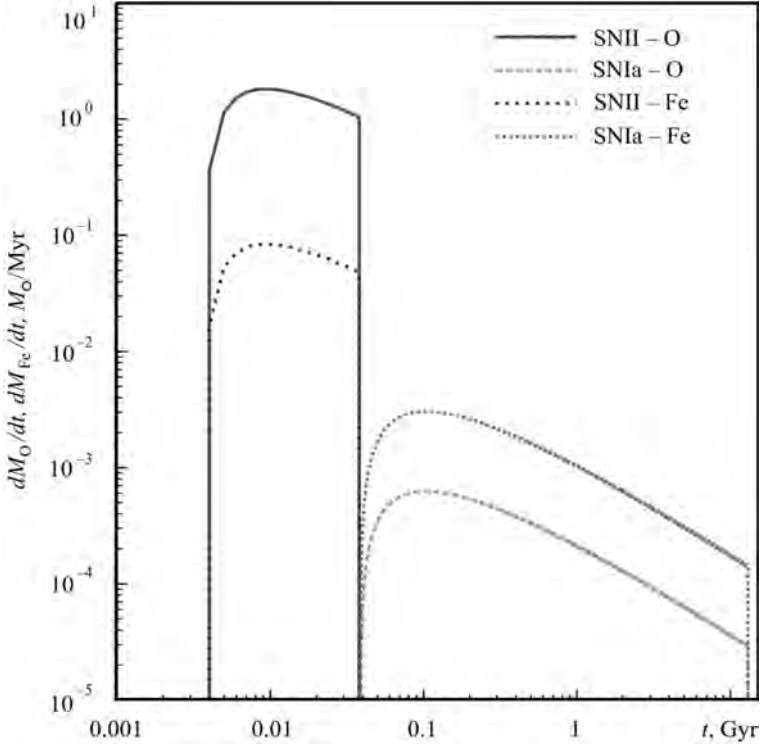


Fig. 4.59. The returned mass rate of ^{16}O and ^{56}Fe from the SSP with the $10^4 M_{\odot}$ and with solar metallicity $Z_{\odot} = 0.02$ due to SNIi and SNIa events

The gas rotates initially in centrifugal equilibrium (in the total “dm” + “gas” gravitational field) around the z -axis.

In some of the models we also use the idea of clouds initial mass function (CIMF) [95]. We use the power law CIMF with index -1.5 with lower and upper mass limits $10^4 M_{\odot}$ and $10^6 M_{\odot}$.

In Fig. 4.54 and Fig. 4.55 we present the time evolution of mass exchange rate via condensation/evaporation for different models. In the basic model VER-01 we use 5,000 same mass hot/warm (SPH) gas particles and 5,000 same mass cold gas particles. In the next model VER-02 we use the 10,000 + 10,000 particles. In the model VER-03 we use the same particle numbers as in VER-01, but for the mass distribution of the cold clumps we use the CIMF. In the model VER-04 we use the same particle numbers as in the model VER-02 but also with CIMF.

The figures show that the basic behavior of mass exchange rate between the hot/warm and cold phase described well with our model (practically independently from particle number and initial mass distribution of cold clumps) and also have a same rate as in the 2d multi phase mesh code [66, 123].

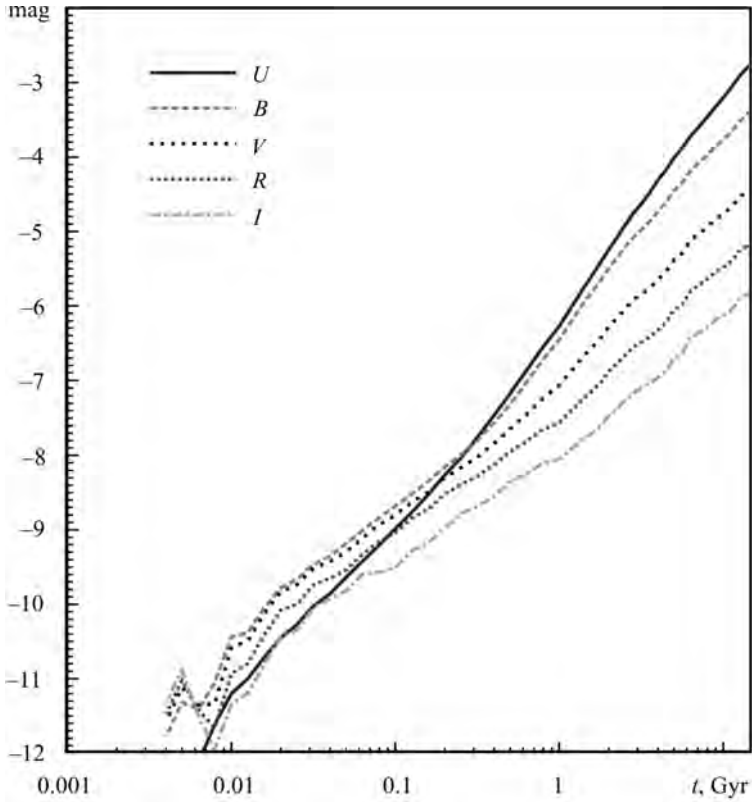


Fig. 4.60. The time evolution of the magnitudes for the SSP with the $10^4 M_{\odot}$ and with solar metallicity $Z_{\odot} = 0.02$

Star formation. Stars inject a significant amount of mass, momentum and energy (both mechanical and thermal) in the galactic system through supernova (SN) explosions, Planetary Nebulae (PN) events and stellar winds (SW). The gas dynamics then strongly depend on the star formation (SF) and a feed back (FB) processes.

Stars are supposed to be formed from collapsing and fragmenting cold gaseous clouds. Different SF criteria for numerical simulations have been examined [61, 72, 106]. In our code we use the “standard” Jeans instability criterion inside the “cold” cloud particle, with randomized efficiency for SF. Basically, we form “star” not from the “hot/warm” SPH gas (as in a many other previous SPH codes because of their single gas-phase representation) but in the “cold” clouds which, of course, intensively interact with the “hot/warm” phase via condensation vs. evaporation.

As a first step for the SF criterion we select the capability of “cloud” particles by:

$$h_{\text{cl}} > \lambda_{\text{J}} \equiv c_{\text{cl}} \sqrt{\frac{\pi}{G\rho_{\text{cl}}}}.$$

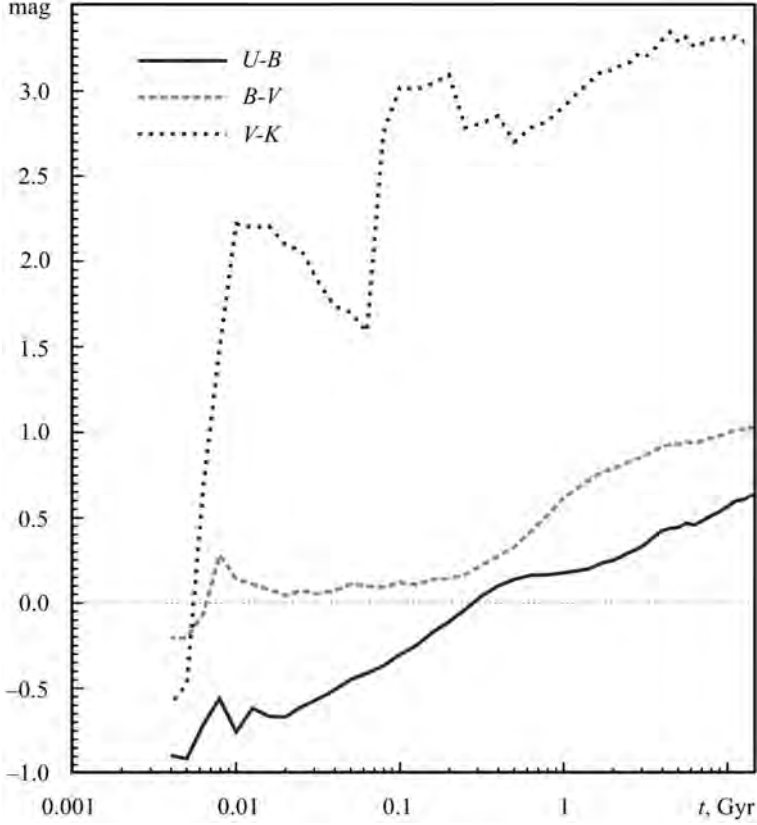


Fig. 4.61. The time evolution of the color indexes for the SSP with the $10^4 M_{\odot}$ and with solar metallicity $Z_{\odot} = 0.02$

After this we calculate the maximum SFR using the idea, that in this case the whole Jeans mass M_J inside the Jeans volume V_J is converted into a star particle during the free-fall time τ_{cl}^{ff} :

$$\frac{d\rho_*^{\max}}{dt} \equiv \frac{M_J}{\tau_{cl}^{ff} V_J} = \frac{4}{3} \sqrt{\frac{6G}{\pi}} \cdot \rho_{cl}^{3/2}$$

with

$$\tau_{cl}^{ff} \equiv \sqrt{\frac{3\pi}{32G\rho_{cl}}}.$$

The actual SFR in each current SF step is set by randomizing each maximum SFR:

$$\frac{d\rho_*}{dt} = \mathbf{RAND}(0.1 \div 1.0) \cdot \frac{d\rho_*^{\max}}{dt}.$$

The mass of newly formed “star” particle we can derive as:

$$m_{\text{star}} = \frac{d\rho_*}{dt} \cdot \tau_{cl}^{ff}.$$

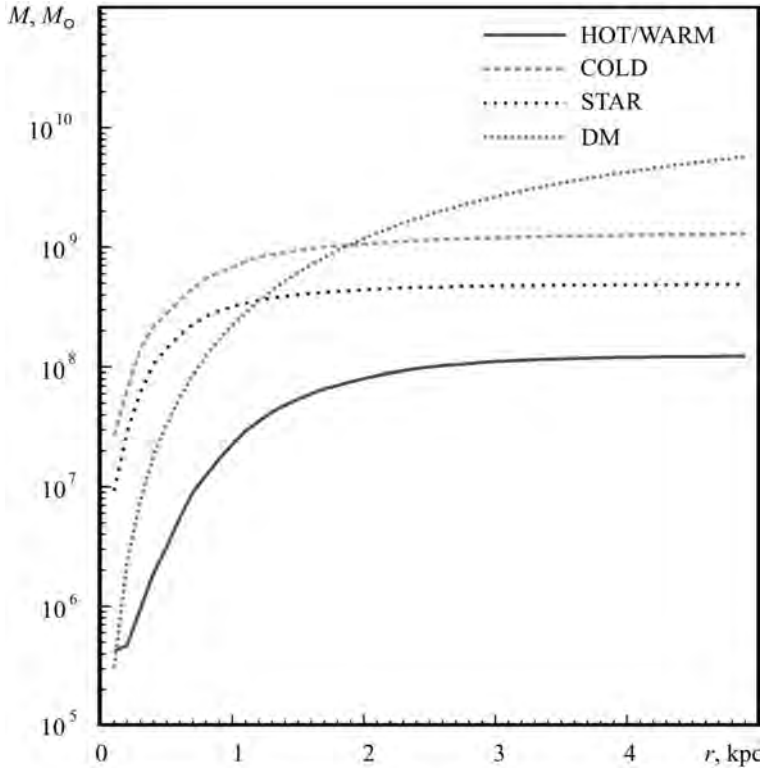


Fig. 4.62. The radial distribution of the cumulative mass for the different components in the central region of the model galaxy after 1 Gyr

Each “cold” cloud we check for the next SF only if we have at least the τ_{cl} from the last time of the SF act in the particle. These condition prevent the unphysically high SF activity in some low temperature “cold” particles and add the element of self-regulation in our SF algorithm.

Feedback processes from stars. SSP-chemo. Every new “star” particle in our SF scheme represents a separate, gravitationally bound star formation macro region i.e. a SSP. The “star” particle is characterized its own date of birth t_{SF} when it is formed. We assume that in the moment of creation the “star” particle, the individual stars inside our macro “star” particle distributed according to the [77] Initial Mass Function (IMF):

$$\Phi(m) = A \begin{cases} 2^{0.9} \cdot m^{-1.3}, & 0.1 \leq m < 0.5, \\ m^{-2.2}, & 0.5 \leq m < 1.0, \\ m^{-2.7}, & 1.0 \leq m < 100, \end{cases}$$

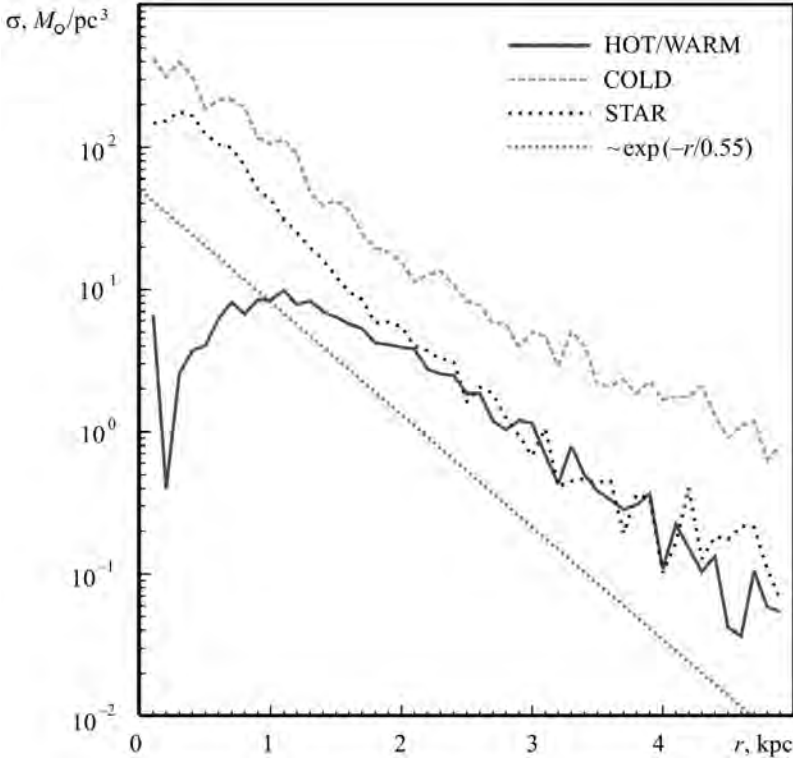


Fig. 4.63. The radial distribution of the surface density for the different components in the central region of the model galaxy after 1 Gyr

where the value $A = 0.310146$ is given by the normalization of the IMF:

$$\int_{m_{low}}^{m_{upp}} m \cdot \Phi(m) dm = 1.$$

The values of $m_{low} = 0.1 M_{\odot}$ and $m_{upp} = 100 M_{\odot}$ define the lower and upper mass limit of the IMF.

In the paper [25] in more detail describe our software for the calculation of the chemical output from the selected SSP (check the dependence from the selected IMF, initial metallicities and other parameters)⁴. In this complex N -body/SPH code, in numerical reason, we fix the IMF and use the, more simple, metallicity independent chemical output as in our previous paper [11]. We also consider only the production of ^{16}O and ^{56}Fe . During the evolution, these “star” particles return the chemically enriched gas to surrounding “gas” particles due to SNII, SNIa, PN events.

⁴ SSP: see <http://ssp-chemo.pbwiki.com/>

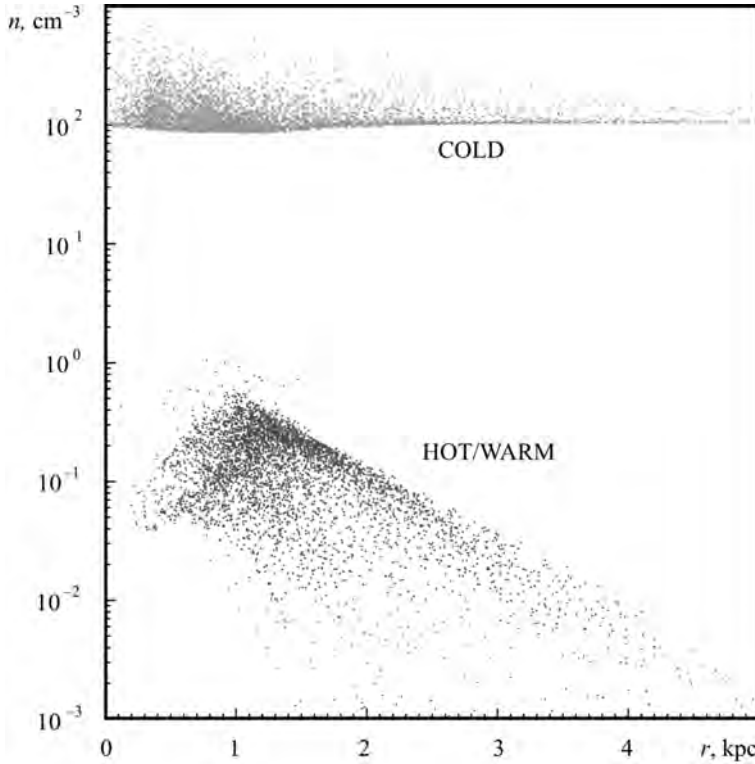


Fig. 4.64. The radial distribution of the volume density for the individual particles in both gaseous phases of the model galaxy after 1 Gyr

For the calculation of the stellar lifetime in the program we using the metal dependent approximation formula base on the theoretical stellar track of the Padova group [26, 36, 120]:

$$\lg t_{dead} = a_0(Z) - a_1(Z) \cdot \lg m + a_2(Z) \cdot (\lg m)^2,$$

where a_0 , a_1 , a_2 defined as:

$$\begin{cases} a_0(Z) = 10.130 + 0.0755 \cdot \lg Z - 0.0081 \cdot (\lg Z)^2, \\ a_1(Z) = 4.4240 + 0.7939 \cdot \lg Z + 0.1187 \cdot (\lg Z)^2, \\ a_2(Z) = 1.2620 + 0.3385 \cdot \lg Z + 0.0542 \cdot (\lg Z)^2, \end{cases}$$

here t_{dead} calculates in years, m given in M_\odot and Z given in the absolute values (the mass fraction off all elements heavier as He). This approximation give the very good results for the wide range of masses and mettalicities (m from $0.6 M_\odot$ up to $120 M_\odot$ and Z from $7 \cdot 10^{-5}$ up to 0.03).

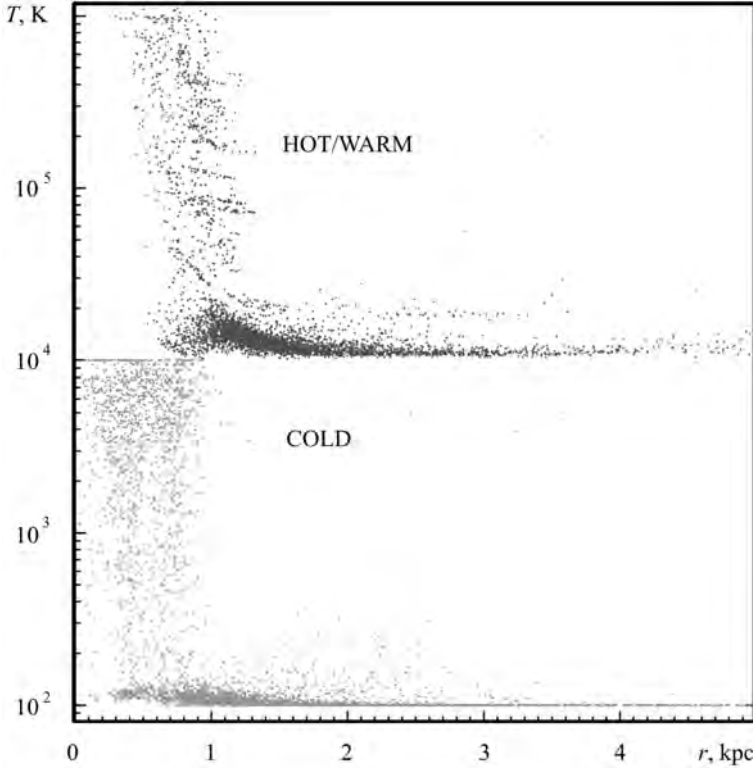


Fig. 4.65. The radial distribution of the temperature for the individual particles in both gaseous phases of the model galaxy after 1 Gyr

The “star” particles return to ISM the energy due to the SW, SNII, SNIa, PN processes. We assume what each SNII and SNIa events return to the ISM $\sim 10^{44}$ J energy, in the moment of the star death. Due to the SW the “star” particle return to the neighbor “gas” the $\sim 10^{44}$ J, but during the whole lifetime of the high mass stars. The PN event return to the surrounding gas the $\sim 10^{40}$ J also in one moment, like in the SNII and SNIa events. The total energy released by all processes from “star” particles calculated at each time step and distributed (in the form of thermal energy) between gas particles. Due to the different energetic scale of the events the energy coming from the SNII and SNIa distributed between the neighbor ($N_B = 50$) “hot/warm” SPH gas particles and the energy from SW and PN returned to the neighbor (50) “cold” gas clumps.

SNII. We can define the number of SNII explosions inside a given “star” particle during the time from t to $t + \Delta t$ using a simple equation:

$$\Delta N_{\text{SNII}} = \int_{m_{\text{dead}}(t+\Delta t)}^{m_{\text{dead}}(t)} \Phi(m) dm,$$

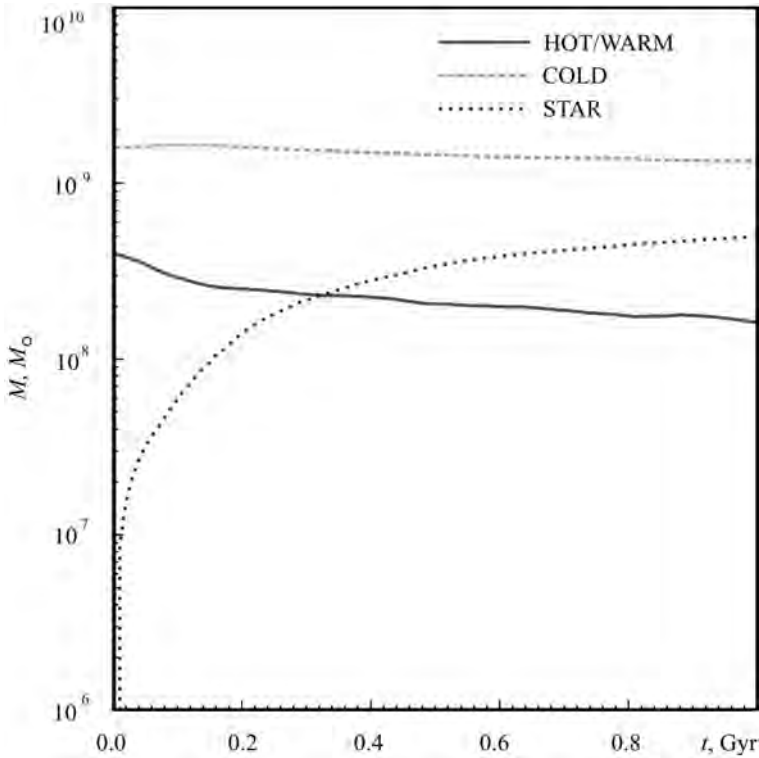


Fig. 4.66. The temporal evolution of the mass for the different components of the model galaxy

where $m_{dead}(t)$ and $m_{dead}(t + \Delta t)$ are masses of stars that end their lifetimes at the beginning and at the end of the respective time step. We assume that all stars with high masses between $8 M_{\odot}$ and $40 M_{\odot}$ produce SNI, for which we use the yields from [118, 161].

PN. To take into account PN events inside the “star” particle we use the equation:

$$\Delta N_{\text{PN}} = \int_{m_{dead}(t+\Delta t)}^{m_{dead}(t)} \Phi(m) dm.$$

We assume that all stars with intermediate masses between $1 M_{\odot}$ and $8 M_{\odot}$ produce PN, for which we use the yields from [152].

SNIa. The method described in [120] and proposed in [63, 88] is used to account for SNIa. In simulations, the number of SNIa exploding inside a selected “star” particle during each time step is given by:

$$\Delta N_{\text{SNIa}} = \int_{m_{dead}(t+\Delta t)}^{m_{dead}(t)} \Phi_2(m_2) dm_2.$$

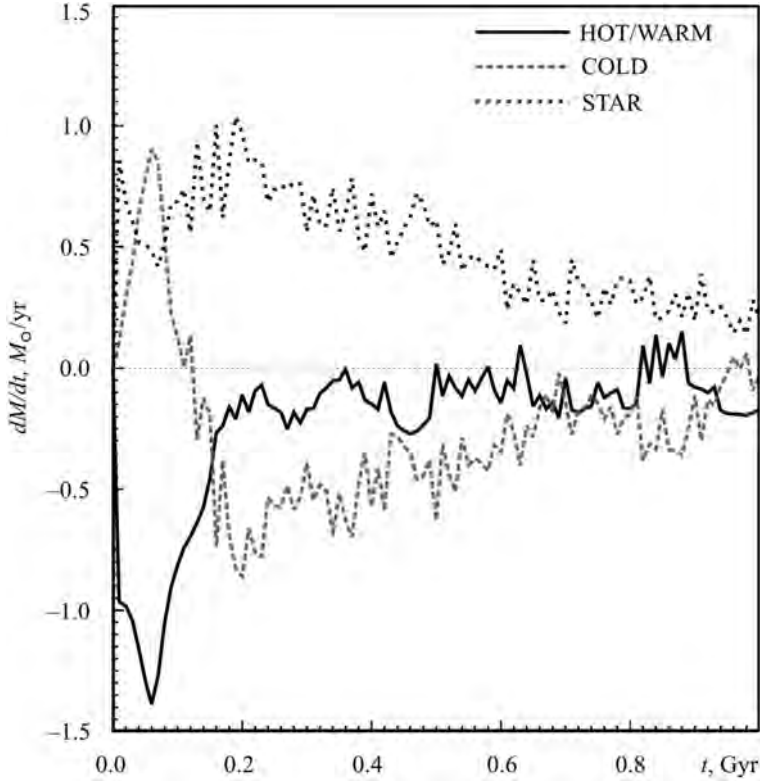


Fig. 4.67. The temporal evolution of the mass exchange rate for the different components of the model galaxy

The quantity $\Phi_2(m_2)$ represents the initial mass function of the secondary component and includes the distribution function of the secondary's mass relative to the total mass of the binary system m_B [88]:

$$\Phi_2(m_2) = A_2 \int_{m_{inf}}^{m_{sup}} \left(\frac{m_2}{m_B}\right)^\xi m_B^{-\gamma-1} dm_B,$$

where $m_{inf} = \max(2 \cdot m_2, 3 M_\odot)$ and $m_{sup} = m_2 + 8 M_\odot$. We set the parameter $\xi = 2$ following the paper [63]. The value of $\gamma = 2.7$ for the intermediate mass stars (between $1 M_\odot$ and $8 M_\odot$) according to the accepted [77] IMF. A_2 is a normalization constant which is connected with the IMF normalization constant A and with the parameter ξ with equation:

$$A_2 = \zeta \cdot 2^{1+\xi} (1 + \xi) \cdot A,$$

where we set the second parameter $\zeta = 0.05$ [63, 88]. For the chemical output of the SNIa process we use the “updated W7” model presented in the paper

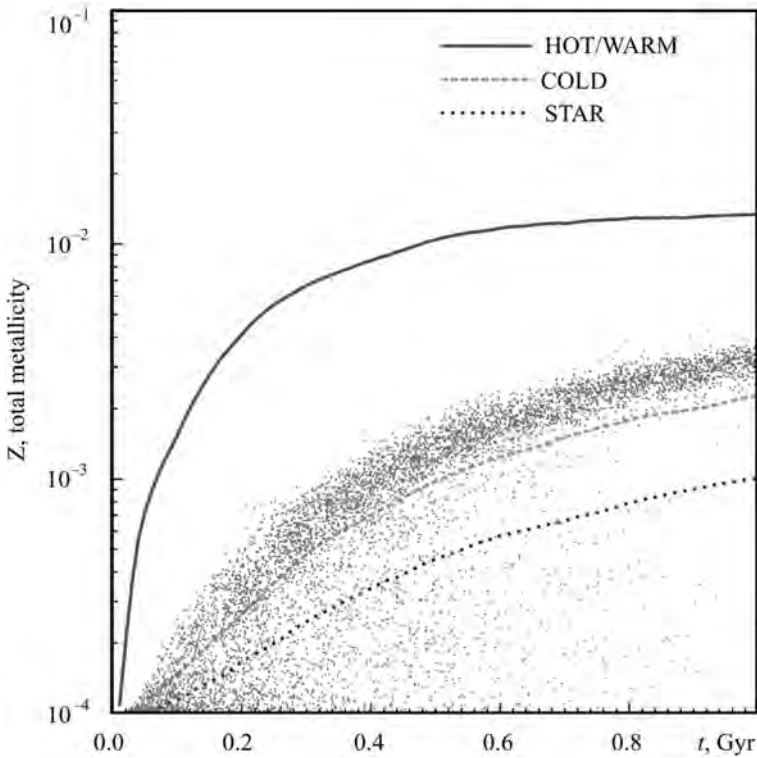


Fig. 4.68. Temporal evolution of the metallicities. Individual metallicities of newly born stars are marked by dots

[107]. This model is an extended and updated variant of the very successful previous SNIa model [145].

In Fig. 4.56 we present the number rate of SNII, SNIa, PN and SW events for the SSP with the $10^4 M_{\odot}$ and with solar metallicity $Z_{\odot} = 0.02$.

In Fig. 4.57 we present the energy returned rate from the SSP with the $10^4 M_{\odot}$ and with solar metallicity $Z_{\odot} = 0.02$ due to SNII, SNIa, PN and SW events.

In Fig. 4.58 we present the returned mass rate from the SSP with the $10^4 M_{\odot}$ and with solar metallicity $Z_{\odot} = 0.02$ due to SNII, SNIa and PN events.

In Fig. 4.59 we present the returned mass rate of ^{16}O and ^{56}Fe from the SSP with the $10^4 M_{\odot}$ and with solar metallicity $Z_{\odot} = 0.02$ due to SNII and SNIa events.

Photometric evolution of stellar component. SSP-photo. The code also includes the photometric evolution of each “star” particle, based on the idea of the SSP [35, 141]. At each time-step, absolute magnitudes: M_U , M_B , M_V , M_R , M_I , M_K , M_M and M_{BOL} are defined separately for each “star” particle.

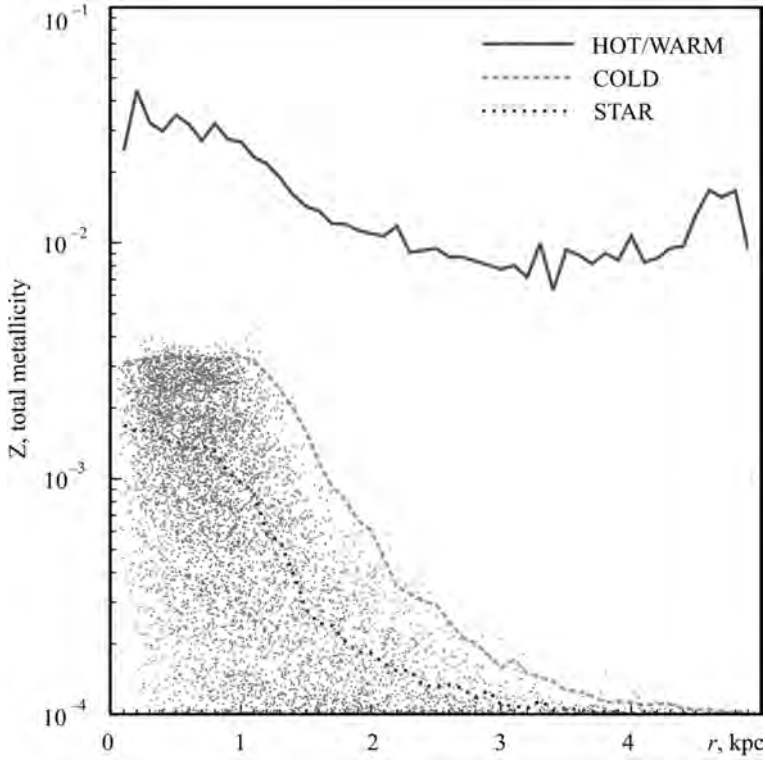


Fig. 4.69. Radial distribution of the metallicities after 1 Gyr. Individual metallicities of newly born stars are marked by dots

The spectro-photometric evolution of the overall ensemble of “star” particles forms the Spectral Energy Distribution (SED) of the galaxy.

In the Fig. 4.60 and Fig. 4.61 we present the time evolution of the magnitudes and the color indexes for the SSP with the $10^4 M_{\odot}$ and with solar metallicity $Z_{\odot} = 0.02$, based on the paper [141].

4.7.3. Model

Initial conditions. As a test of our new code, we calculate the evolution of an isolated star forming dwarf galaxy. The initial total gas content of our dwarf galaxy is $2 \times 10^9 M_{\odot}$ (80% “cold” + 20% “hot/warm”) which is placed inside a fixed dark matter halo with parameters $r_0 = 2$ kpc and $\rho_0 = 0.075 M_{\odot}/\text{pc}^3$ [37].

With these parameters the dark matter mass inside the initial distribution of gas (20 kpc) is $\simeq 2 \times 10^{10} M_{\odot}$. The initial temperatures for the cold gas we set 10^3 K, for the hot/warm gas 10^5 K. For the initial gas distribution we use a Plummer–Kuzmin disk with parameters $a = 0.1$ kpc and $b = 2$ kpc [94].

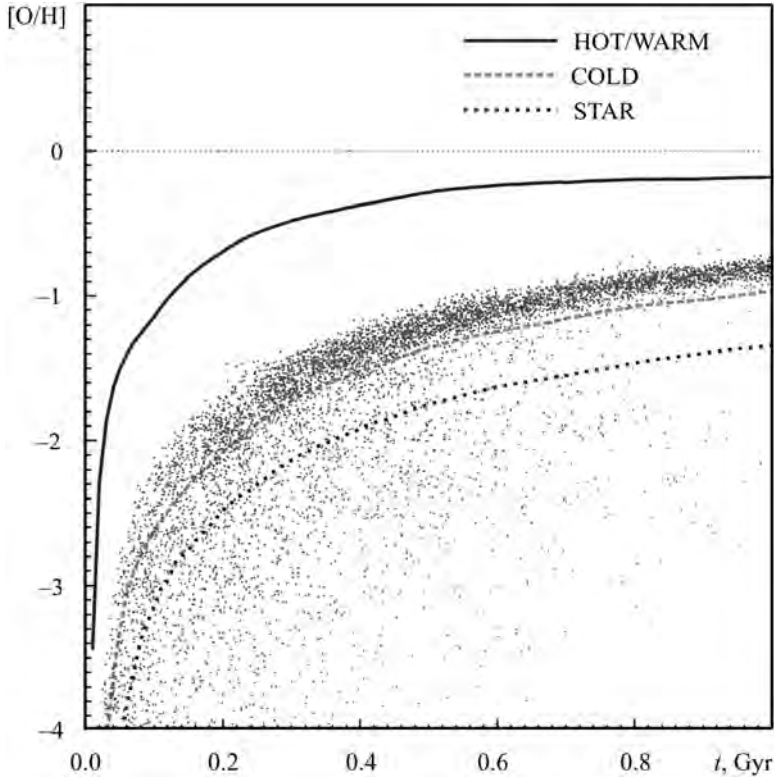


Fig. 4.70. Temporal evolution of the [O/H]. Individual metallicities of newly born stars are marked by dots

The gas initially rotates in centrifugal equilibrium (in the total “dm” + “gas” gravitational field) around the z-axis.

We choose the dwarf galaxy as an appropriate object for our code, because in this case even with a relatively “small” number of cold “clouds” ($\sim 10^4$) we achieve the required physical resolution for a realistic description of individual molecular clouds ($\sim 10^5 M_\odot$) as a separate “cold” particle. In the simulation we use $N_{\text{hot}} = 10^4$ SPH and $N_{\text{cold}} = 10^4$ “cold” particles. After 1 Gyr more than 10^4 additional “stellar” particles are created.

Results. After a moderate collapse phase the stars and the molecular clouds follow an exponential radial distribution, whereas the diffuse gas shows a central depression as a result of stellar feedback. The metallicities of the galactic components behave quite differently with respect to their temporal evolution as well as their radial distribution. Especially, the ISM is at no stage well mixed.

In Fig. 4.62 and Fig. 4.63 we present the mass and surface density distribution of the different components in the central region of the model after

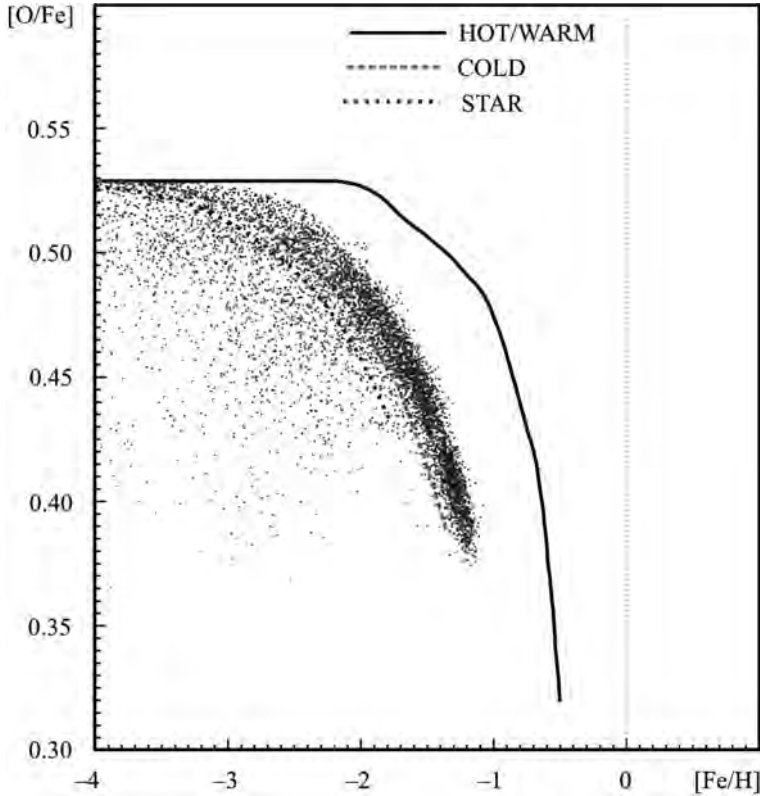


Fig. 4.71. Relative metallicity evolution $[O/Fe]$ vs. $[Fe/H]$. Individual metallicities of newly born stars are marked by dots

1 Gyr of evolution. In the region up to ≈ 2 kpc the baryonic matter dominates over the DM. The surface density of the stars can be well approximated by an exponential disk with a scale length of 0.55 kpc.

In the distribution of hot gas (see Fig. 4.50, Fig. 4.51), we see a central “hole” (≈ 1 kpc), as a result of gas blow-out from the center mainly due to SNI explosions but not for the cold gas. This results disagrees with the model by [101] where a density hole occurs caused by their single gas-phase treatment.

In Fig. 4.66 and Fig. 4.67 we present the evolution of the mass and the mass exchange rate of the different components. The SFR (i.e. dM_{STAR}/dt) peaks to a value of $1 M_{\odot}\text{yr}^{-1}$ after 200 Myrs. Afterwards it drops down to $0.2 M_{\odot}\text{yr}^{-1}$ within several hundred Myrs. I.e. that after 1 Gyrs the stellar mass has already reached $5 \times 10^8 M_{\odot}$. Another interesting feature is the behavior of the hot gas phase mass exchange. After the initial violent phase of condensation an equilibrium is established which gives a hot gas fraction of about 10% of the total gas mass.

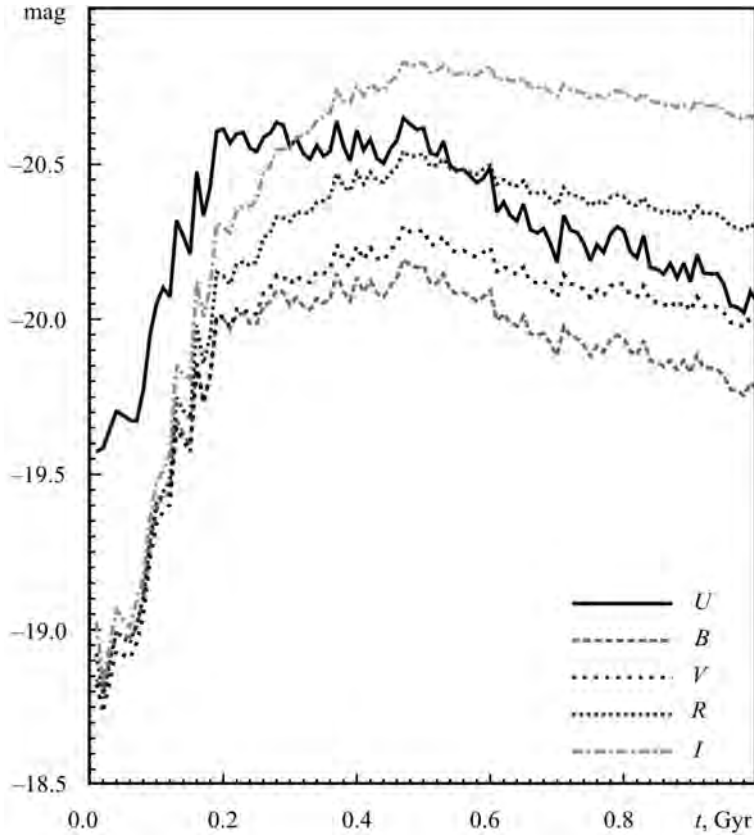


Fig. 4.72. Temporal evolution of the model galaxy magnitudes in different spectral branch

The metal content of the diffuse gas and the clouds differs significantly over the whole integration time (see Fig. 4.68 and Fig. 4.69). Due to SNII and SNIa events the metallicity of the hot phase exceeds that of the clouds by almost one order of magnitude (~ 5 times). The clouds mainly get their metals by condensation from the hot phase.

The central metallicity plateau (up to 1 kpc) of the cold component is explained by the fact, that condensation of metal-enriched material does not work efficiently in that region. This signature agrees well with the observed abundance homogeneity in dIrrs over up to 1 kpc (e.g. in I Zw 18: [71]). Moreover, the conditions in the center lead mainly to evaporation of clouds which also prevents the mixing with the metal enriched hot gas.

In the Fig. 4.72 and Fig. 4.73 we present the evolution of the model galaxy magnitudes in different spectral branch and also the color indexes.

FUSE observations. One of the key feature in our multi-phase SPH model description is a fact, that the “hot/warm” and “cold” gas phase have

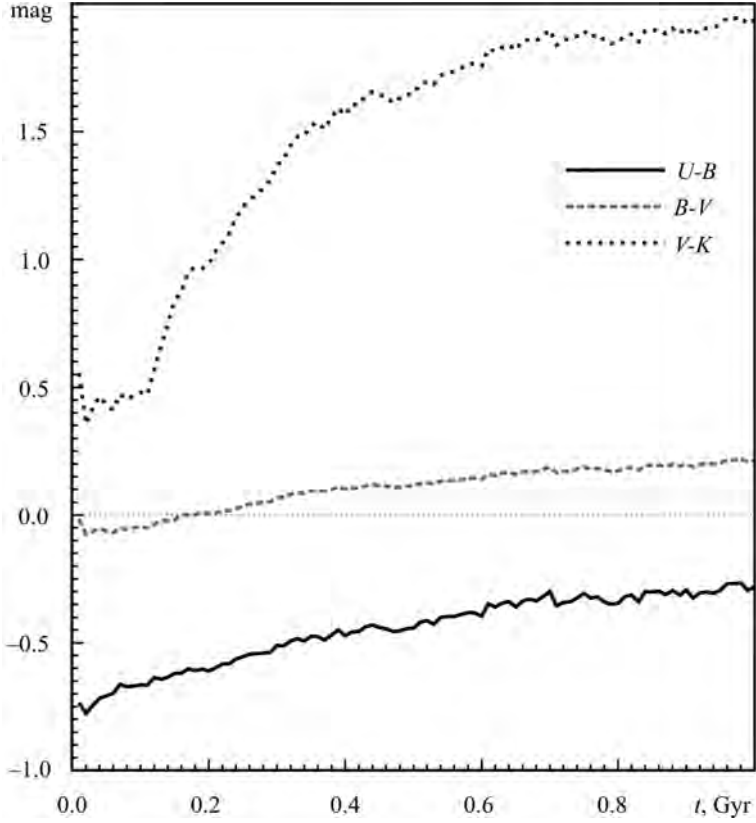


Fig. 4.73. Temporal evolution of the model galaxy color indexes

a different metal content. As we already mention in the discussion of the figures Fig. 4.68 and Fig. 4.69 the total metal content of our model dwarf galaxy in the different gas phases significantly differ (~ 5 times). Only for a very few selected dwarf galaxies [38] using the high resolution FUSE (*Far Ultraviolet Spectroscopic Explorer*, [100]) spectroscopic observational data we can check directly the metallicity differences between the “hot/warm” (i.e. nebular gas, using emission lines) and “cold” (i.e. neutral gas, using absorption lines) gas phases.

The “cumulative” resulting table from the paper [38] (see Table 3.) show the Oxygen [O/H] metallicity differences between the nebular and neutral gas phases for 5 dwarf galaxies (NGC 625, NGC 1705, IZw 18, IZw 36, Mrk 59). In average the metallicity in the “hot/warm” phase for these selected dwarf galaxies higher in a factor of ~ 6 compare to the “cold” phase. Such a large metallicity differences, as we see from our plots (Fig. 4.68, Fig. 4.69, Fig. 4.70 and Fig. 4.71), can be easily explained in our multi-phase SPH model.

4.7.4. Conclusions

We present our recently developed 3-dimensional chemodynamical code for galaxy evolution. It follows the evolution of all components of a galaxy such as dark matter, stars, molecular clouds and diffuse interstellar matter (ISM). Dark matter and stars are treated as collisionless N -body systems. The ISM is numerically described by a smoothed particle hydrodynamics (SPH) approach for the diffuse (hot) gas and a sticky particle scheme for the (cool) molecular clouds. Additionally, the galactic components are coupled by several phase transitions like star formation, stellar death or condensation and evaporation processes within the ISM. As an example here we present the dynamical, chemical and photometric evolution of a star forming dwarf galaxy with a total baryonic mass of $2 \times 10^9 M_{\odot}$.

4.8. Conclusion

1. Based on our numerical N -body “sticky-particle” simulations with the additional artificial viscosity, presented in [17, 18, 22], we showed that to provide the required surface density of the baryonic matter in the Galactic disk solar neighborhood ($\sigma \approx 50 M_{\odot}/\text{pc}^2$) we need to have a significant baryonic halo with mass $\sim 2 \cdot 10^{11} M_{\odot}$. Most of the baryonic material of the evolving Galactic disk in our model formed by the accretion of the baryonic halo material on to the disk. These theoretical calculations describe the nature of the baryonic component of the Galactic halo, which may be in a cold “clumpy” gas phase of molecular hydrogen H_2 . Such “clumps” can have a complex internal, fragmented or even “fractal”, structure.

2. Having developed our own Smoothed Particle Hydrodynamics (SPH) code [20], we used it to carry out a large set of calculations of the collapse of triaxial fragments. Our models [15, 21] shows that the complex distorted “bar-like” disk structures (including the galactic bar itself) and associated spiral arms mainly formed during the initial collapse phase of the gas, roughly during the first ~ 1 Gyr of isolated fragment evolution. We use some general initial conditions for our triaxial protogalactic fragments, i.e. the clouds have sizes A , B , C – such that $A > B > C$. We set the three-dimensional field of initial velocities in our models as: $\mathbf{V}(x, y, z) = [\Omega \times \mathbf{r}]$. In this way we have described the initial process of galactic substructure and galactic disk formation.

3. We propose [16, 23] the new “energetic criteria” of star formation and of star formation efficiency itself ϵ_{SF} in our complex N -body/SPH programs. We tested our new star formation recipes thoroughly [24] and showed that using our method we model the star formation in a self-consistent way and that the mass of the stellar component in our galaxy models is almost independent from the initial number of gas fragments (number of SPH particles) in our model. This algorithm makes it possible to interpret the results which were obtained

using moderate SPH-particle numbers and to use them for the whole galaxy, which, of course, contains a much larger number of fragments of gas than we use for our model calculations.

4. Using our new “energetic criteria” for both star formation and the star formation efficiency ϵ_{SF} [16, 23, 24] allowed to us construct the model for qualitative and quantitative analysis of the chemo-dynamical evolution of our own Galaxy [10–12]. The proposed gas-dynamic CD-SPH code allowed a self-consistent description of global and local (in the solar neighborhood) dynamical and chemical evolution of disk galaxies (with general parameters close to those of our Milky Way). Numerical model suggested by the author in [11, 12] within the general model, successfully described in a self-consistent way the global dynamical properties of the disk (surface density distribution and rotation curve of the disk), and global chemical properties (metallicity gradient inside the disk). Simultaneously, the model also well-described the chemical properties of the solar neighborhood (the distribution of stars by metallicities, as well as the “age—metallicity” relation). This comprehensive modelling of gas-dynamic evolution and star formation, as well as the return of chemical elements and energy from the stars back into the gas phase allowed to us offer the solution for the so-called “G-dwarfs problem” in the solar neighborhood.

5. We first applied our Multi-Phase Chemo-Dynamical SPH (MP-CD-SPH) code to chemodynamical modelling of the evolution of actively star forming dwarf galaxies [13, 14]. Our models showed that the different gas components of galaxies also have a significantly different history of heavy element enrichment. Abundance differences, for example in oxygen [O/H], between the hot gaseous inter-cloud medium and the oxygen in cold gas clouds, can reach almost one order of magnitude. Emission spectral lines and absorption spectra of the same dwarf galaxies NGC 625, NGC 1705, I Zw 18, I Zw 36 and Mrk 59, obtained by the recent FUSE space telescope observations, showed just such a difference between the amount of oxygen in the hot inter-cloud and cold cloudy phases of interstellar gas material in these sites.

Acknowledgments

The authors are grateful to their colleagues and friends L.S. Pilyugin, Yu.I. Izotov, A.A. Veles, Ch. Theis, D. Merritt, S. Harfst, S. Aarseth, P. Kroupa, Ch. Boily, N. Nakasato and S. Justham for fruitful discussions and help during the preparation of this work.

The authors are also grateful to the whole staff of the Astro-Space Information and Computing Center and the Department for Physics of Stars and Galaxies of the Main Astronomical Observatory, National Academy of Sciences of Ukraine.

The authors are also grateful to the whole staff of the Astro-Space Information and Computing Center and the Department for Physics of Stars

and Galaxies of the Main Astronomical Observatory, National Academy of Sciences of Ukraine.

The work of the authors was supported by: the International Science Foundation (ISF) under grants No. UC 9000 and No. UC 9200 (1994–1995); the INTAS under grant No. 94-4069 (1995–1996); the Open Society Institute grant No. TE7 100 (1996); the American Astronomical Society (AAS) under International Small Research Grant (1998); the NATO under grant No. NIG 974675 (1999–2000); the German Science Foundation (DFG) under grants No. 436 UKR 18/2/99, 436 UKR 17/11/99 (1999–2000); the Domus Hungarica Scientiarum et Artium grants (2000–2004); the INTAS under Infrastructure grant No. 03-59-11 (2005–2006); the German Science Foundation (DFG) under SFB 439 (sub-project B11) “Galaxies in the Young Universe” at the University of Heidelberg (2005–2008); the Volkswagen Foundation project “GRACE” I/80041-043 and the Ministry of Science, Research and the Arts of Baden–Württemberg (Az: 823.219-439/30 and /36) (2005–2008).

The special GPU accelerated supercomputer *laohu* at the Center of Information and Computing at National Astronomical Observatories, Chinese Academy of Sciences, funded by Ministry of Finance of People’s Republic of China under the grant ZDYZ2008-2, has been used for some of the largest simulations. We also used smaller GPU clusters *titan*, *hydra* and *kepler*, funded under the grants I/80041-043 and I/84678/84680 of the Volkswagen Foundation and grants 823.219-439/30 and /36 of the Ministry of Science, Research and the Arts of Baden–Württemberg, Germany.

Some code development was also done on the Milky Way supercomputer, funded by the Deutsche Forschungsgemeinschaft (DFG) through Collaborative Research Center (SFB 881) “The Milky Way System” (subproject Z2), hosted and co-funded by the Jülich Supercomputing Center (JSC).

We acknowledge support by Chinese Academy of Sciences through the Silk Road Project at NAOC, through the Chinese Academy of Sciences Visiting Professorship for Senior International Scientists, Grant Number 2009S1-5, and through the “Qianren” special foreign experts program of China.

P. Berczik is thankful for the special support of his work by the National Academy of Sciences of Ukraine under the Main Astronomical Observatory, “GPU/GRID” computing cluster project and the German “AstroGrid-D” project, which links together the two GPU clusters in Kiev and Heidelberg. P. Berczik is especially thankful for the hospitality of the Astronomisches Rechen Institut (ARI) University of Heidelberg, where the significant parts of this work has been done.

■

BIBLIOGRAPHY

1. L.A. Aguilar, D. Merritt, The structure and dynamics of galaxies formed by cold dissipationless collapse, *Astrophys. J.* **354** (1990), 33–51.
2. C. Alcock, C.W. Akerlof, R.A. Allsman, T.S. Axelrod, D.P. Bennett et al., Possible gravitational microlensing of a star in the Large Magellanic Cloud, *Nature* **365** (1993), 621–623.
3. M. Alongi, G. Bertelli, A. Bressan, C. Chiosi, F. Fagotto et al., Evolutionary sequences of stellar models with semiconvection and convective overshoot. I — $Z = 0.008$, *Astron. Astrophys. Supp.* **97** (1993), 851–871.
4. E. Bajaja, W.K. Huchtmeier, U. Klein, The extended HI halo in NGC 4449, *Astron. Astrophys.* **285** (1994), 385–388.
5. D.S. Balsara, von Neumann stability analysis of smooth particle hydrodynamics—suggestions for optimal algorithms, *Journal of Computational Physics* **121** (1995), 357–372.
6. J.M. Bardeen, J.R. Bond, N. Kaiser, A.S. Szalay, The statistics of peaks of Gaussian random fields, *Astrophys. J.* **304** (1986), 15–61.
7. M. C. Begelman, C. F. McKee, Global effects of thermal conduction on two-phase media, *Astrophys. J.* **358**, (1990) 375–391.
8. C.L. Bennett, N.W. Boggess, M.G. Hauser, J.C. Mather, G.F. Smoot et al., Recent Results from COBE, in *The Environment and Evolution of Galaxies*, edited by J.M. Shull & H.A. Thronson, volume 188 of *Astrophysics and Space Science Library* (1993), pp. 27–58.
9. P. Berczik, SPH code for dynamical and chemical evolution of disk galaxies, ArXiv Astrophysics e-prints: astro-ph/9807059.
10. P. Berczik, Chemo-Dynamical Evolution of Disk Galaxies, Smoothed Particles Hydrodynamics Approach, *Astrophys. Sp. Sci.* **265** (1999), 473–477.
11. P. Berczik, Chemo-dynamical smoothed particle hydrodynamic code for evolution of star forming disk galaxies, *Astron. Astrophys.* **348** (1999), 371–380.
12. P. Berczik, Modeling the Star Formation in Galaxies Using the Chemo-Dynamical SPH Code, *Astrophys. Sp. Sci.* **271** (2000), 103–126.
13. P. Berczik, G. Hensler, C. Theis, R. Spurzem, Chemodynamical Modelling of Galaxy Formation and Evolution, *Astrophys. Sp. Sci.* **281** (2002), 297–300.
14. P. Berczik, G. Hensler, C. Theis, R. Spurzem, A multi-phase chemo-dynamical SPH code for galaxy evolution. Testing the code, *Astrophys. Sp. Sci.* **284** (2003), 865–868.

15. P. Berczik, I.G. Kolesnik, Gasodynamical model of the triaxial protogalaxy collapse, *Astronomical and Astrophysical Transactions* **16** (1998), 163–185.
16. P. Berczik, S.G. Kravchuk, 3D Modelling of Forming Galaxies; The History of Star Formation Activity, *Astrophys. Sp. Sci.* **245** (1996), 27–42.
17. P. Berczik, S.G. Kravchuk, On the Galactic Baryonic Halo, *Astronomical and Astrophysical Transactions* **14** (1997), 61–64.
18. P. Berczik, S.G. Kravchuk, Dissipative N-body code for galactic evolution, *Astronomical and Astrophysical Transactions* **18** (2000), 829–838.
19. P.P. Berczik, I.G. Kolesnik, Particle orbits in triaxial potentials of two ellipsoids, *Kinematics and Physics of Celestial Bodies* **9** (1993), 51–64.
20. P.P. Berczik, I.G. Kolesnik, Smoothed particle hydrodynamics and its application to astrophysical problems, *Kinematics and Physics of Celestial Bodies* **9** (1993), 1–11.
21. P.P. Berczik, I.G. Kolesnik, Dynamical collapse of isothermal and adiabatic triaxial protogalaxies, *Kinematics and Physics of Celestial Bodies* **12** (1996), 13–26.
22. P.P. Berczik, S.G. Kravchuk, Galaxy as a dynamical system with accreting cold gaseous halo, *Kinematics and Physics of Celestial Bodies* **13** (1997), 32–38.
23. P.P. Berczik, S.G. Kravchuk, Three-dimensional simulation of the evolution of protogalaxies. Rapidly rotating objects, *Kinematics and Physics of Celestial Bodies* **13** (1997), 51–60.
24. P.P. Berczik, M.I. Petrov, Analysis of the star formation modeling algorithm in the hydrodynamic SPH code, *Kinematics and Physics of Celestial Bodies* **17** (2001), 153–161.
25. P.P. Berczik, N.I. Petrov, Calculation of the SSP chemical evolution, *Kinematics and Physics of Celestial Bodies* **19** (2003), 23–33.
26. G. Bertelli, A. Bressan, C. Chiosi, F. Fagotto, E. Nasi, Theoretical isochrones from models with new radiative opacities, *Astron. Astrophys. Suppl. Ser.* **106** (1994), 275–302.
27. F. Bertola, M. Vietri, W.W. Zeilinger, Triaxiality in disk galaxies, *Astrophys. J. Lett.* **374** (1991), L13–L16.
28. O. Bienaymé, The local stellar velocity distribution of the Galaxy. Galactic structure and potential, *Astron. Astrophys.* **341** (1999), 86–97.
29. J. Binney, On the rotation of elliptical galaxies, *Mon. Not. Roy. Astron. Soc.* **183** (1978), 501–514.
30. J. Binney, Testing for triaxiality with kinematic data, *Mon. Not. Roy. Astron. Soc.* **212** (1985), 767–781.
31. J. Binney, WARPS, *Annu. Rev. Astron. Astrophys.* **30** (1992), 51–74.
32. G.S. Bisnovatyi-Kogan, R.A. Syunyaev, Quasars and the Nuclei of Galaxies: A Single Object or a Star Cluster?, *Sov. Astron.* **16** (1972), 201–208.
33. L. Blitz, D.N. Spergel, Direct evidence for a bar at the Galactic center, *Astrophys. J.* **379** (1991), 631–638.
34. L. Blitz, D.N. Spergel, The shape of the Galaxy, *Astrophys. J.* **370** (1991), 205–224.
35. A. Bressan, C. Chiosi, F. Fagotto, Spectrophotometric evolution of elliptical galaxies. 1: Ultraviolet excess and color-magnitude-redshift relations, *Astrophys. J. Suppl. Ser.* **94** (1994), 63–115.

36. A. Bressan, F. Fagotto, G. Bertelli, C. Chiosi, Evolutionary sequences of stellar models with new radiative opacities. II — $Z = 0.02$, *Astron. Astrophys. Suppl. Ser.* **100** (1993), 647–664.
37. A. Burkert, The Structure of Dark Matter Halos in Dwarf Galaxies, *Astrophys. J. Lett.* **447** (1995), L25–L28.
38. J.M. Cannon, E.D. Skillman, K.R. Sembach, D.J. Bomans, Probing the Multi-phase Interstellar Medium of the Dwarf Starburst Galaxy NGC 625 with Far Ultraviolet Spectroscopic Explorer Spectroscopy, *Astrophys. J.* **618** (2005), 247–258.
39. G. Carraro, C. Lia, C. Chiosi, Galaxy formation and evolution — I. The Padua tree-sph code (pd-sph), *Mon. Not. Roy. Astron. Soc.* **297** (1998), 1021–1040.
40. S. Chandrasekhar, *Ellipsoidal figures of equilibrium* (Mir, Moscow, 1973), p. 243.
41. A.D. Chernin, The nature of the angular momentum of galaxies: The hydrodynamical theory, *Astron. Astrophys.* **267** (1993), 315–336.
42. R. Courant, K.O. Friedrichs, *Supersonic flow and shock waves* (Interscience Publishers, New York, 1948).
43. L.L. Cowie, C.F. McKee, J.P. Ostriker, Supernova remnant evolution in an inhomogeneous medium. I — Numerical models, *Astrophys. J.* **247** (1981), 908–924.
44. A. Curir, A. Diaferio, Angular momentum redistribution and spin tilt during N-body collapse: phenomenological implications, *Astron. Astrophys.* **285** (1994), 389–392.
45. A. Dalgarno, R. A. McCray, Heating and Ionization of HI Regions, *Annu. Rev. Astron. Astrophys.* **10** (1972), 375–424.
46. A. Dar, Baryonic Dark Matter and Big Bang Nucleosynthesis, *Astrophys. J.* **449** (1995), 550–553.
47. B. Dauphole, J. Colin, Globular clusters as a new constraint for the potential of our Galaxy., *Astron. Astrophys.* **300** (1995), 117–125.
48. J.I. Davies, Searching for Hidden Galaxies, in *The Environment and Evolution of Galaxies*, edited by J.M. Shull & H.A. Thronson, volume 188 of *Astrophysics and Space Science Library* (1993), pp. 105–126.
49. F. de Paolis, G. Ingrosso, P. Jetzer, M. Roncadelli, A scenario for a baryonic dark halo, *Astron. Astrophys.* **295** (1995), 567–570.
50. A. de Rujula, P. Jetzer, E. Masso, On the Nature of the Dark Halo of Our Galaxy, *Astron. Astrophys.* **254** (1992), 99–104.
51. T. de Zeeuw, M. Franx, Structure and dynamics of elliptical galaxies, *Annu. Rev. Astron. Astrophys.* **29** (1991), 239–274.
52. R. Duerr, C.L. Imhoff, C.J. Lada, Star formation in the Lambda Orionis region. I — The distribution of young objects, *Astrophys. J.* **261** (1982), 135–150.
53. B. Edvardsson, J. Andersen, B. Gustafsson, D.L. Lambert, P.E. Nissen et al., The Chemical Evolution of the Galactic Disk — Part One — Analysis and Results, *Astron. Astrophys.* **275** (1993), 101–150.
54. D.J. Eisenstein, A. Loeb, An analytical model for the triaxial collapse of cosmological perturbations, *Astrophys. J.* **439** (1995), 520–541.
55. A.E. Evrard, Beyond N-body — 3D cosmological gas dynamics, *Mon. Not. Roy. Astron. Soc.* **235** (1988), 911–934.

56. K.M. Ferriere, The hot gas filling factor in the vicinity of the Sun, *Astrophys. J.* **441** (1995), 281–299.
57. C. Flynn, B. Fuchs, Density of dark matter in the Galactic disk, *Mon. Not. Roy. Astron. Soc.* **270** (1994), 471–479.
58. M. Franx, G. Illingworth, T. de Zeeuw, The ordered nature of elliptical galaxies: Implications for their intrinsic angular momenta and shapes, *Astrophys. J.* **383** (1991), 112–134.
59. M. Franx, G. Illingworth, T. Heckman, Major and minor axis kinematics of 22 ellipticals, *Astrophys. J.* **344** (1989), 613–636.
60. C.S. Frenk, S.D.M. White, M. Davis, G. Efstathiou, The formation of dark halos in a universe dominated by cold dark matter, *Astrophys. J.* **327** (1988), 507–525.
61. D. Friedli, W. Benz, Secular evolution of isolated barred galaxies. II. Coupling between stars and interstellar medium via star formation, *Astron. Astrophys.* **301** (1995), 649–665.
62. T. Fukushige, J. Makino, A. Kawai, GRAPE-6A: A Single-Card GRAPE-6 for Parallel PC-GRAPE Cluster Systems, *Publ. Astron. Soc. Jap.* **57** (2005), 1009–1021.
63. L. Greggio, A. Renzini, The binary model for type I supernovae — Theoretical rates, *Astron. Astrophys.* **118** (1983), 217–222.
64. S. Harfst, C. Theis, G. Hensler, Modelling galaxies with a 3d multi-phase ISM, *Astron. Astrophys.* **449** (2006), 509–518.
65. R.N. Henriksen, L.M. Widrow, Hydrogen clouds and the MACHO/EROS events, *Astrophys. J.* **441** (1995), 70–76.
66. G. Hensler, A. Rieschick, Star Formation in Dwarf Irregular Galaxies: From Self-regulation to Starbursts (Invited), in *Modes of Star Formation and the Origin of Field Populations*, edited by E.K. Grebel & W. Brandner, volume 285 of *Astronomical Society of the Pacific Conference Series* (2002), pp. 341–348.
67. L. Hernquist, N. Katz, TREESPH — A unification of SPH with the hierarchical tree method, *Astrophys. J. Suppl. Ser.* **70** (1989), 419–446.
68. N. Hiotelis, N. Voglis, Smooth particle hydrodynamics with locally readjustable resolution in the collapse of a gaseous protogalaxy, *Astron. Astrophys.* **243** (1991), 333–340.
69. N. Hiotelis, N. Voglis, G. Contopoulos, Hydrodynamics in a collapsing gaseous protogalaxy, *Astron. Astrophys.* **242** (1991), 69–76.
70. G. Illingworth, Rotation in 13 elliptical galaxies, *Astrophys. J. Lett.* **218** (1977), L43–L47.
71. Y.I. Izotov, Helium abundances in the most metal-deficient dwarf galaxies, in *The Low Surface Brightness Universe*, edited by J.I. Davies, C. Impey, & S. Phillips, volume 170 of *Astronomical Society of the Pacific Conference Series* (1999), pp. 390–392.
72. N. Katz, Dissipational galaxy formation. II — Effects of star formation, *Astrophys. J.* **391** (1992), 502–517.
73. N. Katz, J.E. Gunn, Dissipational galaxy formation. I — Effects of gasdynamics, *Astrophys. J.* **377** (1991), 365–381.
74. J. Koppen, C. Theis, G. Hensler, Condensation and evaporation of interstellar clouds in chemodynamical models of galaxies, *Astron. Astrophys.* **331** (1998), 524–534.

75. J. Kormendy, S. Djorgovski, Surface photometry and the structure of elliptical galaxies, *Annu. Rev. Astron. Astrophys.* **27** (1989), 235–277.
76. A.V. Kravtsov, A.A. Klypin, J.S. Bullock, J.R. Primack, The Cores of Dark Matter-dominated Galaxies: Theory versus Observations, *Astrophys. J.* **502** (1998), 48–58.
77. P. Kroupa, C.A. Tout, G. Gilmore, The distribution of low-mass stars in the Galactic disc, *Mon. Not. Roy. Astron. Soc.* **262** (1993), 545–587.
78. K. Kuijken, G. Gilmore, The mass distribution in the galactic disc. I – A technique to determine the integral surface mass density of the disc near the sun, *Mon. Not. Roy. Astron. Soc.* **239** (1989), 571–603.
79. R.B. Larson, A model for the formation of a spherical galaxy, *Mon. Not. Roy. Astron. Soc.* **145** (1969), 405–422.
80. R.B. Larson, Turbulence and star formation in molecular clouds, *Mon. Not. Roy. Astron. Soc.* **194** (1981), 809–826.
81. C. Leitherer, C. Robert, L. Drissen, Deposition of mass, momentum, and energy by massive stars into the interstellar medium, *Astrophys. J.* **401** (1992), 596–617.
82. J.R.D. Lepine, G. Duvert, Star formation by infall of high velocity clouds on the galactic disk, *Astron. Astrophys.* **286** (1994), 60–71.
83. J. Lequeux, Large amounts of cold molecular hydrogen in the Small Magellanic Cloud, *Astron. Astrophys.* **287** (1994), 368–370.
84. J. Lequeux, R. J. Allen, S. Guilloteau, CO absorption in the outer Galaxy: Abundant cold molecular gas, *Astron. Astrophys.* **280** (1993), L23–L26.
85. F. Li, S. Ikeuchi, Formation of a giant Galactic gaseous halo – Metal absorption lines and high-velocity clouds, *Astrophys. J.* **390** (1992), 405–422.
86. W.J. Maciel, J. Koppen, Abundance gradients from disk planetary nebulae: O, Ne, S, and Ar, *Astron. Astrophys.* **282** (1994), 436–443.
87. P. Maloney, Are molecular clouds in virial equilibrium?, *Astrophys. J. Lett.* **348** (1990), L9–L12.
88. F. Matteucci, L. Greggio, Relative roles of type I and II supernovae in the chemical enrichment of the interstellar gas, *Astron. Astrophys.* **154** (1986), 279–287.
89. C.F. McKee, M.C. Begelman, Steady evaporation and condensation of isolated clouds in hot plasma, *Astrophys. J.* **358** (1990), 392–398.
90. D. Mera, G. Chabrier, R. Schaeffer, Towards a consistent model of the Galaxy. I. Kinematic properties, star counts and microlensing observations, *Astron. Astrophys.* **330** (1998), 937–952.
91. D. Mera, G. Chabrier, R. Schaeffer, Towards a consistent model of the Galaxy. II. Derivation of the model, *Astron. Astrophys.* **330** (1998), 953–962.
92. H. Meusinger, B. Stecklum, H. Reimann, The age-metallicity-velocity dispersion relation in the solar neighborhood and a simple evolution model, *Astron. Astrophys.* **245** (1991), 57–74.
93. J.C. Mihos, L. Hernquist, Gasdynamics and Starbursts in Major Mergers, *Astrophys. J.* **464** (1996), 641–663.
94. M. Miyamoto, R. Nagai, Three-dimensional models for the distribution of mass in galaxies, *Publ. Astron. Soc. Jap.* **27** (1975), 533–543.

95. A. Miyazaki, M. Tsuboi, Dense Molecular Clouds in the Galactic Center Region. II. Statistical Properties of the Galactic Center Molecular Clouds, *Astrophys. J.* **536** (2000), 357–367.
96. J.J. Monaghan, Smoothed particle hydrodynamics, *Annu. Rev. Astron. Astrophys.* **30** (1992), 543–574.
97. J.J. Monaghan, R.A. Gingold, Shock Simulation by the Particle Method SPH, *J. Comput. Phys.* **52** (1983), 374–389.
98. J.J. Monaghan, J.C. Lattanzio, A refined particle method for astrophysical problems, *Astron. Astrophys.* **149** (1985), 135–143.
99. B. Moore, F. Governato, T. Quinn, J. Stadel, G. Lake, Resolving the Structure of Cold Dark Matter Halos, *Astrophys. J. Lett.* **499** (1998), L5–L8.
100. H.W. Moos, W.C. Cash, L.L. Cowie, A.F. Davidsen, A.K. Dupree et al., Overview of the Far Ultraviolet Spectroscopic Explorer Mission, *Astrophys. J. Lett.* **538** (2000), L1–L6.
101. M. Mori, Y. Yoshii, K. Nomoto, Dissipative Process as a Mechanism of Differentiating Internal Structures between Dwarf and Normal Elliptical Galaxies in a Cold Dark Matter Universe, *Astrophys. J.* **511** (1999), 585–594.
102. N. Nakasato, M. Mori, K. Nomoto, Numerical Simulations of Globular Cluster Formation, *Astrophys. J.* **535** (2000), 776–787.
103. J.F. Navarro, Dark Matter Halos and Disk Rotation Curves, in *Galactic Halos*, edited by D. Zaritsky, volume 136 of *Astronomical Society of the Pacific Conference Series* (1998), pp. 409–417.
104. J.F. Navarro, C.S. Frenk, S.D.M. White, The Structure of Cold Dark Matter Halos, *Astrophys. J.* **462** (1996), 563–575.
105. J.F. Navarro, C.S. Frenk, S.D.M. White, A Universal Density Profile from Hierarchical Clustering, *Astrophys. J.* **490** (1997), 493–508.
106. J.F. Navarro, S.D.M. White, Simulations of Dissipative Galaxy Formation in Hierarchically Clustering Universes — Part One — Tests of the Code, *Mon. Not. Roy. Astron. Soc.* **265** (1993), 271–300.
107. K. Nomoto, K. Iwamoto, N. Nakasato, F. Thielemann, F. Brachwitz et al., Nucleosynthesis in type Ia supernovae, *Nucl. Phys. A* **621** (1997), 467–476.
108. K. Nomoto, F. Thielemann, K. Yokoi, Accreting white dwarf models of Type I supernovae. III — Carbon deflagration supernovae, *Astrophys. J.* **286** (1984), 644–658.
109. B.E.J. Pagel, Chemical Evidence on Galaxy Formation and Evolution, in *The Formation and Evolution of Galaxies*, edited by C. Munoz-Tunon & F. Sanchez (1994), pp. 149–230.
110. P.J.E. Peebles, Origin of the Angular Momentum of Galaxies, *Astrophys. J.* **155** (1969), 393–401.
111. P.J.E. Peebles, *Principles of physical cosmology* (Princeton University Press, Princeton, 1993).
112. M. Peimbert, Chemical evolution of the galactic interstellar medium: Abundance gradients, in *The Large-Scale Characteristics of the Galaxy*, edited by W.B. Burton, volume 84 of *IAU Symposium* (1979), pp. 307–315.
113. D. Pfenniger, The 3D dynamics of barred galaxies, *Astron. Astrophys.* **134** (1984), 373–386.

114. D. Pfenniger, F. Combes, Is dark matter in spiral galaxies cold gas? II. Fractal models and star non-formation, *Astron. Astrophys.* **285** (1994), 94–118.
115. D. Pfenniger, F. Combes, L. Martinet, Is dark matter in spiral galaxies cold gas? I. Observational constraints and dynamical clues about galaxy evolution, *Astron. Astrophys.* **285** (1994), 79–93.
116. L.S. Pilyugin, M.G. Edmunds, Chemical evolution of the Milky Way Galaxy. I. On the infall model of galactic chemical evolution, *Astron. Astrophys.* **313** (1996), 783–791.
117. L. Portinari, C. Chiosi, A. Bressan, Galactic chemical enrichment with new metallicity dependent stellar yields, *Astron. Astrophys.* **334** (1998), 505–539.
118. L. Portinari, C. Chiosi, A. Bressan, Galactic chemical enrichment with new metallicity dependent stellar yields, *Astron. Astrophys.* **334** (1998), 505–539.
119. W.H. Press, S.A. Teukolsky, W.T. Vetterling, B.P. Flannery, C. Lloyd et al., Book Review: Numerical recipes in C: the art of scientific computing / Cambridge U Press, 1993, *The Observatory* **113** (1993), 214–263.
120. C.M. Raiteri, M. Villata, J.F. Navarro, Simulations of Galactic chemical evolution. I. O and Fe abundances in a simple collapse model, *Astron. Astrophys.* **315** (1996), 105–115.
121. A. Renzini, M. Voli, Advanced evolutionary stages of intermediate-mass stars. I – Evolution of surface compositions, *Astron. Astrophys.* **94** (1981), 175–193.
122. O. Richter, R. Sancisi, Asymmetries in disk galaxies. How often? How strong?, *Astron. Astrophys.* **290** (1994), L9–L12.
123. A. Rieschick, G. Hensler, Chemodynamical gas flow cycles and their influence on the chemical evolution of dwarf irregular galaxies, *Astrophys. Space Sci.* **284** (2003), 861–864.
124. T.R. Saitoh, H. Daisaka, E. Kokubo, J. Makino, T. Okamoto et al., Toward First-Principle Simulations of Galaxy Formation: I. How Should We Choose Star-Formation Criteria in High-Resolution Simulations of Disk Galaxies?, *Publ. Astron. Soc. Jap.* **60** (2008), 667–681.
125. M. Samland, Modeling the Evolution of Disk Galaxies. II. Yields of Massive Stars, *Astrophys. J.* **496** (1998), 155–171.
126. M. Samland, G. Hensler, Modelling the Evolution of Galaxies, in *Reviews in Modern Astronomy*, edited by R.E. Schielicke, volume 9 of *Reviews in Modern Astronomy* (1996), pp. 277–306.
127. M. Samland, G. Hensler, C. Theis, Modeling the Evolution of Disk Galaxies. I. The Chemodynamical Method and the Galaxy Model, *Astrophys. J.* **476** (1997), 544–559.
128. B. Semelin, F. Combes, Formation and evolution of galactic disks with a multi-phase numerical model, *Astron. Astrophys.* **388** (2002), 826–841.
129. P.A. Shaver, R.X. McGee, L.M. Newton, A.C. Danks, S.R. Pottasch, The galactic abundance gradient, *Mon. Not. Roy. Astron. Soc.* **204** (1983), 53–112.
130. F.H. Shu, V. Milione, W. Gebel, C. Yuan, D.W. Goldsmith et al., Galactic Shocks in an Interstellar Medium with Two Stable Phases, *Astrophys. J.* **173** (1972), 557–592.
131. J. Silk, Star formation and galactic evolution – From protogalaxies to starbursts, in *Star Forming Regions*, edited by M. Peimbert & J. Jugaku, volume 115 of *IAU Symposium* (1987), pp. 663–689.

132. P.M. Solomon, A.R. Rivolo, J. Barrett, A. Yahil, Mass, luminosity, and line width relations of Galactic molecular clouds, *Astrophys. J.* **319** (1987), 730–741.
133. V. Springel, L. Hernquist, Cosmological smoothed particle hydrodynamics simulations: a hybrid multiphase model for star formation, *Mon. Not. Roy. Astron. Soc.* **339** (2003), 289–311.
134. V. Springel, N. Yoshida, S.D.M. White, GADGET: a code for collisionless and gasdynamical cosmological simulations, *New Astronomy* **6** (2001), 79–117.
135. M. Steinmetz, GRAPESPH: cosmological smoothed particle hydrodynamics simulations with the special-purpose hardware GRAPE, *Mon. Not. Roy. Astron. Soc.* **278** (1996), 1005–1017.
136. M. Steinmetz, M. Bartelmann, On the spin parameter of dark-matter haloes, *Mon. Not. Roy. Astron. Soc.* **272** (1995), 570–578.
137. M. Steinmetz, E. Mueller, On the capabilities and limits of smoothed particle hydrodynamics, *Astron. Astrophys.* **268** (1993), 391–410.
138. M. Steinmetz, E. Mueller, The formation of disk galaxies in a cosmological context: Populations, metallicities and metallicity gradients, *Astron. Astrophys.* **281** (1994), L97–L100.
139. M. Steinmetz, E. Muller, The formation of disc galaxies in a cosmological context: structure and kinematics, *Mon. Not. Roy. Astron. Soc.* **276** (1995), 549–562.
140. R.S. Sutherland, M.A. Dopita, Cooling functions for low-density astrophysical plasmas, *Astrophys. J. Suppl. Ser.* **88** (1993), 253–327.
141. R. Tantalò, C. Chiosi, A. Bressan, F. Fagotto, Spectro-photometric evolution of elliptical galaxies. II. Models with infall, *Astron. Astrophys.* **311** (1996), 361–383.
142. R.J. Thacker, E.R. Tittley, F.R. Pearce, H.M.P. Couchman, P.A. Thomas, Smoothed Particle Hydrodynamics in cosmology: a comparative study of implementations, *Mon. Not. Roy. Astron. Soc.* **319** (2000), 619–648.
143. C. Theis, A. Burkert, G. Hensler, Chemo-dynamical evolution of massive spherical galaxies, *Astron. Astrophys.* **265** (1992), 465–477.
144. C. Theis, G. Hensler, Dynamical evolution of dissipative cloud systems, *Astron. Astrophys.* **280** (1993), 85–104.
145. F. Thielemann, K. Nomoto, K. Yokoi, Explosive nucleosynthesis in carbon deflagration models of Type I supernovae, *Astron. Astrophys.* **158** (1986), 17–33.
146. J. Tomkin, M. Lemke, D.L. Lambert, C. Sneden, The carbon-to-oxygen ratio in halo dwarfs, *Astron. J.* **104** (1992), 1568–1584.
147. M. Tosi, The effect of metal-rich infall on galactic chemical evolution, *Astron. Astrophys.* **197** (1988), 47–51.
148. G. Toth, J.P. Ostriker, Galactic disks, infall, and the global value of Ω , *Astrophys. J.* **389** (1992), 5–26.
149. A. Udalski, M. Szymanski, J. Kaluzny, M. Kubiak, W. Krzeminski et al., The optical gravitational lensing experiment. Discovery of the first candidate microlensing event in the direction of the Galactic Bulge, *Acta Astronomica* **43** (1993), 289–294.
150. J.P. Vallee, Galactic magnetism and the rotation curves of M31 and the Milky Way, *Astrophys. J.* **437** (1994), 179–183.

151. S. van den Bergh, R.D. McClure, Rediscussion of extragalactic supernova rates derived from Evans's 1980–1988 observations, *Astrophys. J.* **425** (1994), 205–209.
152. L.B. van den Hoek, M.A.T. Groenewegen, New theoretical yields of intermediate mass stars, *Astron. Astrophys. Suppl. Ser.* **123** (1997), 305–328.
153. N. Voglis, A new distribution function fitting a nearly spherical cold-collapsed N-body system, *Mon. Not. Roy. Astron. Soc.* **267** (1994), 379–389.
154. N. Voglis, N. Hiotelis, Simulations of galaxy formation in tidal fields, *Astron. Astrophys.* **218** (1989), 1–14.
155. M.S. Warren, P.J. Quinn, J.K. Salmon, W.H. Zurek, Dark halos formed via dissipationless collapse. I — Shapes and alignment of angular momentum, *Astrophys. J.* **399** (1992), 405–425.
156. M.D. Weinberg, Detection of a large-scale stellar bar in the Milky Way, *Astrophys. J.* **384** (1992), 81–94.
157. S.D.M. White, M.J. Rees, Core condensation in heavy halos: A two-stage theory for galaxy formation and clustering, *Mon. Not. Roy. Astron. Soc.* **183** (1978), 341–358.
158. S.D.M. White, J. Silk, The growth of aspherical structure in the universe — Is the Local Supercluster an unusual system, *Astrophys. J.* **231** (1979), 1–9.
159. B.A. Wilking, C.J. Lada, The discovery of new embedded sources in the centrally condensed core of the Rho Ophiuchi dark cloud — The formation of a bound cluster, *Astrophys. J.* **274** (1983), 698–716.
160. T.L. Wilson, R. Mauersberger, On the question of dark matter and cold H₂, *Astron. Astrophys.* **282** (1994), L41–L44.
161. S.E. Woosley, T.A. Weaver, The Evolution and Explosion of Massive Stars. II. Explosive Hydrodynamics and Nucleosynthesis, *Astrophys. J. Suppl. Ser.* **101** (1995), 181–235.
162. W.H. Zurek, P.J. Quinn, J.K. Salmon, Rotation of halos in open and closed universes — Differentiated merging and natural selection of galaxy types, *Astrophys. J.* **330** (1988), 519–534.

CATAclysmic VARIABLES — THE FAINT INTERACTING CLOSE BINARY STARS AT THE LATE STAGE OF EVOLUTION

E.P. Pavlenko

5.1. Introduction

Cataclysmic variables (CVs) represent significant part of baryonic matter in our Galaxy according to the modern data of X-ray observations [55, 59]. Their space density estimated as 10^{-4} – 10^{-5} per pc^{-3} [1, 52, 55]. CVs are the close binary stars at the late stage of their evolution, they are formed on timescale of 0.1–10 Gyr [66]. CVs contain a primary compact component (white dwarf, or neutron star, or black hole) and the late type component. The later component fills in its Roche lobe and loses material via inner Lagrangian L1 point onto the compact star. If the primary is a non-magnetic star, accretion occurs from an accretion disk orbiting the primary. If the primary is magnetic white dwarf with field strength of 10^7 – 10^8 G, accretion happens directly onto magnetic poles without creating an accretion disk. In intermediate cases when a white dwarf possesses magnetic field of $\sim 10^6$ G, there could be both disc and pole accretion [78]. The main components of a CV are shown in Fig. 5.1 schematically.

CVs exhibit a wide range of phenomenology — dwarf nova eruptions which are thought to be caused by thermal instabilities in the accretion disks [5], and classical nova explosions which are thermonuclear runaways of the accreted matter on the white dwarf [78]. The range of observed phenomena depends on the mass transfer rate (that for CVs is $\sim 10^{-8}$ – 10^{-11} [78]), the mass ratio of the stellar components, and the magnetic field strength of the accreting white dwarf. The orbital periods of the majority of CVs

lay in a region ~ 6 hours – 76.2 minutes (period minimum) [31,32].

The mass transfer and secular evolution of CVs is driven by angular momentum loss caused mostly by magnetic braking [71] for orbital periods > 3 hr and by gravitational radiation [35] for orbital periods < 2 hr. Passing the minimal period, the secondary component continues to lose its mass. There must be a population of an extremely low-mass secondaries with mass < 0.1 solar masses (brown dwarf donor stars or so-called “period bouncers” or “bouncers”) in CVs.

Period bounce should occur when the thermal timescale of a secondary $\sim M_2^{-1}$ becomes longer than the mass-transfer timescale $\sim M_2$ [51], so they cross over when M_2 is sufficiently low. When mass-transfer is driven by angular momentum loss from gravitational radiation alone, this occurs when M_2 is near 0.07 solar masses [53,58].

Period bouncers have been proposed as the final stage of CV evolution since 1981 [53,58]. According to the theoretical predictions [6,17,18,33,34,52] ~ 70 – 75% of the current CV population have evolved past the orbital period minimum since their evolution at this stage is much slower than at earlier stage.

CVs on the final stage of evolution are presented by WZ Sge type stars (see Kato et al. [23]), having the shortest orbital period, large amplitude of the superoutburst and long (tens of years) recurrence time.

The real number of the observed bouncers is much smaller than predicted one. The reason is a selection effect. As it was describes by Knigge et al. [31,32] the donors in close binaries exhibits a fairly sharp drop in temperature, luminosity, and optical/ infrared flux well before the minimum period. That is why the detection of brown dwarf secondaries in CVs is extremely difficult task. Since CVs are intrinsically faint binaries (the candidate period bouncers should have the quiescent magnitude $M_v = 13$ – 14 [63]), they are unknown objects

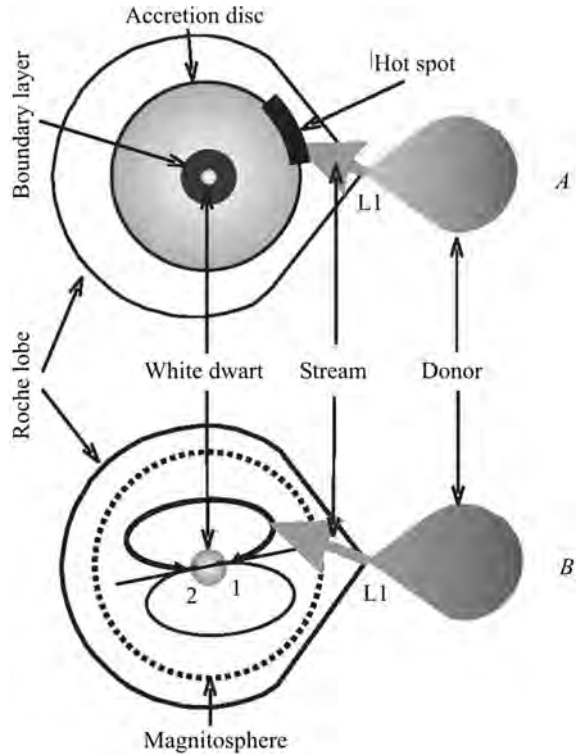


Fig. 5.1. Schematic view of a nonmagnetic (A) and magnetic (B) binary

until they manifest themselves via bright outburst. The discoveries of new CVs happen sporadically due to a different monitoring projects. Some projects serve for discovery of the CVs outbursts, for example the Catalina Real-Time Survey [12], watch by amateurs, etc. Another way is a search for outbursts of CVs that happened in the past by inspecting of a photographic plates available through a virtual observatories and private collections. A majority of these stars are located in the solar neighborhood. The attempt to estimate a “missed population” was done by Uemura [68].

The SDSS projects (see for example [64]) are able to extract a CVs in their quiescent state up to 21^m , so penetrate deeper into Galaxy and to detect CVs at distance as far as 10498 pc [24].

The white dwarf masses according to the study of most recent measurement of single non-magnetic DA white dwarfs discovered by SDSS are distributed between 0.59 and 1.4 solar masses [30], and the mean mass for the stars brighter than $g = 19$ and hotter than $T_{eff} = 12000$ K, is 0.593(16) solar masses. A last measuring of WD masses in CVs (observations of 17 intermediate polars with X-ray telescope Suzaku [79]) revealed the WDs in region of 0.4–1.2 solar masses with mean mass 0.88 ± 0.25 solar masses.

The accumulating of accretion matter leads to the thermonuclear runaway on the WD, that could happen (as it is believed) once 10^4 years. Much faster, typically once a week — several tens of years, the thermal instability of accretion disk accompanied by accretion onto the WD and outburst, occurs ([41, 78] and references therein). As a whole, the WDs in binaries are hotter then isolated WD of the same age. Urban and Sion [69] found that the average temperature of white dwarfs in dwarf novae with orbital periods less then 2 hr is ~ 18000 K and those with orbital periods larger than 3 hr, ~ 26000 K. A long accretion history forces WDs in close binaries many times to enter the instability strip and leave it. The latest investigations [65] showed that instability strip for the accreting WDs is wider the instability strip for isolated WDs.

Using the Spitzer Space Telescope, Howell et al. [19] have discovered that the accretion disk in the late type CV, WZ Sge is far more complex than previously believed. They found that the well known gaseous accretion disk is surrounded by an asymmetric disk of dusty material with a radius approximately 15 times larger than the gaseous disk. This dust ring is completely invisible at optical and near-IR wavelengths, hence consisting of “dark matter”. Assuming that the mass transfer rate of donor star in WZ Sge system is $\dot{M} = 10^{-12} M_{\odot} \text{yr}^{-1}$, while a dust disk mass estimate is $10^{-16} M_{\odot}$, authors calculated that the dust torus can easily be replenished continuously by a small amount of dusty material transferred from the cool brown dwarf-like secondary star.

Another Spitzer observations discovered an invisible matter — in form of circumbinary dust disks [7, 18] around magnetic CVs also.

5.2. Observations and results

The goal of our observations was: 1) search for potential brown dwarfs, 2) study of the interaction of a late type donor (particularly, brown dwarf) with white dwarf, 3) explore the structure of accretion discs among selected CVs. The main observations have been carried out in the primary focus of the 2.6-m mirror Shajn telescope [45–50]. Also the observations at 2-m and 60-cm telescopes in the observatory at peak Terskol, at 60-cm telescope of the Crimean laboratory of the Sternberg University and at 50-cm telescope of Tatranska Lomnica observatory have been carried out. Mostly we used filters R or V or no filters in order (if necessary) to reach a high time resolution. The selected targets were SDSS J080434.20 + 510349.2 = EZ Lyn, SDSS J102146.44 + 234926.3 = IK Leo, OT J012059.6 + 325545, V1108 Her, WZ Sge, V455 And, 1RXS J184542 + 483134.

5.2.1. White dwarf — late type donor star interaction

The study of the WDs masses is very important from a point of view of the SN Ia progenitors. The question is whether the accretion onto the white dwarf in some CVs actually grows the white dwarf mass to the Chandrasekhar limit. Wheeler [74] in his recent work considered the peculiarity of accretion that in the close pairs of white dwarf + M dwarf, could avoid the classical nova event and could be the single degenerate progenitors of type Ia supernovae.

It is amazing that extremely low mass donor, which is invisible in optic, continues to lose its material onto white dwarf and this interaction eventually leads to the tidal instability of accretion disc and its powerful optical outburst. In this subsection we present our contribution to an observational investigation of interaction of a low-mass late type donor star and white dwarf. Here we consider a rare light curves of the superoutbursts of several WZ Sge type CVs, accompanied by a series of peculiar events — rebrightenings (EZ Lyn, OT J012059.6 + 325545 [25, 26, 45]), and one prolonged rebrightening (IK Leo [67]).

EZ Lyn was first discovered as a CV and was considered as a potential dwarf nova with an underlying white dwarf (WD) in quiescence prior to the 2006 outburst [64]. It was first found in outburst by Pavlenko et al. [45] in 2006. Despite there was some reason to believe that EZ Lyn is similar to WZ Sge, possessing the outburst activity once per tens of years, it displayed the second outburst four years after the 2006 outburst [26, 50]. The overall light curve is shown in Fig. 5.2.

The 2010 outburst differed from the previous one at least in a sequence of rebrightenings (they are not seen in a presented scale). The comparison of rebrightenings is given in Fig. 5.3. Besides their different number during the first and second outbursts, rebrightenings in 2010 have a larger amplitude. Also

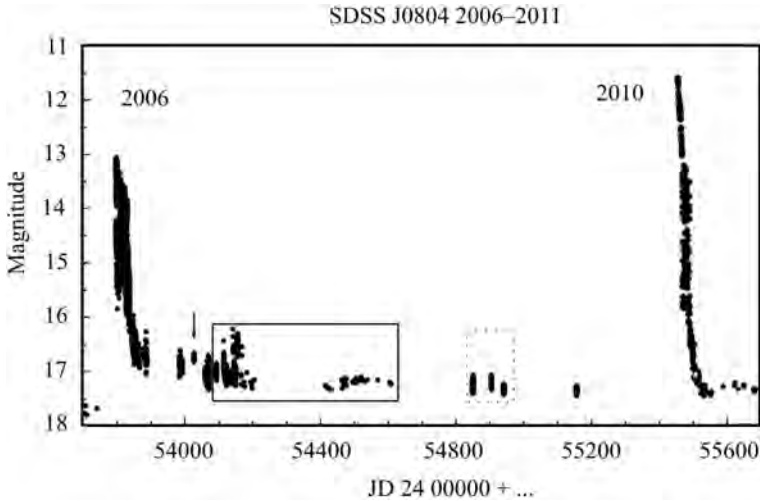


Fig. 5.2. The light curve of EZ Lyn in 2006–2010. The arrow points to the first detection of a non-radial pulsations of the white dwarf. The first prolonged box designates the time interval where pulsations were observed. The second small box indicates the period of unstable appearance of observed pulsations

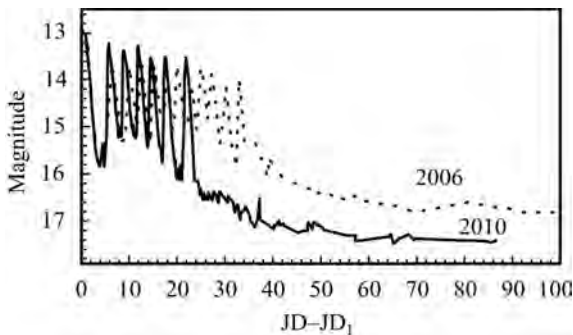


Fig. 5.3. The comparison of the rebrightenings of the EZ Lyn that occurred after the 2006 outburst (dotted line) and the 2010 outburst (solid line). The zero-point of the X axis starts at the rapid decline after the main outburst plateau. Data are combined, using $T_0 = \text{JD } 2453801$ for the 2006 outburst and $T_0 = \text{JD } 2455470$ for the 2010 outburst

the system became fainter much more quickly in 2010 than in 2006 at the same epoch following the end of the main outburst. In \sim one month since the end of the main outburst, EZ Lyn was one magnitude fainter in the 2010 than in the 2006.

OT J012059.6 + 325545 was first discovered in outburst by Itagaki [22] in 2010. This dwarf nova displayed a spectacular sequence of at least 9 rebrightenings. It has been observed by us in a framework of the VSNET campaign [26]. Here we present the part of the superoutburst light curve obtained in Crimea, Terskol and Tatranska Lomnica (Fig. 5.4).

IK Leo was discovered in its outburst ($V = 13^m.9$) by Christensen [8] on CCD images obtained in the course of the Catalina Sky Survey in 2006. It

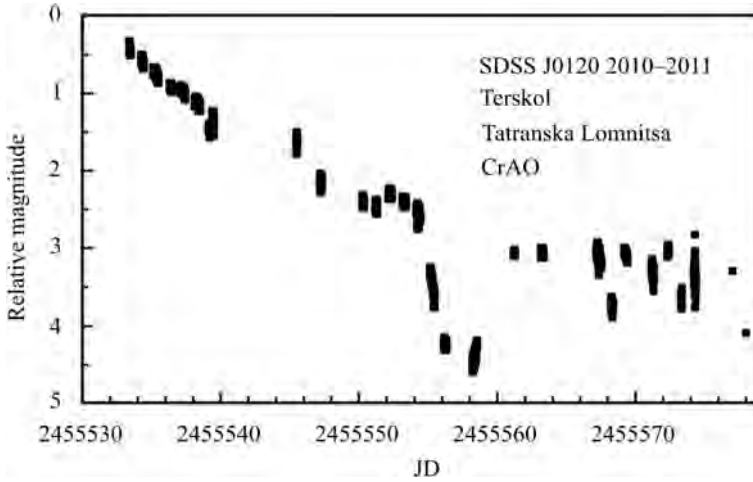


Fig. 5.4. The light curve of the OT J012059.6 + 325545 during the 2010–2011 superoutburst

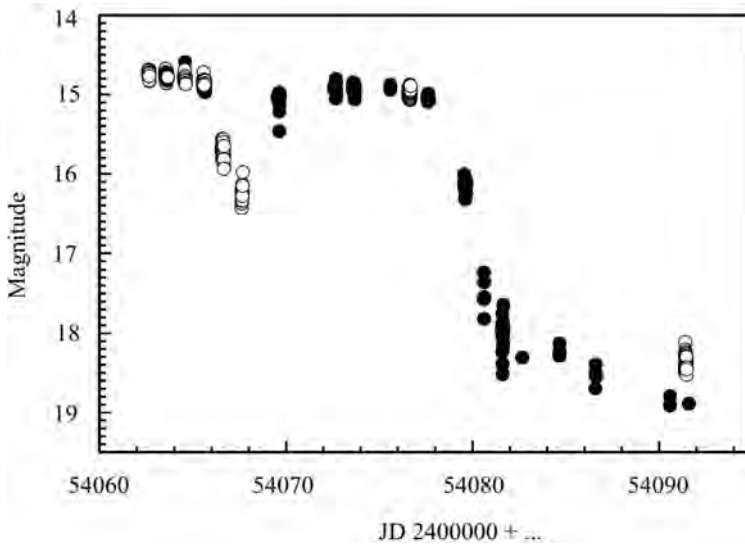


Fig. 5.5. The light curve of the IK Leo during the 2006 superoutburst

is the WZ Sge type star that displayed a superoutburst in 2006. We studied this CV in the framework of VSNET campaigns [20, 67]. The light curve of the outburst plotted based on our observations is shown in Fig. 5.5. Contrary to the SDSS J0804 and SDSS J0120, this binary had only one prolonged rebrightening.

A sequence of rebrightenings is rather rare phenomenon that potentially could be registered in some of WZ Sge type stars [23]. The importance of this phenomenon for search for the invisible matter in CVs will be described below.

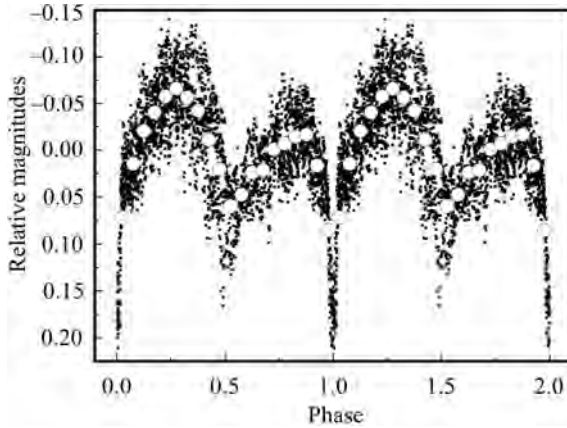


Fig. 5.6. The data of WZ Sge in 2008 quiescence folded on the orbital period. The mean points are shown by open circles. For clarity data are plotted twice

Similar to EZ Lyn, V1108 Her is a WZ Sge type star that has the respectively short recurrence time of outbursts that could be as short as 2 years [57]. There were no outbursts during a course of our observations in 2008.

5.2.2. The structure of accretion discs

Here we describe the peculiarities of accretion discs in the WZ Sge type stars, V455 And, V1108 Her, EZ Lyn and IK Leo that may have much larger extension and reservoir of poorly visible matter in an outermost parts of discs.

The WZ Sge type stars as a subclass of SU UMa stars show the periodical brightness variations “superhumps” (P_{sh}) that can be considered as the beat period (P_{beat}) between the orbital period (P_{orb}) and precession period (P_{prec}) of the elliptical disc [72]:

$$P_{prec}/P_{sh} = P_{prec}/P_{orb} - 1. \quad (5.1)$$

The disc became elliptical and begins to precess [73] if its outer edge achieves the 1 : 3 resonance for the systems with mass ratio $q < 0.3$. In the systems that have evolved past the period minimum ($q < 0.1$), the disc can be larger and achieve more stronger 1 : 2 resonance [16].

Generally the CVs with high enough inclination may display a brightness modulation with orbital period. The typical “orbital” light curve has a one-humped profile like for example U Gem [78]. It is caused by different visibility of a hot spot on the accretion disk in the classical model [61] or of a hot line in terms of an alternative model (see for example [14]). However a subgroup of the WZ Sge stars stands out among CVs displaying (typically) a two-humped orbital light curves in quiescence ([49] and references therein). The examples of the phase-averaged light curves are presented in Figs. 5.6–5.8.

Fig. 5.7. The data of V455 And folded on the orbital in 2011 quiescence. The mean points are shown by open circles. For clarity data are plotted twice

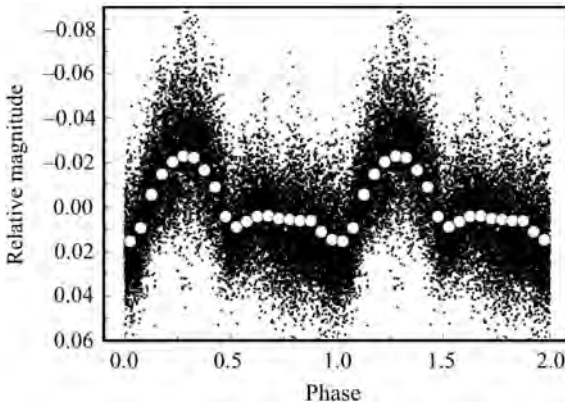
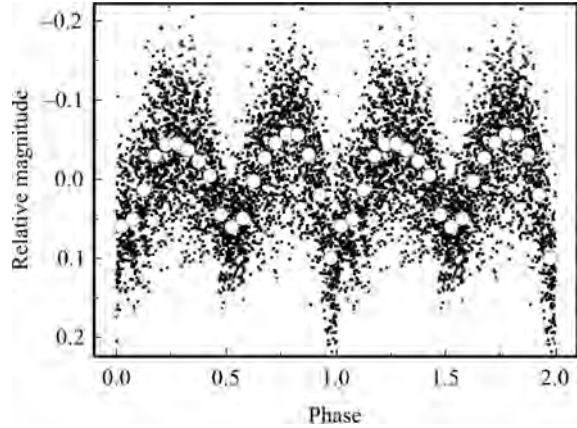


Fig. 5.8. The data of V1108 Her in 2008 quiescence folded on the orbital period. The mean points are shown by open circles. For clarity data are plotted twice

The profiles of the known orbital light curves of WZ Sge systems do differ. They can consist of a single sinusoidal wave as, for example, in HV Vir [37], EG Cnc [39], or a two-humped wave with well separated humps, each of which lasts half a period and has an equal (or almost equal) amplitude. Two-humped light curves are also known in systems such as WZ Sge [36], V455 And [2, 28], AL Com [43], EZ Lyn [47], SDSS J123813.73–033933.0 [81], BW Scl [3], SDSS J161033.64–010223.3 [77], and SDSS J013701.06–091234.9 = FL Cet [56]. Rogoziecki and Schwartzberg–Cherny [60] have found that switching from a single-humped curve to a two-humped curve can occur in WX Cet, and noted that this phenomenon has also been detected in WZ Sge [36]. Sometimes one or both humps in the light curves of WZ Sge systems undergo “splitting” (or have a “dip”), so that a peak at 1/4 of the orbital period can also appear in a periodogram. In 1971, Krzeminski and Smak [36] offered their explanation of the two-humped orbital light curve of WZ Sge: each of the humps is associated with the same hot spot on the disk, but only one of them corresponds to a

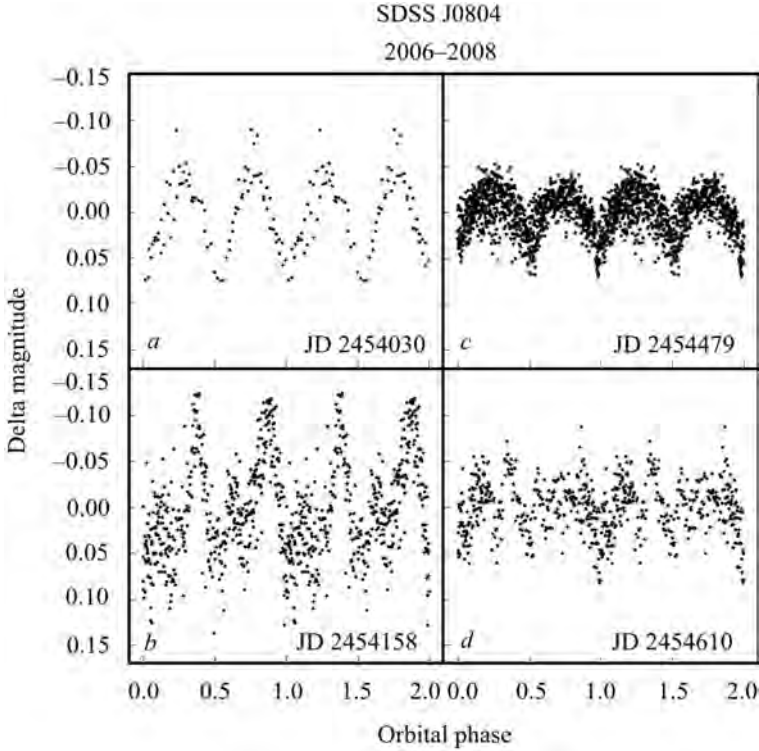


Fig. 5.9. The data folded on the orbital period for EZ Lyn in quiescence. In separate cuts four types of the light curve shape is shown

position of the hot spot on the leading edge of the disk relative to the observer, while the other is on the opposite edge and is observed through the transparent disk. Obviously, the central region of the disk is only partially transparent and, when the hot spot lies exactly behind this region, a sudden drop in the brightness may be detected at the second hump. A similar effect is also seen in WZ Sge at the brightness minimum. The transparency of the disk in WZ Sge stars may be a consequence of a very low rate of transfer of matter from the secondary star.

As it is seen on the Fig. 5.9, an original light curves of EZ Lyn can be two-humped with equal amplitudes and no splitting, or with splitting of one or both humps [43, 48].

Dramatic change of the orbital profile from night to night and even from cycle to cycle could be observed in V1108 Her (Fig. 5.10).

This last circumstance contradicts the proposed model, at least for EZ Lyn. Another explanation of the two-humped curve is related to a spiral structure of the accretion disk predicted in 1979 by Lin and Papaloizou [38] using the light curve of WZ Sge as an example. They calculated that such a structure occurs

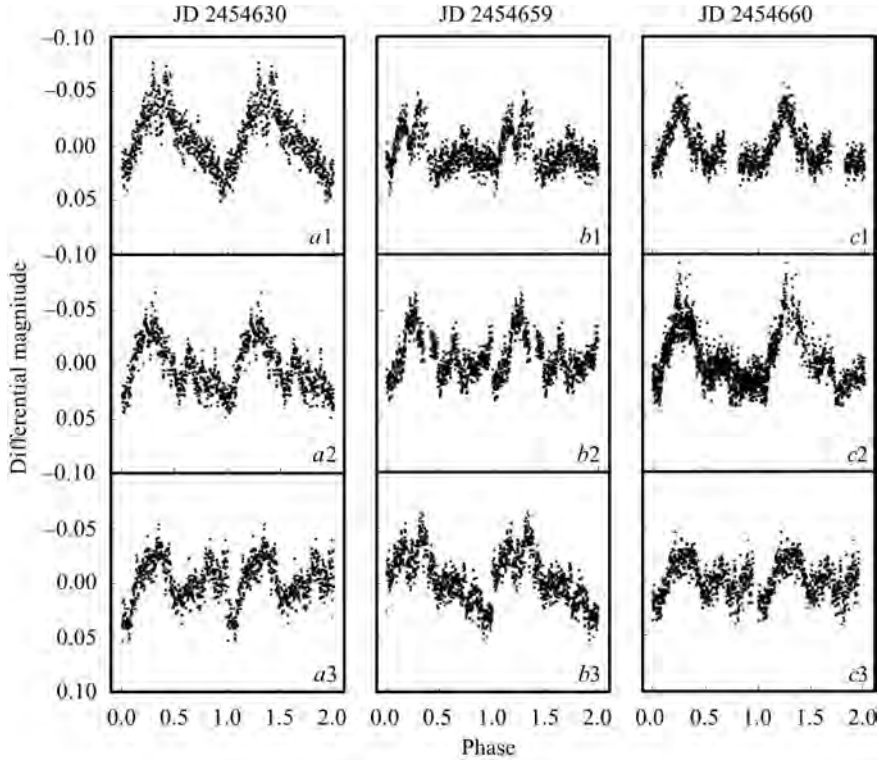


Fig. 5.10. Data folded with the orbital period for the three longest series of observations of V1108 Her (arranged vertically). Each series is represented by curves from three successive orbital cycles ($a1$ – $a3$, $b1$ – $b3$, $c1$ – $c3$)

only in disks extending to the 2 : 1 resonance, which can happen only when the mass ratio of the components is extremely small, <0.1 . In their model a two-armed structure is maintained even when transfer of matter from the donor star to the acceptor star is cut off, while the width of the spiral branches depends on the viscosity. Osaki and Meyer [42] were the first who demonstrated that the reason for the so-called “early superhumps” is also a 2 : 1 resonance that is attained when $q < 0.09$. The calculations of Aviles et al. [4], show that the two-humped structure of the short-period dwarf nova SDSS J123813.73 – 033933.0 is well described by a model with a 2 : 1 resonance with a low viscosity of the accretion disk. As for V1108 Her, the orbital light curve of this dwarf nova is not similar to either the typical single-humped or the typical two-humped curves encountered in WZ Sge stars. V1108 Her differs from the two-humped light curves of WZ Sge stars in that the structure of the smaller hump is highly variable; it can vanish entirely, while its averaged profile looks more like a low plateau (although in individual cycles, both humps can be well separated and have similar amplitudes (see Fig. 5.10, $a3$)). V1108 Her differs

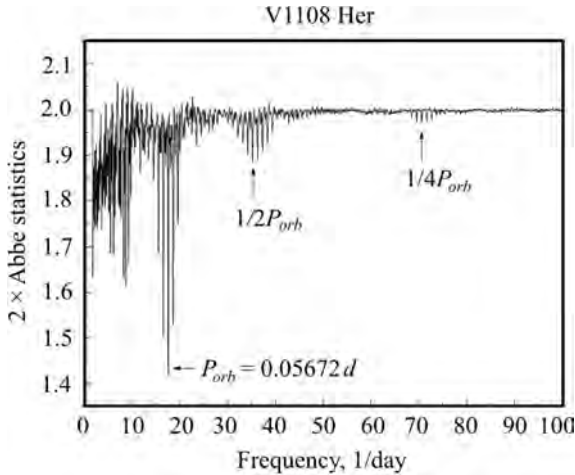


Fig. 5.11. The periodogram for the data of the V1108 Her in 2008 quiescence

from the single-humped sinusoidal orbital curves of the sort found in HV Vir and EG Cnc, in that the main hump in its light curve lasts all of half the orbital period. In this representation, the average curve for V1108 Her can be regarded as single-humped with a grazing eclipse at phase 0.5. One common property of the light curve of V1108 Her and the two-humped curves for WZ Sge stars is a sporadic doubling of each of the humps, i.e., a periodicity equal to a quarter of the orbital period. Such peculiarity produces additional peak at $1/4 P_{orb}$ on periodograms, as it is seen for the data of V1108 Her (Fig. 5.11). In analysis of time series we used the “ISDA” package [54].

This periodicity vanishes after subtraction of the orbital modulation with harmonics from the data; hence, it cannot be related to nonradial pulsations of the white dwarf. Kato, et al. [27], have estimated the radius of the accretion disk of V1108 Her at the end of the 2004 outburst ($0.499a \pm 0.149a$, where a is the distance between the components) and shown that, to within the limits of error, it may correspond to the radius where a 2 : 1 resonance occurs. On the other hand, the mass ratio $q = 0.068$ and the two-humped profile for at least some of the curves also indicate (in accordance with [38]) that the accretion disk in this system has reached a 2 : 1 resonance. An accretion disk close to a 2 : 1 resonance has a rotation period equal to half the orbital period and any structure (such as a blob) encounters a tidal perturbation twice during this period, thereby creating a signal equal to $1/4$ of the orbital period, which has also been observed in the light curves of V1108 Her.

We studied the superhumps evolution of the IK Leo during the VSNET campaign [67]. The IR observations have been performed with KANATA 1.5-m telescope at Higashi-Hiroshima Observatory led to discovery of unprecedented infrared activity during a rebrightening phase in a form of a prominent infrared superhumps. These provide evidence for the presence of mass reservoir at the

outermost part of the accretion disk. It was proposed that a moderately high mass-accretion rate at this infrared active region could be a source of the long-lived rebrightening observed in IK Leo.

5.2.3. White dwarf pulsations

In most CVs, the luminosity caused by accretion dominates the total luminosity from a binary. The white dwarf itself, having $M_V \sim 10^m - 13^m$, is seldom seen. So there is a great interest on CVs with detectable and pulsating WD because study of pulsations could reveal information about the stellar mass, core composition, age, rotation rate, magnetic field strength, and distance [40] (see the review papers [13, 75, 76]).

Using the astroseismology techniques, it is possible to measure a cooling rate of WD. There are some evidences from observations that the real WD cooling is much faster than expected from theoretical models. Isern et al. (1992) [21] declared that the cooling rate of the WD G117–B15a is a factor of 2–6 higher relatively theoretical calculations. The authors assumed that axions could provide the extra cooling necessary to account for the observed cooling rate and estimated the mass of axions. In this respect the study the drift of pulsation period on a long time scale is very important because this period depends on the WD temperature.

In this paragraph we point attention on a peculiarities of the WD nonradial pulsations in the WZ Sge type dwarf nova, EZ Lyn that are induced by a low-mass donor star. We also suspect that the WD in the IK Leo probably displays sporadically appearing nonradial pulsations.

Pavlenko (2007) [45] first discovered the non-radial pulsations of the WD in EZ Lyn. Now there are fifteen accreting pulsating WDs belonging to the SU UMa stars [40, 70]. Among the accreting pulsators that have experienced a dwarf novae outburst, EZ Lyn has the most dramatic history of events in a short time scale. Remind that during 2006–2010 interval EZ Lyn underwent two outbursts in 2006 and 2010, accompanied by 11 and 6 rebrightenings consequently [26, 45]. Additionally a series of mini-outbursts have been observed in December, 2006–January, 2007 [80]. Thus EZ Lyn gives a unique opportunity to study the evolution of the WD pulsations under such rare conditions as frequent accretion events.

The first pulsations were detected 8 months after the 2006 outburst and lasted for ~ 2 years. In Fig. 5.12 (*a–k*) the examples of original light curves of the EZ Lyn are shown. For each data the Fourier transform (FT) after orbital period subtraction was calculated and correspondent periodograms are performed in Fig. 5.12 (*l–u*). One could see that every periodogram (with exception of (*m*)) shows a sequence of significant peaks. These series concentrate within $40–150 d^{-1}$. The most stable pulsation corresponds to

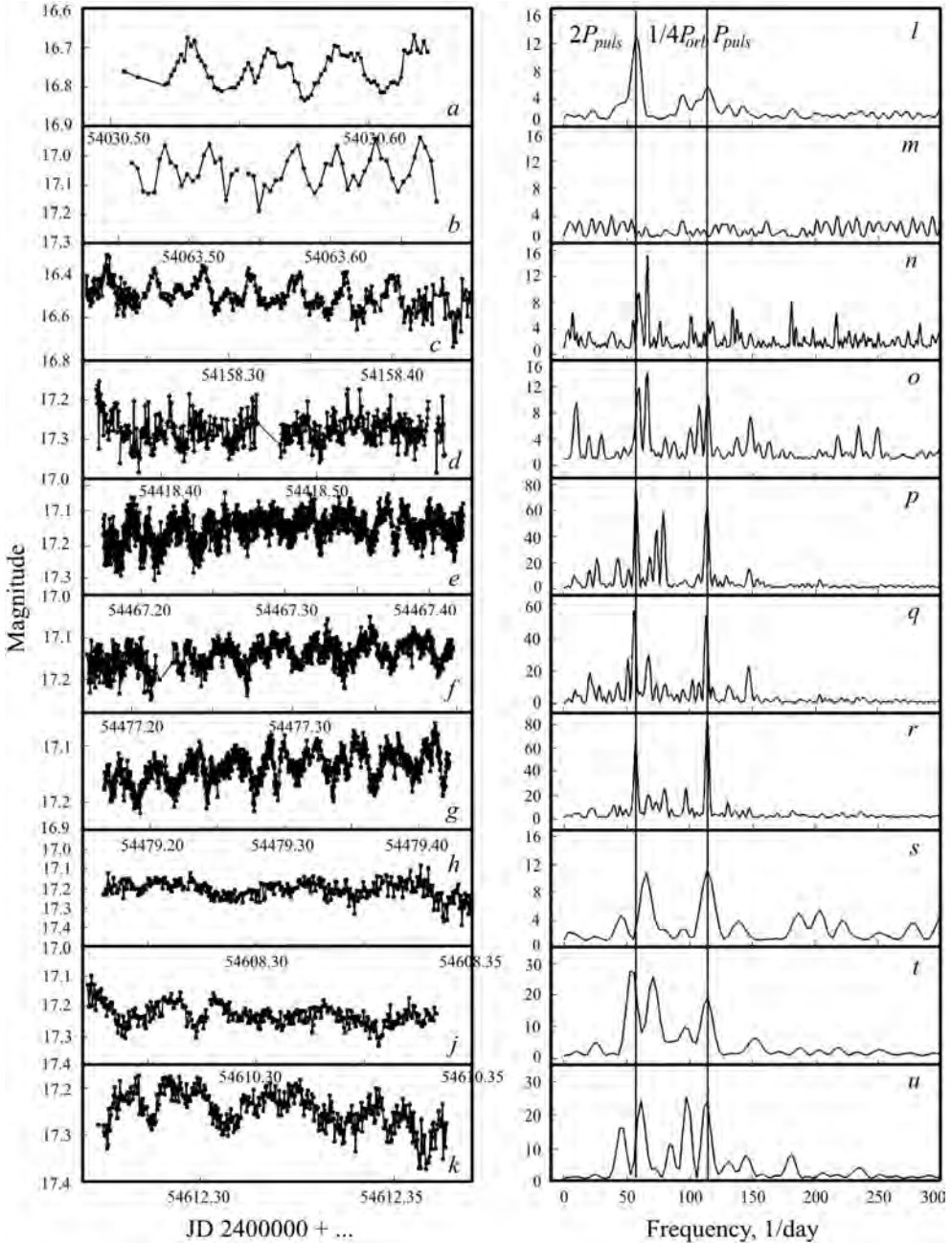


Fig. 5.12. The light curves (a–k) and corresponding Fourier transforms (l–u) for the separated observations of EZ Lyn in 2006–2008. The solid line are drawn through the frequencies 57 and $114 d^{-1}$ while the dotted one — through the $68 d^{-1}$

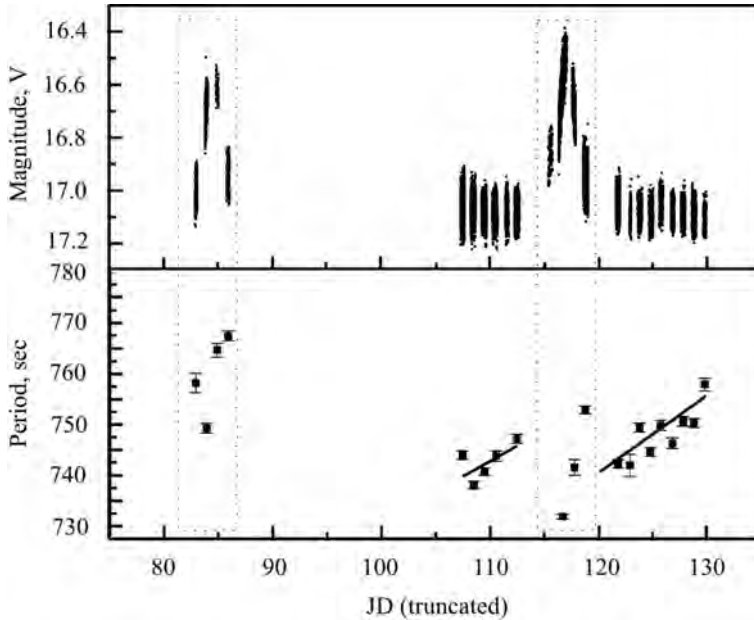


Fig. 5.13. The light curve of EZ Lyn including two minioutbursts (above) an corresponding drift of 12.6-min pulsation (below). The zero-point of the time scale is JD 2454000

$114 d^{-1}$ (12.6 min) and its twice value $57 d^{-1}$. The peak at $68 d^{-1}$ could be caused by the four-humped structure of the orbital light curve profile because it coincides just with $1/4P_{orb}$. The less stable peak could be seen at frequency near $74 d^{-1}$ and $148 d^{-1}$. Many of peaks probably are not connected with WD pulsations.

We did not find any significant pulsations in 1–1.5 months before the outburst. The first detection of the most stable 12.6-min. pulsations was in ~ 8 months after the expected start of the outburst. It is not clear whether the lack of pulsations at JD 2454063 was their temporary disappearance or caused by the insufficient data statistics. It is already known that the pulsators in dwarf novae could stop their pulsations by some reason contrary to the ZZ Ceti stars [62]. So the lack of pulsations in EZ Lyn in two occasions before outburst at JD 2453384 [64] and at JD 2453856 [45] could not be the argument that before outburst the white dwarf never pulsated. However it is possible to suggest that the compressional heating during the outburst and further fast cooling forced the white dwarf in the EZ Lyn to enter the instability strip.

On every night when the 12.6-min period was recorded, we estimated its snapshot value. The drift of this period in a region of 732–768 s is obvious.

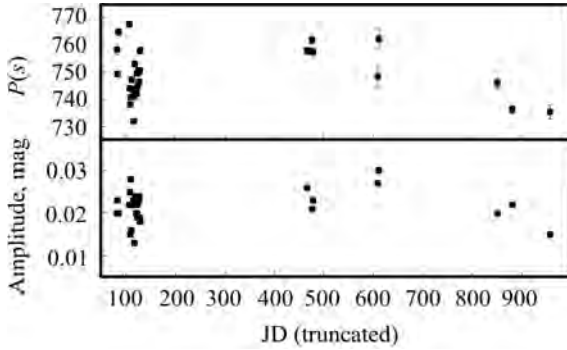


Fig. 5.14. The drift of periods and amplitudes of the 12.6-min pulsations of EZ Lyn during ~ 900 days since the appearance of pulsations. Zero-point of the time scale is JD 245400

This region is ~ 10 times wider than those found by Mukadam et al. [40] for SDSS J161033.64–010223.3 on a time scale that is ~ 100 times shorter than ours. Meantime Uthas et al. ([70]) found even larger drift of pulsations for SDSS J1457+51 and BW Scl occurred within 86 s during 47 d.

In Fig. 5.13 we presented the details of period drift around the minioutbursts. It is seen that during the minioutbursts themselves there is a larger scatter of periods, while after the every of minioutburst the periods lengthened. In a whole during the ~ 900 days this period varied in the same region regardless of the presence of minioutbursts. The drift of this period together with amplitude of pulsations is shown in Fig. 5.14. The amplitudes varied from 0.013^m to 0.030^m . The last data at JD ...600—...960 showed a decrease in period together with a decrease in amplitude. There was, however, no correlation between periods and amplitudes for the entire data.

The brightness variations of the IK Leo in quiescence (4 years after the 2006 outburst) show no modulation with expected orbital period. However during one from four nights Leo06 displayed a strong variability with short period 0.0136877-d. The corresponding periodogram and data folded on the best period are shown in Fig. 5.15. It is seen that the mean amplitude of these variations is about 0.01^m . This periodicity can't be the orbital one because it has not been keeping in other nights. The periodicity may be rather WD nonradial pulsations that could appear and disappear unexpectedly as in our observations of EZ Lyn [50].

5.2.4. Search for the masses of donors

There is an attractive way of indirect estimation the mass of a star-donor among a subclass of CVs, SU UMa type stars using a photometry. These close binaries are characterizing by a normal outbursts lasting 3–5 days and superoutbursts typically lasting 10–14 days [78]. There are brightness variations during the superoutbursts several percents longer the orbital variations

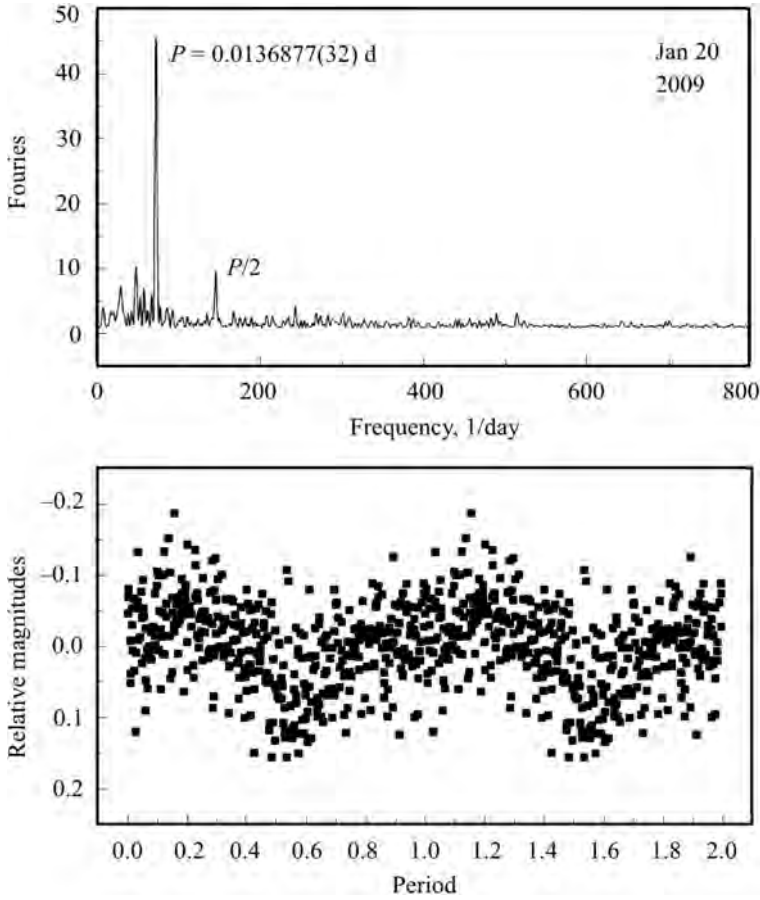


Fig. 5.15. The Fourier periodogram for the IK Leo (above) and the data folded on the 0.0136877-d period (below)

(positive superhumps). Once the orbital period P_{orb} and the superhump period P_{sh} are known, it is possible to find from observations a fractional period excess ϵ :

$$\epsilon = (P_{sh} - P_{orb})/P_{orb}, \quad (5.2)$$

where P_{orb} is an orbital period and P_{sh} is period of superhumps.

Using the relationship between ϵ and the ratio q of the masses of the secondary (m_2) and primary (m_1) components found by Patterson [52],

$$\epsilon = 0.18q + 0.29q^2, \quad (5.3)$$

or in linear form independently obtained by Knigge et al. [32]:

$$q(\epsilon) = (0.114 \pm 0.005) + (3.97 \pm 0.41)\epsilon - 0.025, \quad (5.4)$$

one could calculate a mass ratio of the components $q = m_2/m_1$.

To find candidates for brown dwarfs among the cataclysmic variables, we undertook the observations of a newly discovered dwarf novae. While detection of a superhumps during the superoutbursts is available with the small telescopes due to a relatively high brightness of system at this stage of its activity, the search for the orbital period in quiescence demands bigger telescopes. Optical modulation with orbital period could be detected in systems with rather high inclinations.

For this task we used the photometric observations of the follow targets as potential stars-bouncers: EZ Lyn, V1108 Her and IK Leo.

From our observations we found $P_{sh} = 0.059539$ and $P_{orb} = 0.0590048$ d for the EZ Lyn [46], [25] and $P_{orb} = 0.05672$ d for the V1108 Her [49]. Period of superhumps for V1108 Her (0.05778 d) was first found by Price et al. [57].

Using equations 1.3.1 and 1.3.2 we obtained $\epsilon = 0.009$, $q = 0.047$ for EZ Lyn and $\epsilon = 0.0135$, $q = 0.068$ for V1108 Her. The mass of the secondary component is constrained to be 0.028–0.065 solar masses for the EZ Lyn and by 0.041–0.095 solar masses for V1108 Her (if we put the mass of the white dwarf to be 0.6–1.4 solar masses). So the secondary component (donor) of the EZ Lyn and V1108 Her, could be the brown dwarf with a high probability.

Observations of IK Leo did not identify the orbital modulation probably because of a low inclination of the system [48].

5.2.5. New potential bouncer candidate among the magnetic CVs

The ROSAT source 1RXS J184542+483134 (hereafter 1RXS J1845) was first identified as an eruptive star by Denisenko and Sokolovsky [10]. Later on Denisenko and Smirnov [11] found from photometry that the star exhibited high-amplitude (1.6 magnitudes) brightness variations with a period of 79 min. They suggested that this source is a non-magnetic cataclysmic variable with a strong reflection effect. Such suggestion implied that the compact component, which produces the heating of the secondary so strong, must be a neutron star or a black hole.

In order to study this system in detail we have been carried out a photometry in BVRI or without usage of filters at ZTSh during several nights in May, 2011. Additionally we applied to the SWIFT for UV and X-ray observations and obtained them successfully partially simultaneously with our optical photometry [44]. The resulting data in BVRI folded on the orbital period are shown in Fig. 5.16. The previously unknown short-lasting eclipse is clearly seen. Its depth is probably different in BVRI, reaching the biggest value of 2^m in V. However the time resolutions have been used during a quasi-simultaneous multi-color observation did not allow to define the difference correctly.

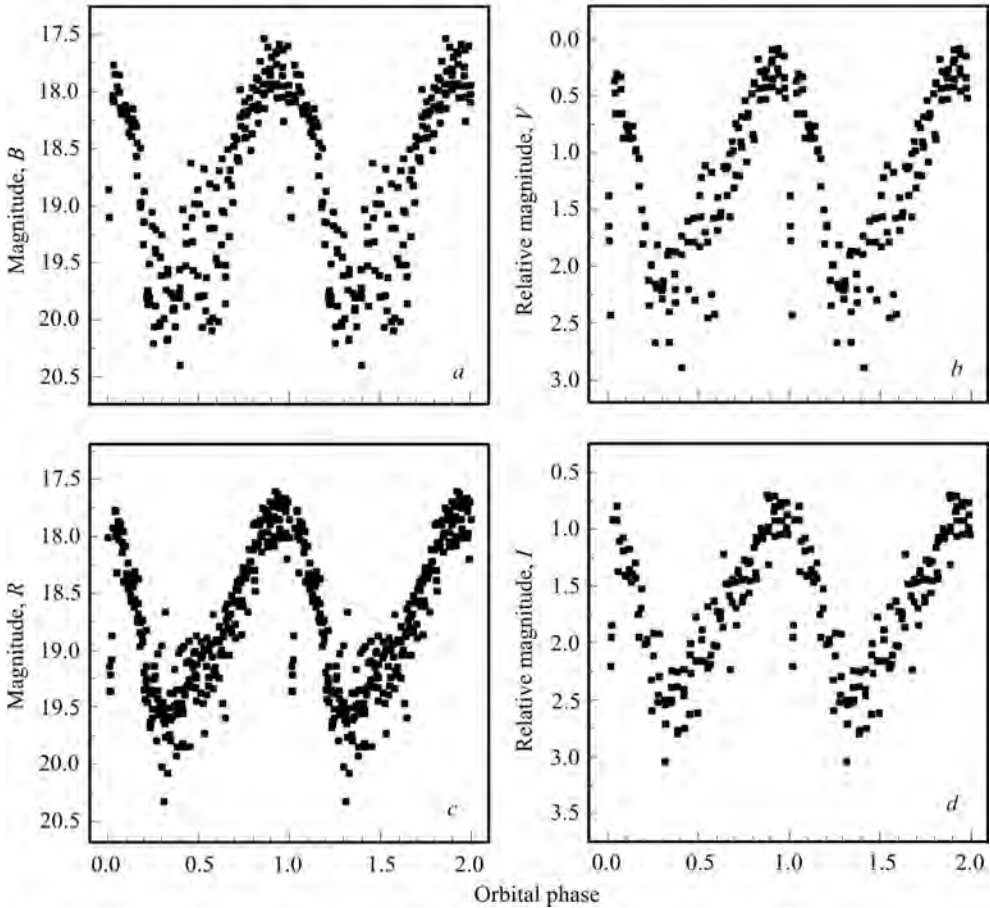


Fig. 5.16. The BVRI data of 1RXS J1845 folded on the orbital period 0.0549082 d. The B data are shown in cut a , V , R and I data are shown in cuts b , c and d correspondingly

The light curves appear to be asymmetric with steeper declining branch and enhanced scattering of the data around phase 0.5 in all spectral bands (that is opposite to eclipse).

The SWIFT UV data and time of X-ray quanta arrival correlated with the orbital period.

In order to define the eclipse profile with higher time resolution, we observed it without filters (Fig. 5.17). The depth of eclipse was about $1^m.4$ that is close to those obtained in R . The eclipse ingress and egress are very sharp, lasting about 0.005 of P_{orb} corresponding to eclipse of a compact source of a radiation.

Taking into account the X-ray and optical peculiarities described above, we concluded that previous interpretation [11] was wrong. The object is a cataclysmic variable indeed, but is not a disc system with reflection effect.

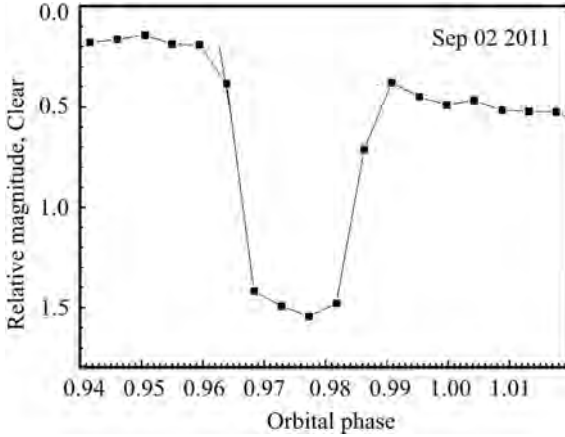


Fig. 5.17. The unfiltered eclipse profile of 1RXS J0038 in 2011 quiescence

Actually it consists of a late type companion donor and highly magnetic white dwarf with simultaneous and unequal accretion onto both magnetic poles. The brighter compact accretion region (accretion column) having a size of ~ 0.034 white dwarf radius is eclipsing by companion.

Using timing of eclipses, we refined the orbital period and obtained the ephemeris for the mid-eclipse time:

$$HJD_{ecl} = 2455677.37609 + 0.0549082E, \quad (5.5)$$

where E is a number of orbital cycles.

This period falls to the region of the shortest orbital period for magnetic CVs close to the minimum period.

According to theoretical models [32], all CVs with orbital periods < 90 min could be a potential bouncers — systems containing a brown dwarf that passed the period minimum in their evolution. All known bouncer candidates are nonmagnetic CVs. Until now it has been proven that only magnetic CV EF Eri contains a brown dwarf mass donor [15]. More over, Chun et al. [9] suggested that the stars donors in magnetic CVs are “more normal” then their cousins in a non-magnetic CVs. So the search for and studies of a short-period magnetic CVs is very important for understanding of a role of the white dwarf magnetic field on the late evolution of CVs, and for estimation of a magnetic CVs fraction containing brown dwarf among entire bouncers.

■

BIBLIOGRAPHY

1. T. Ak, S. Bilir, S. Ak, Z. Eker, Spatial distribution and galactic model parameters of cataclysmic variables, *NewA* **13** (2008), 133–143.
2. S. Araujo-Betancor, B.T. Gansicke, H.-J. Hagen et al., HS 2331 + 3905: The cataclysmic variable that has it all, *Astron. Astrophys.* **430** (2005), 629–642.
3. T. Augusteijn, L. Wisotzki, HE 2350–3908: a dwarf nova with a 78^m orbital period, *Astron. Astrophys.* **324** (1997), L57–L60.
4. A. Aviles, S. Zharikov, G. Tovmassian et al., SDSS J 123813.73–033933.0: A cataclysmic variable evolved beyond the period minimum, *Astron. J.* **711** (2010), 389–398.
5. S.A. Balbus, J.F. Hawley, A powerful local shear instability in weakly magnetized disks. I — Linear analysis. II — Nonlinear evolution, *Astrophys. J.* **376** (1991), 214–233.
6. I. Baraffe, U. Kolb, On the late spectral types of cataclysmic variable secondaries, *Mon. Not. R. Astron. Soc.* **318** (2000), 354–360.
7. C.S. Brinkworth, D.W. Hoard, S. Wachter et al., Spitzer Space Telescope Observations of Circumbinary Dust Disks around Polars, *Astrophys. J.* **372** (2007), 333–336.
8. E.J. Christensen, Variable Star in Leo, *CBET* **746** (2006), 1–1.
9. H. Chun, S. Howell, D. Daou et al., Detecting Brown Dwarfs in Interacting Cataclysmic Binaries, *Sptz. prop.* (2005), 238.
10. D.V. Denisenko & K. V. Sokolovsky, Identification of new cataclysmic variables in the 1RXS and USNO-B1.0 catalogs, *Pis'ma v Astronomicheskii Zhurnal* **37** (2011), 110–119.
11. D. Denisenko & E. Smirnov, 1RXS J 184542.4 + 483134: a New Cataclysmic Variable with Short-Period Photometric Variations, *PZP* **11** (2011), 10.
12. A.J. Drake, et al., First Results from the Catalina Real-Time Transient Survey, *Astrophys. J.* **696** (2009), 870–874.
13. G. Fontaine, & P. Brassard, The Pulsating White Dwarf Stars, *PASP* **120** (2008), 1043–1096.
14. A.M. Fridman, & D.V. Bisikalo, REVIEWS OF TOPICAL PROBLEMS: The nature of accretion disks of close binary stars: overreflection instability and developed turbulence, *PhyU* (2008), 551–576.

15. T.E. Harrison, S. B. Howell, P. Szkody et al., Phase-Resolved Infrared H- and K-Band Spectroscopy of EF Eridani, *Astrophys. J.* **614** (2004), 947–954.
16. K. Hellier, Cataclysmic variable stars. How and why they vary, Springer-Praxis books in astronomy and space sciences. Praxis Publishing Ltd, Chichester, UK (2001), 206 p.
17. S.B. Howell, D.R. Ciardi, Spectroscopic Discovery of Brown Dwarf-like Secondary Stars in the Cataclysmic Variables LL Andromedae and EF Eridani, *Astrophys. J.* **550L** (2001), 57–59.
18. S.B. Howell, C. Brinkworth, D. Hoard et al., First Spitzer Space Telescope Observations of Magnetic Cataclysmic Variables: Evidence of Excess Emission at 3–8 μm ?, *Astrophys. J.* **646** (2006), 65–68.
19. S.B. Howell, D.W. Hoard, C. Brinkworth et al., “Dark Matter” in Accretion Disks, *Astrophys. J.* **685** (2008), 418–427.
20. A. Golovin et al., Multicolor Observations of ASAS 002511 + 1217.2, *IBVS* **5611** (2005), 1–4.
21. J. Isern, M. Hernantz, E. Garcia-Berro, Axion cooling of white dwarfs, *Astrophys. J.* **392** (1992), L23–L25.
22. Itagaki, VSNET-alert 12431 (2010).
23. T. Kato, S. Yoshiyuki, H. Ryuko, HV Virginis and WZ Sge-Type Dwarf Novae, *PASJ* **53** (2001), 1191–1210.
24. T.Kato, H. Maehara, M. Uemura, Characterization of Dwarf Novae Using SDSS Colors, *PASJ* **64** (2012), 63 p.; arXiv:1111.4286 (2011), 69 p.
25. T. Kato et al., SDSS J 080434.20 + 510349.2: Eclipsing WZ Sge-Type Dwarf Nova with Multiple Rebrightenings, *Publ. Astron. Soc. Jap.* **61** (2009), 601–613.
26. T. Kato et al., Survey of Period Variations of Superhumps in SU UMa-Type Dwarf Novae. III. The Third Year (2010–2011), *PASJ* **64** (2012), 21–100.
27. T. Kato, et al., Survey of Period Variations of Superhumps in SU UMa-Type Dwarf Novae, *Publ. Astron. Soc. Jap.* **61** (2009), S395–S616.
28. N. Katysheva & S. Shugarov, J. V455 and a life before the outburst, *Phys.: Conf. Ser.* **172** (2009), 012044, 1–4.
29. N. Katysheva, I. Voloshina, Cataclysmic Variables with Magnetic White Dwarfs, *ASP Conf. Ser.* **372** (2007), 527–530.
30. S.O. Kepler, S.J. Kleinman, A. Nitta et al., The White Dwarf Mass Distribution, *ASP Conf. Ser.* **372** (2007), 35–40.
31. C. Knigge, Cataclysmic Variables: Eight Breakthroughs in Eight Years, arXiv: 1101.2901(2011).
32. C. Knigge, I. Baraffe, J. Patterson, The Evolution of Cataclysmic Variables as Revealed by Their Donor Stars, *Astrophys. J. Suppl. Ser.* **194** (2011), 28–90.
33. U. Kolb, A model for the intrinsic population of cataclysmic variables, *Astron. Astrophys.* **271** (1993), 149–166.
34. U. Kolb, I. Baraffe, Brown dwarfs and the cataclysmic variable period minimum, *Mon. Not. R. Astron. Soc.* **309** (1999), 1034–1042.
35. R.P. Kraft, J. Methews & J.L. Greenstein, Binary Stars among Cataclysmic Variables. II. Nova WZ Sagittae: a Possible Radiator of Gravitational Waves, *Astrophys. J.* **136** (1962), 312–315.

36. W. Krzeminski, J. Smak, Eruptive Binaries. III. The Recurrent Nova WZ Sagittae, *Acta Astronomica* **21** (1971), 133–184.
37. E. Leibowitz, H. Mendelson, A. Bruch, et al., The 1992 outburst of the SU Ursae Majoris-type dwarf nova HV Virginis, *Astrophys. J.* **421** (1994), 771–778.
38. D.N.C. Lin, & J. Papaloizou, Tidal torques on accretion discs in binary systems with extreme mass ratios, *Mon. Not. R. Astron. Soc.* **186** (1979), 799–812.
39. K. Matsumoto, T. Kato, K. Ayani, T. Kawabata, On the Orbital Period of EG Cancri, *IBVS* **4613** (1998), 1–4.
40. A.S. Mukadam et al., Multi-site Observations of Pulsation in the Accreting White Dwarf SDSS J 161033.64–010223.3 (V386 Ser), *Astrophys. J.* **714** (2010), 1702–1714.
41. Y. Osaki, Dwarf-Nova Outbursts, *Publications of the Astronomical Society of Pacific* **108** (1996), 39–60.
42. Y. Osaki, F. Meyer, Early humps in WZ Sge stars, *Astron. Astrophys.* **383** (2002), 574–579.
43. J. Patterson, T. Augusteijn, D. Harvey et al., Superhumps in Cataclysmic Binaries. IX. AL Comae Berenices, *Publications of the Astronomical Society of Pacific* **108** (1996), 748–761.
44. E. Pavlenko, K. Sokolovsky, A. Baklanov et al., 1RXS J 184542.4 + 483134 is a new eclipsing polar, *ATel* **3436** (2011), 1–1.
45. E. Pavlenko et al., Discovery of the New WZ Sge Star SDSS J 080434.20 + 510349.2, *ASPC* **372** (2007), 511–514.
46. E.P. Pavlenko, V.P. Malanushenko, Unique components of the WZ Sge-type dwarf nova SDSS J 080434.20 + 510349.2, *KBCB* **25** (2009), 48–53.
47. E.P. Pavlenko, The white dwarf in dwarf nova SDSS J 080434.20 + 510349.2: Entering the instability strip?, *J. Phys.: Conf. Ser.* **172** (2009), 012071, IOP Publ.
48. E. Pavlenko, O. Antonyuk, K. Antonyuk et al., Activity of five WZ Sge-type systems in a few years after their outbursts, *AIP Conf. Proc.* **1273** (2010), 332–337.
49. E.P. Pavlenko, T. Kato, O.I. Antonyuk et al., Features of the orbital variability in the brightness of the WZ Sge type dwarf nova V1108 Her, *Astrophysics* **54** (2011), 483–495.
50. E. Pavlenko, V. Malanushenko, G. Tovmassian et al., SDSS J 080434.20 + 510349.2: Cataclysmic Variable Witnessing the Instability Strip?, *ArXiv:1111.2339* (2011).
51. J. Patterson, Distances and Absolute Magnitudes of Dwarf Novae: Murmurs of Period Bounce, *ArXiv:0903.1006* (2009), 57 p.
52. J. Patterson, Late Evolution of Cataclysmic Variables, *Publications of the Astronomical Society of Pacific* **110** (1998), 1026–1031.
53. B. Paczynski, R. Sienkiewicz, Gravitational radiation and the evolution of cataclysmic binaries, *Astrophys. J.* **248** (1981), L27–L30.
54. Ja. Pelt, *Irregularly Spaced Data Analysis. User Manual*, Helsinki (1992).
55. M.L. Pretorius, & C. Knigge, The space density and X-ray luminosity function of non-magnetic cataclysmic variables, *arXiv: 1109.3162* (2012).
56. M.L. Pretorius, P.A. Woudt, B. Warner, et al., High-speed photometry of SDSS J 013701.06–091234.9, *Mon. Not. R. Astron. Soc.* **352** (2004), 1056–1060.

57. A. Price, B. Gary, J. Bedient et al., A New Cataclysmic Variable in Hercules, *Publ. Astron. Soc. Pacif.* **116** (2004) 1117–1122.
58. S. Rappaport, P.C. Joss, R.F. Webbink, The evolution of highly compact binary stellar systems, *Astrophys. J.* **254** (1982), 616–640.
59. M. Revnivtsev, E. Churazov, S. Sazonov et al., Universal X-ray emissivity of the stellar population in early-type galaxies: unresolved X-ray sources in NGC 3379, *Astron. Astroph.* **490** (2008), 37–43.
60. P. Rogoziecki, A. Schwarzenberg-Cherny, The dwarf nova WX Cet: a clone of WZ Sge or a pretender?, *Mon. Not. R. Astron. Soc.* **323** (2001), 850–858.
61. J. Smak, Eruptive Binaries. II. U Geminorum, *Acta Astronomica* **21** (1971), 15–47.
62. J. Southworth, D.M. Townsley, B.T. Gansicke, Orbital periods of cataclysmic variables identified by the SDSS – IV. SDSS J220553.98 + 115553.7 has stopped pulsating, *Mon. Not. R. Astron. Soc.* **388** (2008), 709–715.
63. L.N.S. Sproats, S.B. Howell, K.O. Mason, Infrared colours, distance determination and absolute magnitudes of a sample of faint cataclysmic variables, *Mon. Not. R. Astron. Soc.* **282** (1996), 1211–1222.
64. P. Szkody, A. Henden, M. Agueros et al., Cataclysmic Variables from Sloan Digital Sky Survey. V. The Fifth Year (2004), *Astron. J.* **131** (2006), 973–983.
65. P. Szkody, et al., Finding the Instability Strip for Accreting Pulsating White Dwarfs From Hubble Space Telescope and Optical Observations, *Astrophys. J.* **710** (2010), 64–77.
66. D.W. Townsley, L. Bildsten, The Thermal Structure and Evolution of Accreting White Dwarfs, *ASP Conf. Ser.* **372** (2007), 557–562.
67. M. Uemura et al., Discovery of a WZ Sge-Type Dwarf Nova, SDSS J102146.44 + 234926.3: Unprecedented Infrared Activity during a Rebrightening Phase, *Publ. Astron. Soc. Jap.* **60** (2008), 227–236.
68. M. Uemura, T. Kato, D. Nogami, H. Ohsugi, Dwarf Novae in the Shortest Orbital Period Regime: II. WZ Sge Stars as the Missing Population near the Period Minimum, *Publ. Astron. Soc. Jap.* **62** (2010), 613–620.
69. J.A. Urban, E.M. Sion, The Dwarf Novae during Quiescence, *Astrophys. J.* **642** (2006), 1029–1041.
70. H. Uthas et al., Two new accreting, pulsating white dwarfs: SDSS J1457+51 and BW Sculptoris, *Mon. Not. R. Astron. Soc.* **420** (2012), 379–387.
71. F. Verbunt, C. Zwaan, Magnetic braking in low-mass X-ray binaries, *Astron. Astrophys.* **100** (1981), L7–L9.
72. N. Vogt, The structure and outburst mechanisms of dwarf novae and their evolutionary status among cataclysmic variables, *MitAG* **57** (1982), 79–118.
73. R. Whitehurst, Numerical simulations of accretion disks. I – Superhumps – A tidal phenomenon of accretion disks, *Mon. Not. R. Astron. Soc.* **232** (1988), 35–51.
74. J.C. Wheeler, White dwarf/Red dwarf binaries as a single degenerate progenitors of type Ia supernovae, *Astrophys. J.* (2012), in press, arXiv: 1209.1021.
75. D.E. Winget, Asteroseismology of white dwarf stars, *Journal of Physics* **10** (1998), 11247–11261.

76. D E. Winget, S.O. Kepler, Pulsating White Dwarf Stars and Precision Asteroseismology, *Ann. Rev. Astron. Astrophys.* **46** (2008), 157–159.
77. P.A. Woudt, B. Warner, SDSS J 161033.64–010223.3: a second cataclysmic variable with a non-radially pulsating primary, *Mon. Not. R. Astron. Soc.* **348** (2004), 599–602.
78. B. Warner, *Cataclysmic Variables*, Cambridge University Press, Cambridge, 1995.
79. T. Yuasa, K. Nakazawa, K. Makishima et al., White dwarf masses in intermediate polars observed with the Suzaku satellite, *Astron. & Astroph.* **520** (2010), 25–41.
80. S.V. Zharikov, et al., Cyclic brightening in the short-period WZ Sge-type cataclysmic variable SDSS J080434.20+510349.2, *Astron. Astrophys.* **486** (2008), 505–509.
81. S.V. Zharikov, G.H. Tovmassian, R. Napiwotzki et al., Time-resolved observations of the short period CV SDSS J 123813.73–033933.0, *Astron. & Astropys.* **449** (2006), 645–653.

6

CHAPTER

ULTRACOOOL DWARFS IN OUR GALAXY

Ya. V. Pavlenko

6.1. Introduction

Observations of galaxies and their clusters and modelling of their gravitational properties, provided one of the major enigma in astronomy for a long time, at least from 70-th (see [103]). In the framework of the conventional paradigma, clusters contain matter galaxies with stars formed billions of years ago. However, the “visible” amount of mass in clusters are not enough to make them gravitationally bound. In other words, the observed masses are not sufficient to prevent the galaxies from “escaping”. There must be some kind of invisible mass (dark matter) to provide a stability of these complicate dynamical systems (see [24]).

Another indication of the presence of dark matter in galaxies we found in the flatness of the rotation curves of galaxies and clusters (see [23]). Namely, there are no downward turns. It means the mass distribution extends far beyond the measured values, probably in the forms of massive haloes of dark matter, i.e their masses increase outward [68].

These and the other ideas about invisible matter gained powerful confirmations by the end of the last century on the basis of cosmological data. The very first observations of Supernovae 1a and CMB anisotropy showed that about 30 % of the whole cosmological density is due to the matter with a non-relativistic equation of state, which is often assumed as the “cold” matter having negligible pressure. From considerations of nuclear reactions in the Early Universe and the elements abundance we know that the content of usual

baryonic matter cannot exceed 4–5%. Therefore, most of this “cool” matter must be non-baryonic. This view gains support from WMAP and PLANK observations, weak lensing (cf. Bullet Cluster), etc.

On the other hand, a huge fraction of baryonic matter is also in some “invisible” or almost “invisible” form! From the viewpoint of the conventional science, possibility is that this invisible matter is concentrated in objects of low luminosity.

- Gas in the intergalactic space. Large amounts of the intergalactic gas may exist in a form of low density clouds in the space in galaxies and between galaxies can be detected by only radio observations on 21 cm^{-1} . Till now we have known a little to proper account its mass which is invisible in optical and infrared spectral region (de Paolis et al. [65]). The mass of intergalactic gas is calculated to be a considerable amount, perhaps greater than the amount in galaxies and stars.

- Stellar Remnants, i.e white dwarfs, neutron stars or black holes, could make up the Dark Matter [64]. However, our understanding of the history of the Milky Way makes it unlikely that stars could have formed and died sufficiently rapidly in the past to make up the necessary mass of 10 or more times the current mass of stars (see [28]).

- Ultracool dwarfs (UCD), i.e dwarfs of masses less than $0.1 M_{\odot}$. We use here the definition “ultracool dwarfs” for all low mass objects of spectral classes later than M6. In general, the number of dwarfs increases dramatically as we go to the lower bottom of the Main sequence. We do not know definitely if this trend continues beyond the cutoff for the ignition of nuclear reactions. If so, population of ultracool dwarfs might account for a significant fraction of the Dark Matter. Unfortunately, UCDs are hard to spot since they are cool and very low in luminosity. Recent infrared studies found a lot of ultracool dwarfs, but not in sufficient numbers to make up the dark matter needed in the Milky Way.

In this chapter we draw our main attention to the physical properties of the ultracool dwarfs. Populations of ultracool dwarfs occupy the right-bottom quadrant below the bottom of the conventional Main sequence. A lot of ultracool dwarfs in the solar vicinity were discovered after 1995 (see [5] for review). Up to now, more than two-thirds of stars within 10 parsecs are M dwarfs and it is very probable that this number density prevails throughout our Galaxy. Unless there is a sharp turn-down in the stellar mass function, they and even lower mass objects are an important component of the Galaxy’s mass.

6.2. M-dwarfs of later spectral classes

Studies of M dwarf spectra are of interest to many branches of modern astrophysics. Indeed, perhaps 70 % of stars within 10 parsecs are M dwarfs and it is very probable that this number density prevails throughout our Galaxy. The population of these numerous low-mass stars ($0.08 M_{\odot} < M < 0.6 M_{\odot}$), together with substellar objects (brown dwarfs; $M \leq 0.075 M_{\odot}$, see section 6.3) would contain an appreciable amount of the baryonic matter in the Galaxy.

M-dwarfs are occupied the right-bottom corner of the classical diagram of Hertzsprung—Russel diagram. Before 1995 two M-dwarfs, i.e. VB8 and VB10 were known as the coolest dwarfs of the Galaxy. Effective temperatures of M-dwarfs cover the wide range $2200 < T_{\text{eff}} < 3800$ K, gravity parameter $\log g$ in atmospheres of young M-dwarfs are of $\log g = 4.0\text{--}5.0$. In fact M-dwarfs of $\log g = 4.0\text{--}4.5$ lies above their Main Sequence. Due to the low masses ($M < 0.1 M_{\odot}$ times of their evolution toward Main sequence are huge (>10 Gyr).

M-dwarfs are fully convective objects. Due to the low temperatures in their interiors and atmospheres the radiative transfer processes there is not effective enough due to the low opacity. Therefore convective envelope extends from the core to the lower photosphere.

The verification of the theory of stellar evolution and structure of stars, the detection among M dwarfs of a subset of young brown dwarfs, and the physical state of plasma in their low temperature atmospheres are among a few of the interesting problems that may be addressed through the detailed study of M-dwarfs.

6.2.1. Procedure of synthetic spectra computation

Hereafter we discuss the results of theoretical spectra computation and comparison of them with observations.

First of all, to analyse spectrum of any M-dwarf, as well as any other star we should determine a long range of input data:

- model atmosphere. In the most general case the model atmosphere is a table of physical parameters, i.e. pressure, number densities, temperature, etc, vs depth in stellar atmosphere. As a depth parameter we use rosseland mean optical depth or column density $\rho_x = \int \rho dx$, here ρ is the density on the geometrical depth x . In our work we use two grids of model atmospheres computed by Tsuji [106] and Hauschildt et al. [32], These two grids of atmospheres were computed in the framework of similar paradigmas, therefore provide similar results.

- The data set of constants needed to model ionization-dissociation equilibrium. The detailed descriptions of the procedure of computations of the molecular densities in stellar atmospheres can be found in the papers of

Tsuji [104] and Kurucz [48]. Here we note that in the case of M-dwarfs the system of the equations of chemical equilibrium should include all chains of possible reactions for ions, neutral atoms and molecules, including polyatomic molecules.

— A set of continuum and pseudocontinuum opacity sources. It is worth noting that in the case of M-dwarfs negative ion of hydrogen is not the main source of opacity, because number of free electrons sharply decreases with lowering temperatures in atmospheres of M-dwarfs. Main donors of free electrons here are metals of low ionization potential, especially alkali metals (see Pavlenko et al. [69]).

— Lists of lines of molecular bands and atomic lines that are the significant absorbers in the cool oxygen-rich atmospheres.

Theoretical spectral energy distributions¹ were computed for model atmospheres of M-dwarfs with effective temperatures $T_{\text{eff}} = 2500\text{--}3200$ K from the NextGen grid of Hauschildt et al. [32] for solar metallicity [1]. Hereafter we use the syntax “effective temperature/ gravity/metallicity”, e.g. 2800/5.0/0 to signify the model atmosphere. Unless otherwise mentioned all models are for $\log g = 5.0$. Computations of synthetic spectra were carried out by the program WITA6 [70] assuming LTE, hydrostatic equilibrium for a one-dimensional model atmosphere and without sources and sinks of energy. The equations of ionization-dissociation equilibrium were solved for media consisting of atoms, ions and molecules. We took into account ~ 100 components [76]. The constants for equations of chemical balance were taken from [104].

Molecular line data were taken from different sources. TiO line lists were taken from Plez [86] and Schwenke [96]. CN lines came from CDROM 18 [49]; Atomic line list was taken from VALD [47]. In our modelling spectra of M-dwarfs and ultracool dwarfs we account CrH and FeH lines provided by Burrows et al. [12] and Dulick et al. [22], respectively. Lines of H₂O were computed using the lists by Partridge & Schwenke [67], Jorgensen [39], Barber et al. [4]. The partition functions of H₂O were also computed from these data. Then, we accounted ¹²C¹⁶O and ¹³C¹⁶O line lists were computed by Goorvitch [29].

The profiles of molecular and atomic lines were determined using the Voigt function $H(a, v)$. Parameters of their natural broadening C_2 and van der Waals broadening C_4 were taken from Kupka et al. [47] or in their absence computed following Unsöld [107]. Owing to the low temperatures in M dwarf atmospheres and consequently, electron densities, Stark broadening could be neglected. As a whole the effects of pressure broadening prevail. Most of our computations for synthetic spectra were carried out for the fixed microturbulent velocity $V_t = 2$ km/s. The instrumental broadening was modelled by gaussian profiles set to approximate the resolution of the observed spectra.

¹ Hereafter we use the term “synthetic spectra” to simplify the text.

6.2.2. Spectra of late M-dwarfs in the optical spectral regions

Optical spectra of late M-dwarfs, as well as spectra of all stars of spectral type M, are governed by absorption features created by TiO bands (Fig. 6.1). VO bands (B-X) are seen in the optical region, too (see [70, 75, 81] for more details). In general, TiO bands are used to identify the spectral class of M-dwarf.

Only a few atomic lines can be seen in spectra of late M-dwarfs, see Fig. 6.1. Most of them are the resonance lines or subordinate lines of low excitation energies of the neutral alkalis. Due to the low temperatures in atmospheres of late dwarfs only the alkali metals are presumably in the form of neutral atoms. Analysis of alkali lines in spectra of M-dwarfs is not easy deal, due to strong blending molecular lines.

Indeed, in spectra of M-dwarfs, and in more common case, spectra of ultracool dwarfs, we cannot determine continuum in the conventional sense (see Fig. 6.1). Specifically in case of M-dwarf spectra the haze of molecular lines covers the whole range of spectral regions available for analysis. Well, to study limited spectral ranges we can use some kind of pseudocontinuums in spectra. Still, in more general case spectral energy distributions provide much more detailed information about star of our interest. Indeed, blue and red part of any spectral regions show the different sensitivity on the temperature in the spectrum formation layers. Then, the shape and intensity of molecular bands response on the variation of physical parameters in stellar atmosphere.

All problems of theoretical modelling of M-dwarfs spectra can be seen on the example of investigation of spectrum GJ406 provided by Pavlenko et al. [82], see also [81]. The relative importance of the different opacities contributing to our synthetic spectra is shown in Fig. 6.2.

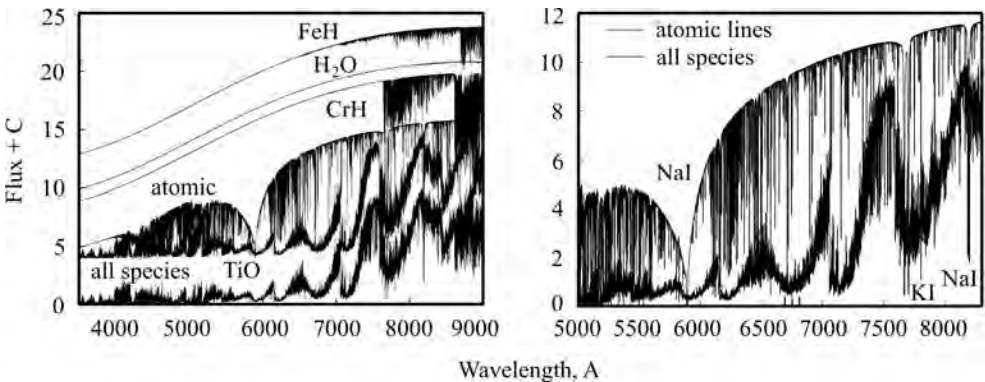


Fig. 6.1. Formation of M-dwarf spectra. Main source opacities in spectral region $\lambda\lambda$ 3500–9000 Å (left), Spectral region with the strongest atomic lines shown in large scale (right)

6.2.3. Infrared spectra of M-dwarfs

The dominant source of opacity in the infrared spectral region for the late-type M dwarfs is water vapor (Fig. 6.2) which easily forms at relatively high pressures and low temperatures.

In general, water vapor opacity is important for computations/modelling of theoretical spectra in the infrared spectral region, as well as to compute the

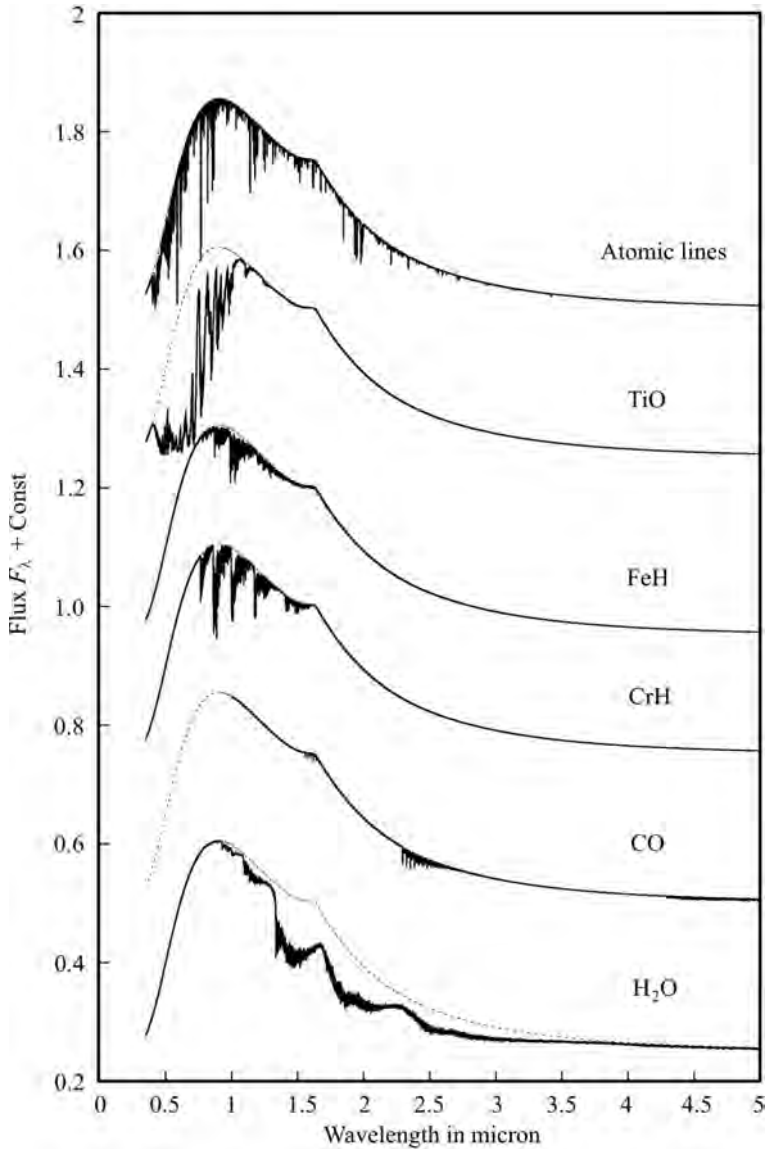


Fig. 6.2. The different molecules contribution to the synthetic spectrum formation in $T_{\text{eff}}/\log g/[Fe/H] = 2800/5.0/0.0$ model atmosphere

modern model atmospheres. The attempts of computation of the astrophysically significant line list of H₂O lines began in the early 60-th. First concept of developing astrophysical applications for lists of H₂O absorption lines was suggested by Auman [2]. He managed the known characteristics of this molecule's levels and transitions (line intensities, molecular constants, relative band intensities) to compute the opacity due to the water vapour band absorption.

Auman [2] was the first who computed so called direct mean absorption coefficients in the frequencies of H₂O bands in the infrared spectral region. He used of relatively simple techniques to account the H₂O absorption, due to the incompleteness of the existing at those days data on the relevant molecular transitions, as well as a lack of computational capacities.

Recent progress in theoretical molecular quantum mechanics allows us to perform ab initio calculations to accurately predict the frequency and intensity for ro-vibrational transitions for water vapor. This means that it is no longer necessary to extrapolate laboratory measurements for water vapor to untestable temperature regimes of which are found in the atmospheres of M dwarfs.

On another hand, the appearance of more advanced techniques for account opacity sampling opacities and opacity distribution functions (see Michalas [62] for more details) shows again the necessity for more refined computations using more complete lists of H₂O lines, so that their positions (and, ideally, intensities) should coincide with those measured in laboratory and/or stellar spectra.

The Jorgenssen [39] list was used in model-atmosphere computations for late-type stars for a number of years. However, later investigations by Jones et al. [38] showed that the list by Jorgenssen [39] is not suitable for studies requiring a description of the fine structure of rotational-vibrational H₂O bands.

Naturally, any computed line list should be tested by comparison with observations. Spectra of M-dwarfs at wavelengths beyond 1.35 μm are dominated by water vapor. Unfortunately, bands of terrestrial water vapor at these wavelengths make it notoriously difficult to make accurate measurement from ground-based observations in that spectral region. In some cases terrestrial water vapor makes it impossible to make accurate measurement from ground-based observations at all.

Using the observed by the high resolution Infrared Space Observatory (ISO) spectra beyond 1.35 μm Jones et al. [37] performed the extensive study of water bands in spectra of M-dwarfs and showed that M star spectra at these wavelengths are dominated by water vapor absorption. Jones et al. [37] used the short wavelength spectrometer on the ISO at four wavelength settings to cover the 2.5–3. μm region for a range of M stars. The synthetic spectra computed with AMES Partridge & Schwenke [67] line list can be fitted well to the observed ISO spectra, see Fig. 6.3. The AMES list was computed ab initio, using modified potential energy surfaces and theoretical dipole moments

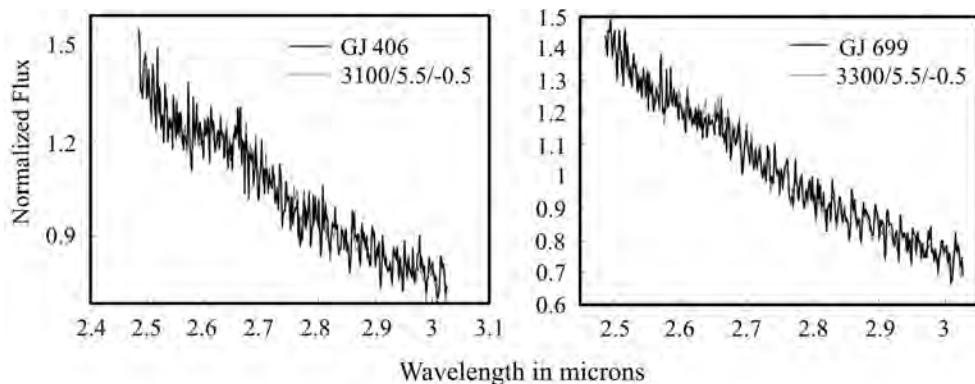


Fig. 6.3. Fits of computed with Partridge & Schwenke [67] water vapour line list spectra to the observed by ISO fluxes of GJ 406 and GJ 699, shown on the left and right panels, respectively

chosen so that the computed positions of the H_2O absorption lines coincided with the HITRAN data [91]. The full AMES line list contains 307 721 352 lines. This list essentially includes the HITRAN list of water vapor lines: 66% of the observed transitions were reproduced with accuracies better than 0.05 cm^{-1} . Moreover, the detailed analysis demonstrated that about 3% of all lines in HITRAN96 had incorrect wavelengths. Still, Partridge & Schwenke acknowledge the possible presence of imperfections in the AMES line list. They note, in particular, the growth of computational uncertainties with increasing angular momentum. The data on the H_2O levels were derived by optimizing the potential energy surfaces for levels with $j < 5$. Comparison of AMES and SCAN lists shows that SCAN list of H_2O lines by Jorgensen et al. [39] provide much less confident results, see Jones et al. [37] for more details.

Jones et al. [37] used a least-squared minimisation technique to systematically find best fit parameters for the sample of stars. However, the effective temperatures of late M-dwarfs that were found indicate a relatively hot temperature scale for M dwarfs. By the way, this could be a consequence of problems with the Partridge & Schwenke linelist which leads to synthetic spectra predicting water bands which are too strong for a given temperature. Such problems need to be solved in the next generation of water vapor line lists which will extend the calculation of water vapor to higher energy levels with the good convergence necessary for reliable modelling of hot water vapor. Then water bands can assume their natural role as the primary tool for the spectroscopic analysis of M stars.

The existing uncertainties in AMES line list can be reduced via further refinement of the potential energy surfaces for higher j values. In fact, next generation of H_2O line list was provided by Barber et al. [4]. Barber et al. [4] computed BT2 list of H^{16}O infrared transition frequencies and intensities.

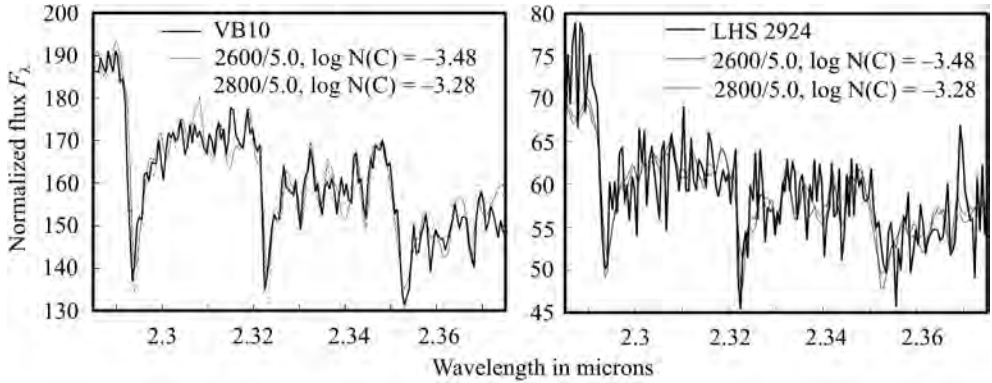


Fig. 6.4. Best fits of synthetic spectra to the observed VB10 (M8) and LHS2924 (M7) spectra

The list, BT2, was produced using a discrete variable representation two-step approach for solving the rotation-vibration nuclear motions. It is the most complete water line list in existence, comprising over 500 million transitions (65% more than any other list) and it is also the most accurate (over 90 percent of all known experimental energy levels are within 0.3 cm^{-1} of the BT2 values). Its accuracy has been confirmed by extensive testing against astronomical and laboratory data. More detailed comparison of different line lists was done by Tennyson et al. [98].

A few other molecular bands can be found of having significant strength in the IR spectrum of M-dwarfs. Pavlenko & Jones [79] fitted the theoretical spectra of the $\Delta v = 2$ CO bands to the observed fluxes of some M dwarfs. They investigated the dependence of theoretical spectra on effective temperatures as well as carbon abundance and found that the synthetic CO bands fit the observed data extremely well and therefore they are excellent diagnostics (Fig. 6.4). In particular the synthetic spectra reasonably match observations and the best fit temperatures are similar to those found by empirical methods. Pavlenko & Jones [79] also examined the possibility of determination of $^{12}\text{C}/^{13}\text{C}$ isotopic ratio in atmospheres of M-dwarf. They showed that fundamental ^{13}CO bands around 2.345 and $2.375 \mu\text{m}$ are good discriminators for the $^{12}\text{C}/^{13}\text{C}$ ratio in M dwarfs. The $2.375 \mu\text{m}$ band is more useful because it does not suffer such serious contamination by water vapor transitions. Unfortunately, the used dataset did not quite have the wavelength coverage to perform a reliable determination of the $^{12}\text{C}/^{13}\text{C}$ ratio in M dwarfs. For this observing the region $2.31\text{--}2.40 \mu\text{m}$ at a resolution of better than 1000 was recommended. Furthermore, Pavlenko & Jones [79] claimed the observational problems of contamination by water vapour at $2.345 \mu\text{m}$ might be solved by observing at resolutions of around 50000. They investigated also the possibility of using the $\Delta v = 1$ CO bands around $4.5 \mu\text{m}$ and found that the contamination due to water vapor is even more of a problem at these wavelengths.

The project was continued by Jones et al. [38] who fitted theoretical spectra to the high resolution infrared observations of the CO 3-1 bands in the 2.297–2.310 μm region of M and L dwarfs. They found a good match between the observational and synthetic spectra throughout the 2000–3500 K temperature regime investigated. Nonetheless, for the 2500–3500 K temperature range the temperatures that we derive from synthetic spectral fits are higher than expected from more empirical methods by several hundred K. In order to reconcile our findings with the empirical temperature scale it is necessary to invoke warming of the model atmosphere used to construct the synthetic spectra. We consider that the most likely reason for the back-warming is missing high temperature opacity due to water vapor. While the AMES line list is a reasonable spectroscopic match for the new BT2 [4] line list at 2000 K, by 4000 K it is missing around 25% of the water vapor opacity. Jones et al. [38] thus considered that the offset between empirical and synthetic temperature scales can be explained by the lack of hot water vapor used for computation of the synthetic spectra. Then, for the coolest objects with temperatures below 2500 K were found the best fits of synthetic spectra which include hot dust emission. Jones et al. [38] constrain the rotational velocities of our sources, the determined velocities are consistent with the broad trend of rotational velocities increasing from M to L.

6.3. Brown dwarfs

Brown dwarfs are low mass objects without hydrogen H^1 fusion reactions in their cores (see D’Antona & Mazzitelli [19], Chabrier et al. [17]), which is the conventional characteristic of stars on the main sequence. Brown dwarfs have fully convective envelopes, so they are chemically homogeneous by depth. Other definitions of brown dwarfs are “failed stars”, “substellar objects”. Brown dwarfs occupy the mass range $13 M_J < M < 85 M_J$, i.e. on the mass-luminosity diagram they are located between the low-mass stars and large gas giant planets. Here M_j is the mass of Jupiter: $1M_j = 0.001M_\odot$.

6.3.1. First theoretical predictions

The existence of dwarfs without hydrogen burning in their core was predicted by Kumar [45, 46] and Hayashi & Nakano [33]. Kumar [45] constructed completely convective models for low mass objects 90–40 M_J . The non-relativistic degeneracy of their interiors was taken into account. He claimed that there should be a lower limit to their mass of the main sequence, i.e. objects with burning hydrogen core in the center part. The objects with mass less than this limit should be completely degenerate objects, or “black” dwarfs in the end of gravitational contraction. They never go the normal stellar evolution.

6.3.2. First discoveries

In fact, predictions of Kumar [45, 46] were forgotten for many years. Only huge technological breakthrough of the CCD technologies and application of the new telescopes and approaches in the infrared spectral region in the later 80-th give the second life for these ideas. And on the times, main impetus came from the side of observers. A few groups uses different methods to discover brown dwarfs (see [5] for more details). The first brown dwarfs Teide1 and Gl 229B were discovered by Rebolo, Zapatero Osorio & Martín [89] and Nakajima et al. [63], respectively. Interestingly, in both cases very different methods were used. First brown dwarfs of the late M-dwarf was found in a deep CCD-based *IZ* survey at 80 cm telescope of Teide observatory covering an area of 1 deg^2 in the central region of Pleyades, which is a the comparatively young cluster. In contrary, Nakajima et al. [63] discovered low mass companion of Gl229A by the very sophisticated techniques. They obtained measurements at the Hale 5-m and the Keck 10-m telescopes. After proper account of the scattered light of Gliese 229A they refined the main parameters of Gl229B.

6.3.3. Lithium test

It is currently believed that the rate of depletion of lithium and deuterium in the interiors of low-mass stars is primarily determined by the mass of the star or substellar object. For stars $M > 85 M_J$, the burning of lithium, $\text{Li} (p, \alpha) {}^4\text{He}$, becomes efficient at early evolutionary stages preceding the main sequence at interior temperatures of $T \sim 2.5 \text{ MK}$ (D’Antona & Mazzitelli [19]). Young, low-mass stars possess developed convective envelopes, so that lithium depletion in their central regions is manifest on relatively short time scales (several tens of million years) as a weakening or complete disappearance of lithium lines in their spectra. The temperatures in the interiors of brown dwarfs of masses less than $60 M_J$ are not high enough for lithium burning. Thus, in principle, their primordial lithium abundance should not change with time. This circumstance led to the idea of the lithium test (Rebolo et al. [88]), which essentially consists of searching for lithium absorption lines in the spectra of late M dwarfs as evidence of their substellar nature. The practical applicability of the lithium test was demonstrated in Pavlenko et al. [69, 76]. Subsequently, the lithium test was successfully used to prove the substellar nature of several late-type dwarfs (see Rebolo et al. [90], Ruiz et al. [92]).

The lithium abundances in the atmospheres of young stars are also of interest for other problems. In particular, the position of the line in the Hertzsprung—Russell diagram separating stars burning lithium from lower-mass objects that still have lithium in their atmospheres can be used to derive independent age estimates for young open clusters with ages $t < 150$ million

years, see [19]. The prospects for applying the lithium test to the identification of brown dwarfs among L dwarfs were studied by Pavlenko et al. [75], see section 6.4.1.

6.3.4. Teide 1

Low luminosity M-dwarfs close to the bottom of the Main Sequence are the best brown dwarf candidates in young clusters of the solar neighborhood. These young brown dwarfs are comparatively bright. Zapatero Osorio et al. in 1993–1995 performed a deep CCD CCD-based *IZ* survey covering an area of 1 deg^2 in the central region of the Pleyades and found several very low luminosity objects using well equipped 80 cm telescope of Teide Observatory (Tenerife). A few objects of spectral class M6-M8 (Martín et al., [57]) definitely belongs to the cluster of coolest known members of the Pleiades [110]. After discovery of the first brown dwarf candidates in the Pleyades they a special spectroscopic observation program was performed on Keck.

Rebolo et al. [90] using 10 m Keck spectra of the two Pleyades brown dwarfs Teide 1 and Calar 3 showing a clear detection of the 670.8 nm Li resonance line, despite strong blending by lines of TiO molecule. Indeed, lithium lines in spectra of late M-dwarfs are severely blended by TiO bands (Fig. 6.5). In fact in that case the main problem of the “lithium test” is to observe and to model lithium lines at the background of the strong molecular spectrum formed by TiO bands mainly (Pavlenko et al. [69, 70, 76]). We can

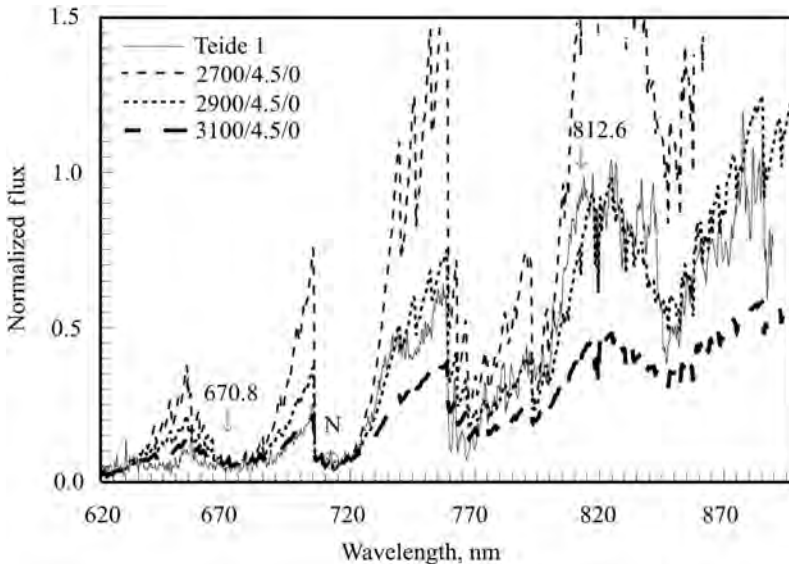


Fig. 6.5. Fit of observed spectrum of young brown dwarf Teide1 (Rebolo et al. [90]) by theoretical spectra computed for several NextGen [32] “non-dusty” model atmospheres. Positions of Li I lines are labelled

only measure relatively strength of lithium lines in respect to the molecular background formed by molecular bands, so called pseudoequivalent widths [70, 76]. In general, pEW are lower than the true equivalent widths. The formally determined lithium abundance from pseudo-equivalent widths analysis should increase in comparison with the case of the true curves of growth.

It is worth noting that in atmospheres of late M-dwarfs Ti and other metals are depleted due to formation of dust particles (Tsuji et al. [105], Jones & Tsuji [36], Pavlenko [74]). Simulation of the impact of the “dusty effects” on the output spectra of the latest M-dwarfs shows, that:

- in the “TiO non-depleted” spectra Li I lines disappear in TiO bands at $T_{\text{eff}} = 2000$ K.
- Processes of TiO and VO depletion may substantially reduce the strength of molecular bands around Li I lines (Fig. 6.4). Strictly speaking, the effect depends on T_{eff} , $\log g$, metallicity.

In fact observations of the Li I in spectrum Teide1 confirmed early prediction of Pavlenko et al. [69] that the core of Li doublet at 6708 Å can be observed even in the late M-dwarf spectra. Since Pleyades brown dwarfs are unable to burn Li the significant preservation of this fragile element confirms the substellar nature of our two objects. Regardless of their age, their low luminosities and Li abundance place Teide1 and Calar3 comfortably in the genuine brown dwarf realm. Given the probable age of the Pleyades cluster, their masses are estimated at $55 \pm 15 M_J$.

Rebolo et al. [90] determined the lower limit of lithium abundance in atmosphere Teide1, i.e. $\log N(\text{Li}) > 2.5$. Later Pavlenko [70, 71] provided more detailed analysis of lithium lines in spectra of Teide1 and Calar3. Using procedures of spectral synthesis he showed that the spectrum of Teide1 may be reasonably well fitted in the visible region, and pseudoequivalent width analysis provide even higher lithium abundances ($\log N(\text{Li}) = 3.2$).

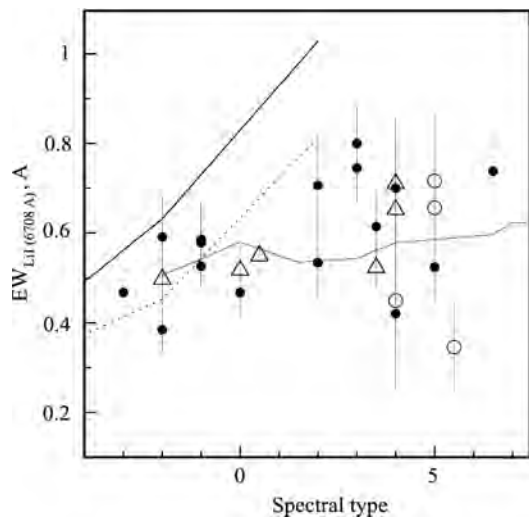
In fact, these works initiated intermediate and low resolution optical and near infrared spectroscopy of a few faint, very red objects ($20 > I \geq 17.8$, $I - Z \geq 0.5$) discovered in a open clusters [110–113]. These objects are very cool dwarfs, having spectral types in the range M6–M9. Some of them can be considered as members of young clusters on the basis of their radial velocities, H α emission and other gravity sensitive atomic features like the Na I doublet at 818.3 and 819.5 nm. The latest observations prove that the cloud fragmentation process extends well into the brown dwarf realm, suggesting a rise in the initial mass function below the substellar limit.

6.3.5. Brown dwarfs in σ Ori cluster

For some young open clusters the lithium test can be used for the assessing of subpopulations of brown dwarfs. Computed equivalent widths for cosmic abundance of $\log N(\text{Li}) = 3.3$ (Rebolo et al. [88]) yield true equivalent widths exceeding 1 \AA for M-stars of $T_{\text{eff}} = 3500 \text{ K}$. However, up to 90 % of profiles of strong lithium lines are covered under the haze of molecular lines. Still saturated cores are still detectable and can be used to confirm the substellar nature of many low mass objects in young open clusters.

Zapatero Osorio et al. [112] followed very refined procedure of determination of age of low-mass objects bound in open cluster σ Ori. Analysis was performed in the framework of LTE approach. Complex investigation of the “lithium age” and $H\alpha$ age was carried out on the basis of analysis of intermediate- and low-resolution optical spectra between 6100 \AA and 7000 \AA , covering $H\alpha$ and Li I at $\lambda 6708 \text{ \AA}$, for a sample of a sample of low mass stars. Radial velocities (except for one object) are found by Zapatero Osorio et al. to be consistent with membership in the Orion complex [112]. The found spectral classes are in the interval K6–M8.5, which correspond to masses from $1.2 M_{\odot}$ down to $0.02 M_{\odot}$ after comparison with state-of-the-art evolutionary models (Baraffe et al. [3], Chabrier et al. [17]). All cluster members from the sample show considerable $H\alpha$ emission and the Li I resonance doublet in absorption, which is typical of very young ages. Two brown dwarfs with confirmed membership in the pre-main sequence stellar σ Orionis cluster were investigated. The pseudo-equivalent widths of $H\alpha$ and Li I (measured relative to the observed local pseudo-continuum formed by molecular absorptions) appear rather dispersed (and intense in the case of $H\alpha$) for objects cooler than M3.5 spectral class, occurring at the approximate mass where low mass stars are

Fig. 6.6. Pseudoequivalent widths (pEW) of the Li I resonance doublet lines 670.8 nm computed for the “cosmic” lithium abundance $\log N(\text{Li}) = 3.2$ and the measured in observed spectra in young dwarfs of σ Ori cluster. TiO line list by Plez [86] and NextGen model atmospheres [32] of solar metallicity were used in theoretical computations. Solid and dashed lines in the left part of the plot show the conventional curves of growth for the line computed for $\log N(\text{Li}) = 3.2$ and 2.0 , respectively. Open circles and open triangles label sources with $H\alpha$ emission of pEW > 1 nm and objects with forbidden emission lines, respectively — see Zapatero Osorio et al. [112] for more details



expected to become fully convective. The least massive brown dwarf in the sample of Zapatero Osorio et al. sample, S Ori 45 (M8.5, $\sim 0.02 M_{\odot}$), displays variable H α emission and a radial velocity that differs from the cluster mean velocity [112]. Tentative detection of forbidden lines in emission by Zapatero Osorio et al. indicates that this brown dwarf may be accreting mass from a surrounding disk. Zapatero Osorio et al. [112] presented computations of Li I $\lambda 6708 \text{ \AA}$ curves of growth for low gravities ($\log g = 4.0$ and 4.5), cool temperatures ($T_{\text{eff}} = 4000\text{--}2600 \text{ K}$), and lithium abundances in the interval $\log N(\text{Li}) = 1.0\text{--}3.4$. The distribution of our observed Li I pEWs appears to be well reproduced by the theoretical pEWs computed for the cosmic lithium abundance of $\log N_0(\text{Li}) = 3.1$. This leads us to conclude that lithium has not yet been depleted in the σ Orionis cluster (Fig. 6.6).

After comparison to various lithium depletion curves available in the literature, Zapatero Osorio et al. [112] imposed an upper limit to the cluster age of 8 Myr, while the most likely age is in the interval 2–4 Myr.

6.3.6. LP944-20

LP944-20 (other names are APMPM J0340–3526, BRI B 0337–3535, LEHPM 3451, 2MASSW J0339352–352544) is an archetypal dwarf of spectral type M9.5. Dim red dwarf-like Luyten Palomar (LP) 944-20 (M9 V) was cataloged by Luyten & Kowal [55]. The dwarf is comparatively bright ($M_{\text{bol}} = 14.22$, Dahn et al. [20]) and appears to be a young object. The SIMBAD database lists more than 180 references for this object up to January 2012.

LP944-20 shows significant rotation broadening in high-resolution spectra. The $v \sin i$ values determined by different authors are in the range of $30 \pm \pm 2 \text{ km/s}$ (Tinney & Reid [100], Jones et al. [38]). The rotation period has not been determined yet, but photometric variability was reported by Tinney & Tolley [101]. Surface inhomogeneities could be due to magnetic spots or dusty clouds. “Dusty effects” in the atmospheres of cool dwarfs with $T_{\text{eff}} < 2600 \text{ K}$ were predicted by Tsuji et al. [105].

Presence of large amounts of dust in the highly dynamical atmospheres of fast rotating ultracool dwarfs can yield “weather phenomena” (Jones & Tsuji [36], Gelino et al. [26]; Martín, Zapatero Osorio & Lehto [59]; Caballero et al. [14]; Koen et al. [43]). Indeed, Pavlenko et al. [83] find a complete absence of the TiO molecule in the outermost layers of the atmosphere of LP944-20 and the presence of an additional opacity produced by dusty cloud structures over the photosphere. Only by adopting a semi-empirical model, Pavlenko et al. [83] were able to fit the theoretical spectra to the observed spectrum across a wide spectral region ($0.65\text{--}0.9 \mu\text{m}$), and reproduce the profiles of resonance lines of K I and Rb I.

An unexpectedly strong, solar like X-ray flare ($\log(L_x/L_{\text{bol}} = -4.1)$) of duration ~ 2 hours was registered by *Chandra* [93]. Later XMM-Newton observations by Martín & Bouy [60] did not detect any X-ray activity. The quiescent X-ray luminosity of LP944-20 is lower than that of the active Sun, therefore X-ray flares on LP944-20 are very rare events in comparison with more massive M-dwarfs (Hambaryan et al. [30]). Generally speaking, LP944-20 is not the only M9 dwarf showing X-ray flares. Stelzer [97] observed an X-ray flare ($\log(L_x/L_{\text{bol}} = -3.3)$) from the brown dwarf binary with spectral types M8.5/M9 G1569 B, which has an age of about 300 Myr (see Zapatero Osorio et al. [113]).

Tinney [99] provides a lithium abundance $\log N(\text{Li}) = 0.0 \pm 0.5$ from analysis of the “equivalent width” of lithium resonance doublet at $0.6708 \mu\text{m}$. However, the use of the equivalent width method to derive the lithium abundance in atmospheres of late M-dwarfs is difficult by definition: equivalent widths are values measured with respect to the true continuum, which is not seen in their spectra. In optical spectra of late M-stars we see only the cores of some atomic lines on a background of TiO bands [70, 71].

Taking into account the processes of blending lithium lines by TiO bands, Pavlenko et al. [83] determined the much higher lithium abundance $\log N(\text{Li}) = 3.2 \pm 0.25$ in the atmosphere of LP944-20. However, here much sophisticated procedure of spectra synthesis was used. As the first step of analysis, Pavlenko et al. [83] obtained the best fits to the CASPEC ($R = 1500$) spectrum of LP944-20 for a few model atmospheres with $T_{\text{eff}} = 2000\text{--}2400$ K. These values are in good agreement with estimations of Luhman [56] and Basri et al. [6] for M9 dwarfs, despite our model atmospheres differences from those used by them.

Then, fits of theoretical spectra to observed 670.8 nm Li I resonance line doublet profiles observed with VLT/UVES ($R = 40000$), provided the lithium abundance of over two orders magnitude larger than previous estimates in the literature (Fig. 6.7, see more details in Pavlenko et al. [83]).

The found lithium abundance $\log N(\text{Li}) = 3.2 \pm 0.25$ shows a rather weak dependence on input parameters. However, the lithium abundance determination was carried out in the frame of LTE. Fortunately, the resonance lines of alkali metals are rather insensitive to chromospheric-like features (CLF) because processes of their formation are controlled by photoionisation [102]. By definition, these lines should show rather weak dependence on temperature structure of the outermost layers of atmosphere. Indeed, direct NLTE modelling formation of lithium lines in the atmospheres of ultracool dwarfs with CLF showed their rather weak response to temperature inversions [73]. Lithium lines can be affected only in the case of the strongest CLF producing additional flux in the blue part of the spectra. As we know LP944-20 is of age greater than 300 Myr, we cannot expect the appearance of strong CLF here.

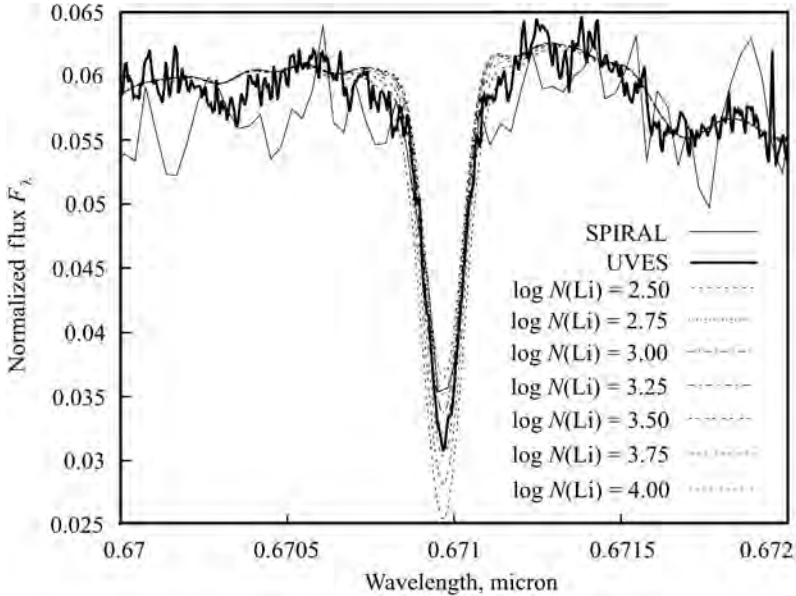


Fig. 6.7. Fit to profile of resonance Li line with $v \sin i = 32$ km/s FWHM = 0.17 \AA ($R = 40000$)

The result of the lithium abundance determination pseudo-equivalent widths (pEW) of atomic lines can be measured in respect to the background formed by the haze of TiO lines [70, 71, 112].

Nonetheless, analysis of pseudoequivalent widths of lithium resonance lines provides the proof of our main result. Pseudo-equivalent widths of Li resonance doublet pEW, i.e. measured in respect to the local background/pseudo-continuum formed by molecular lines in UVES spectrum is of order $0.65 \pm 0.05 \text{ \AA}$ (Tinney measured $0.53 \pm 0.05 \text{ \AA}$ [99]). Using curves of growth measured by Zapatero Osorio for young M-dwarfs in σ Ori (see Fig. 16 in Zapatero Osorio et al. [112]) we obtain $\log N(\text{Li}) = 3.2 \pm 0.3$. This confirmed results of Pavlenko et al. [83] in a qualitative sense, because our T_{eff} is lower and we used different model atmospheres.

Nevertheless, results of Pavlenko et al. [83] for LP944-20 provided a strong confirmation of the effectiveness of the lithium test for the identification of the brown dwarfs. Brown dwarf LP944-20 has preserved its initial lithium abundance, as expected for the dwarfs of masses less than $0.055 M_{\odot}$.

6.4. Low mass objects of spectral classes L-T-Y

M-dwarf sequence belongs to the classical part of the Herzprung—Russell diagram. As was noticed in the previous section, their spectra are governed by the TiO. However, in spectra of late M-dwarfs molecular bands of TiO weakens due to the processes of depletion of Ti as well as other metals into dust particles. In spectra of cool dwarfs of effective temperatures 2000 K and below only remnants of TiO are observed. General shape of spectra of ultracool dwarfs changes drastically [74]. Strong and extended wings of potassium and sodium resonance doublets form the most intensive features in the observed spectra [72]. This was a reason to implement the new spectral class (L) and to extend the classical Main sequence down to lower masses and effective temperatures (Martín et al. [58], Kirkpatrick et al. [41]).

In fact, one of the first brown dwarfs G1229B discovered by Nakajima et al. (1995) became soon after its discovery known as archetype of the new spectral class T. Optical spectra of T dwarfs differ much from L-dwarfs (see [75]). In the infrared methane and water bands are dominated (see section 6.4.5).

6.4.1. L-dwarfs

Practically before 1995—1996 only one L-dwarf was known. GD165B is the secondary component of the binary consists of L-dwarf and white dwarf (WD). For a long time its spectrum was considered as something very peculiar (Kirkpatrick et al. [40]). However, after 1996 numerous discoveries of L-dwarfs were done by analysis of 2MASS and DENIS data.

Even first models of L-dwarfs showed that the resonance lines of KI and NaI are of huge intensity in spectra of L-dwarfs. Formally computed equivalent widths of these lines in spectra of the coolest L-dwarfs are of order of a few thousand angstroms [74, 77, 78]. Wings of absorption lines of NaI and KI resonance doublet extend on a few thousand angstroms from their cores (Fig. 6.8).

It is worth noting that shown in Fig. 6.8 spectra were computed in the framework of the classical collisional theory of line broadening. Burrows and Volobuyev [13] showed that this approach cannot be applied for modelling superstrong alkali lines in spectra of L-dwarfs.

6.4.2. Formation of strong Na and K resonance lines in spectra of L-dwarfs

Indeed, as was shown by Burrows & Volobuyev [13], under high pressure and low temperatures the energy levels of Na and K are considerably perturbed by surrounding atoms and molecules. That is the real reason of why far wings of Na and K resonance lines extend at thousands Angstroms

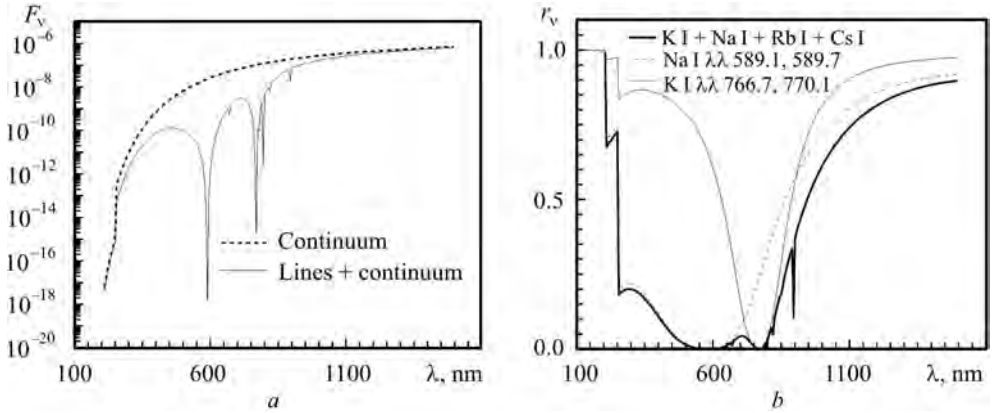


Fig. 6.8. Fluxes (a) and residual fluxes (b) in frequencies of resonance lines of KI ($\lambda\lambda$ 766.6, 770.1 nm) and NaI ($\lambda\lambda$ 589.1, 589.7 nm) computed in the frame of collisional broadening theory (van der Waals broadening) for 1200/5.0 C-model atmosphere of Tsuji [106], see [77] for more details

defining the pseudocontinuum of the spectra of ultracool dwarfs. Pavlenko et al. [84] performed ab initio calculations of energy shifts of the ground and excited states of sodium and potassium atoms in immersed in H_2 - and helium rich atmospheres. First three excited states of Na and K atoms involved in formation of their resonance doublets are considered.

Pavlenko et al. [84] considered energy states forming resonance doublets for sodium and potassium and correspond transitions $3s^2S_{1/2} - 3p^2P_{3/2,1/2}$ (Na-D doublet) and $4s^2S_{1/2} - 4p^2P_{3/2,1/2}$ respectively. The components of doublets, the D_1 (5896 Å) and the D_2 (5890 Å) of D-Na and 7665 Å and 7699 Å for potassium are formed by transition to 1/2 and to 3/2 excited state. In the molecular theory $P_{3/2}$ state includes p_x and p_y states referred as 2B_1 and 2B_2 state. At small distances they can form bonding states with H_2 molecule. The $P_{1/2}$ state corresponds p_z state denoted as 2A_1 , which is always repulsive to H_2 molecule.

For the calculation of the interaction potentials was used quantum-chemical package PC GAMESS. It is improved and developed by Alex A. Granovsky version of original GAMESS US [95] allowing to find self-consistent solution of many-electron Schrodinger equation.

We apply two-step approach including UHF (unrestricted Hartree–Fock) calculation of initial orbitals and then account for configuration interaction and electron correlation effects using post-HF method as proposed by Burrows & Volobuyev [13]. We use a special case of full CI (configuration interaction), CASSCF (complete active space self-consistent field) or FORS (fully optimized reaction space) approach.

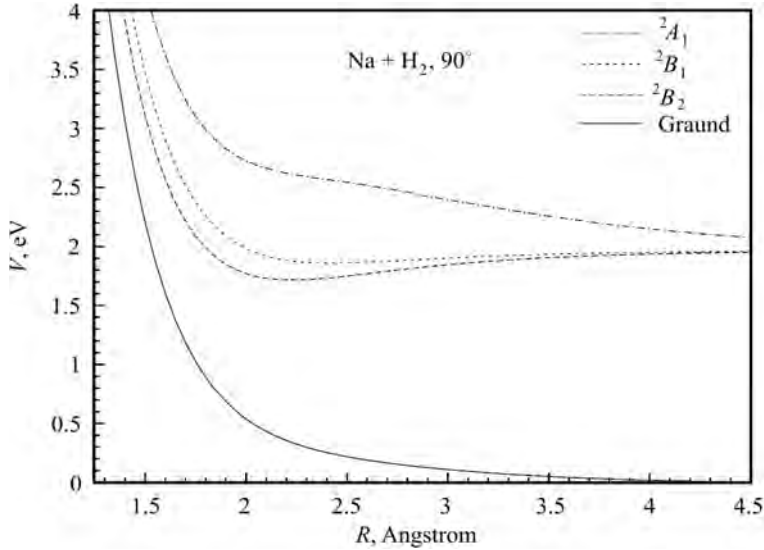


Fig. 6.9. Interaction potentials for ground and excited states (relative to zero at infinity) for Na + H₂ system oriented perpendicularly

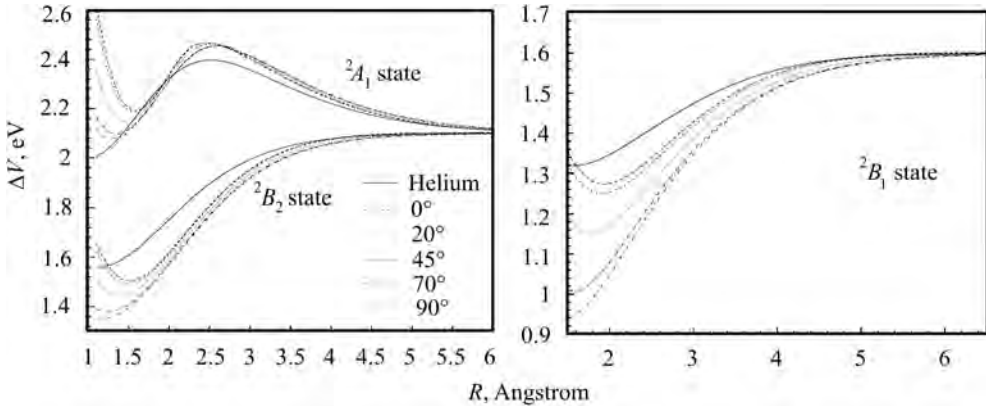


Fig. 6.10. Energy shifts of Na+H₂/He systems relative to the ground state as function of separations and orientation angles

Pavlenko et al. [84] calculated interaction potential for all states 2A_1 , 2B_1 , and 2B_2 of Na + H₂, K + H₂, Na + He, and K + He systems as a function of distance and orientation (for H₂), see Figs 6.9 and 6.10. To compare our results with previous calculations we include the same set of angles (0°, 20°, 45°, 70°, 90°) and cover all range of separations up to values of energy state shifts less 1%. In present calculations we manage to increase accuracy of ab initio calculations. Wavelength of the isolated line of Na atom now is reproduced with 6% (0.13 eV) accuracy in contrast to 14% (0.3 eV) in B&V computati-

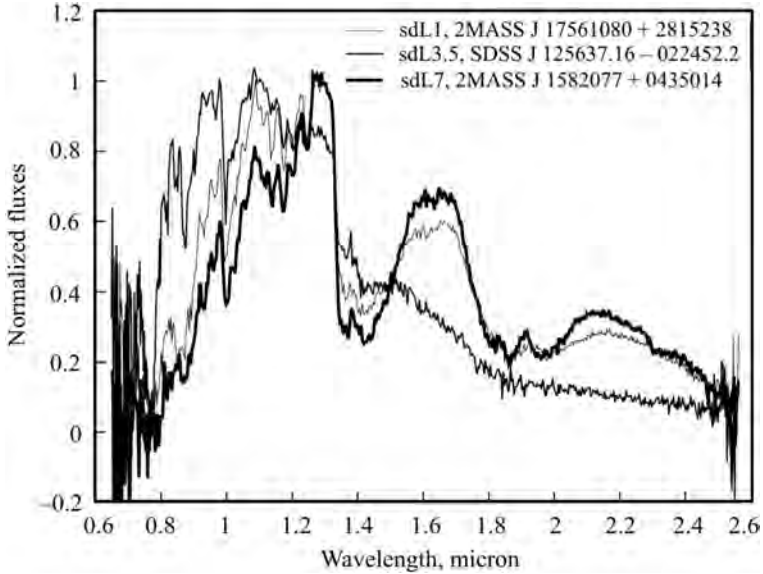


Fig. 6.11. Spectra of L-dwarfs from the sample of Burgasser et al. [10]

ons. Similar improvements are carried out for potassium where accuracy has increased from 21 % (0.34 eV) to 12 % (0.19 eV). To provide exact reproducing of the core of unperturbed resonance line for Na and K atom we shift interaction potentials by constant amount in analogous to B&V way.

The theory was successfully applied to the simulation of L-dwarf spectra [84]. It is worth to noting that wings of K I and Na I resonance lines form some kind of pseudocontinuum for Li lines. So proper modelling K I and Na I lines as well as “dusty effects” if of crucial importance for the determination of physical parameters of these objects.

6.4.3. Spectral classification of L-dwarfs

First spectral classifications of L-dwarfs were provided by Kirkpatrick et al. [41] and Martín et al. [58]. Today we can assess their spectra (see libraries of spectra on of L-dwarfs provided by Burgasser et al. [10]). Some optical spectra from the database is shown in Fig. 6.11)

It is worth noting, than in the case of L-dwarfs the definition of metallicity lost its conventional sense. In their atmospheres metals are depleted in the dust particles, it means that observed abundances of metals in atmospheres of L-dwarfs are lower in comparison with their interiors, where abundances of elements with atomic number larger than 3 are the same from the times of the contraction of protostellar cloud.

6.4.4. Lithium test for L-dwarfs

We expect that L dwarfs are a mixture of very low-mass stars and sub-stellar objects (brown dwarfs). The spectral classes of low mass stars may be changed during their evolution. The L-dwarfs of masses less than $65 M_J$ preserve their lithium abundance from the formation times. The "lithium test" should work for L-dwarfs, too. Practically first attempt to use the lithium test to assess L-dwarf population was carried out by Pavlenko et al. [75]. After detailed consideration of chemical equilibrium, they showed that the lithium resonance doublet at 670.8 nm can be detected in the whole spectral range (down to 1000 K). In the coolest L-dwarfs the strength of the resonance line is more affected by the amount of additional (dusty) opacity needed to explain the spectra than by the depletion of neutral lithium atoms into molecular species. In those atmospheres where the additional opacity is low, the lithium test can provide a useful discrimination of substellar nature. Still changes in the physical conditions governing dust formation in L-dwarfs, will cause variability of the lithium resonance doublet. Taking into account the need for additional opacity Pavlenko et al. [75] found that the lithium abundance in atmosphere of L-dwarf Kelu 1 can be as high as $\log N(\text{Li}) = 3.0$, i.e. consistent with complete preservation, see Fig. 6.12.

However, later Liu and Leggett [53] the Keck sodium laser guide star adaptive optics (LGS AO) system as part of a high angular resolution survey found that Kelu 1 is a binary. They estimated spectral types of L1.5-L3 and L3-L4.5 for the two components, giving model-derived masses of 5–7 and 45–65 M_J for an estimated age of 0.3–0.8 Gyr. More distant companions are not

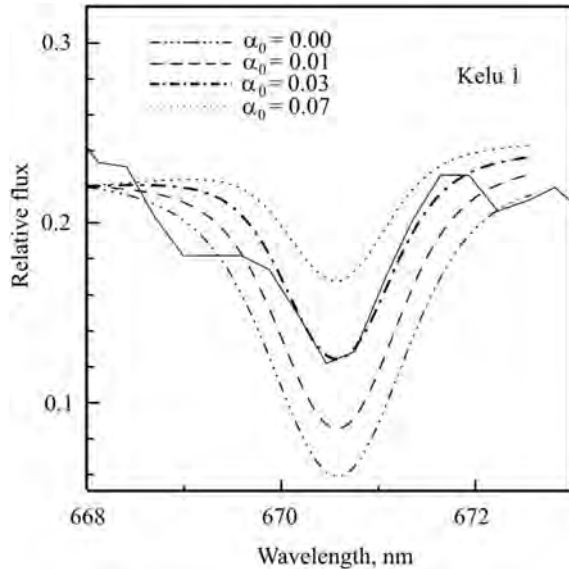


Fig. 6.12. Fitting of the Li I resonance line of Kelu 1 (full line) using the Tsuji's C-type model atmosphere for $T_{\text{eff}} = 2000$ K, $\log g = 5$. Computations have been performed for a lithium abundance of $\log N(\text{Li}) = 3.0$ and considering different amounts of dust opacity. The resolution of all theoretical spectra is the same than the one of the observed data

detected to a limit of 5–9 MJup. The presence of Li 6708 Å absorption indicates that both components are substellar, but the weakness of this feature relative to other L dwarfs can be explained if only Kelu-1B is Li-bearing.

6.4.5. T-dwarfs

In fact discovered by Nakajima et al. [63] brown dwarf Gliese 229B became later the prototype of a second new spectral class, namely the T dwarfs. Whereas near-infrared (NIR) spectra of L dwarfs show strong absorption bands of H₂O and carbon monoxide (CO), the NIR spectrum of Gliese 229B is dominated by the methane absorption bands. Similar features created by CH₄ absorption were known in spectra of the giant planets of the solar system and Titan.

We know a lot of T-dwarfs of different physical spectral classes for the time being. Pienfield et al. [66] present the discovery of 15 new T2.5–T7.5 dwarfs (with estimated distances 24–93 pc), identified in the first three main data releases of the United Kingdom Infrared Telescope (UKIRT) Infrared Deep Sky Survey. This brings the total number of T dwarfs discovered in the Large Area Survey (LAS) (to 10/2008) to 28. These discoveries are confirmed by near-infrared spectroscopy, from which we derive spectral types on the unified scheme of Burgasser et al. Seven of the new T dwarfs have spectral types of T2.5–T4.5, five have spectral types of T5–T5.5, one is a T6.5p and two are T7–7.5. Pienfield et al. [66] assess spectral morphology and colours to identify T dwarfs in our sample that may have non-typical physical properties (by com-

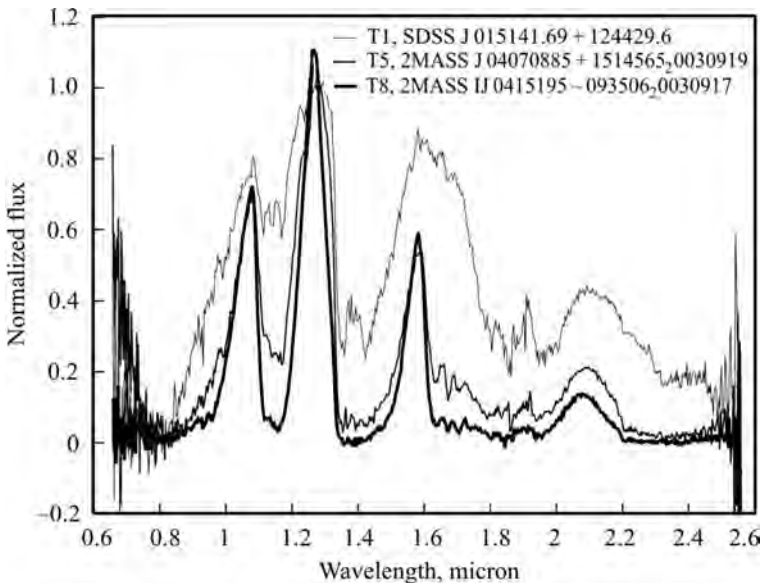


Fig. 6.13. Spectra of T-dwarfs from the sample of Burgasser et al. [9]

parison to solar neighbourhood populations), and find that three of these new T dwarfs may have unusual metallicity, two may have low surface gravity, and one may have high surface gravity (see [54] for other sample of T4–T8 dwarfs).

In general, Gliese 229B has blue near-infrared colors due to the presence of CH₄, H₂O bands and molecular hydrogen (H₂) collision-induced absorption (CIA), see Fig. 6.13. Naturally in regime of low temperature and high pressure the resonance lines of sodium and potassium are very stronger, than in the case of L-dwarfs. Fluxes in visible spectral region of T dwarf spectra is reduced due to the strong absorption of the sodium and potassium resonance doublet lines, so the actual appearance of T dwarfs to human visual perception is estimated to be not brown at all. Wikipedia defines the colors of T dwarfs as similar to “magenta coal tar dye”. Then, the FeH and CrH bands that characterize L dwarfs are weak or even absent. These differences led the astronomical community to propose the T spectral class for objects exhibiting H- and K-band CH₄ absorption. Up to now a few hundred T dwarfs are known. We expect that all T dwarf class is composed entirely of brown dwarfs.

6.4.6. Y-dwarfs

The most low temperature objects are Y-dwarfs. They all are brown dwarfs, which are of effective temperatures below 600 K.

Due to they low effective temperatures these objects are practically unobservable in visible light, but with the infrared vision of NASA’s WISE space telescope, researchers finally detected the faint glow of a few Y dwarfs (WISE 0410 + 1502, WISE 1405 + 5534, WISE 1738 + 2732, WISE 1828 + 2650, WISE 2056 + 1459) relatively close to our Sun, within a distance of about 40 light-years Cushing et al. [18].

WISE (Wide-field Infrared Survey Explorer) team members found this coldest Y dwarf, known as WISE 1541–2250 (full designation is WISEPA J154151.66–225025.2), was colder than 30 degrees Celsius.

The closest of the known Y dwarfs, WISE 1541–2250, is of 9 light-years distant. In comparison, the alien star closest to us, Proxima Cen, is about 4 light-years away.

Interestingly, these objects are often observed as members of binary and multiple systems (Gellino et al. [27]).

6.5. Exoplanets

Exoplanet, or an extrasolar planet, is a planet outside the Solar System. Up to now in total more than 700 confirmed exoplanets are listed in the Extrasolar Planets Encyclopedia.

In fact, the first published discovery to receive subsequent confirmation was made in 1988 by the Canadian astronomers Bruce Campbell, G.A.H. Walker

& Stephenson Yang [15]. They obtained relative radial velocities with a mean external error of 13 m/s rms for 12 late-type dwarfs and four subgiants over the past six years. Campbell et al. [15] claimed that two stars, χ^1 Ori A and γ Cep, show large velocity variations *probably* due to stellar companions. In contrast, other observed 14 stars are virtually constant in velocity. In some sense these observations can be considered as state-of-art. Restricted by limits of instrumental capabilities at the time most astronomers remained rather skeptical for several years about this discovery. Some astronomers thought, that these objects might instead have been brown dwarfs, i.e. objects intermediate in mass between planets and stars. Fortunately, the ideas of Campbell et al. [15] were not forgotten. Additional investigations by Lawton & Wright [50] supported the existence of the planet orbiting γ Cephei. Still serious doubts remain. Walker et al. [108] claimed that γ Cep is almost certainly a velocity variable yellow giant. Finally, more sophisticated investigation by Hatzes et al. [31] confirmed the planetary companion existence.

Another story began four years later, when Wolszczan & Frail [109] announced the discovery of a planetary system around the millisecond pulsar PSR 1257 + 12. Namely, they claimed that two planets orbits the pulsar. This discovery was confirmed, and is generally and formally considered to be the first definitive detection of exoplanets. These pulsar planets are believed to have formed from the unusual remnants of the supernova that produced the pulsar, in a second round of planet formation, or else to be the remaining rocky cores of gas giants that survived the supernova and then decayed into their current orbits.

Still the modern epoch began on 1995. Mayor and Queloz [61] announced the first definitive detection of an exoplanet orbiting a main-sequence star, namely the nearby G-type star 51 Pegasi. Technological advances, most notably in high-resolution spectroscopy, led to the rapid detection of many new exoplanets: astronomers could detect exoplanets indirectly by measuring their gravitational influence on the motion of their parent stars. More extrasolar planets were later detected by observing the variation in a star's apparent luminosity as an orbiting planet passed in front of it.

Surprisingly, the first discovered planetary systems were very different from the solar system. First exoplanets were massive planets, i.e. "hot Jupiters", that orbited very close to their hosting stars. It was not predicted by the classical theories of planetary formation which indicated that giant planets should only form at large distances from stars. However, later eventually more planets of other sorts were found, and it is now clear that hot Jupiters are a minority of exoplanets.

New technologies trigger new discoveries. Lissauer [52] claimed the discovery of three planets in the system of ϵ And. In that way this star became the first main-sequence star known to have multiple planets. Up to now we know

definitely more than 1500 planets (May 2014) in planetary systems and more than 80 planets within multiple planetary systems. Recently Doyle et al. [21] claimed the discovery of the Kepler-16 system in which a planet orbit surrounds a pair of low-mass stars. The eclipsing stars are 20 and 69% as massive as the Sun and have an eccentric 41-day orbit.

Now we are in the post-era of the discoveries of the NASA's Kepler mission. Kepler mission had identified more than 3700 planetary candidates associated with approximately 1500 host stars by the space-based telescope. Some of them may be in the habitable zone. However, these objects should be investigated by direct astrophysical methods to confirm or reject any discovery. Former history of science provides numerous evidences that only confirmed discoveries have sense.

Study of exoplanets should be followed by the onvestigation of the hosting stars. Indeed, only from modelling of the spectra of hosting stars we can get the detailed information about abundances, and, respectively, the evolutionary status of these systems. Furthermore, we cannot get these data from the fine analysis of of the spectrum of the exoplanets. Good examples of the investigations of the hosting stars can be found in papers of Jenkins et al. [34, 35], Capetta et al. [16], Koppenhoefer et al. [44].

6.5.1. Deuterium test

The deuterium test is largely analogous to the so-called lithium test. In turn, deuterium is burned in stellar interiors in the reaction ${}^2\text{D}(p, \gamma) {}^3\text{He}$ at lower temperatures ($T > 8 \times 10^5$ K) than Li. This means that the temperatures in the interiors of substellar objects with $M < 13M_J$ are insufficient for deuterium burning. Their deuterium abundances have remained unchanged since their formation (Saumon et al. [94], Burrows et al. [11]). This fact makes it possible to define planets as objects with no deuterium burning (or lithium burning) in their interiors. Deuterium burns inside brown dwarfs, observation of the deuterium or deteriorated species in atmospheres of ultracool dwarf can be used as evidence of planetary masses. The deuterium test was suggested bt Bejar et al. [7] to isolate planets among low-mass objects. In practice, it was proposed to search for absorption lines of molecules containing deuterium (HDO, CrD, FeD, etc.) in the spectra of low-mass objects. The discovery of such objects in the solar neighborhood (see Zapatero Osorio et al. [111]) increased interest in the idea of using these deuterium-containing molecules for the classification of extremely cool objects. It is not possible to observe lines of the deuterium atom itself (in absorption or emission, blended with the hydrogen $L\alpha$ lines) due to the very nature of substellar objects: their photospheres are immersed in "coats" of cool matter that effectively absorbs ultraviolet radiation. On the other hand, deuterium emission lines should arise at significant distances from these objects, where the matter may be enriched

in deuterium from the interstellar medium. In principle, the deuterium test can also be used to investigate other problems. For instance, the position of the line separating objects that still contain deuterium from those whose deuterium has all been burned can be used to determine the ages of open clusters within several million years.

Furthermore, in objects of higher masses, such as stars, deuterium burning is completed comparatively quickly ($t \sim 1\text{--}3$ million years, see D’Antona & Mazzitelly [19]) during the evolution prior to the star’s period on the main sequence. The deuterium depletion rate depends on the mass of the star or brown dwarf.

On early stages of evolution, the luminosity of low-mass objects exhibits a strong time dependence (D’Antona & Mazzitelly [19]). Thus, the deuterium test can be used in connection with at least three problems: a) identifying planets in samples of low-mass objects (naturally, this is possible only for very nearby objects with $T_{\text{eff}} < 1000$ K); b) clarifying the evolutionary status of young objects in open clusters with ages of several million years; c) studying evolutionary changes of the deuterium abundances in low-mass substellar objects (such investigations can usefully be combined with the “lithium test”).

However, the practical realization of the deuterium test seems to be much more complex than for the “lithium test”. The main reason is the low deuterium abundance in atmospheres in the interstellar medium ($D/H = 2 \cdot 10^{-5}$).

Pavlenko [80] investigated the applicability of the “deuterium test” for the classification of low-mass objects in our Galaxy. To compute spectra of deuterated water HDO line lists from AMES database were used. The AMES database contains data on HDO transition systems derived under the same assumptions as for H_2O . However, the number of HDO levels taken into account was lower than the number of H_2O levels. By the way, this circumstance affects the computed sums over states of the HDO molecule. In general, HDO spectrum is much less studied in comparison with H_2O due to the one simple reason. Namely, molecule HDO is non-symmetrical at all, it means that here more types of transitions can be realised. The positions of the HDO lines show poorer agreement even with the HITRAN values: the rms error of the transition energies corresponding to the HDO lines is 0.25 cm^{-1} (Partridge & Schwenke [67]).

Nevertheless, the simplest case would be to propose the analysis of HDO/ H_2O spectra in the IR spectra of ultracool dwarfs. $H_2O + HDO$ spectrum was computed in wide range of wavelengths and showed that HDO lines are severely blended by H_2O lines (Fig. 6.14, see [80] for more details). To analyse the comparatively weak features created by the HDO absorption in spectra of ultracool dwarfs we should have very accurate line lists both H_2O and HDO. Observed intensities of HDO lines cannot exceed a few percent (see *ibid* and Chabrier [17]). Moreover, IR spectra of ultracool dwarfs contain lines of other

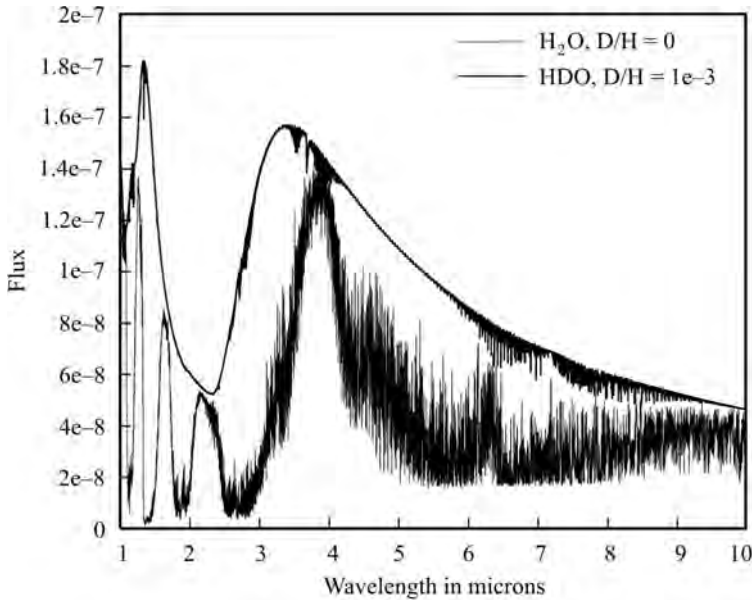


Fig. 6.14. Computed spectra of H_2O and HDO for different ratios D/H . Computations were carried for model atmosphere 1200/5.0 by Tsuji [106], AMES line lists, see [80] for more details

polyatomic species (CH_4 and others). These factors increase the demands for a capacity of observational facilities and the quality of theoretical data to identify and to carry the analysis of HDO lines in spectra of UC dwarfs. In fact the realisation of the “deuterium test” provides the real challenge for the observers and theoreticians.

Lines and bands of other deteriorated molecules can be used for a realisation of “deuterium test” Pavlenko et al. [85] discussed the problems of computations of molecules CrH , CrD , MgH , MgD in spectra of ultracool dwarfs. Namely, authors propose techniques and results of computations of the molecular band systems $A^6\Sigma^+ - X^6\Sigma^+$ of CrH , CrD , and the $A^2\Pi - X^2\Sigma^+$ band systems MgH , MgD in spectra of late-type dwarfs. Strong molecular bands of diatomic hydrides such as MgH and CrH , can be observed in the optical spectrum of ultracool dwarf stars. The MgH band system $A^2\Pi - X^2\Sigma^+$ can be observed at 4700–6000 Å, and the CrH band system $A^6\Sigma^+ - X^6\Sigma^+$ show strong absorption features at 6000–15000 Å. The computations of the synthetic spectra and spectral energy distributions in the optical and infrared (0.3–1.7 μm) were carried out assuming LTE, for the grids of M- and L-dwarf model atmospheres of $T_{\text{eff}} = 1800$ and 1200 K, taking into account molecular absorption of CrH , CrD , MgH and MgD at the background of K I and Na I resonance line wings. Pavlenko et al. [85] discussed the use of CrD and MgD electron bands formed in the optical and near infrared spectra of

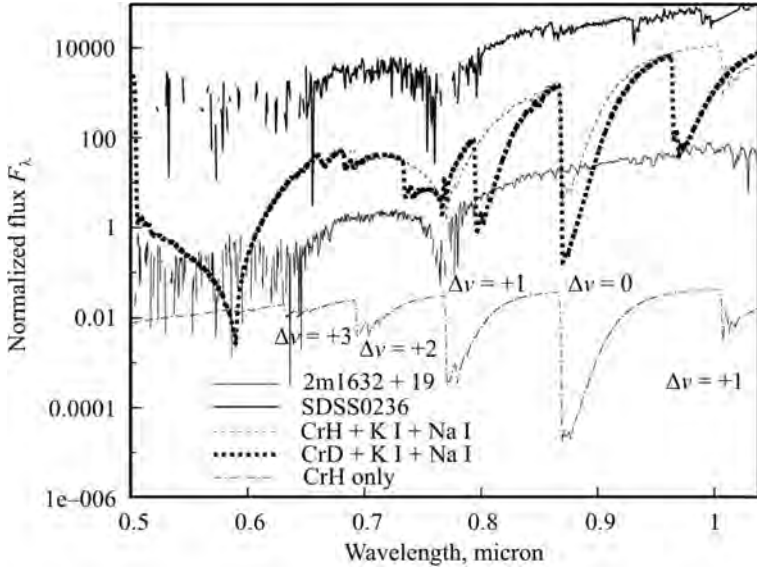


Fig. 6.15. Molecular bands of $A^6\Sigma^+ - X^6\Sigma^+$ system of CrH and CrD in theoretical spectrum computed with $D/H = 1$ for 1800/5.0/0 COND model atmosphere. For a comparison the observed spectra of two L-dwarfs 2MASS 1632 + 19 [58] and SDSS0236 [51] are shown by solid lines

ultracool dwarfs for a realisation of the “deuterium test” recently proposed for the identification of substellar-mass objects and large planets and to refine scenarios for the evolution of young stars and substellar objects. They claim that more realistic would be search of CrD molecular lines. Indeed, the band heads of this molecule is located far enough from the band heads of CrH (Fig. 6.15). Bands of CrH are observed in the spectra of the latest L dwarfs. Then, bands CrD are located in the near IR spectra, where fluxes are much higher, than in the blue or even green spectral regions.

Again, more efforts should be applied to compute the line lists of CrD and CrH of the high enough quality. Some problems of theoretical modelling of the spectrum of CrH are caused by the multiplicity of the terms of the molecule. Anyway, the problems here are less difficult with the case of polyatomic molecules, i.e. H_2O or CH_4 .

6.6. Conclusions

Estimates of brown dwarf number densities currently suggest the same order as for stars (~ 0.1 per pc^{-3}), therefore their contribution to the total mass should not exceed 15% [87]. Nonetheless, the large errors associated with age and mass determinations for brown dwarfs make such estimates very uncertain.

For the time being the general situation with a contribution of brown dwarfs to the dark/barionic matter in our Galaxy and the Universe is rather controversial. Definitely we know the populations of ultracool dwarfs only in the close vicinity to the Sun. Our studies are still rather phenomenological, because we know very little about abundances and basic parameters of low mass dwarfs. We can mention at least two non-solved problems of cosmological importance:

- Discovery of free-floating dwarfs with large deficit of metals. These objects are unevolved from the time of their formation on the early epochs.
- Mass ditribution of ultracool dwarfs and their evolutionary changes are poorly known.

OK, as example of pessimistic view we can quote from Gates [25] who discussed some results a survey of where we stand on dark energy and dark matter studies on gravitational lensing by MACHO, i.e Massive Astrophysical Compact Halo Objects:

“The final paper of the MACHO collaboration, published in 2000, concluded that a Galactic halo consisting entirely of MACHOs was now ruled out, and estimated that about 20% of the Galactic halo was in the form of MACHOs. The EROS team preferred to present its results as an upper limit on the number of MACHOs in the halo, with no more than about 8% of the halo in MACHOs having masses of about one-tenth to one times the mass of the Sun. A combined analysis of the two experiments showed that, within the uncertainties of each experiment, they are consistent with each other and that less than 20% of the halo is in the form of MACHOs”.

... and:

“MACHOs, the least exotic candidates for dark matter, have now been effectively ruled out as the *main* component of the dark matter, leaving WIMPs (Weakly Interacting Massive Particles) to dominate the Galaxy... Nevertheless, there seems to be evidence for some MACHOs in the Galactic halo, even if not enough to be interesting from a dark matter point of view”.

On the other hand, ultracool dwarfs of spectral classes T and L could be more common than all the other classes combined, at least in disk of Galaxy. As we know, physical properties and history of disk and halo are very different. Taking into account the number of protoplanetary discs, clumps of gas in nebulae from which stars and solar systems are formed one may see that the number of low mass objects in the galaxy should be several orders of magnitude higher than was known recently. The first one to form will become a proto-star, which are very violent objects and will disrupt other proplyds in the vicinity, stripping them of their gas. The victim proplyds will then probably go on to become main sequence stars or brown dwarf stars of the L and T classes, but quite invisible to us. Since they live so long, these smaller stars will accumulate over time.

■

BIBLIOGRAPHY

1. E. Anders, N. Grevesse, Abundances of the elements — meteoritic and solar, *Geochim. Cosmochim. Acta* **53** (1989), 197–214.
2. J.R. Auman, Opacity of Hot Water Vapor, *Astron. J.* **14** (1966), 171–171.
3. I. Baraffe, G. Chabrier, F. Allard, P.H. Hauschildt, Evolutionary models for solar metallicity low-mass stars: mass-magnitude relationships and color-magnitude diagrams, *Astron. Astrophys.* **337** (1998), 403–412.
4. R.J. Barber, J. Tennyson, G.J. Harris, R.N. Tolchenov, A high-accuracy computed water line list, *Mon. Not. R. Astron. Soc.* **368** (2006), 1087–1094.
5. G. Basri, The discovery of brown dwarfs, *Scientific American* **282**, No. 4 (2000), 76–83.
6. G. Basri, S. Mohanty, F. Allard et al., An Effective Temperature Scale for Late-M and L Dwarfs, from Resonance Absorption Lines of Cs I and Rb I, *Astrophys. J.* **538** (2000), 363–385.
7. V.J.S. Bejar, M.R. Zapatero Osorio, and R. Rebolo, A Search for Very Low Mass Stars and Brown Dwarfs in the Young Sigma Orionis Cluster, *Astrophys. J.* **521** (1999), 671–681.
8. W.J. Borucki, D.G. Koch, G. Basri, N. Batalha, T.M. Brown et al., Characteristics of Planetary Candidates Observed by Kepler. II. Analysis of the First Four Months of Data, *Astrophys J.* **736** (2011), 19–22.
9. A. Burgasser, M.W. McElwain, J.D. Kirkpatrick et al., The 2MASS Wide-Field T Dwarf Search. III. Seven New T Dwarfs and Other Cool Dwarf Discoveries, *Astron. J.* **127** (2004), 2856–2870.
10. A. Burgasser, S. Witte, Chr. Helling et al., Optical and Near-Infrared Spectroscopy of the L Subdwarf SDSS J125637.13–022452.4, *Astrophys. J.* **697** (2009), 148–159.
11. A. Burrows, M. Marley, W.B. Hubbard et al., A Nongray Theory of Extrasolar Giant Planets and Brown Dwarfs, *Astrophys. J.* **491** (1997), 856–875.
12. A. Burrows, S.R. Ram, P. Bernath et al., New CrH Opacities for the Study of L and Brown Dwarf Atmospheres, *Astrophys. J.* **577** (2002), 986–998.
13. A. Burrows, M. Volobuyev, Calculations of the Far-Wing Line Profiles of Sodium and Potassium in the Atmospheres of Substellar-Mass Objects, *Astrophys. J.* **583** (2003), 985–995.

14. J.A. Caballero, V.J.S. Bejar, R. Rebolo, Variability of L Dwarfs in the Near Infrared, in E.L. Martín, ed., Proc. IAU211 Symp. Brown dwarfs, ASP, San Francisco (2003), 455–456.
15. B. Campbell, G.A.H. Walker, S. Yang, A search for substellar companions to solar-type stars, *Astrophys. J.* **331** (1988), 902–921.
16. M. Cappelletta, R.P. Saglia, J.L. Birkby et al., The first planet detected in the WTS: an inflated hot Jupiter in a 3.35 d orbit around a late F star, *Mon. Not. R. Astron. Soc.* **427** (2012), 1877–1890.
17. G. Chabrier, I. Baraffe, F. Allard, P. Hauschildt, Deuterium Burning in Substellar Objects, *Astrophys. J.* **542** (2000), L119–L122.
18. M.C. Cushing, J.D. Kirkpatrick, C.R. Gelino et al., The Discovery of Y Dwarfs using Data from the Wide-field Infrared Survey Explorer (WISE), *Astrophys. J.* **743** (2011), 50–66.
19. F. D’Antona and I. Mazzitelli, in *Brown Dwarfs and Extrasolar Planets*, edited by R. Rebolo, E. Martín, and M.R. Zapatero Osorio, *Astron. Soc. Pac. Conf. Ser.* **134** (1998), 442–445.
20. C.C. Dahn, H.C. Harris, F.J. Vrba et al., Astrometry and Photometry for Cool Dwarfs and Brown Dwarfs, *Astron. J.* **24** (2002), 1170–1189.
21. L.R. Doyle, J.A. Carter, D.C. Fabrycky et al., Kepler-16: A Transiting Circumbinary Planet, *Science* **333** (2011), 1602–1614.
22. M. Dulick, C.W. Bauschlincher, A. Burrows, Line Intensities and Molecular Opacities of the FeH $F^4\Delta_i - X^4\Delta_i$ Transition, *Astrophys. J.* **594** (2003), 651–663.
23. K.C. Freeman, On the Disks of Spiral and so Galaxies, *Astrophys. J.* **160** (1970), 811–830.
24. C.S. Frenk, C.M. Baugh, S. Cole, and C. Lacey, Numerical and Analytical Modelling of Galaxy Formation and Evolution, in *Dark and visible matter in Galaxies*, edited by M. Persic and P. Salucci, *Astron. Soc. Pac. Conf. Ser.* **117** (1997), 335–347.
25. E. Gates, *Einstein’s Telescope: The Hunt for Dark Matter and Dark Energy in the Universe* (W.W. Norton & Co, New York, 2009), 1.
26. C.R. Gelino, M.S. Marley, J.A. Holtzman et al., L Dwarf Variability: I-Band Observations, *Astroph. J.* **577** (2002), 433–446.
27. C.R. Gelino, D. Kirkpatrick, M.C. Cushing et al., WISE Brown Dwarf Binaries: The Discovery of a T5 + T5 and a T8.5 + T9 System, *Astron. J.* **142** (2011), 57–65.
28. B.K. Gibson, C. Flynn, White Dwarfs and Dark Matter, *Science* **292** (2001), 2211–2213.
29. D. Goorvitch, Infrared CO line for the X $^1\Sigma^+$ state, *Astrophys. J. Suppl. Ser.* **95** (1994), 535–552.
30. V. Hambaryan, A. Staude, A.D. Schwöpe, R.-D. Scholz, S. Kimeswenger, and R.E. Neuhaus, A new strongly X-ray flaring M9 dwarf in the solar neighborhood, *Astron. Astrophys.* **415** (2004), 265–272.
31. A.P. Hatzes, W.D. Cochran, M. Endl, B. McArthur, D.B. Paulson, B. Diane, G.A.H. Walker, B. Campbell, S. Yang, A Planetary Companion to γ Cephei A, *Astrophys. J.* **599** (2003), 1383–1394.

32. P.H. Hauschildt, F. Allard, E. Baron, The NextGen Model Atmosphere Grid for $3000 \leq T_{eff} \leq 10\,000$ K, *Astrophys. J.* **512** (1999), 377–385.
33. C. Hayashi, T. Nakano, Evolution of Stars of Small Masses in the Pre-Main-Sequence Stages, *Prog. Theor. Phys.* **30** (1963), 460–474.
34. J.S. Jenkins, Y.V. Pavlenko, O. Ivanyuk et al., Benchmark cool companions: ages and abundances for the PZ Telescopii system, *Mon. Not. R. Astron. Soc.* **420** (2012), 3587–3598.
35. J.S. Jenkins, H.R.A. Jones, M. Tuomi et al., A Hot Uranus Orbiting the Super Metal-rich Star HD 77338 and the Metallicity-Mass Connection, *Mon. Not. R. Astron. Soc.* **766** (2013), 67–80.
36. H.R.A. Jones, T. Tsuji, Spectral Evidence for Dust in Late-Type M Dwarfs, *Astrophys. J.* **480** (1997), L39–L41.
37. H.R.A. Jones, Ya. Pavlenko, S. Viti, J. Tennyson, *Mon. Not. R. Astron. Soc.* **330** (2002), 675–684.
38. H.R.A. Jones, Ya.V. Pavlenko, S. Viti, R.J. Barber, La.A. Yakovina, D. Pinfield, J. Tennyson, Carbon monoxide in low-mass dwarf stars, *Mon. Not. R. Astron. Soc.* **358** (2005), 105–112.
39. U.G. Jorgensen, Molecular opacity data for stellar atmospheres, *Rev. Mex. Astron. Astrofis.* **23** (1992), 49–62.
40. J.D. Kirkpatrick, T.J. Henry, J. Liebert, The unique spectrum of the brown dwarf candidate GD 165B and comparison to the spectra of other low-luminosity objects, *Astrophys. J.* **406** (1993), 701–707.
41. J.D. Kirkpatrick, I.N. Reid, J. Liebert et al., Dwarfs Cooler than “M”: The Definition of Spectral Type “L” Using Discoveries from the 2 Micron All-Sky Survey (2MASS), *Astrophys. J.* **519** (1999), 802.
42. J.D. Kirkpatrick, D.L. Looper, D.J. Burgasser et al., Discoveries from a Near-infrared Proper Motion Survey Using Multi-epoch Two Micron All-Sky Survey Data, *Astrophys. J. Suppl. Ser.* **190** (2010), 100–146.
43. C. Koen, N. Matsunaga, J. Menzies, A search for short time-scale JHK variability in ultracool dwarfs, *Mon. Not. R. Astron. Soc.* **354** (2004), 466–476.
44. J. Koppenhoefer, R.P. Saglia, L.Fossati et al., A hot Jupiter transiting a mid-K dwarf found in the pre-OmegaCam Transit Survey, *Mon. Not. R. Astron. Soc.* **435** (2014), 3133–3147.
45. S.S. Kumar, The Structure of Stars of Very Low Mass, *Astrophys. J.* **137** (1963), 1121–1125.
46. S.S. Kumar, The Helmholtz-Kelvin Time Scale for Stars of Very Low Mass, *Astrophys. J.* **137** (1963a), 1126–1128.
47. F. Kupka, N. Piskunov, T.A. Ryabchikova, H.C. Stempels, W.W. Weiss, VALD-2: Progress of the Vienna Atomic Line Data Base, *Astron. Astrophys. Suppl. Ser.* **138** (1999), 119–133.
48. R.L. Kurucz, Atlas: a Computer Program for Calculating Model Stellar Atmospheres, *SAO Spec. Rept.* **309** (1970), 1–291
49. R.L. Kurucz, CDROMs 1-22, Harvard-Smithsonian Observatory (1993), 1.
50. A.T. Lawton, P. Wright, A planetary system for Gamma Cephei?, *Journ. of the British Interplanetary Soc.* **42** (1989), 335–336.
51. S.K. Leggett, F. Allard, T.R. Geballe, P.H. Hauschildt, A. Schweitzer, Infrared Spectra and Spectral Energy Distributions of Late M and L Dwarfs, *Astrophys. J.* **548** (2001), 908–918.

52. J.J. Lissauer, How common are habitable planets?, *Nature* **398** (1999), 659–662.
53. M.C. Liu, S.K. Leggett, Kelu-1 Is a Binary L Dwarf: First Brown Dwarf Science from Laser Guide Star Adaptive Optics, *Astrophys. J.* **634** (2005), 616–624.
54. N. Lodieu, D.J. Pinfield, S.K. Leggett et al., Eight new T4.5–T7.5 dwarfs discovered in the UKIDSS Large Area Survey Data Release 1, *Mon. Not. R. Astron. Soc.* **379** (2007), 1434–1430.
55. W.J. Luyten, C.T. Kowal, Proper motion Survey with 48 inch Schmidt telescope. XLIII. One hundred and six Faint Stars with Large Proper Motion, University of Minnesota, Minneapolis **43** (1975), 1–2.
56. K.L. Luhman, Young Low-Mass Stars and Brown Dwarfs in IC 348, *Astrophys. J.* **525** (1999), 466–465.
57. E.L. Martín, R. Rebolo, M.R. Zapatero-Osorio, Spectroscopy of New Substellar Candidates in the Pleiades: Toward a Spectral Sequence for Young Brown Dwarfs, *Astrophys. J.* **469** (1996), 706–714.
58. E.L. Martín, X. Delfosse, G. Basri, B. Goldman, Th. Forveille, M.R. Zapatero Osorio, Spectroscopic Classification of Late-M and L Field Dwarfs, *Astron. J.* **118** (1999), 2466–2482.
59. E.L. Martín, M.R. Zapatero Osorio, and H. Lehto, Photometric Variability in the Ultracool Dwarf BRI 0021–0214: Possible Evidence for Dust Clouds, *Astrophys. J.* **557** (2001), 822–830.
60. E.L. Martín, H. Bouy, XMM-Newton observations of the nearby brown dwarf LP 944-20, *New Astronomy* **7** (2002), 595–602.
61. M. Mayor, D. Queloz, A Jupiter-mass companion to a solar-type star, *Nature* **378** (1995), 355–359.
62. D. Michalas, *Stellar Atmospheres* (Freeman, San Francisco, 1980).
63. T. Nakajima, B.R. Oppenheimer, S.R. Kulkarni, D.A., Golimowski, K. Matthews, S.T. Durrance, Discovery of a cool brown dwarf, *Nature* **378** (1995), 463–465.
64. B.R. Oppenheimer, N.C. Hambly, A.P. Digby, S.T. Hodgkin, D. Saumon, Direct Detection of Galactic Halo Dark Matter, *Science* **292** (2001), 698–702.
65. F. de Paolis, G. Ingrosso, Ph. Jetzer, and M. Roucadelli, MACHOs and molecular clouds in galactic halos, *Phys. Rev. Lett.* **74** (1995), 14–18.
66. D.J. Pinfield, B. Burningham, M. Tamura et al., Fifteen new T dwarfs discovered in the UKIDSS Large Area Survey, *Mon. Not. R. Astron. Soc.* **390** (2008), 304–322.
67. H. Partridge and D. Schwenke, The determination of an accurate isotope-dependent potential energy surface for water from extensive ab initio calculations and experimental data, *J. Chem. Phys.* **106** (1997), 4618–4628.
68. D. Pfenniger, Galactic Dynamics and the Nature of Dark Matter, in *Dark and visible matter in Galaxies*, edited by M. Persic and P. Salucci, *Astron. Soc. Pac. Conf. Ser.* **117** (1997), 249–257.
69. Y.V. Pavlenko, R. Rebolo, E.L. Martín, and R.J. García López, Formation of lithium lines in very cool dwarfs, *Astron. Astrophys.* **303** (1995), 807–818.
70. Ya.V. Pavlenko, Analysis of the spectra of two Pleiades brown dwarfs: Teide 1 and Calar 3, *Astrophys. Space Sci.* **253** (1997), 43–53.
71. Y.V. Pavlenko, Lines in Late-Type M Dwarfs: Teide1, *Astron. Rept.* **41** (1997a), 537–542.

72. Ya.V. Pavlenko, Depletion of TiO and spectra of the coolest brown dwarfs, *Odessa Astron. Publ.* **10** (1997b), 76–77.
73. Ya.V. Pavlenko, Lithium lines in the spectra of late M-dwarfs: the effects of chromosphere-like structures, *Astron. Rept.* **42** (1998), 501–507.
74. Ya.V. Pavlenko, The “lithium test” and the Spectra of Late M Dwarfs and Brown Dwarfs: Condensation Effects, *Atron. Rept.* **42** (1998b), 787–792.
75. Y. Pavlenko, M.R. Zapatero Osorio, R. Rebolo, On the interpretation of the optical spectra of L-type dwarfs, *Astron. Astrophys.* **355** (2000), 245–255.
76. Ya.V. Pavlenko, Lithium Lines in the Spectra of M Dwarfs: UX Tau C, *Astron. Rept.* **44** (2000), 219–226.
77. Ya.V. Pavlenko, Modeling the Spectral Energy Distributions of L Dwarfs, *Astron. Rept.* **45** (2001b), 144–156.
78. Ya.V. Pavlenko, Formation of the optical spectra of L dwarfs, in *Ultracool dwarfs*, edited by H.R.A. Jones, I.A. Steele (Springer, 2001a), 33–49.
79. Ya.V. Pavlenko, H.R.J. Jones, Carbon Monoxide bands in M dwarfs, *Astron. Astrophys.* **397** (2002), 967–975.
80. Ya.V. Pavlenko, H₂O and HDO bands in the spectra of late-type dwarfs, *Astron. Rept.* **46** (2002), 567–578.
81. Ya.V. Pavlenko, Ultracool dwarfs, in *Proceedings of MAO2004, 2005, astro-ph 0506263*, 1.
82. Ya.V. Pavlenko, H.R.A. Jones, Yu. Lyubchik, J. Tennyson, *Astron. Astrophys.* **447** (2006), 709–717.
83. Ya.V. Pavlenko, H.R.A. Jones, E.L. Martín, E. Guenther, M.A. Kenworthy, M.R. Zapatero Osorio, Lithium in LP 944-20, *Mon. Not. R. Astron. Soc.* **380** (2007), 1285–1296.
84. Ya.V. Pavlenko, S.V. Zhukovskaya, M. Volobuev, Resonance potassium and sodium lines in the spectra of ultracool dwarfs, *Astron. Rept.* **51** (2007a), 282–290.
85. Ya.V. Pavlenko, G.J. Harris, J. Tennyson, H.R.A. Jones, J.M. Brown, C. Hill, L.A. Yakovina, The electronic bands of CrD, CrH, MgD and MgH: application to the ‘deuterium test’, *Mon. Not. R. Astron. Soc.* **386** (2008), 1338–1346.
86. B. Plez, A new TiO line list, *Astron. Astrophys.* **337** (1998), 495–500.
87. I.N. Reid, M Dwarfs, L Dwarfs, T Dwarfs and Subdwarfs: $\Phi(M)$ at and below the Hydrogen-Burning Limit, in *Proceedings of Star Formation*, held in Nagoya, Japan, June 21–25, 1999, edited by T. Nakamoto, Nobeyama Radio Observatory, 327–322
88. R. Rebolo, E.L. Martín, and A. Magazzu, Spectroscopy of a brown dwarf candidate in the Alpha Persei open cluster, *Astrophys. J.* **389** (1992), L83–L86.
89. R. Rebolo, M.R. Zapatero-Osorio, E.L. Martín, Discovery of a brown dwarf in the Pleiades star cluster, *Nature* **377** (1995), 129–131.
90. R. Rebolo, E.L. Martín, G. Basri et al., Brown Dwarfs in the Pleiades Cluster Confirmed by the Lithium Test, *Astrophys. J.* **469** (1996), L53–L56.
91. L.S. Rothman, C.P. Rinsland, A. Goldman et al., The HITRAN Molecular Spectroscopic Database and HAWKS (HITRAN Atmospheric Workstation): 1996 Edition, *J. Quant. Spectrosc. Radiat. Transfer* **60** (1998), 665–710.
92. M.T. Ruiz, S.K. Leggett, and F. Allard, Kelu-1: A Free-floating Brown Dwarf in the Solar Neighborhood, *Astrophys. J.* **491** (1997), L107–L110.

93. R.E. Rutledge, G. Basri, E.L. Martín, L. Bildsten, Chandra Detection of an X-Ray Flare from the Brown Dwarf LP 944-20, *Astrophys. J.* **538** (2000), L141–L144.
94. D. Saumon, W.B. Hubbard, A. Burrows et al., A Theory of Extrasolar Giant Planets, *Astrophys. J.* **460** (1996), 993.
95. M.W. Schmidt, M.S. Gordon, The Construction and Interpretation of MCSCF wavefunctions, *Ann. Rev. Phys. Chem.* **49** (1998), 233–266.
96. D. Schwenke, Opacity of TiO from a coupled electronic state calculation parametrized by AB initio and experimental data, *Faraday Discuss.* **109** (1998), 321–334.
97. B. Stelzer, X-ray emission probing the limiting cases of stellar dynamos, *Mem. S. A. It.* **76** (2005), 410–415.
98. J. Tennyson, G.J. Harris, R.J. Barber, S. La Delfa, B.A. Voronin, B.M. Kaminsky, Ya.V. Pavlenko, Molecular line lists for modelling the opacity of cool stars, *Mol. Pharm. J.* **105** (2007), 701–714.
99. C.G. Tinney, The intermediate-age brown dwarf LP 944-20, *Mon. Not. R. Astron. Soc.* **296** (1998), L42–L44.
100. C.G. Tinney, I.N. Reid, High-resolution spectra of very low-mass stars, *Mon. Not. R. Astron. Soc.* **301** (1998a), 1031–1048.
101. C.G. Tinney, A.J. Tolley, Searching for weather in brown dwarfs, *Mon. Not. R. Astron. Soc.* **304** (1999), 119–126.
102. R.N. Thomas, The Source Function in a Non-Equilibrium Atmosphere. I. The Resonance Lines, *Astrophys. J.* **125** (1957), 260–274.
103. V. Trimble, *Ann. Rev. Astron. Astrophys.* **25** (1987), 425–472.
104. T. Tsuji, Molecular abundances in stellar atmospheres. II. *Astron. Astrophys.* **23** (1973), 411–431.
105. T. Tsuji, K. Ohnaka, W. Aoki, T. Nakajima, *Astron. Astrophys.* **308** (1996), L29–L32.
106. T. Tsuji, Dust in Very Cool Dwarfs, in *Very Low-mass Stars and Brown Dwarfs*, edited by R. Rebolo and M.R. Zapatero-Osorio (The Cambridge University Press, 2000), 156–168.
107. A. Unsöld, *Physics der Sternatmosphären* (Springer, 1955), 1.
108. G.A.H. Walker, D.A. Bohlender, A.R. Walker, A.W. Irwin, Yang, L.S. Stephenson, A. Larson, γ Cephei — Rotation or planetary companion?, *Astrophys. J.* **396** (1992), L91–94.
109. A. Wolszczan, D.A. Frail, A planetary system around the millisecond pulsar PSR1257 + 12, *Nature* **355**, 6356 (1992), 145–147.
110. M.R. Zapatero Ozorio, R. Rebolo, E.L. Martín, New Brown Dwarfs in the Pleiades Cluster, *Astrophys. J.* **491** (1997), L81–L84.
111. M.R. Zapatero Ozorio, V.J.S. Bejar, R. Rebolo et al., Discovery of Young, Isolated Planetary Mass Objects in the σ Orionis Star Cluster, *Science* **290** (2000), 103–107.
112. M.R. Zapatero Osorio, V.J.S. Bejar, Ya. Pavlenko, R. Rebolo, C. Allende Prieto, E.L. Martín, R.J. Garcia Lopez, Lithium and H α in stars and brown dwarfs of sigma Orionis, *Astron. Astrophys.* **384** (2002b), 937–953.
113. M.R. Zapatero Osorio, B.L. Lane, Ya. Pavlenko, E.L. Martín, M. Britton, S.R. Kulkarni, Dynamical Masses of the Binary Brown Dwarf GJ 569 Bab, *Astrophys. J.* **615** (2004), 958–971.



ABOUT THE AUTHORS

Valery SHULGA (16.08.1944), Academician of National Acad. Sci. of Ukraine, Doctor of Science in physics and mathematics, Professor in astrophysics and radioastronomy. Vice-Director of the Institute of Radioastronomy, Nat. Acad. Sci. of Ukraine; Head of department. Research interests: astrophysics and radioastronomy (quantum radiophysics, radio-astronomy, low temperature physics, gravitational lensing).

Valery ZHDANOV (07.07.1950), Doctor of Science in physics and mathematics, Professor in astrophysics and radioastronomy. Head of the Astrophysics department of Astronomical observatory, Taras Shevchenko Nat. Univ. of Kyiv. Research interests: relativistic gravity and cosmology, relativistic dynamics (gravitational lensing, relativistic reference frames, relativistic hydrodynamics, equations of motion).

Alexander ALEXANDROV (11.07.1944), Candidate of Science in Physics and Mathematics, Senior Researcher of the Astrophysics department of Astronomical observatory, Taras Shevchenko Nat. Univ. of Kyiv. Research interests: relativistic gravitation, relativistic dynamics (gravitational lensing, dynamics of test bodies, relativistic reference frames).

Peter BERCZIK (16.09.1964) Doctor of Science in Physics and Mathematics, Vice-Director of Main Astronomical Observatory, Nat. Acad. Sci. of Ukraine, Head of the Astro-Space Information and Computing Centre. Research interests: Galactic and extragalactic astrophysics (Formation and evolution of galactic and sub-galactic structures. Star cluster evolution in galactic disk. Single and Binary Black Hole dynamics. N-body/Smoothed Particle Hydrodynamics. Chemo-Dynamical simulations. High Performance Computing).

Elena PAVLENKO (08.01.1951), Doctor of Science in Physics and Mathematics, Leading Researcher of Crimean Astrophysical Observatory. Research interests: astrophysics (double stars, cataclysmic variables).

Yakiv PAVLENKO (24.01.1954) Doctor of Science in Physics and Mathematics, Chief Research Fellow of Main Astronomical Observatory, Nat. Acad. Sci. of Ukraine. Research interests: astrophysics (brown dwarfs, ultra cool dwarfs, evolved stars, temporal changes of abundances).

Leonid PILYUGIN (25.04.1955), Doctor of Science in Physics and Mathematics, Professor in astrophysics and radioastronomy. Head of the Laboratory for physics of galaxies with active star formation of Main Astronomical Observatory, Nat. Acad. Sci. of Ukraine. Research interests: extragalactic astronomy (chemical evolution of galaxies, diagnostics of the physical conditions and element abundances in extragalactic HII regions).

Victoria TSVETKOVA (28.03.1939), Candidate of Science in Physics and Mathematics, Senior Researcher of the Institute of Radio Astronomy, Nat. Acad. Sci. of Ukraine. Research interests: astrophysics and cosmology, gravitational lensing, image processing.

Монографія є другим томом тритомного видання під загальною назвою “Темна енергія і темна матерія у Всесвіті”. Основну увагу приділено астрофізичним аспектам проблеми невидимої маси і темної матерії, включно з проблемами гравітаційного лінзування, дослідження розподілів маси та елементів у Всесвіті, фізики компактних зірок та моделями галактичної еволюції. Монографія призначена для науковців-фахівців, викладачів та студентів магістратури, що спеціалізуються в галузі позагалактичної астрономії, космології та загальної теорії відносності.

Наукове видання

НАЦІОНАЛЬНА АКАДЕМІЯ НАУК УКРАЇНИ

РАДІОАСТРОНОМІЧНИЙ ІНСТИТУТ

ГОЛОВНА АСТРОНОМІЧНА ОБСЕРВАТОРІЯ

КИЇВСЬКИЙ НАЦІОНАЛЬНИЙ УНІВЕРСИТЕТ імені ТАРАСА ШЕВЧЕНКА

ХАРКІВСЬКИЙ НАЦІОНАЛЬНИЙ УНІВЕРСИТЕТ імені В.Н.КАРАЗІНА

ТЕМНА ЕНЕРГІЯ І ТЕМНА МАТЕРІЯ У ВСЕСВІТІ

За редакцією академіка НАН України В. ШУЛЬГИ

У ТРЬОХ ТОМАХ

ШУЛЬГА Валерій, ЖДАНОВ Валерій, АЛЕКСАНДРОВ Олександр,
БЕРЦИК Петер, ПАВЛЕНКО Олена, ПАВЛЕНКО Яків,
ПЛЮГІН Леонід, ЦВЕТКОВА Вікторія

ТЕМНА МАТЕРІЯ: АСТРОФІЗИЧНІ АСПЕКТИ ПРОБЛЕМИ

ТОМ 2

Англійською мовою

Літературний редактор *О. Сергієнко*
Художнє оформлення *Є. Ільницького*

Технічний редактор *О. Бурдік*
Комп'ютерна верстка *Л. Шмагайло*

Підп. до друку 02.07.2014. Формат 70×100/16. Папір офс.

Гарн. Computer Modern. Друк офс. Ум. друк. арк. 28,93. Обл.-вид. арк. 30,62.

Тираж 300 прим. Зам. 3947.

Видавець і виготовлювач Видавничий дім “Академперіодика” НАН України
01004, Київ-4, вул. Терещенківська, 4

Свідоцтво суб'єкта видавничої справи ДК № 544 від 27.07.2001 р.